

ENG 371-(EQC 2008/U575)

**An experimental study on geosynthetic reinforced soil walls  
under seismic loading**

*Perry Jackson, supervised by Elisabeth Bowman and Misko  
Cubrinovski, University of Canterbury*

# Progressive failure and shear band development within model-scale reinforced soil walls subject to seismic shaking

E. T. BOWMAN\*, P. JACKSON†, M. CUBRINOVSKI\* and R. J. FANNIN‡

This paper discusses the results of an experimental study on model geosynthetic-reinforced soil (GRS) walls constructed with full-height rigid (FHR) facing. Ground accelerations, external deformations and localised strain fields were tracked, while stepped-amplitude sinusoidal seismic shaking events were applied via a shake table. The results of one of seven shake table tests are presented here, with a focus on the evolution of the pre-failure deformation of the wall at the end of the reinforced zone. This study shows that the deformation of ductile GRS walls with FHR facing subjected to seismic shaking is a progressive process of shear band development with depth as the wall rotates and, ultimately, translates towards failure.

doi: 10.1680/geolett.11.00030

**KEYWORDS:** earthquakes; failure; model tests; reinforced soils; retaining wall; strain localisation

ICE Publishing: all rights reserved

## INTRODUCTION

Geosynthetic-reinforced soil (GRS) walls constructed in seismic areas have been found to perform well during earthquakes, behaving in a ductile manner rather than failing catastrophically (Ling *et al.*, 2001). For the purposes of design, a distinction is made between collapse at the ultimate limit state (ULS) and tolerable deformation at the serviceability limit state (SLS). Although considerable progress has been made on design guidance for the former, the nature of the progressive failure mechanisms that govern the latter are not well reported. Moreover, GRS walls may be subject to a series of seismic episodes during their lifetimes that do not necessarily cause wholesale failure but result in progressive deformation. It is therefore important to understand how such deformation may be manifested within and proximate to the reinforced soil mass, in terms of localised strain.

This paper discusses the results of an experimental study on GRS walls constructed with full-height rigid (FHR) facing conducted at the University of Canterbury. In the tests, ground accelerations, external deformations and localised strain fields were tracked while stepped-amplitude sinusoidal seismic shaking events were applied via a shake table. The results of one of seven shake table tests are presented here with a focus on the evolution of the pre-failure deformation of the wall at the end of the reinforced zone via progressive shear band formation. Further details and results of the testing programme may be found in the literature (Jackson, 2010).

## MODEL CONSTRUCTION AND TEST PROCEDURE

The tests were conducted in a rigid box (3.0 m long, 0.8 m wide, 1.1 m high) with a transparent glass window on one

side and a base that was roughened with glued sand. A model-to-prototype scale of 1 : 5 was chosen, with a model wall height of 900 mm thus corresponding to a prototype wall height of 4.5 m. Similar experimental configurations have been used in previous works (Matsuo *et al.*, 1998; Watanabe *et al.*, 2003; El-Emam & Bathurst, 2007). The box was mounted onto a 4.0 m long by 2.0 m wide shake table for the application of sinusoidal shaking.

Similitude rules as developed by Iai (1989) were considered in order to appropriately scale the soil, the reinforcement and the GRS wall design. While these yielded realistic model and excitation characteristics in relation to the prototype, the limitations of scaled-down 1 *g* models in quantifying the stress-dependent soil response and its effects on the soil-reinforcement interaction restricted a direct comparison with the prototype structure. This paper thus only discusses behaviour relating to the specific physical model test conditions.

The model soil, Albany sand, had a mean particle size  $D_{50}$  of 0.3 mm, maximum and minimum void ratios  $e_{max}$  and  $e_{min}$  of 0.83 and 0.51, respectively, and a critical state friction angle  $\phi'_{crit}$  of 31°. The model reinforcement was Stratagrid Microgrid with an axial stiffness  $J_{2\%}$  of 220 kN/m, resulting in an equivalent stiffness of 5500 kN/m (Iai, 1989); this corresponds to 'inextensible' reinforcement at the prototype scale.

The wall face was an FHR aluminium panel (5 mm thick, 795 mm wide, 960 mm long) that was fitted with a low-friction seal against the sidewalls and was free to move at the base. The reinforcement, placed at a vertical spacing of 150 mm, was rigidly connected to the face, but was flexible enough that no moment connection would be developed at the connection. For the test described here, the constructed wall of height 900 mm was inclined at an angle of 70° to the horizontal and the reinforcement length was 675 mm, yielding a length to wall height ratio  $L/H$  of 0.75. Figure 1 shows the general arrangement of the model wall.

The instrumentation scheme consisted of six accelerometers to record the model and dynamic soil response, six linear variable differential transformers (LVDTs) to record wall face displacement and two high-speed cameras to

Manuscript received 10 May 2011; first decision 30 June 2011; accepted 12 July 2011.

Published online 12 August 2011.

\*Department of Civil and Natural Resources Engineering, University of Canterbury, Christchurch, New Zealand

†Arup, Melbourne, Victoria, Australia

‡Civil and Mechanical Engineering Building, University of British Columbia, Vancouver, Canada

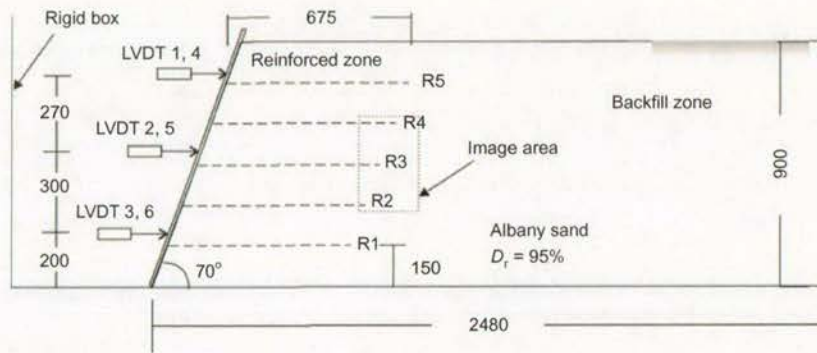


Fig. 1. General arrangement of the model (dimensions in millimetres)

record deformation within two selected areas (one within the reinforced soil zone and one at the end of the reinforced zone). During testing, images were taken at a frame rate of 200 frames/s and an exposure time of 5 ms; this was to enable within-cycle deformation to be tracked for further analysis (not shown here). Only the results of the wall displacement and images from the camera placed at the end of the reinforcement are discussed here; further details can be found in Jackson (2010).

The sand was placed to a relative density  $D_r$  of 95% using a weighted-vibration method. Horizontal and vertical marker lines of black sand were incorporated at the window to enable final deformation patterns to be visible after each test (Fig. 2). Grid reinforcement was placed after every second compaction layer and instrumentation was embedded as the model wall was constructed.

Multi-stage tests were performed: model excitation consisted of a sinusoidal motion at frequency 5 Hz for duration 10 s (i.e. 50 cycles of uniform amplitude), commencing at 0.1 g (0.2 g peak-to-peak (Fig. 3)), with an increase in amplitude of 0.1 g between stages until the test was stopped. Tests were stopped when the wall slid or rotated to produce at least 100 mm displacement at the top of the wall. A rest period of approximately 15 min between each stage enabled data to be downloaded and additional measurements and photos to be taken.

#### LOCAL STRAIN ANALYSIS USING PARTICLE IMAGE VELOCIMETRY

GeoPIV software enables particle image velocimetry (PIV) (also known as digital image correlation) on soil bodies for the tracking of displacement fields (White *et al.*, 2003) by following the movement of 'patches' of soil in sequential images. This paper discusses the results from one camera (resolution 1280 × 1024 pixels) and progressive deformation at the embedded ends of the reinforcement (Fig. 1).

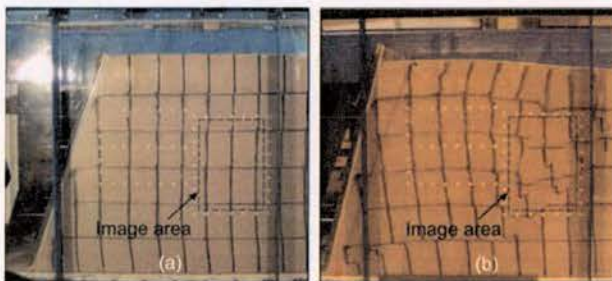


Fig. 2. Close-up of reinforced zone: (a) end-of-construction, with region of image capture as shown; (b) end of test, after 0.7 g horizontal shaking.

Images taken before and after each stage of testing were analysed using GeoPIV software and photogrammetry to obtain displacement and strain fields generated by the increment of shaking.

For the GeoPIV analysis reported here, 32 pixel patches were used that overlapped at 8 pixel intervals (equating to a measurement point spacing of ~0.6 mm or  $2D_{50}$  for the chosen field of view). The resulting precision is approximately 0.019 pixels (1/67400th of the field of view or  $\approx 5 \mu\text{m}$ ) (see White *et al.* (2003)). Overlapping the patches ensured that interfaces between the reinforcement and soil, where large differences in displacement may develop, would be accurately reflected in the strain field produced and that developing shear bands could be resolved in sufficient detail.

#### RESULTS

The cumulative displacement at the top of the wall facing at the end of each shaking stage through to failure at 0.7 g is shown in Fig. 4, with rotational and sliding components as indicated. It is notable that the wall generally rotates with each increment of shaking before finally sliding in the last stage – this behaviour is clearly a function of the toe fixity, which is purely frictional in this case. El-Emam & Bathurst (2007) define the critical acceleration, whereupon failure is deemed to occur (Matsuo *et al.*, 1998), as the acceleration at which a sharp increase in incremental displacement takes place. Referring to Fig. 4, this may be taken as 0.5 g or 0.6 g according to this criterion.

Figures 5 to 9 show strain field plots at the position of the camera as defined horizontally rightwards ( $X$ ) and vertically upwards ( $Y$ ) from the toe of the wall. Figure 5 shows, on a plot of cumulative shear strain  $\epsilon_s$ , the progressive development of shear at increasing levels of shaking from 0.1 g to 0.6 g (strains developed at 0.7 g were too large to resolve with GeoPIV and may be viewed in Fig. 2(b)). In total, four fully developed shear bands (labelled sequentially S1–S4) are visible. The depth of development increased with wall rotation (see Fig. 2), and the ends of reinforcement layers R2 to R4 are coincident with kinks in the bands of shear strain.

Figure 6 shows the companion development of incremental shear strain  $\Delta\epsilon_s$  between incremental test stages. This suggests that the exact positions of the failure surfaces vary as the amplitude of shaking increases. Figure 7 shows the corresponding incremental volumetric strain  $\Delta\epsilon_{vol}$  between each shaking stage. Zones of contraction and dilation are seen to develop near-alternately, with contraction appearing as a relatively more diffuse process, in contrast to dilation that tends to occur in thinner bands (refer to Fig. 6).

To examine the response more closely, the development of  $\Delta\epsilon_s$  and  $\Delta\epsilon_{vol}$  in shear band S2 is illustrated in Figs 8 and

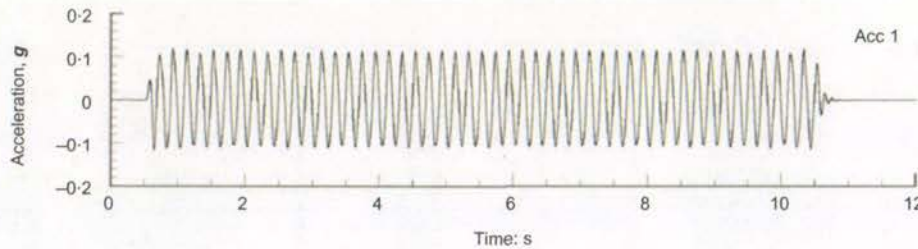


Fig. 3. Acceleration-time history at 0.1 g, for accelerometer Acc 1 placed on the shake table base

9, respectively. Figures 8(b) and 9(b) reveal that, prior to a shear surface fully developing, the soil contracts and dilates in adjacent zones and it is not clear where the shear band will eventually develop: contraction of up to 2% occurs within these zones over an accumulated shear strain of approximately 2.5%. With increased shaking (from 0.2 g to 0.3 g), dilation of up to -4.5% occurs over approximately 8–12% shear strain (cumulatively -2.5% volumetric strain over 10–15% shear strain). Thereafter, shearing continues at constant volume (Figs 8(c) and 9(c)), as evinced by alternating zones of contraction and dilation along the shear band.

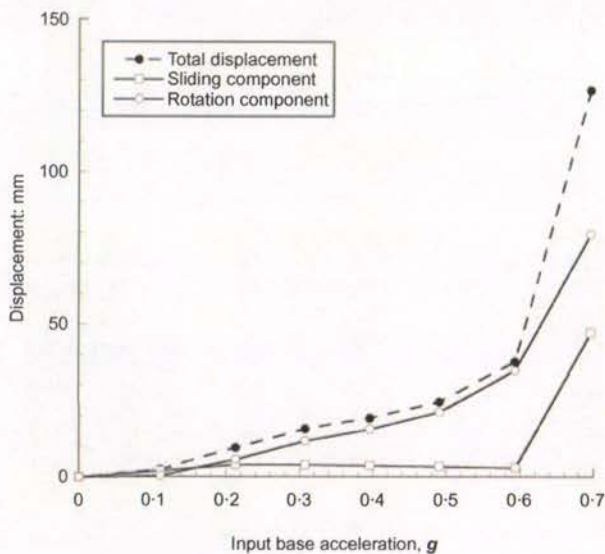


Fig. 4. Permanent (irrecoverable) displacement of wall face at the end of each stage of seismic shaking. Sliding (translational) and rotational components determined from LVDT measurements

For shaking at 0.2 g, shear band S2 has a width of 9–12 mm, or a normalised thickness of 30–40D<sub>50</sub>. At this stage, the shear band is still developing and the soil is not yet mobilising peak friction. At 0.3 g, the shear band thickness reduces to 4–6 mm (13–20D<sub>50</sub>) and finally to 3–5 mm at 0.6 g (10–17D<sub>50</sub>). The final values are typical of those reported for fine to medium sands (Yoshida & Tatsuoka, 1997; Rechenmacher & Finno, 2004).

It is interesting to examine the forking shear band evident in Figs 8(b)–(f) and 9(b)–(f). Shear strain accumulates in both the upper and lower branches of the fork by the end of the 0.2 g stage, with contraction evident in the upper branch and dilation in the lower; this is suggestive of a more developed shear surface along the lower branch. However, the failure surface is not fully formed and its progressive development is subject to kinematic constraints (Muir Wood, 2002). In work using biaxially loaded dense sand specimens, Rechenmacher (2006) also found ‘competition’ between two or more preliminary shear bands prior to peak strength development, with persistent shear band formation closely linked to post-peak strain softening towards the end of dilation. In the test reported here, further shaking causes the position of dominant shearing to shift between the two branches after constant volume shearing to the critical state. This is most evident in a comparison of Fig. 8(e), where, at 0.5 g, a fully strain-softened shear band has developed in the upper-right corner with a secondary shear band beginning to develop below this, with Fig. 8(f), where, at 0.6 g, all further shear strain accumulates on the lower shear band. By the end of the 0.6 g stage, the shear band has straightened out and trends to the ground surface at approximately 39° to the vertical, with some radiating planes of lesser shear strain evident at shallower angles (Fig. 6). Radiating lines of volumetric compression and dilation outside of major shear bands (Fig. 7(c)) are also reported from model footings in work by Lesniewska & Muir Wood (2009), suggesting early micro-straining of soil to be common in granular materials subject to complex loading conditions.

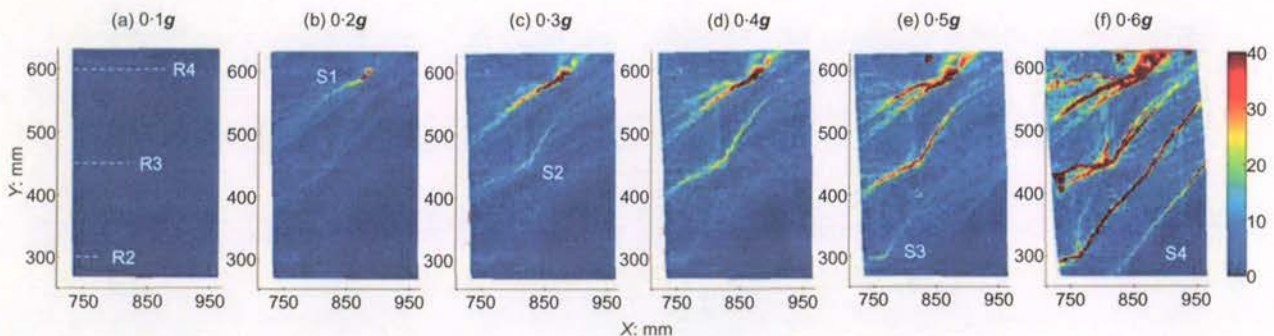


Fig. 5. Accumulated shear strain (%) from (a) 0.1 g to (f) 0.6 g. In (a) the positions of the reinforcement layers R2 to R4 are indicated. As they develop, shear bands S1 to S4 are as indicated

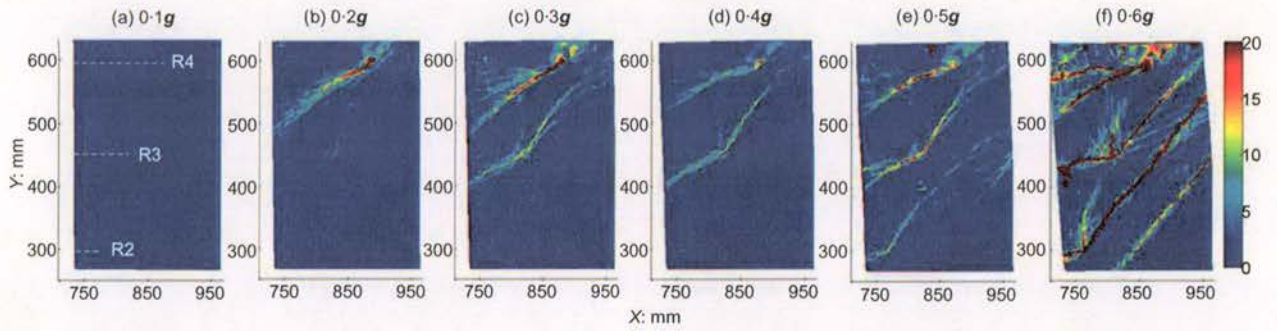


Fig. 6. Incremental shear strain (%) from (a) 0.1 *g* to (f) 0.6 *g*. The positions of the reinforcement layers R2 to R4 are indicated in (a)

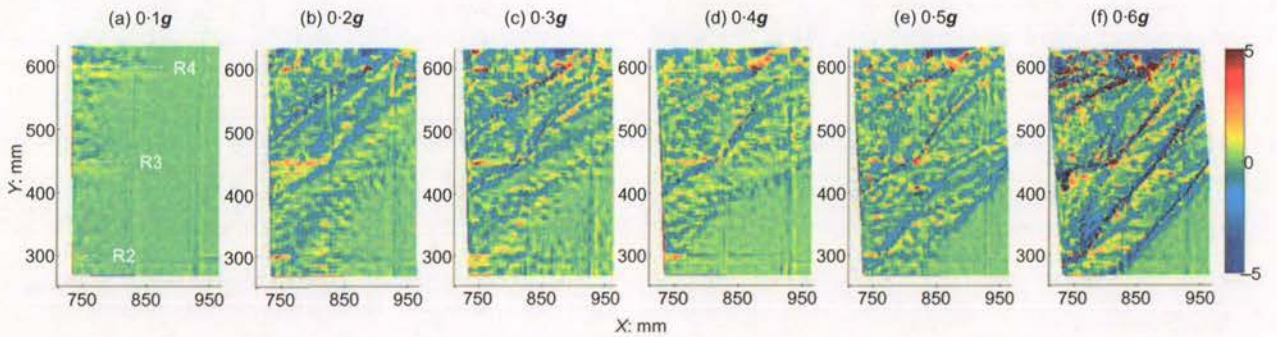


Fig. 7. Incremental volumetric strain (%) from (a) 0.1 *g* to (f) 0.6 *g*. Positive (red, orange yellow colours) indicates contraction; negative (green, blue colours) indicates dilation

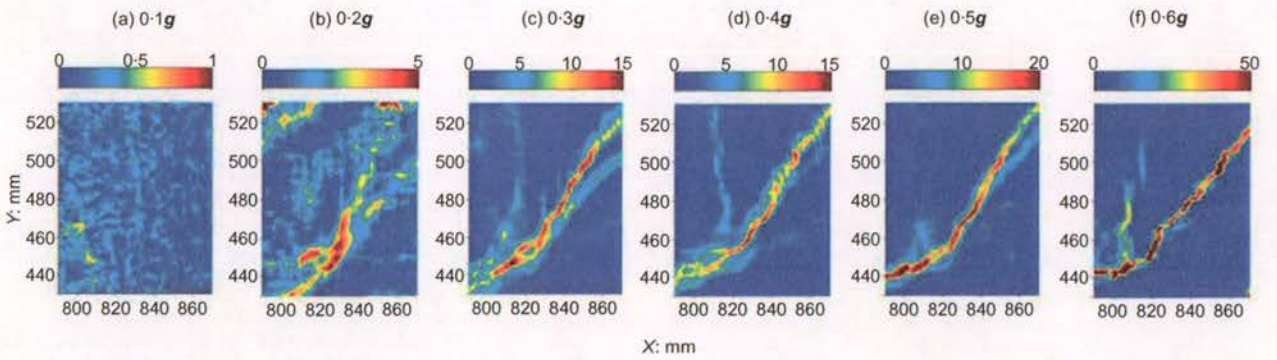


Fig. 8. Incremental shear strain for shear band S2 from (a) 0.1 *g* to (f) 0.6 *g*. Corresponding scales of shear strain (%) are indicated above each plot

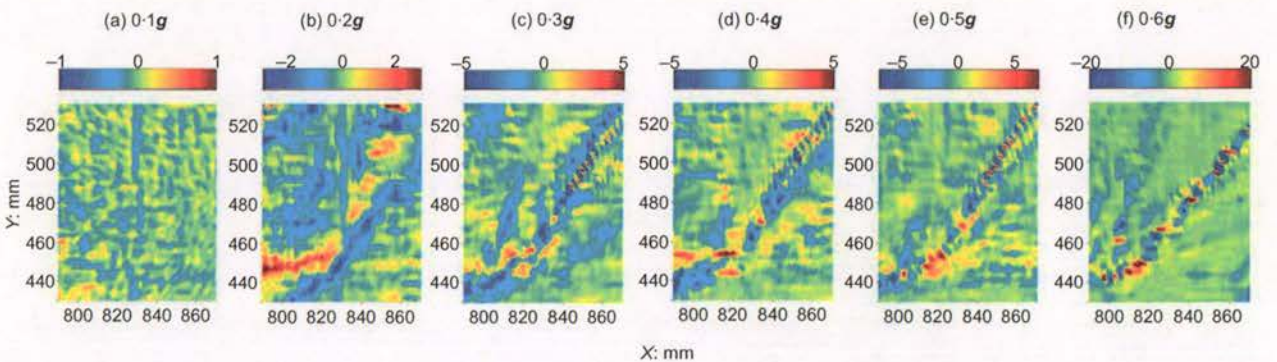


Fig. 9. Incremental volumetric strain for shear band S2 from (a) 0.1 *g* to (f) 0.6 *g*. Corresponding scales of volumetric strain (%) are indicated above each plot. Positive (red, orange yellow colours) indicates contraction; negative (green, blue colours) indicates dilation

Consider now the vertical failure plane from the end of reinforcement layer R3, which is embryonic in the 0.2 *g* stage (Fig. 5(b)), but clearly develops in the 0.3 *g* stage (Fig. 5(c)). Its full development is arrested until the 0.6 *g* stage – a response of the model that is attributed to the reinforcement layer above (R4). This clearly shows how the provision of longer reinforcement at the top of the reinforced zone can act to improve seismic resistance (Watanabe *et al.*, 2003).

## CONCLUSIONS

This study shows that the deformation of ductile GRS walls with FHR facing subjected to seismic shaking is a progressive process of shear band development with depth as the wall rotates toward failure. The results show, even at relatively low levels of shaking and with little apparent external deformation, fully softened shear bands extending from the soil reinforcement into the backfill. Indeed, this progressive failure occurs well before any 'critical' acceleration may be defined (e.g. Matsuo *et al.*, 1998), whereupon failure by sliding at the ULS is deemed to occur. Instead, the results suggest a mechanism of progressive shear band development that is related to the acceleration level (induced rotation and translation of the wall) and is both influenced and constrained by the reinforcement layers.

## Acknowledgements

This work was financially supported by the Earthquake Commission (EQC) of New Zealand via a postgraduate student award for the second author. The assistance of University of Canterbury technicians John Maley and Siale Faitotonu in constructing the rigid box and model and conducting the tests is also gratefully acknowledged.

## REFERENCES

- El-Emam, M. M. & Bathurst, R. J. (2007). Influence of reinforcement parameters on the seismic response of reduced-scale reinforced soil retaining walls. *Geotext. Geomem.* **25**, No. 1, 33–49.
- Iai, S. (1989). Similitude for shaking table tests on soil–structure–fluid model in 1 *g* gravitational field. *Soils and Found.* **29**, No. 1, 105–118.
- Jackson, P. (2010). *An investigation into the deformation behaviour of geosynthetic reinforced soil walls under seismic loading*. ME thesis, University of Canterbury, Christchurch.
- Lesniewska, D. & Muir Wood, D. (2009). Observations of stresses and strains in a granular material. *J. Engng Mech.* **135**, No. 9, 1038–1054.
- Ling, H. I., Leshchinsky, D. & Chou, N. N. S. (2001). Post-earthquake investigation on several geosynthetic-reinforced soil retaining walls and slopes during the Ji-Ji earthquake of Taiwan. *Soil Dynam. Earthquake Engng* **21**, No. 4, 297–313.
- Matsuo, O., Yokoyama, K. & Saito, Y. (1998). Shaking table tests and analyses of geosynthetic-reinforced soil retaining walls. *Geosynth. Int.* **5**, No. 1–2, 97–126.
- Muir Wood, D. (2002). Some observations of volumetric instabilities in soils. *Int. J. Solids Struct.* **39**, 3429–3449.
- Rechenmacher, A. L. (2006). Grain-scale processes governing shear band initiation and evolution in sands. *J. Mech. Phys. Solids* **54**, No. 1, 22–45.
- Rechenmacher, A. L. & Finno, R. J. (2004). Digital image correlation to evaluate shear banding in dilative sands. *Geotech. Test. J.* **27**, No. 1, 1–10.
- Watanabe, K., Munaf, Y., Koseki, J., Tateyama, M. & Kojima, K. (2003). Behaviors of several types of model retaining walls subjected to irregular excitation. *Soils and Found.* **43**, No. 5, 13–27.
- White, D. J., Take, W. A. & Bolton, M. D. (2003). Soil deformation measurement using particle image velocimetry (PIV) and photogrammetry. *Géotechnique* **53**, No. 7, 619–631.
- Yoshida, T. & Tatsuoka, F. (1997). Deformation property of shear band in sand subjected to plane strain compression and its relation to particle characteristics. *Proc. 14th Int. Conf. Soil Mech. Found. Engng.* Hamburg: AA Balkema, pp. 237–240.

## WHAT DO YOU THINK?

To discuss this paper, please email up to 500 words to the editor at journals@ice.org.uk. Your contribution will be forwarded to the author(s) for a reply and, if considered appropriate by the editorial panel, will be published as a discussion.

# Non-biennial Project 6UNI/575

## *An experimental study on geosynthetic reinforced soil walls under seismic loading*

Report prepared for the New Zealand Earthquake Commission (EQC)

Project Leaders: Dr. Elisabeth Bowman  
Assoc. Prof. Misko Cubrinovski

Principal Investigator: Perry Jackson

Department of Civil and Natural Resources Engineering  
University of Canterbury, July 2010

Civil and Natural Resources Engineering

# Non-biennial Project 6UNI/575

*An experimental study on geosynthetic  
reinforced soil walls under seismic loading*

Report prepared for the New Zealand  
Earthquake Commission (EQC)

Project Leaders: Dr. Elisabeth Bowman  
Assoc. Prof. Misko Cubrinovski

Principal Investigator: Perry Jackson

Department of Civil and Natural Resources Engineering  
University of Canterbury, July 2010

# **An Investigation into the Deformation Behaviour of Geosynthetic Reinforced Soil Walls under Seismic Loading**

## **Executive Summary**

### **Background**

Reinforcement of soil enables a soil slope or wall to be retained at angles steeper than the soil material's angle of repose. Geosynthetic Reinforced Soil (GRS) systems involve the incorporation of geosynthetic reinforcement (a strong and flexible engineering plastic) layered horizontally into select engineering backfill for the purposes of slope stabilisation and/or retaining slopes or walls.

GRS systems enable shortened construction time, increase seismic performance, potentially improve aesthetic benefits, and lower cost (by up to 50% less in one study) than their conventional retaining wall counterparts such as gravity and cantilever type retaining walls. They also meet many of the goals associated with sustainable development such as reduced carbon emissions and embodied energy, in addition to cost reductions noted when compared to conventional type retaining walls.

### **Motivation**

Design of GRS in New Zealand is made using several different overseas standards and design guidelines (i.e. Federal Highways Administration, 2001; British Standards Institute, BS8006:1995; Australian Standard, AS4678-2002), in addition to manufacturers' own in-house design methods and guidelines (Tensar, for example). Hence, GRS structures in New Zealand have been built with varying resistance to static and seismic loads, and thus different seismic risk.

Experience in previous earthquakes such as Northridge (1994), Kobe (1995), and Ji-Ji (1999) indicate good performance of GRS under high seismic loads, in comparison to their conventional retaining wall counterparts. However, this good performance is not necessarily due to advanced understanding of their behaviour, but rather highlights the inherent stability of GRS against high seismic loads and conservatism in static design practices. Hence further experimental research is required to better understand seismic behaviour and to evaluate earth pressures, displacements and/or deformation under high seismic loads to advance design practice.

A further innovation in GRS is the use of a Full-Height Rigid (FHR) facing (adopted as standard technology for vulnerable lifeline assets such as high-speed railways in Japan), quite

different to the typically utilised (at least in New Zealand) flexible wrap-around, or segmental-block faced GRS systems. New Zealand has a similar seismic risk, yet to date, the use of FHR for vulnerable roadways and the recently nationalised railways, has been limited or non-existent. Thus the use of FHR facing panels for increased seismic performance was investigated in the test series.

### **Experimental Study**

The experimental study consisted of a series of seven reduced-scale GRS model walls under seismic excitation conducted using the University of Canterbury shake-table. The models were 900 mm high, reinforced by five layers of stiff Microgrid geosynthetic reinforcement, and were founded on a rigid foundation. The models were faced by a FHR panel connected rigidly to the reinforcement. The soil deposit backfill was constructed of dry dense (target  $D_r = 90\%$ ) Albany sand, compacted by vibration of each layer by the shake-table with a weighted steel plate placed on top of the layer. The influence of the L/H ratio and wall inclination on seismic performance was investigated by varying these important design parameters throughout the testing programme. The L/H ratio tested ranged from 0.6 – 0.9, and the walls were primarily vertical except for one test inclined at  $70^\circ$  to the horizontal.

During testing, measurements of the facing displacement and the acceleration within the backfill were recorded at varying levels of shaking intensity. Mechanisms of deformation, in particular, were of interest in this study. Global and local deformations within the backfill were investigated using two methods. The first used coloured horizontal and vertical sand markers placed within the backfill. The second utilised high-speed camera imaging for subsequent analysis using Geotechnical Particle Image Velocimetry (GeoPIV) software. GeoPIV enabled shear strains to be identified within the soil at far smaller levels than that rendered visible by eye using the coloured sand markers. The complementary methods allowed the complete spatial and temporal development of deformation within the backfill to be visualised.

### **Key Findings**

All models displayed a critical acceleration, below which deformations were minor, and above which ultimate failure occurs. Failure was predominantly by overturning, with some small sliding component. During failure, the rate of sliding increased significantly.

An increase in the L/H ratio from 0.6 to 0.9 increased the stability of the wall and decreased deformations accrued prior to failure. Accelerations at failure also increased, from 0.5g to 0.7g, respectively. A similar trend of increased seismic performance was observed for the wall inclined at  $70^\circ$  to the horizontal.

Overturning was accompanied by the development of inclined shear surfaces which started at the wall crest and extended down to the back of the reinforced soil block. With increasing acceleration amplitude, further inclined shear surfaces developed progressively deeper within the retained backfill. Additional shear surfaces also propagated near-vertically up the back of the reinforced soil block, and horizontal failure surfaces propagated from the reinforcement tail, along the reinforcement layer and/or into the reinforced soil block. The initiation of the surfaces were observed to occur at much lower shaking amplitudes (0.1g-0.2g) than is considered in design, highlighting the ductile nature of GRS walls. Failure of the model was observed when an inclined failure surface developed from the wall crest downwards towards the back of the reinforced soil block and intersected with the lowest layer of reinforcement.

For all tests, the reinforced soil block was observed to demonstrate non-rigid behaviour, with simple shearing along horizontal planes as well as strain localisations at the reinforcement or within the back of the reinforced soil block. This observation is contrary to design, which assumes the reinforced soil block zone to behave rigidly.

### **Future Research**

The study examined the influence of the L/H ratio and wall inclination on seismic performance, but further work is required in order to determine in detail the existence of an 'optimum' L/H ratio, and more details into the effect of wall inclination on behaviour. This study is the first of a research programme which investigates the seismic performance of GRS walls, and determined the methodology to enable future studies to possibly investigate, among other things, the use of local soils as backfill, the addition of a surcharge load, facing connections, and their impacts on seismic performance.

# **An Investigation into the Deformation Behaviour of Geosynthetic Reinforced Soil Walls under Seismic Loading**

## **Plain English Summary**

Reinforcement of soil enables a soil slope or wall to be retained at steeper angles than the soil on its own could manage. Geosynthetic Reinforced Soil (GRS) wall structures incorporate geosynthetic reinforcement (a strong and flexible engineering plastic grid) layered horizontally into soil walls to stabilise and/or retain the soil. They take less time to construct at a reduced cost (with savings of up to 50%) and perform better in earthquakes than their conventional retaining wall counterparts such as large concrete based gravity and cantilever type retaining walls. Further, GRS walls tend to be more environmentally sustainable, with reduced carbon emissions and embodied energy.

In countries like Japan which has a high earthquake risk, GRS technology is used for important and vulnerable lifeline assets such as high-speed railways. New Zealand has a similar earthquake risk, yet the use of GRS technology has been limited. To help increase the uptake of GRS technology on New Zealand's roads and railways, a better understanding of GRS behaviour in the New Zealand earthquake environment is required.

To investigate GRS behaviour under earthquake loading, a series of seven reduced-scale GRS model walls were subjected to earthquake shaking on the University of Canterbury shake-table. The models were 0.9 m high, 2.4 m long, and 0.8 m wide, and comprised dry dense sand, reinforced by five layers of stiff geosynthetic reinforcement and rigid front face. Scaling laws applied to seismic shaking were employed so that the wall effectively represented a prototype 4.5m high wall. The length of reinforcement, and the slope of the wall face was varied to investigate these parameters' influence on wall stability. Each model was shaken with increasing intensity until failure occurred. During testing, acceleration and displacement measurements, as well as three high-speed cameras were used to plot the progression of how the model deformed. This deformation generally occurred with the wall collapsing over its base and sliding forward. The results of the study demonstrated that GRS walls built with longer geosynthetic reinforcement and shallower slopes were more stable and able to withstand stronger earthquakes.

Finally, advanced image analysis software was used to show deformation previously undetectable by eye at relatively low amplitudes of shaking. These results highlight the relative ductility of GRS walls, and have implications to the way GRS systems are designed.

**AN INVESTIGATION INTO THE  
DEFORMATION BEHAVIOUR  
OF  
GEOSYNTHETIC REINFORCED SOIL WALLS  
UNDER SEISMIC LOADING**

A thesis submitted in partial fulfilment

of the requirements for the Degree of

Master of Engineering

at the

University of Canterbury

By Perry Jackson

2010



## ABSTRACT

Reinforcement of soil enables a soil slope or wall to be retained at angles steeper than the soil material's angle of repose. Geosynthetic Reinforced Soil (GRS) systems enable shortened construction time, lower cost, increased seismic performance and potentially improve aesthetic benefits over their conventional retaining wall counterparts such as gravity and cantilever type retaining walls. Experience in previous earthquakes such as Northridge (1994), Kobe (1995), and Ji-Ji (1999) indicate good performance of reinforced soil retaining walls under high seismic loads. However, this good performance is not necessarily due to advanced understanding of their behaviour, rather this highlights the inherent stability of reinforced soil against high seismic loads and conservatism in static design practices.

This is an experimental study on a series of seven reduced-scale GRS model walls with FHR facing under seismic excitation conducted using a shake-table. The models were 900 mm high, reinforced by five layers of stiff Microgrid reinforcement, and were founded on a rigid foundation. The soil deposit backfill was constructed of dry dense Albany sand, compacted by vibration (average  $D_r = 90\%$ ). The influence of the L/H ratio and wall inclination on seismic performance was investigated by varying these important design parameters throughout the testing programme. The L/H ratio ranged from 0.6 – 0.9, and the walls were primarily vertical except for one test inclined at  $70^\circ$  to the horizontal.

During testing, facing displacements and accelerations within the backfill were recorded at varying levels of shaking intensity. Mechanisms of deformation, in particular, were of interest in this study. Global and local deformations within the backfill were investigated using two methods. The first utilised coloured horizontal and vertical sand markers placed within the backfill. The second utilised high-speed camera imaging for subsequent analysis using Geotechnical Particle Image Velocimetry (GeoPIV) software. GeoPIV enabled shear strains to be identified within the soil at far smaller strain levels than that rendered visible by eye using the coloured sand markers. The complementary methods allowed the complete spatial and temporal development of deformation within the backfill to be visualised.

Failure was predominantly by overturning, with some small sliding component. All models displayed a characteristic bi-linear displacement-acceleration curve, with the existence of a critical acceleration, below which deformations were minor, and above which ultimate failure occurs. During failure, the rate of sliding increased significantly.

An increase in the  $L/H$  ratio from 0.6 to 0.9 caused the displacement-acceleration curve to be shallower, and hence the wall to deform less at low levels of acceleration. Accelerations at failure also increased, from 0.5g to 0.7g, respectively. A similar trend of increased seismic performance was observed for the wall inclined at  $70^\circ$  to the horizontal, when compared to the other vertical walls.

Overturning was accompanied by the progressive development of multiple inclined shear surfaces from the wall crest to the back of the reinforced soil block. Failure of the models occurred when an inclined failure surface developed from the lowest layer of reinforcement to the wall crest. Deformations largely confirmed the two-wedge failure mechanism proposed by Horii et al. (2004).

For all tests, the reinforced soil block was observed to demonstrate non-rigid behaviour, with simple shearing along horizontal planes as well as strain localisations at the reinforcement or within the back of the reinforced soil block. This observation is contrary to design, which assumes the reinforced soil block to behave rigidly.

## ACKNOWLEDGEMENTS

This research project was carried out at the Department of Civil and Natural Resources Engineering, University of Canterbury, New Zealand, under the guidance of Dr. Elisabeth Bowman and Dr. Misko Cubrinovski.

Many people have been involved in the project design, testing, analysis and write up. I would like to particularly thank my supervisors' Dr. Elisabeth Bowman and Dr. Misko Cubrinovski for their technical insights, encouragement, understanding, and patience during difficult periods of the study. I would also like to thank Dr. Jan Kupec and Dr. Jonathan Fannin for their input from a New Zealand and Canadian design practice perspective, respectively.

The study was predominantly experimental, and as such, considerable time was invested in the laboratory for the construction of the experiment apparatus, model preparation, and testing. I have all of the technical staff to thank, but in particular, Mr A. Stokes and Mr. J. Maley, both for their skills, but also their humour and ready conversation during this period.

I gratefully acknowledge the generous financial assistance provided to me by the New Zealand Earthquake Commission.

I would also like to express my thanks to my office mates, as our many technical discussions contributed to a better understanding of the problems at hand. My friendship with postgraduate colleagues' Messrs. R. Fleury and A. Sundaresan and Ms. B. Bell and Ms. S. Nutsford, guaranteed my enjoyment of postgraduate life.

But most importantly, the unswerving nature and support of my mother and sister, Erice and Alexandra Jackson, and of my wonderful partner, Lucy McGregor, has been the single most important factor of my life these last two years, and made this work possible.

Perry Jackson

Christchurch, New Zealand



# TABLE OF CONTENTS

ABSTRACT	iii
ACKNOWLEDGEMENTS	v
TABLE OF CONTENTS	vii
CHAPTER 1 INTRODUCTION	1
1.1 Introduction	1
1.2 Geosynthetic-Reinforced Soil retaining walls	3
1.2.1 General characteristics of GRS retaining walls	3
1.2.2 Design of Geosynthetic-Reinforced Soil	4
1.2.3 Seismic design	7
1.3 Performance during some recent earthquakes	7
1.4 New Zealand context	9
1.4.1 New Zealand use of GRS	9
1.4.2 Full-Height Rigid facing	11
1.4.3 Sustainable development agenda	13
1.5 Research objectives	14
1.5.1 Research aims	14
1.5.2 Organisation of Thesis	15
References	16
CHAPTER 2 LITERATURE REVIEW	19
2.1 Introduction	19
2.2 Seismic design aspects	20
2.2.1 General	20
2.2.2 Inertia forces	22
2.2.3 Seismic earth pressure	23
2.2.4 Acceleration amplification	26

2.2.5	Critical acceleration	29
2.2.6	Performance-based design	31
2.3	Parameters which influence seismic performance	33
2.3.1	Influence of Length-to-Height Ratio on seismic performance	33
2.3.2	Influence of wall face inclination on seismic performance	38
2.4	Mechanisms of deformation	38
2.4.1	Observed failure modes of GRS	40
2.4.2	Formation of failure surfaces	42
2.4.3	Rigid-block assumption	43
2.5	Summary	43
	References	45
 CHAPTER 3 EXPERIMENTAL DESIGN AND TESTING PROCEDURES		47
3.1	Introduction	47
3.2	Wall Design	48
3.3	Experimental Box	49
3.3.1	Box design in previous studies	49
3.3.2	Box design	50
3.3.3	Seal design	51
3.4	Physical model	53
3.4.1	Similitude aspects	53
3.4.2	Soil	53
3.4.3	Reinforcement	58
3.4.4	Soil-Reinforcement interaction	60
3.4.5	Full-height Rigid (FHR) facing	62
3.4.6	Connections	62
3.4.7	Model excitation	62
3.4.8	Summary of model geometry	64
3.5	Shake-table and motion dynamics	65
3.6	Instrumentation	66

3.6.1	Facing displacements	67
3.6.2	Shake-table and soil accelerations	67
3.6.3	High-speed camera imaging	69
3.7	Model construction	70
3.7.1	Reinforcement connections	71
3.7.2	FHR panel bracing	72
3.7.3	Construction of model deposit	73
3.7.4	Reinforcement and accelerometer placement	78
3.7.5	Vertical columns and horizontal layers of black marker sand	78
3.8	End of construction and static self-weight response	80
3.9	Model deposit density	83
3.9.1	Sensitivity study	84
3.10	Model fundamental frequency	87
3.10.1	Impulse test	89
3.11	Summary	94
	References	95
CHAPTER 4 EXPERIMENTAL RESULTS		98
4.1	Introduction	98
4.2	Testing summary	99
4.3	Results of Test-6 – A typical case	100
4.3.1	Test-6 model wall	100
4.3.2	Base input shaking	101
4.3.3	Step-by-step deformation	104
4.3.4	Acceleration-time histories	108
4.3.5	Facing displacement-time histories	114
4.3.6	Investigation of irregular displacement response	120
4.4	Analysis of Test-6 results	125
4.4.1	Cumulative wall face displacement	125
4.4.2	Overtopping and sliding components of deformation	127

4.4.3	Critical Acceleration	128
4.4.4	Soil response	131
4.4.5	Peak acceleration amplification	132
4.4.6	RMS acceleration amplification	134
4.4.7	Acceleration amplification during shaking	135
4.5	Parametric study	137
4.5.1	Detailed summary of testing series	137
4.5.2	Displacement-acceleration curves	139
4.5.3	Repeatability of experimental results	140
4.6	Influence of L/H ratio and wall inclination on seismic performance	142
4.6.1	Accumulation of residual displacement	142
4.6.2	Modes of failure	146
4.6.3	Critical Acceleration	149
4.6.4	RMS acceleration amplification	152
4.7	Design implications	156
4.7.1	Discussion of acceleration amplification effects	156
4.7.2	Performance-based design	158
4.8	Summary	159
	References	161
<b>CHAPTER 5 PRE-FAILURE DEFORMATION OF GRS</b>		165
5.1	Introduction	165
5.2	General description of observed failure mechanisms	166
5.3	Interpretation of deformation from images	168
5.3.1	Development of deformation	168
5.3.2	Effect of L/H ratio on deformation	174
5.3.3	Effect of wall face inclination on deformation	174
5.3.4	Progressive failure	174
5.3.5	Comparison of angle of failure surfaces observed with those predicted by Mononobe-Okabe theory	176

5.3.6	Comment on sidewall friction	179
5.4	Geotechnical Particle Imaging Velocimetry	180
5.4.1	Background of GeoPIV technique	180
5.4.2	Discussion of error in GeoPIV analysis	182
5.4.3	Selected regions within the wall for GeoPIV analysis	185
5.4.4	Validation of GeoPIV for the current application	185
5.4.5	Determination of appropriate patch size	189
5.5	Deformation of the reinforced soil block-retained backfill interface prior to failure	189
5.5.1	Deformation of the Test-6 model using GeoPIV	191
5.5.2	Interpretation of localised shear strains	198
5.5.3	Development of deformation within the 0.2g shaking step	200
5.5.4	Cyclic development of deformation	203
5.5.5	Residual analysis on Tests-5 and 7 interface region	207
5.5.6	Comparison of shear strain development within the interface region	210
5.6	Deformation of the reinforced soil block	212
5.6.1	Shear surfaces within the reinforced soil block	212
5.6.2	GeoPIV analysis of reinforced soil block	213
5.6.3	GeoPIV analysis of inclined reinforced soil block	222
5.7	Idealised model for progression of deformation	224
5.7.1	General model of deformation for vertical walls	224
5.7.2	Comparison of idealised deformation model with other research	227
5.7.3	General model of deformation for inclined walls	228
5.8	Summary	228
	References	230

CHAPTER 6	CONCLUSIONS AND RECOMMENDATIONS	233
6.1	Geosynthetic Reinforced Soil Walls	233
6.2	Conclusions from the experimental study	234
6.2.1	Shake-table tests	234
6.2.2	Influence of L/H ratio and wall inclination on seismic performance	235
6.2.3	Development of deformation	236
6.2.4	Implications to design	238
6.3	Model limitations	239
6.4	Recommendations for future research	240
	References	243
APPENDIX A	WALL DESIGN AND SOIL PROPERTIES	I
A.1	Model Wall Design	II
A.2	Seal Friction Measurements	IV
A.3	Particle Size Distribution	VI
APPENDIX B	TIME HISTORIES	VII
B.1	Test-1 Time Histories	IX
B.2	Test-2 Time Histories	XV
B.3	Test-3 Time Histories	XX
B.4	Test-4 Time Histories	XXVIII
B.5	Test-5 Time Histories	XXXIX
B.6	Test-6 Time Histories	L
B.7	Test-7 Time Histories	LVIII
APPENDIX C	TESTING IMAGES	LXIX
C.1	Test-2 Testing Images	LXXI
C.2	Test-3 Testing Images	LXXIII
C.3	Test-4 Testing Images	LXXV
C.4	Test-5 Testing Images	LXXVII

C.5	Test-6 Testing Images	LXXX
C.6	Test-7 Testing Images	LXXXI
APPENDIX D GEOPIV PLOTS OF MAXIMUM SHEAR STRAIN		LXXXV
D.1	Test-6 Residual Maximum Shear Strain	LXXXVII
D.2	Test-5 Residual Maximum Shear Strain	LXXXVII
D.3	Test-5 Maximum Shear Strain developed during 0.7g shaking step	I
D.4	Test-7 Residual Maximum Shear Strain	LXXXIX
D.5	Test-7 Maximum Shear Strain developed during 0.7g shaking step	XCI

## LIST OF FIGURES

Figure 1-1. Conventional cantilever type retaining wall (a) and the alternative reinforced soil retaining wall (b) with reinforced zone, facing and connection (between reinforcement and facing) highlighted. Redrawn from FHWA, 2001.	3
Figure 1-2. Pullout (adherence) capacity, tieback wedge method. From BS8006:1995.	5
Figure 1-3. Failure modes of external instability. From Murashev (1998).	5
Figure 1-4: Internal modes of failure. From Murahsev (2003).	6
Figure 2-1. Inertia forces and dynamic earth pressure increments additional to static forces acting on a GRS wall during an earthquake. From Murashev (2003).	22
Figure 2-2. Failure plane interpreted from inclinometer tubes and extensimeters compared with the predicted failure surface by MO theory. From El-Emam and Bathurst (2004).	25
Figure 2-3. Effect of soil properties on the dynamic amplification of acceleration within the reinforced soil wall. (From Law and Ko)	27
Figure 2-3. Normalised residual wall top displacement, $d_{h3}/H$ , as a function of increasing base input acceleration for a number of different model wall types. The relationships are	

approximately bi-linear and demonstrate evidence of model type-specific critical acceleration.	30
Figure 2-4. Permanent displacement calculation using Newmark's sliding-block method. From Cai and Bathurst (1996)	32
Figure 2-5. Influence of reinforcement properties, including $L/H$ , vertical spacing ( $S_v$ ) and reinforcement stiffness ( $J_m$ ) for GRS models. NB: The model's toe condition was hinged (i.e. base sliding completely restricted). (From El-Emam and Bathurst 2007).	35
Figure 2-6. Lateral displacement measured at wall top, $\Delta X_T$ for three walls of varying facing mass and inclination ( $L/H = 0.6$ ). From El-Emam and Bathurst (2005).	38
Figure 2-7. Residual displacement of 6 types of retaining wall, observed after the final shaking step. From Watanabe et al (2003).	39
Figure 2-8. Two-wedge failure mechanism used in Japanese design. From Tatsuoka (2008).	41
Figure 3-1. Experimental setup in Box for $L/H = 0.75$ .	51
Figure 3-2. Plan view of seal against the Perspex sidewall (a) and schematic (not-to-scale) detailing of the seal and friction force components (b). Note that the backup seal is used to prevent leakage (if any) during compaction and is removed for testing.	52
Figure 3-3. Schematic detailing critical state soil mechanics and its use in scaling model density (point m) with prototype density (point p) at medium-to-large strains as suggested by Wood (2004)	56
Figure 3-4. Comparison of reinforced backfill recommended PSD from the NZ Guidelines (Murashev, 2003) and Albany Sand used in the tests.	60
Figure 3-5. Model geometry inside strong box for: a) vertical model reinforced the longest at $L/H = 0.9$ , and b) inclined wall at $70^\circ$ , reinforced at $L/H = 0.75$ .	64

Figure 3-6. Sign convention of shake-table and model dynamics	65
Figure 3-7. Model instrumentation for (a) the vertical wall reinforced the longest at $L/H = 0.9$ (Test-3 and 5); b) plan view of vertical wall (reinforced by $L/H = 0.9$ ); and, (c) the inclined wall, reinforced by $L/H = 0.75$ (Test-7).	66
Figure 3-8. Kyowa AS-2GA accelerometer mounted on aluminium plate.	67
Figure 3-10. Rigid mechanical connection between reinforcement and aluminium panel.	70
Figure 3-11. FHR aluminium panel with attached stiffeners and guides for wall bracing: a) side view, and b) front view.	71
Figure 3-12. The facing panel is rigidly braced against the box by six steel tubes attached by screws to the facing panel: a) side view through transparent sidewall, and b) schematic plan view.	72
Figure 3-13. Storage container lifted into position above the box to record initial combined mass of container and sand (a) and sand deposition into the box (b).	73
Figure 3-14 (a) – (l). Describes the layer construction process in detail.	76
Figure 3-15. Reinforcement unfolded from the wall and placed in position on the surface of layer 2 (a), accelerometer embedded into the top of layer 3 at a distance of 250 mm from the wall face and along the box centreline (400 mm from the box sidewall) (b).	77
Figure 3-16. The tubes are filled with black sand when taped (a), after two layers have been compacted the tape is removed by pulling upwards (b) leaving just the plastic tube held against the wall by the sand pressure (c) which is then removed (d).	78
Figure 3-17. Average lateral displacement of the wall face under self-weight at the end of construction of walls a) Test-6, $L/H = 0.6$ ; b) Test-1, $L/H = 0.75$ ; and c) Tests-3 and 5, $L/H = 0.9$ .	81

Figure 3-18. Relative density of each layer during and after construction. Post compaction of each layer, layer heights were recorded at two locations and are plotted separately: Dark for density measurements at the face, and grey for density measurements at mid-length (1400 mm) along the wall. Note each measurement has a possible absolute 11% error.	85
Figure 3-19. Hammer impact time history.	89
Figure 3-20. Acceleration response during hammer test. Acc 5 records the first pulse as it is closest to the back-wall. However there is also a difference in arrival time between accelerometers located in vertical array (Acc 2, Acc 3, Acc 4).	90
Figure 3-21. Free-vibration Fourier spectrum of the embedded accelerometers	92
Figure 4-1. Completed Test-6 at End of Construction (EoC) prior to shaking.	100
Figure 4-2. Summary of staged testing procedure.	101
Figure 4-3. The first shaking step of Test-6 at 0.1g: (a) Raw shake-table acceleration and displacement time history data, (b) Fast Fourier Transformation, and (c) filtered shake-table acceleration and displacement time history data.	102
Figure 4-4. Deformation of Test-6 visible at the end of acceleration inputs of 0.1g, 0.2g, 0.3g, 0.4g, and 0.5g upon which the wall failed. The numbered dashed lines highlight the location and progression of failure planes once they become readily discernible by the naked eye.	105
Figure 4-5. Acceleration time history recorded by Acc 4 for Test-6 during 0.5g shaking step and the data processing applied: (a) raw accelerometer data, (b) filtered accelerometer data using an 8 <sup>th</sup> order 10 Hz low-pass Butterworth filter, and (c) filtered data after baseline correction.	108
Figure 4-6. Correction of accelerometer tilt	109
Figure 4-7. Acceleration time histories for 0.1g shaking step.	110
Figure 4-8. Acceleration time histories for 0.3g shaking step.	111

Figure 4-9. Acceleration time histories for 0.5g (final) shaking step.	112
Figure 4-10. Facing and shake-table displacement time histories at 0.1g shaking step	114
Figure 4-11. Facing and shake-table displacement time histories at 0.2g shaking step.	114
Figure 4-12. Facing and shake-table displacement time histories at 0.3g shaking step	115
Figure 4-13. Facing and shake-table displacement time histories at 0.4g shaking step.	115
Figure 4-14. Facing and shake-table displacement time histories at 0.5g shaking step	116
Figure 4-15. Facing displacement time history of Disp. 3 (lowest North Array displacement transducer).	118
Figure 4-16. Facing and shake-table raw (unfiltered) displacement time histories at 0.3g shaking step.	120
Figure 4-17. Fast fourier transforms for 0.3g shaking step for: (a) wall face top displacement, (b) acceleration at the top of the reinforced soil zone, (c) the base input acceleration (d) shake-table displacement.	121
Figure 4-18. Fast fourier transforms for 0.5g shaking step for: (a) wall face top displacement, (b) acceleration at the top of the reinforced soil zone, (c) the base input acceleration (d) shake-table displacement.	122
Figure 4-19. Cumulative lateral displacement of the wall face as a function of the base input acceleration and number of cycles for Test-6, reinforced at $L/H = 0.6$ . NB: “c” denotes the peak for the number of cycles completed.	125
Figure 4-20. Rotation and sliding components of cumulative residual horizontal displacement of the wall top with increasing base input acceleration (PGA). Reinforced at $L/H = 0.60$ (T6).	126
Figure 4-21. Normalised sliding and rotation components of wall response for $L/H = 0.6$ .	129

- Figure 4-22. Fast Fourier Transformations for the base input and response accelerations for the 0.1g, 0.3g and 0.5g base shaking levels for Test-6. The values in parentheses correspond to peak values. 130
- Figure 4-23. Amplification of peak outwards accelerations with wall elevation is plotted for each shaking step: (a) reinforced soil and (b) backfill. 131
- Figure 4-24. Amplification of RMS acceleration up the wall for each shaking step: (a) Reinforced zone and (b) Backfill. 134
- Figure 4-25. Acceleration amplification factors for a 5 cycle period starting at cycles 0, 20c and 45c for shaking steps a) 0.1g, b) 0.3g and c) 0.5g. 135
- Figure 4-26. Displacement-acceleration curves for Tests-1, 5, 6, and 7. Note that Test-1 data prior to 0.5g is not plotted, for reasons as discussed above. 138
- Figure 4-27. Comparison of displacement-acceleration curves for repeatability purposes of Test-2 and 6 both reinforced at  $L/H = 0.6$ . 140
- Figure 4-28. Comparison of displacement-acceleration curves for tests of different  $L/H$  ratio. NB: Test-1 is dashed to represent unreliable data. 142
- Figure 4-29. Comparison of displacement-acceleration curves for the effect of wall face inclination on stability. 144
- Figure 4-30. Comparison of failure modes during Tests-5, 6, and 7 for walls reinforced at  $L/H = 0.6, 0.9$  and  $0.75$  inclined at  $70^\circ$  to the horizontal. The letters represent the different definitions of critical acceleration proposed by various researchers and are discussed further in Section 4.6.3. 146
- Figure 4-31. Test-7 cumulative displacement recorded at the wall face showing the geometry of failure from the start of testing (EoC), through to 0.7g. 148

- Figure 4-32. Comparison of critical acceleration of Tests-7 and 5 reinforced at  $L/H = 0.75$  and  $0.9$ ; Test-7 with facing inclined at  $70^\circ$ . 149
- Figure 4-33. Comparison of sliding components of deformation for Tests-5, 6 and 7. 150
- Figure 4-34. Comparison of RMS Amplification factors measured near the wall top within the reinforced zone (Acc 4) and backfill (Acc 5) for Tests-5 and 6 reinforced at  $L/H = 0.9$  and  $0.6$  respectively. 152
- Figure 4-35. RMS acceleration amplification up the wall during Test-7 for: a) Reinforced soil vertical accelerometer array (Acc 2, 3, 4) and b) Accelerometers Acc 1 and 5 where a linear relationship has been assumed. 153
- Figure 4-36. Comparison of RMS Amplification factors for Tests-5 and 7 reinforced at  $L/H = 0.9$  and  $0.75$ ; Test-7 inclined facing at  $70^\circ$ . 154
- Figure 4-37. RMS Amplification of acceleration measured near the wall top within the reinforced zone (Acc 4) and backfill (Acc 5) for Test-5 and 6 reinforced at  $L/H = 0.9$  and  $0.6$  respectively. 156
- Figure 5-1. Deformation visible after failure of Test-6 (a), Test-5 (b) and Test-7 (c) reinforced at  $L/H = 0.6, 0.9$  and  $0.75$  (and inclined at  $70^\circ$  to the horizontal) respectively. 165
- Figure 5-2. Progression of deformation within the backfill in Test-6 reinforced  $L/H = 0.6$  at the completion of: a)  $0.3g$ , b)  $0.4g$  and c)  $0.5g$  (failure). 168
- Figure 5-3. Progression of deformation within the backfill in Test-5 reinforced  $L/H = 0.9$  at the completion of: a)  $0.3g$ , b)  $0.5g$ , c)  $0.6g$ , and d)  $0.7g$  (failure). 169
- Figure 5-4. Progression of deformation within the backfill in Test-7 reinforced  $L/H = 0.75$  with a facing inclination of  $70^\circ$  at the completion of: a)  $0.4g$ , b)  $0.6g$  and c)  $0.7g$  (failure). 170
- Figure 5-5. Progressive failure at wall heel during the final  $0.5g$  shaking step (Test-6) 174

Figure 5-6. Schematic diagram showing the definition of the failure surface angle, $\alpha_{AE}$ , for the MO prediction and that observed.	175
Figure 5-7. Principles of GeoPIV (from White and Take (2002)).	179
Figure 5-8. GeoPIV precision and measurement array size vs camera CCD resolution (from White and Take (2002)).	181
Figure 5-9. Location of “windows” in Test-6 (identified by dashed white lines), used for image capture by cameras C1 and C2. The images captured of these windows were then analysed using GeoPIV.	183
Figure 5-10. Displacement-time history of the shake-table used for PIV validation test. NB: The circled points are images taken for validation of GeoPIV.	184
Figure 5-11. Calibration of GeoPIV for this application: (a) Window for analysis, (b) mesh of patches to track soil texture, and (c) mesh of patches tracking reference points on the box window.	185
Figure 5-12. Displacement vector field of interface region in u-v space (pixels). Vectors plotted between: (a) Time history points 1 and 2, and (b) points 2 and 3.	186
Figure 5-13. Calibrated displacement vector field of interface region in x-y space (mm). Vectors plotted between: (a) Time history points 1 and 2, and (b) points 2 and 3.	187
Figure 5-14. Displacement vector plot for comparison of patch size for GeoPIV analysis: a) 16 by 16 pixels, b) 32 by 32 pixels, c) 64 by 64 pixels. Each vector has been scaled up by a factor of 3.	188
Figure 5-15. Displacement plot of interface region for shaking steps 0.1g, 0.2g, 0.3g and 0.4g. (Note vectors have been scaled by 3). The plotting region is the extent of the viewing window. Vector circled for inspection below.	190

Figure 5-16. Triangular element mesh for strain calculation plotted in xy coordinates. Note that because some "wild" vectors were evident in the displacement plots, the associated patches have been removed from the element mesh. 192

Figure 5-17. Residual shear strain of the reinforced/retained backfill interface of Test-6 reinforced with  $L/H = 0.6$  and accumulated by the completion of: (a) 0.1g, (b) 0.2g, (c) 0.3g and (d) 0.4g shaking steps. 193

Figure 5-18. Residual shear strain accumulated by the completion of 0.1g (replotted at a finer scale for better visualisation) of the reinforced/retained backfill interface of Test-6 reinforced with  $L/H = 0.6$ . 194

Figure 5-19. Comparison of location of failure surfaces plotted and seen within the image after 0.3g (a) and 0.4g (b). 195

Figure 5-20. Residual shear strain accumulated by the completion of 0.4g shaking step for Test-6 plotted with the maximum strain scale set to: (a) 50% and (b) 80%. 197

Figure 5-21. Shear strain accumulated during 0.2g shaking step and cycle peak: a) 1, b) 5, c) 10, d) 20, e) 30, f) 50. The cycle peaks are shown in the shake-table time-history (g). 199

Figure 5-22. Shear strain developed within the first complete shake-table displacement cycle of the 0.2g shaking step for Test-6. The initial position of reinforcement layers R2, R3 and R4 are indicated with a dashed white line in (a). 202

Figure 5-23. Schematic showing the direction of shake-table displacement and the corresponding inertial force,  $F_{IR}$ , acting on the wall face. 203

Figure 5-24. Selected peaks and troughs of facing displacement transducer Disp 1, for use in the GeoPIV analysis. 203

Figure 5-25. Shear strain developed within the complete first four cycles of the 0.2g shaking step for Test-6. The timing of the images was made to coincide with the peaks (a – c) and troughs (d

– f) for cycles 1, 2, and 4, respectively, as shown in the attached facing displacement time history. 204

Figure 5-26. The "windows" (identified by dashed white lines) used for image capture by cameras C1 and C2 in Test-5 (a) and Test-7 (b), used for subsequent analysis using GeoPIV.205

Figure 5-27. Maximum shear strain in Test-5 reinforced at  $L/H = 0.9$  accumulated by the completion of: a) 0.1g, b) 0.2g, c) 0.3g, d) 0.4g, e) 0.5g and f) 0.6g shaking steps. 206

Figure 5-28. Maximum shear strain in Test-7 reinforced at  $L/H = 0.75$  and inclined at  $70^\circ$  accumulated by the completion of: a) 0.1g, b) 0.2g, c) 0.3g, d) 0.4g, e) 0.5g and f) 0.6g shaking steps. 207

Figure 5-29. Comparison of residual maximum shear strain after 0.3g shaking step for Test-6 (a), Test-5 (b), and Test-7 (c). 209

Figure 5-30. Comparison of reinforced block regions post-failure illustrating strain localisations within the reinforced soil block: (a) Test-5,  $L/H = 0.9$ ; (b) Test-6,  $L/H = 0.6$ ; (c) Test-7,  $L/H = 0.75$  and inclined  $70^\circ$  to the horizontal. 210

Figure 5-31. Simple shear deformation of the reinforced soil block. 211

Figure 5-32. Maximum shear strain within the reinforced soil block at reinforcement layer, R4, for Test-6 reinforced at  $L/H = 0.6$  at the completion of: a) 0.1g, b) 0.2g, c) 0.3g, d) 0.4g. 213

Figure 5-33. High-speed camera images used in the GeoPIV analysis of the reinforced soil block of Test-6: (a) before testing, (b) after 0.4g shaking step, and (c) after failure at 0.5g shaking. The vertical sand marker lines have been numbered to indicate the movement of these lines between shaking steps. Note that a strain localisation is visible in the 5<sup>th</sup> vertical marker line and has been circled. 214

Figure 5-34. Components of strain accumulated up to 0.4g shaking step for Test-6: a) Maximum shear strain, $\gamma$ (replotted for comparison), b) shear strain, $\gamma_{xy}$ , c) linear strains in the horizontal direction, $\epsilon_x$ , and d) linear strain in the vertical direction, $\epsilon_y$ .	216
Figure 5-35. Development of shear strain during the 0.5g shaking step for Test-6.	218
Figure 5-36. Geometry and mode of failure of Test-6 during 0.5g (final) shaking step.	219
Figure 5-37. Maximum shear strain accumulated within the reinforced soil block by: a) 0.1g, b) 0.2g, c) 0.3g, d) 0.4g, and e) 0.5g shaking steps, centred on reinforcement layer, R4, for Test-7 reinforced at $L/H = 0.75$ and inclined at $70^\circ$ top the horizontal. Note that the 0.7g shaking steps are not plotted due to the large sliding component during these steps, impacting on the results as discussed.	221
Figure 5-38. Idealised model of progression of deformation mechanism for GRS model walls undergoing increasing stages of seismic excitation from (a) to (e).	222
Figure A-1. Particle Size Distribution of Albany Sand	VI
Figure B-1. Test-1 acceleration time histories at 0.1g shaking step	IX
Figure B-2. Test-1 acceleration time histories at 0.2g shaking step	IX
Figure B-3. Test-1 acceleration time histories at 0.3g shaking step	X
Figure B-4. Test-1 acceleration time histories at 0.4g shaking step	X
Figure B-5. Test-1 acceleration time histories at 0.5g shaking step	XI
Figure B-6. Test-1 acceleration time histories at 0.6g shaking step	XI
Figure B-7. Test-1 displacement time histories at 0.1g shaking step	XII
Figure B-8. Test-1 displacement time histories at 0.2g shaking step	XII

Figure B-9. Test-1 displacement time histories at 0.3g shaking step	XIII
Figure B-10. Test-1 displacement time histories at 0.4g shaking step	XIII
Figure B-11. Test-1 displacement time histories at 0.5g shaking step	XIV
Figure B-12. Test-1 displacement time histories at 0.6g shaking step	XIV
Figure B-13. Test-2 acceleration time histories at 0.3g shaking step	XV
Figure B-14. Test-2 acceleration time histories at 0.4g shaking step	XVI
Figure B-15. Test-2 acceleration time histories at 0.5g shaking step	XVII
Figure B-16. Test-2 displacement time histories at 0.3g shaking step	XVIII
Figure B-17. Test-2 displacement time histories at 0.4g shaking step	XVIII
Figure B-18. Test-2 displacement time histories at 0.5g shaking step	XIX
Figure B-19. Test-3 acceleration time histories at 0.6g, 10 Hz frequency shaking step	XX
Figure B-20. Test-3 acceleration time histories at 0.4g, 5Hz shaking step, as per standard protocol	XXI
Figure B-21. Test-3 acceleration time histories at 0.5g shaking step	XXII
Figure B-22. Test-3 acceleration time histories at 0.6g shaking step	XXIII
Figure B-23. Test-3 acceleration time histories at 0.7g shaking step	XXIV
Figure B-24. Test-3 displacement time histories at 0.6g, 10 Hz frequency shaking step	XXV
Figure B-25. Test-3 displacement time histories at 0.4g shaking step	XXV
Figure B-26. Test-3 displacement time histories at 0.5g shaking step	XXVI

Figure B-27. Test-3 displacement time histories at 0.6g shaking step	XXVI
Figure B-28. Test-3 displacement time histories at 0.7g shaking step	XXVII
Figure B-29. Test-4 acceleration time histories at 0.1g shaking step	XXVIII
Figure B-30. Test-4 acceleration time histories at 0.2g shaking step	XXIX
Figure B-31. Test-4 acceleration time histories at 0.3g shaking step	XXX
Figure B-32. Test-4 acceleration time histories at 0.4g shaking step	XXXI
Figure B-33. Test-4 acceleration time histories at 0.5g shaking step	XXXII
Figure B-34. Test-4 acceleration time histories at 0.6g shaking step	XXXIII
Figure B-35. Test-4 acceleration time histories at 0.65g shaking step	XXXIV
Figure B-36. Test-4 displacement time histories at 0.1g shaking step	XXXV
Figure B-37. Test-4 displacement time histories at 0.2g shaking step	XXXV
Figure B-38. Test-4 displacement time histories at 0.3g shaking step	XXXVI
Figure B-39. Test-4 displacement time histories at 0.4g shaking step	XXXVI
Figure B-40. Test-4 displacement time histories at 0.5g shaking step	XXXVII
Figure B-41. Test-4 displacement time histories at 0.6g shaking step	XXXVII
Figure B-42. Test-4 displacement time histories at 0.65g shaking step	XXXVIII
Figure B-43 Test-5 acceleration time histories at 0.1g shaking step.	XXXIX
Figure B-44. Test-5 acceleration time histories at 0.2g shaking step.	XL
Figure B-45. Test-5 acceleration time histories at 0.3g shaking step.	XLI

Figure B-46. Test-5 acceleration time histories at 0.4g shaking step.	XLII
Figure B-47. Test-5 acceleration time histories at 0.5g shaking step.	XLIII
Figure B-48. Test-5 acceleration time histories at 0.6g shaking step.	XLIV
Figure B-49. Test-5 acceleration time histories at 0.7g shaking step.	XLV
Figure B-50. Test-5 displacement time histories at 0.1g shaking step	XLVI
Figure B-51. Test-5 displacement time histories at 0.2g shaking step	XLVI
Figure B-52. Test-5 displacement time histories at 0.3g shaking step	XLVII
Figure B-53. Test-5 displacement time histories at 0.4g shaking step	XLVII
Figure B-54. Test-5 displacement time histories at 0.5g shaking step	XLVIII
Figure B-55. Test-5 displacement time histories at 0.6g shaking step	XLVIII
Figure B-56. Test-5 displacement time histories at 0.7g shaking step	XLIX
Figure B-57. Test-6 acceleration time histories at 0.1g shaking step.	L
Figure B-58. Test-6 acceleration time histories at 0.2g shaking step.	LI
Figure B-59. Test-6 acceleration time histories at 0.3g shaking step.	LII
Figure B-60. Test-6 acceleration time histories at 0.4g shaking step.	LIII
Figure B-61. Test-6 acceleration time histories at 0.5g shaking step.	LIV
Figure B-62. Test-6 displacement transducer time histories at 0.5g shaking step.	LV
Figure B-63. Test-6 displacement time histories at 0.2g shaking step.	LV
Figure B-64. Test-6 displacement time histories at 0.3g shaking step.	LVI

Figure B-65. Test-6 displacement time histories at 0.4g shaking step.	LVI
Figure B-66. Test-6 displacement time histories at 0.5g shaking step.	LVII
Figure B-67. Test-7 acceleration time histories at 0.1g shaking step.	LVIII
Figure B-68. Test-7 acceleration time histories at 0.2g shaking step.	LIX
Figure B-69. Test-7 acceleration time histories at 0.3g shaking step.	LX
Figure B-70. Test-7 acceleration time histories at 0.4g shaking step.	LXI
Figure B-71. Test-7 acceleration time histories at 0.5g shaking step.	LXII
Figure B-72. Test-7 acceleration time histories at 0.6g shaking step.	LXIII
Figure B-73. Test-7 acceleration time histories at 0.7g shaking step.	LXIV
Figure B-74. Test-7 displacement transducer time histories at 0.1g shaking step.	LXV
Figure B-75. Test-7 displacement transducer time histories at 0.2g shaking step.	LXV
Figure B-76. Test-7 displacement time histories at 0.3g shaking step.	LXVI
Figure B-77. Test-7 displacement time histories at 0.4g shaking step.	LXVI
Figure B-78. Test-7 displacement time histories at 0.5g shaking step.	LXVII
Figure B-79. Test-7 displacement time histories at 0.6g shaking step.	LXVII
Figure B-80. Test-7 displacement time histories at 0.7g shaking step.	LXVIII
Figure C-1. Test-2 prior to testing	LXXI
Figure C-2. Test-2 after 0.3g shaking (first step to reduce sand leakage).	LXXI
Figure C-3. Test-2 after 0.4g shaking.	LXXI

Figure C-4. Test-2 after 0.5g shaking.	LXXII
Figure C-5. Test-2 prior to testing	LXXIII
Figure C-6. Test-3 after first shaking step of 0.6g, at 10Hz (due to experimental error).	LXXIII
Figure C-7. Test-3 after 0.4g, 5 Hz shaking step (standard testing protocol resumed).	LXXIII
Figure C-8. Test-3 after 0.5g shaking step.	LXXIV
Figure C-9. Test-3 after 0.6g shaking step.	LXXIV
Figure C-10. Test-3 after 0.7g shaking step.	LXXIV
Figure C-11. Test-4 prior to testing	LXXV
Figure C-12. Test-4 after 0.1g shaking step.	LXXV
Figure C-13. Test-4 after 0.2g shaking step.	LXXV
Figure C-14. Test-4 after 0.3g shaking step.	LXXVI
Figure C-15. Test-4 after 0.4g shaking step.	LXXVI
Figure C-16. Test-4 after 0.5g shaking step.	LXXVI
Figure C-17. Test-4 after 0.6g shaking step.	LXXVII
Figure C-18. Test-4 after 0.65g shaking step.	LXXVII
Figure C-19. Test-5 prior to testing.	LXXVIII
Figure C-20. Test-5 after 0.1g shaking step.	LXXVIII
Figure C-21. . Test-5 after 0.2g shaking step	LXXVIII
Figure C-22. Test-5 after 0.3g shaking step	LXXIX

Figure C-23. Test-5 after 0.4g shaking step	LXXIX
Figure C-24. Test-5 after 0.5g shaking step	LXXIX
Figure C-25. Test-5 after 0.6g shaking step	LXXX
Figure C-26. Test-5 after 0.7g shaking step	LXXX
Figure C-27. Test-7 prior to testing.	LXXXI
Figure C-28. Test-7 after 0.1g shaking step.	LXXXI
Figure C-29. Test-7 after 0.2g shaking step.	LXXXI
Figure C-30. Test-7 after 0.3g shaking step.	LXXXII
Figure C-31. Test-7 after 0.4g shaking step.	LXXXII
Figure C-32. Test-7 after 0.5g shaking step.	LXXXII
Figure C-33. Test-7 after 0.6g shaking step	LXXXIII
Figure C-34. Test-7 after 0.7g shaking step	LXXXIII
Figure D-1. Maximum shear strain within the reinforced soil region for Test-6, vertical wall reinforced at $L/H = 0.6$ , by shaking steps: a) 0.1g, b) 0.2g, c) 0.3g, d) 0.4g.	LXXXVII
Figure D-1. Maximum shear strain within the reinforced soil region for Test-5, vertical wall reinforced at $L/H = 0.9$ , by shaking steps: a) 0.1g, b) 0.2g, c) 0.3g, d) 0.4g, e) 0.5g, and f) 0.6g.	LXXXIX
Figure D-1. Development of maximum shear strain within the reinforced soil region during 0.7g shaking step for Test-5, vertical wall reinforced at $L/H = 0.9$ . Strains accumulated from the end of 0.6g shaking step to: a) 10 cycles (c), b) 20 cycles, c) 30 cycles, d) 40 cycles, and e) 50 cycles.	XC

Figure D-1. Maximum shear strain within the reinforced soil region for Test-7, wall reinforced at  $L/H = 0.9$  and inclined at  $70^\circ$  to the horizontal, by shaking steps: a) 0.1g, b) 0.2g, c) 0.3g, d) 0.4g, e) 0.5g, and f) 0.6g. XCII

Figure D-1. Development of maximum shear strain within the reinforced soil region during 0.7g shaking step for Test-7, wall inclined at  $70^\circ$  to the horizontal and reinforced  $L/H = 0.75$ . Strains accumulated from the end of 0.6g shaking step to: a) 10 cycles (c), b) 20 cycles, c) 30 cycles, d) 40 cycles, and e) 50 cycles. XCIII

## LIST OF TABLES

Table 3-1. Summary of previous model tests' and this study's dimensions and materials.	50
Table 3-2. Similitude derived scaling factors for 1-g shaking table tests	54
Table 3-3: Albany Sand soil properties	55
Table 3-4. Manufacturers and Geosynbthetic product stiffness properties	58
Table 3-5: Properties of Microgrid manufactured by Stratagrid	59
Table 3-6 Accelerometer AS-2GB Specifications	67
Table 3-7. Camera specifications	69
Table 3-8. Calculated average wall densities	83
Table 3-9. Measurement quantities and possible errors	84
Table 3-10. Estimation of fundamental frequency from the longitudinal shear wave velocities caclulated via the delay time between the first hammer impulse and that recorded within the backfill.	

# **CHAPTER 1**

## **INTRODUCTION**

### **1.1 Introduction**

Reinforcement of soil enables a soil slope or wall to be retained at angles steeper than the soil material's angle of repose. Systems comprising soil and reinforcement are collectively termed "reinforced soil" and involve the incorporation of reinforcement layered horizontally into select engineering backfill for the purposes of slope stabilisation and/or retaining slopes or walls.

Reinforced soil systems enable shortened construction time, lower cost, increase seismic performance and potentially improve aesthetic benefits over their conventional retaining wall counterparts such as gravity and cantilever type retaining walls (see Fairless 1989; FHWA 2001; Murahsev 2003; El-Emam and Bathurst 2004 as examples). Further, soil reinforcement meets many of the goals associated with sustainable development such as reduced carbon emissions and embodied energy, in addition to cost reductions noted when compared to conventional type retaining walls (Jones 1996; Tatsuoka 2008).

The concept of Reinforced Earth (RE) was first introduced in 1966 by the French engineer Henri Vidal, with the inclusion of steel reinforcing strips into engineering backfill, and connecting these to a stiff concrete facing. Geosynthetic reinforcement was first used in 1971. Both RE and geosynthetic reinforcement are part of a large family of reinforced soil systems that comprise different reinforcement, facing products and design methods.

Geosynthetic reinforcement, with a Full-Height Rigid (FHR) facing panel is the focus of this thesis.

This is an experimental study on the seismic performance of Geosynthetic Reinforced Soil (GRS) retaining walls. The study consisted of a series of seven reduced-scale model tests conducted on the University of Canterbury shake-table. Two key parameters that influence seismic behaviour, namely the reinforcement length to height ratio, and the wall inclination, were systematically varied during testing. Facing displacements, accelerations within the backfill, and backfill deformation was measured during each test.

Mechanisms of deformation, in particular, were of interest in this study. Global and local deformations within the backfill were investigated using a combination of sand markers, and high-speed camera imaging and subsequent analysis using Geotechnical Particle Image Velocimetry (GeoPIV) software. GeoPIV allowed a more in-depth picture of the strain field in selected regions of the backfill to be determined (White et al. 2003).

This Chapter will first briefly introduce the concept of GRS retaining walls and the basis of their design. A general overview of GRS retaining wall performance during previous earthquakes in the United States, Japan and Taiwan is provided in Section 1.3. Their recorded performance has in general, been described as “excellent” (Sandri 1997), and provides further impetus for their increased use in New Zealand, a country of similarly significant seismic risk.

The New Zealand context is discussed in Section 1.4 and first provides a brief overview of GRS use in New Zealand. An argument advocating the use of Full-Height Rigid (FHR) facing panels in New Zealand is presented; as FHR is the preferred facing method in Japan for high-speed rail that demands high rigidity and seismic resistance. The benefits to sustainable development associated with GRS are discussed subsequently.

The objectives of this research project, the experimental scope and the organisation of this thesis is provided in Section 1.5.

## 1.2 Geosynthetic-Reinforced Soil retaining walls

### 1.2.1 General characteristics of GRS retaining walls

Geosynthetic-Reinforced Soil (GRS) is a derivative of the original reinforced earth concept developed in 1966. The original reinforcement comprised steel strips layered into the retained soil; this system is now trademarked Reinforced Earth<sup>®</sup>. Different reinforcement materials, design methodologies and construction techniques have since been derived from the original Reinforced Earth concept; however the fundamental engineering principles of soil reinforcement are the same. The use of geosynthetic reinforcement, a polymeric material, is the subject of this study.

A reinforced soil wall and a conventional cantilever retaining wall are compared in Figure 1-1 below. The following key features of the reinforced soil wall are of note: a reinforced soil block comprised of reinforcement layered into select cohesionless granular fill, a facing type (which can vary with design), a connection between the reinforcement and facing, a retained backfill behind the reinforced soil block, and a reduction in the concrete and foundations necessary as compared to the conventional cantilever retaining wall (RW).

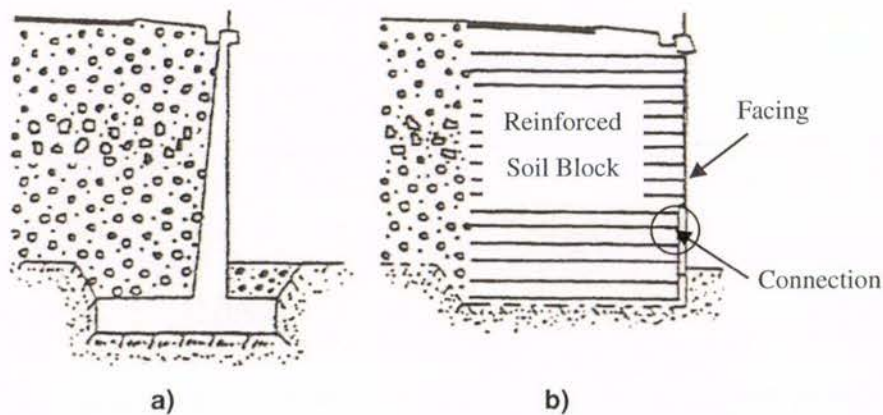


Figure 1-1. Conventional cantilever type retaining wall (a) and the alternative reinforced soil retaining wall (b) with reinforced zone, facing and connection (between reinforcement and facing) highlighted. Redrawn from FHWA, 2001.

The important components of a GRS retaining wall are described below:

*Geosynthetic-reinforcement* – A polymeric material comprised either of polyester, polyethylene or polypropylene which is manufactured into geotextile (sheets) or geogrid (planar grid-like arrangement). The reinforcement provides tensile capacity to the soil.

*Engineering backfill* – Generally cohesionless, free-draining granular fill. This ensures a good frictional interaction with the reinforcement and prevents the build-up of pore water pressures.

*Facing* – A number of facing types exist for GRS structures, based on aesthetic requirements, proprietary aspects, and structural design considerations. Two types are commonly used in New Zealand: Wrap-around facing whereby the layered geosynthetic is looped around the wall face; and Segmental Retaining Wall (SRW) facing where discrete concrete panels or brick units are stacked and connected to the reinforcement with lips, shear pins and/or friction.

The method of Full-Height Rigid (FHR) panel facings as used in Japan (Tatsuoka 2008) is discussed in Section 1.4.2 below and is used in this study.

*Connections* – Specifies the method used to connect the reinforcement layered into the fill with the facing system. The connection can be either rigid as in the case of mechanical connection to a concrete panel, or non-rigid as in the case of a SRW, which relies on friction generated between the concrete facing panels and reinforcement.

## **1.2.2 Design of Geosynthetic-Reinforced Soil**

Current design techniques for GRS walls utilise either limit equilibrium or limit state approaches. There are a number of different methods and codes available. For instance, the British Standard (BS 8006:1995) (1995) specifies a limit state design, while the FHWA (2001) specifies a limit equilibrium approach. The New Zealand design guidelines prepared by Murashev (2003) adopt a limit state approach.

Aside from differing design philosophies; the underlying concept of geosynthetic reinforced soils is simple: geosynthetic reinforcement inclusion provides tensile capacity to the soil and allows slopes and walls to be constructed at angles steeper than the soil material's angle of repose.

Figure 1-2 below shows the reinforcing mechanism. It can be seen that the reinforcement resists the formation of a potential failure surface within the reinforced soil block and is anchored in the resistant zone. The 'pullout' capacity of the reinforcement is hence determined by the length of reinforcement,  $L_{ej}$ , within the resistant zone, and the interaction between the soil and reinforcement.

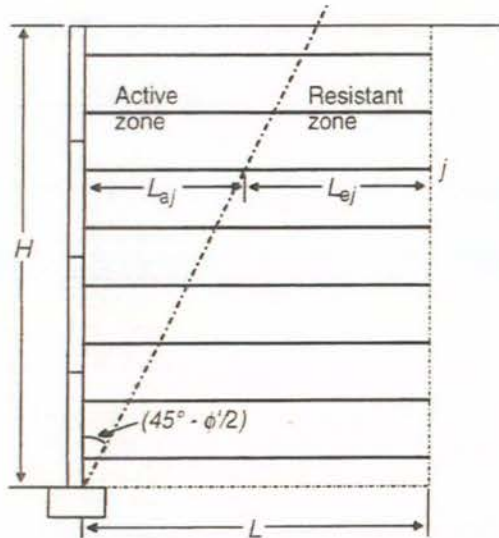


Figure 1-2. Pullout (adherence) capacity, tieback wedge method. From BS8006:1995.

Design separates possible failure modes into external stability of the reinforced block as a rigid composite mass, and the internal stability of the reinforced block. Modes of failure considered in an external stability analysis are shown in Figure 1-3 and include: (a) Sliding, (b) Overturning, (c) Bearing Capacity Failure, and (d) Deep-Seated Failure.

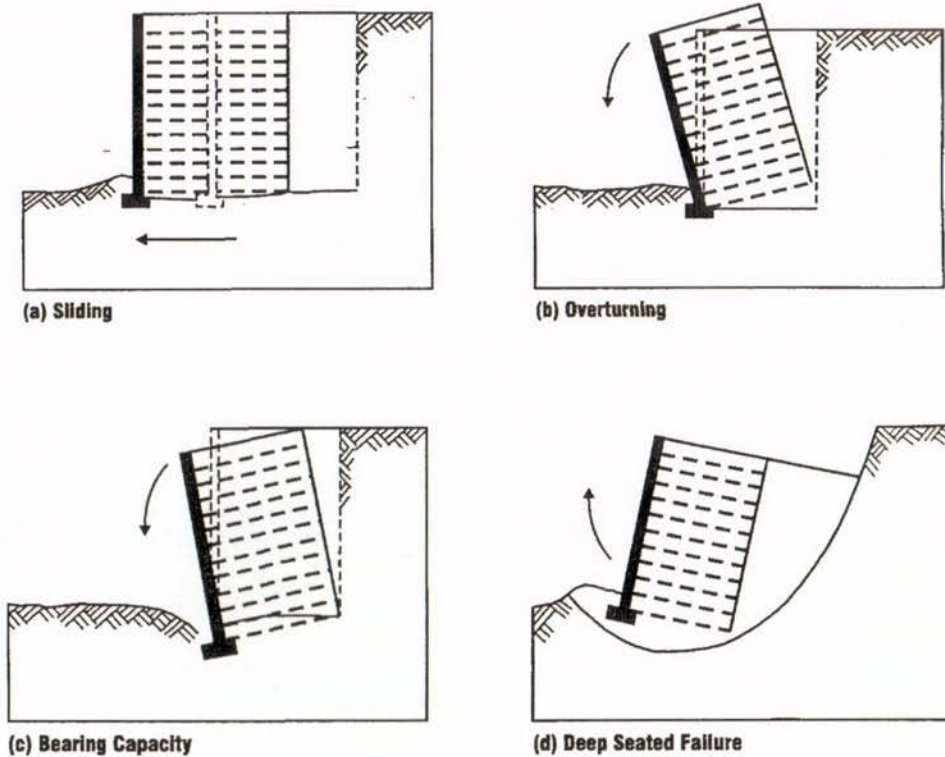
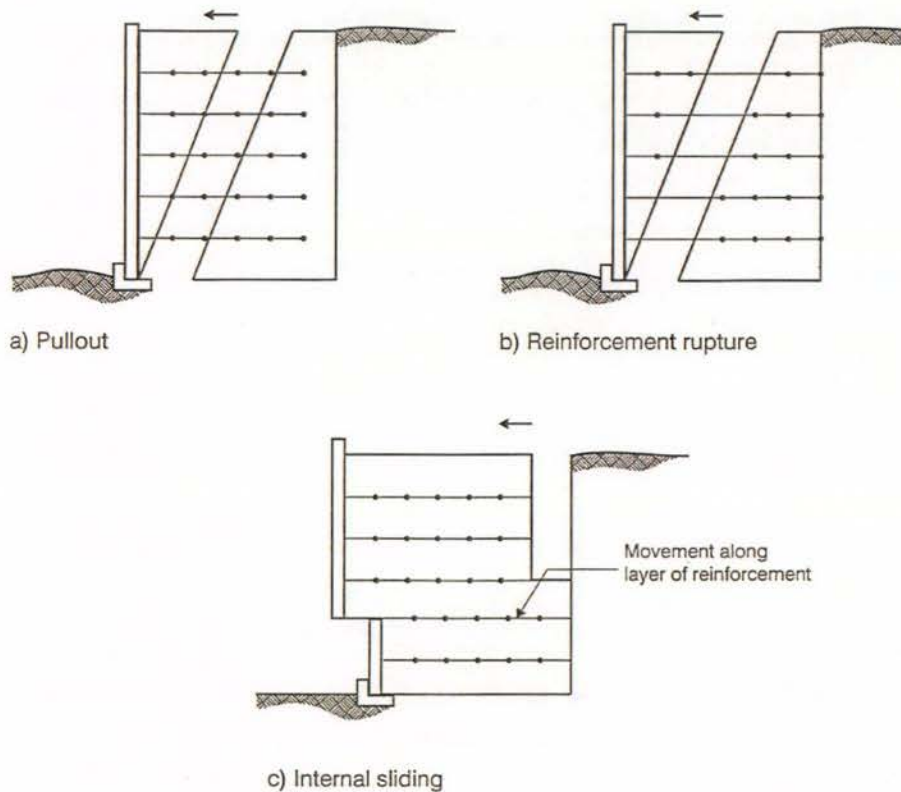


Figure 1-3. Failure modes of external instability. From Murashev (1998).



**Figure 1-4: Internal modes of failure. From Murahsev (2003).**

Internal stability analysis is concerned with the integrity of the reinforced soil block. This can lead to the failure modes shown in Figure 1-4 and includes: (a) Reinforcement pullout (b) Reinforcement rupture, and (c) Internal sliding of layers upon one another.

It is obvious that three key design parameters of the reinforced soil block are: reinforcement layout which concerns the vertical spacing between reinforcement layers ( $S_v$ ), and length-to-wall-height ratio ( $L/H$ ); and the inclination of the wall. These design parameters affect wall stability under self-weight, external and seismic loading.

In general static design, different design methods will predict generally similar vertical spacing and length of reinforcement requirements. However in the case of seismic design, different design methods can predict very different vertical spacing and length of reinforcement, indicating that the behaviour of GRS structures under seismic loading is still not fully understood.

### **1.2.3 Seismic design**

There is no widely held consensus on seismic design procedures (Murashev 2003), and many design codes (for instance BS 8006:1995) do not include seismic design at all. Despite this, GRS walls have performed very well in recent earthquakes and this is discussed in Section 1.3 below. Hence the behaviour of GRS walls during earthquakes requires further clarification (Watanabe et al. 2003). The current knowledge of the GRS behaviour under seismic excitation and the seismic aspects of design are discussed in Chapter 2.

## **1.3 Performance during some recent earthquakes**

There is considerable evidence to highlight the good performance of reinforced soil retaining walls during recent earthquakes such as that in Northridge (1994), Kobe (1995), and Chi-Chi (1999). During these earthquakes, significant damage of conventional retaining wall structures was reported, whilst reinforced soil structures demonstrated limited to no damage (Ling et al. 2001; Sandri 1997; Tatsuoka et al. 1996). In many cases, the reinforced soil walls either had no seismic design, or seismic design which considered a Peak Ground Acceleration (PGA) of only 20% of that actually experienced (Gazetas et al. 2004). This highlights the inherent stability of reinforced soil against high seismic loads and conservatism in current design practices (White and Holtz 1997).

The field experiences of the abovementioned earthquakes are summarised briefly below.

#### *Northridge Earthquake (1994)*

The 1994 Northridge earthquake of California, United States, was of moment magnitude 6.7, with the duration of strong shaking lasting 10 to 15 seconds. Vertical shaking components up to 1.5 times higher than horizontal accelerations were recorded by Shakal et al. (1994), as reported by Sandri (1997), and this was a large factor contributing to the earthquake's relative destructiveness.

Sandri (1997) conducted a review of known geogrid-reinforced Segmental Retaining Walls (SRW) over 4.6 m high. All 11 GRS walls assessed by Sandri (1997) post-earthquake were in "excellent" condition. In particular, the Valencia water treatment plant GRS wall, 6.4 m high and approximately 8 km long, was subjected to peak horizontal accelerations of 0.5g, however the design considered only a peak horizontal acceleration of 0.3g (Cai and Bathurst

1996). Post-earthquake inspection by Sandri (1997) revealed no residual displacement between the segmental block face and soil, indicating a good connection between reinforcement and the facing blocks. Some intermittent surface tension cracks (< 6 mm wide) were noted near the back of the reinforced soil block, and this would indicate mass movement of similar magnitude. In comparison, two cantilever walls located close by experienced significant residual deformation, and required extensive repairs.

#### *Kobe Earthquake (1995)*

The Kobe earthquake of Japan in 1995 was magnitude 7.2 and caused widespread structural damage (Tatsuoka 2008). Peak ground accelerations of around 0.5g were recorded (Koseki et al. 2006).

Tatsuoka (2008) reports a number of old gravity, leaning and masonry type retaining walls which demonstrated complete collapse, while a number of modern reinforced concrete cantilever walls were also seriously damaged. In contrast, a number of GRS walls with Full-Height Rigid (FHR) facings, subjected to similar severe ground motions, performed very well.

One GRS wall with FHR facing called the Tanata wall, supported a railway line and was investigated in detail by Tatsuoka (2008). The 6.2 m high Tanata wall was subjected to an estimated PGA of 0.7g and survived the earthquake with limited deformation that included tilting of the wall of 26 cm and sliding at the base of 10 cm. Tatsuoka (2008) notes that the Tanata wall did not have extended top layers of reinforcement as was the case for the other walls which performed better than the Tanata wall.

Next to the GRS wall was a reinforced concrete cantilever retaining wall supported by a row of large-diameter bored piles (even though the subsoil conditions were the same as for the GRS wall). This wall demonstrated similar displacements as the GRS wall, however cost approximately double to triple that of the GRS wall due to the bored-pile foundations required. Hence, the relative performance of the GRS wall was considered satisfactory.

Given the good performance of GRS walls, reconstruction efforts of a number of conventional retaining walls which failed during the Kobe earthquake have since focussed on the use of GRS walls with a FHR facing.

### *Chi-Chi Earthquake (1999)*

The Chi-Chi earthquake of Taiwan in 1999 was a 7.3 magnitude earthquake that resulted in 2200 people being killed and extensive structural damage. PGA's larger than 1.0g were recorded. Significant vertical accelerations was also a feature of the ground motion (Ling et al. 2001).

The geography, population density and construction and design methods utilized make GRS application in Taiwan unique. For instance, because of the hilly terrain and high land costs, wall heights of up to 40 m are quite common with the use of in-situ soils in place of select granular backfill. Because of the proprietary nature of the wall systems employed, the majority of walls were faced with modular blocks in a SRW fashion (Ling et al. 2001).

Design of GRS walls is often carried out by geosynthetic reinforcement manufacturers rather than geotechnical specialists. Thus the design risk is carried by the manufacturers rather than geotechnical specialists, and may result in conservative design for static conditions and higher costs. However, there is often limited attention paid to seismic design aspects.

Ling et al. (2001) conducted a post earthquake review of some of the GRS structures around the central Taiwan region. In general, Ling et al. (2001) found many failure cases of stone, reinforced concrete, and tie-back retaining walls. Additionally, a number of geogrid reinforced SRW were also found to have failed. These walls failed primarily with deformation of the modular block facing via sliding, toppling or local instability with bulging evident near the base of the structures. These deformation patterns demonstrated the importance of both seismic design and good connections between the facing blocks and the reinforcement.

In one example, a SRW approximately 10 m high in the Chung Hsin New Village consisted of both reinforced and un-reinforced sections and provided a good comparison of their relative performance. The un-reinforced section had collapsed, whereas the reinforced wall remained stable. This demonstrated the earthquake resistance of the reinforced soil wall.

## **1.4 New Zealand context**

### **1.4.1 New Zealand use of GRS**

Design of GRS in New Zealand is made using several different overseas standards and design guidelines i.e. Federal Highways Administration (FHWA 2001), British Standards Institute (BS8006:1995), Australian Standard (AS4678-2002), and the Deutsches Institut Bautechnik (DIBt). Manufacturers of reinforcement such as Tensar and Stratagrid, also produce design methods and guidelines. Hence, GRS structures in New Zealand have been built with varying resistance to static and seismic loads, and thus different seismic risk (Murashev 2003).

Because of this uncertainty in design, and because the use of GRS in New Zealand was increasing, Transfund New Zealand (now part of the New Zealand Transport Agency) commissioned 'Guidelines for Design and Construction of Geosynthetic-Reinforced Soil Structures in New Zealand' prepared by Murashev (2003). The Guidelines are based on a limit state approach and combine the BS 8006:1995 and FHWA (2001) standards, as well as research to formulate a New Zealand approach to GRS design.

Murashev (1998) also conducted a survey of all GRS structures constructed in New Zealand up to 1998. The survey found at least 54 GRS structures that had been completed. The structures ranged in wall height from 2 m to 13 m. Roughly an equal number of walls (defined as structures inclined at angles larger than  $70^\circ$  to the horizontal) and slopes (inclined at angles less than  $70^\circ$  to the horizontal) were surveyed.

Of the structures surveyed, nearly all were for road applications including slip rehabilitation, embankments, and slope stabilisation. The majority of these roads were minor State Highways or rural roads. Only 4 structures were recorded as for private purposes and included support for a carparking facility, and landscaping.

The predominant method of facing for both slopes and walls was wrap-around methods, and this reflects the low structural performance necessary for the mostly rural applications. Around 30% of the walls were faced by modular keystone blocks or precast concrete blocks.

All of the walls and slopes surveyed by Murashev (1998) were reported to have performed satisfactorily under static conditions. As yet however, no GRS structure in New Zealand has undergone significant seismic excitation, and therefore there is little local experience of their seismic performance. Hence the field experiences of the abovementioned earthquakes can be generalised and applied to the New Zealand context.

The case histories above demonstrate that there has been some cases of large deformation and/or failure of GRS Segmental Retaining Walls (SRW). It should be restated that segmental blocks, and wrap-around geogrids, are the predominant facing types of existing GRS structures in New Zealand (up to 1998, at least). Hence, a similar performance as that which occurred in the Northridge and Chi-Chi earthquakes could be expected.

In contrast, Japan has adopted the use of GRS walls with a Full-Height Rigid facing as standard technology for vulnerable lifeline assets such as high-speed railways. New Zealand has a similar seismic risk, yet to date, the use of FHR facings for vulnerable roadways and the recently nationalised railways, has been limited or non-existent. Thus the use of FHR facing panels, as opposed to the more typical (at least in New Zealand) SRW and wrap-around faced GRS walls, is the facing method used for model tests in this research.

#### **1.4.2 Full-Height Rigid facing**

After the good performance of GRS walls with a Full-Height Rigid (FHR) panel facing during the 1995 Kobe earthquake, Tatsuoka (2008) reports that reconstruction of failed conventional type retaining walls utilised the GRS FHR technology. Because New Zealand has a similarly high seismic risk, it is argued that this technology could also be used in New Zealand. Tatsuoka (2008) provides details of the construction and additional stability achieved during seismic events as compared to conventional retaining walls.

The staged-construction procedure of GRS FHR walls is described in the following steps:

1. A small foundation is constructed for the FHR facing.
2. The geosynthetic reinforced wall is faced with gravel-filled gabions wrapped-around by reinforcement and is compacted in layers as is typical of standard construction for wrap-around faced GRS walls.

The gravel-filled gabions provide three services: a) They create a temporary facing structure for good backfill compaction; b) they act as a drainage layer directly behind the wall face; and, c) they protect the geosynthetic reinforcement and FHR panel connection from relative displacement of the reinforcement and backfill soil post-completion of the wall.

3. At completion of the wrap-around GRS wall, the wall is left to consolidate (if at all) under static conditions.
4. Finally, a thin and lightly steel-reinforced concrete facing is cast in place once ultimate deformation is complete. This creates a single rigid facing panel and a good connection with the exposed geosynthetic reinforcement wrapped around the gravel-filled gabion baskets.

It is noted that there is no need for an external propping support as in the case of conventional reinforced concrete retaining walls. This is especially advantageous in sites with restricted access or difficult terrain.

Tatsuoka (2008) explains a number of advantageous features, as compared with a conventional reinforced concrete retaining wall, that the completed GRS wall with FHR facing demonstrates. These are summarised as follows:

#### *Activation of high earth pressure at the rigid connection with the FHR facing*

A rigid connection ensures that high earth pressures and thus high tensile stresses can be activated in the reinforcement. This condition generates high lateral confining pressures and hence high strength of the reinforced soil.

#### *Full-Height Rigid facing panel*

The FHR facing panel has a high structural integrity which acts to resist localised failures of the wall face (failures such as those demonstrated by GRS SRW faced structures in the Chi-Chi earthquake of 1999). Instead, the location of the critical failure surface is forced to intersect with the FHR toe, resulting in greater resistance against earthquake loading. Additionally, three-dimensional effects make the wall very stable against concentrated vertical and lateral loads.

#### *Geosynthetic reinforcement*

The geosynthetic reinforcement acts to support the FHR facing panel at regular intervals and reduces the overturning moments and sliding forces acting at the facing toe. Hence there is a reduced need for foundations than compared with a conventional cantilever reinforcement concrete structure, whereby the sole resistance to sliding and overturning is activated at the wall toe. In these cases there is often the need for pile foundations.

The above mentioned advantages of FHR faced GRS walls over SRW GRS and wrap-around faced walls are evidenced by increased performance during previous earthquakes and model tests as reported by Matsuo et al. (1998).

### **1.4.3 Sustainable development agenda**

Definitions of sustainable development in New Zealand often converge on the 'Brundtland' definition. For engineering purposes, this relates to the equitable use of economic, social and environmental resources between current and future generations (Statistics New Zealand 2009). Further, the future introduction of a price on carbon will likely have an impact upon private and public decision-making and the selection of one particular retaining wall system over another.

In this context, GRS wall systems are compared with conventional reinforced concrete retaining wall systems along economic, environmental and social criteria to determine its potential in achieving national and international sustainable development goals.

#### *Economic benefits*

A number of advantages of reinforced soil structures over conventional reinforced-concrete (RC) cantilever retaining walls (RW) include: Rapid construction without the need for large construction equipment and many experienced labourers, reduction in space required/land acquisition, reduced need for rigid/deep foundations (FHWA 2001). These advantages lead to reported cost reduction of up to 75% in the UK (Jones 1996) and 50% in the USA compared to RC cantilever RWs (Koerner et al. 1998) as reported by Koseki et al. (2006). In Japan, Tatsuoka (2008) also comments on the cost-effectiveness of GRS FHR walls as compared to RC cantilever RWs.

#### *Environmental benefits*

Jones (1996) conducted an ecological audit of GRS systems to remove possible commercial distortions in the above described economic cost of GRS systems. The audit was made with reference to a RC cantilever RW system over the life-cycle of both structures. For ecological parameters such as energy, labour, dust and sulphur dioxide emissions, and despoiling of land, the GRS system is ecologically cheaper by roughly 30% than RC cantilever RWs. However the GRS system requires roughly 20% more process water than the compared RC cantilever RW.

Further, Tatsuoka (2008) notes that the use of a GRS FHR system results in a reduction in total CO<sub>2</sub> emissions compared to conventional retaining technology. Thus in addition to the environmental benefits, the cost on carbon is likely to also result in further cost reductions for a GRS wall, when compared to conventional RC RWs.

### *Social benefits*

It is unlikely there is any particular substantive social benefit in the trade-off between GRS vs conventional RWs systems as defined by the Statistics New Zealand social dimension definition (2009). However, as noted above, the need for experienced labour and construction machinery is reduced (FHWA 2001), and this could be an advantage in developing countries where such skills and equipment is in short supply.

From the above arguments it can be seen that GRS systems offer substantial benefits in meeting sustainable development goals and that as part of this, substantial benefits in cost effectiveness over conventional RW systems. However Murashev (2003) notes that unless GRS systems in New Zealand are fully understood, and the uncertainty in design is removed, consultants will prefer to use conventional structures. Further, if a GRS design is selected, consultants often impose strict performance-based specifications upon contractors to carry all design and construction risks. This results in higher costs to Road Controlling Authorities in New Zealand than could otherwise be achieved.

## **1.5 Research objectives**

### **1.5.1 Research aims**

This study focuses on the seismic performance of GRS retaining walls, particularly pre-failure deformation. The influence of reinforcement length-to-height ratio (L/H) and the inclination of the wall on this seismic performance is investigated at varying levels of shaking intensity. The specific objectives of the project were to:

- Develop procedures for shake-table tests on GRS walls.
- Quantify the influence of the L/H ratio and wall inclination on seismic behaviour.
- Identify failure mechanisms and patterns of deformation. Utilise GeoPIV to examine in detail deformation within the wall during seismic loading.

- Identify critical issues for further research studies.

To achieve the abovementioned research aims, a series of 7 reduced-scale model tests were conducted using the University of Canterbury shake-table. The L/H ratio and wall inclination was varied from test to test and wall facing displacement, acceleration within the backfill, and deformations within the backfill were measured during testing. Details of the experimental model are provided in Section 3.

## **1.5.2 Organisation of Thesis**

This thesis consists of six main chapters.

Chapter 2 examines the additional aspects considered in a seismic design, which consider the inertia force, seismic earth pressure, acceleration amplification and the critical acceleration threshold of the structure. The static and seismic performance of GRS walls under field and model scale conditions is discussed. Chapter 3 provides the details of the experimental model and in particular provides details of the model similitude such that results at model scale can be generalised at prototype scale.

Chapter 4 presents the main body of results from the shake-table tests. It is divided into 2 parts. The first part presents the raw results from one of the tests, Test-6, followed by analysis of these results using established techniques. The second part presents the raw results from the entire tests series and conducts parametric analysis to determine the influence of the L/H ratio and wall inclination on seismic performance.

The deformation data obtained from the test series is presented in Chapter 5 in two different forms. The first method uses sand markers within the backfill to plot the progression of deformation throughout the wall during testing and enable final deformation patterns to be viewed by eye. The second method utilises GeoPIV to more accurately determine and quantify the deformation in detail, in particular, at early stages in its development, when deformation was not visible to the naked eye.

Chapter 6 concludes the study and makes some recommendations for design and future research.

## References

- British Standards Institute. (1995). *BS8006:1995 - Code of Practice for strengthened/reinforced soils and other fills.*
- Cai, Z., and Bathurst, R. J. (1996). "Seismic-induced permanent displacement of geosynthetic-reinforced segmental retaining walls." *Canadian Geotechnical Journal*, 33(6), 937-955.
- Fairless, G. J. (1989). "Seismic Performance of Reinforced Earth Walls," University of Canterbury, Christchurch.
- FHWA. (2001). "Mechanically Stabilized Earth Walls and Reinforced Soil Slopes Design and Construction Guidelines".
- Gazetas, G., Psarropoulos, P. N., Anastasopoulos, I., and Gerolymos, N. (2004). "Seismic behaviour of flexible retaining systems subjected to short-duration moderately strong excitation." *Soil Dynamics and Earthquake Engineering*, 24(7), 537-550.
- Jones, C. J. F. P. (1996). *Earth reinforcement and soil structures*, Thomas Telford London.
- Koerner, R., Soong, T. Y., and Koerner, R. M. (1998). "Earth retaining wall costs in USA." Geosynthetics Research Institute, Folsom, Pennsylvania.
- Koseki, J., Bathurst, R. J., Guler, E., Kuwano, J., and Maugeri, M. "Seismic stability of reinforced soil walls." *8th International Conference of Geosynthetics (ICG)*, Yokohoma, Japan, 51 - 77.
- Ling, H. I., Leshchinsky, D., and Chou, N. N. S. (2001). "Post-earthquake investigation on several geosynthetic-reinforced soil retaining walls and slopes during the ji-ji earthquake of Taiwan." *Soil Dynamics and Earthquake Engineering*, 21(4), 297-313.
- Matsuo, O., Yokoyama, K., and Saito, Y. (1998). "Shaking table tests and analyses of geosynthetic-reinforced soil retaining walls." *Geosynthetics International*, 5(1-2), 97-126.
- Murashev, A. K. (1998). "Design and construction of geosynthetic-reinforced soil structures in New Zealand.", Transfund New Zealand.
- Murashev, A. K. (2003). "Guidelines for Design and Construction of Geosynthetic-Reinforced Soil Structures." Transfund New Zealand.
- Sandri, D. (1997). "Performance summary of reinforced soil structures in the Greater Los Angeles area after the Northridge earthquake." *Geotextiles and Geomembranes*, 15(4-6), 235-253.
- Shakal, A., Huang, M., Darragh, R., Cao, T., Sherburne, R., Malhotra, P., Cramer, C., Sydnor, R., Graizer, V., Maldonado, G., Peterson, C., and Wampole, J. (1994). "CSMIP Strong-Motion Records from the Northridge, California Earthquake of January 17, 1994." *OSMS 94-07*, Office of Strong Motion Studies, Division of Mines and Geology, California Department of Conservation.

- Statistics New Zealand. (2009). "Measuring New Zealand's Progress Using a Sustainable Development Approach: 2008." Wellington: Statistics New Zealand.
- Tatsuoka, F. "Geosynthetic-reinforced soil structures: A cost-effective solution combining two engineering disciplines." *19th Carillo Lecture - Mexican Society for Soil Mechanics*, Aguascalientes.
- Tatsuoka, F., Tateyama, M., and Koseki, J. (1996). "Performance of soil retaining walls for railway embankments." *Soils and Foundations*(Special), 311-324.
- Watanabe, K., Munaf, Y., Koseki, J., Tateyama, M., and Kojima, K. (2003). "Behaviors of several types of model retaining walls subjected to irregular excitation." *Soils and Foundations*, 43(5), 13-27.
- White, D. J., Take, W. A., and Bolton, M. D. (2003). "Soil Deformation measurement using particle image velocimetry (PIV) and photogrammetry." *Geotechnique*, 53(7), 619 - 631.
- White, D. M., and Holtz, R. D. (1997). "Performance of geosynthetic-reinforced slopes and walls during the Northridge, California Earthquake of January 17, 1994." *Earth Reinforcement*, 2, 965-972.



## **CHAPTER 2**

### **LITERATURE REVIEW**

#### **2.1 Introduction**

A review of current static design methodology is not the purpose of this literature review. However, such a review may be found in the New Zealand Guidelines prepared by Murashev (2003). Rather, the extra design considerations for GRS walls under seismic loading, and their treatment, are discussed in Section 2.2. Specifically, this includes inertial and earth pressure forces active on the GRS structure during an earthquake. The impact of acceleration amplification on these additional seismic forces is explained.

The critical acceleration of a structure is discussed as a threshold acceleration above which, theoretically, permanent deformation occurs. Hence, the structure-specific critical acceleration provides an important measure of stability and is a key parameter in performance-based design approaches.

Significant research has been conducted to support key design assumptions and determine behaviour under seismic loading. However, Koseki et al. (2006) states the need for experimental research that further clarifies:

- Methods to evaluate earth pressures under high seismic loads

- Methods to evaluate displacements and/or deformation of earth structures under high seismic loads

In light of these needs, Section 2.3 discusses research relating to the reinforcement length-to-wall-height ratio ( $L/H$ ) and wall inclination on stability and seismic performance. Section 2.4 looks at the mechanisms of deformation of GRS walls and how these contribute to their seismic performance.

## **2.2 Seismic design aspects**

### **2.2.1 General**

Static design methods produce GRS wall designs that perform well under seismic loading conditions, though often without any form of seismic design (Gazetas et al. 2004; Ling et al. 2001). This implies a high degree of conservatism in current static design methods, and underlines a lack of understanding of GRS behaviour under high seismic loading (Koseki et al, 2006).

Seismic design is considered in codes/guidelines such as FHWA (2001) and Murashev (2003) and is based mostly on pseudo-static methods. However different methodologies still predict different reinforcement densities (i.e. vertical spacing and lengths). Additionally, there are further differences in how researchers believe seismic issues should be treated. These differences centre mostly on:

- The use of partial factors vs global factors of safety
- Selection of an appropriate horizontal acceleration coefficient for design and its relationship with a site specific Peak Ground Acceleration (PGA)
- How amplification of design accelerations within the backfill should be treated
- Prediction of stability and deformation.

The first issue is code-dependant, while the second issue is out of scope of this report and a discussion of local site effects and PGA selection can be found in Kramer (1996). The latter two issues are discussed in the following sections.

A number of methods are available which consider additional seismic forces. Shukla (2002) divides seismic analysis procedures into roughly three categories:

- Pseudo-static methods
- Allowable-displacement methods
- Dynamic finite element/finite difference methods.

Pseudo-static methods are based on conventional static limit equilibrium analysis extended to include additional destabilising forces resulting from an earthquake ground motion. Mononobe-Okabe (MO) earth pressure theory is used to determine seismically induced forces (Okabe 1926). This method is specified by Murashev (2003) and FHWA (2001) for the design of GRS structures.

Where large ground motions are predicted, greater than a PGA of 0.3g, large scale deformation and/or sliding could be expected. Design based on Pseudo-static methods using MO theory is often highly uneconomical and impractical (Murashev 2003). In these cases, Murashev (2003) and FHWA (2001) suggest an allowable displacement approach should be used where some deformation would not result in structural failure. This allows the design to be based on a reduced horizontal acceleration coefficient,  $k_h$ , resulting in a more economical and practical design (Murashev 2003).

Further, the limit equilibrium approach cannot predict deformation or displacements, only the onset of instability. Thus a number of approaches, based on Newmark sliding-block theory (Newmark 1965) exist to predict order-of-magnitude displacement of the structure under earthquake loading. However, these approaches depend on an accurate estimation of critical acceleration (i.e. the acceleration at which the permanent deformation occurs), otherwise it is difficult to predict displacement accurately (Koseki et al. 1998). Researchers' opinions also differ on the best method to estimate a structure's critical acceleration.

Dynamic finite element/finite difference methods have been reported in the literature for the analysis of GRS structures with seismic loading (El-Emam et al. 2004; Hatami and Bathurst 2000; Ling et al. 2004; Ling et al. 2005; Segrestin and Bastick 1988). However a discussion of these advanced methods is out of scope of this report.

## 2.2.2 Inertia forces

During an earthquake, horizontal and vertical acceleration components are propagated up through the GRS wall; these accelerations act to increase the earth pressure, and create inertial loads on the facing and active wedge. The additional seismic forces acting on the reinforced soil block are shown in Figure 2-1 below.

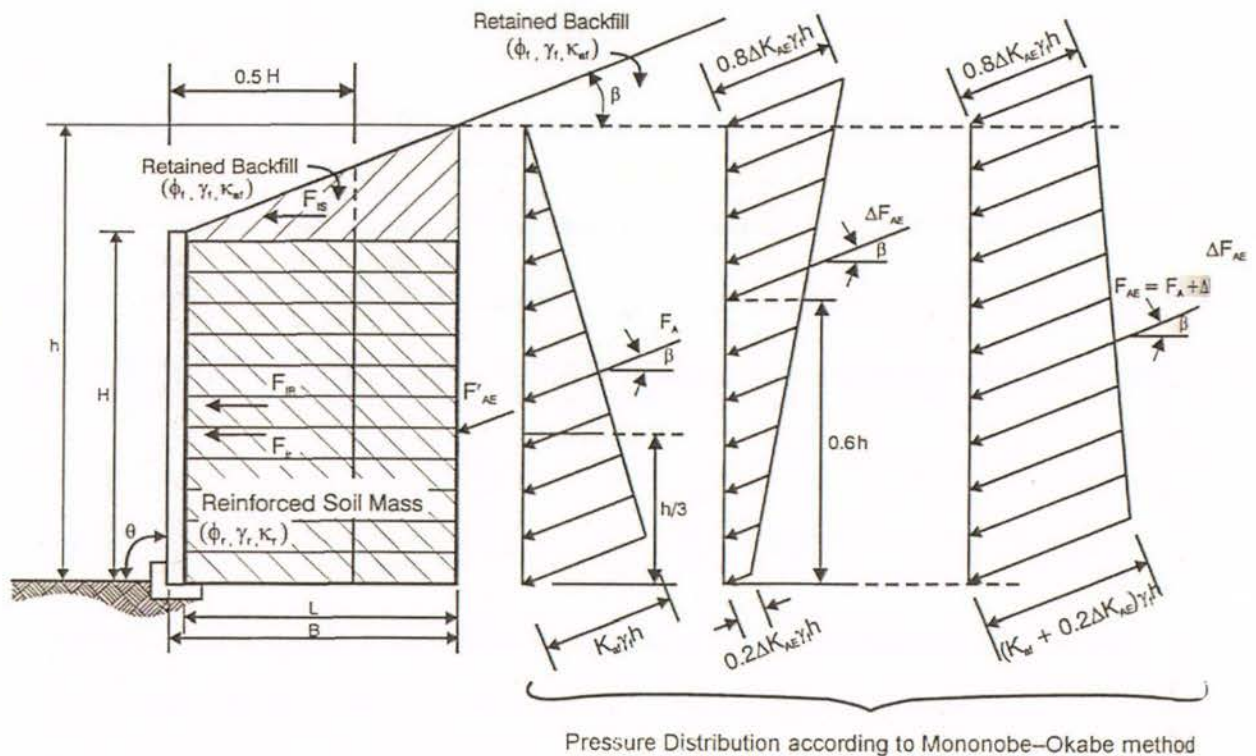


Figure 2-1. Inertia forces and dynamic earth pressure increments additional to static forces acting on a GRS wall during an earthquake. From Murashev (2003).

Figure 2-1 shows the inertia force, and earth pressure distribution acting on the wall. The inertia force is equal to the mass,  $m$ , factored by the design seismic acceleration coefficient,  $k_h$ , and acceleration due to gravity,  $g$ . The inertia forces are shown for the reinforced soil block,  $F_{ir}$ , and the inclined backfill,  $F_{is}$ , which contribute to the total inertia force,  $F_{IR}$ . Should there be a substantial difference in the weight of the facing type used and the soil, then the facing mass should also be considered to contribute to the total inertia force.

Murashev (2003) specifies that only the mass contained in the front  $0.5H$  of the reinforced soil block is considered to contribute to the inertial force,  $F_{ir}$ . This is because the inertia

forces of the reinforced soil block and retained backfill will be unlikely to reach peak values at the same time.

Figure 2-1 also shows the total earth pressure distribution acting on the back of the wall made up of its static and dynamic seismic earth pressure components. The resultant total dynamic seismic force,  $F_{AE}$ , comprises the resultant static force,  $F_A$ , and the resultant dynamic increment force,  $\Delta F_{AE}$ . The derivation of the resultant earth pressure forces is explained below.

### 2.2.3 Seismic earth pressure

GRS walls are flexible structures (Gazetas et al. 2004) and as such develop minimum active and maximum passive earth pressures (Kramer 1996). The pseudo-static MO approach is used to determine the seismic earth pressure acting to destabilise the wall Murashev (2003). MO theory is an extension of Coulomb theory with the addition of pseudo-static horizontal and vertical accelerations acting upon the Coulomb failure wedge. Thus for the purposes of design, the total dynamic active soil pressure,  $F_{AE}$ , can be expressed as in Equation 2-1 (based on Murahev 2003; Kramer 1996).

$$F_{AE} = 0.5 (1 - k_v) K_{AE} \gamma h^2 \quad (2-1)$$

Where  $k_v$  is the design vertical seismic coefficient (as a fraction of acceleration due to gravity,  $g$ ),  $\gamma$  is the soil density,  $h$  is the wall height, and  $K_{AE}$  is the total earth pressure coefficient expressed as Equation 2-2.

$$K_{AE} = \frac{\cos^2(\phi - \xi - 90 + \theta)}{\cos \xi \cos^2(90 - \theta) \cos(\beta + 90 - \theta + \xi) \left[ 1 + \sqrt{\frac{\sin(\phi + \beta) \sin(\phi - \xi - \beta)}{\cos(\beta + 90 - \theta + \xi) \cos(\beta - 90 + \theta)}} \right]^2} \quad (2-2)$$

Where  $\beta$  is the backfill slope angle with the horizontal,  $\theta$  is the inclination of the face with the horizontal,  $\phi$  is the soil angle of friction and  $\xi$  is the seismic inertia angle (Shukla 2002) as defined in Equation 2-3. All other angles are shown in Figure 2-1.

$$\xi = \tan^{-1} \left[ \frac{k_h}{(1 - k_v)} \right] \quad (2-3)$$

Where  $k_h$  is the horizontal seismic coefficients (as a fraction of acceleration due to gravity,  $g$ ).

As seen in Figure 2-1 above,  $F_{AE}$ , can be divided into its static,  $F_A$ , and dynamic increment,  $\Delta F_{AE}$ , components. The static earth pressure is distributed hydrostatically, thus the resultant force acts at  $h/3$ . Seed and Whitman (1970) assume the dynamic force increment to act at  $0.6h$ . Hence the location of the resultant total dynamic earth force normally acts at around half the wall elevation, or  $0.5h$  (Kramer 1996).

An approximate solution for the critical failure surface was determined by Zarrabi-Kashani (1979) and reported by Kramer (1996) as shown in Equation 2-4a.

$$\alpha_{AE} = \phi - \psi + \tan^{-1} \left[ \frac{-\tan(\phi - \psi - \beta) + C_{1E}}{C_{2E}} \right] \quad (2-4a)$$

Where  $\alpha_{AE}$  is the critical failure surface angle with the horizontal plane and  $\delta$  is the interface friction angle between soil and wall face. Factors  $C_{1E}$  and  $C_{2E}$  are defined in Equations 2-4 (b) and (c).

$$C_{1E} = \sqrt{\tan(\phi - \psi - \beta) \left[ \tan(\phi - \psi - \beta) + \frac{1}{\tan(\phi - \psi - \theta^*)} \right] \left[ 1 + \frac{\tan(\delta + \psi + \theta^*)}{\tan(\phi - \psi - \theta^*)} \right]} \quad (2-4b)$$

$$C_{2E} = 1 + \left\{ \tan(\delta + \psi + \theta^*) \left[ \tan(\phi - \psi - \beta) + \frac{1}{\tan(\phi - \psi - \theta^*)} \right] \right\} \quad (2-4c)$$

It is important to note that the wall face inclination angle,  $\theta^*$ , is made with respect to the *vertical*, as defined by Kramer (2006).

The inclination of the wedge is shallower than the static case (Kramer 2006), and this reflects a larger active wedge formed due to the introduction of seismic forces.

As MO theory is an extension of Coulomb theory, the limitations associated with Coulomb theory are applicable. One of these is that the reinforced soil block is considered rigid, and by definition, the shear wave velocity of the soil profile is considered infinite, and the base acceleration propagates instantly into the block. The pseudo-static analysis precludes

deformation of the rigid block and the dynamic changes in the peak ground acceleration during wave propagation. It thus becomes difficult to assess the appropriate design seismic coefficient to determine dynamic earth pressures (Kramer 2006).

An additional problem with the MO pseudo-static method is that it has been demonstrated to over-predict earth pressures and it generally results in a highly conservative design (e.g. Kramer 1996; Murashev 2003; Wood 2008). Further, Koseki et al. (1998) conducted reduced-scale model tests on both conventional type and reinforced soil walls, and compared the MO-predicted failure plane angles with those observed at failure. The MO calculated failure planes were shallower than those observed, with the largest discrepancy observed for the reinforced soil wall.

Contrasting with these results are studies conducted by El-Emam and Bathurst (2004) on reduced-scale reinforced soil models which showed the predicted MO failure planes to be steeper than the observed failure plane. The comparison of the calculated failure surface angle, and that interpreted from inclinometer tube measurements is shown in Figure 2-2.

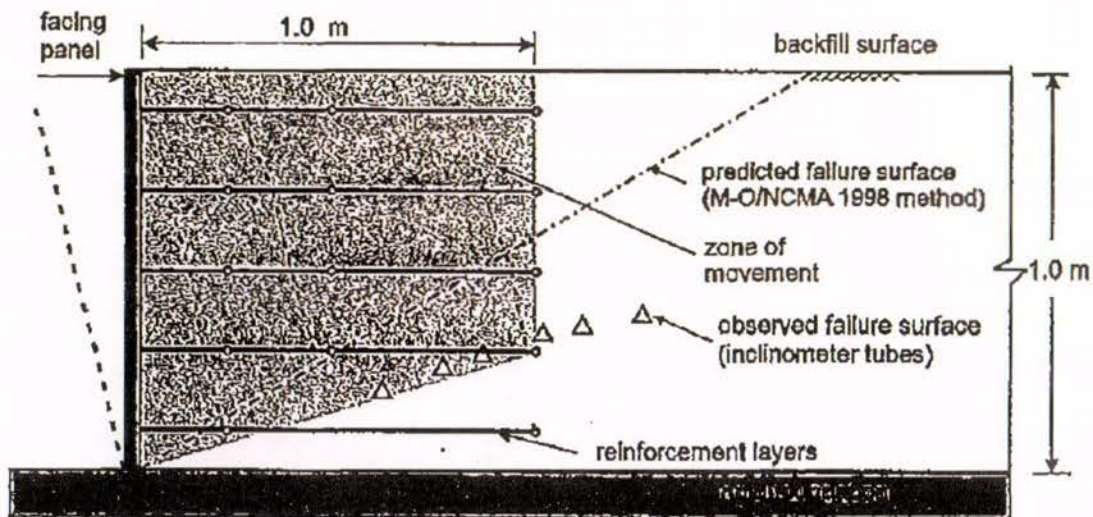


Figure 2-2. Failure plane interpreted from inclinometer tubes and extensimeters compared with the predicted failure surface by MO theory. From El-Emam and Bathurst (2004).

The discrepancy between the observed and predicted failure planes made by MO analysis for both studies, in general, shows that the behaviour and deformation of reinforced soil walls is not well understood.

## 2.2.4 Acceleration amplification

Considerable evidence from previous earthquakes notes local site effects (Kramer 2006). Experimental evidence from reduced-scale model tests on reinforced soil models show that these structures are no exception, and that the ground motion is modified within the structure (El-Emam and Bathurst 2004; Law and Ko 1995; Nova-Roessig and Sitar 2006). Further, De and Zimmie (1998) show the soil-reinforcement interaction to influence ground motion propagation through the structure in reduced-scale model tests in a geotechnical centrifuge.

Whilst an in-depth discussion of the fundamentals of acceleration amplification is not the subject of this chapter, a single degree of freedom (SDOF) model is used to briefly illustrate the problem and soil parameters involved. The SDOF model has a stiffness,  $k$ , and is undergoing forced vibration by ground motion at frequency,  $\omega$ . The model has a fundamental circular frequency,  $\omega_0$  as shown in Equation 2-6 below, proportional to its stiffness and mass,  $m$ .

$$\omega_0 = \sqrt{k/m} \quad (2-5)$$

The second order differential equation describing the motion of the soil system is solved for the soil profile's displacement response as a function of the input ground motion and an amplification factor, AF. The amplification factor is dependent on the system damping characteristics and the ratio of the frequency of the input ground motion to the fundamental frequency of the soil structure.

Figure 2-3 plots the amplification factor for the SDOF model as a function of damping ratio and ratio of the excitation frequency to the SDOF natural frequency.

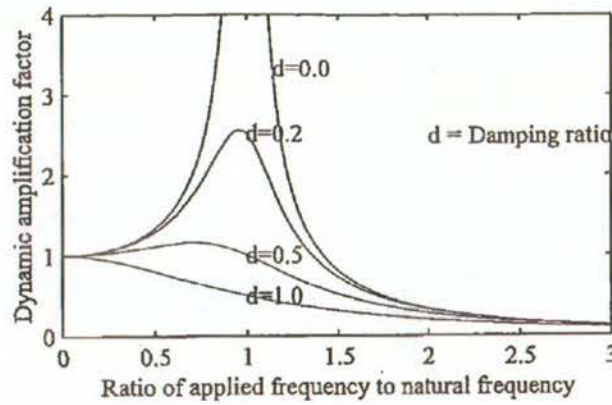


Figure 2-3. Effect of soil properties on the dynamic amplification of acceleration within the reinforced soil wall. (From Law and Ko)

As seen in Figure 2-3, a ‘resonance’ condition occurs when the applied frequency of ground motion is equal to the natural frequency of the SDOF model. This would lead to excessive amplification of motion within the soil profile.

It should be noted that during an earthquake, strain development leads to a reduction in soil stiffness,  $G$ , and an increase in damping. Using the SDOF analogy shown in Equation 2-5, this alters the fundamental frequency of the soil profile and soil wall system. Hence the amplification factor will also change during an earthquake.

Amplification of acceleration is a design concern because it can generate larger accelerations leading to larger destabilizing dynamic earth pressure and wall inertia. The Australian Standard (AS4678-2002) notes that acceleration amplification can act to increase seismically induced displacements. However, as noted above in Section 2.2.3, the pseudo-static methods assume that the acceleration is uniform over the height of the structure. Hence to account for amplification of design accelerations in their pseudo-static analyses, FHWA (2001) modify the design horizontal acceleration coefficient,  $k_{h,des}$ , as in Equation 2-6.

$$k_{h,des} = (1.45 - k_h) k_h \quad (2-6)$$

Where  $k_h$  is limited to 0.45, whereby after that  $k_{h,des}$  is assumed to equal  $k_h$ . The design acceleration,  $k_{h,des}$ , is used for both external and internal stability calculations and applied at around mid-height of the wall.

In contrast, where some lateral movement of the wall can be tolerated, Murashev (2003) suggests the design acceleration,  $k_{h,des}$  can be reduced 40% for external and internal sliding stability analyses, and acceleration amplification is not considered. However, internal stability analysis of reinforcement pullout and rupture *does* consider acceleration amplification with Equation 2-7.

$$k_{h,int} = (1.3 - k_h) k_h \quad (2-7)$$

Again,  $k_{h,int}$  is applied at around mid-height of the wall.

The effect of Equations 2-6 and 2-7 is an amplified design horizontal acceleration coefficient for seismic coefficients less than 0.45 and 0.3, respectively. The limit of 0.45g is based on some finite element modelling work by Segrestin and Bastick (1988). The authors note that the work is highly idealised and limited. The different limiting coefficient of 0.3 proposed by Murashev (2003) is unexplained.

Experimental and numerical modeling shows that both amplification and de-amplification occurs in GRS walls. Nova-Roessig and Sitar (2006) showed that wall top motion was amplified by up to 2.3 times for accelerations less than 0.15g, and that de-amplification generally occurred for base input accelerations larger than 0.46g. This would seem to validate the Equation 2-6 used by FHWA (2001).

However, other studies show that the amplification can be more significant than suggested by Equations 2-6 and 2-7. Fairless (1989) reported accelerations at the wall top up to three times larger than that at the wall base. El-Emam and Bathurst (2004) showed amplification of the acceleration at the top of the facing panel up to 2.25 times, with accompanied amplification of the backfill soil up to 1.75 for accelerations larger than 0.5g.

Matsuo et al. (1998) separated the amplification of motions into that in the forward and backward directions. The results showed an amplification of forward accelerations for all levels of shaking, however a de-amplification of backward accelerations at accelerations larger than around 0.3g. The authors attributed this to the soil along the sliding surface being unable to transmit the restoring acceleration up into the sliding block.

In addition to the variant amplification factors used by FHWA (2001) and Murashev (2003) for external and internal stability analyses, further debate also centers on how best to take into account acceleration amplification for design purposes. Cai and Bathurst (1996) argue that the location of dynamic earth pressure increment at 60% the wall height from the bottom of the wall may indirectly account for acceleration amplifications.

Steedman and Zeng (1990) modeled the soil profile with MO assumptions, but with a finite shear wave velocity of the soil profile, instead of infinite shear wave velocity, as in a rigid block assumption. Thus the acceleration within the soil varies as a function of depth and soil behavior such as phase change of ground motion and amplification can be accounted for pseudo-dynamically.

### 2.2.5 Critical acceleration

The critical acceleration is defined by Bracegirdle (1980) as “the horizontal pseudo-static acceleration acting uniformly over the structure to achieve limiting equilibrium.” For each mechanism of failure, considered typically as rotation and sliding of the reinforced soil block, the structure will have an associated critical acceleration at which point the dynamic factor of safety against this failure mechanism will be less than 1, and permanent displacement will be induced.

A general form of the dynamic factor of safety,  $FS_d(t)$  is shown in Equation 2-8 below.

$$FS_d(t) = \frac{\text{available resisting force}(t)}{\text{driving force}(t)} \quad (2-8)$$

Note that  $FS_d(t)$  varies during an earthquake as both the driving and resisting forces are functions of the ground motion response and therefore time. For instance, considering limiting equilibrium against sliding, i.e. setting  $FS_d(t)$  equal to unity, the critical acceleration which would induce sliding can be determined. Hence, accelerations larger than this value may generate large permanent displacements.

Model studies have demonstrated the existence of threshold critical acceleration values for gravity retaining walls (Lai 1979) and for reinforced soil walls (El-Emam and Bathurst 2004; Koseki et al. 1998; Matsuo et al. 1998; Nova-Roessig and Sitar 2006; Sakaguchi 1996;

Watanabe et al. 2003). In these studies, accelerations larger than some threshold value generate large permanent displacements.

Matsuo et al. (1998) conducted multiple reduced-scale model tests on geosynthetic-reinforced soil walls. Figure 2-4 shows the normalized residual wall top displacement, ( $d_{h3}/H$ ) for each wall type with increasing base input acceleration.

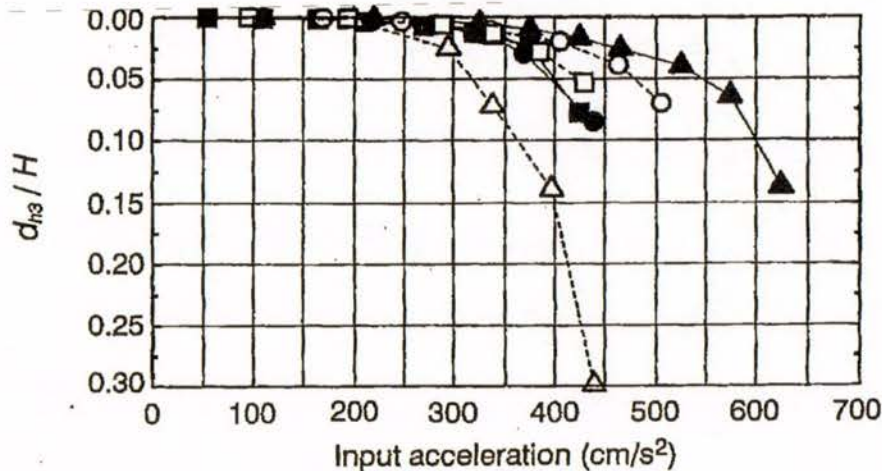


Figure 2-4. Normalised residual wall top displacement,  $d_{h3}/H$ , as a function of increasing base input acceleration for a number of different model wall types. The relationships are approximately bi-linear and demonstrate evidence of model type-specific critical acceleration (From Matsuo et al, 1998).

The residual displacement of the wall top demonstrates a bi-linear trend for each wall type. That is, deformation is small until some threshold base input acceleration, at which point deformation is suddenly increased. The critical acceleration for the model walls is seen to be around  $200 \text{ cm/s}^2$  to  $350 \text{ cm/s}^2$  (0.2g to 0.35g).

Critical acceleration is thus an important parameter which can quantify the outset of instability. A high critical acceleration implies a higher acceleration necessary to induce failure, and reduced deformation at low accelerations.

A number of methods exist to estimate the critical acceleration, based generally on Equation 2-8 above. Elms and Richards (1979) extended MO-theory to include wall inertia forces and base friction, to estimate earthquake-induced rigid-block sliding displacements of gravity retaining walls.

In order to account for other possible modes of failure evident for reinforced soil walls, Cai and Bathrust (1996) extended the sliding block model to determine seismically-induced permanent displacement of GRS SRW. In addition to rigid-block sliding, limit equilibrium stability analysis considered two extra potential failure modes for the GRS SRW as: Sliding along individual reinforcement layers ('internal type failure'); and internal sliding between SRW facing units (facing failure). Analytical equations for the critical acceleration for each mode of failure were determined.

The estimation of critical acceleration suffers from the limitations of pseudo-static limit equilibrium analysis. Matsuo et al. (1998) best illustrated this with a calculation of critical acceleration using pseudo-static methods for GRS models of different reinforcement length and vertical spacing and wall inclination. Despite these differences, the model walls' calculated critical acceleration for overturning varied between 0.45g – 0.55g and for sliding, varied between 0.6g – 0.75g. However, as shown in Figure 2-4, the observed critical acceleration varied between 0.2g – 0.35g.

## **2.2.6 Performance-based design**

Performance-based design allows designers to predict the behaviour of a structure during an earthquake. The design methodology allows designers to first select an allowable displacement, i.e. performance, which can be tolerated during an earthquake. Tolerance of some movement can lead to a reduction in the seismic coefficient used for design and hence create a more cost effective solution (Richards and Elms 1979). For instance, Wood (2008) determined that in areas of the highest seismic hazard in New Zealand, where up to 100 mm movement of the RW can be tolerated, the PGA can be reduced by up to 50%.

To calculate the permanent displacement of the structure during an earthquake, the sliding block theory proposed by Newmark (1965) is used. The reinforced soil block is treated as a rigid-plastic monolithic mass with a critical acceleration calculated as described in Section 2.2.5. An appropriate acceleration time history is applied to the soil block; permanent displacement occurs only when the ground acceleration exceeds the soil block critical acceleration, or the velocity of the soil block is greater than zero. This concept, and the process of double-integration of the acceleration time history is shown graphically in Figure 2-5 below.

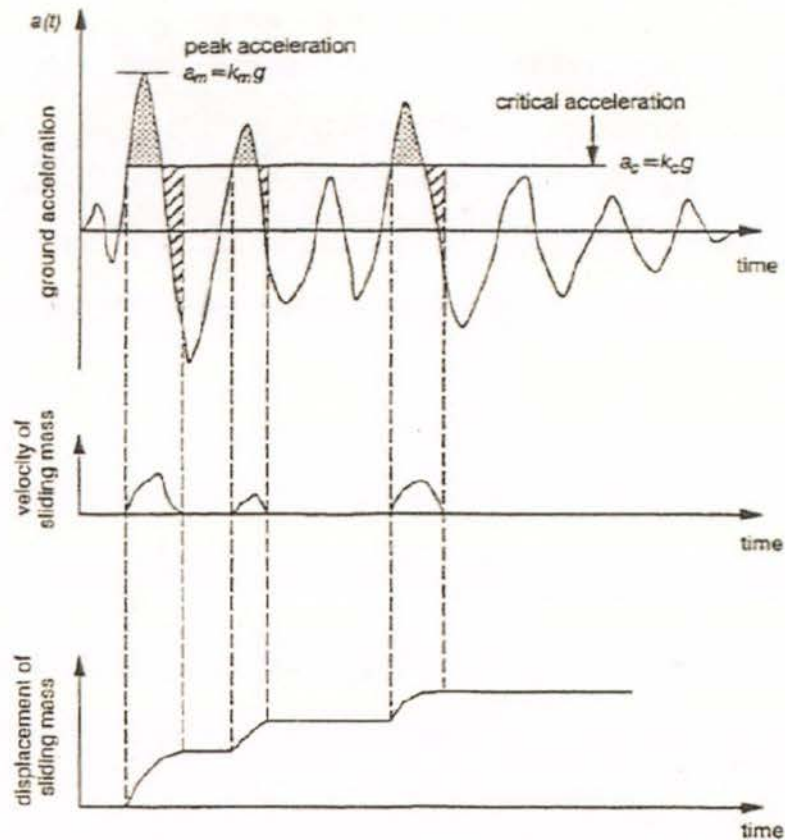


Figure 2-5. Permanent displacement calculation using Newmark's sliding-block method. From Cai and Bathurst (1996)

The predicted displacement can then be compared with that considered tolerable and the design evaluated against the desired performance.

Where ultimate wall failure is by sliding, and hence closest to the original assumptions made by Newmark (1965), reduced-scale tests by Fairless (1989) and Nagel (1985) demonstrate that the Newmark predicted displacement is in good agreement with experimental results.

However, Matsuo et al. (1998) notes that the GRS walls are subjected to continuous deformation (i.e. do not obey rigid-perfectly plastic behaviour), and this results in an underestimation of displacement when using sliding block models. Further, displacement prediction is highly sensitive to the selection of critical acceleration values for each particular mode of failure. It is therefore vulnerable to the issues described in Section 2.2.5.

## **2.3 Parameters which influence seismic performance**

Leshchinsky (2000) postulated that the main objective of design is to produce safe and economical structures. The non-collapse of GRS in recent earthquakes indicates that the first objective has, in the large part, been achieved with modern design techniques. However, GRS walls predominantly fail in a ductile manner, where displacements, not necessarily ultimate failure, are of concern. Hence, the performance of GRS, at an acceptable cost, is the subject of considerable research (Koseki et al., 2006).

Two important parameters which influence ultimate stability and performance of a GRS wall are the reinforcement arrangement, and the wall inclination. For the static case, there are limited examples of fully instrumented GRS structures in the field, thus there is minimal field data that can be used to assess performance and/or critical design assumptions (Fannin and Hermann, 1990; Zornberg and Arriaga, 2003). Even less field data exists under seismic loading and in many cases the soil properties have not been modelled appropriately making analysis difficult (Ling et al. 2004).

Hence the influence of L/H ratio and wall inclination on static and seismic performance has been the subject of some previous experimental research using tilt-table, shake-table and seismic centrifuge tests (El-Emam and Bathurst 2004; Koseki et al. 1998; Sabermahani et al. 2009; Sakaguchi 1996; Watanabe et al. 2003) as discussed in Sections 2.3.1 and 2.3.2 below.

It should be noted that reduced-scale tests have their limitations and the response of the model can be influenced by low confining pressure, boundary effects and improperly scaled reinforcement mechanical properties (Koseki et al. 2006). Thus an important aspect of all model scale experimental tests is the need to ensure model similitude; otherwise the results at model scale are not directly transferable to proto-type scale.

### **2.3.1 Influence of Length-to-Height Ratio on seismic performance**

Section 1.2.2 shows that the L/H ratio is a key design parameter for wall stability. However, seismic design with large seismic coefficients can lead to MO-theory being indeterminate or can result in a large failure wedge. In these cases, design might specify an unreasonably large or impractical L/H ratio to guarantee stability. This implies a greater cost in geosynthetic-

reinforcement; however the cost is minor compared to the additional cost of select granular backfill and excavation required with a larger L/H ratio.

Both Murahsev (2003) and FHWA (2001) indicate that for seismic design, L/H should be limited to  $L/H \leq 1.0$  or 1.2. Further, for seismic coefficients,  $k_h$ , larger than 0.3, and where some movement can be tolerated, the seismic coefficient can be reduced, based on an assessment of the seismic performance of the GRS wall.

As part of wider experimental parametric studies, various researchers have investigated the influence of L/H on static and seismic performance. Two general research objectives were to examine:

- The impact of the L/H ratio on performance *during* an earthquake
- The determination of optimum L/H ratio for cost-effective design for seismic events

Investigations of particular interest include those by El-Emam and Bathurst (2004, 2005, 2007), Watanabe et al. (2003), Sakaguchi et al. (1996), Sabermahani et al. (2009) and Nova-Roessig and Sitar (2006), and are discussed in some detail below.

El-Emam and Bathurst (2004; 2005; 2007) conducted a series of reduced-scale model tests using a shake-table and a scaled geosynthetic geogrid with sand glued to its surface to ensure good soil-reinforcement interlock. Parameters such as facing toe condition, wall mass and inclination, vertical spacing, reinforcement stiffness, and L/H were investigated. L/H was set to 0.6 and 1.0. The models were subjected to incrementally increasing base shaking and the influence of these parameters on seismic performance is shown in Figure 2-6.

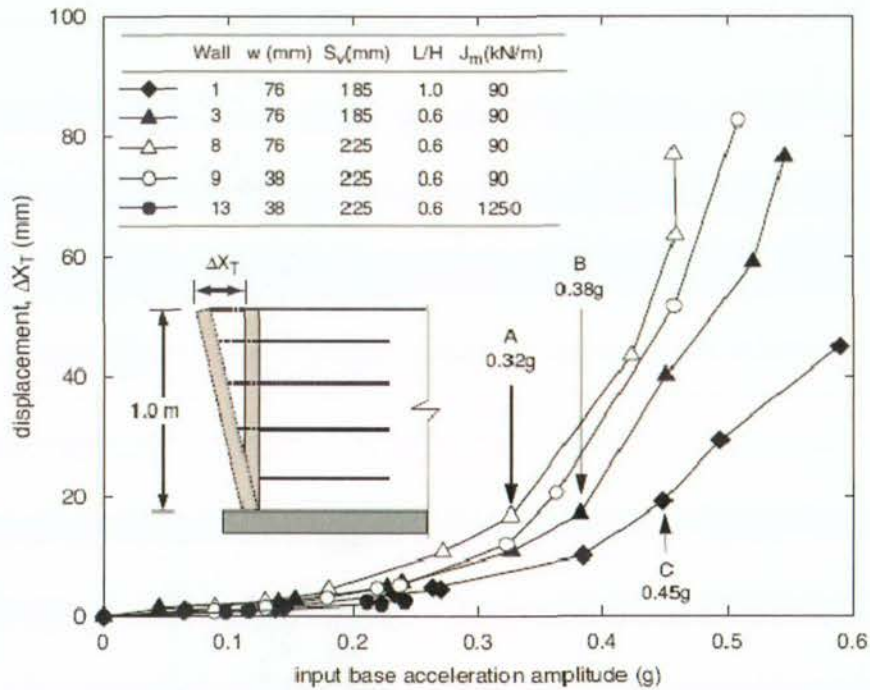


Figure 2-6. Influence of reinforcement properties, including L/H, vertical spacing ( $S_v$ ) and reinforcement stiffness ( $J_m$ ) for GRS models. NB: The model's toe condition was hinged (i.e. base sliding completely restricted). (From El-Emam and Bathurst 2007).

Figure 2-6 plots residual wall top displacement,  $\Delta X_T$ , due to increasing base acceleration amplitude. A shallower curve, i.e. smaller displacement for increasing base input acceleration indicates a higher resistance to seismic loading. As seen in Figure 2-6, an increase in L/H from 0.6 to 1.0 (Walls 1 and 3) resulted in a smaller displacement response. Specifically, from a base input acceleration of 0.45g, the wall reinforced at 0.6 had displacement around 40 mm, roughly twice that of the wall reinforced at L/H = 1.0.

Similar increases in performance due to increased L/H have been noted in other shake-table studies. Watanabe et al. (2003) conducted shake-table tests on 3 conventional and 3 reinforced soil retaining walls with a FHR facing at 1:10 scale. The models were 0.5 m high, constructed to a relative density of 90% and had a 1KPa surcharge load applied. The reinforced-soil models were reinforced by a “geogrid” that comprised soldered phosphor and bronze strips. An irregular acceleration time history based on a Kobe (1995) earthquake record with a predominant frequency of 5 Hz was used as the base excitation. The record was scaled to an initial PGA of 100 gal (~ 0.1g), and then increased incrementally by 100 gal.

Watanabe et al. (2003) set  $L/H$  to 0.4 and 0.7 using a scaled reinforcement of phosphor bronze strips. The wall reinforced at  $L/H = 0.7$  had reinforcement roughly 80% longer than the other models; however seismic performance was no better. Again, this indicates an optimum value for reinforcement length. In one model, two upper reinforcement layers were increased in length from  $L/H = 0.6$  to 0.9 and 1.6. This was found to be effective at resisting wedge deformation, and the increased length effectively improved the seismic stability of the GRS wall.

Sakaguchi (1996) conducted reduced-scale model tests using both a shake-table and tilt-table with reinforcement lengths set at  $L/H = 0.33, 0.66,$  and 1.0. Scaled geosynthetic geogrid reinforcement was used in the model tests. An increase in  $L/H$  from 0.66 to 1.0 was found to be less effective at resisting deformation than an increase in  $L/H$  from 0.33 to 0.66 and this suggested an optimum  $L/H$  value equal to 0.67.

The geotechnical centrifuge may be used to better model prototype stresses in the ground and thus soil behaviour, than model studies using a 1-g shake-table. Nova-Roessig and Sitar (2006) set  $L/H = 0.7$  and 0.9 with scaled reinforcement of a geosynthetic-textile and mesh of wire strips. As in the above shake-table tests, an increase in reinforcement length decreased the residual displacement of the wall during increasing base excitation.

Section 2.2.4 noted that the composite stiffness of the reinforced soil block is an important factor in dynamic wall response. The impact of  $L/H$  on the reinforced soil block stiffness, and thus stability has been studied by Sabermahani et al. (2009). A number of reduced-scale model tests were conducted on verticals walls with wrap-around facing, and varying reinforcement type and lengths. The authors defined a new parameter,  $G_{\text{global}}$ , as the stiffness of the entire wall.  $G_{\text{global}}$  is equal to the stiffness of one layer within the wall, normalised by the confining stress at that layer. The parameter was found to be unique for each reinforcement layout used.

$G_{\text{global}}$  was found to be apparently larger for models with a larger  $L/H$  ratio. Thus models with a larger  $L/H$  demonstrate a stiffer response than shorter reinforced  $L/H$  models at low strains. The parameter displayed conventional strain degradation, and at larger strains corresponding to 0.1%,  $G_{\text{global}}$  seemed to approach some limit and was unaffected by the  $L/H$  ratio.

These investigations among others suggest an optimum reinforcement ratio,  $L/H$ , at which point any increase, is not met by a proportional increase in performance (Sakaguchi, 1996; Watanabe et al. 2003; Nova-Roessig and Sitar, 2006). However it is difficult to draw this conclusion precisely as reinforcement properties, approaches to similitude, and testing procedures vary greatly between test arrangements.

### **2.3.2 Influence of wall face inclination on seismic performance**

Codes define a GRS slope as one that is inclined at less than  $70^\circ$  to the horizontal, and a GRS “wall” as that inclined greater than  $70^\circ$  to the horizontal. The design procedures for each structure type are different, reflecting differences in structural requirements, reinforcement loads and failure modes.

The effect of slope inclination on slope stability is a basic problem; earth pressure theory predicts a decrease in lateral forces on the wall with an increase in inclination from the vertical (El-Emam and Bathurst, 2005). The impact of wall inclination on stability has also been investigated experimentally (El-Emam and Bathurst 2005; Lo Grasso et al. 2005; Matsuo et al. 1998).

One of the parameters varied during the above noted experiments by El-Emam and Bathurst (2005) was wall inclination, and 2 of the 14 models tested were inclined at  $80^\circ$  to the horizontal. The residual wall displacement with increasing base input acceleration is compared for three walls of different facing inclination and mass in Figure 2-7.

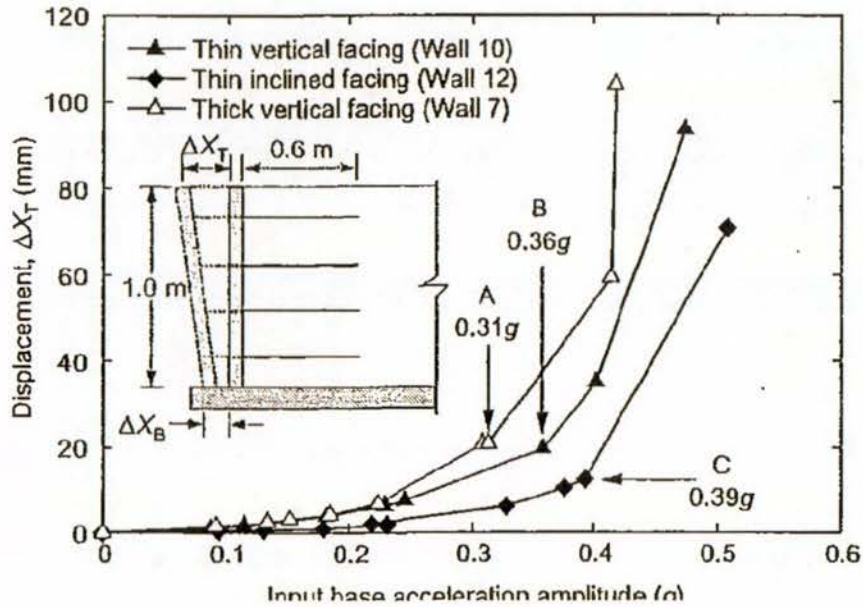


Figure 2-7. Lateral displacement measured at wall top,  $\Delta X_T$  for three walls of varying facing mass and inclination ( $L/H = 0.6$ ). From El-Emam and Bathurst (2005).

As seen in Figure 2-7, the parameters governing behaviour was the facing thickness and inclination. At all base accelerations, the model inclined at  $80^\circ$  (Wall 12) showed the smallest displacement, and demonstrated the largest critical acceleration. The results indicated that increasing the facing inclination was more effective in increasing wall stability, than increasing facing mass (El-Emam and Bathurst 2005).

Similarly, Matsuo et al. (1998) reported a 10% increase in the PGA required to generate the same displacement for a wall inclined  $79^\circ$  to the horizontal compared to a vertical wall.

## 2.4 Mechanisms of deformation

### 2.4.1 Observed failure modes of GRS

Matsuo et al. (1998) notes that deformation modes due to shaking are dependant on wall facing and inclination. Hence, a number of experimental studies have been undertaken to validate failure mechanisms used in design (El-Emam and Bathurst 2004; Matsuo et al. 1998; Sabermahani et al. 2009; Watanabe et al. 2003).

The modes of deformation observed in reduced-scale model GRS wall shaking table tests conducted by Watanabe et al. (2003) are shown in Figure 2-8. The experimental details of Watanabe et al. (2003) have been described previously in Section 2.3.1.

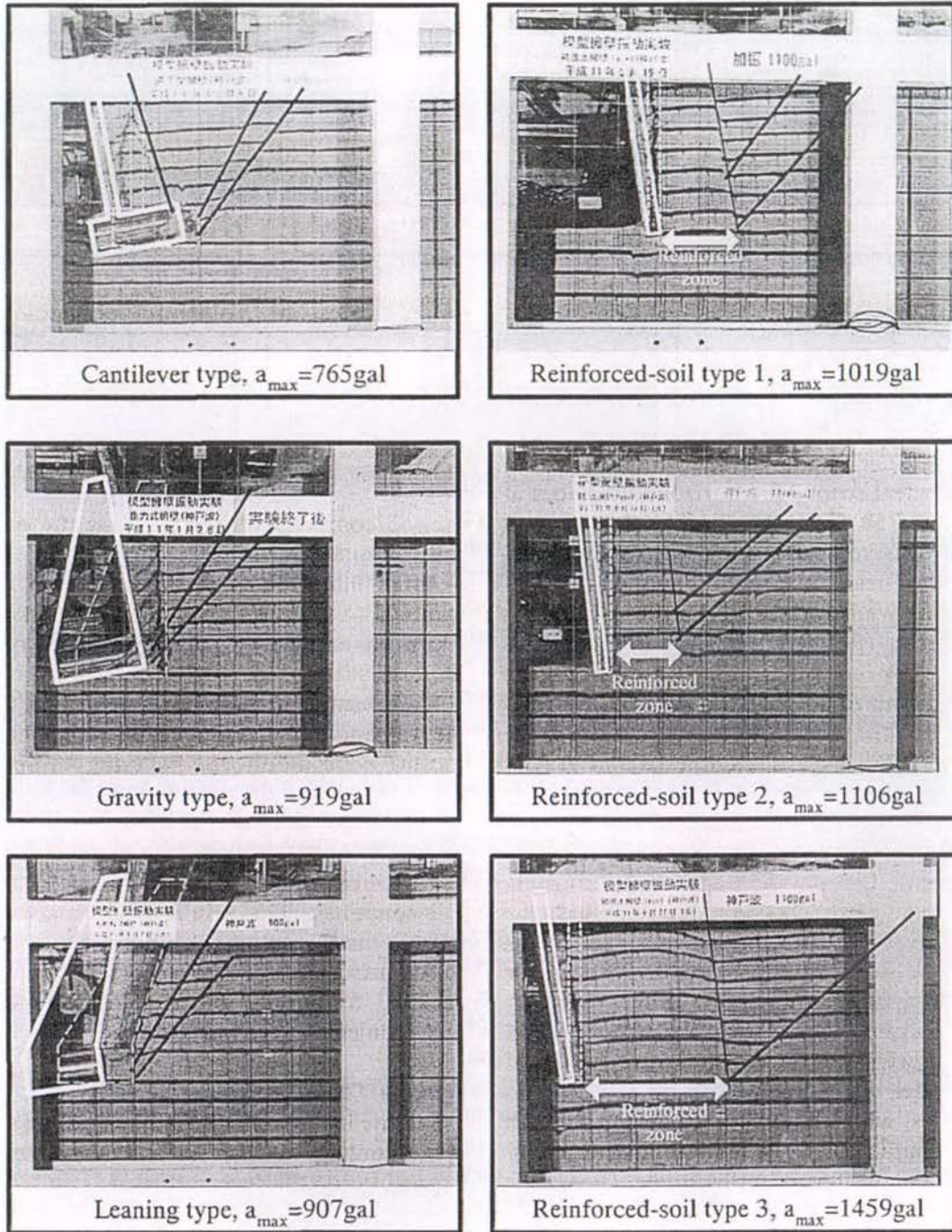


Figure 2-8. Residual displacement of 6 types of retaining wall, observed after the final shaking step. From Watanabe et al (2003).

It can be seen in Figure 2-8 that the predominant failure type for all six walls was overturning, with some small component of sliding failure. The conventional-type retaining walls demonstrated varying degrees of overturning, sliding and bearing capacity failures. All types of failure were accompanied by multiple failure surfaces formed within the retained backfill. This is discussed in Section 2.4.2.

El-Emam and Bathurst (2007) conducted a number of reduced-scale tests using a shake-table. All models were 1 m high, had a FHR panel facing, and had varied reinforcement arrangement and toe condition (either free-sliding or hinged). Again, overturning was the predominant mode of failure.

Comparison of the failure modes of the reinforced soil walls reveals that despite different L/H ratios and reinforcement layout, the failure comprised similar overturning and sliding components. Thus the overturning mode is significant and cannot be ignored in stability analyses as proposed by Newmark (1965) and Richards and Elms (1979).

#### **2.4.2 Formation of failure surfaces**

Figure 2-8 shows that for the tests conducted by Watanabe et al. (2003), the vertical walls exhibited multiple failure planes with the second failure plane forming upon larger amplitude shaking. For the reinforced soil model walls, the failure planes originated at the base of the interface between the reinforced and retained soil zones. No failure planes were observed within the reinforced zone. This pattern of deformation indicates that when the reinforcement is arranged sufficiently it resists the formation of a failure plane within the reinforced soil block.

In one test conducted by El-Emam and Bathurst (2004), the model was toe-hinged and reinforced with 5 layers of length  $L/H = 1.0$ . Overturning accompanied the formation of a failure surface which intersected both the reinforced zone and retained backfill (contrary to the above model tests by Watanabe et al., 2003). This deformation is shown above in Figure 2-2.

Sabermahani et al. (2009) tested vertical walls with a wrap-around facing on the shake-table. Overturning failure was accompanied by multiple failure surfaces which formed in the backfill and extended down to the second or third layer (from the base) of reinforcement.

Bulging of the wall face occurred for walls reinforced with reinforcement of very low stiffness and resulted in the largest displacement being recorded around mid-height of the face (and not at the wall top as in the overturning failure). This failure mode was accompanied by an internal slip surface within the reinforced soil block.

These observations highlight the importance of facing type and reinforcement material properties on GRS seismic behaviour. When a wall is faced with an FHR panel, the failure surface formed on ultimate failure is located at the wall heel or back of the reinforced soil block. In contrast, for non-rigid walls, failure surfaces at ultimate failure may not necessarily form at the heel or base of the reinforced soil block (Tatsuoka 2008). Additionally, depending on the reinforcement material properties and/or reinforcement layout, a failure surface may form within the reinforced soil block.

The two-wedge failure mechanism used in current Japanese design practice is shown below in Figure 2-8 and shows a near vertical failure surface and an inclined failure surface which form behind the reinforced soil block. The deformation observed in the Watanabe et al. (2003) models, in general confirmed the use of this mechanism. However, in these models, no failure plane was observed within the reinforced soil block, shown as dashed line A – B in Figure 2-8.

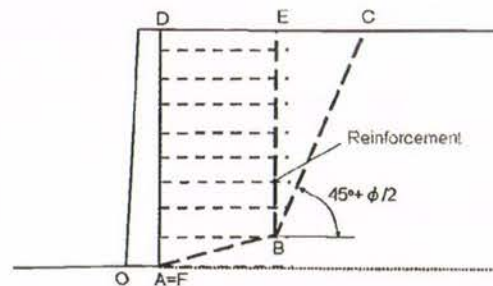


**Figure 2-9. Two-wedge failure mechanism used in Japanese design. From Tatsuoka (2008).**

For the case of an inclined wall, Matsuo et al. (1998) noted in general a more rotational movement with model wall inclined at  $77^\circ$ . This deformation involved the largest horizontal wall face displacement occurring at one third the height of the wall and was accompanied by the formation of a more circular slip surface (than the corresponding base-case vertical wall).

Lo Grasso et al. (2005) observed similar behaviour in reduced-scale shake-table tests on model walls inclined at  $70^\circ$ . Rotational behaviour accompanied the formation of somewhat curved failure surfaces within the backfill, that could be approximated with the two-wedge failure mechanism (Lo Grasso et al. 2005).

However, there are differences in the development of failure between GRS models on the geotechnical centrifuge and shake-table. For instance, a well-defined failure by overturning and sliding (with distinct failure surfaces clearly visible within the backfill) is seen in shake-table models. In contrast, a well-defined failure mechanism is not always visible in model testing using a centrifuge (Howard et al. 1998; Nova-Roessig and Sitar 2006).

Nova-Roessig and Sitar (2006) conducted an experimental study using a centrifuge on slopes inclined at  $63^\circ$  to the horizontal, with wrap-around facing. The model slopes failed in a 'ductile' manner with an absence of a defined failure surface within the backfill, and high vertical settlements and outwards slumping of the slope face. Howard et al. (1998) report a centrifuge study on six vertical face model walls faced with discrete panels. For all tests (except one with the shortest reinforcement,  $L/H = 0.5$ ) a vertical failure surface behind the reinforced soil block was observed. However, for the test reinforced at  $L/H = 0.5$ , deformation *was* accompanied by a defined inclined failure surface and graben wedge behind the reinforced soil block.

The difference in behaviour between the two centrifuge tests, again shows the importance of facing type and model inclination on model response. However, the general absence of inclined failure surfaces observed, indicates that the centrifuge could have influenced model behaviour to occur in a more 'ductile' manner as opposed to testing at 1-g on the shake-table. This difference is likely due to higher confining stress levels achieved with a centrifuge.

### **2.4.3 Rigid-block assumption**

For design purposes, the reinforced soil block is considered as a rigid coherent mass. Sandri (1997) observed post-earthquake deformation of GRS retaining walls in the field and noted behaviour, that for vertical walls, could validate the rigid block assumption.

However, both Watanabe et al. (2003) and Sabermahani et al. (2009) observed simple shear deformation within the reinforced soil block for models faced with a FHR panel or wrap-

around facing, respectively. Whilst the predominant mode of failure for the FHR faced models was overturning, Watanabe et al. (2003) note that this actually comprised simple shear along horizontal planes of the reinforced soil.

Further, Watanabe et al. (2003) note that the interaction of the soil and reinforcement requires further clarification. The lack of understanding of the reinforced soil block and simple shear behaviour under seismic excitation impedes the accurate prediction of seismic performance as discussed in Section 2.2.6.

## **2.5 Summary**

Additional factors of seismic design, such as inertial and seismic earth pressures have been discussed. Observed phenomena such as amplification of ground motion, and threshold critical acceleration help to conceptually explain the behaviour of GRS structures, and this has been examined to enable the interpretation of behaviour observed in the current series of model tests.

An accurate measure of structure-specific critical acceleration, combined with valid mechanisms of deformation, and selection of an appropriate acceleration time history can lead to the development of performance-based design methods. However these methods are subject to many limitations as discussed. This thesis investigates particularly the development of deformation within GRS walls under seismic loading.

It was shown that facing type, reinforcement properties and wall inclination strongly impact on the mode of failure, and the mechanisms of deformation observed. However, there has been limited work on the systematic variation of L/H and wall inclination that has had sole focus on its influence on deformation under seismic conditions, and hence on the underlying mechanisms of deformation. Therefore a series of experimental tests is required to further investigate this. Such tests and their interpretation are the topic of this thesis.

## **References**

- Bracegirdle, A. (1980). "SEISMIC STABILITY OF REINFORCED EARTH RETAINING WALLS." *Bulletin of the New Zealand National Society for Earthquake Engineering*, 13(4), 347-354.

- Cai, Z., and Bathurst, R. J. (1996). "Seismic-induced permanent displacement of geosynthetic-reinforced segmental retaining walls." *Canadian Geotechnical Journal*, 33(6), 937-955.
- De, A., and Zimmie, T. F. (1998). "Estimation of dynamic interfacial properties of geosynthetics." *Geosynthetics International*, 5(1-2), 17-39.
- El-Emam, M. M., and Bathurst, R. J. (2004). "Experimental Design, Instrumentation and Interpretation of Reinforced Soil Wall Response Using A Shaking Table." *International Journal of Physical Modelling in Geotechnics*, 4 (2004), 13-32.
- El-Emam, M. M., and Bathurst, R. J. (2005). "Erratum: Facing contribution to seismic response of reduced-scale reinforced soil walls (Geosynthetics International (2005) vol. 12 (5) (215-238))." *Geosynthetics International*, 12(6), 344.
- El-Emam, M. M., and Bathurst, R. J. (2007). "Influence of reinforcement parameters on the seismic response of reduced-scale reinforced soil retaining walls." *Geotextiles and Geomembranes*, 25(1), 33-49.
- El-Emam, M. M., Bathurst, R. J., and Hatami, K. (2004). "Numerical Modeling of reinforced soil retaining walls subjected to base acceleration." 13th World Conference on Earthquake Engineering, Vancouver, B.C. Canada.
- Fairless, G. J. (1989). "Seismic Performance of Reinforced Earth Walls," University of Canterbury, Christchurch.
- Fannin, R. J., and Hermann, S. (1990). "Performance data for a sloped reinforced soil wall." *Canadian geotechnical journal*, 27(5), 676-686.
- FHWA. (2001). "Mechanically Stabilized Earth Walls and Reinforced Soil Slopes Design and Construction Guidelines".
- Gazetas, G., Psarropoulos, P. N., Anastasopoulos, I., and Gerolymos, N. (2004). "Seismic behaviour of flexible retaining systems subjected to short-duration moderately strong excitation." *Soil Dynamics and Earthquake Engineering*, 24(7), 537-550.
- Hatami, K., and Bathurst, R. J. (2000). "Effect of structural design on fundamental frequency of reinforced-soil retaining walls." *Soil Dynamics and Earthquake Engineering*, 19, 137-157.
- Howard, R., Kutter, B., and Siddharthan, R. "Seismic deformation of reinforced soil centrifuge models." *Geotechnical Earthquake Engineering and Soil Dynamics III*, University of Washington, Seattle, Washington, USA.
- Koseki, J., Bathurst, R. J., Guler, E., Kuwano, J., and Maugeri, M. (2006) "Seismic stability of reinforced soil walls." *8th International Conference of Geosynthetics (8ICG)*, Yokohoma, Japan, 51 - 77.

- Koseki, J., Munaf, Y., Tatsuoka, F., Tateyama, M., Kojima, K., and Sato, T. (1998). "Shaking and tilt table tests of geosynthetic-reinforced soil and conventional-type retaining walls." *Geosynthetics International*, 5(1-2), 73-95.
- Kramer, S. L. (1996). *Geotechnical Earthquake Engineering*, Prentice-Hall, Upper Saddle River, New Jersey.
- Lai, C. S. (1979). "Behaviour of Retaining Walls Under Seismic Loading," University of Canterbury, Christchurch, New Zealand.
- Law, H. K., and Ko, H.-Y. "Dynamic response of uniform level ground deposits." *Earthquake Geotechnical Engineering*, Balkema, Rotterdam.
- Leshchinsky, D. (2000). "Discussion: Performance of Geosynthetic-Reinforced Slopes at Failure." *Journal of Geotechnical and Geoenvironmental Engineering*.
- Ling, H. I., Leshchinsky, D., and Chou, N. N. S. (2001). "Post-earthquake investigation on several geosynthetic-reinforced soil retaining walls and slopes during the ji-ji earthquake of Taiwan." *Soil Dynamics and Earthquake Engineering*, 21(4), 297-313.
- Ling, H. I., Liu, H., Kaliakin, V. N., and Leshchinsky, D. (2004). "Analyzing Dynamic Behaviour of Geosynthetic-Reinforced Soil Retaining Walls." *Journal of Engineering Mechanics*, 130(8).
- Ling, H. I., Mohri, Y., Leshchinsky, D., Burke, C., Matsushima, K., and Liu, H. (2005). "Large-scale shaking table tests on modular-block reinforced soil retaining walls." *Journal of Geotechnical and Geoenvironmental Engineering*, 131(4), 465-476.
- Lo Grasso, A. S., Maugeri, M., and Recalcati, P. (2005). "Seismic Behaviour of Geosynthetic-Reinforced Slopes with Overload by Shaking Table Tests." Slopes and Retaining Structures Under Seismic and Static Conditions (GSP 140), M. A. Gabr, J. J. Bowders, D. Elton, and J. G. Zornberg, eds., Austin, Texas.
- Matsuo, O., Yokoyama, K., and Saito, Y. (1998). "Shaking table tests and analyses of geosynthetic-reinforced soil retaining walls." *Geosynthetics International*, 5(1-2), 97-126.
- Murashev, A. K. (2003). "Guidelines for Design and Construction of Geosynthetic-Reinforced Soil Structures." Transfund New Zealand.
- Nagel, R. B. (1985). "Seismic Behaviour of Reinforced Earth Walls," University of Canterbury, Christchurch, New Zealand.
- Newmark, N. M. (1965). "Effects of Earthquakes on Dams and Embankments." *Geotechnique*, 15(2), 139 - 160.
- Nova-Roessig, L., and Sitar, N. (2006). "Centrifuge model studies of the seismic response of reinforced soil slopes." *Journal of Geotechnical and Geoenvironmental Engineering*, 132(3), 388-400.

- Okabe, S. (1926). "General theory of earth pressures." *Journal of Japan Society of Civil Engineers*, 12(1).
- Richards, R., and Elms, D. (1979). "SEISMIC DESIGN OF GRAVITY RETAINING WALLS." *Bulletin of the New Zealand National Society for Earthquake Engineering*, 12(2), 114-121.
- Sabermahani, M., Ghalandarzadeh, A., and Fakher, A. (2009). "Experimental study on seismic deformation modes of reinforced soil-walls." *Geotextiles and Geomembranes*, 27, 121-136.
- Sakaguchi, M. (1996). "Study of the seismic behavior of geosynthetic reinforced walls in Japan." *Geosynthetics International*, 3(1), 13-30.
- Sandri, D. (1997). "Performance summary of reinforced soil structures in the Greater Los Angeles area after the Northridge earthquake." *Geotextiles and Geomembranes*, 15(4-6), 235-253.
- Segrestin, P., and Bastick, M. J. "Seismic design of Reinforced Earth retaining walls - The contribution of finite element analysis." *International Geotechnical Symposium on Theory and Practice of Earth Reinforcement*, Fukuoka, Japan.
- Shukla, S. K. (2002). "Geosynthetics and their applications." ThomasTelford.
- Standards Australia International. (2002). "Australian Standard AS 4678-2002, Earth-retaining Structures." Standards Australia International.
- Steedman, R. S., and Zeng, X. (1990). "The influence of phase on the calculation of pseudo-static earth pressure on a retaining wall." *Geotechnique*, 40(1), 103-112.
- Tatsuoka, F. "Geosynthetic-reinforced soil structures: A cost-effective solution combining two engineering disciplines." *19th Carillo Lecture - Mexican Society for Soil Mechanics*, Aguascalientes.
- Watanabe, K., Munaf, Y., Koseki, J., Tateyama, M., and Kojima, K. (2003). "Behaviors of several types of model retaining walls subjected to irregular excitation." *Soils and Foundations*, 43(5), 13-27.
- Wood, J. H. "Design of Retaining Walls for Outward Displacement." *2008 New Zealand Seismology and Earthquake Engineering*, Christchurch.
- Zarrabi-Kashani, K. (1979). "Sliding of Gravity Retaining Wall During Earthquakes Considering Vertical Acceleration and Changing Inclination of Failure Surface," Massachusetts Institute of Technology.
- Zornberg, J. G., and Arriaga, F. (2003). "Strain distribution within geosynthetic-reinforced slopes." *Journal of Geotechnical and Geoenvironmental Engineering*, 129(1), 32-45.

## **CHAPTER 3**

### **EXPERIMENTAL DESIGN AND TESTING**

#### **PROCEDURES**

##### **3.1 Introduction**

This chapter discusses in detail the experimental model, construction methodology, and testing procedures used in this study. Section 3.2 discusses the model GRS wall design, designed at prototype scale, and geometrically scaled down. Equipment that required design and construction prior to physical model testing is discussed in Section 3.3 and included: a rigid box within which model GRS walls could be built and subsequently tested on the shake-table; sand storage units that were also used for sand deposition into the box; a weighted plate used for compaction of the wall; and a removable bracing system for the GRS wall face. Additionally, a seal to prevent sand leakage around the wall face was also investigated.

Scaling considerations are discussed in the terms of the model geometry, soil, reinforcement, facing and the selection of a model excitation in Section 3.4. The shake-table motion dynamics are shown in Section 3.5, followed by the instrumentation used to measure the dynamic response of the GRS physical model in Section 3.6. The instrumentation included: seven accelerometers, six displacement transducers, and three high-speed cameras used to track soil texture and observe soil deformation through the transparent acrylic sidewall for subsequent analysis using Geotechnical Particle Imaging Velocimetry (GeoPIV) software.

Model construction and experimental set-up are discussed in Section 0. The remaining sections show the static performance of the wall, the as-constructed relative density, and an attempt to measure the fundamental frequency of the models' soil deposit.

### **3.2 Wall Design**

Full-scale and large-scale testing of GRS walls some 4.8m, 2.8 m and 2.0 m high has been undertaken by Fannin and Hermann (1990), Sakaguchi (1996) and Ling et al. (2005) respectively, however due to material and spacing limitations, the majority of model-scale tests in the literature have been conducted on smaller models of 1 m high or less (El-Emam and Bathurst 2004; Sabermahani et al. 2009; Watanabe et al. 2003). While larger models are able to generate more realistic results than small model-scale tests (Sabermahani et al. 2009), similar limitations on model size, and in particular, those imposed by the dimensions of the University of Canterbury shake-table meant that a model wall height of 900 mm was selected for use in the current tests.

The GRS model wall was designed at prototype scale using the well-established simplified coherent gravity method (FHWA 2001) considering also the experimental objectives. The failure modes considered during design were overtopping and sliding (external), and reinforcement pullout (internal). Reinforcement rupture was not considered. Obviously, the absence of foundation sub-soil and the use of a Full-Height Rigid (FHR) panel facing preclude failure mechanisms such as deep seated slip, bearing capacity, and internal block sliding failures as discussed in Chapter 2. Details of the prototype's design are given in Appendix A.

A 4.5 m high wall was designed at prototype scale with a typical reinforcement length to wall height ratio, of  $L/H = 0.75$ . This is slightly larger than the minimum  $L/H = 0.70$  specified by FHWA (2001). Factors of safety against sliding, overturning and pullout failures were all larger than 2. A geometric scale factor of 1:5 was used to scale the prototype design down to the model height of 0.9 m.

The prototype design required only 5 layers of reinforcement, with a vertical spacing between layers of 750 mm. This spacing is larger than the 500 mm recommended by FHWA (2001) for GRS walls with a wrap-around facing, and equates to a vertical spacing at model scale of 150 mm.

The length of reinforcement is initially defined as 75% of the wall height of 900 mm and is (initially) 675 mm long. The L/H ratio is a key variable throughout testing and will vary from 0.6 to 0.9.

Where possible, appropriate parameters and components of the wall, such as facing, reinforcement, and soil were selected based on the scaling rules suggested by Iai (1989) to satisfy geometric, dynamic and kinematic similitude. This ensured that behaviour at model scale can be used to infer behaviour at prototype scale and is further examined in Section 3.4.

### **3.3 Experimental Box**

A strong rigid box was designed to allow easy construction, testing and dismantling of the reduced-scale model GRS walls. For the purpose of high-speed digital image capture during testing (for subsequent GeoPIV analysis) one side of the box was made of 20 mm thick transparent acrylic. Two further criteria for the box included: a high rigidity and that it would not inhibit the natural behaviour of the sand model (i.e. small boundary effects).

#### **3.3.1 Box design in previous studies**

The literature contains many examples of reinforced soil wall physical modelling. These examples were consulted to help determine important parameters for the box design. The predominant consideration concerns that of minimising boundary effects.

Various theories exist as to wall height-to-width ratios (H/W) that minimise frictional boundary effects. Side friction effects can in general be reduced by constructing the model in a box wide enough such that the boundary effects are insignificant at its center-line. Fairless (1989) reported on different wall height-to-width ratios (H/W) for reinforced soil walls that, in theory, minimize boundary effects. He reports Terzaghi (1932) that a wall should be twice as wide as it is high in order to avoid edge effects, and Rowe (1971) who detailed this further stating H/W ratios of 0.5 to 0.3 reduce edge effects. Finally, Fairless (1989) notes that for  $H/W = 0.5$ , frictional effects from the boundary will impact on the active earth pressure coefficient,  $K_a$ , less than 10% and “probably much less.”

Box designs reviewed included those by Sakaguchi (1996), Watanabe et al. (2003), and El-Emam and Bathurst (2004). Sakaguchi (1996) built four large-scale model geosynthetic-reinforced soil segmental block faced walls within a box 4.0 m long, 0.9 m wide, and 2.0 m

high ( $H/W = 2.2$ ) and conducted 1-g shake-table tests that compared the seismic behaviour of three conventional retaining wall structures and one GRS retaining wall. Watanabe et al. (2003) compared three conventional and three FHR panel faced reinforced soil retaining walls scaled by 1:10, again using 1-g shake-table testing. The models were 1.4 m long, 0.5 m high and 0.6 m wide ( $H/W = 0.83$ ). Both box side walls were transparent allowing deformation to be observed.

El-Emam and Bathurst (2004) conducted multiple 1:6 reduced-scale model shake-table tests that investigated the influence of reinforcement layout and facing geometry on seismic behaviour. The model walls were 1.0 m high and faced by a FHR panel which was isolated from the frictional base and instead was founded on slide rails to enable determination of toe loads and displacements. The wall was built in a box 2.4 m long and 1.0 m wide ( $H/W = 1.0$ ). The rigid box was lined with plywood and the base covered with glued sand layer that provided friction between the wall and the base.

A summary of the model properties used in each study is provided in Table 3-1.

**Table 3-1. Summary of previous model tests' and this study's dimensions and materials.**

Reference	Scale	Box dimensions (L, W, H) (m)	Model height (m)	Height-to-width ratio	Construction materials
Sakaguchi (1996)	1:3	(4.0, 0.9, 2.0)	1.5	1.7	Steel, sand paper glued to base
Watanabe et al. (2003)	1:10	(2.6, 0.6, 1.4)	0.5	0.8	Steel and plexiglass. Greased Teflon used on side of model wall
El-Emam and Bathurst (2004)	1:6	(2.4, 1.0, 1.0)	1.0	1.0	Rigid steel lined with plywood and a glued sand base layer
This study	1:5	(3.0, 0.8, 1.1)	0.9	1.1	Rigid steel lined with plywood and a glued sand base layer, transparent acrylic 20 mm thick

### 3.3.2 Box design

In addition to an adequate width to reduce boundary effects, the box was designed such that the anticipated failure surface in the model deposit formed during shaking would be contained within the box and not affected by the back wall boundary. This ensured that the effect of the backwall on the model wall was negligible. To predict the theoretical location of a failure surface formed on application of a pseudo-static 0.6g horizontal acceleration, Mononobe-Okabe (MO) theory was used.

The theoretical model was a vertical wall with horizontal backfill, soil with a peak friction angle of  $33^\circ$ , and wall face-soil interface friction angle of  $25^\circ$  ( $3/4$  of the peak friction angle as used by Watanabe et al. 2003). The failure surface was predicted to be  $10.7^\circ$  to the horizontal and was assumed to extend from the wall toe to the backfill surface 5.1 m from the wall. It is unlikely the failure surface would extend this far, considering that the model experiments summarised in Table 3-1 all observed failure surfaces which formed entirely within the strong-box. Hence similar box dimensions are maintained in the current experiments as those noted above and a compromise set the model length to be  $\sim 2.4$  m.

It should be noted that the rigid back wall boundary could reflect seismic energy back into the model. This effect has been reduced in other experiments with the inclusion of a foam barrier to absorb this energy. However, due to the need to calculate an accurate soil deposit density and the construction method chosen, this strategy was not utilized in the present experiment and the model length was assumed long enough to reduce this effect.

A cross section of the box and model inside is shown in Figure 3-1. One side of the box is transparent acrylic (Perspex), allowing high-speed imaging during testing and subsequent Geotechnical Particle Imaging Velocimetry (GeoPIV) analysis.

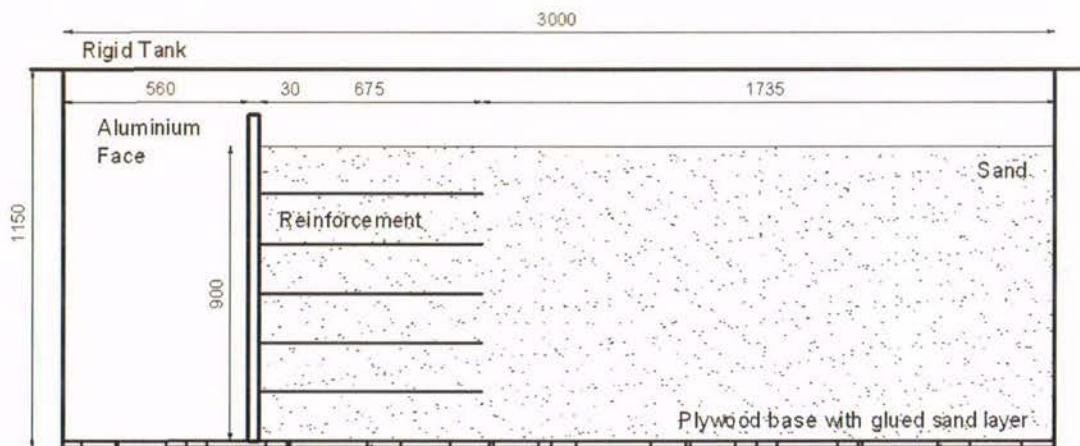


Figure 3-1. Experimental setup in Box for  $L/H = 0.75$ .

### 3.3.3 Seal design

One important detail of the facing panel is the seal it makes with the box sidewall. The seal should meet two important functions: First it should minimise its influence on model behaviour by generating low friction with the box sidewall; second, it should prevent the

leakage of sand around the wall face. Friction force,  $F_f$ , under static loading comprises two components as shown in Equation 3-1.

$$F_f = \mu_s F_N \quad (3-1)$$

Where  $\mu_s$  is the static coefficient of friction, and  $F_N$  is the force normal against the box sidewall. It is therefore apparent that the former can be treated with appropriate selection of materials and the latter through seal design.

Of the research identified above, the seal was mentioned in only the experimental methods reported by Watanabe et al. (2003). Here the seal consisted of a thin strip of foam with Teflon tape wrapped around it and attached to the edge of the facing panel. While Watanabe et al. (2003) did not quantify the friction force, it is assumed negligible. This is because the foam would have generated minimal normal force on the sidewall, and, coupled with the low frictional properties of the Teflon contact, would have resulted in a very low friction force between the wall panel and strong-box sidewall.

Difficulties in fabrication of a wall panel similar to that used by Watanabe et al. (2003) precluded its use and a variety of other designs were trialed with varied success. A variation of that used by Watanabe et al (2003) was selected and consisted of Teflon tape and foam as shown in Figure 3-2.

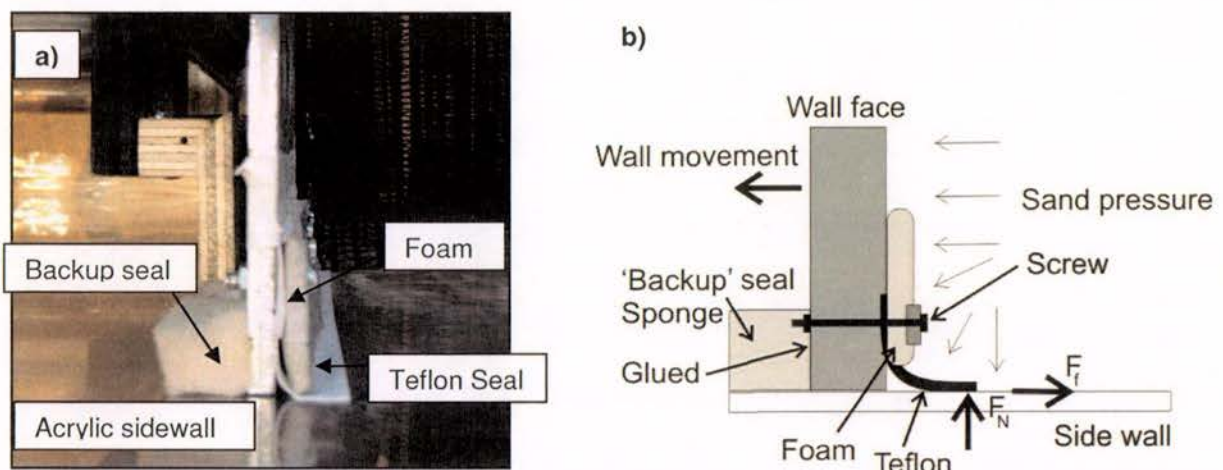


**Figure 3-2.** Plan view of seal against the Perspex sidewall (a) and schematic (not-to-scale) detailing of the seal and friction force components (b). Note that the backup seal is used to prevent leakage (if any) during compaction and is removed for testing.

The seal comprised of two parts. The first part was comprised of a Teflon strip attached to the side of the facing panel and curved to fit the box side wall. A strip of foam was attached on top of this to apply a small normal force on the box sidewall which ensured a good seal. The second part consisted of a 'backup seal' and this consisted of a piece of sponge attached to the front of the facing panel. The 'backup' seal was forced against the box side wall to prevent any leakage of sand during model construction with a wooden strip. During testing, the wooden strip was removed and the backup seal taped away such that there was no contact between it and the sidewall of the strong-box. The seal designed as above, prevented any serious sand leakage both during model preparation and testing.

Tilt table tests and spring force tests were used to quantify the frictional properties of the seal and friction force of the wall in rotation (see Appendix A). The friction force required to generate rotation was a low  $F_f = 1$  N, equating to roughly  $\sim 0.1\%$  of the theoretical total force on the back of the wall (corresponding to the active state). A further comparison of friction force with the earth pressures near the top of the wall was made, as earth pressures are lower near wall top and friction could have a larger impact on wall response. The friction equated to just  $1.3\%$  of the earth pressure force acting against the top 200 mm of the wall. This was again deemed to have a minimal impact on model response.

It should be noted that the seal described above was developed during the process of testing, and was the solution generated during the second half of testing. Tests in which a different seal was used are identified in the results.

### **3.4 Physical model**

Important for all reduced-scale model tests is the need to ensure model similitude to allow behaviour at prototype scale to be inferred from that at model scale. In this section, aspects of similitude are defined and used to select (where applicable) model components of soil, reinforcement, reinforcement-soil interface, facing and reinforcement-facing connections. Similitude also applies during testing; hence the selection of model excitation parameters is discussed.

#### **3.4.1 Similitude aspects**

In order to model behaviour at prototype scale correctly with reduced-scale models, it is important not only to scale down its geometry, but also to consider stress dependant

behaviour (Sabermahani et al. 2009). Further, the response of the model may be influenced by low confining pressure, ill considered boundary effects and improperly scaled reinforcement mechanical properties (Koseki et al. 2006). Thus Iai (1989) derived similitude specifically for geotechnical applications whereby the basic definitions of effective stress, strain, the constitutive law, overall equilibrium, pore water equilibrium and mass balance at model and proto-type scales are proportional.

The geometric scale factor,  $\lambda$ , is the proportionality constant between the model (subscript m) and prototype (subscript p) geometry, as shown in Equation 3-2. Similar proportional equations are assumed for other parameters such as stress-strain, overall equilibrium, mass balance and pore water pressure.

$$(x)_p = \lambda(x)_m \quad (3-2)$$

Inspection of the combined proportionality equations finds that each scale factor can be reduced down to a function of just three independent scale factors,  $\lambda$ ,  $\lambda_p$ ,  $\lambda_\varepsilon$ , namely the geometry, saturated soil density, and soil strain scale factors as shown in Table 3-2.

**Table 3-2. Similitude derived scaling factors for 1-g shaking table tests (From Iai 1989)**

Parameter	Symbol	Scaling factor (prototype/model)
Density	$\rho$	$\lambda_p$
Effective stress of soil	$\sigma'$	$\lambda \lambda_p$
Length	$x$	$\lambda$
Strain of soil	$\varepsilon$	$\lambda_\varepsilon$
Displacement of soil and/or structure	$u$	$\lambda \lambda_\varepsilon$
Velocity of soil and/or structure	$u'$	$(\lambda \lambda_\varepsilon)^{0.5}$
Acceleration	$u''$	1
Time	$t$	$(\lambda \lambda_\varepsilon)^{0.5}$

For the present experiments, the geometric scale factor,  $\lambda$ , is equal to 5. However, scale factors relating the saturated soil density,  $\lambda_p$ , and soil strain,  $\lambda_\varepsilon$ , at model and prototype scales are more difficult to determine. Iai (1989) suggests that for the simple case when  $\lambda_p = 1$ , i.e. the soil density is the same for both prototype and model scales, then the strain scale factor,  $\lambda_\varepsilon = \lambda^{0.5}$ .

The derived similitude by Iai (1989) was tested in a series of saturated plane strain compression tests and was found to hold for low soil strains and confining pressures 5 –

392 kPa. Thus the similitude is not valid at model failure and/or large shear strains,  $\gamma > 10\%$  at prototype scale. The similitude also has the following assumptions that limit its applicability:

- The soil skeleton is regarded as a continuous medium (reinforcement inclusion makes this invalid).
- The strain is small such that the linear strain approximation  $d\varepsilon = Ldu$  holds and that the equations of equilibrium before and after deformation are the same.

As the main project aim was to investigate the performance of GRS walls prior to failure, data was obtained at low shaking levels and also during and post failure. This initial data is deemed to meet the similitude conditions; whilst the data obtained at large strains corresponding to failure requires special interpretation in light of violating the abovementioned similitude conditions.

Further, the inclusion of reinforcement into the model is obviously necessary, and the effects on the fundamental model similitude conditions are deemed to be minor. However, correct scaling of reinforcement, and reinforcement layout (length and vertical spacing) is important, as these parameters affect the formation and location of failure wedges (Watanabe et al. 2003) and can generate results not indicative of full-scale behaviour (Nova-Roessig and Sitar 2006).

### 3.4.2 Soil

Albany sand was selected for the model soil; it is relatively rounded with the properties specified in Table 3-3. Reasons for its selection included that it is commercially available, that it is a clean sand, and that it generates minimal dust during sand deposition and wall construction.

**Table 3-3: Albany Sand soil properties**

Property	Symbol	Value
Solid particle density	$\rho_s$	2.65 t/m <sup>3</sup>
Mean particle size	$D_{50}$	0.3 mm
Maximum void ratio	$e_{max}$	0.83
Minimum void ratio	$e_{min}$	0.51
Peak friction angle <sup>1</sup>	$\Phi_p$	33°
Critical state friction angle <sup>1</sup>	$\Phi_{ss}$	31°

Notes: <sup>1</sup> As determined by Roper (2006)

In geotechnical engineering, the confining stress level is a dominant factor behind soil behaviour (strength, stiffness and strain) and requires correct modelling. For instance, some modes of failure documented in previous 1-g tests have not been observed in the field, due to low model stress levels (Nova-Roessig and Sitar 2006). Thus in order to model accurate prototype soil stress-strain behaviour, the geotechnical centrifuge has been used in some cases (Howard et al. 1998; Ling et al. 2004; Nova-Roessig and Sitar 2006; Viswanadham and Konig 2009), where gravity, and thus soil stress is increased N-times.

However the current tests are to be conducted at 1-g, and special consideration of soil density, vertical confining stress, and stiffness is necessary. Where the same soil material, and thus density, is used for both the prototype and model, Iai (1989) provides the simple case where the density scale factor is 1. Thus effective stress is scaled only by the geometric scale factor of 5. At small strain, the initial (elastic) shear modulus of the soil is dependent on the effective stress of the soil as in Equation 3-3.

$$G \propto \sigma'^{\alpha} \quad (3-3)$$

Where  $G$  is the shear modulus (stiffness),  $\sigma'$  is the effective stress, and  $\alpha$  is some exponent of order 0.5 for sands or 1 for clays. Thus the model soil stiffness at small strains should be reduced from that of the prototype by  $(5)^{0.5} = 2.2$  (Wood 2004).

At larger strain associated with permanent deformation, Wood (2004) recommends invoking critical state soil mechanics to ensure representative model behaviour. The schematic in Figure 3-3 shows the initial states of the prototype and model with reference to the critical state line.

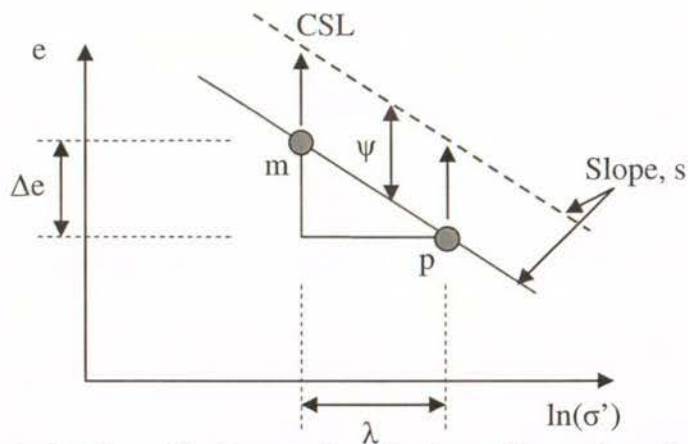


Figure 3-3. Schematic detailing critical state soil mechanics and its use in scaling model density (point m) with prototype density (point p) at medium-to-large strains as suggested by Wood (2004)

To achieve similar values of state variable,  $\psi$ , the relative change in void ratio,  $e$ , from the initial state to the critical state needs to be retained. Assuming a typical sand has a critical state line with a local slope,  $s$ , of roughly 0.03 (Wood 2004), and reducing the confining stress between prototype and model scales by the geometric scale factor of 5, then the difference in initial void ratios is calculated as shown in Equation 3-4:

$$\Delta e = s \ln \lambda \quad (3-4)$$

Thus to ensure similar behaviour between prototype and model scales, the difference in void ratios should be roughly 0.05. Hence for the prototype constructed with Albany sand at relative density,  $D_r = 90\%$ , the model should be constructed at  $D_r = 75\%$ . Sabermahani et al. (2009) similarly noted that in theory the model should be looser than for the prototype and as such, selected model target relative density's of 47% and 84%, lower than that used in the field.

However, any scaling of soil density needs to be balanced with the:

- Desire for good soil-reinforcement interlock;
- Capability of model preparation procedures to generate mid-range (50 – 75%) densities consistently;

Hence it was deemed simpler to create a model of sufficiently high density with minimal variation in density across the test series. A target relative density of  $D_r = 90\%$  was selected. Section 3.9 shows the density achieved during model construction.

### 3.4.3 Reinforcement

Modelling of geosynthetics for similitude is difficult; contrary to soil, the same material often cannot be used (Viswanadham and Konig 2004). Viswanadham and Konig (2004) consider two aspects of the reinforcement that require appropriate scaling: 1) frictional bond behaviour of the reinforcement-soil interface, and 2) the tensile strength–strain behaviour of geosynthetics. El-Emam and Bathurst (2004) report that stiffness, not ultimate tensile capacity, governs deformation behaviour, and is thus one of the most important parameters to model correctly. This is in contrast to current design codes that select reinforcement based on the ultimate tensile capacity of the reinforcement.

Geosynthetic-reinforcement available in New Zealand is manufactured by Stratagrid and Tensar, supplied by Stevensons and Maccaferri respectively. Reinforcement selection was confined to these makes and based on the best value for stiffness similitude. Table 3-4 shows the stiffness of various geogrid products.

**Table 3-4. Manufacturers and Geosynthetic product stiffness properties**

Manufacturer	Product	Use	Stiffness measure	Value (kN/m)
Tensar	UX1800HS	Reinforced Soil	$J_{5\%}^a$	1900
		Slopes (RSS)	$J_{2\%}^b$	2375 <sup>d</sup>
	Uniaxial 3326	Tunnels	$E^c (J_{0\%})$	1400
	UX1000HS	RSS	$J_{5\%}$	460
	Biaxial 3326	Tunnels	$E$	321
Stratagrid	Microgrid	RSS	$J_{2\%}$	220

<sup>a, b</sup> Axial stiffness at 5%, 2% strain respectively

<sup>c</sup> Initial elastic axial stiffness (i.e. stiffness at 0% strain)

<sup>d</sup> Calculated by assuming stiffness degradation of 25% occurs between 2% and 5%.

Tensar UX1800HS was selected as comparable to typical reinforcement stiffness at prototype scale (El-Emam and Bathurst 2004). UX1800HS has an axial stiffness,  $J_{2\%} = 2375$  kN/m. To determine an appropriate corresponding model scale stiffness the similitude rules proposed by Iai (1989) were used to determine the stiffness scale factor as in Equation 3-5.

$$J_m = \frac{J_p}{\lambda^2} = \frac{2375}{5^2} = 95 \text{ kN/m} \quad (3-5)$$

Where  $J_p$  and  $J_m$  are the axial stiffness at prototype and model scale respectively, and  $\lambda$  is the geometric scale factor. Therefore the model scale stiffness (at 2% strain) should be roughly 95 kN/m.

Nakajima et al. (2007) performed scale-model tests on two models of different reinforcement

stiffness, using a polyester and a phosphor bronze reinforcement. The axial stiffness of each reinforcement was determined by direct tension testing, and at 2% axial strain, the axial stiffness was approximately 185 kN/m and 60 kN/m respectively. Even though the material properties were largely different, upon testing, the models demonstrated little observed difference in seismic performance (Nakajima et al. 2007).

Therefore Microgrid was selected for the model reinforcement. Whilst the axial stiffness of Microgrid is 220 kN/m and is approximately double that of the similitude derived stiffness of around 95 kN/m, the difference in stiffness, and order of magnitude, is similar to that of the abovementioned experiment by Nakajima et al. (2007), and was thus deemed to model the reinforcement sufficiently.

Microgrid is a polyester geogrid manufactured by Stratagrid, with the relevant design properties detailed in Table 3-5.

**Table 3-5: Properties of Microgrid manufactured by Stratagrid**

Parameter	Value	Units	Testing method
Axial stiffness, $J_{2\%}$	220	kN/m	
Ultimate Tensile Strength, $T_{ult}$	29.2	kN/m	ASTM D 4595
Creep Limited Tensile Strength	18.5	kN/m	ASTM D 5262
Long term design Tensile Strength (LTDS) <sup>a</sup> , $T_{al}$	14.0	kN/m	

Notes: <sup>a</sup> LTDS or  $T_{al}$  is based on the ultimate tensile strength,  $T_{ult}$  reduced by reduction factors due to creep, installation damage, and durability.

The Microgrid reinforcement stiffness ( $J_{2\%}$ ) is higher than that used in previous research by Sabermahani et al. (2009) and El-Emam and Bathurst (2004) of 0.09 - 29 kN/m and 90 kN/m respectively. Hence the Microgrid is considered an extensible reinforcement at prototype scale; its higher stiffness at model scale may mean the reinforcement behaves more like a non-extensible reinforcement.

Reinforcement extensibility is an important reinforcement parameter which alters the formation of lateral earth pressures within the reinforced soil block. FHWA (2001) defines an extensible reinforcement as one where “The deformation of the reinforcement at failure is comparable to or even greater than the deformability of the soil”. This means that loading induces a strain response in the reinforcement which allows the soil to relax and induce the active earth pressure condition. In contrast, an inextensible reinforcement (larger axial stiffness) resists the formation of active earth pressure conditions; rather the earth pressure approximates the at-rest earth pressure conditions, especially within the upper sections of a

GRS wall (FHWA 2001). In light of this, lateral earth pressure conditions at model scale need to be interpreted carefully.

### **3.4.4 Soil-Reinforcement interaction**

The soil-reinforcement interface is the second issue for appropriate reinforcement scaling and selection as specified by Viswanadham and Konig (2004). The bond strength between the soil and reinforcement comprises frictional and passive resistance, which are functions of interface friction, reinforcement geometry and vertical confining stress (which has been discussed in Section 3.4.2 above).

Frictional resistance is determined by the interaction between the soil and reinforcement. The soil-reinforcement interaction is defined by manufacturer specified coefficients for pullout and direct sliding, determined via pullout testing in different soils. Microgrid has a soil-reinforcement interaction coefficient of 0.8 – 0.9 for a uniformly-graded Sand or Silty Sand such as Albany sand. Thus this coefficient is the same at both prototype and model scale because the same materials have been used.

To scale the passive resistance, i.e. the interlock of soil particles with the reinforcement, the reinforcement grid mesh size and characteristic soil particle size diameter (PSD) requires scaling. A comparison between the PSD of reinforced soil backfill recommended in the NZ Guidelines (Murashev 2003) and the PSD of Albany sand is shown in Figure 3-4. The NZ Guidelines provide upper and lower bounds on the PSD of soil suggested for use in the reinforced zone, with a mean  $D_{50} = 4.35$  mm. Albany sand has a  $D_{50} = 0.3$  mm, roughly 15 times smaller, and, in terms of prototype scale, is over-scaled by 3 times (15/5).

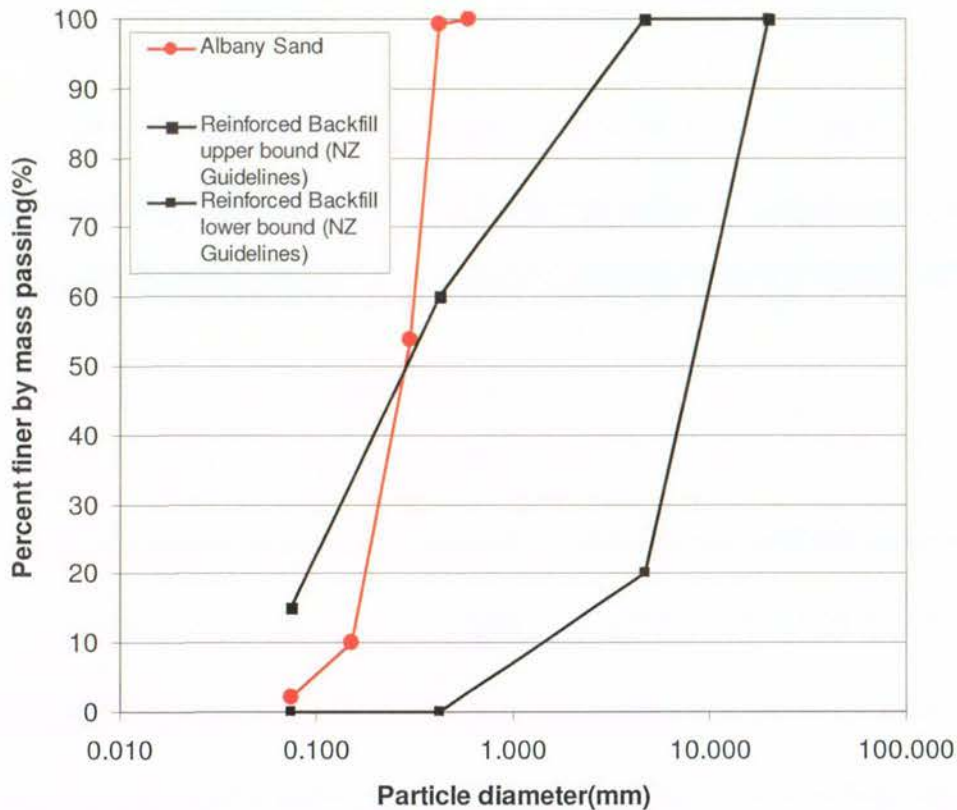


Figure 3-4. Comparison of reinforced backfill recommended PSD from the NZ Guidelines (Murashev, 2003) and Albany Sand used in the tests.

The Microgrid mesh size is 7.5 by 2.5 mm, with a mesh area of  $\sim 19 \text{ mm}^2$ . Compared to a typical geogrid mesh area of  $3300 \text{ mm}^2$ , the Microgrid mesh is smaller by 175 times. This means that the reinforcement does not meet the requirements of scaled geometry for passive resistance. Viswanadham and Konig (2004) notes that this has been a factor in past experimental testing and that researchers have been more concerned with modes of failure and qualitative rather than quantitative comparisons. However, Nova-Roessig and Sitar (2006) report research conducted by Richardson and Lee (1975) where sufficient soil-reinforcement interlock in the scale model was only achieved through setting the reinforcement at an impractical  $L/H = 2.5$ . As noted by Watanabe et al. (2003) above, this would impact on failure patterns and modes observed.

The above analysis indicates that the mean grain size to reinforcement mesh size has not been geometrically scaled well, and this could impact on observed behaviour due to a reduced passive resistance. However it was deemed as being of secondary importance to reinforcement stiffness, reinforcement-soil interlock, and reinforcement  $L/H$ , to obtain results more consistent with those observed at prototype scale.

### **3.4.5 Full-height Rigid (FHR) facing**

The facing is more difficult to scale quantitatively, as there is large variety in how facing structures are designed, constructed and used. In these tests, Full-Height Rigid (FHR) facings were used due to their 'excellent' performance in previous earthquakes in Japan (Tatsuoka 2008).

El-Emam and Bathurst (2005) considered the effects of facing condition by constructing the wall face from rectangular steel cross sections bolted rigid together. The sections could be rotated and stacked to double wall thickness from 36 to 72 mm, with a doubling of facing weight also. Facing geometry and type had a large influence on wall behaviour; very stiff facings transferred up to 60% of dynamic reinforcement loads to the facing toe. The results indicated decreasing stability with increasing wall mass for the ranges tested; thus a stiff panel of low weight was selected for the current experiments.

The facing comprises an aluminium panel nominally 960 mm by 800 mm and 5 mm thick, stiffened in the vertical and horizontal directions with steel angles. The entire face weighs 30 kg and was constructed with the aim that its influence on behaviour was minimal, and that facing rigidity was maintained during preparation and testing. This ensured that the conditions of a typical FHR facing panel were achieved, without other characteristics such as the weight and geometry influencing results considerably.

### **3.4.6 Connections**

The mechanical properties of the connection govern the transfer of stress from the reinforcement to the wall face and visa versa. Connections between the reinforcement can either be rigid, in which case the full benefits of a FHR panel facing are realised, or imperfectly rigid. For the tests conducted, a rigid connection was created with a steel strip clamping the reinforcement to the face. This prevented slippage of the reinforcement, simplifying interpretation of results.

### **3.4.7 Model excitation**

The three important components of an earthquake motion for engineering purposes are the acceleration amplitude, frequency content and its duration (Kramer 1996). With reference to

the similitude discussed previously, motion frequency was scaled appropriately as discussed below. The effects of amplitude and duration are considered in the model results.

A typical medium to high intensity strong motion earthquake has a predominant frequency of 2 – 3 Hz (0.3 – 0.5 seconds) (Hatami and Bathurst 2000). As noted previously, Iai (1989) allowed for the simple case where the model soil density is the same both at prototype and model scales, and the soil strain scale factor  $\lambda_\epsilon$  is unity. The similitude rules govern the selection of an appropriate frequency of input motion at model scale as shown in Equation 3-6:

$$(t)_p = \lambda_t (t)_m = (\lambda \lambda_\epsilon)^{0.5} (t)_m \quad (3-6)$$

Where  $(t)_p$  and  $(t)_m$  are the time dimensions at prototype and model scale,  $\lambda_t$  is the time scaling factor,  $\lambda$  the geometric scale factor, and  $\lambda_\epsilon$  the soil strain scale factor. Equation 3-7 calculates the predominant frequency at model scale:

$$(t)_m = \frac{(t)_p}{(\lambda \lambda_\epsilon)^{0.5}} = \frac{0.5}{(5)^{0.5}} = 0.2 \text{ sec} \quad (3-7)$$

Hence a predominant frequency of 5 Hz was selected, allowing comparison of results with other model studies conducted at this frequency of excitation (El-Emam and Bathurst 2004; El-Emam and Bathurst 2005; Watanabe et al. 2003).

For modeling purposes, the shape of the driving motion is also important. A series of studies conducted by Watanabe et al. (2003) showed that the intensity of loading increased in the order of: shaking with an irregular time-history, shaking sinusoidally and pseudo-static loading with a tilt-table. Whilst an irregular time-history is more realistic, its analysis and repeatability to enable comparisons across tests is difficult, and a sinusoidal motion was chosen for its high repeatability and easier interpretation of results. As discussed later, this simple base excitation contains more energy than an earthquake time history of similar predominant frequency and peak acceleration amplitude (El-Emam and Bathurst 2005; Watanabe et al. 2003). In other words, in a sinusoidal excitation, the PGA occurs every cycle, while an irregular time history scaled to the same PGA, might only have a single occurrence of this PGA. Hence, in terms of duration of time at PGA, the sinusoid is a more intense excitation than the irregular ground motion.

For completeness, a sinusoidal excitation of 5 Hz frequency with an acceleration amplitude of 0.1g for a duration of 10 seconds (50 cycles) was applied for the first shaking step. The acceleration amplitude was then increased in 0.1g increments until model failure.

### 3.4.8 Summary of model geometry

The previous sections detail the similitude considerations behind the selection of various model parameters and geometry. These issues are summarised in Figure 3-5 (a) and (b).

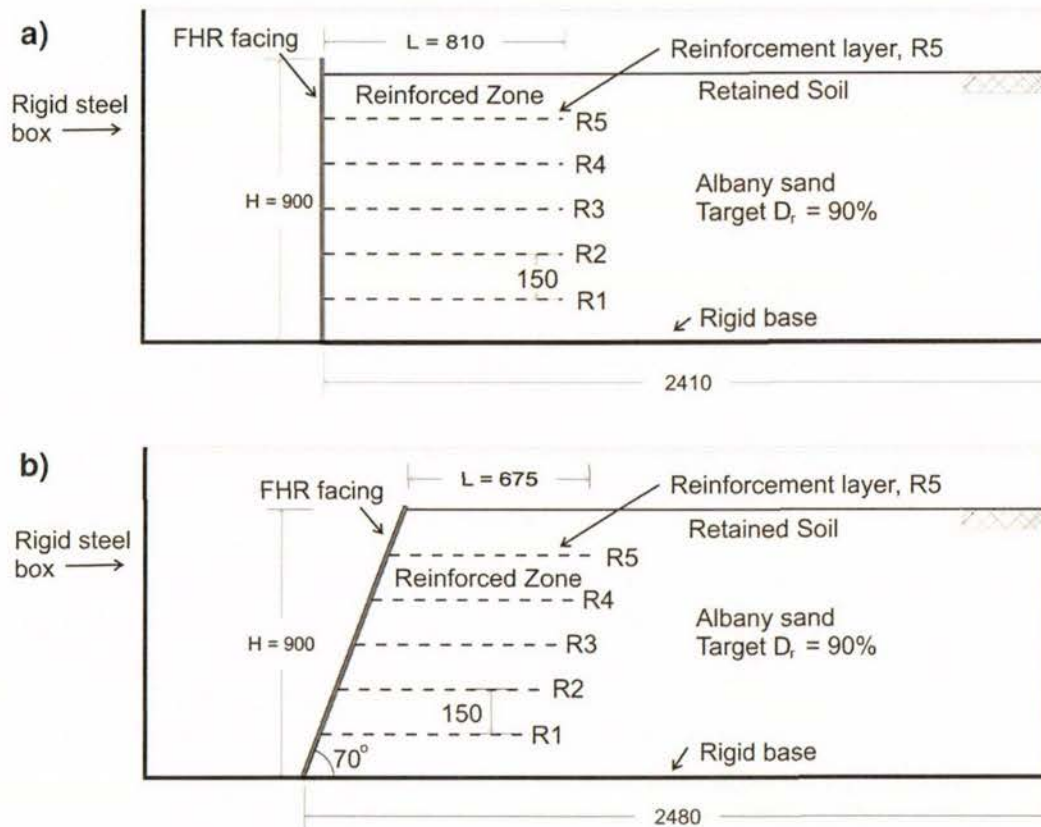


Figure 3-5. Model geometry inside strong box for: a) vertical model reinforced the longest at  $L/H = 0.9$ , and b) inclined wall at  $70^\circ$ , reinforced at  $L/H = 0.75$ .

The wall face is a FHR aluminium panel 5 mm thick and 960 mm high which fits into the 800 mm wide box mounted onto a 4.0 m long by 2.0 m wide shake-table. (Note the extra 60 mm wall facing in height is to allow the same panel to be used for the inclined model wall). The backfill is Albany Sand compacted to a target relative density of  $D_r = 90\%$  deposited upon the base of the rigid box with a glued sand layer to ensure sufficient friction between the rigid base and backfill. The sand deposit consists of six layers up to a total height of 900 mm.

Based on stiffness similitude Microgrid reinforcement was selected. This reinforcement is a polyester geogrid and can be classified as 'extensible' at prototype scale. The reinforcement length was varied to achieve a reinforcement-to-wall height ratio,  $L/H = 0.6, 0.75$  and  $0.9$ . The vertical spacing between reinforcement layers for all models was  $150$  mm. Figure 3-5 (a) shows the longest reinforcement length of  $810$  mm ( $L/H = 0.9$ ).

Figure 3-5 (a) and (b) also shows the reinforcement numbering used for the description of model deformation in Chapter 5.

### 3.5 Shake-table and motion dynamics

The box and GRS model within were mounted on the University of Canterbury shake-table. The uni-directional shake-table is dimensioned  $4.0$  m by  $2.0$  m, has a maximum velocity of  $240$  mm/s, maximum payload of  $20$  T and a peak displacement amplitude stroke of  $\pm 120$  mm.

The shake-table is displacement controlled; displacement amplitude and frequency with time generate the desired acceleration as shown in the governing dynamic Equation 3-8.

$$\begin{aligned} a(t) &= -\omega^2 d(t) \\ \omega &= 2\pi f \end{aligned} \tag{3-8}$$

Where  $a(t)$  and  $d(t)$  are the shake-table acceleration and displacement, and  $\omega$  and  $f$  are the angular and temporal frequencies of motion. Thus a sinusoidal wave of frequency  $5$  Hz and displacement amplitude of  $1$  mm creates a sinusoidal acceleration with an amplitude of  $0.1g$ .

The experimental sign convention is positive for outward displacements, velocities and accelerations (with respect to the backfill) and is shown in Figure 3-6 below. The minus sign in Equation 3-8 means that the acceleration and displacement vectors are always  $180^\circ$  out of phase, that is, outward wall accelerations are positive and occur when the wall is negatively displaced.

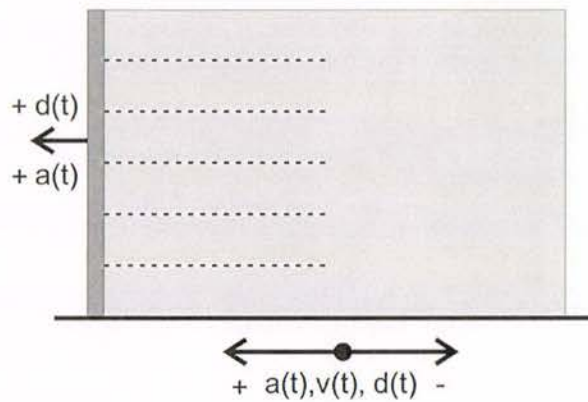


**Figure 3-6. Sign convention of shake-table and model dynamics**

The shake-table system is driven by a 280 kN double-acting hydraulic actuator, powered by a 300 Hp motor operating at 4000 psi. The hydraulic actuator is controlled by a set of two E072-054 servovalves controlled by a TestStar control system supplied by MTS Systems Corporation. The system has a built in Linear Variable Differential Transducer (LVDT) that measures table displacement. Ang (1985) reviews the shake-table capabilities in-depth.

The shake table at the University of Canterbury has an unloaded resonance frequency of around 17.5 Hz (Murahidy 2004). Murahidy (2004) further developed a relationship between shake-table payload and natural frequency. This relationship was used to predict the natural frequency of the shake-table, box and sand mass of the current testing system. The box filled with sand had a combined weight of 3600 kg, and according to Murahidy's (2004) relationship, the combined system had a natural frequency of around 13.7 Hz; larger than the testing frequency of 5 Hz. Little can be done to mitigate possible resonance effects, however they are considered minimal.

### **3.6 Instrumentation**

Instrumentation was designed to effectively quantify the seismic response at varying intensity levels and is shown in Figure 3-7 (a - c).

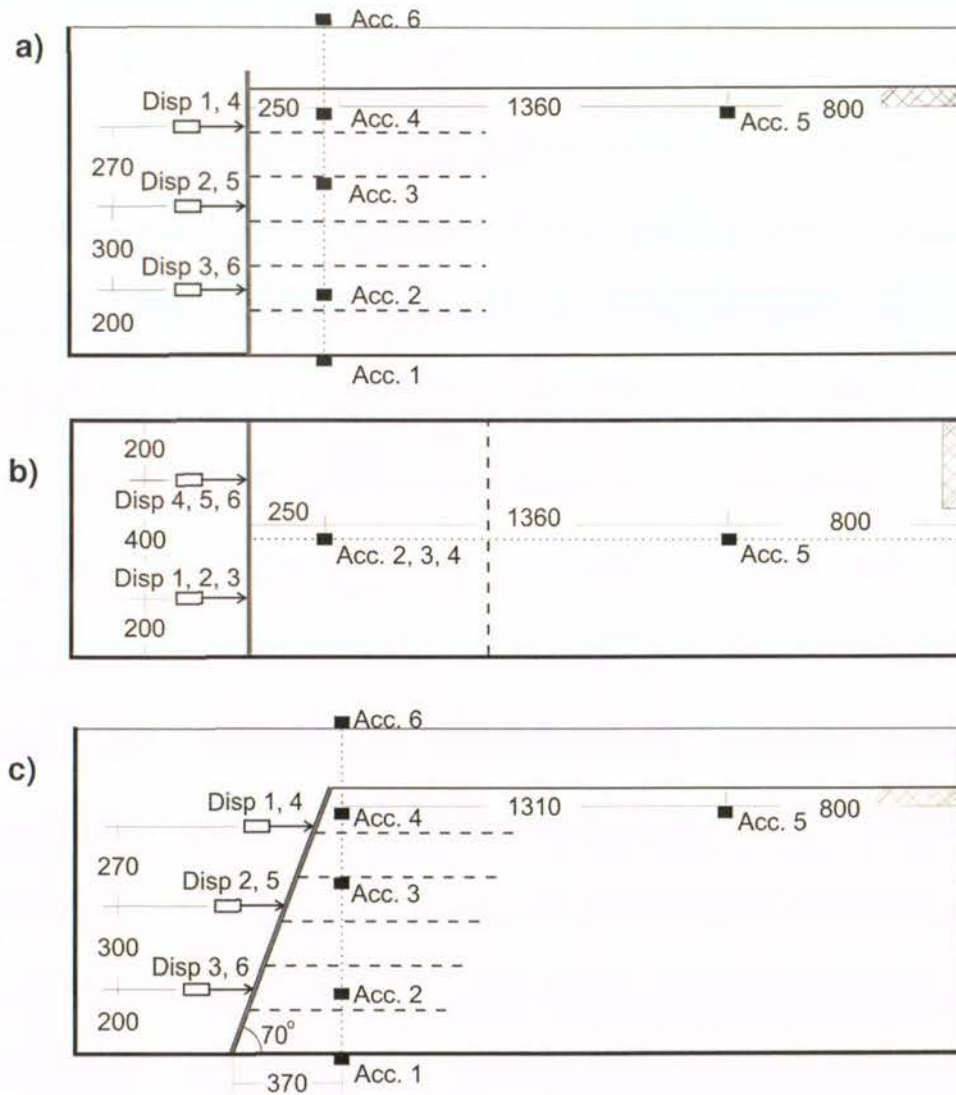


Figure 3-7. Model instrumentation for (a) the vertical wall reinforced the longest at  $L/H = 0.9$  (Test-3 and 5); b) plan view of vertical wall (reinforced by  $L/H = 0.9$ ); and, (c) the inclined wall, reinforced by  $L/H = 0.75$  (Test-7).

### 3.6.1 Facing displacements

Two arrays of three displacement transducers (Disp. 1 – 6) were located in series at the front of the wall at heights 775, 500 and 200 mm as seen in Figure 3-7 (a) and (c). Each array was located 200 mm from the side-wall and named the North (Disp. 1 – 3) and South (Disp. 4 – 6) Array, as seen in Figure 3-7 (b).

### 3.6.2 Shake-table and soil accelerations

Four accelerometers to be placed into the soil deposit at varying heights were purchased for the experiment. A number of factors influenced their selection which included:

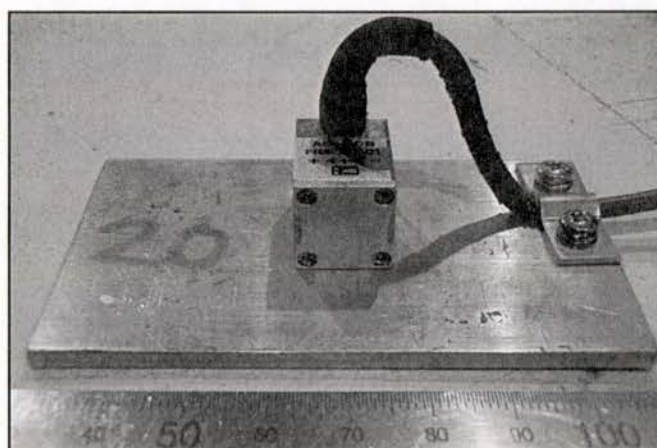
- Size (minimal impact on natural vibration of the soil)
- Ability to withstand the abrasive sand environment as well as high soil pressures
- Measurement range and safe overload capacity
- Natural frequency
- Data sampling rate.

Accelerometer model AS-2GB manufactured by Kyowa was selected as it met all of the above listed criteria. The compact accelerometer weighed 25 g and is dimensioned nominally at 14 x 14 x 20 mm resulting in minimal impact on the vibration mode of the soil deposit.

**Table 3-6 Accelerometer AS-2GB Specifications**

Parameter	Value
Rated Capacity	$\pm 9.807 \text{ m/s}^2$
Frequency Response (at 23°C)	DC to 60 Hz ( $\pm 5\%$ )
Resonance Frequency	100 Hz

The accelerometers were mounted on aluminum plates measuring nominally 50 mm by 80 mm and 3 mm thick, with the total height of the accelerometer being 14 mm off the plate's surface. The cable is integrated with the accelerometer perpendicular to the plate surface and extended roughly 15 mm above the accelerometer.



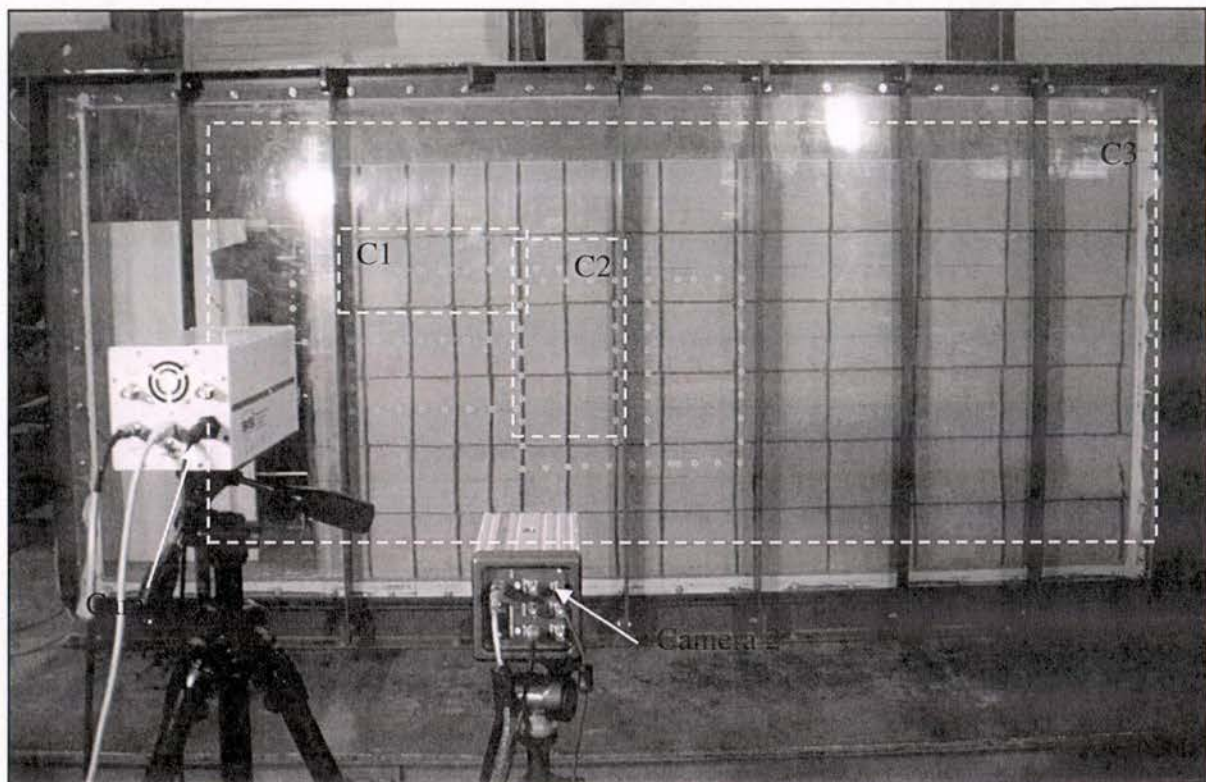
**Figure 3-8. Kyowa AS-2GA accelerometer mounted on aluminium plate.**

Figure 3-7 (a) and (b) shows the location of the accelerometers within the soil deposit and on the shake-table and top of the box. In total, six accelerometers were used in the experiment. Acc. 1 and Acc. 6 were mounted on the shake-table and the rigid box itself, respectively. Acc. 2 – 4 were located vertically in line 250 mm from the wall face, and along the box centre-line to reduce boundary effects, and were used to measure the reinforced soil block

response. For the inclined wall, the accelerometers were still placed vertically and on average, 250 mm from the wall face. Acc. 5, was used to quantify the far-field response and was positioned along the box centerline, 800 from the box back wall (again to minimise boundary effects).

### 3.6.3 High-speed camera imaging

Three high-speed cameras were used to record deformations during testing. Camera 1 focused on the reinforcement layer R4 within the reinforced soil block and Camera 2 focused on the interface between the reinforced and retained backfill zones. Camera 3 was used to capture the global deformation of the entire wall. Figure 3-9 shows the regions recorded by each camera. Cameras 1 and 2 are visible in the picture mounted on tripods.



**Figure 3-9.** Regions recorded by each camera are shown in as the white dashed lines for Camera 1 – C1, Camera 2 – C2, and Camera 3 – C3 (not shown).

Camera 1 is a SVSi Camera (USA), and Camera 2 and 3 are MotionPro X3 Cameras (USA). The camera properties are summarised in Table 3-7. High-speed Nikon lenses were used for Cameras 1 and 2, to ensure sufficient light for texture tracking, whereas a standard Nikon lens was able to be used for Camera 3, which operated at a slower frame rate.

**Table 3-7. Camera specifications**

Camera	Purpose	Resolution (pixels)	Frame Rate (fps)	Exposure (msec)	Acquisition time (s)	Colour
Camera 1	Reinforced soil block	512 x 1280	200	5	12	Monochrome
Camera 2	Interface between reinforced and retained backfill	1280 x 1024	200	5	12	Monochrome
Camera 3	Global deformation	1280 x 1024	100	10	12	Colour

The nature of high-speed photography means that the images recorded are stored within the camera RAM during image capture. Hence the limited RAM of each camera controlled the selection of frame rate, resolution and acquisition duration. At the completion of each shaking step, the acquired image data was transferred to hard disk; this process could take up to 15 minutes between shaking steps.

### 3.7 Model construction

The staged construction procedure for GRS walls with FHR panel was discussed in Section 1.4.2. The model wall was not constructed in the staged manner for full-scale walls as described by Tatsuoka (2008). Rather, the construction method braced a single aluminium panel against the box, and the sand was layered and compacted behind it. A similar method was used by El-Emam and Bathurst (2004) who argued it to be a construction technique somewhat similar to the field case of an incrementally constructed (unbraced) segmental (modular block) wall and a FHR panel process.

Because soil behaviour depends on parameters such as confining stress, packing and density, the most important aspect of model construction is soil placement. Two methods considered for the placement and compaction of soil were those reported by Watanabe et al. (2003) and El-Emam and Bathurst (2004). Watanabe et al. (2003) constructed 500 mm high models in layers by air-pluviation to achieve a relative density of  $D_r = 90\%$ . El-Emam and Bathurst (2004) constructed their 1000 mm high models by first distributing sand in 100 mm thick layers, and then vibrating the shake-table and box after each layer to achieve a relative density of  $D_r = 86\%$ . Because air-pluviation is time intensive and requires the use of robotic-automated equipment the latter method used by El-Emam and Bathurst (2004) was selected for the current experiments and is described in Section 3.7.3 below.

Therefore, the staged construction of the model wall involved a number of steps: Connection of reinforcement to the FHR aluminium panel face; bracing the wall face for construction; layered placement and compaction of backfill; reinforcement placement; accelerometer

placement; incorporation of marker sand in both vertical and horizontal lines; and finally, the un-bracing of the wall face to produce the static self-weight condition for subsequent testing. Throughout the construction, layer-by-layer measurements of soil height and mass were made to enable calculation of average soil density. The movement of the wall during un-bracing was also recorded. These stages are described in the following sections.

### 3.7.1 Reinforcement connections

It is important to ensure the connection between reinforcement and facing panel is rigid (Section 3.4.6 above). This ensures that the wall deformations measured are the result of soil and reinforcement interaction as opposed to some (un-measured) degree of reinforcement slippage at the facing connection, thus simplifying the analysis.

The reinforcement is first connected to the FHR aluminium panel prior to being braced in the box. Five steel strips 16 mm wide and 3 mm thick were used to provide the rigid mechanical connection. The reinforcement was cut with an extra 16 mm in length which was clamped in between the facing and steel strip and bolted at 100 mm centres, as shown in Figure 3-10. Nakajima et al. (2007) used a similar method for reinforcement connection.

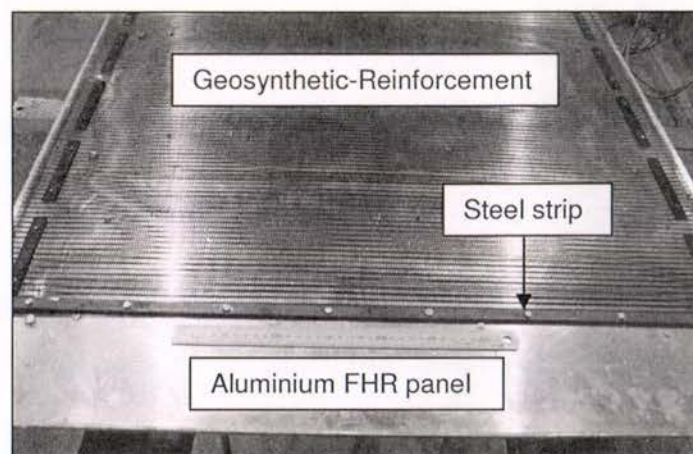


Figure 3-10. Rigid mechanical connection between reinforcement and aluminium panel.

The strength of the reinforcement at the connection sometimes limits design strength achievable in the reinforcement, and FHWA (2001) recommends long-term testing of this strength should this be a factor. No physical testing on the connection was conducted; however on visual inspection of the connection after deconstruction, slippage was never identified and the rigid assumption appeared validated.

### 3.7.2 FHR panel bracing

The FHR facing was an aluminium panel dimensioned 960 mm by 798 mm and 5 mm thick. The panel was stiffened symmetrically in the vertical direction by 4 steel angles with cross section dimensions of 41 mm by 41 mm and 15 mm thick. Three further steel angles of the same dimensions were used to stiffen the face in the horizontal direction at heights of 120, 100 and 730 mm. The panel and stiffeners are shown in Figure 3-11.

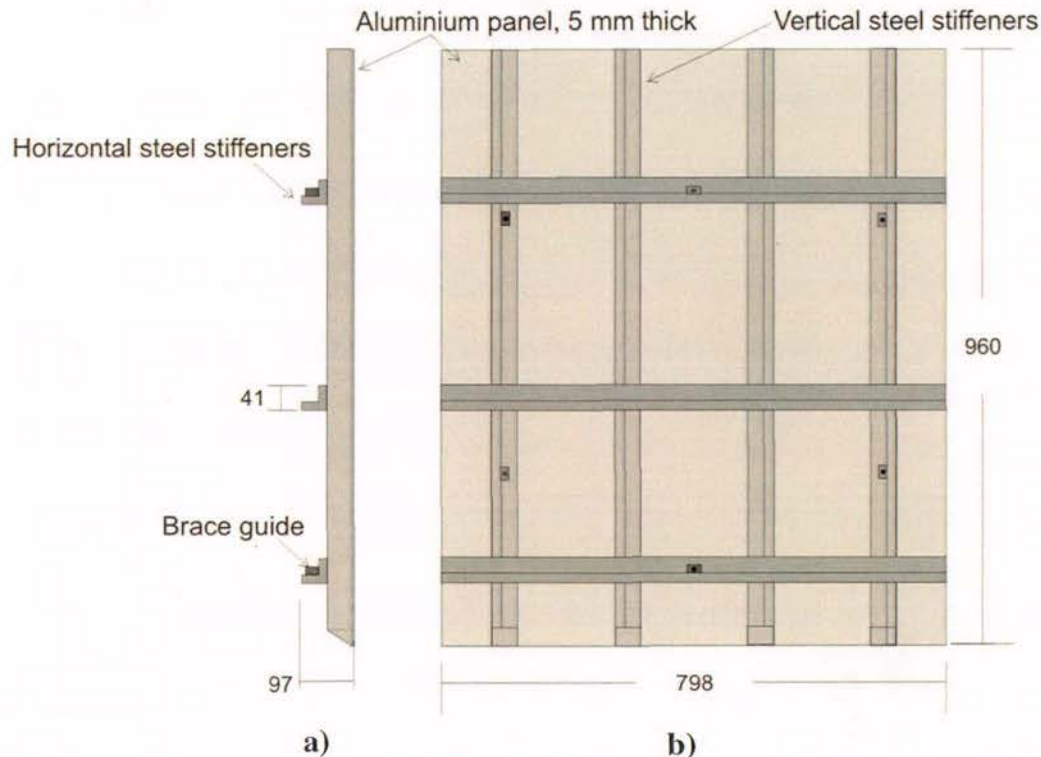
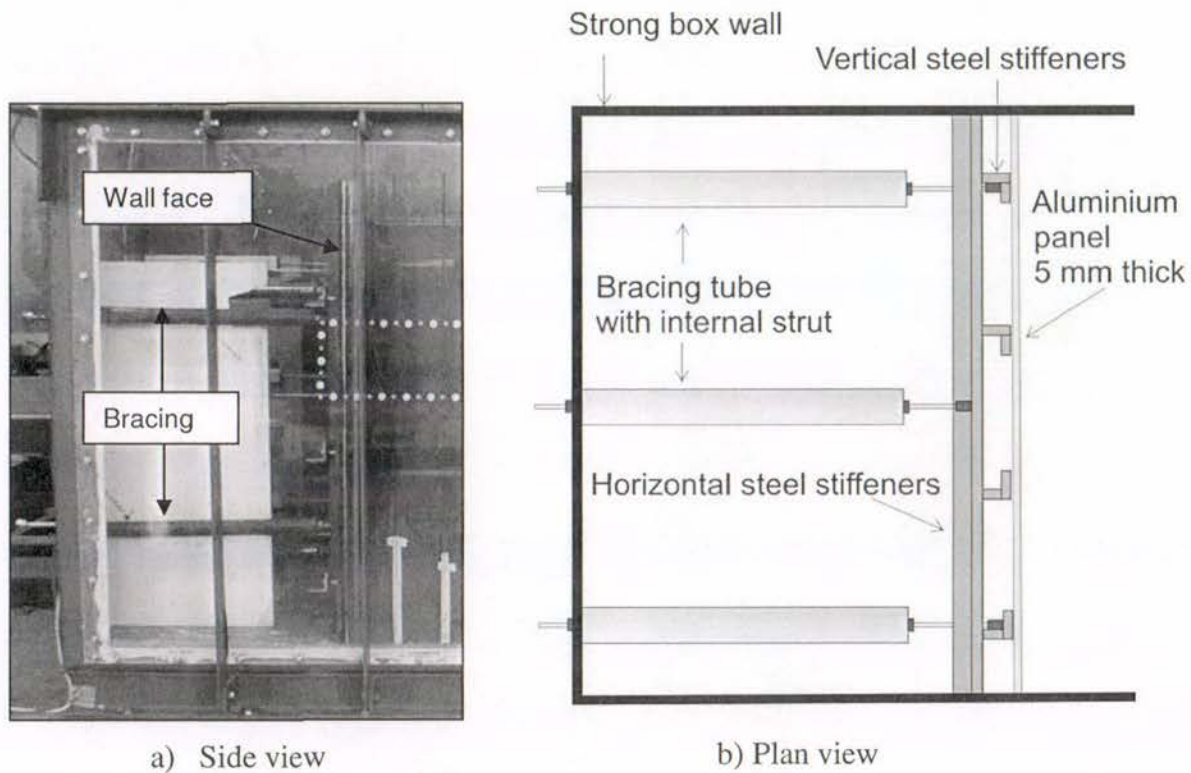


Figure 3-11. FHR aluminium panel with attached stiffeners and guides for wall bracing: a) side view, and b) front view.

The facing was placed squarely within the box and braced by six steel tubes arranged in two rows and three columns. The steel tubes were screwed tightly into guides mounted on the vertical and horizontal angle stiffeners. The wall face is shown fully braced in the box in Figure 3-12 (a). Figure 3-12 (b) shows a schematic plan view of the facing braced within the box.



**Figure 3-12.** The facing panel is rigidly braced against the box by six steel tubes attached by screws to the facing panel: a) side view through transparent sidewall, and b) schematic plan view.

### 3.7.3 Construction of model deposit

The soil deposit was constructed in layers 75 mm thick. Prior to sand placement, plastic tubes were taped against the acrylic wall for vertical columns of coloured sand to be poured in, as described in Section 3.7.5 below. The first stage of layer construction involved the determination of the mass of sand necessary to achieve the target density. Slight changes in face position would change the box volume, and thus mass required to achieve target soil density; hence internal length and widths were measured manually once the wall face was braced.

Four storage containers were constructed each able to contain 900 kg of sand. A crane scale calibrated to 1000 kg and accurate to  $\pm 0.2$  kg was connected to the container and crane. The container was lifted above the box and the combined mass of the container and sand recorded (Figure 3-13 (a)). The container sliding trapdoor was opened until the required sand mass for the layer (usually 245 kg) was deposited in the box. The sand was deposited evenly across the wall (Figure 3-13 (b)).

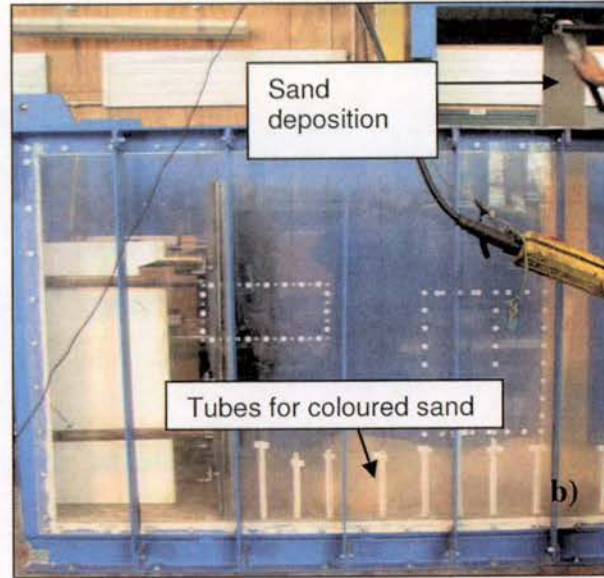
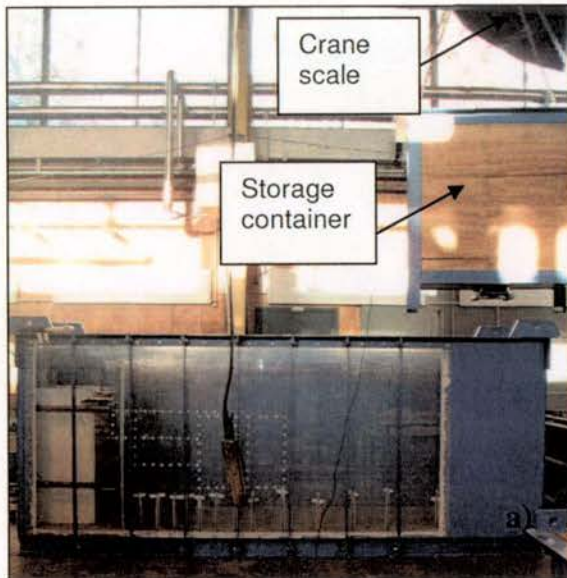
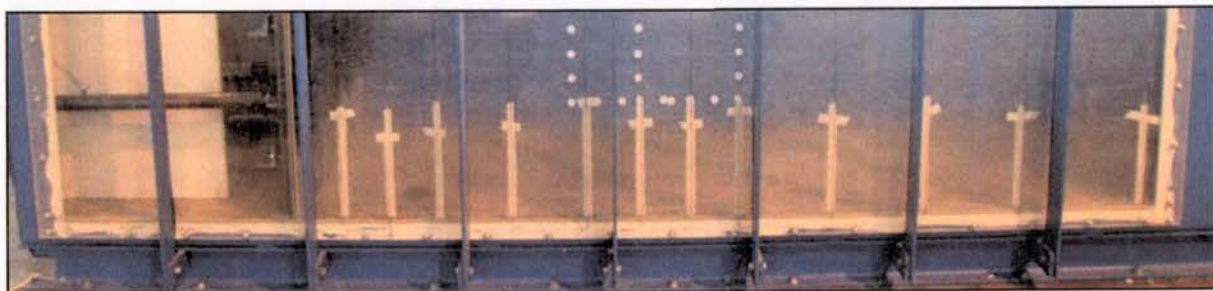


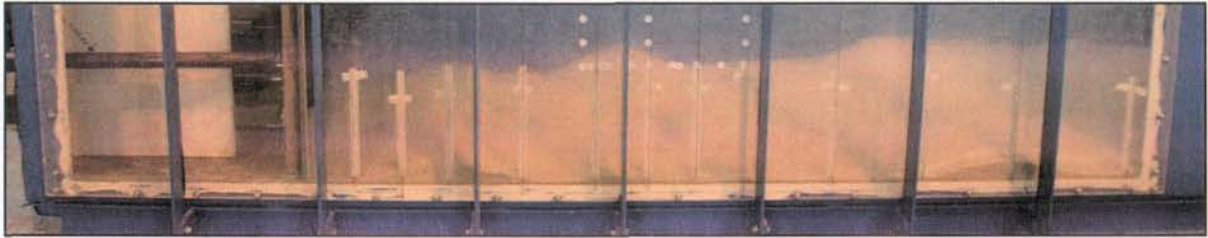
Figure 3-13. Storage container lifted into position above the box to record initial combined mass of container and sand (a) and sand deposition into the box (b).

Figure 3-14 (a – l) shows the construction process up the placement of the bottom layer of reinforcement. Figure 3-14 (a) shows the empty box with vertical tubes in position ready for the first layer of sand to be deposited as described above.

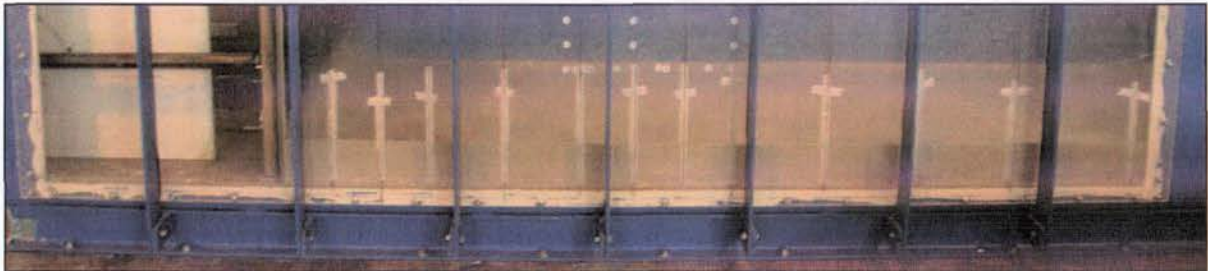
To ensure consistent compaction of each layer of sand, the surface of the sand layer had to be horizontal. Hence the deposited sand (Figure 3-14 (b)) was first raked, and then flattened with an adjustable wooden board, which was dragged across the surface of the layer. Depending on how loose the deposited sand was, the board's depth (with respect to the top of the box) was adjusted. Normally, the loose sand deposit was flattened to a level approximately 10 mm above the target layer thickness of 75 mm. The sand deposit after this process is shown in Figure 3-14 (c).



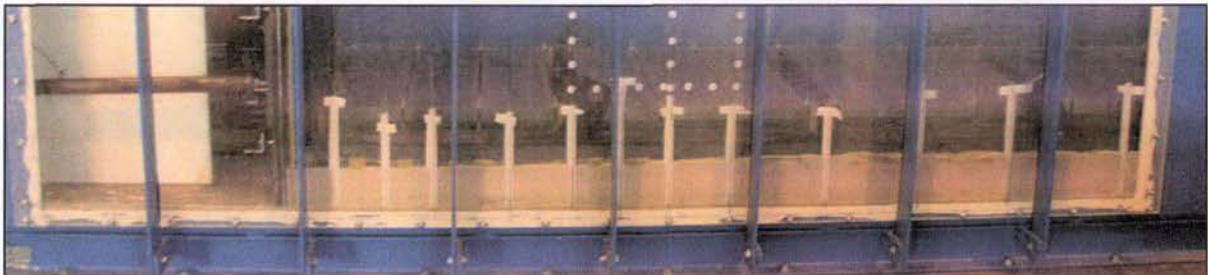
a) Empty box with vertical tubes taped into position.



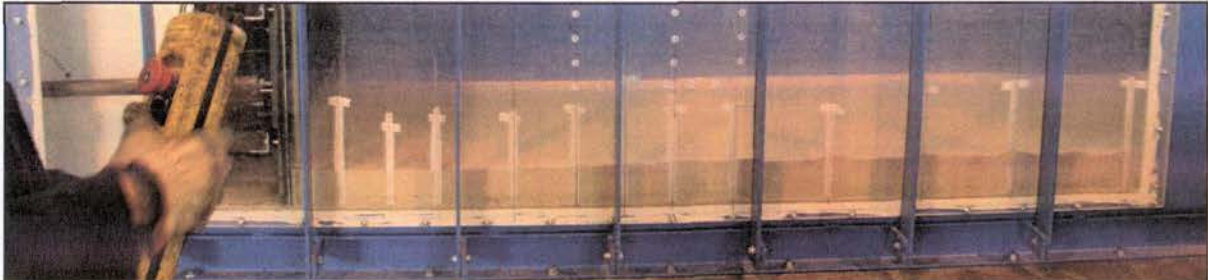
b) Loose sand after deposition.



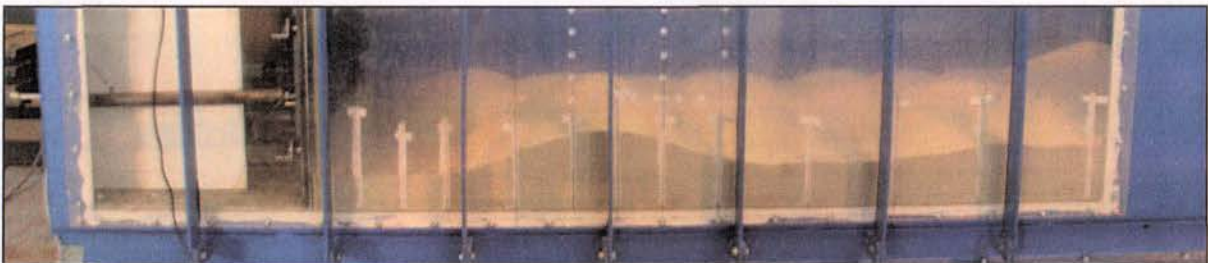
c) Loose sand after raking, and using the wood panel to make the sand surface flat.



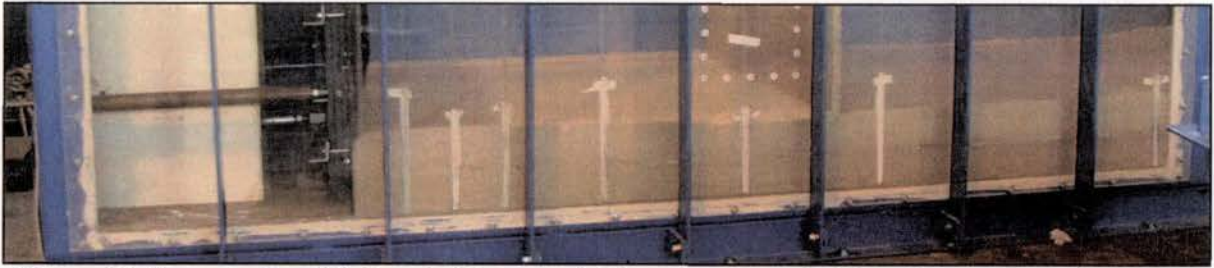
d) The compactor plate is lowered onto Layer 1 of flat loose sand. The shake-table is vibrated at 13 Hz for 10 seconds to compact the sand Layer. Layer height is then measured to the top of the compactor plate at both sidewalls at intervals of 30 cm. The known thickness of the compactor plate is removed to determine the sand layer thickness.



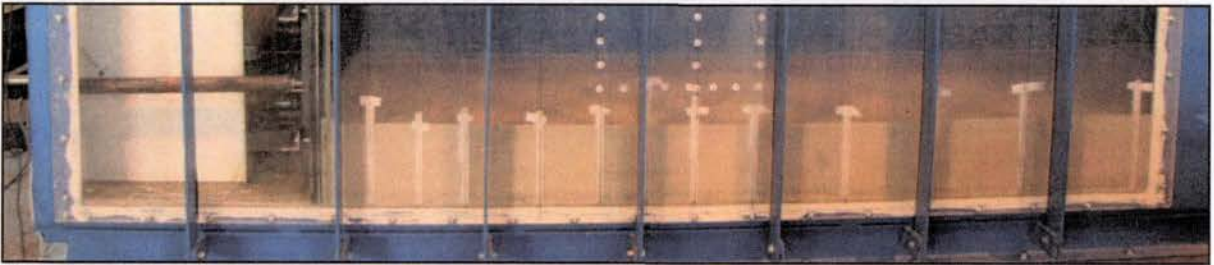
e) Layer 1 post compaction and removal of the compactor plate.



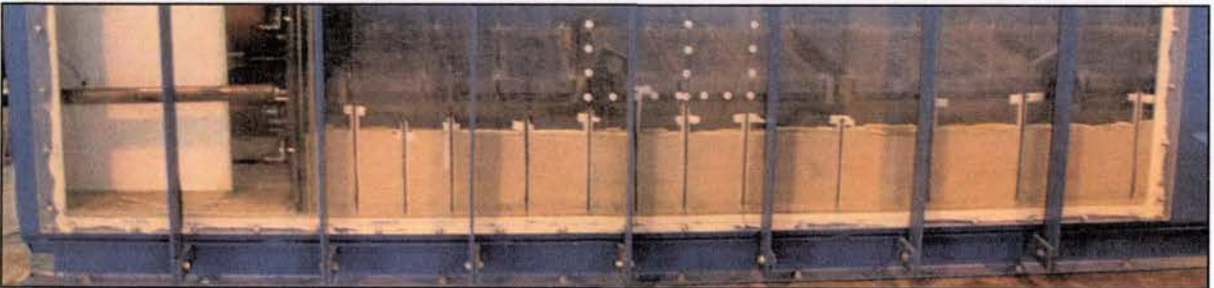
f) Sand is deposited for Layer 2 on top of compacted Layer 1.



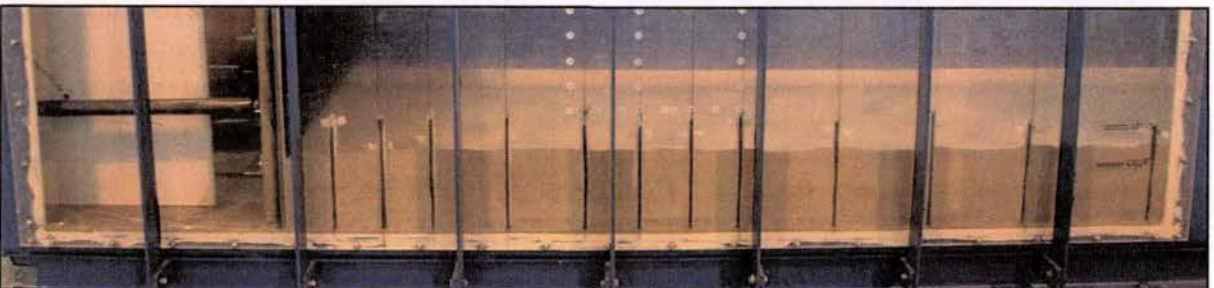
**g) Layer 2 is then raked and flattened with suspended board to known height prior to compaction.**



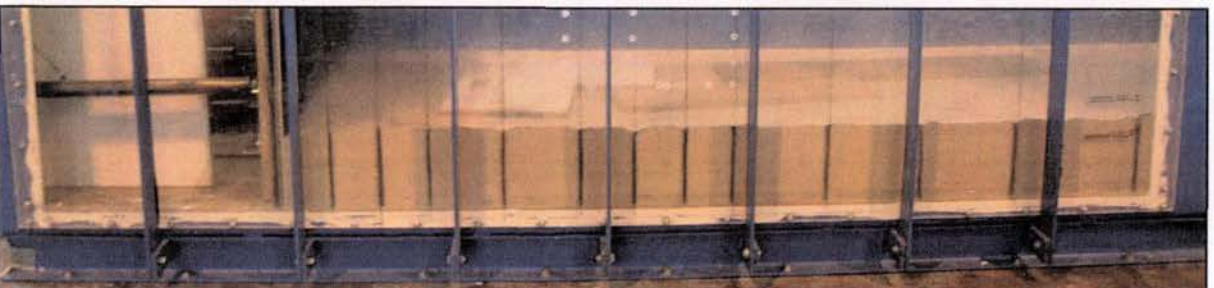
**h) Flattened Layer 2, ready for compaction.**



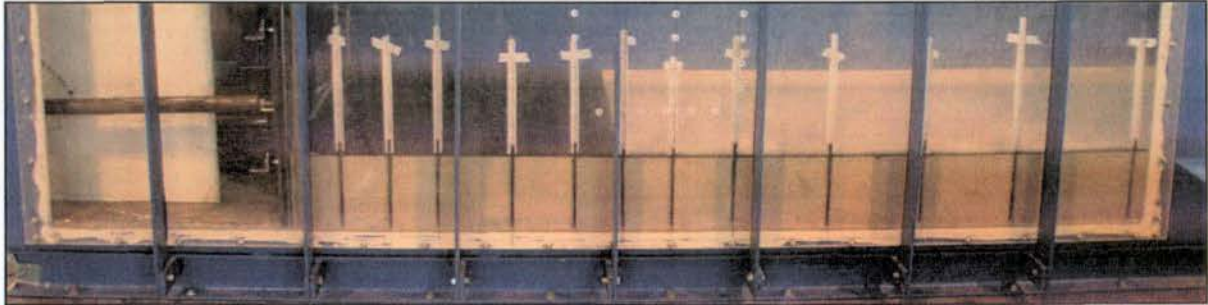
**i) Compactor plate on Layer 2, post compaction. Soil height is measured post compaction.**



**j) Layer 2 post compaction with compactor plate removed.**



**k) Boards are carefully placed on top of Layer 2 to enable access to the inside of the box. The tape holding the vertical coloured sand lines is carefully removed.**



l) Finally, Layer 2 is scraped flat at the sidewall to correspond with the surface at the box centreline and the reinforcement is pulled out horizontally from the wall face. A coloured sand line is created against the sidewall window (flattened to a thickness of 4 mm), and the vertical tubes reset for the next two layers.

Figure 3-14 (a) – (l). Describes the layer construction process in detail.

Three methods were trialled to compact flat the sand layer:

- Manual hand-held plate compaction;
- Shake-table vibration with no surcharge weights;
- Shake-table vibration with surcharge.

The first two were deemed unsatisfactory: for the first method, it was impossible to uniformly compact layers; and for the second method, the shake-table/box/sand system dynamics were such that, in contrast to the construction methodology used by El-Emam and Bathurst (2004), simple shake-table vibration was found to be unable to compact the sand. The third method, whereby a surcharge weighing approximately 950 kg was used during vibration was selected, and Figure 3-14 (c) shows the compactor plate resting on the flat sand layer. For this method, the shake-table was vibrated with a displacement stroke amplitude of 2 mm at 13 Hz for a duration of 10 seconds. This equates roughly to an acceleration amplitude of 1.4g.

Post-compaction, the height of the compaction plate with respect to target layer heights marked along both sidewalls of the box was measured and recorded at 30 cm intervals. As the compactor plate is rigid, these measurements gave an indication of the average layer compaction response along the centreline of the box. The compactor plate was removed and the process repeated for the second layer of sand as shown in Figure 3-14 (e) – (i). Figure 3-14 (j) – (k) shows the horizontal layers and vertical columns of black sand that were then created as discussed in Section 3.7.5 below.

### 3.7.4 Reinforcement and accelerometer placement

The reinforcement was placed before the horizontal coloured sand layer was made and the reinforcement pulled taut ready for deposition of the next sand layer. Care was taken not to impart any tension to the reinforcement, as this could alter the stress condition of the model prior to shaking as shown in Figure 3-15 (a).

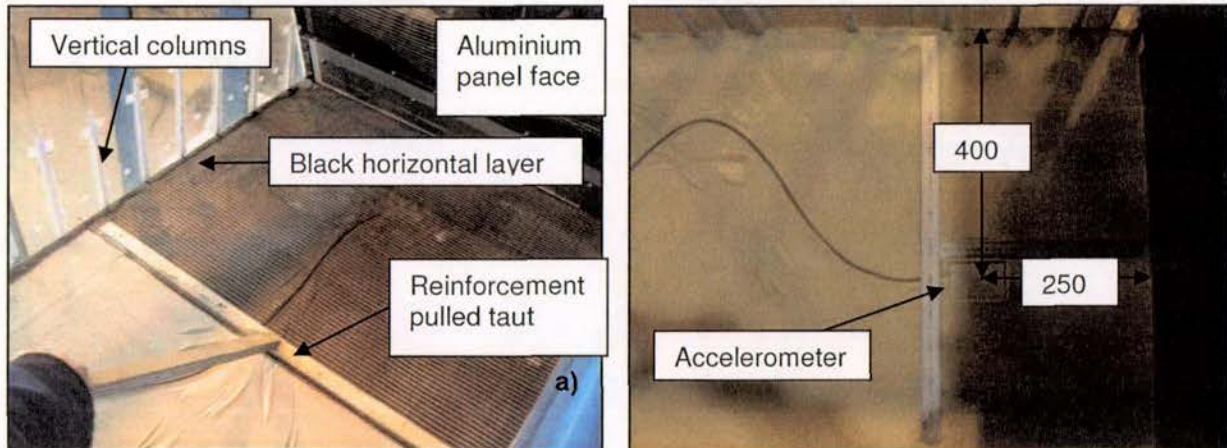


Figure 3-15. Reinforcement unfolded from the wall and placed in position on the surface of layer 2 (a), accelerometer embedded into the top of layer 3 at a distance of 250 mm from the wall face and along the box centreline (400 mm from the box sidewall) (b).

After the compaction of layers 3, 8 and 11, accelerometers (Acc 2, Acc 3, and Acc 4) were embedded upside down at the top of the layer along the box centreline 250 mm from the wall face as shown in Figure 3-15 (b). Acc 5 was placed 800 from the box back-wall.

### 3.7.5 Vertical columns and horizontal layers of black marker sand

Use of horizontal coloured sand lines to clarify deformation in some form or another is common in the literature for tilt-table, 1-g shake-table and geotechnical centrifuge tests (see for example Koseki et al. (1998), Watanabe et al. (2003), El-Emam and Bathurst (2004), Nova-Roessig and Sitar (2006)). In particular centrifuge tests by Nova-Roessig and Sitar (2006) used white sand along each reinforcement layer to identify the reinforced zone, green sand layered within the backfill to show the location of potential failure surfaces and black sand markers arranged in a grid to monitor lateral and horizontal displacements. While the grid arrangement used by Nova-Roessig and Sitar (2006) was able to fully resolve visualisation of deformation, using only horizontal coloured marker layers limits visualisation to vertical and rotational movements.

Relatively few researchers have used vertical columns of coloured sand to monitor translational movement deformation within the reinforced-soil block. Lo Grasso et al. (2004) and Howard et al. (1998) utilised coloured columns of black sand in shake-table tests 0.35 m high and centrifuge models 0.33 m high respectively to better visualise mechanisms of failure. This allowed both failure planes within the backfill and horizontal displacement of the reinforced soil zone to be clearly visible. However, these were constructed in models of relatively small dimensions and the use of a similar construction technique for models 900 mm high was found difficult to replicate.

A method for constructing vertical columns of black sand into models almost 3 times taller than that constructed in the abovementioned studies was created for the purposes of this research. Plastic tubes ~ 200 mm in length (longer than the reinforcement spacing of 150 mm) were taped to the inside of the transparent wall as visible in Figure 3-14 (a) – (l) which described the layer construction process in detail. The initial tube set up for the entire layer is shown in Figure 3-14 (a). The tape was looped back up to the top of the tube such that when pulled, the tape would be gradually removed from the bottom of the tube until the tube was no longer taped to the inside of the wall, as shown in Figure 3-16 (a – d).

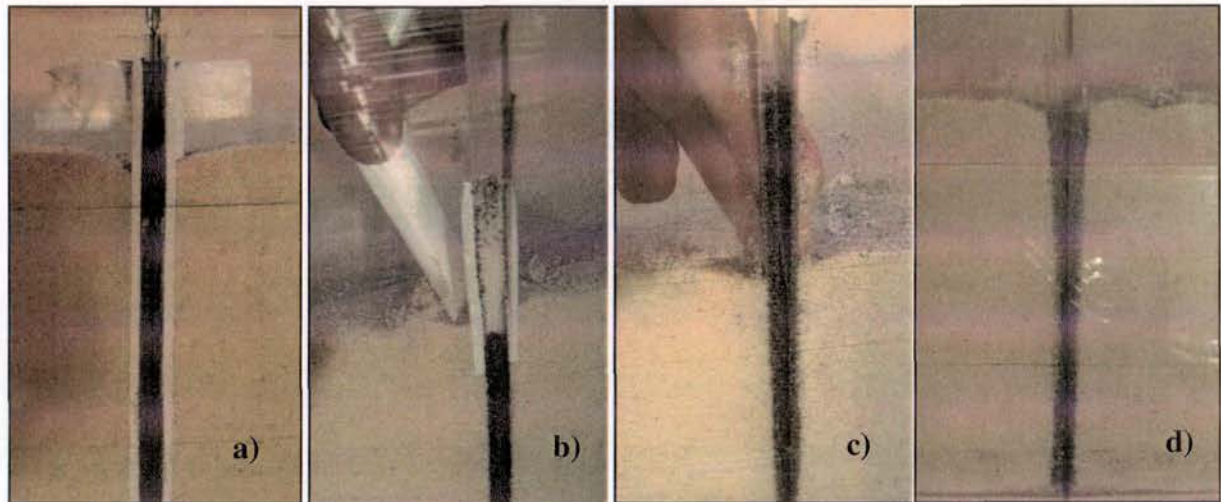


**Figure 3-16.** The tubes are filled with black sand when taped (a), after two layers have been compacted the tape is removed by pulling upwards (b) leaving just the plastic tube held against the wall by the sand pressure (c) which is then removed (d).

Once taped, the tubes could be filled with black sand, a close up of which is shown in Figure 3-16 (a). After two layers have been compacted the tape was removed by pulling upwards (Figure 3-16 (b)) and this left the plastic tube held against the wall by sand pressure only.

Figure 3-16 (c) shows the tube then being manually removed. This staged construction ensured:

- The plastic tubes could be removed (high soil density prevented un-taping of the tubes and subsequent tube removal when tube sections were longer);
- The plastic columns did not interfere with the reinforcement placement at the box sidewalls;
- The soil disturbed on removal of the plastic tubes is able to be subsequently re-densified during compaction of above layers.

During compaction some sand would be vibrated upwards around the compaction plate at the box sidewalls (see Figure 3-14 (h)), this, and the removal of the vertical tubes left the sand in an uneven and loose state at the box sidewalls (see Figure 3-16 (d)); as mentioned above, this sand was scraped flat and the layer surface made flat for subsequent reinforcement placement and horizontal line construction.

The horizontal black sand lines were made against the acrylic wall above the placed reinforcement and across the retained backfill. Each line was made by funnelling the coloured sand; it too was scraped level to achieve a layer thickness of 4 mm. Once the reinforcement was placed, the vertical tubes were re-positioned above ready for construction of the next two layers as shown in Figure 3-14 (I). While care was taken to ensure that the columns were placed vertically in-line to enable inter-layer displacement to be visible, sometimes during compaction the sand layers beneath that being compacted underwent some lateral displacement. This resulted in the vertical lines sometimes being slightly curved prior to testing, as can be seen in photos in subsequent sections. Thus only qualitative measures of deformation can be inferred from the black marker lines.

### **3.8 End of construction and static self-weight response**

Upon completion of compaction of all layers, the facing braces were removed. At this point, some movement of the wall occurred (on the order of 0.5 – 1.5 mm at wall top) as lateral earth pressures reduced towards the active earth pressure,  $K_a$ , and the reinforcement was fully/partially engaged. The initial displacement is governed primarily by the stiffness of the reinforcement (inextensible vs extensible) and connections, the amount of slack in the

reinforcement, and the compaction of the retained fill. The displacement of the wall upon the removal of the braces was recorded at each displacement transducer and is shown in Figure 3-17 for each reinforcement layout:  $L/H = 0.6, 0.75$  and  $0.9$  (Tests-6, 1 and 5 respectively). Note that for Figure 3-17 (a) and (c), the points of lateral displacement are averaged from the North and South Arrays, and also that Figure 3-17 (c) shows the results from both Tests-3 and 5. This position of the wall under self-weight was taken as the initial position prior to shaking.

Note that the lines linking lateral displacements are extrapolated to both the wall toe and top. From these extrapolations - which may not be valid at such small displacements - both sliding and overturning modes of deformation are apparent.

The largest displacement upon removal of the bracing occurred at the top of the wall. It can be seen that a decrease in facing displacement from 1.5 mm to 1.1 mm at wall top occurred with an increase in  $L/H$  from 0.75 to 0.9. No difference in facing deformation is noticeable for reinforcement ratios of  $L/H = 0.6$  and 0.75. Factors that may act to reduce the movement of the wall under static self-weight loading include:

- Minimal slackness of reinforcement present during construction
- The retained fill density is high
- The reinforcement is considered extensible at prototype scale, however as noted is likely under-scaled at model scale in the current experiments (i.e. the model reinforcement acts inextensibly).

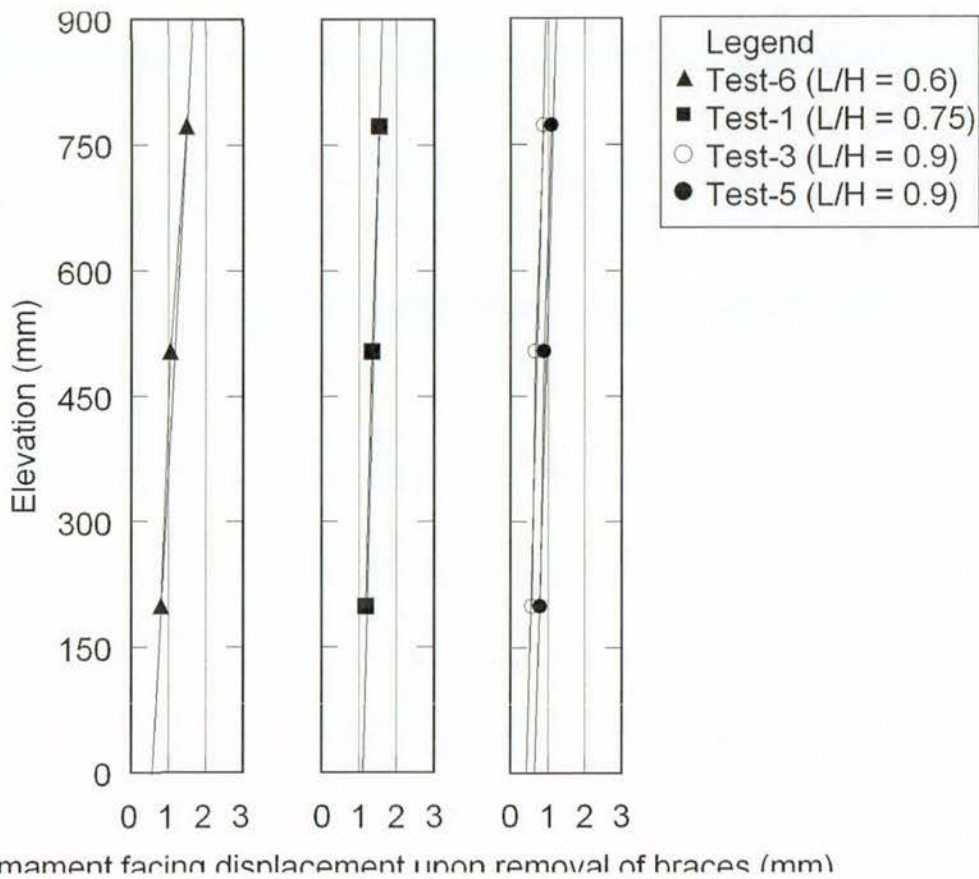


Figure 3-17. Average lateral displacement of the wall face under self-weight at the end of construction of walls a) Test-6, L/H = 0.6; b) Test-1, L/H = 0.75; and c) Tests-3 and 5, L/H = 0.9.

The deformations equate to displacements at the wall top of around ~ 0.17% of the wall height for L/H = 0.6 and 0.75 (Test-6 and 1), and around ~ 0.11% for L/H = 0.9 (Tests-3 and 5). Ling et al. (2004) measured facing displacements during and post-construction of a full-scale 6 m high GRS segmental-panel faced retaining wall. The largest lateral facing displacements under static self-weight were recorded at mid-height (due to the non-rigid segmental face) and were of the order of 0.5% of the height, larger than those observed in this study (Figure 3-17).

The NZ Guidelines (Murashev 2003) provide an empirical assessment of lateral displacement post construction based on the FHWA (2001) Guidelines. Equation 3-9 is used to calculate a maximum lateral displacement of the wall assumed to occur at the top of the wall during construction.

$$\delta_{\max} = \delta_R H / 75 \quad (3-9)$$

Where  $\delta_R$  is the relative lateral displacement (dimension-less) based on reinforcement layout for a 6 m high wall, and H (m) is the height of the wall under consideration. An empirical design chart determines the relative lateral displacement,  $\delta_R$ , for reinforcement ratios  $L/H = 0.6, 0.75$  and  $0.9$  as  $1.22, 0.73,$  and  $0.95$  respectively. Thus the method predicts a maximum lateral displacement,  $\delta_{\max}$  during construction to be approximately 9 mm, 11 mm and 15 mm for the 0.9 m high model walls.

The discrepancy between that predicted and observed is large and is probably due to the empirical derivation being based on 6 m high walls. This, and the difference with observations made by Ling et al. (2004) are due to the in-exact nature of modelling of reinforcement and soil properties as detailed above.

### 3.9 Model deposit density

Noted in Section 3.4.2 is the importance and influence of soil density on stiffness and thus model response. Hence the measurement of the model deposit density is necessary to ensure consistency of soil parameters across tests.

The compaction process uses two plates that apply a uniform vertical stress of  $\sim 5.3$  kPa across the soil surface under static conditions. The box, braced wall, soil, and plates are then vibrated by the shake-table at 13 Hz with acceleration amplitude of 1.4g for 10 seconds. Due to densification of the soil underneath, the plate typically drops  $\sim 8$  mm from its pre-compaction position and its final height with respect to the bottom of the box is recorded. In this way, the soil layer's height and thus volume, combined with its known mass is used to determine an average relative density for the layer using Equations 3-10 and 3-11.

$$\rho_d = \frac{m_s}{V_T}, \quad \rho_d = \frac{\rho_s}{1+e}, \quad \text{therefore, } e = \rho_s \frac{V_T}{m_s} - 1 \quad (3-10)$$

$$D_r = \frac{e_{\max} - e}{e_{\max} - e_{\min}} \times 100(\%) \quad (3-11)$$

Where  $m_s$  is the mass of the deposited soil for one layer,  $\rho_d$  is the soil layer dry density,  $\rho_s$  is the solid particle density,  $V_T$  is the total volume of densified sand,  $e$  is void ratio,  $e_{\max}$  and  $e_{\min}$  are the maximum and minimum void ratios for Albany sand (defined in Table 3-3 above), and  $D_r$  is the relative density of the soil. All walls had a target relative density,

$D_r = 90\%$ . The New Zealand Geotechnical Society (2005) thus defines the model as being 'very dense'. The average density for the entire deposit for each test is shown in Table 3-8.

**Table 3-8. Calculated average wall densities**

Test	$m_s$ -total (kg)	$\rho_d$ (kg/m <sup>3</sup> )	e	$D_r$ (%) <sup>1</sup>	Remarks
Test-1	2982.0	1738	0.525	94	
Test-2	2956.5	1708	0.551	93	
Test-3	2939.4	1705	0.554	92	
Test-4	2939.4	1700	0.559	90	
Test-5	2946.2	1706	0.554	92	
Test-6	2938.2	1697	0.562	89	
Test-7	2842.0	1715	0.545	95	Inclined wall

Notes: <sup>1</sup> Maximum error for the entire deposit is determined as below and equals ~ 3.3%.

Table 3-8 shows that the total mass used for each test are similar in value and this suggests consistent preparation procedures and repeatability of density. While similar to the density achieved by Watanabe et al.(2003), it is higher than for tests conducted by other researchers. El-Emam and Bathurst (2004) constructed walls of  $D_r = 86\%$ , and Sabermahani et al. (2009) of  $D_r = 47$  and  $84\%$ . Further, the relative density is higher than some large-scale tests conducted by Ling et al. (2005). In these tests, the walls were 2.8 m high and constructed to  $D_r = 52 - 56\%$ .

### 3.9.1 Sensitivity study

Calculation of relative density is sensitive to volume and mass measurements, particularly when considering a single lift of 75 mm. For instance, consider a single layer of thickness 75 mm in height with width and length of 800 mm and 2410 mm respectively, and with mass of 245.2 kg. A measurement error of +/-1 mm height (1.3% inaccuracy), results in a 7.1% change in the relative density, from  $D_r = 90\%$  to 83.6%.

Sensitivity to mass measurement is similar. The typical mass used in each layer is 245 kg with a known accuracy of +/- 0.2 kg. Again, for a single layer, the possible error results in a relative change of 0.6% from  $D_r = 90.4\%$  to 89.9%. The errors considered are only two, acting in isolation, of those listed in Table 3-9.

**Table 3-9. Measurement quantities and possible errors**

Parameter	Quantity	Possible error	$\Delta D_r$ (%)
Mass / layer (kg)	245	+/- 0.2	- 0.5
Height / layer (mm)	75	+/- 2	- 13.9
Length / layer (mm)	2408	+/- 2	- 0.4
Width / layer (mm)	798	+/- 2	- 1.3
Total Mass (kg)	2940	+/- 2.4	-0.1
Total deposit Height (mm)	900	+/- 2	-1.3
Solid density (kg/m <sup>3</sup> )	2650	-	-
$e_{max}$	0.83	-	-
$e_{min}$	0.53	-	-
		per layer	-16.1
		entire deposit	-3.7

The above parametric study considers a single layer. As construction progresses the calculations of an average relative density for the entire wall become progressively less sensitive, and the final average density for the entire wall is determined as shown in Table 3-8. (There is less relative error with increasing wall height and mass). A maximum worst-case error (when errors are all additive) for the entire wall is calculated as an absolute error in terms of relative density measurement of 3.7%.

Density impacts on the shear modulus which determines acceleration amplification which in turn, has important effects on the magnitude of the lateral earth pressure coefficient (Steedman and Zeng 1990). Thus the uniformity of density with depth is also of interest, and a density calculation for each sand layer is necessary.

However, this is made difficult because, during construction, compaction of layers higher up (and increasing confining pressure with increasing wall height) most likely act to further compact layers below, similar to the concept of under-compaction proposed by Ladd (1978). It should be noted that further densification of lower layers may not always be the case, and that some loosening could occur (as shown in Figure 3-18 below).

In order to gain a measure of this change, the change in elevation of the horizontal black lines (spaced vertically at 150 mm intervals) were measured after compaction of each layer, in order to measure the change in thickness of soil layers below. Figure 3-18 shows the relative density of each layer during and at completion of the wall. Height readings were made at the front of the wall (dark points) and at 1400 mm from the wall face (grey points). Obviously, measurements were confined to the acrylic window and density changes at the back of the wall could not be so measured.

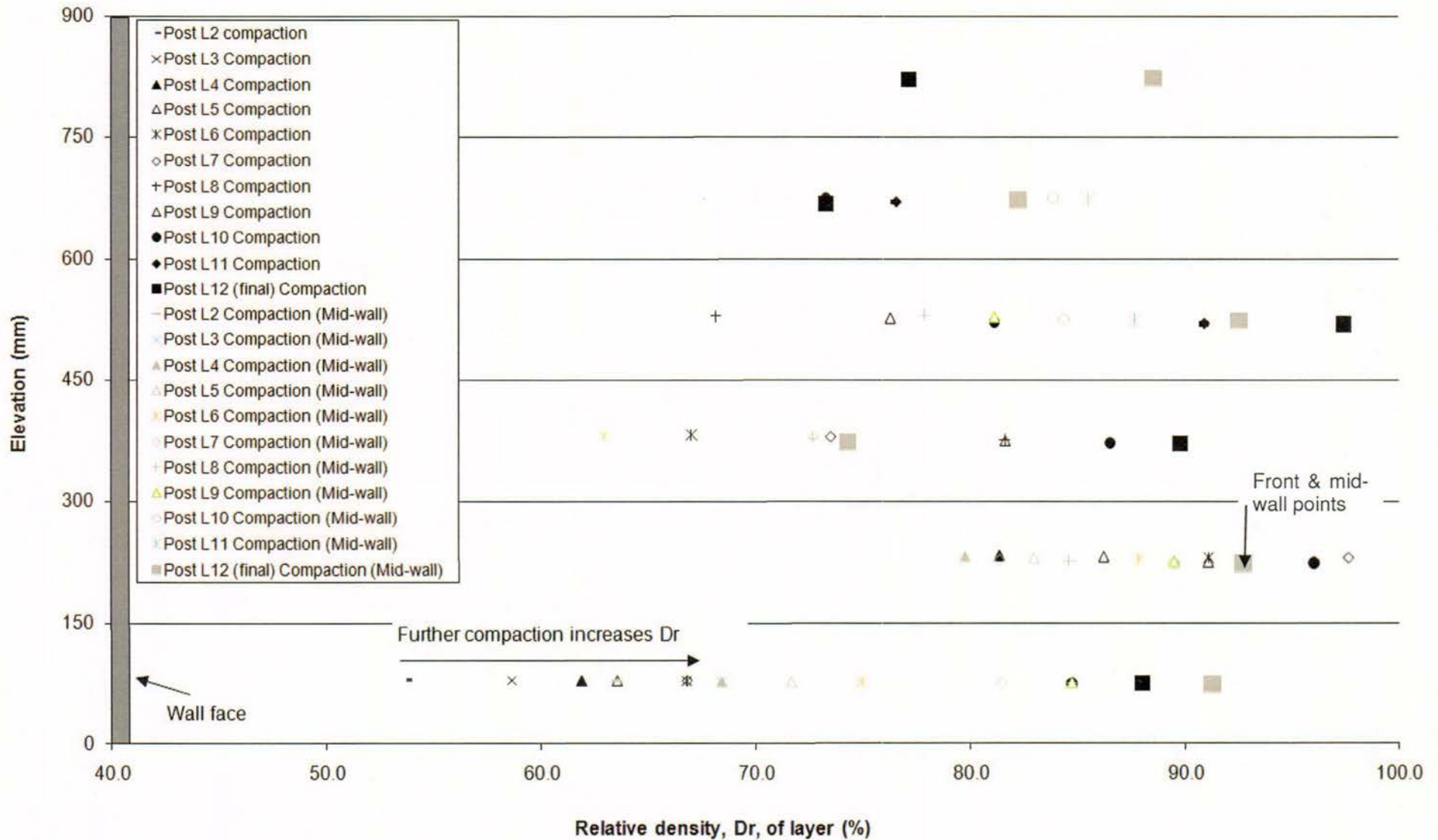


Figure 3-18. Relative density of each layer during and after construction. Post compaction of each layer, layer heights were recorded at two locations and are plotted separately: Dark for density measurements at the face, and grey for density measurements at mid-length (1400 mm) along the wall. Note each measurement has a possible absolute 11% error.

Figure 3-18 shows the relative density of each layer measured at the front of the wall, and mid-way along the wall, with further compaction of layers above. Considering the change in relative density of the bottom most layer, the trend shows increasing density with further compaction steps. In general, the same trend can be seen for other layers, except for L3 - L4 and L9 - L10 where there is an apparent decrease in relative density during compaction of above layers above.

After construction was completed, the relative densities of each layer are spread across the range  $D_r = 74$  to  $98\%$ . No trend was observed relating a layer's relative density with its elevation (L7 - L8 have the highest relative density, whilst L9 - L10 have the lowest). This would indicate that the density of the soil deposit is non-uniform. However, on average, the relative density for the entire Test-6 wall is  $D_r = 89\%$  as specified above.

The inconsistent trend observed for the change in relative density during construction, and the range in final density values achieved, highlights the poor accuracy in the measurement technique. This is because the layer thickness used in the calculation was based upon the elevation of the horizontal coloured sand lines, and these were observed to deform slightly during each vibration compaction. It shows that the density of individual layers is difficult to quantify precisely and that the technique used can not be relied upon.

However, given that one of the most important parameter governing GRS walls behaviour is the stiffness,  $G$ , within the wall, it is unlikely that the recorded non-uniformity in relative density will impact largely on wall response.

### **3.10 Model fundamental frequency**

The fundamental frequency of the model is important to quantify, as this identifies possible resonance conditions that could lead to overamplified response and premature failure (El-Emam and Bathurst, 2004). Additionally, Hatami and Bathurst (2000) state that retaining walls of typical height ( $H < 10$  m) are considered as short-period structures and therefore, their seismic response is dominated by their fundamental frequency.

The fundamental frequency of a soil profile is given by Equation 3-12 and is dependant on the shear wave velocity and soil profile thickness.

$$f_f = \frac{v_s}{4H} \quad (3-12)$$

Where  $f_f$  is the fundamental frequency;  $v_s$  is the shear wave velocity and  $H$  is the soil deposit thickness (in this case equal to 0.9 m). The shear wave velocity is defined by the relationship given in Equation 3-13 and the initial shear modulus,  $G$ , at small strain levels, is in turn proportional to the effective stress level of the wall as shown in Equation 3-14.

$$v_s = \sqrt{\frac{G}{\rho}} \quad (3-13)$$

$$G \propto \sigma'^{\alpha} \quad (3-14)$$

Where  $\rho$  is the soil density,  $\sigma'$  the effective stress level, and the exponent  $\alpha$  is a constant of about 0.5 for sands (Wood 2004).

However, descriptive parameters such as the fundamental frequency, shear wave velocity and model density that describe the state of the soil deposit, change once the soil deposit is subjected to an earthquake motion. This process involves first strain-induced degradation of soil stiffness,  $G$ , and a resultant change in shear wave velocity which in turn affects the fundamental frequency of the model.

Nova-Roessig and Sitar (2006) investigated this effect during a series of centrifuge tests on model-scale GRS walls that were subjected to different scaled earthquakes of varying intensity. In order to quantify earthquake-induced densification of backfill, photographs were used to make an estimate of volume change during testing and from this a density change. From initial relative densities of 55% and 75%, changes in relative density of up 44% were recorded. Further, low-amplitude step displacements were applied intermittently between earthquake motions which enabled changes in the shear wave velocity caused by the earthquake-induced densification to be quantified. Up to a 36% increase in shear wave velocity was recorded indicating that the abovementioned effects are significant.

In model tests of ~ 1.0 m height and relative densities ~ 46 to 86% surveyed in the literature the fundamental frequency was typically 22 Hz (+/- 0.5 Hz) (see Sabermahani et al., 2009; El-Emam and Bathurst, 2004 for examples).

Other parameters, such as reinforcement spacing, length and reinforcement stiffness have been found to have minimal influence on model natural frequencies (Nova-Roessig and Sitar 2006). This is verified by numerical modelling which showed facing condition to also have minimal influence (Hatami and Bathurst 2000).

### **3.10.1 Impulse test**

To determine the fundamental frequency of the model, generally a small acceleration pulse is applied to the base of the soil deposit (to induce shear waves) and the natural vibration frequency of the model is recorded via accelerometers placed within the backfill. This was the methodology used by El-Emam and Bathurst (2004), Nova-Roessig and Sitar (2006) and Sabermahani et al. (2009). The pulse should be small enough such that it is within the elastic range of the soil stress-strain curve so that no permanent deformation occurs; as discussed above, a degraded condition would give an erroneous fundamental frequency for the original model.

It was deemed difficult to apply an acceleration pulse small enough to prevent permanent deformation from occurring using the shake-table. Hence, for the current tests, another method was trailed. This method employed an accelerometer-instrumented hammer which was used to strike the box in order to generate a small acceleration pulse within the soil deposit. The results of this method are summarised herein.

It was impossible to generate an acceleration pulse from below, and the hammer was instead used to strike the back-wall of the box at around mid height of the soil deposit. The back-wall was 2.4 m from the wall face, 2.15 m from the vertical accelerometer array in the reinforced zone (Acc 2, 3, and 4), and the impact was parallel to the direction of accelerometer measurement. Two impacts of roughly 3.5 kN and 4.4 kN impulses spaced roughly one second apart were made to ensure a full frequency content; the impact force-time history is shown in Figure 3-19.

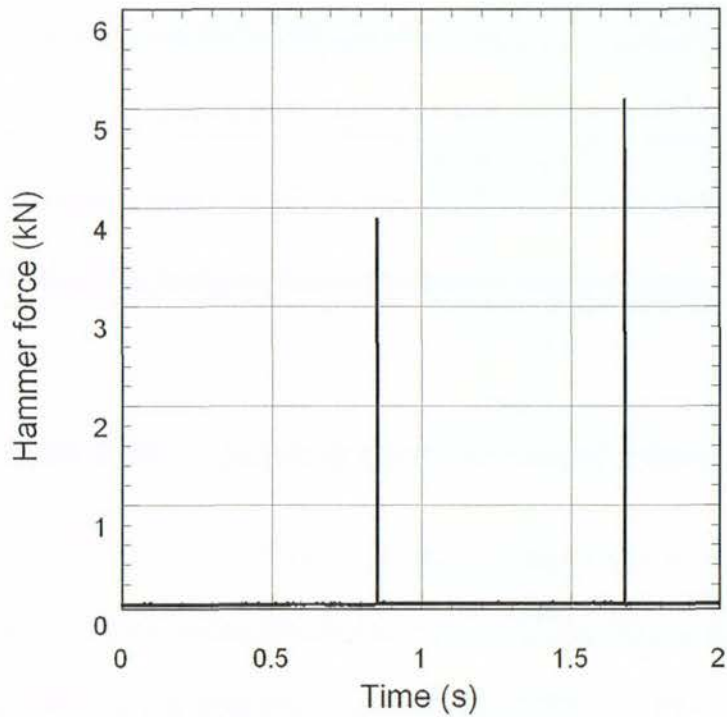


**Figure 3-19. Hammer impact time history.**

Because the hammer struck the box back-wall, an acceleration pulse in the longitudinal direction was induced within the soil deposit. This impulse would be transmitted by a longitudinal wave with velocity,  $v_p$ . It is likely that shear waves within the soil deposit would also be induced, and these are transmitted by velocity,  $v_s$ . The ratio of the two different velocities is shown in Equation 3-15:

$$\frac{v_p}{v_s} = \sqrt{\frac{2-2\nu}{1-2\nu}} \quad (3-15)$$

Where  $\nu$  is poisson's ratio, where a typical ratio for sand is 0.3. Hence the ratio between the longitudinal wave and shear wave velocity is calculated as approximately 1.87.

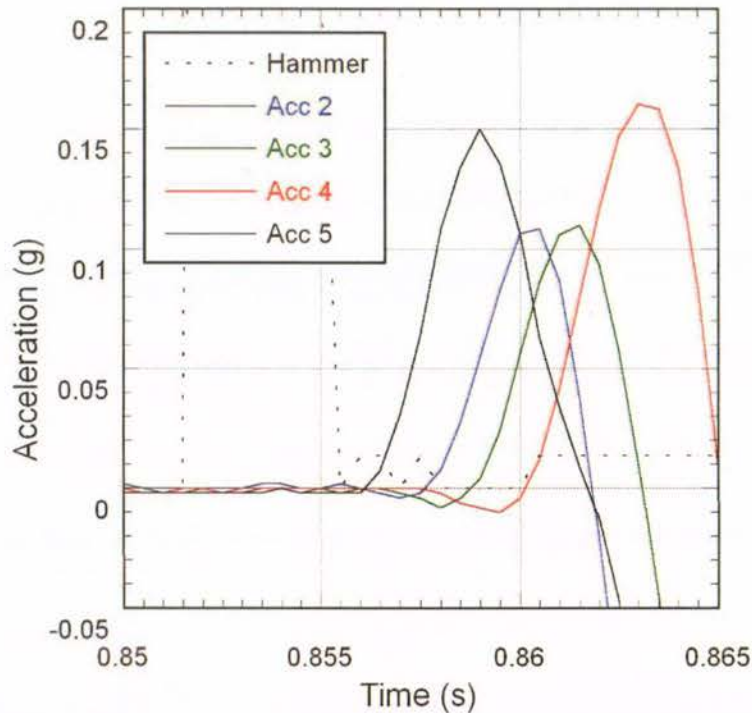


Figure 3-20. Acceleration response during hammer test. Acc 5 records the first pulse as it is closest to the back-wall. However there is also a difference in arrival time between accelerometers located in vertical array (Acc 2, Acc 3, Acc 4).

The time histories of each accelerometer are shown in Figure 3-20. After the initial hammer pulse which peaked at 0.8535 seconds, Acc 5, located 800 mm from the back-wall recorded an acceleration impulse at 0.8595 seconds. This was followed by various delays until pulse arrival was recorded by the accelerometers located in vertical array near the front of the wall. Acc 2 recorded the pulse at 0.8610 seconds.

Care must be taken to determine whether the accelerometers recorded longitudinal wave or shear wave velocity, as this affects the interpretation of arrival times. Because longitudinal waves travel faster, it was assumed that the first pulse recorded by the accelerometers was the result of an induced longitudinal wave.

The delay time between the initial hammer pulse, and its recorded arrival, coupled with the known longitudinal distance between the accelerometers and the back-wall can be used to estimate the longitudinal wave velocity,  $v_p$ . In turn, the shear wave velocity and hence the fundamental frequency of the wall can be estimated via Equations 3-15 and 3-14, respectively. Various estimates for the fundamental frequency are shown in Table 3-10.

**Table 3-10. Estimation of fundamental frequency from the longitudinal shear wave velocities calculated via the delay time between the first hammer impulse and that recorded within the backfill.**

Instrument	Impulse arrival (s)	Delay (s)	Longitudinal distance (m)	Calculated $V_p$ (m/s)	Calculated $V_s$ (m/s) *	Calculated $F_f$ (Hz)
Hammer	0.8535					
Acc 2	0.8610	0.0075	2.16	106.7	199.5	44.9
Acc 3	0.8620	0.0085	2.16	254.1	475.2	107
Acc 4	0.8635	0.01	2.16	216.0	403.9	90.9
Acc 5	0.8595	0.006	0.8	133.3	249.3	56.1

Notes: \*  $V_s$  is calculated assuming poisson's ratio,  $\nu = 0.3$ .

The calculated fundamental frequency ranges from 44.9 Hz – 107 Hz. As Acc 2 recorded the pulse first, it stands to reason that this data is the most reliable record for longitudinal wave velocity. This is because data from accelerometers higher up could be complicated by interference from shear waves originating from lower layers (Acc 2 was the lowest accelerometer at an elevation of 215 mm). Hence a fundamental frequency of approximately 44.9 Hz was assumed.

To check this result, the free-vibration acceleration response of the four accelerometers embedded within the soil deposit was recorded, and the fourier spectrum plotted in Figure 3-21. The figure plots the free-vibration frequency response for the 5 second period recorded, and not just the arrival of the first pulse. It could be assumed that the response includes natural vibration due to both longitudinal and shear wave excitation.

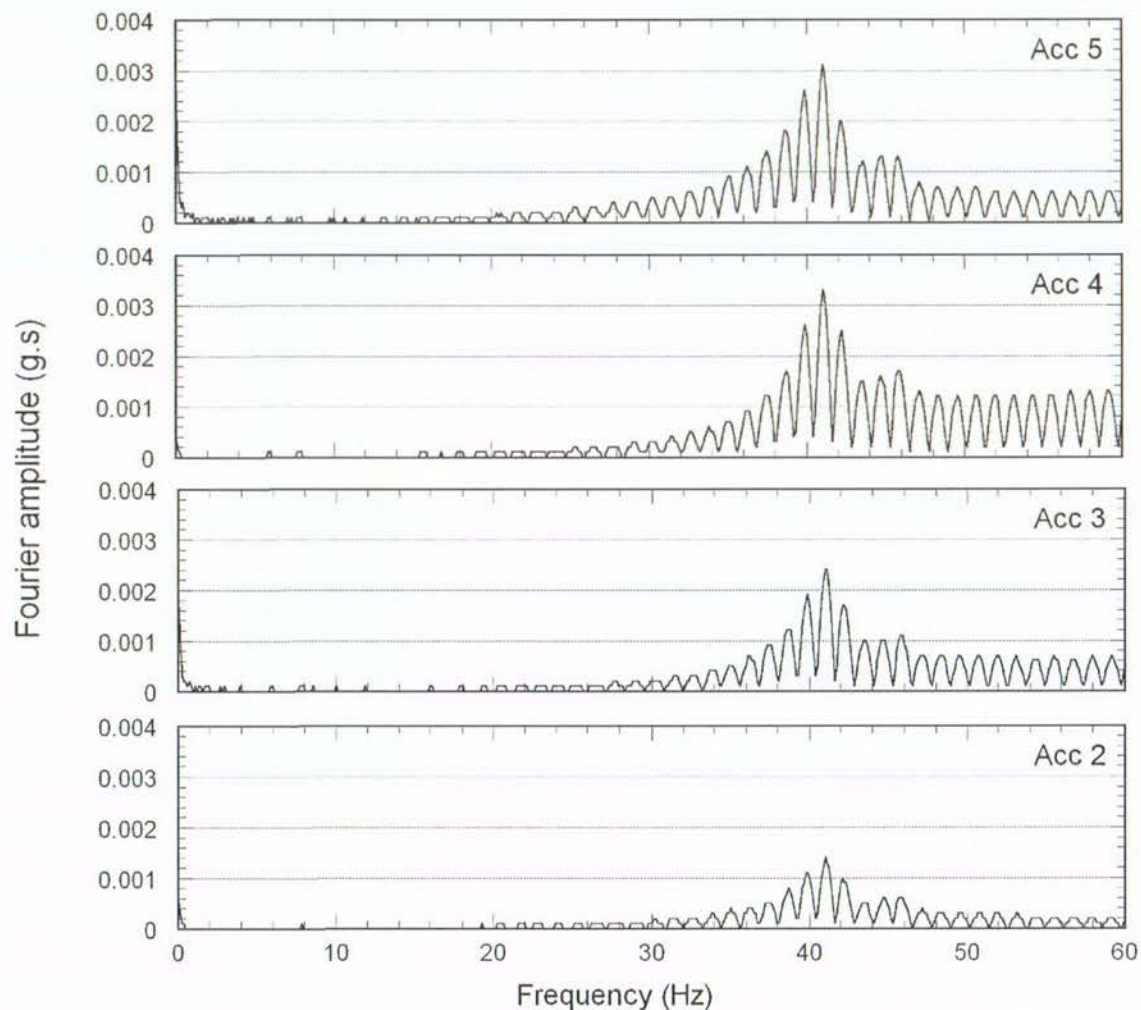


**Figure 3-21. Free-vibration Fourier spectrum of the embedded accelerometers**

Figure 3-21 shows that a peak in the Fourier amplitude response occurred for all accelerometers at 41.0 Hz. This value agrees reasonably well with the 44.9 Hz determined previously based on the arrival time of the impulse longitudinal wave. Because Figure 3-21 shows this value for all accelerometers, and does not include the approximations made to derive Table 3-10, it could be assumed as a more accurate value for the fundamental frequency of the soil deposit.

This value is almost double that of the fundamental frequency determined in the experimental studies by El-Emam and Bathurst (2004) and Sabermahani et al. (2009). However, it should be noted that both these studies had lower model densities ( $D_r = 46\%$  to  $86\%$ ) and larger model heights of 1 m, and that both these parameter values contribute to a reduced fundamental frequency in comparison with that determined for the current tests. It should be noted that these effects are unlikely to contribute to such a large discrepancy.

Hence, the above results are somewhat questionable and show the inadequacy in attempting to measure the fundamental frequency via an impact at the back of the wall. However, the results do confirm that the fundamental frequency of the wall is likely to be significantly higher than the excitation frequency of 5 Hz used during testing. As noted, this reduces the likelihood of an overamplified model response and premature failure.

In the future, a pure shear wave introduced via a small acceleration pulse at the base of the wall (via the shake-table) should be used to more accurately quantify the fundamental frequency of the soil deposit.

### **3.11 Summary**

To conduct shake-table tests on reduced-scale model GRS walls, a strong box was designed and constructed after consulting the literature of typical reduced-scale experimental testing of retaining walls.

Utmost attention was given to various details of the model and preparation procedures. In particular, a methodology to compact the soil deposit and achieve consistent relative density was presented in detail. This involved the soil deposit being constructed in layers and vibration compacted with the shake-table. A weighted plate was placed on top of the soil deposit to aid in the compaction. Additionally, the FHR facing panel and the bracing method used during construction of the wall were described.

Horizontal coloured 'marker' lines of sand were incorporated into the soil deposit and a technique to incorporate vertical 'marker' lines of sand was developed. These enabled deformation patterns to be visible within the soil deposit.

The similitude rules as developed by Iai (1989) and Wood (2004) were considered in order to appropriately scale the soil, reinforcement and GRS wall design to model testing conditions. The reinforcement selected was a Stratagrid Microgrid, supplied by Stevensons Limited. The Microgrid reinforcement is slightly under-scaled in terms of its stiffness and over-scaled in terms of mesh area to reinforcement area.

The model excitation for testing on the University of Canterbury shake-table was based on similitude considerations for the frequency, and a desire observe behaviour at increasing levels of base acceleration. The excitation consisted of a sinusoidal motion at frequency 5 Hz, duration 10 seconds, with steadily increasing amplitude in 0.1g increments. This

frequency is significantly lower than that of the natural frequency of the model deposit, which was found to be ~ 41 Hz (using the free-vibration method).

Seven reduced-scale model GRS walls were constructed and tested with different L/H ratios and wall inclination. A high relative density was achieved for all walls which ranged from 89% to 95% with a possible maximum error in the average relative density for deposit of 3.3%. It was found that there was a certain degree of non-uniformity within the models; however given the high relative density achieved it is unlikely that this will have a major impact on wall response.

The experimental instrumentation consisted of: 6 accelerometers, with 4 of these placed within the soil deposit to record the dynamic soil response within the reinforced soil block and the 'far-field'; 6 LVDT's to record wall face displacement; and 3 high-speed cameras to obtain deformation within two selected areas and globally.

The results of the test series are presented and discussed in Chapter 4.

## References

- Ang, B. G. (1985). "Seismic Response Shear Strength Of Circular Birdge Piers," University of Canterbury, Christchurch.
- El-Emam, M. M., and Bathurst, R. J. (2004). "Experimental Design, Instrumentation and Interpretation of Reinforced Soil Wall Response Using A Shaking Table." *International Journal of Physical Modelling in Geotechnics*, 4 (2004), 13-32.
- El-Emam, M. M., and Bathurst, R. J. (2005). "Erratum: Facing contribution to seismic response of reduced-scale reinforced soil walls (Geosynthetics International (2005) vol. 12 (5) (215-238))." *Geosynthetics International*, 12(6), 344.
- Fairless, G. J. (1989). "Seismic Performance of Reinforced Earth Walls," University of Canterbury, Christchurch.
- Fannin, R. J., and Hermann, S. (1990). "Performance data for a sloped reinforced soil wall." *Canadian geotechnical journal*, 27(5), 676-686.
- FHWA. (2001). "Mechancially Stabilized Earth Walls and Reinforced Soil Slopes Design and Constrcution Guidelines ".
- Hatami, K., and Bathurst, R. J. (2000). "Effect of structural design on fundamental frequency of reinforced-soil retaining walls." *Soil Dynamics and Earthquake Engineering*, 19, 137-157.

- Howard, R., Kutter, B., and Siddharthan, R. "Seismic deformation of reinforced soil centrifuge models." *Geotechnical Earthquake Engineering and Soil Dynamics III*, University of Washington, Seattle, Washington, USA.
- Iai, S. (1989). "Similitude for shaking table tests on soil-structure-fluid model in 1g gravitational field." *Soils and Foundations*, 29(1), 105-118.
- Koseki, J., Bathurst, R. J., Guler, E., Kuwano, J., and Maugeri, M. "Seismic stability of reinforced soil walls." *8th International Conference of Geosynthetics (8ICG)*, Yokohoma, Japan, 51 - 77.
- Koseki, J., Munaf, Y., Tatsuoka, F., Tateyama, M., Kojima, K., and Sato, T. (1998). "Shaking and tilt table tests of geosynthetic-reinforced soil and conventional-type retaining walls." *Geosynthetics International*, 5(1-2), 73-95.
- Kramer, S. L. (1996). *Geotechnical Earthquake Engineering*, Prentice-Hall, Upper Saddle River, New Jersey.
- Ladd, R. S. (1978). "Preparing test specimens using undercompaction." *Geotechnical Testing Journal*, 1(1), 16-23.
- Ling, H. I., Liu, H., Kaliakin, V. N., and Leshchinsky, D. (2004). "Analyzing Dynamic Behaviour of Geosynthetic-Reinforced Soil Retaining Walls." *Journal of Engineering Mechanics*, 130(8).
- Ling, H. I., Mohri, Y., Leshchinsky, D., Burke, C., Matsushima, K., and Liu, H. (2005). "Large-scale shaking table tests on modular-block reinforced soil retaining walls." *Journal of Geotechnical and Geoenvironmental Engineering*, 131(4), 465-476.
- Lo Grasso, A. S., Maugeri, M., Montanelli, F., and Recalcati, P. "Response of geosynthetic - reinforced soil walls under seismic condition by shaking table tests." *Geotechnical Engineering with Geosynthetics*, Munich, Germany.
- Murahidy, A. G. (2004). "Design, Construction, Dynamic Testing and Computer Modelling of a Precast Prestressed Reinforced Concrete Frame Building with Rocking Beam-Column Connections and Adas Elements ", University of Canterbury, Christchurch.
- Murashev, A. K. (2003). "Guidelines for Design and Construction of Geosynthetic-Reinforced Soil Structures." Transfund New Zealand.
- Nakajima, S., Hong, K., Mulmui, S., Koseki, J., Watanabe, K., and Tateyama, M. (2007). "Model tests on seismic performance of reinforced soil retaining walls by using different geo-grids." EHAM - 2007, Guwahati, India.
- New Zealand Geotechnical Society. (2005). "Field Description of Soil and Rock. Guideline for the field classification and description of soil and rock for engineering purposes." New Zealand Geotechnical Society Inc.
- Nova-Roessig, L., and Sitar, N. (2006). "Centrifuge model studies of the seismic response of reinforced soil slopes." *Journal of Geotechnical and Geoenvironmental Engineering*, 132(3), 388-400.

- Richardson, G. N., and Lee, K. L. (1975). "Seismic Design of Reinforced Earth Walls." *American Society of Civil Engineers, Journal of the Geotechnical Engineering Division*, 101(2), 167-188.
- Roper, M. (2006). "Applications and Procedures of Triaxial Tests." Honours Year Project, University of Canterbury.
- Sabermahani, M., Ghalandarzadeh, A., and Fagher, A. (2009). "Experimental study on seismic deformation modes of reinforced soil-walls." *Geotextiles and Geomembranes*, 27, 121-136.
- Sakaguchi, M. (1996). "Study of the seismic behavior of geosynthetic reinforced walls in Japan." *Geosynthetics International*, 3(1), 13-30.
- Steedman, R. S., and Zeng, X. (1990). "The influence of phase on the calculation of pseudo-static earth pressure on a retaining wall." *Geotechnique*, 40(1), 103-112.
- Tatsuoka, F. "Geosynthetic-reinforced soil structures: A cost-effective solution combining two engineering disciplines." *19th Carillo Lecture - Mexican Society for Soil Mechanics, Aguascalientes*.
- Terzaghi, K. (1932). "Record earth-pressure testing machine." *Engineering News-Record*, 109(13), 365-369.
- Viswanadham, B. V. S., and Konig, D. (2004). "Studies on scaling and instrumentation of a geogrid." *Geotextiles and Geomembranes*, 22(5), 307-328.
- Viswanadham, B. V. S., and Konig, D. (2009). "Centrifuge modeling of geotextile-reinforced slopes subjected to differential settlements." *Geotextiles and Geomembranes*, 27(2), 77-88.
- Watanabe, K., Munaf, Y., Koseki, J., Tateyama, M., and Kojima, K. (2003). "Behaviors of several types of model retaining walls subjected to irregular excitation." *Soils and Foundations*, 43(5), 13-27.
- Wood, D. M. (2004). *Geotechnical Modelling*. Spon Press, New York, 246 - 257.

## **CHAPTER 4**

### **EXPERIMENTAL RESULTS**

#### **4.1 Introduction**

A series of seven reduced-scale geosynthetic-reinforced soil wall model tests were conducted using the University of Canterbury shake-table. These tests investigated the influence of reinforcement L/H ratio and facing inclination on the seismic performance of GRS walls. Three of these tests had the same reinforcement layout as other tests, in part to ensure consistency of the construction methodology and repeatability of the testing apparatus, and also due to some errors in the testing protocol.

The first part of this chapter, Sections 4.3 and 4.4, concentrate on the typical results of one of these tests, Test-6. Test-6 has been selected because the construction methodology and testing procedure had been perfected allowing the most representative results of GRS behaviour under seismic loading to be obtained. Section 4.3 illustrates the shake-table input motion and presents a selection of the resulting facing displacement and acceleration time histories during Test-6. These are followed by a discussion of the deformation and failure modes observed. Section 4.4 considers typical analysis of the Test-6 raw data providing further information of deformation pre-failure and at failure. Acceleration amplification is also calculated and compared using two different methods.

The second part of this chapter utilises results from all tests to analyse the effect of the reinforcement ratio L/H and facing inclination on wall deformation. Section 4.5 presents raw data from the entire test series. Section 4.6 then examines this data using the analysis

methods developed in Section 4.4 to investigate the influence of the reinforcement ratio L/H, and wall inclination on wall response. Displacement-acceleration curves, observed modes of failure and acceleration amplification are compared. One measure of stability, critical acceleration, is observed using four different criteria and compared. A comment on repeatability is also made.

Finally, Section 4.7 examines some of the implications of the test findings to design practice.

## 4.2 Testing summary

A series of seven reduced-scale model tests on GRS walls with a FHR facing was conducted on the shake-table. For each test, the reinforcement L/H ratio and the inclination of the wall was varied. Three tests were repeated to ensure construction consistency and also due to issues surrounding the wall seal with the box sidewall, and testing error. Table 4-1 shows how these two parameters were varied throughout the testing programme.

**Table 4-1. Summary of parameters varied during each test**

Test	L/H ratio	Wall angle (°)	Acceleration at failure (g)	Remarks
Test-1	0.75	90	0.6	Seal leakage and brittle failure of cellotape
Test-2	0.6	90	0.5	Seal leakage (Testing initiated at 0.3g*)
Test-3	0.9	90	0.7	Testing initiated at 0.6g, 10 Hz
Test-4	0.75	90	0.65	Seal issue (high friction). Results not used.
Test-5	0.9	90	0.7	-
Test-6	0.6	90	0.5	-
Test-7	0.75	70	0.7	-

NB: \* Testing was initiated at a larger acceleration than planned to reduce the quantity of sand lost around the sides of the facing panel once testing was initiated.

Table 4-1 shows that all tests failed within the range of 0.5g and 0.7g base input acceleration. Two of the repetitions (Tests-6 and 2, and Tests-5 and 3) showed that the wall failed at the same base input acceleration, indicating consistency in the construction methodology. Test-4, an intended repeat of Test-1, failed 0.05g higher at 0.65g due to its high friction seal. This issue is discussed in Section 4.5.1, and resulted in all of the results from Test-4 being considered unreliable and hence they were not used for analysis.

A detailed summary of all tests, including testing issues, is made in Section 4.5.1.

## 4.3 Results of Test-6 – A typical case

### 4.3.1 Test-6 model wall

Of the seven reduced-scale tests conducted, Test-6 was selected to show in detail representative results of GRS model behaviour under seismic loading. This is because the construction methodology and testing procedure had been perfected, compared to earlier tests.

Test-6 was a vertical wall with reinforcement ratio,  $L/H = 0.6$ . This reinforcement layout was the lowest  $L/H$  ratio tested. A comparison with Test-5 (reinforced at  $L/H = 0.9$ ) provides an upper and lower bound on the model seismic response for the range of parameters being tested. The models reinforced at a median  $L/H = 0.75$  (i.e. between that used for Test-5 and Test-6) did not generate results within these upper and lower bounds due to issues surrounding the facing seal, as discussed in Section 4.5.1.

As for all tests, the Test-6 model was 900 mm high, and constructed in the strong box 800 mm wide. The model was 2410 mm long from the wall face to the back wall of the strong box. The model dimensions and the instrumentation used is shown in Section 3.6.

The Test-6 model deposit was constructed to an average relative density of 89%, with the deposit incorporating vertical and horizontal black coloured sand lines to enable better visualisation of failure mechanisms. The as-constructed model prior to testing is shown in Figure 4-1, which also identifies the reinforced soil zone and retained backfill.

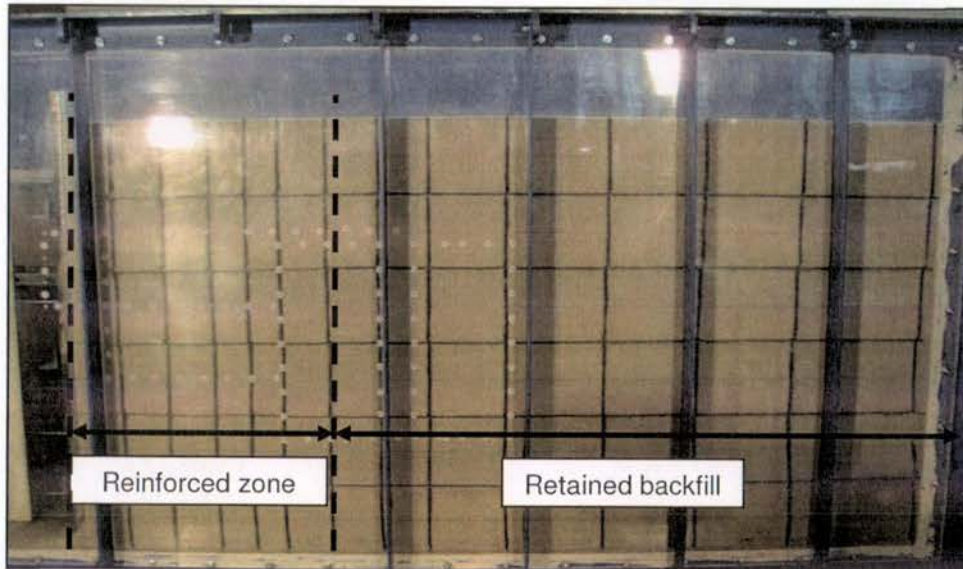


Figure 4-1. Completed Test-6 at End of Construction (EoC) prior to shaking.

The base input shaking, facing deformation and accelerometer time histories recorded during Test-6 are presented in the following sections.

#### 4.3.2 Base input shaking

A sinusoid input motion with predominant frequency of 5 Hz was selected to simplify interpretation of results and enable qualitative comparison with other research. As noted in Section 3.4.7, the selected motion contains more energy than a typical earthquake record of similar predominant frequency and amplitude. This is because the time duration of the peak acceleration is larger in a sinusoidal motion than an irregular acceleration time history (Watanabe et al. 2003).

Hatami and Bathurst (2000) determined that the model response is critically dependant on the structure's fundamental frequency. The selection of 5 Hz as the frequency of input motion was based on two considerations: firstly that the frequency of shaking be sufficiently lower than the model structure fundamental frequency determined in Section 3.10 as ~ 41 Hz to minimise a possible 'resonance' condition; and secondly, model similitude as presented in Section 3.4.7.

The motion duration of 10 seconds corresponds to a long duration earthquake, but was selected so that deformation at different acceleration amplitudes could be observed. Finally, the peak acceleration amplitude was steadily increased in a series of stepped acceleration

sinusoids of 0.1g increments, enabling model response data at various levels of acceleration input to be obtained. The staged testing for Test-6 is shown in Figure 4-2.

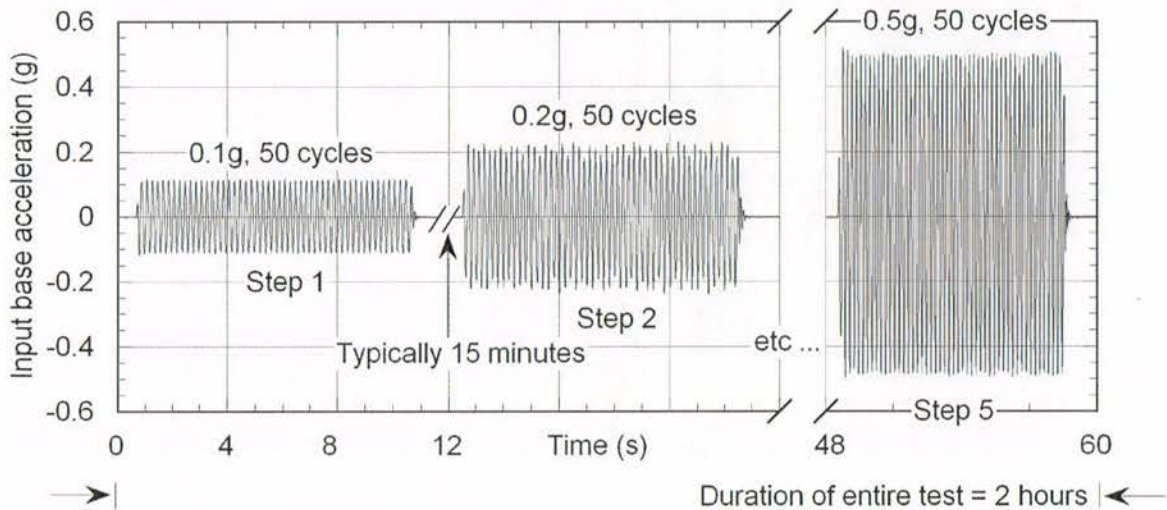


**Figure 4-2. Summary of staged testing procedure.**

The test was terminated when the wall reached the limit of the displacement transducers, which had approximately 200 mm of the travel at the front of wall.

The base acceleration of the model was controlled by the displacement time history of the shake-table. The equations of motion, discussed in Section 3.5, describe the corresponding input acceleration. A displacement transducer and accelerometer mounted on the shake-table recorded the dynamic motion of the shake-table during testing and acted as a check on the acceleration specified.

The raw shake-table displacement time history for the first load step of 0.1g for Test-6, and the recorded acceleration time history are shown in Figure 4-3 (a). Figure 4-3 (b) shows the fast fourier spectrum transformation of the raw data, and Figure 4-3 (c) shows the filtered time histories. An in-depth discussion of the filter and corrections applied to raw time history data is provided in Section 4.3.4.

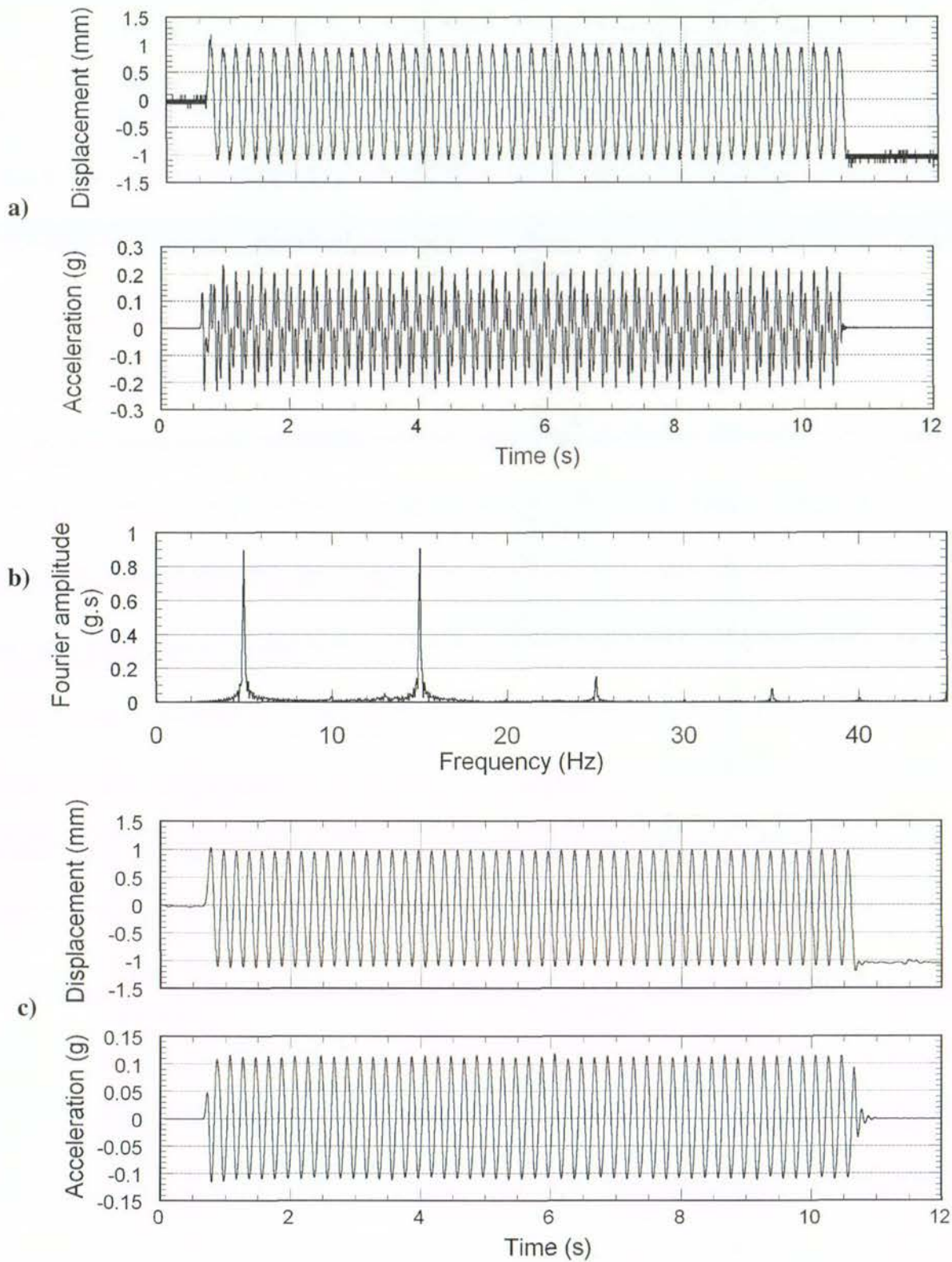


Figure 4-3. The first shaking step of Test-6 at 0.1g: (a) Raw shake-table acceleration and displacement time history data, (b) Fast Fourier Transformation, and (c) filtered shake-table acceleration and displacement time history data.

Figure 4-3 (a) shows the precision of the shake-table system achieved at the lowest acceleration amplitude of 0.1g which is equivalent to a displacement amplitude of +/- 1 mm. As discussed previously, the shake-table acceleration amplitude is controlled through displacement amplitude. It can be seen that the shake-table displacement is asymmetric, and the peak-to-peak, or double amplitude, is approximately 2.1 mm.

The raw acceleration data is shown to overshoot the +/- 0.1g target, to around 0.21g. Figure 4-3 (b) shows the raw data to contain 15 and 25 Hz frequency components (explained in Section 4.3.4), which are of minimal consequence for engineering purposes. Hence these frequencies are filtered using an 8<sup>th</sup> order, 10Hz low-pass Butterworth filter. Figure 4-3 (c) shows the filtered acceleration record which overshoots the +/- 0.1g target by only approximately 0.01g in the positive and negative directions.

The difference between the target acceleration amplitude and the actual measured acceleration of the shake-table is approximately 10% of the acceleration amplitude. This discrepancy is deemed acceptable as the testing methodology ensures that an exact measure of the actual input acceleration time history is made for evaluation of the wall response.

The Fast Fourier Transformation of the input base acceleration is also shown in Figure 4-3 and indicates that the motion consisted predominantly of 5 and 15 Hz components, with further smaller amplitudes at 25 and 35 Hz. The motion contains little other noise and enables an easier study of the results generated, than, say, an irregular time history with rich frequency content.

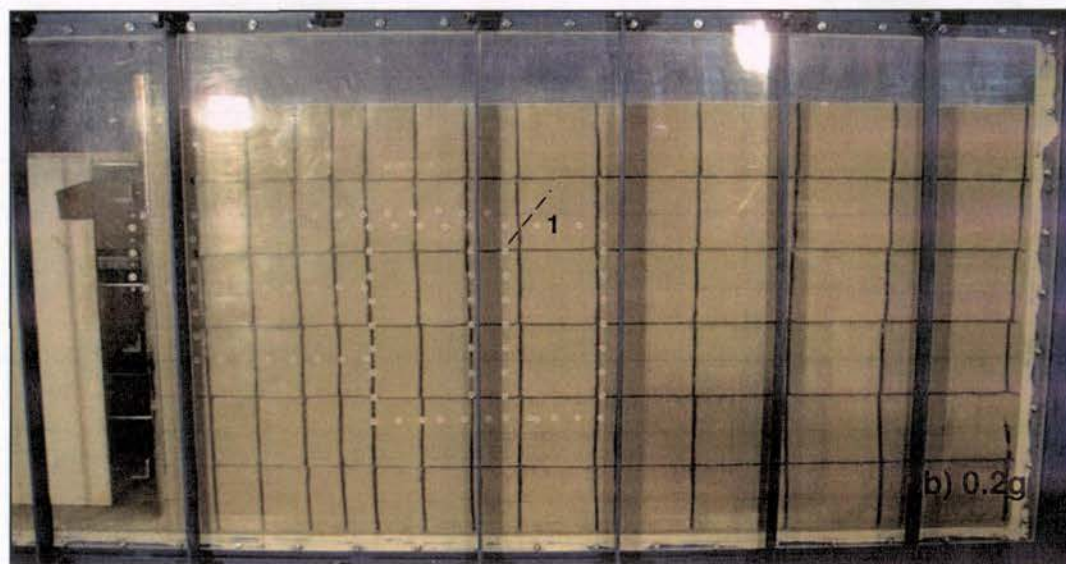
The Test-6 model underwent successive increasing base accelerations up to 0.5g at which point the wall failed, providing deformation information over five shaking steps. Displacement of the wall face, accelerations within the soil deposit, and high-speed camera images were recorded during each acceleration step. Additionally, at the end of each shaking step, photographs showing the global deformation and settlements of the wall crest were taken. A selection of typical data obtained is presented in the following sections.

### **4.3.3 Step-by-step deformation**

Modes of deformation were limited to overturning and sliding (external deformation), and pullout (internal deformation) of the wall.

Figure 4-4 (a – e) shows the formation of these failure modes with the image sequence taken at completion of 0.1g, 0.2g, 0.3g, 0.4g and 0.5g shaking steps, in (a) through (e) respectively.

The predominant mode of deformation of Test-6 was by overturning. This involved the reinforced soil block rotating about the toe, coupled with multiple external failure surfaces which formed within the backfill behind the reinforced soil block. Also evident is some sliding of the base of the wall along the hard foundation, which occurred largely in the final shaking step of 0.5g during wall failure (Figure 4-4 (e)).



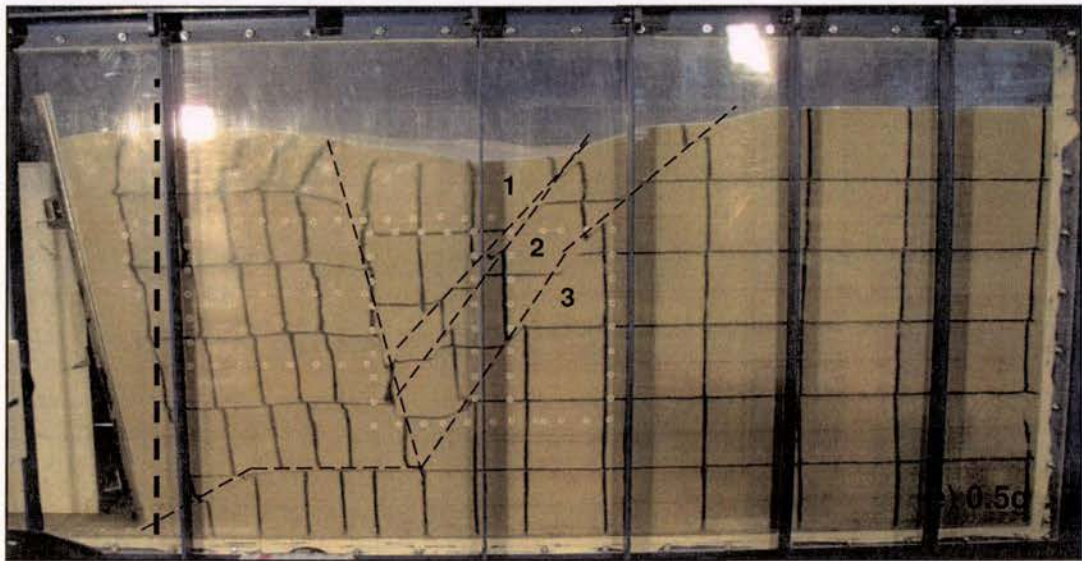
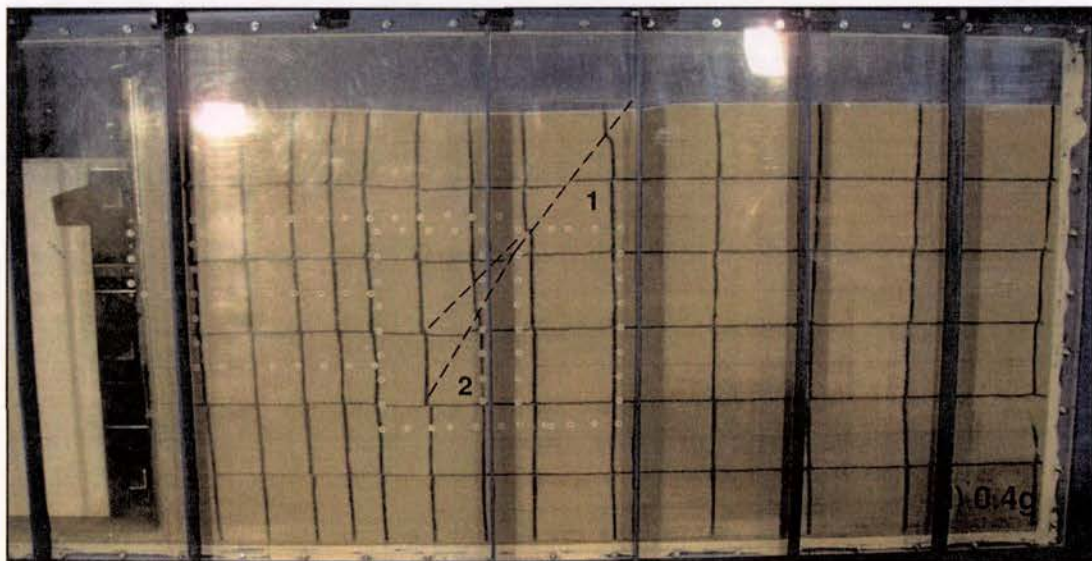
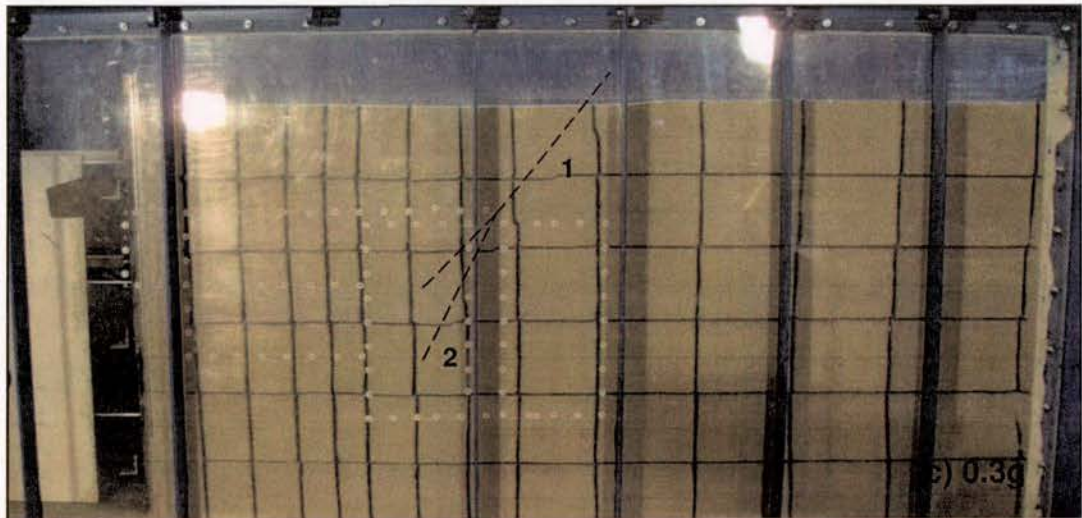


Figure 4-4. Deformation of Test-6 visible at the end of acceleration inputs of 0.1g, 0.2g, 0.3g, 0.4g, and 0.5g upon which the wall failed. The numbered dashed lines highlight the location and progression of failure planes once they become readily discernible by the naked eye.

As seen in Figure 4-4 (a) there is limited deformation evident on completion of 0.1g shaking. On completion of 0.2g shaking (b), an external planar failure surface becomes visible within the top third of the model backfill behind the reinforced soil block (see Section 3.4.8 for reinforcement layer numbering); this is shown by the dashed line number 1. Increased shaking of 0.3g (c) generates a further failure surface that forms deeper within the backfill (dashed line number 2). This failure surface initiated from a point approximately mid-depth along the previously formed (higher) failure plane 1, and extends to the back of the reinforced soil block at around the location of reinforcement R2 tip. This is perhaps evidence of progressive failure and is discussed later in Section 5.3.4. During 0.4g shaking (d) the failure surface initiated at 0.3g is further developed with wedge sliding along the discontinuity and overturning of the wall face.

Finally, upon application of 0.5g shaking (e), a third and lower external failure surface (dashed line numbered 3) is initiated at the soil deposit surface, and propagates down through the backfill until it reaches the bottom layer of reinforcement, R1. This failure surface then propagates horizontally along the soil-reinforcement interface towards the wall face, and meets another failure surface formed between the wall face toe and the bottom layer of reinforcement, R1. The failure surface which formed at the toe would, in a conventional gravity-type retaining wall, continue up through the backfill until it reaches the wall surface; the inclusion of horizontal reinforcement effectively stopped the reinforced soil block from being compromised in this manner. Similar behaviour was commented on by Watanabe et al. (2003).

During the 0.5g shaking, the reinforced soil block rotated about the toe generating maximum lateral displacement at the top of the wall face. This was coupled with some sliding at the bottom of the wall face along the hard foundation. The failure wedge formed by the lowest external failure surface within the backfill then moved down and horizontally into the gap left by the reinforced soil block. As a result, the highest settlement recorded was 108 mm, and occurred some 300 mm behind the reinforced soil block.

Also visible in Figure 4-4 (e) is an inclined failure surface that traces the back of the reinforced soil block and extends from the soil surface down to the lowest layer of reinforcement, R1.

The deformation described during Test-6 was typical for all reinforcement layout and facing inclination tested in this series. However, differences in reinforcement layout and facing

geometry led to differences in the progression of deformation pre-failure. These differences in behaviour are discussed in the parametric studies of Section 4.5.

#### **4.3.4 Acceleration-time histories**

Six accelerometers were used in total, and their location is shown in Figure 3-7. Three Kyowa AS 2GB accelerometers were located within the reinforced zone at the top of soil layers L3, L8 and L11, 250 mm from the wall face; they are named Acc. 2, Acc. 3 and Acc. 4 respectively. Acc. 2 to 4 record the soil response at different elevations within the reinforced soil block. A fourth accelerometer, Acc. 5, is located 1610 mm from the wall face (800 mm from the box back-wall) and records the 'far-field' backfill response. All accelerometers are placed along the centre line of the box to minimise side-wall boundary friction effects. Acc. 6 is fastened securely at the top of the box to check whether the box behaves rigidly.

The accelerometers have a measurement precision of  $\pm 0.002g$ , significantly lower than the smallest PGA applied to the model, with a possible error of 2% for the lowest PGA of 0.1g used. This suggests a high reliability of the accelerometer data for the current application.

An example of raw acceleration data recorded by Acc. 4 within the reinforced soil block during the final shaking step of 0.5g for Test-6 is shown in Figure 4-5 (a). The response contains noise due to the accelerometer instrument (minor) and various other sources. For engineering applications, the consequence of these high-frequency spikes is minimal as the duration of which they occur is so small. Thus an 8<sup>th</sup> order low-pass Butterworth filter is used to filter frequency components higher than 10 Hz from the acceleration record. The raw and filtered time histories are shown in Figure 4-5 (a and b). The filtering process results in a slight phase shift to the right and reduction in peak acceleration values recorded.

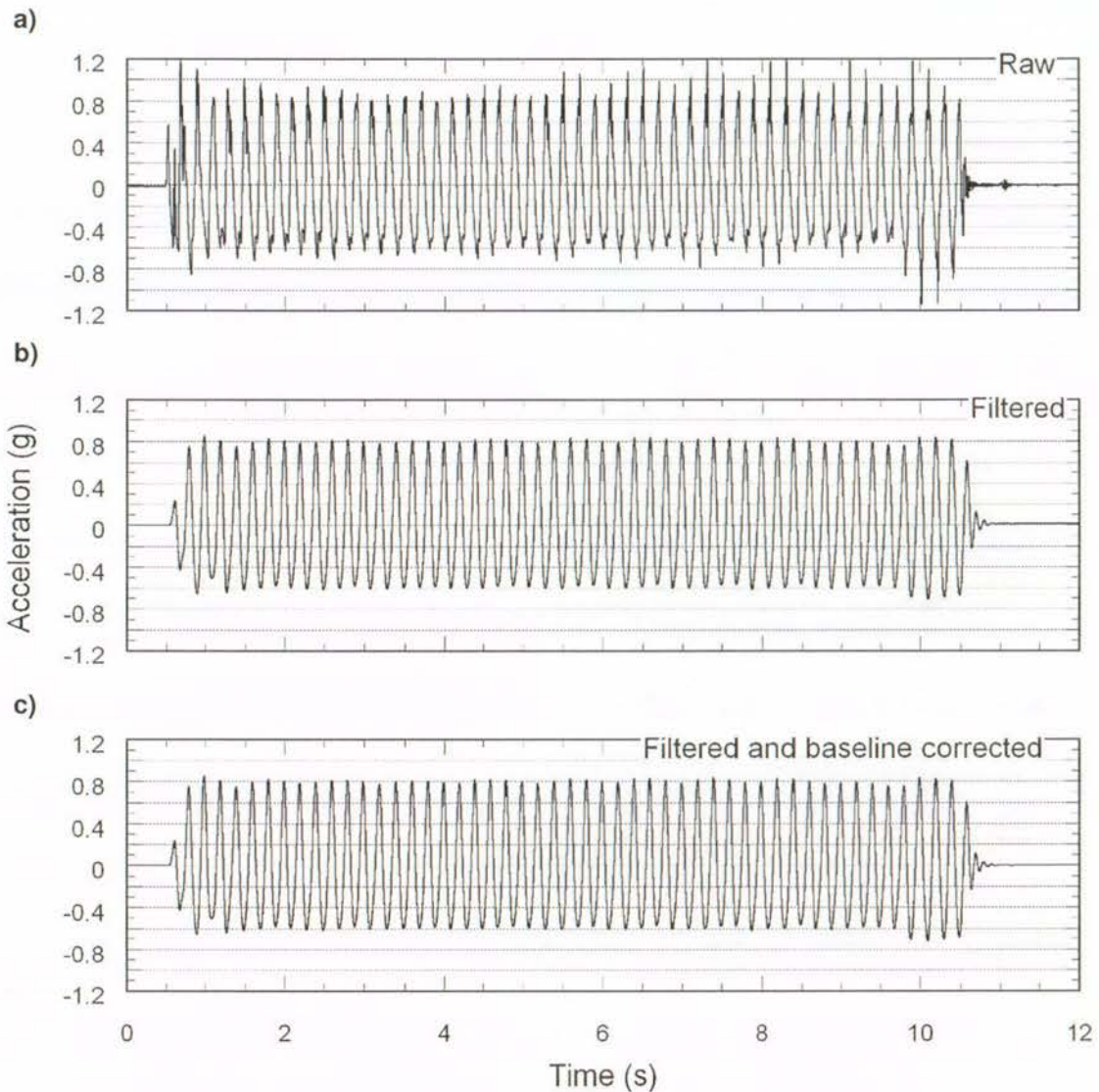
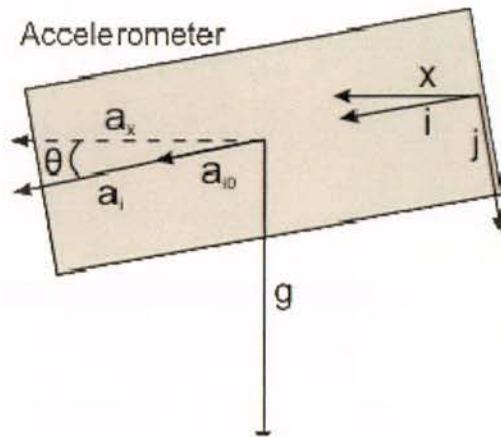


Figure 4-5. Acceleration time history recorded by Acc 4 for Test-6 during 0.5g shaking step and the data processing applied: (a) raw accelerometer data, (b) filtered accelerometer data using an 8<sup>th</sup> order 10 Hz low-pass Butterworth filter, and (c) filtered data after baseline correction.

During testing, the accelerometers record the surrounding soil's response which comprises predominantly rotation, as well as some sliding components. Rotation of the accelerometer compromises its ability to measure accelerations in the horizontal (x) plane as some component of acceleration due to gravity is included. Figure 4-6 shows schematically the effect accelerometer rotation has on the measurement of acceleration in the horizontal plane.



**Figure 4-6. Correction of accelerometer tilt**

Where  $a_{0i}$  is the acceleration recorded before shaking,  $a_i$  is the acceleration recorded during shaking,  $a_x$  is the horizontal acceleration component during shaking, and  $\theta$  is the tilt angle of the accelerometer with the horizontal plane. If the angle of the accelerometer tilt with the horizontal is small, then it can be assumed that  $a_i = a_x$ . However, in some cases the angle was not small and the accelerometer recorded accelerations of up to 0.05g prior to shaking. This corresponded to a tilt of the accelerometer of up to 2.9° to the horizontal.

Thus in addition to the filter applied in Figure 4-5 (b), a correction for the initial accelerometer tilt is made using Equation 4-1 for all accelerations records.

$$a_x = (a_i - a_{i0}) \times \cos(\sin^{-1}(a_{i0})) \quad (4-1)$$

During shaking, the accelerometer can undergo further rotation, and this contributes to the acceleration not returning to zero after the shaking has stopped. This residual acceleration is baseline corrected with a linearly increasing increment over the duration of shaking to return the residual acceleration to zero.

Selected acceleration-time histories of Test-6 for shaking steps 0.1g, 0.3g and 0.5g are presented in Figure 4-7 to 4.9. The complete set of corrected and filtered acceleration time histories, and filtered facing displacement time-histories, for all tests, are presented in Appendix B.

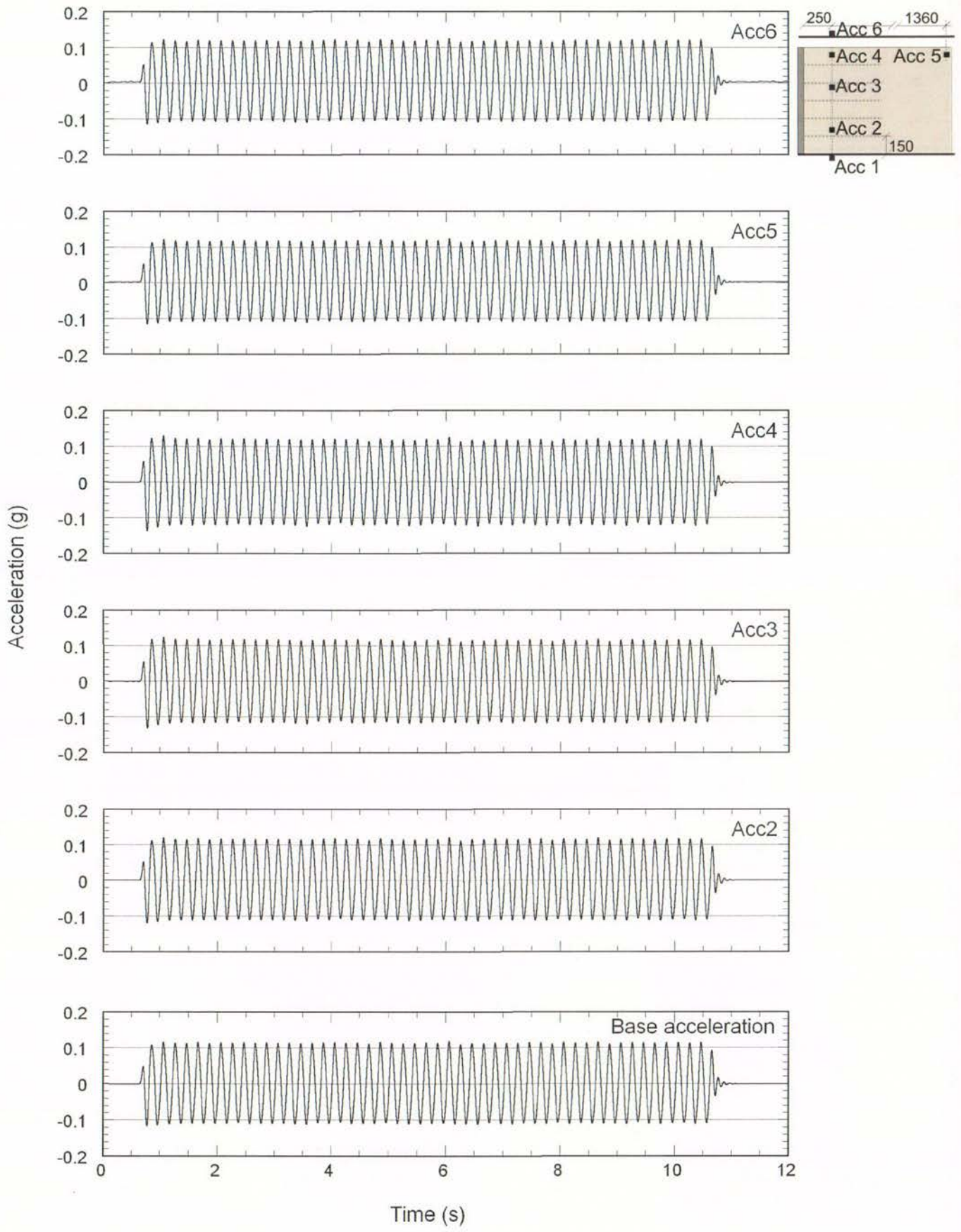


Figure 4-7. Acceleration time histories for 0.1g shaking step.

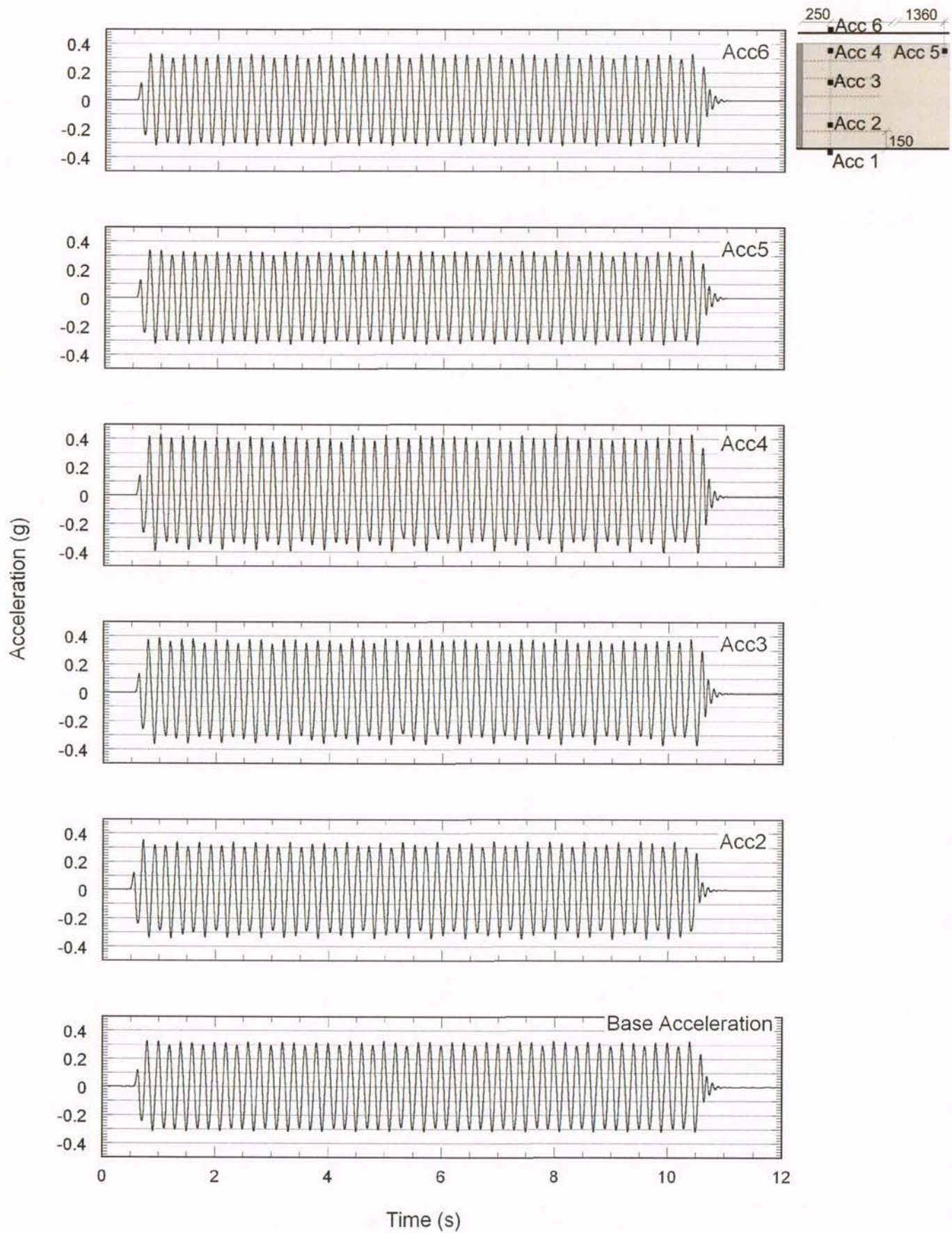


Figure 4-8. Acceleration time histories for 0.3g shaking step.

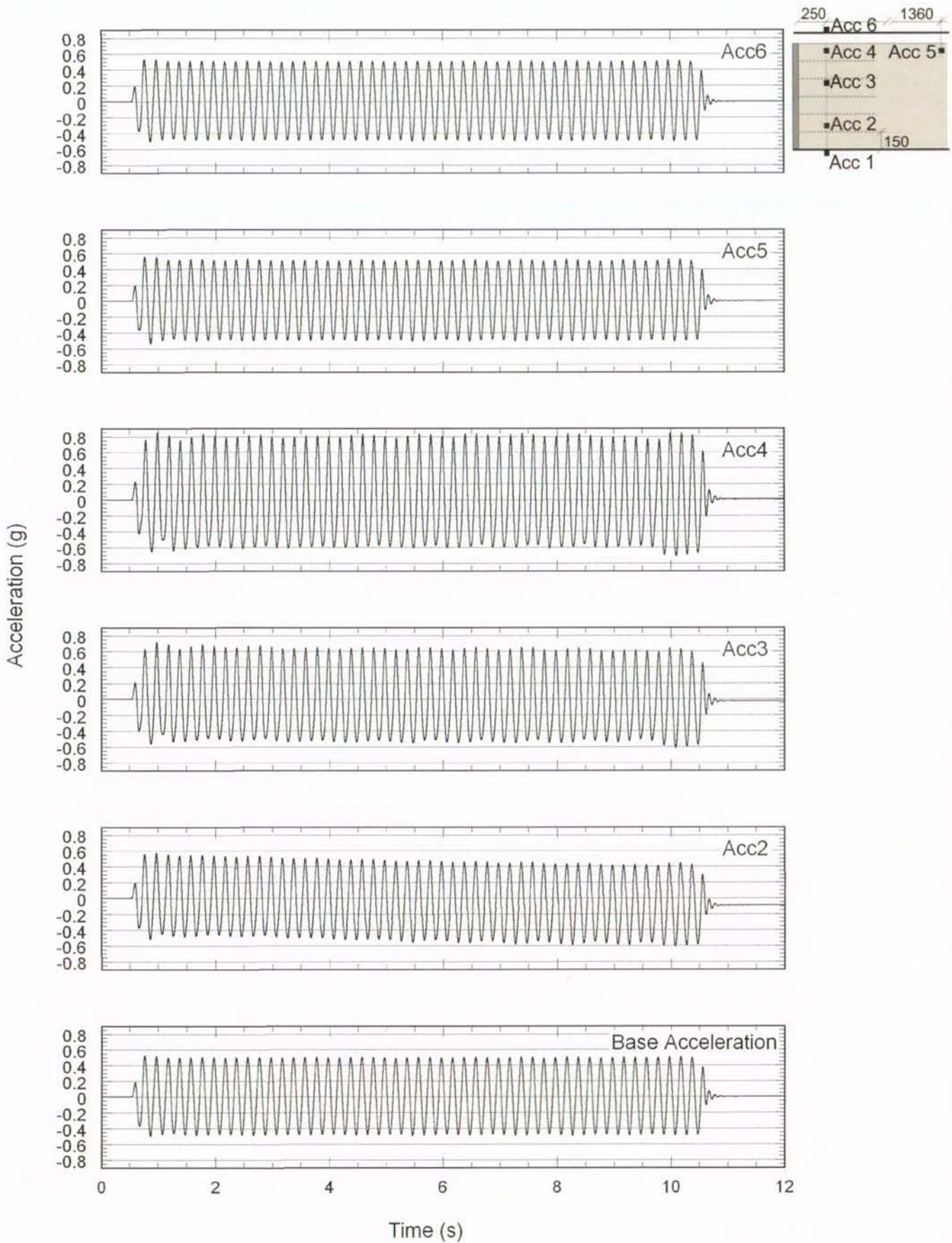


Figure 4-9. Acceleration time histories for 0.5g (final) shaking step.

The acceleration records from Acc. 1 and Acc. 6 were observed to be the same in all tests and confirm that: 1) the box is connected rigidly to the shake-table, and 2) that it does not modify the input motion (due to non-rigid behaviour).

Except for acceleration time histories recorded during 0.1g base input acceleration, accelerometers placed in vertical series within the reinforced soil zone show an increase in the input base acceleration with increasing wall elevation. This could be attributed to the wall face “rocking” about the wall toe, increasing the acceleration amplitude with increasing elevation. In contrast, no increase in acceleration was recorded by Acc. 5 located near the top of the backfill soil; likely due to its increased distance from the deformation at the wall face.

#### **4.3.5 Facing displacement-time histories**

During each shaking step, the wall face oscillates and steadily moves in the outwards (positive) direction. This displacement was recorded by two vertical arrays of displacement transducers located 400 mm apart and 200 mm inwards of their respective North and South side-walls. Both arrays consisted of three displacement transducers numbered Disp 1, 2 and 3 and Disp 4, 5 and 6 in series located at heights of nominally 770 mm, 500 mm and 200 mm from the wall base as shown in Section 3.6.1. Assuming the wall remained rigid during the test, these three transducers enabled displacements at the wall top and bottom to be calculated.

Figure 4-10 to Figure 4-14 show the displacement time histories for all shaking steps 0.1g, 0.2g, 0.3g, 0.4g and 0.5g. The total wall displacement at any time is a combination of cyclic, or recoverable displacement, and residual displacement as the wall deforms permanently outwards (El-Emam and Bathurst, 2004). The cyclic component is clearly dependant on the amplitude of shaking, while the residual component is a function of both the amplitude *and* duration of shaking. The residual displacement at the completion of 0.1g to 0.5g shaking steps increased from 2 mm to 150+ mm respectively.

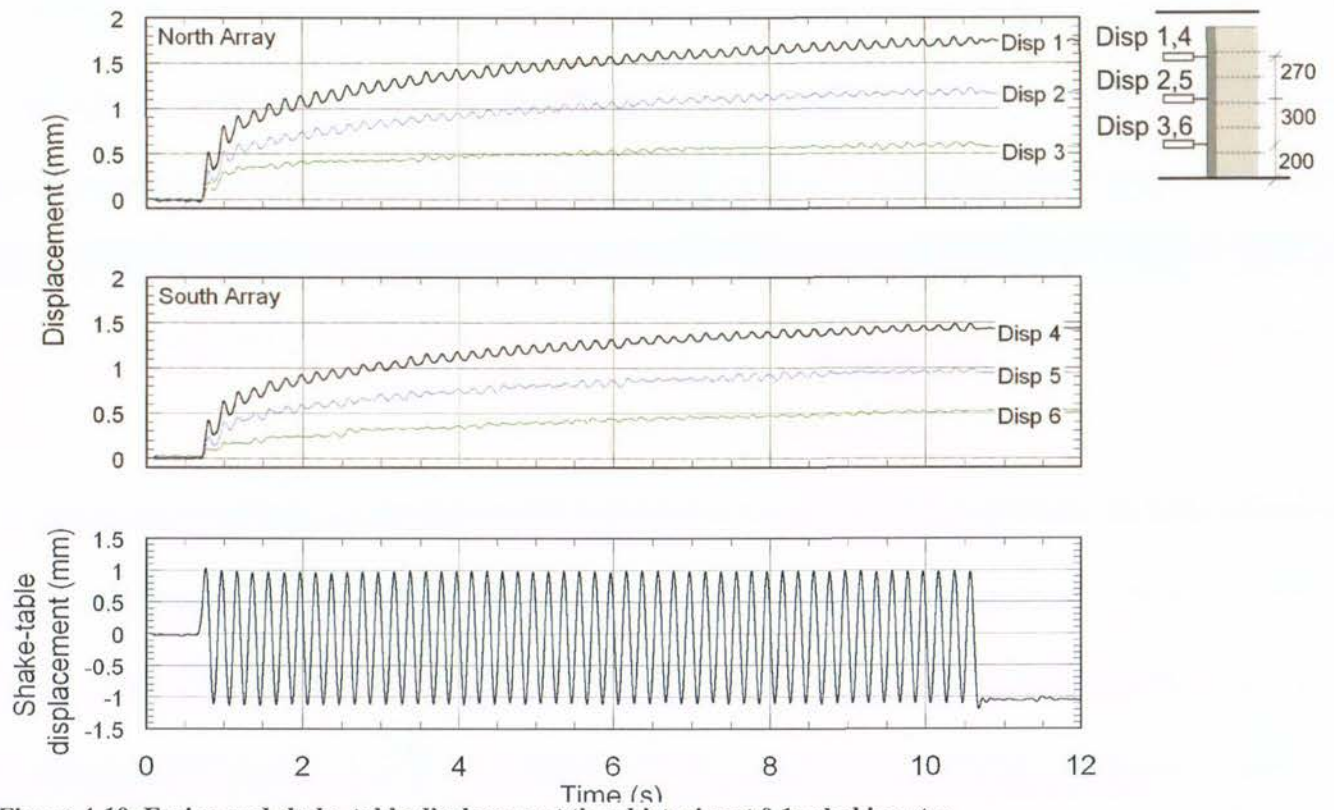


Figure 4-10. Facing and shake-table displacement time histories at 0.1g shaking step

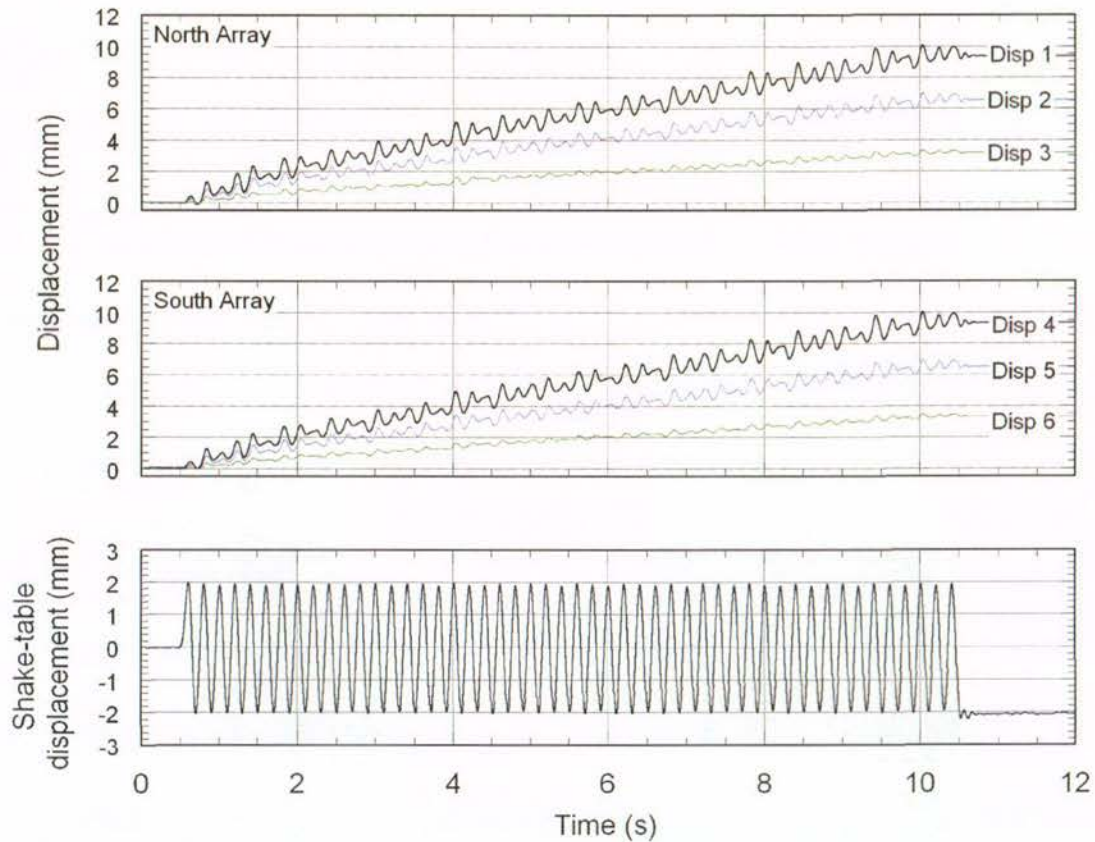


Figure 4-11. Facing and shake-table displacement time histories at 0.2g shaking step.

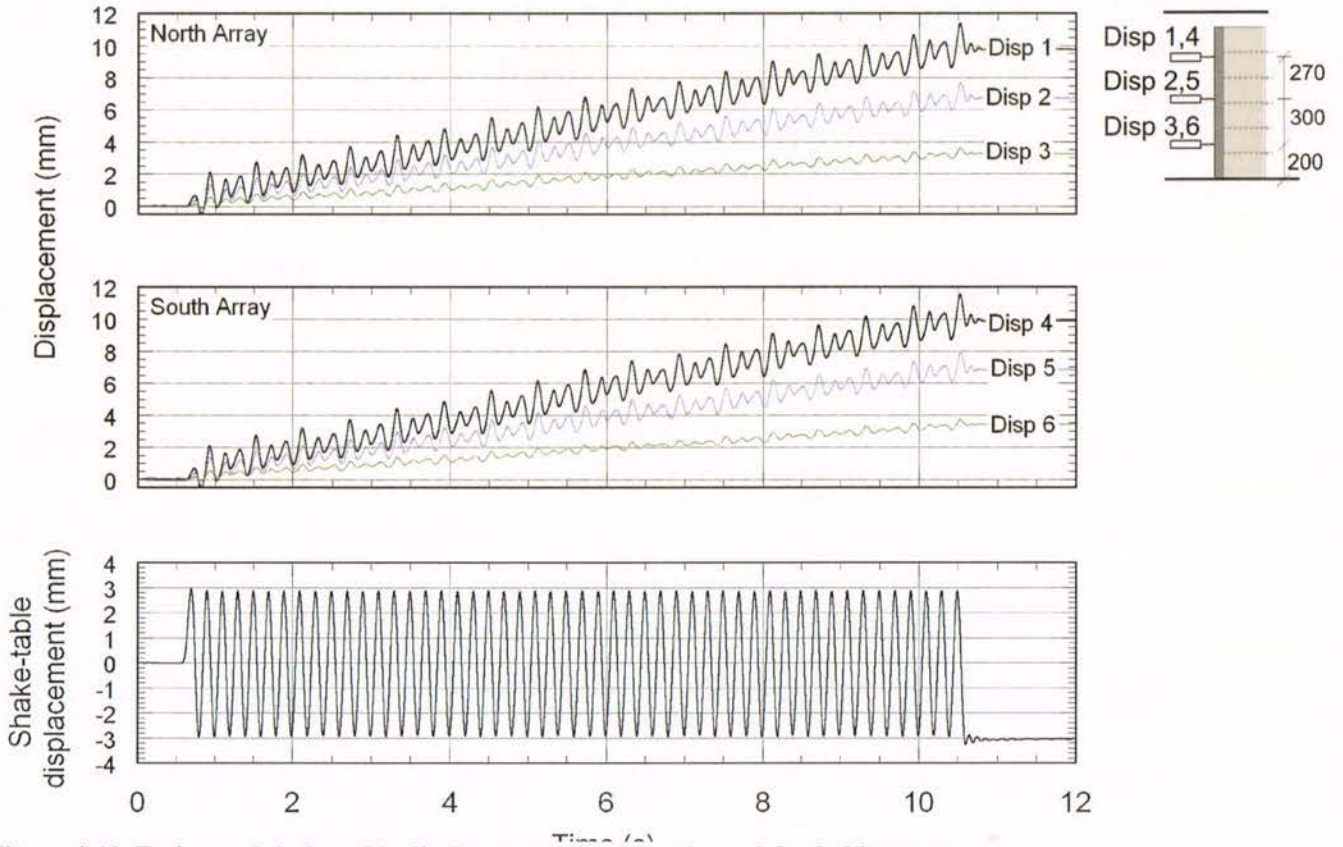


Figure 4-12. Facing and shake-table displacement time histories at 0.3g shaking step

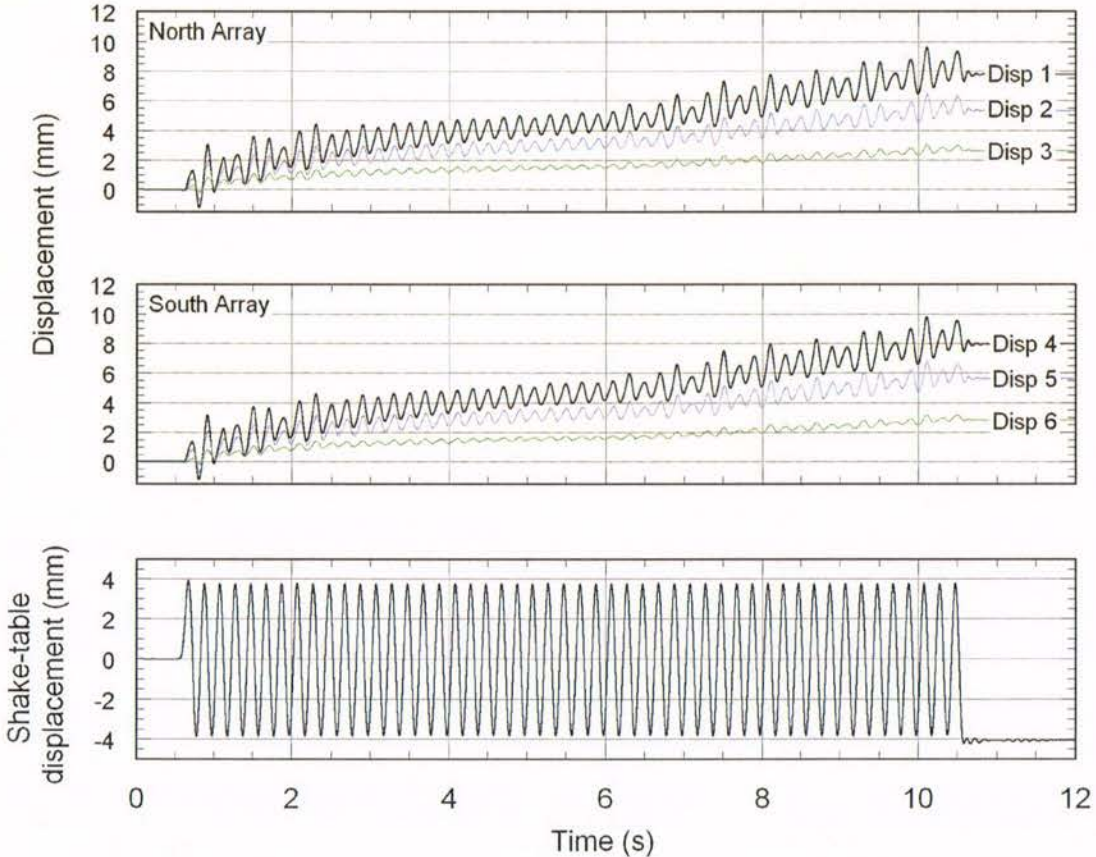


Figure 4-13. Facing and shake-table displacement time histories at 0.4g shaking step.

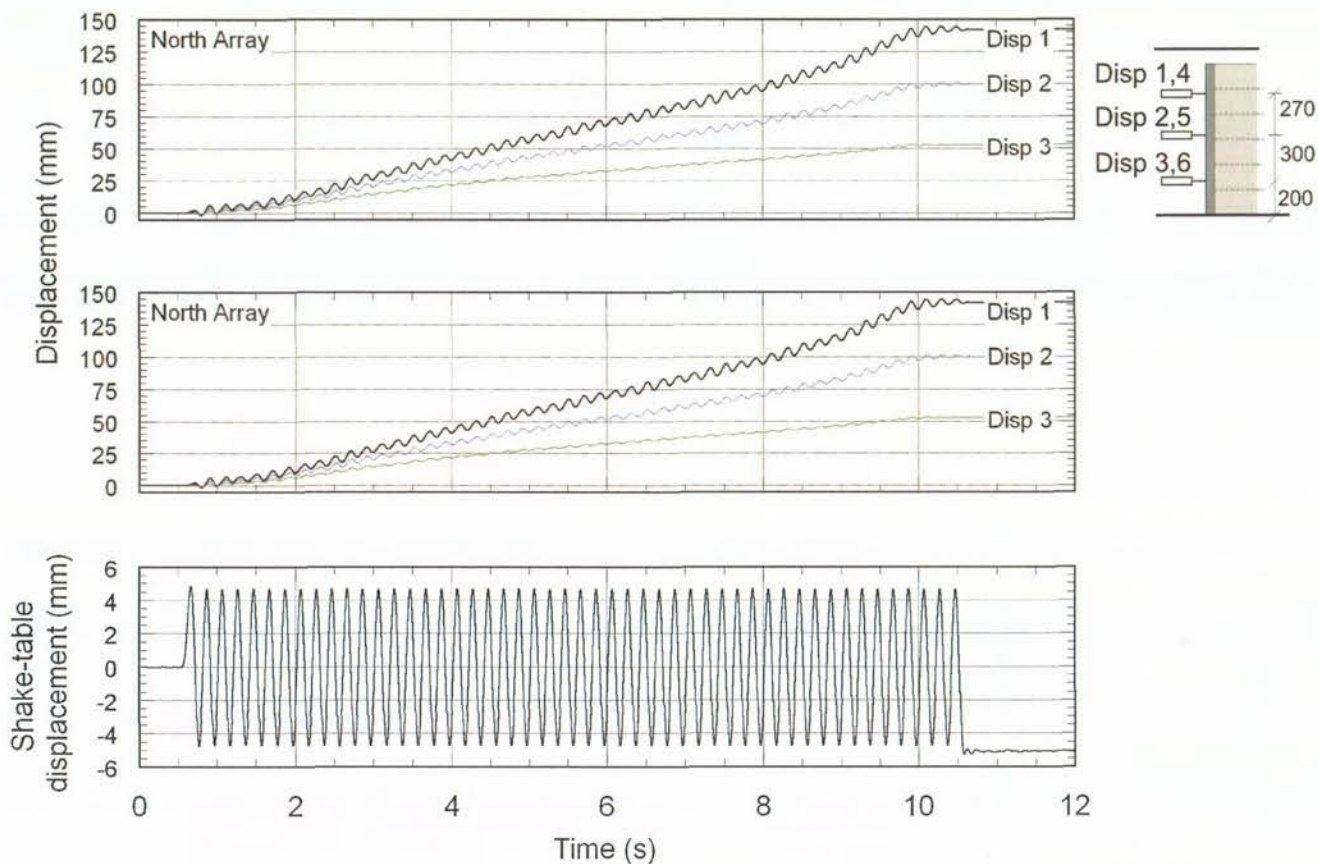


Figure 4-14. Facing and shake-table displacement time histories at 0.5g shaking step

The first cycle of the 0.1g shaking step caused a large residual deformation immediately upon application, which was followed by a reduced response for the rest of the displacement-time history. This behaviour was evident throughout all model walls during the first shaking step and is most likely due to some displacement necessary to completely engage all reinforcement layers. That is, during construction there is some small slack in the reinforcement placement, which, in order for all reinforcement to act in unison and resist deformation of the wall face, must first be removed. The displacement-time history demonstrated non-linear behaviour with decreasing incremental residual displacement throughout the rest of the shaking step, such that the residual displacement seemed to almost plateau at a displacement of 1.75 mm.

The first shaking step also showed evidence of slight asymmetry of movement from the longitudinal direction; there is a 0.35 mm discrepancy in residual wall movement between Displacement transducers 1 and 4 (Figure 4-10). No further movement out of plane was generated during increasing base input acceleration.

In the 0.2g and 0.3g shaking step shown in Figure 4-11 and Figure 4-12, wall deformation was irregular though increased steadily throughout the shaking. An increased response can be seen to occur every third cycle generating an increased recovery of displacement back in the negative direction, and an increased displacement in the positive outward direction of almost double that of the trend seen in the other two cycles.

While the shake-table displacement time history is steady, the base input acceleration of the 0.3g shaking step (Figure 4-8) reveals some small irregularities which appear to have been amplified in the facing displacement response. Amplification of the acceleration response of the wall face has previously been recorded by El-Emam and Bathurst (2007) and it is reasonable to presume that this may translate into an amplification of displacement as well.

The irregular displacement response clearly visible in Figure 4-12 was also exhibited at other shaking levels (it appears “washed-out” for the 0.5g shaking step as shown above) and all other tests. A possible explanation is discussed further in Section 4.3.6.

The 0.4g shaking step (Figure 4-14) shows the residual displacement to be less than that which occurred in the previous lower amplitude shaking at 0.3g. This was also evident in other tests and could be the result of two possible effects: the mode of deformation, and the geometry of wall displacements (i.e. overturning vs sliding). These possible effects are discussed below with reference to Figure 4-15.

It can be seen in Figure 4-4 above that the model undergoes predominantly overturning and some sliding. This failure geometry is evident in the facing displacement time histories with the largest displacement occurring at the top most displacement transducers (Disp. 1 and 4). To remove the influence of failure geometry on the facing displacement time histories, the smaller sliding component of deformation (with some overturning component still present) can be somewhat isolated if we consider the displacement time history of the lowest displacement transducer, Disp. 3 or Disp. 6. Figure 4-15 shows the entire facing displacement time history of Disp. 3 (the lowest North Array displacement transducer located at an elevation of 200 mm) created by connecting the Disp. 3 time histories of Figure 4-10 to Figure 4-14.

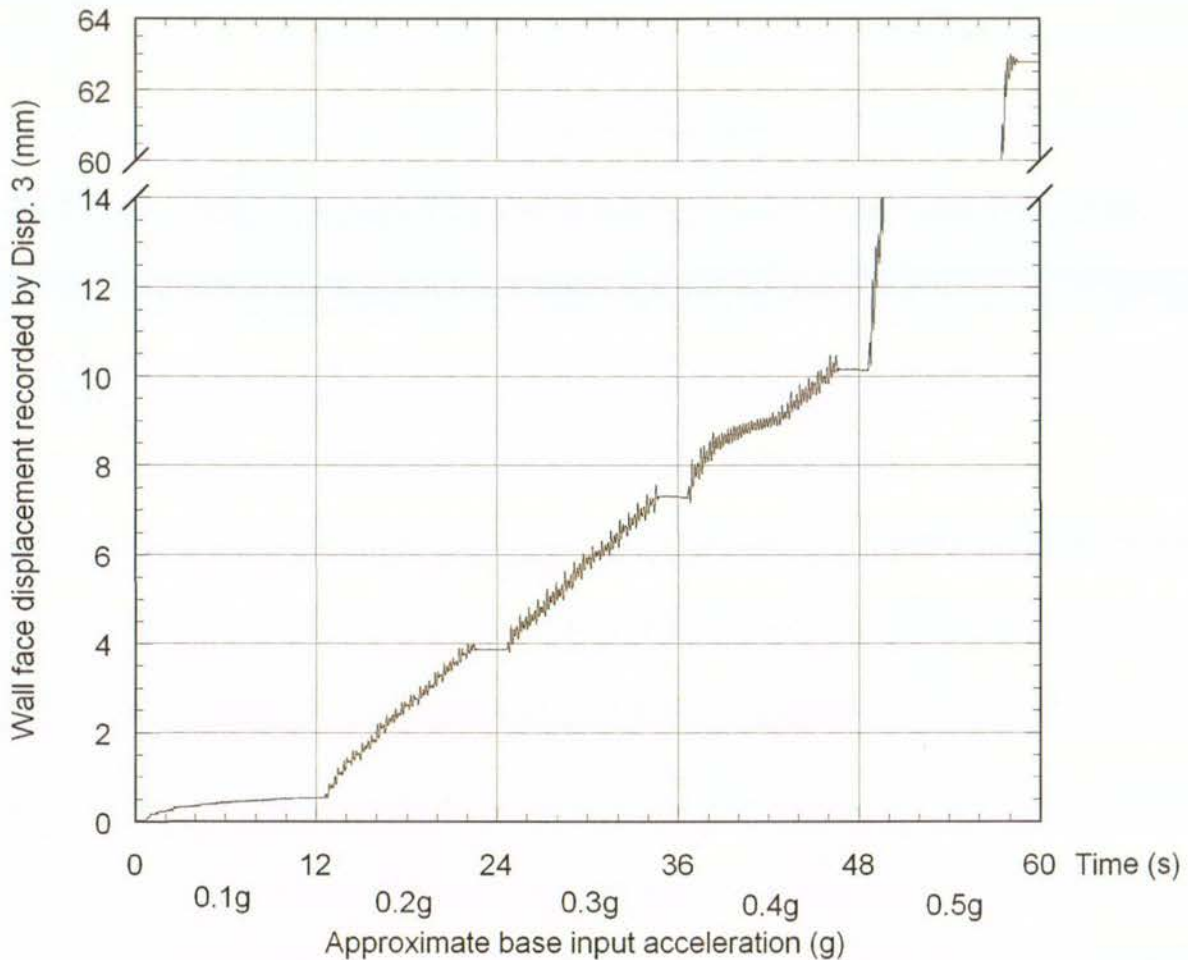


Figure 4-15. Facing displacement time history of Disp. 3 (lowest North Array displacement transducer).

Figure 4-15 shows the response to be a combination of linear and non-linear segments at and within different acceleration levels. Non-linear segments are visible in the 0.1g, 0.2g, 0.4g and 0.5g shaking steps (see Figure 4-14 above for complete 0.5g time history without scale break). For instance, during the 0.4g shaking step, a period of non-linear deformation is followed by a sudden increase in the rate of displacement and a linear response.

The non-linear segment could be due to the further development of failure surfaces already visible in Figure 4-4 (c), and the formation of new failure surfaces, within the backfill, whilst the sudden increase in displacement and a linear response could be the result of the weight of the wall face contributing to an increase in the overturning component of displacement, acting on the previously formed failure surface.

A similar combination of non-linear and linear displacement responses has been noted by Koseki et al. (2006) in reduced-scale shake-table tests on conventional gravity retaining wall models. In one test, displacement was recorded at the wall toe, and a non-linear displacement

response was found to occur for shaking levels prior to approximately 0.35g, before the formation of a failure plane within the backfill. This was attributed to non-linear shear deformation of subsoil layers below the wall. However after the formation of a failure plane within the backfill by 0.35g, displacement accumulated linearly. This was attributed to sliding at the wall base and subsoil interface.

This may help explain the reduction in residual displacement evident between shaking steps 0.3g and 0.4g. That is, progressive failure within the backfill means that the residual displacement accumulated during 0.3g shaking step could be associated with those shallow failure surfaces visible in Figure 4-4 (c), whereas residual displacement accumulated during 0.4g shaking step could be associated with failure surfaces deeper within the backfill, which are more difficult to develop. This would result in a reduction in the displacement recorded at the wall face.

In the final 0.5g shaking step shown in Figure 4-14, the wall deformed with large cyclic components of deformation and almost linear incremental residual (permanent) displacements until the test was terminated. A slight increase in the rate of deformation occurred just prior to the end of the final shaking step, most likely the result of the weight of the wall face as it tilted over, contributing to an increase in the rate of overturning. The test was terminated when the wall reached the maximum displacement of the displacement transducers and experimental set up, which occurred during the final few cycles of the 0.5g shaking step.

#### **4.3.6 Investigation of irregular displacement response**

Discernible in all tests at all shaking steps (except 0.5g where it appears “washed-out”) is a regular increased displacement response every third cycle, for instance that shown in Figure 4-12 and Figure 4-13, and hence occurs at a frequency of  $5/3 = 1.67$  Hz. To investigate this further, raw facing displacement data is shown for 0.3g shaking step in Figure 4-16 below.

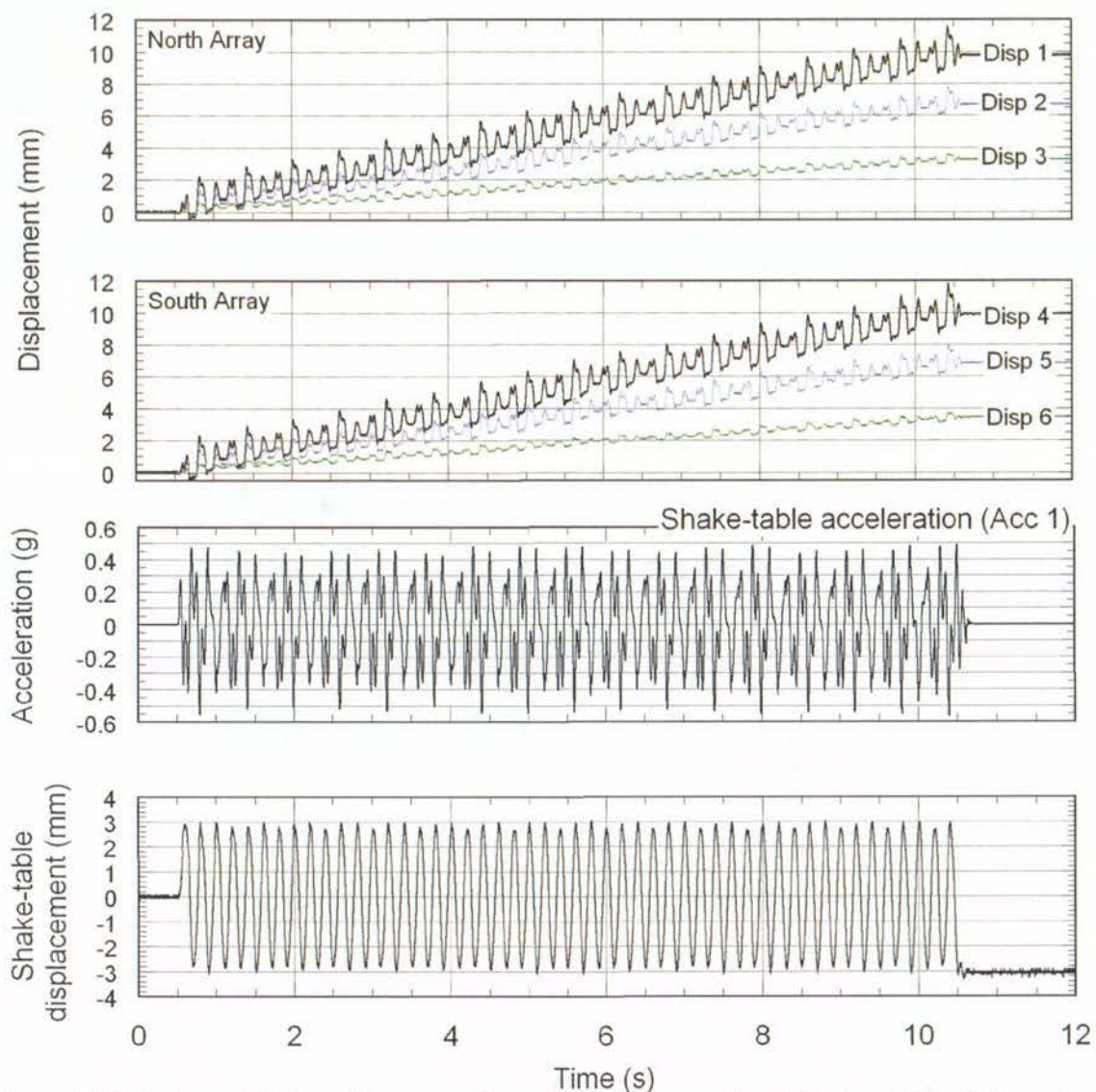


Figure 4-16. Facing and shake-table raw (unfiltered) displacement time histories at 0.3g shaking step.

The raw wall face displacement data plotted in Figure 4-16 shows an increased displacement at every 3<sup>rd</sup> cycle. However, the raw shake-table acceleration data shows two spikes at around 0.4g to 0.5g, for every one cycle hitting the desired 0.3g target acceleration. Additionally, the shake-table displacement does appear to be increased slightly every 3<sup>rd</sup> cycle.

Figure 4-17 (a) – (d) plots the fast fourier transform of the wall, reinforced soil and shake-table system to illustrate their respective frequency components and ascertain the origin of the 1.67 Hz component for the 0.3g shaking step. Figure 4-18 (a) – (d) shows the fast fourier transforms of the system when excited at 0.5g.

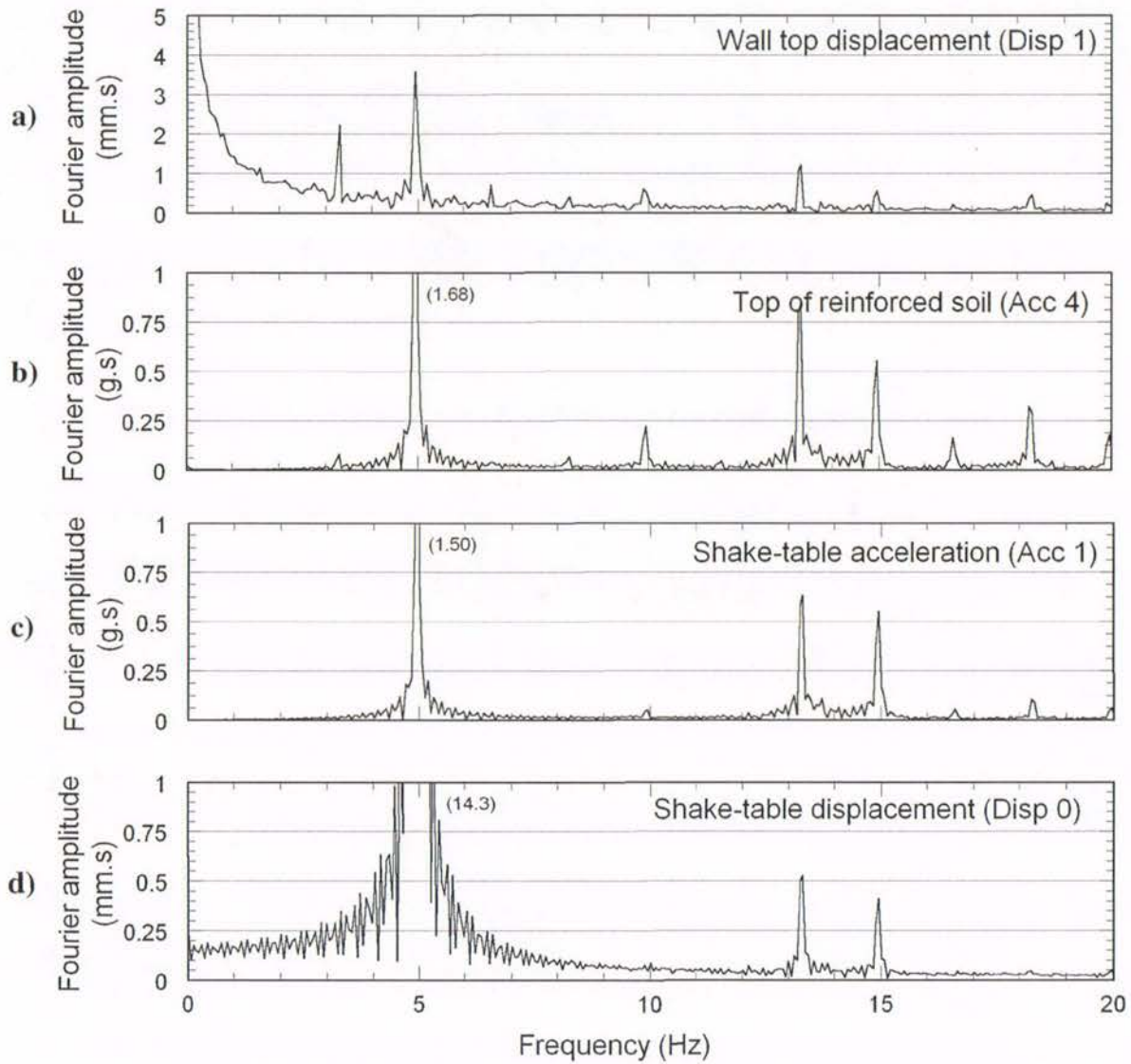


Figure 4-17. Fast fourier transforms for 0.3g shaking step for: (a) wall face top displacement, (b) acceleration at the top of the reinforced soil zone, (c) the base input acceleration (d) shake-table displacement.

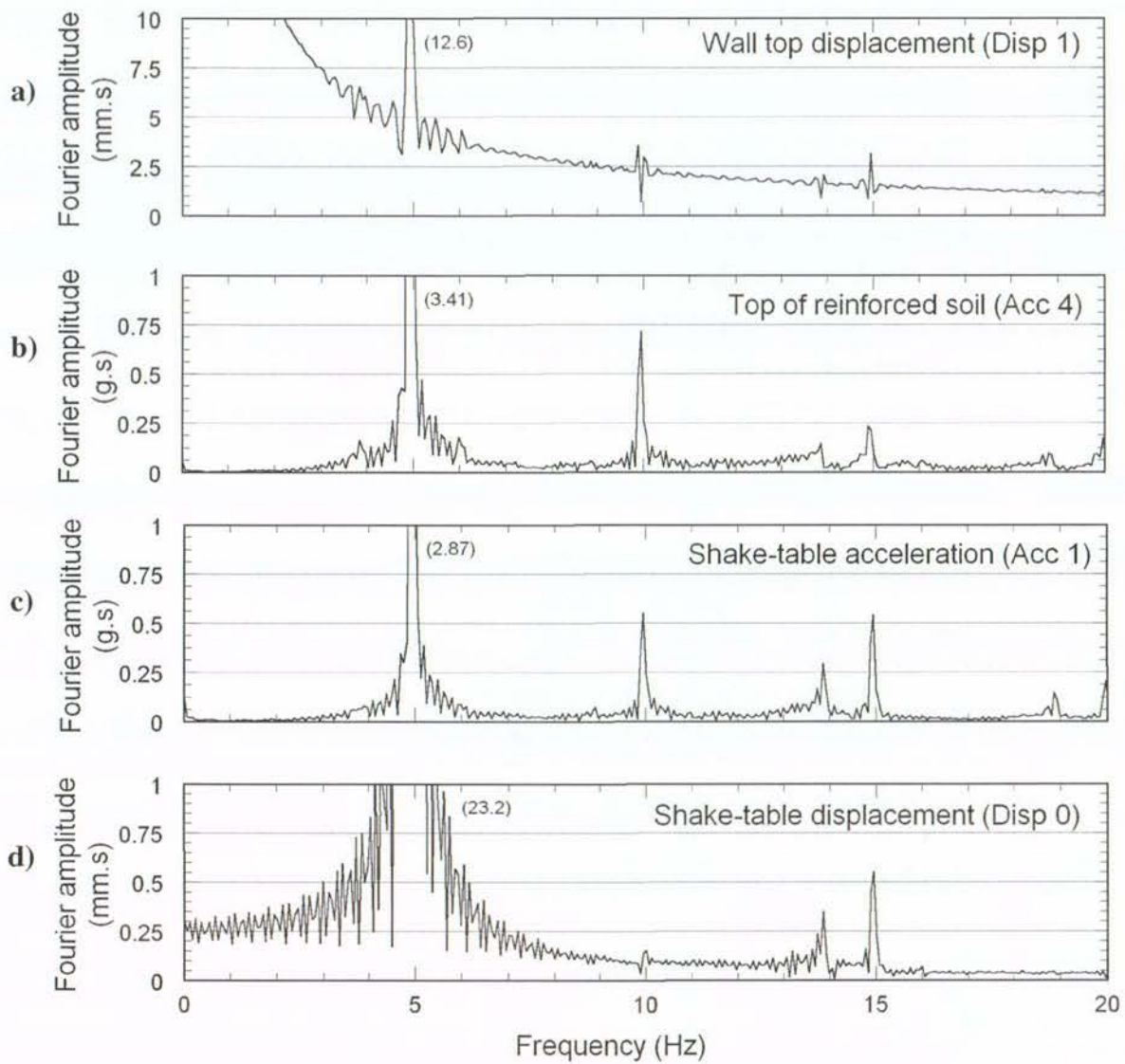


Figure 4-18. Fast fourier transforms for 0.5g shaking step for: (a) wall face top displacement, (b) acceleration at the top of the reinforced soil zone, (c) the base input acceleration (d) shake-table displacement.

The main frequency components of the system as seen in Figure 4-17 and Figure 4-18 (a) – (d) are:

- The driving frequency of the input base motion at 5 Hz, and other modes at 15 Hz and higher.
- The fundamental natural frequency of the loaded shake-table at 13.7 Hz as determined previously in Section 3.5. No other natural modes are visible.
- Long-period (low frequency components) motion associated with the permanent displacement of the wall face visible in Figure 4-17 (a).
- A frequency spike at 3.35 Hz only visible in the wall face displacement and reinforced soil acceleration responses (Figure 4-17 (a) – (b) and Figure 4-18 (b)).

The latter point noted describes a frequency component exactly twice that deduced on inspection of the wall face displacement time histories. Further, it is not visible in the input shake-table displacement and acceleration time histories, but appears within the reinforced soil zone and wall face (Figure 4-17 (a) – (b)). It is quite possibly “washed-out” within the shake-table displacement during 0.5g shaking.

One possible explanation is found upon comparison of the apparatus used to record the shake-table displacement and accelerometer time histories. The shake-table displacement is measured by a linear variable displacement transducer (LVDT) which is fixed to the shake-table foundation and records the relative shake-table top displacement. The base input acceleration is recorded on the shake-table top and, as a result, measures absolute accelerations (which includes shake-table *and* foundation movement).

Marriot (2009) recorded up to 1.1 mm of foundation movement during shaking table tests, and this too was noted in the current tests. This creates increased and irregular shake-table acceleration not recorded in the shake-table displacement time history. Thus it is considered that the response is likely to be the result of the hydraulic actuator driving the shake-table motion as opposed to model-specific behaviour.

## 4.4 Analysis of Test-6 results

This section develops seismic response measures for Test-6, to provide a general framework for the parametric study of L/H ratio and wall inclination influence on seismic performance in later sections.

### 4.4.1 Cumulative wall face displacement

The cumulative facing displacement for Test-6 is plotted as a function of the number of shaking cycles in sequence of increasing base input acceleration in Figure 4-19 (a) – (e). Note that each point is plotted at the displacement peak in the outwards (positive) direction and includes both cyclic and residual components of displacement. This is why the displacement recorded at the 50<sup>th</sup> cycle peak (50c) for 0.1g and 0.3g shaking steps is larger than the residual displacement recorded after shaking had stopped. This method ensures that the measurements recorded at each displacement transducer are time coincident; a displacement peak is better temporarily defined than a completed cycle (i.e. the baseline shifts due to residual displacement).

The residual displacement measured at the end of each shaking step was extrapolated to the wall top and toe at 900 mm and 0 mm respectively. Steel stiffeners attached to the front of the wall face ensured wall rigidity, and both vertical displacement transducer arrays recorded linear displacements, validating this extrapolation. The extrapolated values were then used to infer sliding and rotation components of deformation as discussed below.

Visible in greater detail is the predominance of overturning failure for all shaking steps, with only minor sliding recorded for shaking steps up to 0.5g. Further, upon application of 0.5g base input acceleration, most of the sliding component occurred during the first 30 cycles of shaking, which then decreased throughout the rest of the shaking step. As the wall rotates about the toe, it is likely that the weight of the wall face begins to play an increasing role in the wall response, and generates further rotation and prevents further sliding. In other words, as the wall overturns, the facing weight increases the destabilising moment causing further overturning. This coincides with a similar increase in the rate of displacement recognisable in the displacement-time history shown in Figure 4-14.

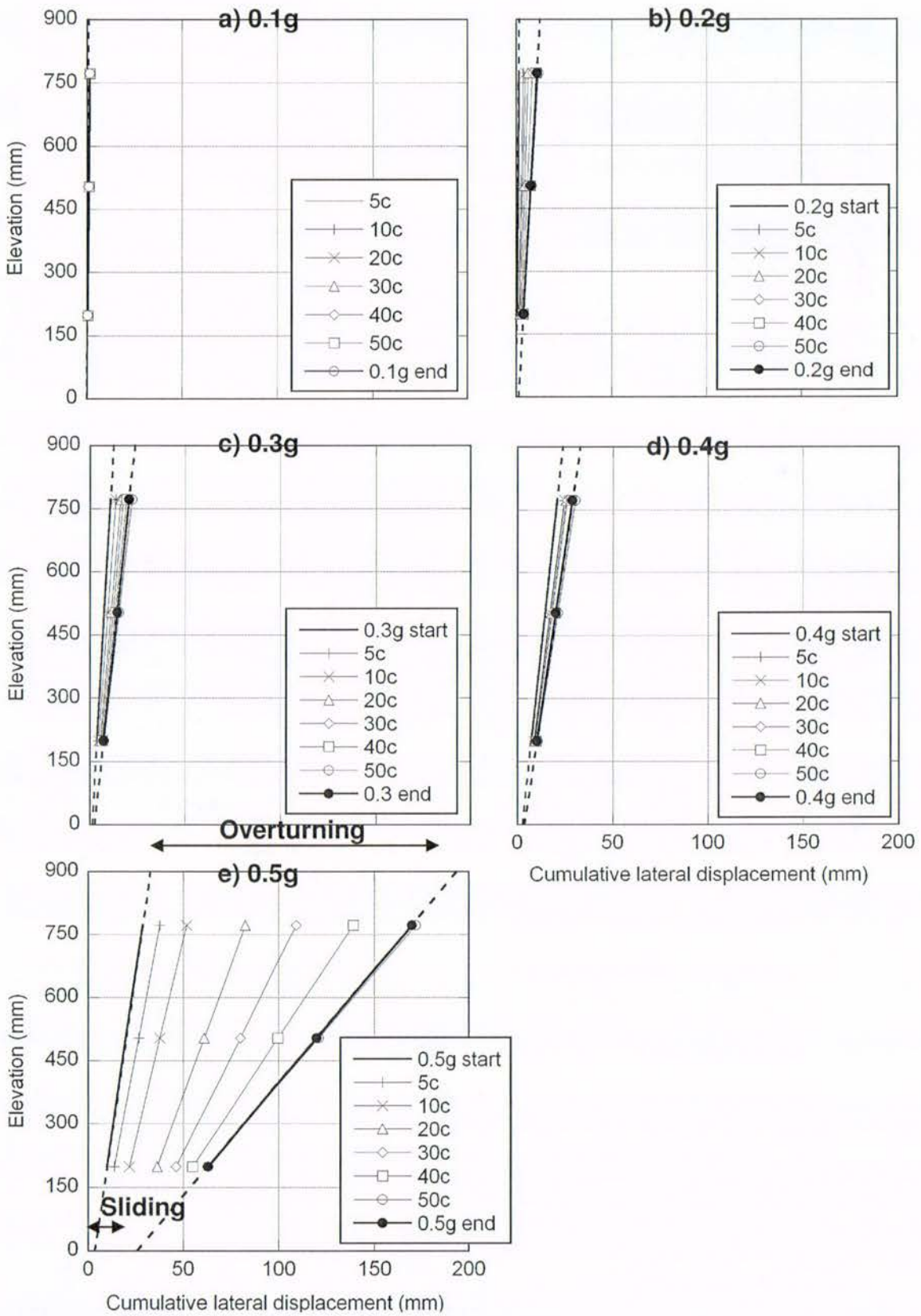


Figure 4-19. Cumulative lateral displacement of the wall face as a function of the base input acceleration and number of cycles for Test-6, reinforced at  $L/H = 0.6$ . NB: "c" denotes the peak for the number of cycles completed.

#### 4.4.2 Overturning and sliding components of deformation

Displacements at the wall top and toe are determined from linear extrapolations in Figure 4-19 shown as dashed lines. The horizontal displacement measured at the wall top,  $x_{top}$ , is dominated by an overturning component ( $x_{rotation}$ ) and includes some sliding component,  $x_{slide}$ , observed at the wall toe. Thus pure rotation of the wall is calculated as the difference between the wall top displacement, and wall toe displacements,  $x_{rotation} = x_{top} - x_{slide}$ .

Total, sliding and rotational components of residual displacement of the wall top at the end of each shaking step are plotted as a function of the input base acceleration in Figure 4-20. The acceleration for each shaking step is calculated as the average amplitude of the input base shaking using the double amplitude method.

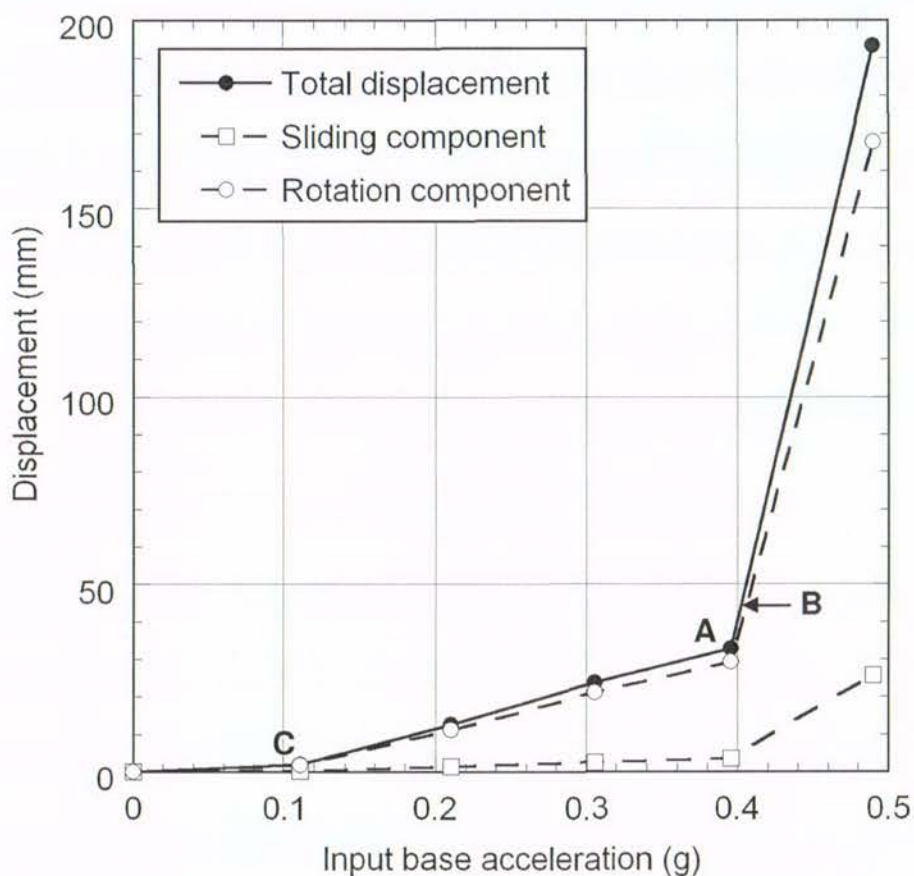


Figure 4-20. Rotation and sliding components of cumulative residual horizontal displacement of the wall top with increasing base input acceleration (PGA). Reinforced at  $L/H = 0.60$  (T6).

A number of comments may be made with respect to Figure 4-20. The total displacement-acceleration curve is bi-linear and typical of other physical model studies (El-Emam and Bathurst 2004; Watanabe et al. 2003). At low base input accelerations, there is small

permanent deformation; at base input accelerations larger than some threshold value – in the above case, 0.4g – the rate of deformation increases significantly. As discussed previously, this value of acceleration could be defined as the critical acceleration for the model wall system and is shown as point A in Figure 4-20. A discussion on the selection of critical acceleration values, and their theoretical derivation is made in Section 2.2.5.

Prior to the critical acceleration being reached, the wall exhibits small sliding with some ~ 4 mm evident by the completion of 0.4g shaking step. Rotation contributes almost entirely to the total deformation of the wall top of ~ 33 mm. At shaking past the critical acceleration, sliding of the wall increases significantly and contributes ~ 27 mm to the total displacement of 195 mm, or about 13 %.

The overturning failure mode is perhaps predominant due to a reduced confinement of the top layers of reinforcement, and thus a reduction in resistance to overturning. The low levels of sliding exhibited in Test-6 and other tests, could be the result of high localised friction between the FHR facing panel toe and the rigid foundation covered with a layer of glued sand. Hence the wall can only slide once this frictional limit is exceeded.

Interestingly, it is noted that even flexibly-faced models on a subsoil foundation (hence with low localised friction at the wall face), tested by Sabermahani et al. (2009) also exhibited small sliding components of deformation. Thus it is considered that the current experimental model does not inhibit the development of sliding deformation.

#### **4.4.3 Critical Acceleration**

Critical acceleration is defined by Bracegirdle (1980) as “the horizontal pseudo-static acceleration acting uniformly over the structure to achieve limiting equilibrium”. In other words, as the critical acceleration generates limit equilibrium (factor of safety equal to unity) any larger acceleration applied will cause the structure to slide.

Critical acceleration is important as a measure of stability; a high critical acceleration value indicates a high stability during an earthquake. Additionally, critical acceleration is also used for predictions of permanent displacement based on rigid block analysis (Richards and Elms 1979). Thus correct selection of a critical acceleration value for the structure under analysis, is one factor which helps the accuracy of such a prediction.

As noted above, the bi-linear displacement-acceleration curve in Figure 4-20 (a) demonstrates the existence of a threshold or critical acceleration; accelerations larger than 0.4g in Test-6 (point A) cause the wall displacement to increase significantly. Thus 0.4g could be considered the model specific critical acceleration value. However, determination of the critical acceleration for the other tests is not so clear. For instance, Section 4.6.3 shows Test-5 to have demonstrated an increase in the rate of wall top displacement both at 0.5g and 0.6g. Hence it is unclear as to what is the critical acceleration for Test-5.

Previous researchers have defined the critical acceleration observed in model studies with different measures. Watanabe et al. (2003) defined it as the acceleration coefficient that generated a cumulative displacement larger than 5% of the wall height (0.05H), or 25 mm, which was recorded at an elevation of 450 mm for the 500 mm high model walls used in their experiments. This definition was justified because wall top displacement increased rapidly after about 25 mm had been accumulated. Because, the models were subjected to amplitude-increasing irregular acceleration-time histories until wall failure, the critical acceleration criterion is based on displacement accumulated by previous shaking steps. This could be problematic as not a single acceleration coefficient can be defined that contributes to an increase in wall top deformation.

While the 0.05H value is specific to the Watanabe et al. (2003) models, the critical acceleration defined by this method is plotted as point B in Figure 4-20.

Nova-Roessig and Sitar (2006) defined critical acceleration as the minimum acceleration that caused the slope to deform permanently. Because permanent deformation occurred at accelerations as little as 0.03g, this was defined as the critical acceleration. With further shaking at higher accelerations, the critical acceleration value was observed to increase, and this was attributed to increased densification of the backfill which was observed. Hence the criterion does not provide a good indication as to when ultimate failure may occur.

For all of the present tests, permanent deformation occurred at the onset of the (initial) 0.1g base input acceleration and thus this would be defined as the critical acceleration (point C in Figure 4-20). However failure is actually observed at base accelerations far larger, and the definition yields little information as to when this failure might occur.

El-Emam and Bathurst (2005) compared rotation and sliding failure modes as a means of observing critical acceleration. The acceleration coefficient that caused a sudden increase in

sliding, compared to rotation, indicated the critical acceleration value. The method is more consistent with the Richard-Elms method (1979) of block sliding, for determining permanent displacements during an earthquake. In the Richard-Elms approach the critical acceleration is the acceleration coefficient that generates limiting equilibrium against sliding failure. Because critical acceleration is an important parameter for the prediction of permanent displacement, it is appropriate that the El-Emam and Bathurst (2005) criteria for observed critical acceleration is the same as its subsequent use for displacement predictions using block sliding.

The displacement data for Test-6 is broken into its components of rotation and sliding components, normalised by the height of the wall, and is replotted in Figure 4-21.

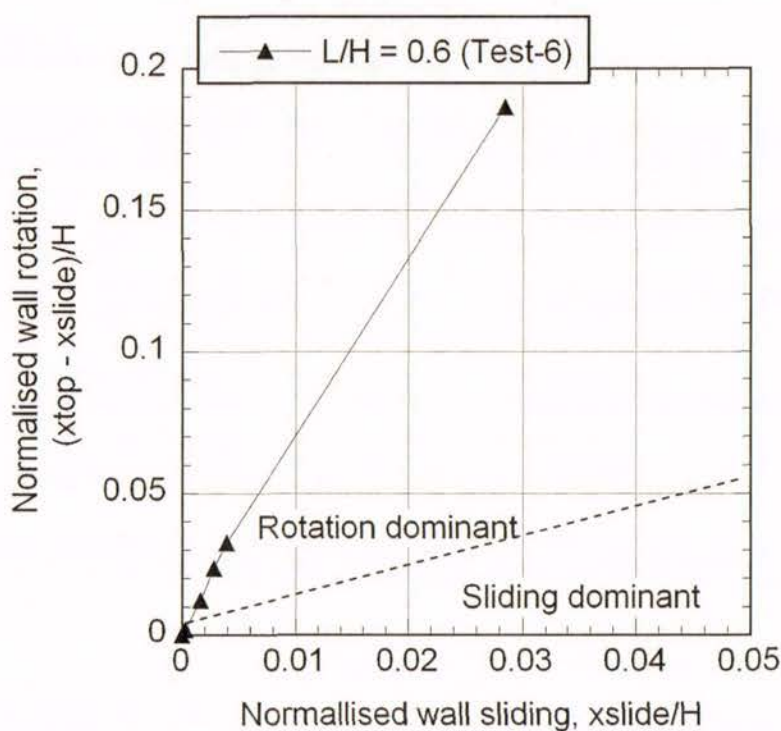


Figure 4-21. Normalised sliding and rotation components of wall response for  $L/H = 0.6$ .

Figure 4-21 shows that this particular criterion is ill-suited to the Test-6 data set, as rotation is always dominant over sliding, even during ultimate failure. In contrast, the data presented by El-Emam and Bathurst (2004, 2005) demonstrated a distinct transition between rotation and sliding modes of deformation, most likely because the model wall's facing panel was founded on roller bearings of low localized friction in order to fully decouple measured vertical and horizontal toe load components. This boundary condition is unlikely to be representative of field structures.

Whilst no *relative* transition from rotation to sliding modes of failure was evident during Test-6, there was a significant increase in the magnitude of sliding prior to failure, and this perhaps, should form the basis of any measure of critical acceleration. This is further investigated with the comparison of all test results in Section 4.6.3.

#### 4.4.4 Soil response

Fast Fourier transformations of the acceleration time histories of Test-6 for shaking steps 0.1g, 0.3g and 0.5g are shown in Figure 4-22.

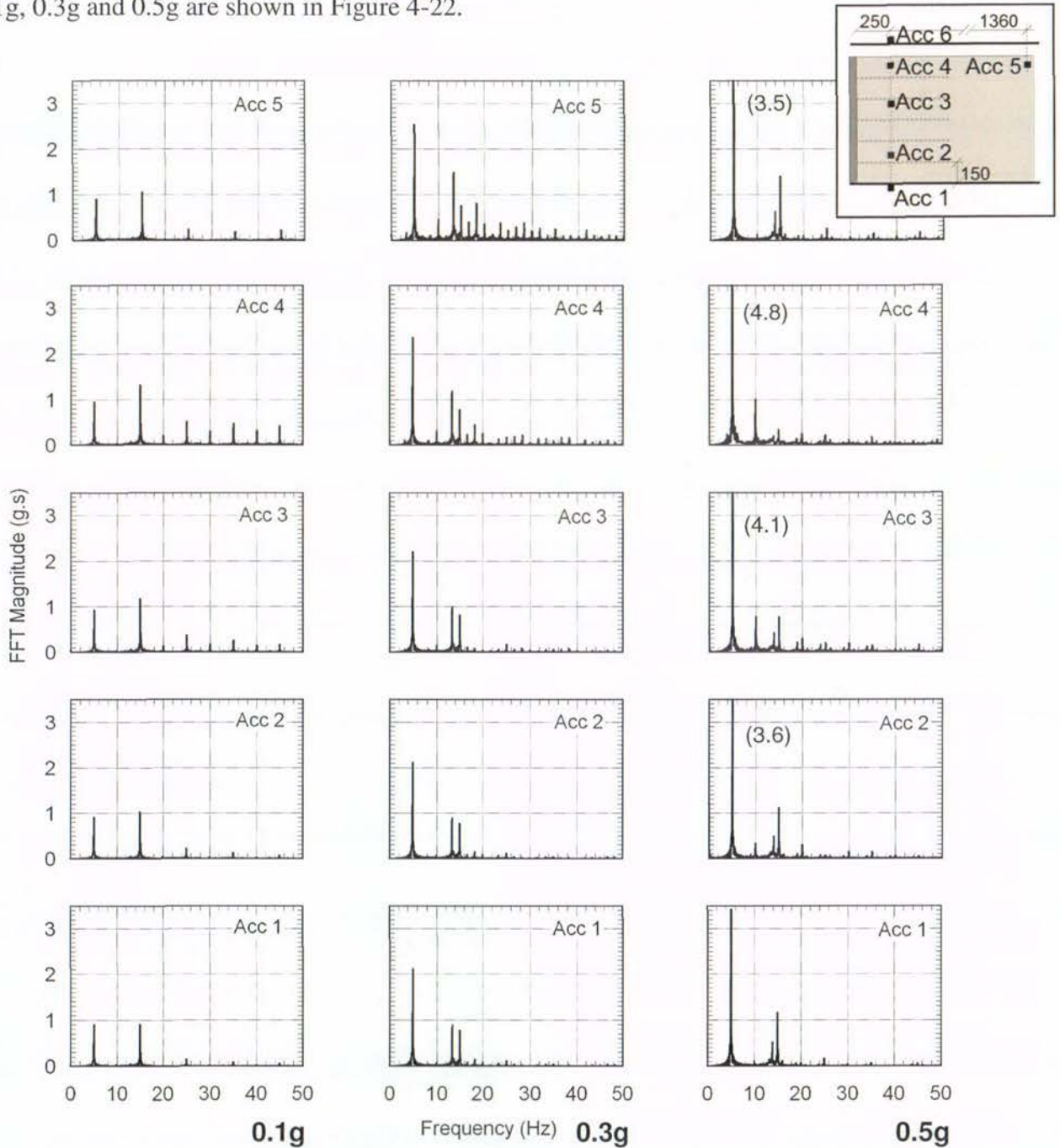


Figure 4-22. Fast Fourier Transformations for the base input and response accelerations for the 0.1g, 0.3g and 0.5g base shaking levels for Test-6. The values in parentheses correspond to peak values.

The response accelerations have the same frequency content as the input base acceleration. This is a further verification of high soil density, as the full frequency content can be transmitted through the system without losses in frequency content associated with frictional damping etc. Conversely, a loose soil would act to dampen out high frequency components (Kramer 1996).

FFT magnitudes increase up the wall for all frequencies and are the result of amplification of the base acceleration. Further, this amplification increases with increasing base input acceleration. This is discussed further below.

#### 4.4.5 Peak acceleration amplification

The average peak accelerations within the soil deposit are normalised with respect to the base input average peak acceleration and plotted in Figure 4-23. Only peaks in the outwards (positive) direction were used in the calculation as these are of primary concern and act to generate a larger destabilising force (accelerations acting inwards act to stabilise the wall).

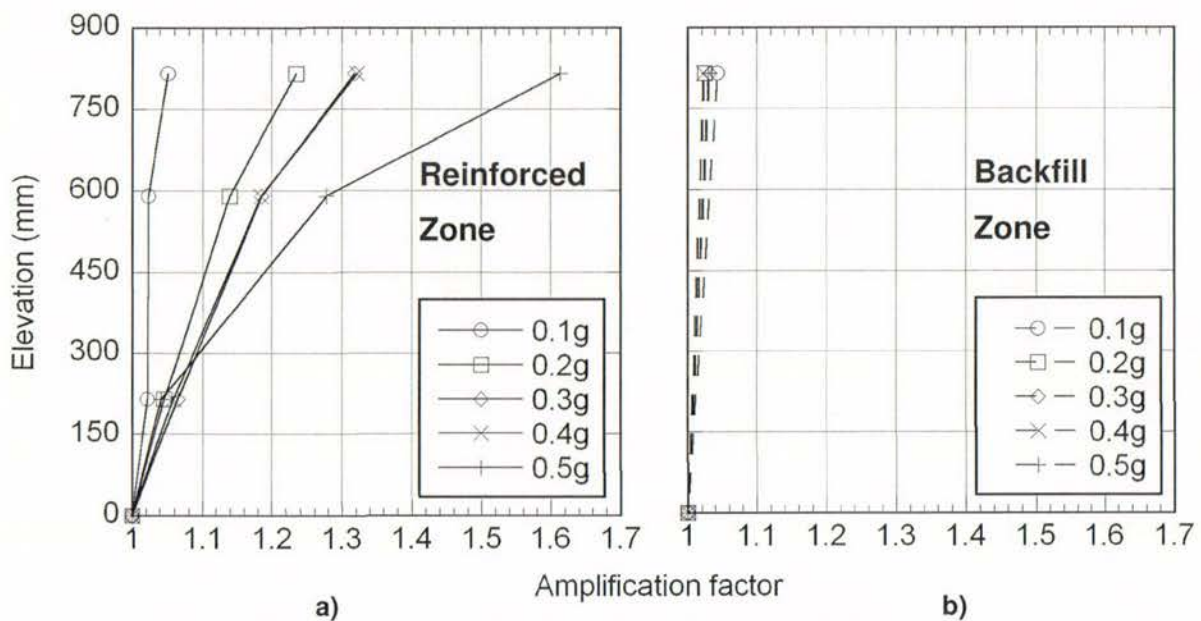


Figure 4-23. Amplification of peak outwards accelerations with wall elevation is plotted for each shaking step: (a) reinforced soil and (b) backfill.

Figure 4-23 (a) demonstrates a significant amplification of the average peak base input acceleration in the reinforced zone up the wall for all shaking steps. This amplification increases with increasing base shaking from 0.1g to 0.5g; behaviour also observed by Matsuo et al. (1998) for flexible reinforcement. The base input acceleration near the wall top

(elevation of 815 mm) is amplified by 1.05 in the first shaking step of 0.1g, which then increases to around 1.2 – 1.3 for the 0.2g, 0.3g and 0.4g shaking steps. In the final shaking step of 0.5g, the soil response significantly amplifies the base input acceleration by 1.6. This is further evidence for some threshold acceleration value being reached at this acceleration level.

Figure 4-23 (a) also demonstrates that amplification in the reinforced zone is non-linear up the wall. This has also been reported by Nova-Roessig and Sitar (2006) in their dynamic centrifuge model tests. Ramifications of this for design are discussed in Section 4.7.1.

Figure 4-23 (b) shows a slight amplification of input base accelerations near the top of the ‘far-field’ backfill; however this is only a single measurement point, hence a dashed line is used to show amplification up the wall assuming a linear amplification response with height from the base of wall.

Larger amplification factors have been reported in the literature for both shaking table and dynamic geotechnical centrifuge tests (El-Emam and Bathurst 2004; Fairless 1989; Nova-Roessig and Sitar 2006). Fairless (1998) reports amplification factors of 3.0 at the top of 0.3 m high 1:6 model scale walls in tests where the acceleration input was pulsed. El-Emam and Bathurst (2004) report amplification factors of 2.25 at the top of 1 m high walls constructed with  $D_r = 84\%$  for shaking table tests just prior to failure, and a decrease in amplification during the final shaking step to 2.0.

Nova-Roessig and Sitar (2006) also reported amplification at wall top of peak acceleration values of up to 2.3; however this occurred at low base input accelerations up to 0.15g. The authors noted that, amplification in general was accompanied by some shearing. In direct contrast to Figure 4-23, the authors reported that de-amplification (attenuation) of peak acceleration occurred at base accelerations larger than about 0.46g.

The difference in behaviour reported by Nova-Roessig and Sitar (2006) and that shown in Figure 4-23 (a) could be contributed to by two effects: the difference in initial model densities and the difference in frequency contents of the input motions used. Nova-Roessig and Sitar (2006) constructed their walls at a  $D_r = 55\%$  and used multiple sinusoidal motions at low amplitudes to examine elastic behaviour, then a series of 8 to 12 time-histories of wide frequency content, amplitude-scaled to 0.11g to shake each model. This is compared to a stepped-sinusoid of predominant frequency 5 Hz used in the present tests.

The peak response accelerations recorded during higher amplitude shaking by Nova-Roessig and Sitar (2006) are typically high frequency components, and these would be dampened out with the accompanying higher rates of shearing deformation to generate deamplification. This did not occur in the present tests because the peak accelerations all occurred at a low frequency of 5 Hz.

Additionally, at low accelerations there is little non-linear soil behaviour (limited damping) and amplification is in general, greater for looser soils (Kramer, 1996). High amplification at low acceleration levels was not evident in the present tests because the initial density of the model backfill was already high ( $D_r = 90\%$ ).

#### 4.4.6 RMS acceleration amplification

Differences in amplification factors between the results can also be attributed to the choice of acceleration measure used to calculate amplification factors. Both El-Emam and Bathurst (2004) and Nova-Roessig and Sitar (2006) reported amplification factors based on peak outwards accelerations. For design purposes this could be misleading since the high frequency peak values occur for a short duration and are rarely important for design purposes. Moreover, as discussed previously, a single parameter, such as Peak Ground Acceleration (PGA) is insufficient to completely describe an earthquake's damage-causing ability.

Thus a number of measures exist that attempt to combine frequency, duration and amplitude to adequately quantify an acceleration time history. These include the Root Mean Squared (RMS) acceleration, Acceleration Power and Arias Intensity, measures that include the duration, acceleration amplitude and frequency content (somewhat) of acceleration-time histories. The first of these, RMS acceleration is defined in Equation 4-2.

$$RMS = \left[ \frac{1}{T} \int_0^T a(t)^2 dt \right]^{1/2} \quad (4-2)$$

Where RMS is the root mean square acceleration,  $a(t)$  is the acceleration time history, and  $T$  is the duration of shaking. Following the method used by Law and Ko (1995), the acceleration time histories were converted to RMS acceleration values. Each RMS response was then normalised with the base input RMS acceleration to generate amplification factors as in Equation 4-3.

$$AF = \frac{RMS(h)}{RMS(base)} \quad (4-3)$$

Where AF is the amplification factor, and RMS(base) and RMS(h) are the root mean squared accelerations at the base and some height, h respectively. RMS acceleration thus quantifies the entire time history (not just positive peak accelerations). The acceleration response data is reinterpreted and RMS based amplification factors are plotted with elevation for the reinforced zone and backfill in Figure 4-24.

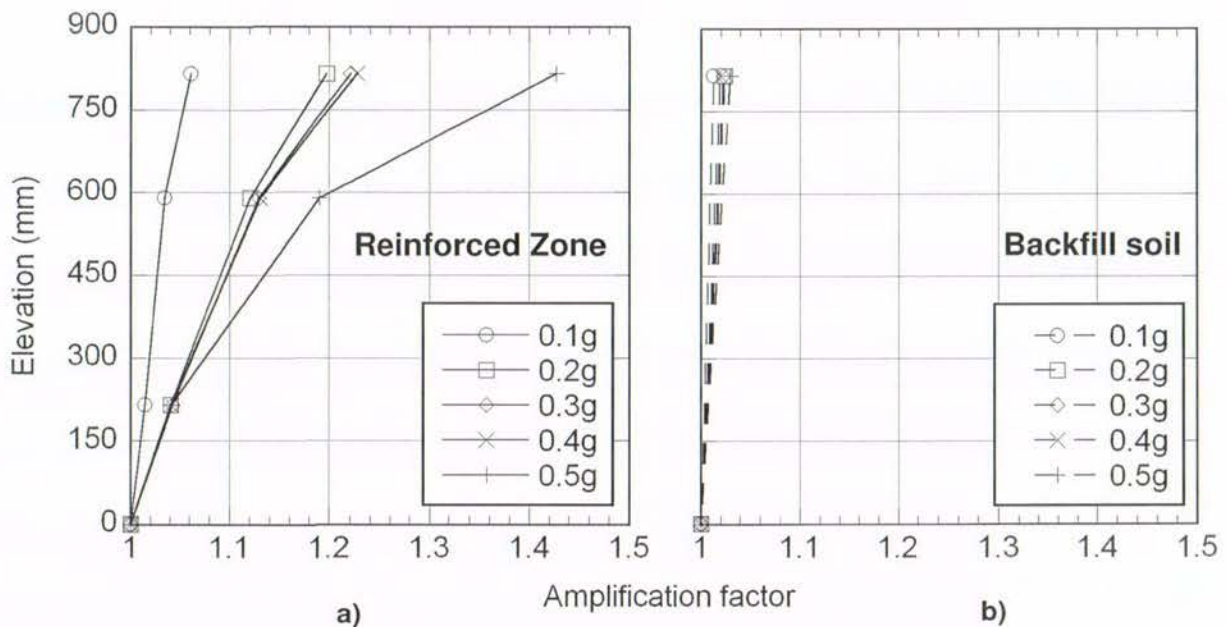


Figure 4-24. Amplification of RMS acceleration up the wall for each shaking step: (a) Reinforced zone and (b) Backfill.

Figure 4-24 shows similar non-linear behaviour of the reinforced soil zone and larger amplification with increasing acceleration amplitude. However amplification factors are smaller than those calculated for peak acceleration. For instance, the RMS amplification factor calculated at 0.5g near the top of the reinforced soil zone is 1.42 compared with a peak amplification of 1.62. This confirms that the peak acceleration amplification can over estimate the acceleration response of the wall overall.

#### 4.4.7 Acceleration amplification during shaking

Amplification of acceleration at each shaking step as discussed above is an average response for the entire duration of shaking. We know that the facing displacement response is non-linear during shaking, thus it could be expected that the soil response would also vary during

each shaking step. Figure 4-25 shows the amplification factors at the beginning, mid-way and end of shaking steps 0.1g, 0.3g and 0.5g. The amplification factors are calculated from RMS acceleration values for 5 cycle periods at 0 - 5 cycles, 20 - 25 cycles, and 45 - 50 cycles for each shaking step.

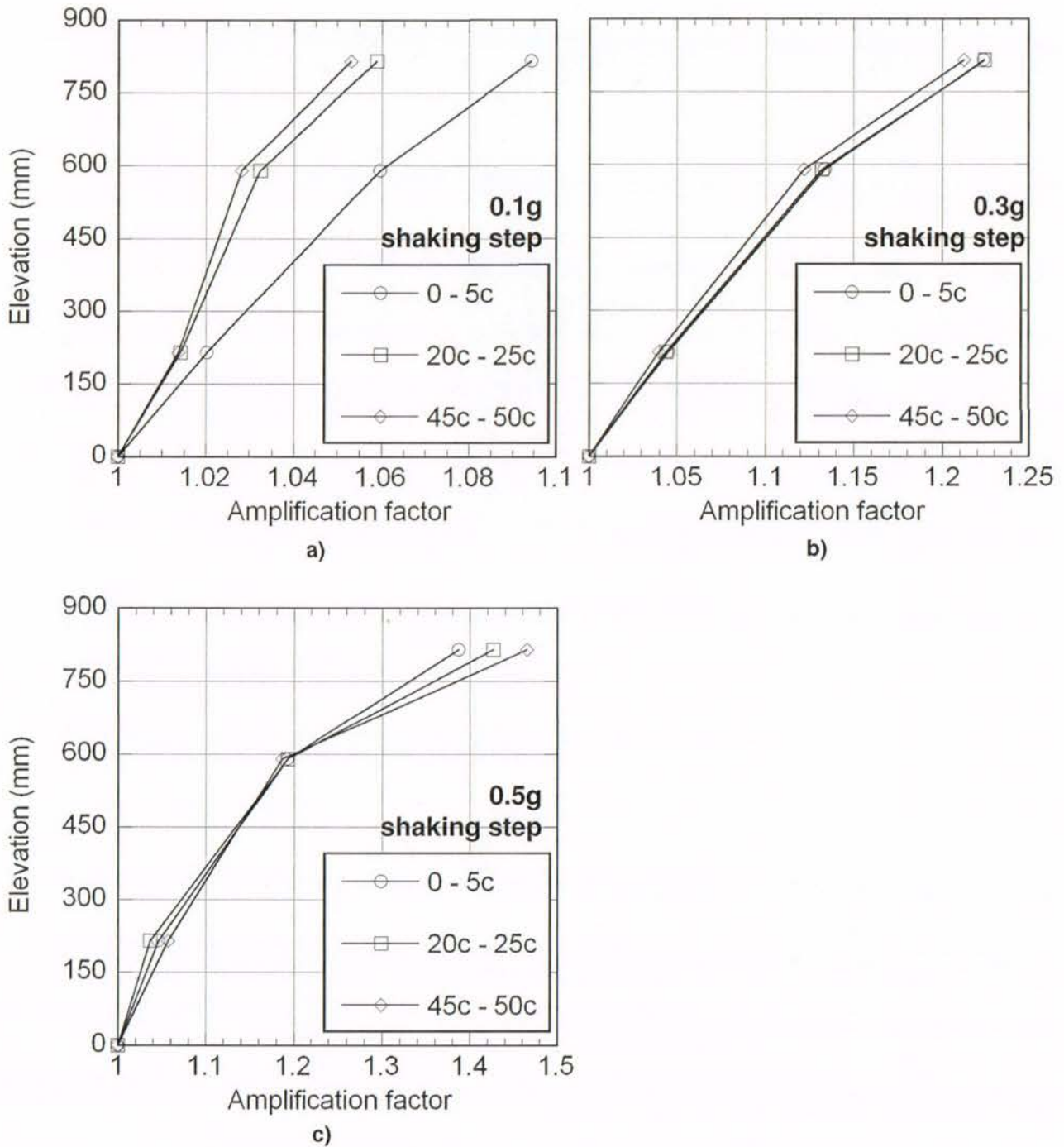


Figure 4-25. Acceleration amplification factors for a 5 cycle period starting at cycles 0, 20c and 45c for shaking steps a) 0.1g, b) 0.3g and c) 0.5g.

Similar to the wall face displacement response during shaking, Figure 4-25 shows that the soil response varies during each shaking step. For instance, as expected, the 0.1g shaking step exhibits a larger amplification factor during the first 5 cycles than at later stages in the shaking step. This response is subsequently reduced as the reinforcement becomes engaged and acts to stiffen the wall.

At later shaking steps of 0.3g and 0.5g, the soil response is more consistent during shaking with similar amplification values recorded. The increased amplification factors recorded in the last 5 cycles of 0.5g shaking is the result of the wall face reaching the physical limit of the box and hitting the brackets supporting the displacement transducer arrays.

## **4.5 Parametric study**

### **4.5.1 Detailed summary of testing series**

During testing, the experimental parametric study investigated the variation of the L/H ratio and wall inclination on seismic performance of the GRS wall models. A summary of the parameters varied for each test, and the issues encountered during testing was presented in Table 4-1.

As stated previously in Section 3.3.3, the seal between the model wall facing panel and the side of box had to achieve two aims: 1) Minimise boundary effects with the lowest possible friction between the wall facing panel and the box sidewall interface, and 2) prevent leakage of sand around the facing panel. The seal design was investigated during the testing process, and as a result, Tests-1, 2, 3 and 4 seals varied from that presented in Section 3.3.3. Where the seal was observed to influence model behaviour, the data was not used. This resulted in Test-1 data pre-failure, and all of Test-4 data to be considered unreliable and not used.

In Test-1, cellotape was used to seal the wall, as the designed seal did not prevent sand from leaking around the side of the wall. The cellotape was observed to impact on wall response at low acceleration levels, restricting free movement. However during the final shaking step, the cellotape failed in a brittle manner and allowed free movement of the wall, and this data during failure was considered reliable.

In Test-2, again the seal did not prevent the leakage of sand between the wall face and box sidewall, and some small quantity of sand was lost prior to testing and during testing. In

order to prevent a further loss of sand, testing was initiated at 0.3g, and continued as per normal procedures. In the 15 minutes between testing stages (necessary to download image data), foam was placed along the side of the panel to prevent further sand leakage. This was removed prior to shaking again. The behaviour during these later stages was similar to behaviour observed for Test-6 (same L/H ratio and geometry), and this would indicate the seal did not significantly affect model behaviour in Test-2.

In Test-3, the model was subjected to a 10 Hz excitation (theoretical PGA of 0.4g) due to testing error, however rather than being a weak point in the testing, this was used as an opportunity to compare the effect of frequency on model response. Because the frequency was higher, an 8<sup>th</sup> order 15 Hz low pass Butterworth filter was used for the time history plots presented in Appendix B. This shows, however, that the model was subjected to an actual acceleration amplitude of approximately 0.6g.

For Test-4, (a repetition of Test-1 reinforced at L/H = 0.75) the facing seal had high friction, evident in the test's time histories presented in Appendix B. This high friction resulted in a reduced facing displacement than could be expected upon comparison with the other tests, and the wall failed at a higher PGA of 0.65g, as opposed Test-1 which failed at 0.6g. Hence it was deemed that all data obtained during Test-4 was impaired and was not used in the study.

For Tests-5, 6, and 7 the seal as described in Section 3.3.3 was used. The seal's friction was tested and was determined to be low (friction force against rotation ~ 1 N), and no sand leaked during testing. Of greater importance were the results generated; these were deemed reliable in general, with parameter variation causing a marked effect on model behaviour which is discussed subsequently.

A comment on the repeatability of the testing apparatus and consistency of the construction methodology is made in Section 4.5.3, with reference to Tests-2 and 6, both vertical walls reinforced at L/H = 0.6. While Test-2 and 6 models were 'sealed' differently, the behaviour at later stages of Test-2 was somewhat similar to Test-6, even though testing was initiated at 0.3g due to sand leakage in Test-2.

The model geometry for all tests is presented in Section 3.4.8. The acceleration and facing displacement time-histories for all tests are presented in Appendix B. A study of the effect of L/H ratio and wall inclination is made in the following sections.

## 4.5.2 Displacement-acceleration curves

The displacement-acceleration curves for Tests-1, 5, 6, and 7 are plotted in Figure 4-26. As noted above, Tests-2, 3, and 4 are not plotted due to issues surrounding the seal and testing procedure.

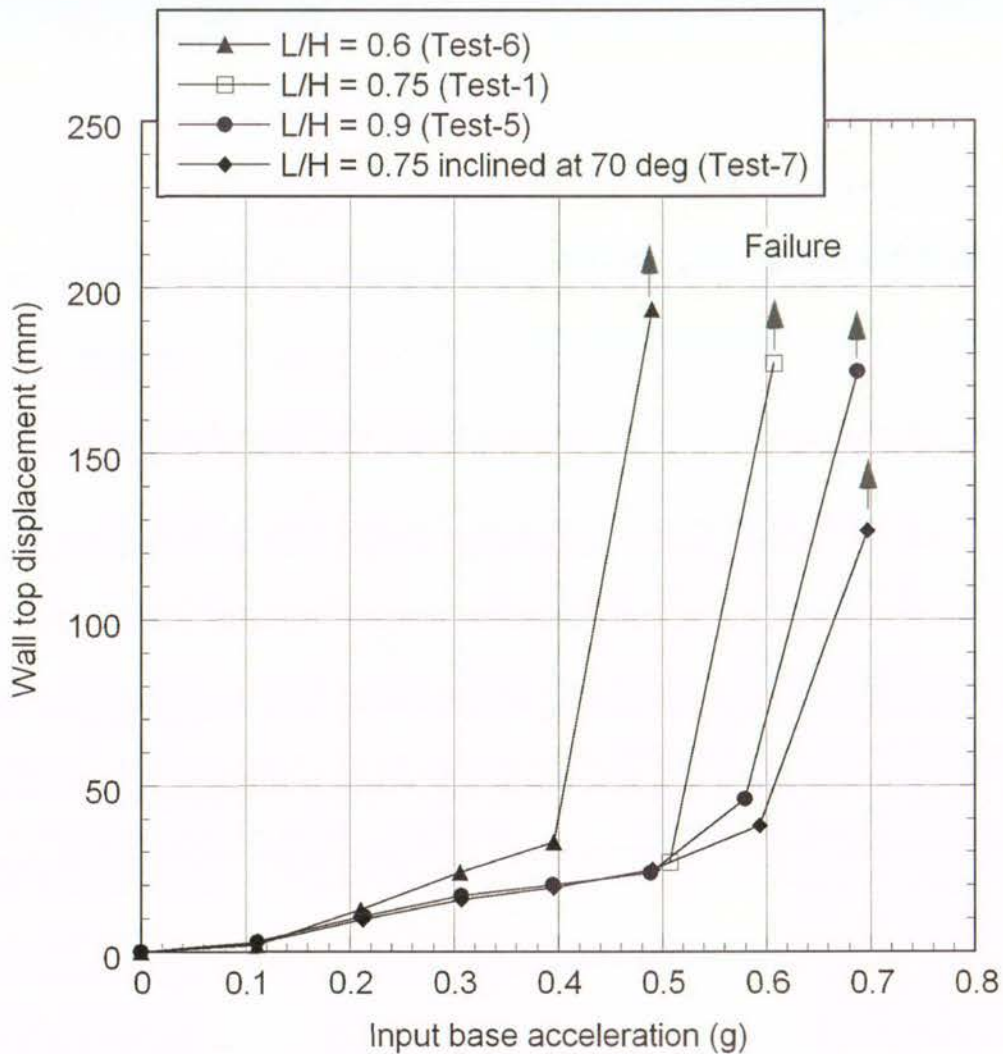


Figure 4-26. Displacement-acceleration curves for Tests-1, 5, 6, and 7. Note that Test-1 data prior to 0.5g is not plotted, for reasons as discussed above.

As can be seen in Figure 4-26, residual displacement was steadily accumulated with each increasing shaking step until some critical acceleration value at which displacement increased markedly, and this confirms the generally bi-linear behaviour expected for GRS models (Watanabe et al. 2003, El-Emam and Bathrust 2004). The tests also demonstrated behaviour consistent with what could be expected for the variation of L/H ratio and wall inclination tested. Specifically, an increase in L/H ratio from 0.6 to 0.9, and a reduction in

inclination of the wall from vertical to  $70^\circ$  with the horizontal, resulted in the displacement-acceleration curve to be shallower (lower residual displacement for increasing acceleration shaking), and an increase in the acceleration required to cause failure.

Failure was defined by a significant increase in rate of wall top displacement, which for the current tests resulted in the limit of the experimental apparatus to be reached. Figure 4-26 shows failure occurred at acceleration shaking levels of 0.5g, 0.6g and 0.7g depending on the L/H ratio for Tests-6, 1, and 5 respectively. Test-7 (the inclined wall) also failed at 0.7g. The increase in acceleration required to cause ultimate failure demonstrates the increase in stability under seismic conditions gained due to the choice of reinforcement and/or wall geometry parameters.

It can be seen in Figure 4-26 that for all tests, the residual displacement accumulated prior to failure at low acceleration levels, was non-linear. In other words, a decrease in incremental displacement (the displacement accumulated within each shaking step) is observed prior to the critical acceleration being reached. This was noted in the facing displacement time-histories of Test-6 and was briefly described in Section 4.3.5. This effect is most marked in Test-5: Except for the 0.1g shaking step, incremental displacement decreased up to 0.5g, when incremental displacement increased suddenly for shaking steps 0.6g and 0.7g (wall failure). This behaviour was not observed in the tests by Watanabe et al. (2003) or El-Emam and Bathurst (2004; 2007).

With reference to the facing displacement time-histories in Appendix B, there are segments of non-linear and linear accumulation of displacement. As stated in Section 4.3.5, this is most likely due to the mode of failure and the progressive nature in the development of failure surfaces within the backfill. The development of deformation within the backfill is discussed further in Chapter 5.

The effect of parameter variation on the rate of residual displacement accumulation, mode of failure, and measures of stability such as critical acceleration and acceleration amplification is presented in detail in Section 4.6.

### **4.5.3 Repeatability of experimental results**

Two vertical walls reinforced at  $L/H = 0.6$  (Tests-2 and 6) were constructed and tested and provide information as to the reliability of the model construction, experimental method, and

results. Test-2 leaked some sand around the wall face and in order to minimise this, shaking was initiated at an acceleration input of 0.3g instead of the usual 0.1g as for Test-6. Except for the seal, both walls were constructed with the same technique and target relative density. It could be surmised that as sand leaked during Test-2, the friction at the facing panel and side of the box was minimal, and hence similar behaviour was expected for both tests.

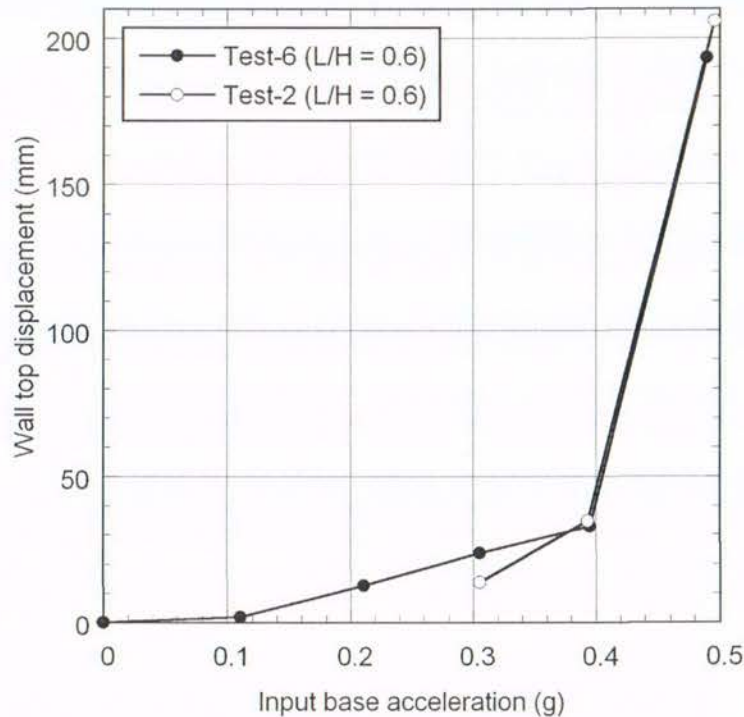


Figure 4-27. Comparison of displacement-acceleration curves for repeatability purposes of Test-2 and 6 both reinforced at  $L/H = 0.6$ .

Figure 4-27 shows good agreement between the Tests-2 and 6, especially at 0.4g and 0.5g shaking steps. Test-2 exhibited less initial sliding, thus the wall top was able to rotate more and register the higher lateral displacement of 205 mm compared to 193 mm during the final shaking step at 0.5g.

For Test-6, the incremental displacement accumulated during the 0.3g shaking step is similar to that recorded for the single 0.3g shaking step in Test-2, even though Test-6 had previously undergone two previous shaking steps at 0.1g and 0.2g. Koseki et al. (1998) notes that for scale model tests, the incremental increase in base input acceleration should be large enough to reduce the possible effects of previous shaking history on subsequent model response. Koseki et al. (1998) assumed that 0.05g increments were sufficient to achieve this; given that similar incremental displacements were recorded during the 0.3g shaking step for both Test-2

and 6, it appears that a 0.1g increment is sufficient in the current tests to reduce the effect of previous shaking history on model response.

## **4.6 Influence of L/H ratio and wall inclination on seismic performance**

### **4.6.1 Accumulation of residual displacement**

Residual displacement was accumulated with each shaking step and its rate of accumulation varied according to reinforcement L/H ratio and model geometry. This is discussed below.

#### *Influence of L/H ratio on accumulation of residual displacement*

Reinforcement L/H ratio was varied across Tests-6, 1, and 5 reinforced by L/H = 0.6, 0.75 and 0.9 respectively to determine the parameter's influence on seismic performance. Figure 4-28 shows the displacement-acceleration curves for the residual displacement at the top of the wall for these three tests.

Figure 4-28 clearly shows the stabilising effect of increasing the reinforcement L/H ratio, for the range of L/H tested. For instance, failure occurred at 0.5g, 0.6g and 0.7g for L/H = 0.6, 0.75 and 0.9, respectively.

Whilst no reliable data pre-failure was recorded for Test-1 reinforced at L/H = 0.75 (for reasons discussed above), pre-failure displacement decreased with increasing reinforcement length via increasing the L/H ratio. For instance, a 50% increase in the L/H ratio from 0.6 to 0.9, caused a 33% decrease in the cumulative lateral displacement recorded up to 0.3g base input acceleration. Similar decreases in lateral facing displacement with increasing L/H ratio have been recorded in reduced-scale GRS wall model tests by Matsuo et al. (1998) and El-Emam and Bathurst (2004).

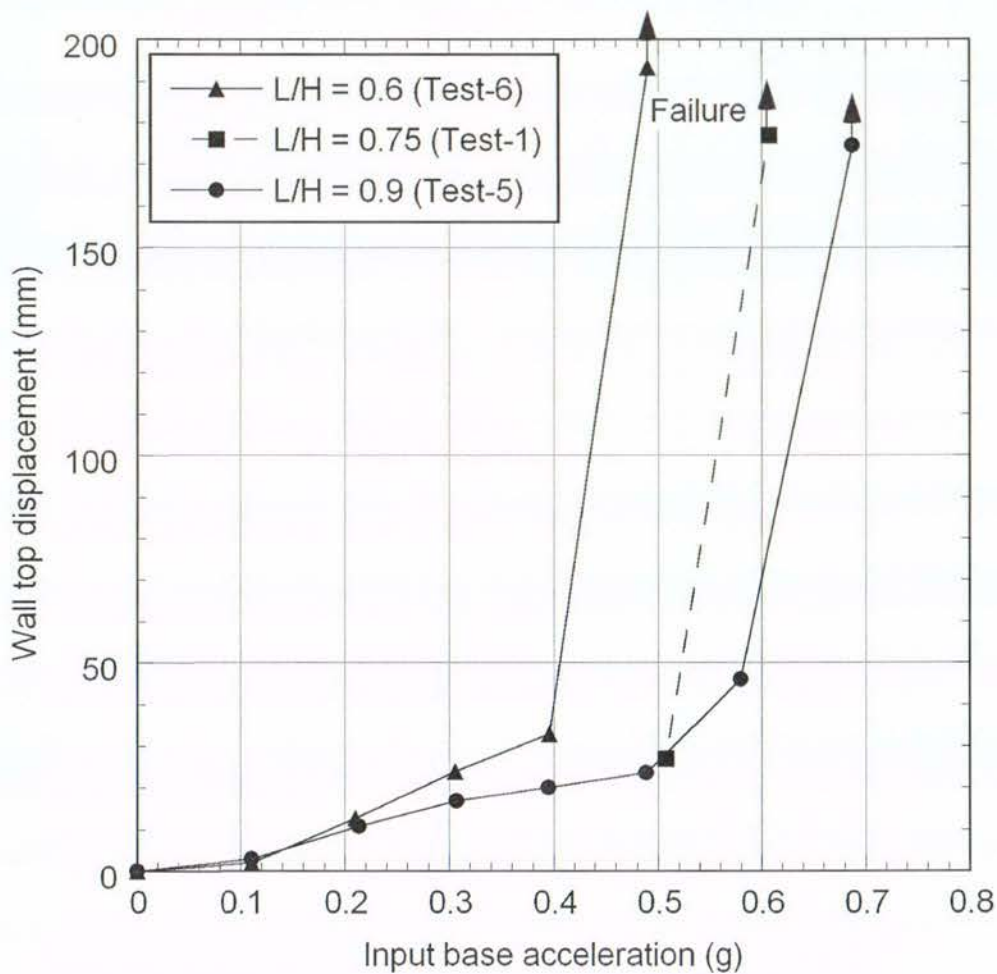


Figure 4-28. Comparison of displacement-acceleration curves for tests of different  $L/H$  ratio. NB: Test-1 is dashed to represent unreliable data.

Whilst a somewhat linear relationship between increasing the  $L/H$  ratio and an increase in the critical acceleration (and ultimate failure) can be seen, this is not clear. For instance, Sakaguchi (1996) showed a diminishing return in the reduction of residual displacements for  $L/H$  ratios larger than 0.67.

A definitive relationship between an increase in the  $L/H$  ratio being met with a proportional increase in seismic performance is unable to be inferred because: 1) the base input acceleration increment is reasonably coarse (increments of 0.1g), 2) both tests reinforced at  $L/H = 0.75$  had some sealing issues, and 3) the range of  $L/H$  ratios (0.6 – 0.9) tested was only small.

Somewhat contrasting the observed increase in seismic performance with an increase in the  $L/H$  ratio from 0.75 to 0.9, is centrifuge work by Nova-Roessig and Sitar (2006). In their

testing, only a minimal reduction in lateral facing displacements was observed when the L/H was increased from L/H = 0.7 to 0.9. However, this range in parameter values is smaller than the current tests, and the absence of a more marked trend could be due to a variety of factors such as different reinforcement spacing, wall density, and the wrap-around facing all perhaps acting to reduce the impact of reinforcement length on lateral residual displacements.

Of interest is the behaviour observed just prior to failure. Test-6 reinforced the shortest at L/H = 0.6 failed abruptly after the critical acceleration of 0.4g was reached. In contrast, Test-5 reinforced the longest at L/H = 0.9, displayed a somewhat 'transitional' region at 0.6g, where displacements markedly increased, however failure did not occur until 0.7g.

This could possibly be attributed to the deformation of the Test-5 reinforced soil block. For instance, the reinforced soil zone of Test-6 behaved more like a rigid block, with minimal internal deformation as compared to the reinforced soil block of Test-5 where larger internal deformation was observed. Hence it was more difficult for the larger reinforced soil block to overturn and slide as a block and this could have reduced the lateral displacement recorded at larger accelerations. This is further discussed in Chapter 5.

#### *Influence of wall inclination on accumulation of residual displacement*

The displacement-acceleration curves of Test-1, 5 and 7 are shown in Figure 4-29. Test-1 is included because it was reinforced with the same reinforcement layout of L/H = 0.75 as Test-7, however deformation data prior to failure is unreliable due to seal issues. Instead, as a pre-failure comparison, displacement data of Test-5, reinforced at a larger L/H = 0.9, is plotted.

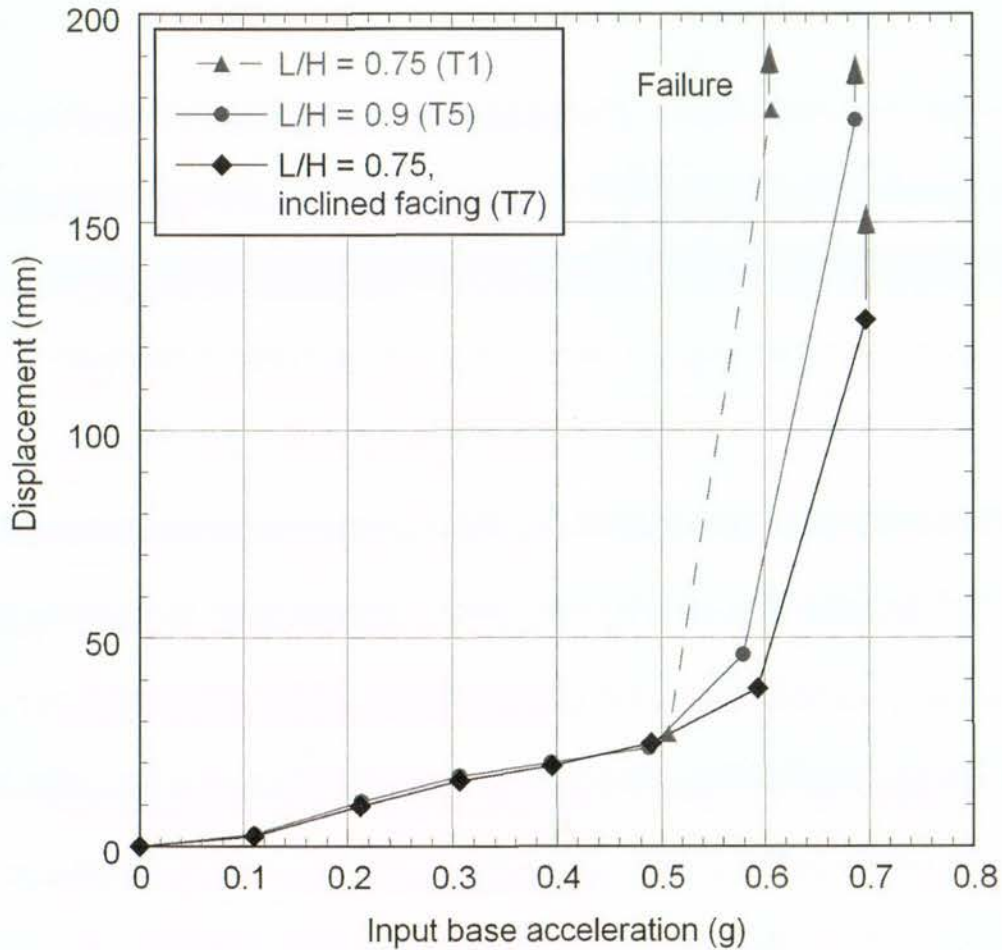


Figure 4-29. Comparison of displacement-acceleration curves for the effect of wall face inclination on stability.

As expected, comparison of the final shaking levels of Tests-1 and 7, Figure 4-29 shows that inclining the wall face acts to increase stability such that failure occurs at 0.6g for the vertical wall and at 0.7g for the wall inclined at  $70^\circ$  to the horizontal. However, in terms of wall top displacement accumulated during low acceleration pre-failure, the effect of wall inclination is almost the same as increasing the reinforcement up to  $L/H = 0.9$  for a vertical wall face. A direct comparison of the effect of the wall inclination cannot be made in the current tests, given that the Test-1 data is unreliable. However, with reference to Figure 4-26, a median response between Tests-5 and 6 reinforced above and below  $L/H = 0.75$  at  $L/H = 0.9$  and 0.6 respectively, can be inferred as indicative of behaviour for a vertical wall reinforced at  $L/H = 0.75$ . This would show that there could have been a significant reduction in facing displacements due solely to wall inclination.

At the same base input acceleration of 0.6g just prior to failure, the inclined wall showed a slightly lower displacement response at the top of the wall than the vertical wall reinforced at

a higher  $L/H = 0.9$ . This indicates that an inclined wall is better able to resist displacement at higher acceleration shaking than a vertical wall.

Similar results have been reported by Matsuo et al., (1998) and El-Emam and Bathurst (2005) with wall inclinations ranging from  $79^\circ$  and  $80^\circ$  to the horizontal, respectively. In these tests, a shallower displacement-acceleration curve, compared to the vertical walls, was observed.

For instance, El-Emam and Bathurst (2005) show that at the vertical wall's critical acceleration of  $0.36g$ , the inclined wall at  $80^\circ$  to the horizontal, accumulated approximately only 50% of the residual displacement as the vertical wall. A similar reduction was recorded for Test-7 inclined  $10^\circ$  further to  $70^\circ$  to the horizontal. Thus it is possible there is a diminishing benefit to wall inclination less at  $80^\circ$  to the horizontal; however this requires further investigation.

#### **4.6.2 Modes of failure**

As noted previously, the walls failed predominantly by overturning and sliding failures. However, lateral displacement recorded at the wall top is a function of both rotation of the wall and sliding of the wall toe; it is convenient to separate these two modes of failure.

Figure 4-30 (a – c) plots the components of rotation and sliding during testing of Tests-5, 6 and 7 reinforced at  $L/H = 0.6, 0.9, 0.75$ , respectively (a – c, respectively). The first two were vertical walls, while Test-7 was inclined at  $70^\circ$  to the horizontal. As mentioned previously, no reliable data at low levels of base input acceleration is available for Test-1, reinforced at  $L/H = 0.75$ , and no comparison is made. It is important to note that the dashed lines representing the rotation and sliding components have been calculated, as discussed previously in Section 4.4.2.

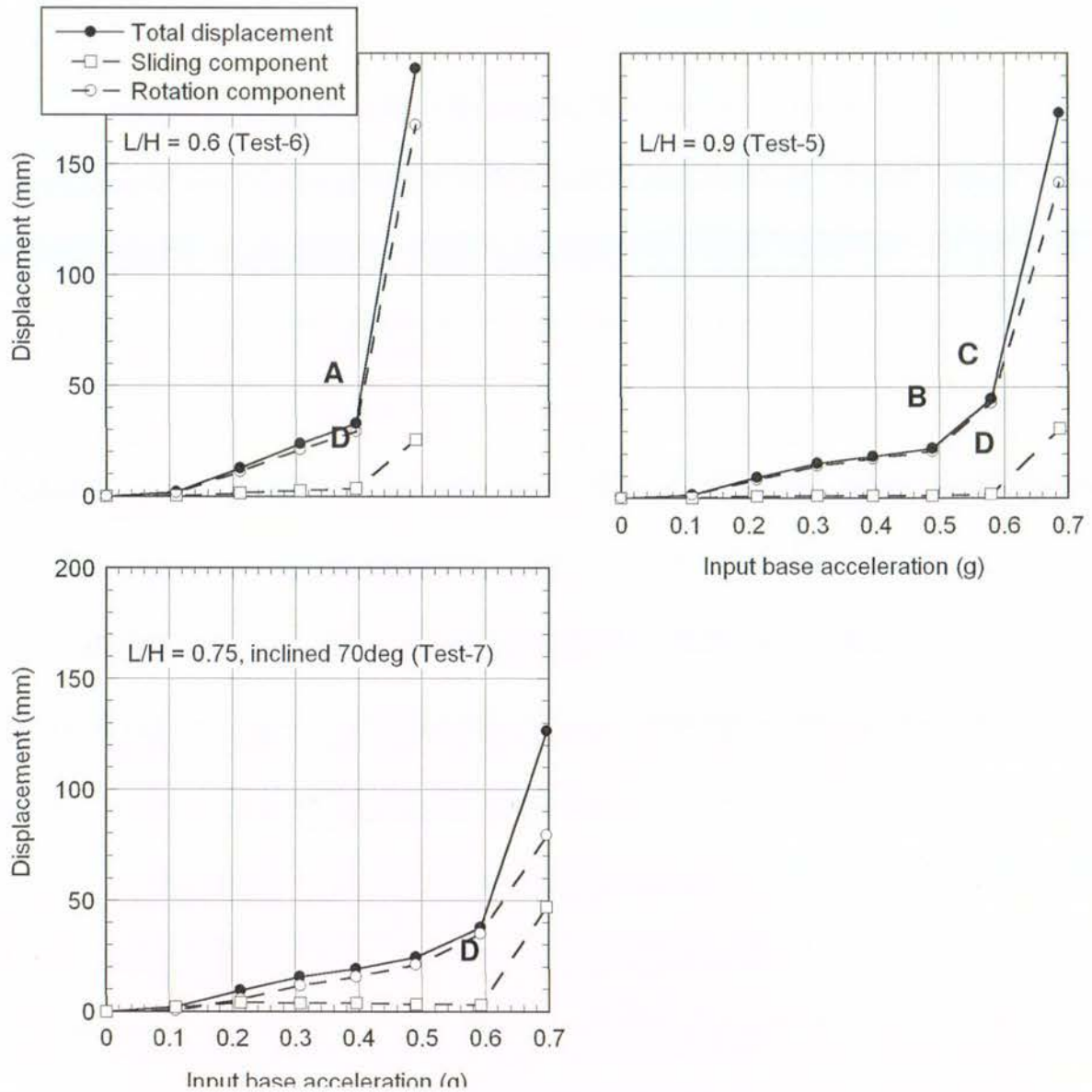


Figure 4-30. Comparison of failure modes during Tests-5, 6, and 7 for walls reinforced at  $L/H = 0.6$ ,  $0.9$  and  $0.75$  inclined at  $70^\circ$  to the horizontal. The letters represent the different definitions of critical acceleration proposed by various researchers and are discussed further in Section 4.6.3.

It can be seen that for all tests, the predominant component of failure was by rotation of the wall top, as opposed to sliding, which was minimal. Sliding only became significant during the final shaking step for each wall.

The effect of the  $L/H$  ratio and wall inclination on different modes of failure is discussed below.

#### *Effect of L/H ratio on components of failure*

For both vertical walls, the L/H ratio had a minimal effect on the components of failure. That is, despite a 50% increase in reinforcement length from  $L/H = 0.6$  to  $0.9$ , failure was predominantly rotational (Figure 4-30 (a and b)). Significant sliding only occurred during the final shaking step of each wall at failure.

However, an increase in the L/H ratio (Test-5) decreased the sliding component of deformation when compared to Test-6 pre-failure. This further highlights the greater stabilising effect of a larger L/H ratio pre-failure.

#### *Effect of wall inclination on components of failure*

Similar to the vertical walls, total wall top deformation largely comprised rotation, with only some small sliding which occurred pre-failure (Figure 4-30 (c)). The cumulative displacement of Test-7 during testing is replotted in Figure 4-31 to better illustrate the geometry of deformation.

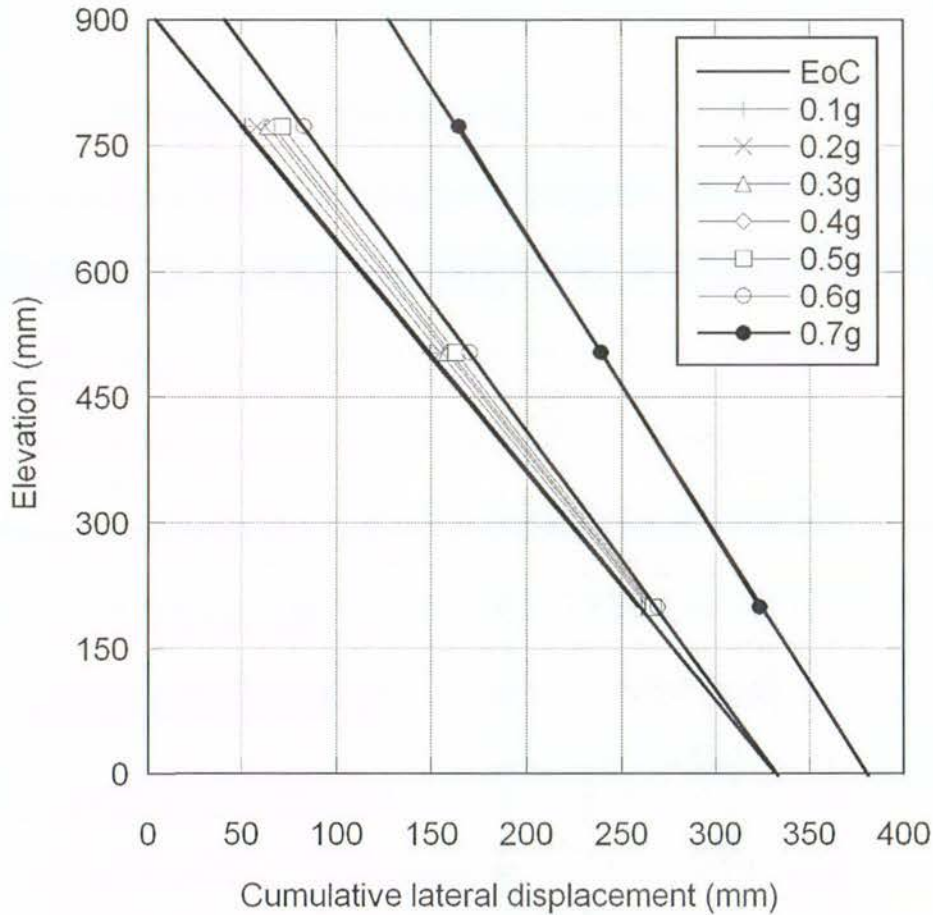


Figure 4-31. Test-7 cumulative displacement recorded at the wall face showing the geometry of failure from the start of testing (EoC), through to 0.7g.

Figure 4-31 shows that significant sliding occurred only during the final 0.7g shaking step. However whilst the predominant mode was rotation, the Test-7 sliding component of 3.9 mm pre-failure was almost twice than that of Test-5 pre-failure of 2.0 mm. Further, at failure, sliding was a major component of failure and was nearly 40% of the total displacement recorded at the wall top. In comparison, the total displacement at the wall top recorded at failure for Test-5 comprised only approximately 30% sliding.

Figure 4-31 shows that because the wall was inclined, there was no increase in the overturning moment of the wall contributing to increased deformation. Instead, sliding was emphasised.

### 4.6.3 Critical Acceleration

The critical acceleration was defined previously by various researchers in Section 4.4.3 and indicated in the plots of Figure 4-30 above. As seen in Figure 4-30 (a), point 'A' describes a

typical definition of the critical acceleration of a sudden change in the rate of deformation. For the Test-6 displacement data, the criterion is clear. However, as noted in Section 4.4.3 above, and seen in Figure 4-30 (b) and (c), the criteria are not clear as to what the appropriate critical acceleration should be, as there is some sort of ‘transition’ region between behaviour at low shaking levels and high shaking levels. Thus the original criterion could be used to define either points ‘B’ or ‘C’.

The El-Emam and Bathurst (2004, 2005) definition of critical acceleration (described in Section 4.4.3) is a relative change between rotation and sliding components. This is plotted Figure 4-32 for both Test-6 and 5, reinforced at  $L/H = 0.6$  and  $0.9$ , respectively (components normalised by wall height,  $H$ ).

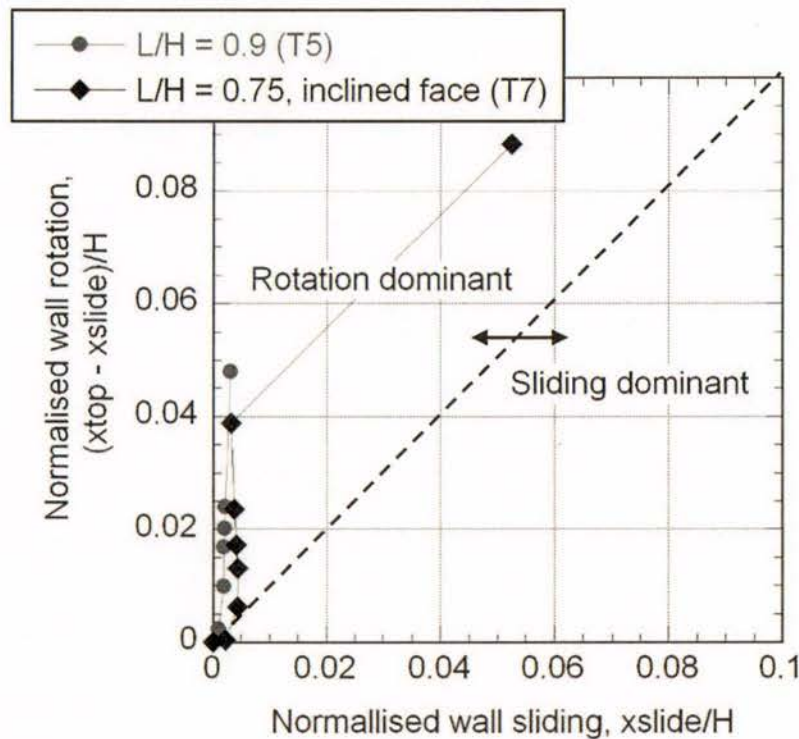


Figure 4-32. Comparison of critical acceleration of Tests-7 and 5 reinforced at  $L/H = 0.75$  and  $0.9$ ; Test-7 with facing inclined at 70 deg.

As shown in Figure 4-32, the prescribed criterion seems to be ill-suited to the present dataset because all walls demonstrated predominantly rotational behaviour.

Instead, because sliding only became significant upon failure, it is proposed that a sudden increase in the rate of sliding is sufficient to describe the critical acceleration of the wall. This is point D plotted in Figure 4-30 (a - c) above.

The sliding component of deformation for Tests-5, 6 and 7 is shown in Figure 4-33. For all tests, there is a significant increase in the magnitude of sliding just prior to failure, and this could be used to indicate the critical acceleration of the model wall. This threshold is exhibited for both vertical and inclined walls and for L/H ratios of 0.6 to 0.9.

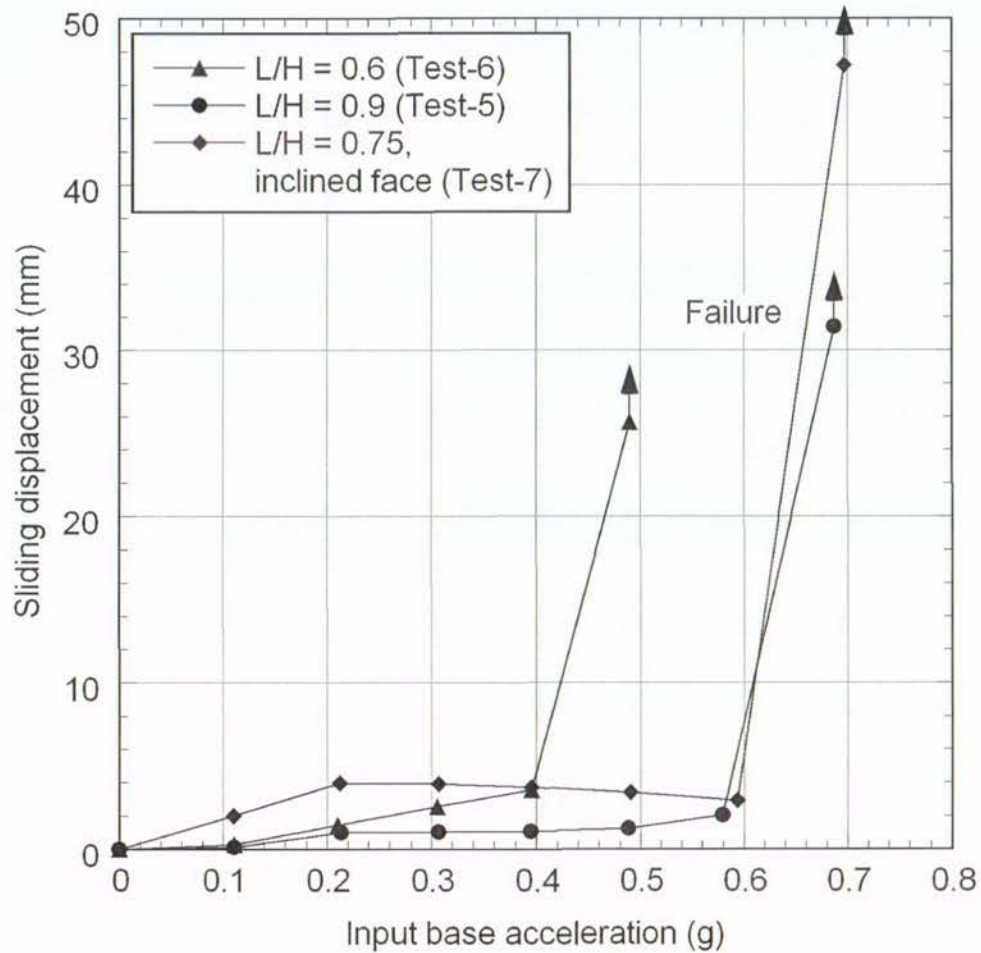


Figure 4-33. Comparison of sliding components of deformation for Tests-5, 6 and 7.

It should be noted that the apparent decrease in cumulative sliding displacement of Test-7 from 3.9 mm (at 0.2g) to 3 mm (at 0.6g) is due to the extrapolation used to determine the displacement at the toe of the wall face. Rather, it is likely that the wall slid until the toe “dug in” at 3.9 mm and the facing panel was subjected to some small deformation (of approximately 0.9 mm) and was not exactly linear as previously assumed. However, this does not have an effect on the overall observation that sliding becomes significant at failure.

Sliding is only one possible mode of external instability considered in design codes. For performance based design, some displacement predictions (Richards and Elms 1979) are

based on limit equilibrium against sliding, and thus should use critical acceleration as determined above. The above evidence would seem to validate the use of critical acceleration based on sliding as opposed to any of the other critical acceleration measures proposed above. The possible reasons for sliding deformation controlling the onset of global failure are discussed in Chapter 5.

#### **4.6.4 RMS acceleration amplification**

Acceleration amplification results in larger destabilising forces acting on the wall. Hence it is important to determine whether the parameters under investigation contribute to a reduction in the acceleration amplification observed.

##### *Effect of L/H ratio on acceleration amplification*

Section 4.4.6 and Figure 4-24 above demonstrated that the amplification of acceleration was non-linear up the vertical wall for Test-6. Figure 4-34 compares amplification factors of the top most accelerometer in the reinforced zones and backfill, Acc 4 and Acc 5, respectively, during all stages of testing for Tests-5 and 6 (reinforced with  $L/H = 0.9$  and  $0.6$  respectively). It should be noted that the filtered and corrected acceleration time-histories were used in the calculations.

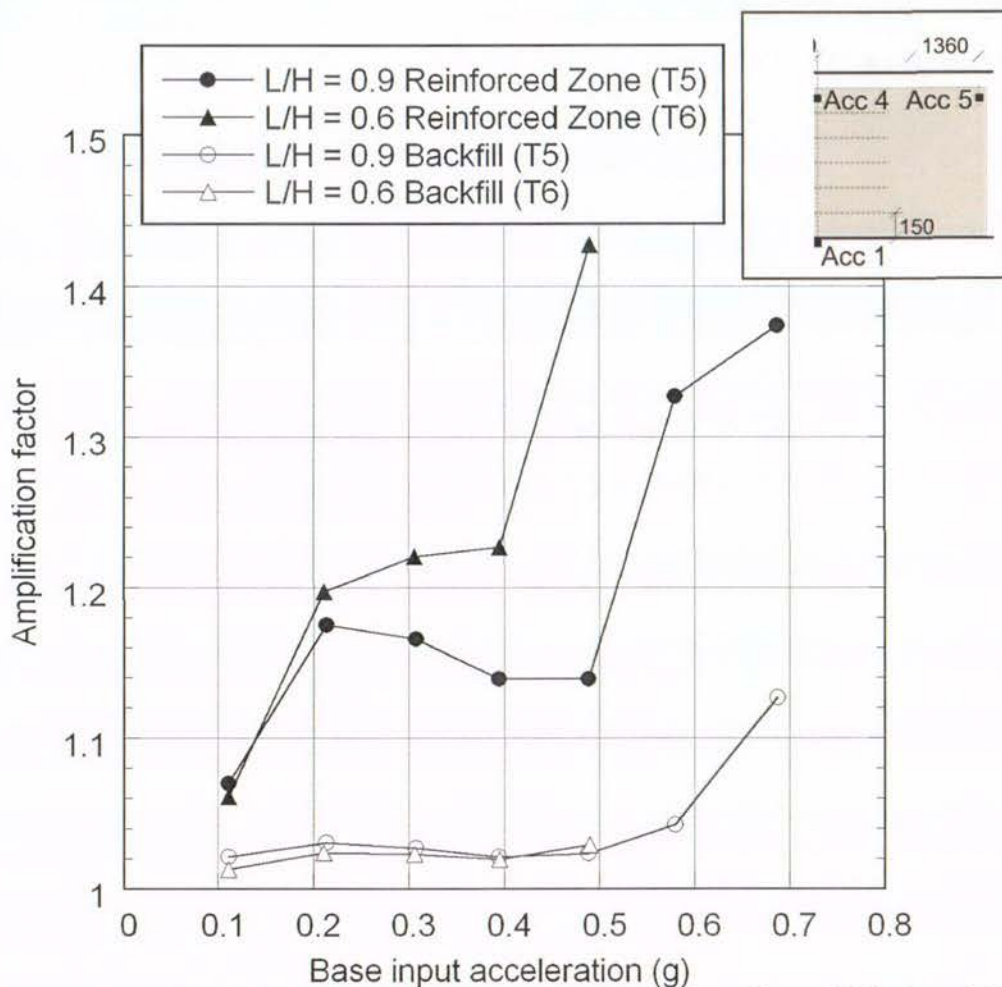


Figure 4-34. Comparison of RMS Amplification factors measured near the wall top within the reinforced zone (Acc 4) and backfill (Acc 5) for Tests-5 and 6 reinforced at  $L/H = 0.9$  and  $0.6$  respectively.

Figure 4-34 shows both tests to demonstrate larger amplification to occur in the reinforced soil than the backfill zone, and exhibit a general trend of increasing amplification with increasing base input acceleration, with the highest amplification factors of 1.43 and 1.38 occurring during the final shaking steps of 0.5g and 0.7g at failure for Tests-6 and 5 respectively.

As noted in Section 4.4.5, these values are slightly lower than recorded by El-Emam and Bathurst (2007), and significantly lower than those recorded as 3.0 by Fairless (1989) and 2.3 by Nova-Roessig and Sitar (2006). This reflects differences in the experimental model as highlighted above.

Up to 0.2g, the amplification response for both walls is similar. At 0.3g, Test-5 reinforced at a larger  $L/H = 0.9$ , demonstrated a decreased amplification response until 0.5g, while Test-6 continued to rise until 0.4g and subsequent failure at 0.5g. Test-5 then demonstrated increased amplification again until failure at 0.7g. The decreased amplification response

exhibited by Test-5 when compared to Test-6 is evident for all shaking levels except 0.1g and could be attributed to its increased stability due to a 50% increase in L/H ratio. A similar decrease in amplifications observed with increasing L/H has been observed by El-Emam and Bathurst (2007).

A sudden increase in backfill amplification recorded by Acc 5 for Test-5 at base input accelerations larger than 0.5g can be attributed to a failure plane which extends from the back of the reinforced soil block and daylights at some distance beyond Acc 5. Hence during 0.6g and 0.7g shaking, Acc 5 records acceleration behaviour attributable to the active wedge, rather than “far-field” conditions. This is further discussed in Chapter 5.

*Effect of wall inclination on acceleration amplification*

Figure 4-35 plots the amplification of acceleration within the reinforced zones and backfill, during all stages of testing for Tests-7. It can be seen that amplification of acceleration is non-linear up the wall as found for the vertical walls.

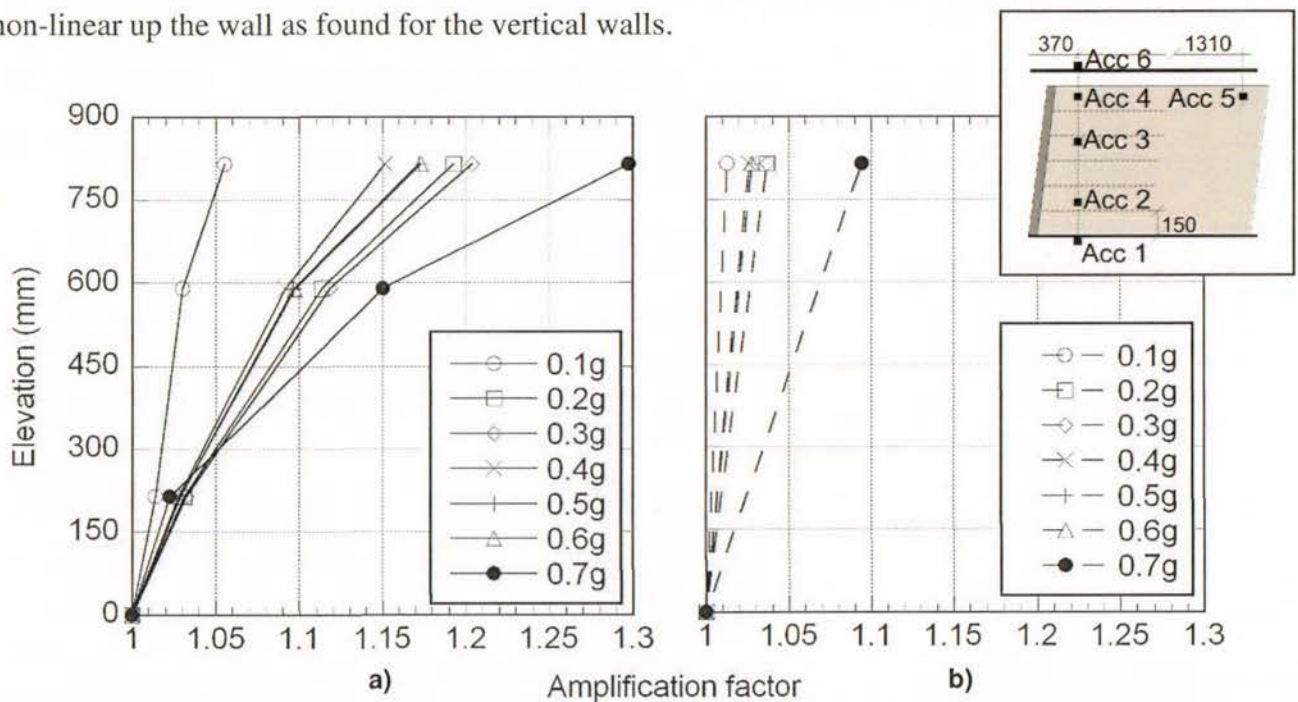


Figure 4-35. RMS acceleration amplification up the wall during Test-7 for: a) Reinforced soil vertical accelerometer array (Acc 2, 3, 4) and b) Accelerometers Acc 1 and 5 where a linear relationship has been assumed.

Figure 4-36 compares the RMS amplification at the top of the wall for Tests-5 and 7 to determine the effect of wall inclination on acceleration amplification.

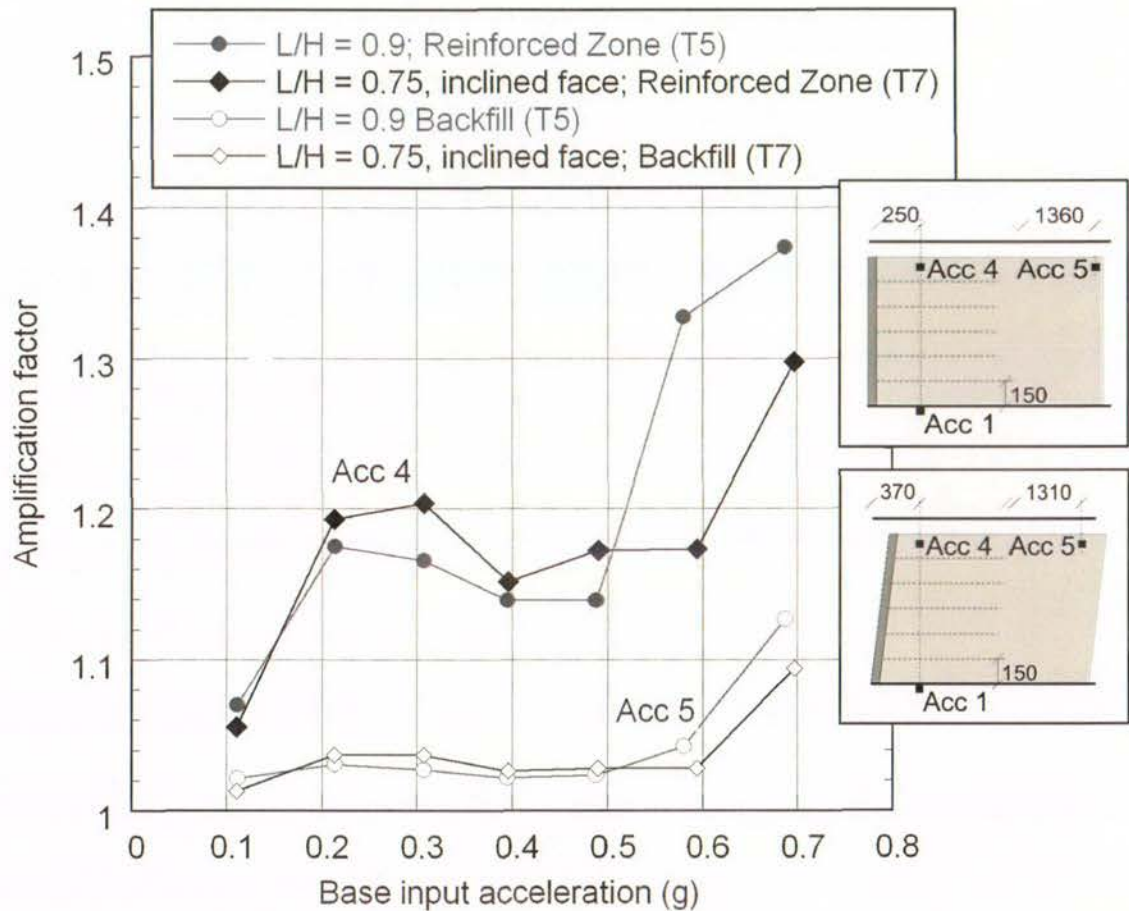


Figure 4-36. Comparison of RMS Amplification factors for Tests-5 and 7 reinforced at L/H = 0.9 and 0.75; Test-7 inclined facing at 70°.

Up to 0.5g, the figure shows a similar amplification response for both walls with the inclined wall demonstrating slightly higher amplification. At 0.6g, Test-5 (vertical), shows an increased amplification while Test-7 (inclined) amplifications remained steady until 0.7g and failure. The reduced amplification response of Test-7 compared to Test-5 is a result of increased stability of the inclined wall compared to the vertical wall, even though the vertical wall was reinforced longer at L/H = 0.9 compared to Test-7 reinforced at only L/H = 0.75.

Figure 4-34 and Figure 4-36 show that generally, amplifications increase for all base input acceleration levels and for all tests, regardless of L/H ratio and wall inclination. Contrasting these results is amplification data for shake-table tests by Matsuo et al. (1998) which showed amplification to be large within the potential sliding block at low acceleration levels, and attenuation to occur once noticeable plastic deformation, i.e. a failure surface has formed. Attenuation of large accelerations was also found in centrifuge tests by Nova-Roessig and Sitar (2006).

## 4.7 Design implications

### 4.7.1 Discussion of acceleration amplification effects

Amplification of acceleration impacts on the magnitude of the lateral earth pressure on the wall (Steedman and Zeng 1990). It also contributes to an increase in the inertial force acting to destabilise the wall face and active zones of the wall. As evidenced in Section 4.4.6 above, this amplification occurs non-linearly up the wall, with the largest amplification occurring near the crest of the wall. This results in a larger inertial and seismic earth pressure component that occurs near the top of the wall.

FHWA (2001) incorporates an artificially modified design acceleration coefficient for use in seismic design using Equation 4-4 proposed by Segrestin and Bastick (1988). The non-linearity of amplification is ignored in favour of a uniform factor for application to the entire reinforced soil block.

$$k_h = \frac{a_g}{g} \left( 1.45 - \frac{a_g}{g} \right) \quad (4-4)$$

The equation is based on the average acceleration amplification over the wall height recorded during finite element analysis on two Reinforced Earth Walls on a hard rock foundation condition subjected to one earthquake time history of predominant frequency 8 Hz scaled to 0.1g, 0.2g and 0.4g peak base acceleration. Thus the results can hardly be generalised. However given that the boundary conditions of the model are highly idealised, Segrestin and Bastick (1988) notes that “any bias will be on the safe side.”

Based on this, the New Zealand Guidelines (Murashev 2003) use the similar Equation 4-5, though without justification for the reduced coefficient of 1.3.

$$k_h = \frac{a_g}{g} \left( 1.3 - \frac{a_g}{g} \right) \quad (4-5)$$

Figure 4-37 compares the amplification factor predicted from Equation 4-5 with the amplification exhibited in the vertical wall Tests-5 and 6 ( $L/H = 0.9$  and  $0.6$ ) and the inclined Test-7 ( $L/H = 0.75$ ; inclined  $70^\circ$ ). Because the design acceleration is normally applied mid-height of the reinforced soil block, a linear interpolation has been used to determine the

amplification factor in the models at an elevation of 450 mm, as opposed to using the amplification factors recorded at wall top previously.

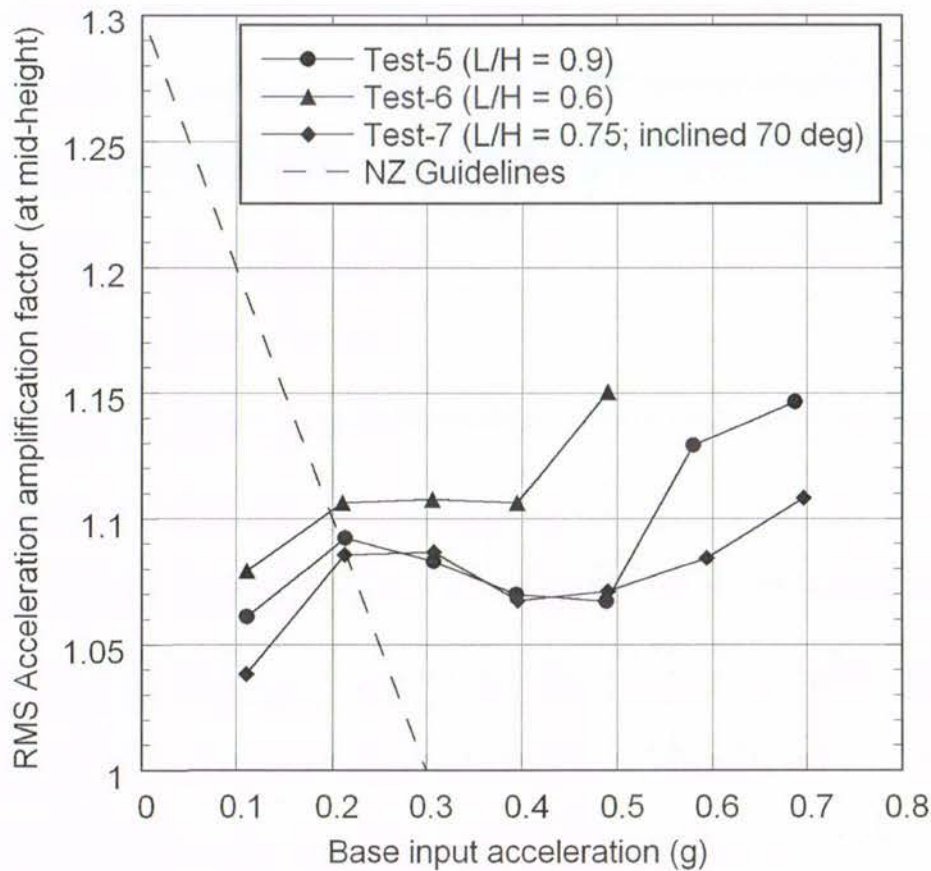


Figure 4-37. RMS Amplification of acceleration measured near the wall top within the reinforced zone (Acc 4) and backfill (Acc 5) for Test-5 and 6 reinforced at  $L/H = 0.9$  and  $0.6$  respectively.

As shown, in practice Equation 4-5 results in amplification being considered for low acceleration levels, and a decrease in design acceleration at acceleration levels larger than  $0.3g$ . Though it should be noted that for areas where the design acceleration is larger than  $0.3g$ , the guidelines recommend a performance-based approach to investigate likely displacements given an earthquake occurs. Figure 4-37 also illustrates the following points:

- Amplification does not decrease with increasing base input acceleration as suggested by the NZ Guidelines, rather an opposite trend was observed and amplification, in general, *increases* with increasing base input acceleration. This was also confirmed by El-Emam and Bathurst (2007).
- The cut-off base input acceleration of  $0.3g$  is too low to accommodate the full range of larger amplification that occurs at higher base input acceleration levels.

- The suggested maximum amplification factor of 1.3 is larger than the amplification factors of around 1.15 exhibited by the vertical models at mid-height of the wall. However, Section 4.6.4 plots a maximum amplification factor recorded at the wall top of around 1.43 for Test-6. Hence the 1.3 coefficient is conservative if the design acceleration is applied at mid-height.

In terms of design, these factors act to reduce design acceleration coefficients because GRS retaining walls have, in the past performed well. Thus they are a 'fudge factor' which seeks to reduce over-design.

Design also models the non-linear amplification as seen in Section 4.4.3 above, with a uniform acceleration applied to a 'rigid' reinforced soil block. Cai and Bathurst (1996) suggests that the discrepancy between actual non-linear amplification behaviour and design using an uniform acceleration can be somewhat rectified by the location of the resultant line of action for the dynamic earth pressure increment set to  $2H/3$ . This rigid block assumption, used in deformation prediction models (Richards and Elms 1979) is violated with the observed acceleration amplification in the current and other tests (Nova-Roessig and Sitar 2006). Deformation observed during the current testing is discussed further in Chapter 5.

#### **4.7.2 Performance-based design**

The basis of performance-based design and prediction of deformation was discussed in Chapter 2. Performance based design has the ability to reduce the design acceleration coefficient by up to 50% in some cases in New Zealand, simply by allowing the occurrence of some movement in the event of an earthquake (Wood 2009).

Whilst there are a number of empirical and analytical models used to predict deformation (Cai and Bathurst 1996; Ling et al. 1997; Newmark 1965), the two most important parameters for the accuracy of any deformation prediction are:

- Determination of the most 'appropriate' ground motion for the simulation of the GRS wall design, and,
- An accurate measure of strength and mechanism of failure. Normally, this is a critical threshold acceleration.

While the first point is not the subject of this thesis, the current series of experiments highlight some issues with the second, that is, the correct identification of the critical acceleration. It was found that the critical acceleration governing ultimate failure occurred just prior to a significant increase in sliding displacement. Research has shown that Newmark sliding block theory is reasonably accurate for prediction of sliding displacement of GRS models (El-Emam and Bathurst 2004; Matsuo et al. 1998), and this method could be used to predict the final sliding response at failure.

However, the test results of these experiments (and others) demonstrate that deformation occurs even at low acceleration levels, and almost continuously. This deformation is predominantly by overturning of the wall. A Newmark-style analysis would not be able to quantify this element of deformation, as firstly the mechanism is not a sliding failure, and secondly, the method uses a constant threshold acceleration (Koseki et al. 2006).

Koseki et al. (2006) describes an attempt to simulate the gradual accumulation of displacement with increasing acceleration of reduced-scale model shake-table tests. The cyclic stress-strain properties of the model were simulated and displacement computed. This was compared to the displacement recorded in the experiments. Prior to ultimate failure which occurred at 750 gal, there was good agreement between the computed and experimental results. Thus accurate knowledge of the soil's properties may help in this method being used for designers to predict deformation prior to ultimate failure, and to compare this with the serviceability limit state criteria. While Newmark-type methods for block sliding could be used to compute sliding deformation at ultimate failure.

Chapter 5 investigates in detail the mechanisms of failure, and the development of deformation within the GRS models, to better aid in the prediction of deformation behaviour at low acceleration levels as discussed.

## **4.8 Summary**

This chapter investigated in detail the seismic performance of reduced-scale GRS wall models with an FHR facing. The models were tested on University of Canterbury Shake-table. The chapter first introduced the test data obtained during one test, namely Test-6, a vertical wall reinforced with  $L/H = 0.6$ . Test-6 was selected because the construction methodology and testing procedure had been perfected allowing the most representative results of GRS behaviour under seismic loading to be obtained. The testing programme

consisted of excitation with a sinusoidal acceleration wave at 5 Hz frequency in stages of 10 second duration. The amplitude of acceleration was increased in 0.1g increments for each stage, with the first stage of testing at 0.1g. This input motion was selected to simplify interpretation of results and enable qualitative comparison with other research.

The deformation of Test-6 was illustrated step-by-step with photos captured at the end of each shaking step. This showed that Test-6, as representative of all other tests, failed predominantly by overturning. This involved the reinforced soil block rotating about the toe, coupled with multiple external shearing surfaces which formed within the backfill, with the first of these surfaces only just visible at the completion of the 0.2g shaking step. These shearing surfaces were inclined away from the reinforced soil block. Also evident is some minor sliding of the base of the facing panel along the rigid foundation, which occurred largely in the final shaking step of 0.5g during wall failure.

The deformation was described with the recorded acceleration and facing displacement time histories. Small deformation was recorded at the wall face at low accelerations up to some threshold acceleration, in this case, 0.4g shaking. Deformation consisted mostly by rotation, with only a small component of sliding observed. Failure occurred during the 0.5g shaking step, and was predominantly by overturning. During failure however, there was also a significant component of sliding.

In general, Test-6 demonstrated behaviour representative of all tests, with a characteristic bilinear displacement-acceleration relationship. This defines a critical acceleration value, below which only minor deformation occurs, and above which, significant deformation and failure is generated. Various definitions for critical acceleration proposed by different researchers were discussed, however, critical acceleration based on a sudden increase in the sliding component was selected as most appropriate to use for the current models. This is because failure for all models occurred concurrently with a significant increase in the sliding component of deformation. Reasons for why sliding might govern failure for the current model tests constructed with a FHR facing panel, are presented in Chapter 5. Critical acceleration can then be used for performance based design, and the prediction of displacements during an earthquake (however this was not discussed).

The parametric study consisted of seven tests designed to investigate the impact of reinforcement ratio  $L/H$  and wall inclination on seismic performance. The reinforcement ratio  $L/H$  was varied between  $L/H = 0.6, 0.75$  and  $0.9$  for vertically faced walls (Tests-6, 1

and 5). One wall was inclined at  $70^\circ$  to the horizontal (Test-7). Three tests were repeated to validate the experimental method and also because of experimental error.

An increase in the L/H ratio from L/H = 0.6 to 0.75 to 0.9 was found to decrease the deformation pre-failure and increase the ultimate stability. For the range tested the acceleration level at which failure occurred increased from 0.5g, 0.6g to 0.7g respectively.

Similarly, wall inclination to  $70^\circ$  to the horizontal (Test-7 reinforced with L/H = 0.75) further decreased deformation pre-failure, with the deformation being somewhat similar to that recorded for the vertical wall, but reinforced at a larger L/H = 0.9 (Test-5). Sliding was small, yet as expected, larger than that observed for all vertical walls. Ultimate failure occurred during the 0.7g shaking step, and included a significant sliding component, again, larger than that observed for the vertical walls.

Amplification of acceleration is important because it increases the destabilising forces active on the wall. Amplification was found, for all tests, to be non-linear up the wall face, and to generally increase with increasing base input acceleration. A peak amplification of around 1.4 occurred during the final shaking step of 0.5g for Test-6. In the current NZ Design Guidelines (Murahsev, 2003) a maximum amplification of only 1.3 is specified, for low acceleration levels, and the trend used in design is of decreasing amplification with increasing base acceleration. The current GRS model experiments with an FHR panel facing, demonstrate that instead, an opposite trend of increasing amplification with increasing base acceleration was observed.

## References

- Bracegirdle, A. (1980). "SEISMIC STABILITY OF REINFORCED EARTH RETAINING WALLS." *Bulletin of the New Zealand National Society for Earthquake Engineering*, 13(4), 347-354.
- Cai, Z., and Bathurst, R. J. (1996). "Seismic-induced permanent displacement of geosynthetic-reinforced segmental retaining walls." *Canadian Geotechnical Journal*, 33(6), 937-955.
- El-Emam, M. M., and Bathurst, R. J. (2004). "Experimental Design, Instrumentation and Interpretation of Reinforced Soil Wall Response Using A Shaking Table." *International Journal of Physical Modelling in Geotechnics*, 4 (2004), 13-32.
- El-Emam, M. M., and Bathurst, R. J. (2005). "Erratum: Facing contribution to seismic response of reduced-scale reinforced soil walls (Geosynthetics International (2005) vol. 12 (5) (215-238))." *Geosynthetics International*, 12(6), 344.

- El-Emam, M. M., and Bathurst, R. J. (2007). "Influence of reinforcement parameters on the seismic response of reduced-scale reinforced soil retaining walls." *Geotextiles and Geomembranes*, 25(1), 33-49.
- Fairless, G. J. (1989). "Seismic Performance of Reinforced Earth Walls," University of Canterbury, Christchurch.
- Hatami, K., and Bathurst, R. J. (2000). "Effect of structural design on fundamental frequency of reinforced-soil retaining walls." *Soil Dynamics and Earthquake Engineering*, 19, 137-157.
- Koseki, J., Bathurst, R. J., Guler, E., Kuwano, J., and Mauerer, M. "Seismic stability of reinforced soil walls." *8th International Conference of Geosynthetics (8ICG)*, Yokohama, Japan, 51 - 77.
- Kramer, S. L. (1996). *Geotechnical Earthquake Engineering*, Prentice-Hall, Upper Saddle River, New Jersey.
- Law, H. K., and Ko, H.-Y. "Dynamic response of uniform level ground deposits." *Earthquake Geotechnical Engineering*, Balkema, Rotterdam.
- Ling, H. I., Leshchinsky, D., and Perry, E. B. (1997). "Seismic design and performance of geosynthetic-reinforced soil structures." *Geotechnique*, 47(5), 933-952.
- Marriot, D. (2009). "The development of high-performance post-tensioned rocking systems for the seismic design of structures," University of Canterbury, Christchurch, New Zealand.
- Matsuo, O., Yokoyama, K., and Saito, Y. (1998). "Shaking table tests and analyses of geosynthetic-reinforced soil retaining walls." *Geosynthetics International*, 5(1-2), 97-126.
- Murashev, A. K. (2003). "Guidelines for Design and Construction of Geosynthetic-Reinforced Soil Structures." Transfund New Zealand.
- Newmark, N. M. (1965). "Effects of Earthquakes on Dams and Embankments." *Geotechnique*, 15(2), 139 - 160.
- Nova-Roessig, L., and Sitar, N. (2006). "Centrifuge model studies of the seismic response of reinforced soil slopes." *Journal of Geotechnical and Geoenvironmental Engineering*, 132(3), 388-400.
- Richards, R., and Elms, D. (1979). "SEISMIC DESIGN OF GRAVITY RETAINING WALLS." *Bulletin of the New Zealand National Society for Earthquake Engineering*, 12(2), 114-121.
- Sabermahani, M., Ghalandarzadeh, A., and Fakher, A. (2009). "Experimental study on seismic deformation modes of reinforced soil-walls." *Geotextiles and Geomembranes*, 27, 121-136.
- Segrestin, P., and Bastick, M. J. "Seismic design of Reinforced Earth retaining walls - The contribution of finite element analysis." *International Geotechnical Symposium on Theory and Practice of Earth Reinforcement*, Fukuoka, Japan.

- Steedman, R. S., and Zeng, X. (1990). "The influence of phase on the calculation of pseudo-static earth pressure on a retaining wall." *Geotechnique*, 40(1), 103-112.
- Watanabe, K., Munaf, Y., Koseki, J., Tateyama, M., and Kojima, K. (2003). "Behaviors of several types of model retaining walls subjected to irregular excitation." *Soils and Foundations*, 43(5), 13-27.

## **CHAPTER 5**

### **PRE-FAILURE DEFORMATION OF GRS**

#### **5.1 Introduction**

Post-earthquake case-studies provide evidence that GRS walls have in the past performed well: GRS walls in general demonstrated minimal to no damage in the 1995 Kobe and 1999 Taiwan earthquakes, when compared to conventional retaining walls which failed (Ling et al. 2001; 1996). While collapse of GRS walls has not been observed during earthquake shaking, the pre-failure structural performance is difficult to understand. Hence pre-failure deformations, that is, deformation because of base input acceleration shaking less than critical acceleration are of particular concern.

To investigate the performance of GRS walls pre-failure, coloured columns and horizontal lines of sand were layered against the transparent window in the model tests, and used to observe mechanisms of deformation within the reinforced soil block and retained backfill. The global mechanism of failure is first discussed in Section 5.2. Plots showing the development of these global failure mechanisms are inferred from photos taken at the end of each shaking step, and presented in Section 5.3. The observed failure surface angles are compared with those predicted by Mononobe-Okabe theory to determine its adequacy in assessing seismic behaviour.

In general, the sand markers were only able to show mechanisms of deformation that occurred with large shear strains. Geotechnical Particle Imaging Velocimetry (GeoPIV)

(White et al. 2003) is a non-invasive measurement technique and was used to accurately measure small strain fields within the reinforced soil block and backfill. This approach is discussed in Section 5.4, including its background and the validation procedures undertaken for its application in the current experiments.

GeoPIV was used to determine small-to-medium shear strains developed at low acceleration shaking, not detectable by the coloured sand markers. The interface between the reinforced soil block and the retained backfill is first analysed using this technique in Section 5.5. Section 5.6 then examines the strain field within the reinforced block itself, to test the design assumption that the reinforced block behaves as a rigid body.

The mechanisms of deformation was thus determined using two methods corresponding to deformation pre- and post-failure, using GeoPIV and sand markers, respectively. This information is combined to infer an idealised model of deformation for the GRS models with a FHR facing.

## **5.2 General description of observed failure mechanisms**

Tests-6, 5 and 7, reinforced at  $L/H = 0.6, 0.9$  and  $0.75$  and inclined at  $90^\circ, 90^\circ$  and  $70^\circ$  to the horizontal respectively, were selected to study deformation mechanisms for different  $L/H$  ratios and wall inclinations. These tests were also un-affected by testing errors and hence allow rigorous evaluation of seismic performance. In general, development of failure was similar for all tests and the step-by-step deformation of Test-6 shown in Section 4.1.3 describes this.

The mechanisms of ultimate failure for Tests-6, 5 and 7 are clearly illustrated in Figure 5-1 (a) – (c) respectively. All walls demonstrated predominantly rotation about the toe, which for the vertical walls resulted in overturning failure with some small components of sliding failure. The inclined wall (c) however, demonstrated a higher component of sliding than the vertical walls; as noted 40% of total deformation was sliding, compared to only 30% of total deformation for the vertical Test-5, and did not overturn (this was prevented by the experimental set-up).

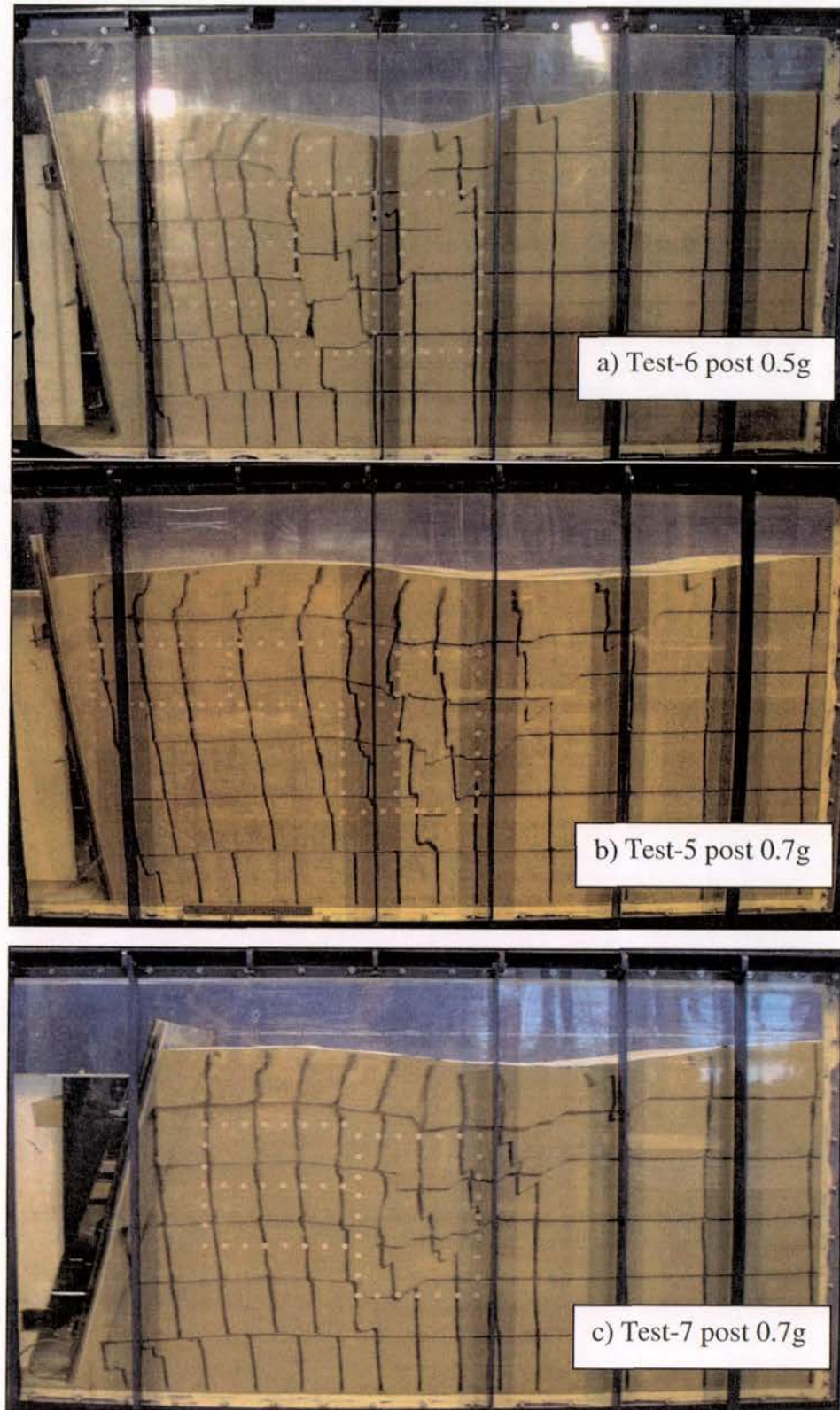


Figure 5-1. Deformation visible after failure of Test-6 (a), Test-5 (b) and Test-7 (c) reinforced at  $L/H = 0.6$ ,  $0.9$  and  $0.75$  (and inclined at  $70^\circ$  to the horizontal) respectively.

For all walls, the rotation was coupled with the formation of multiple failure surfaces within

the retained backfill. It can be seen that the failure wedge was largest for Tests-5 and 7 which failed at 0.7g and the angle of the lowest failure surface was shallower than compared to Test-6 which failed at 0.5g.

Similar observations of failure surfaces external to the reinforced zone have been reported in the literature (Fairless 1989; Howard et al. 1998; Koseki et al. 1998; Matsuo et al. 1998; Sabermahani et al. 2009; Sakaguchi 1996; Watanabe et al. 2003). It should be noted that no inclined failure surfaces formed *within* the reinforced soil block, except for at the toe of the wall (and this is explained in Section 5.3.4) in contrast to other research (El-Emam and Bathurst 2004; El-Emam et al. 2004; Lo Grasso et al. 2005; Sabermahani et al. 2009).

The occurrence of failure surfaces within the reinforced soil block can be attributed to the type of facing chosen (either: FHR panel, discrete segmental retaining, or wrap-around facing) and whether the reinforcement cover is sufficient. For instance, Watanabe et al. (2003) states that where the reinforcement is arranged properly, a failure plane will form with difficulty in the reinforced soil zone. Thus the failure mechanisms visible in the current model study, is consistent with what could be expected for FHR panel faced GRS models.

The vertical and horizontal marker lines in Figure 5-1 (a) – (c) show that the reinforced soil block also suffered some small deformation. This obviously included rotation, but also internal sliding along horizontal planes and settlement of the back of the reinforced soil block. Additionally, further shear surfaces can be seen to have formed at the toe of the reinforced soil block. These issues are discussed in Section 5.5 below.

## **5.3 Interpretation of deformation from images**

### **5.3.1 Development of deformation**

For all tests, the mode of failure included predominantly overturning and sliding. These external modes were accompanied by shear band formation in the backfill behind the reinforced soil block. The development of deformation differed between tests depending on the L/H ratio and wall inclination. Test-6 images viewed through the transparent sidewall and captured at the end of each shaking step are presented in Section 4.3.3, and images of Tests-5 and 7 are presented in Appendix C.

Discontinuities evident in the coloured sand markers were used to plot the progression of

failure within the backfill and reinforced soil block during testing. Figure 5-2, 5-3 and 5-4 (Tests-6, 5 and 7, respectively) plot the failure surfaces visible within the wall at selected acceleration levels.

With regard to identification of the shearing surfaces, it should be noted that video camera recordings enabled the global mechanism of deformation to be viewed and block movement showed the location of shearing surfaces prior to these becoming visible, after shaking. However, a failure surface was only recorded in Figure 5-2, 5-5 and 5-6 when a clear discontinuity became evident in the coloured sand columns or layers, which were around 4 mm thick, at the end of a shaking step. Thus, displacement of around 2-3 mm had to occur for the failure surface to be noted. This somewhat crudeness in measurement is rectified by use of GeoPIV analysis as discussed in Section 5.5.

The location of the reinforcement post-failure was determined by excavation; at shaking steps pre-failure the location of the reinforcement was assumed based on the location of the horizontal layers of coloured sand placed at heights corresponding to the reinforcement (see Section 3.7.3). Excavation revealed that, in general, the coloured sand layer followed the reinforcement closely and hence this assumption was valid.

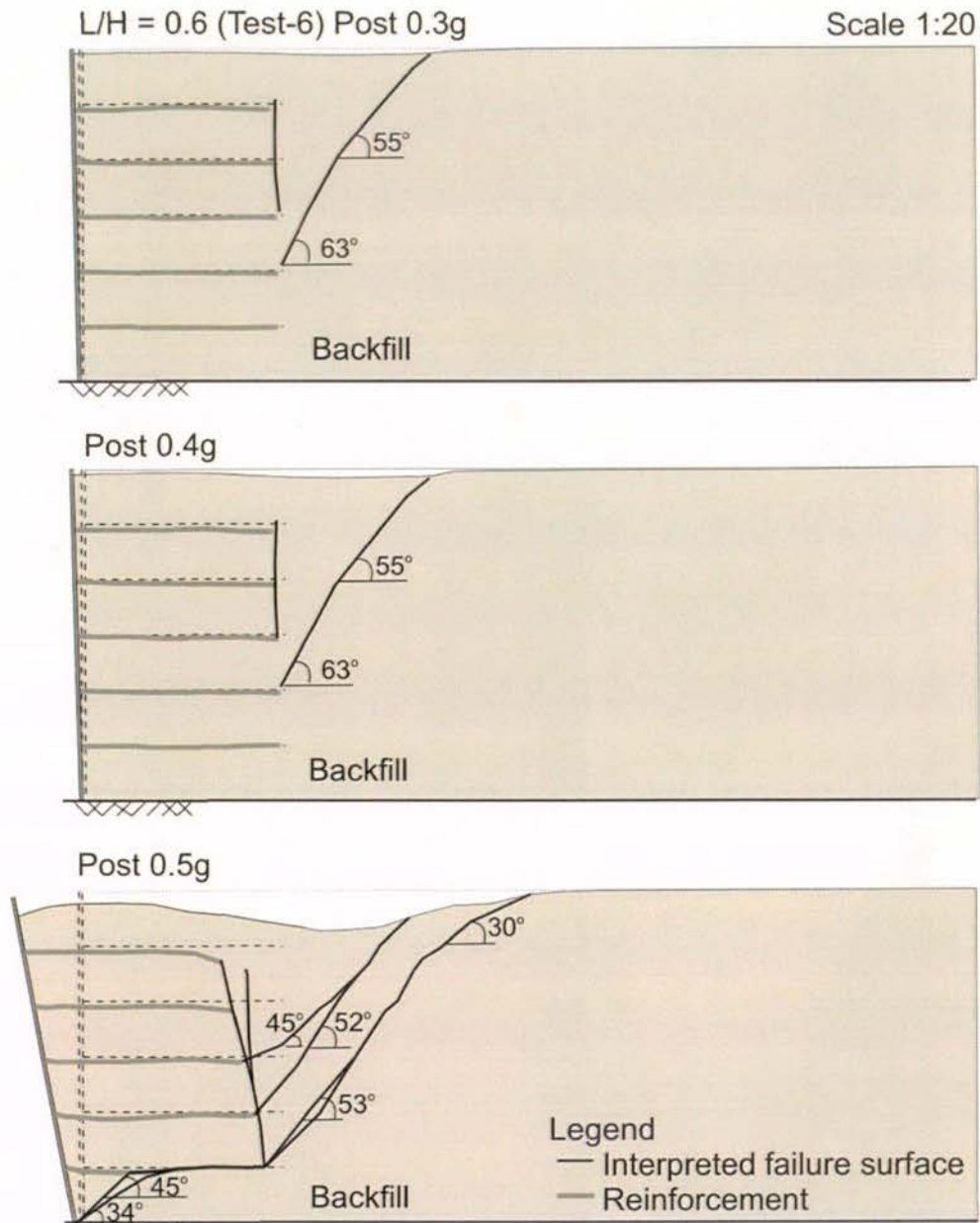
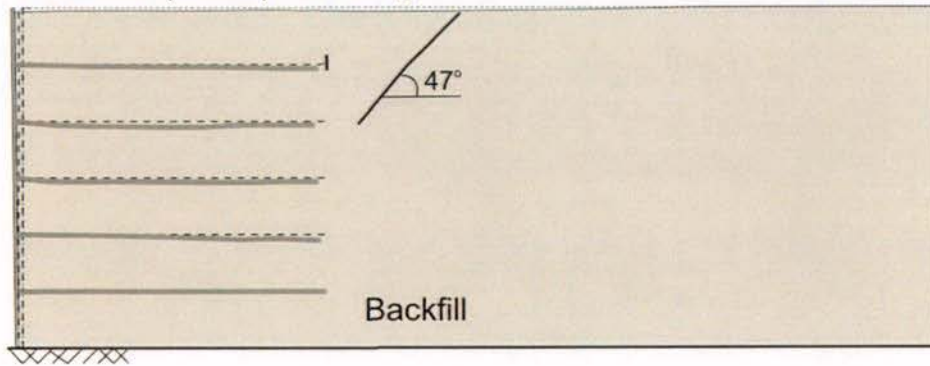


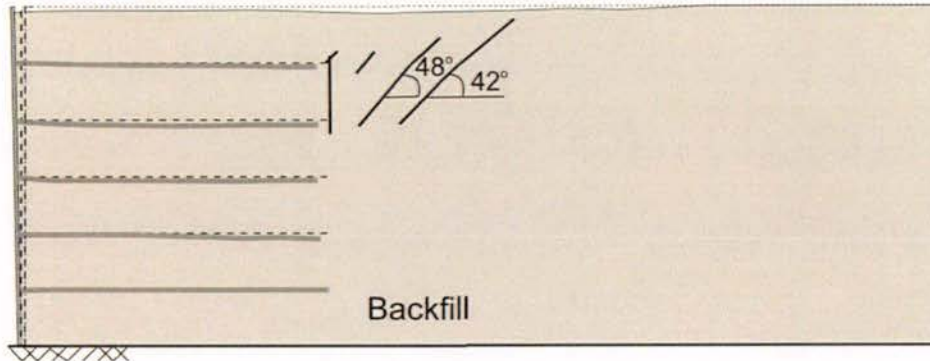
Figure 5-2. Progression of deformation within the backfill in Test-6 reinforced  $L/H = 0.6$  at the completion of: a) 0.3g, b) 0.4g and c) 0.5g (failure).

L/H = 0.9 (Test-5) Post 0.3g

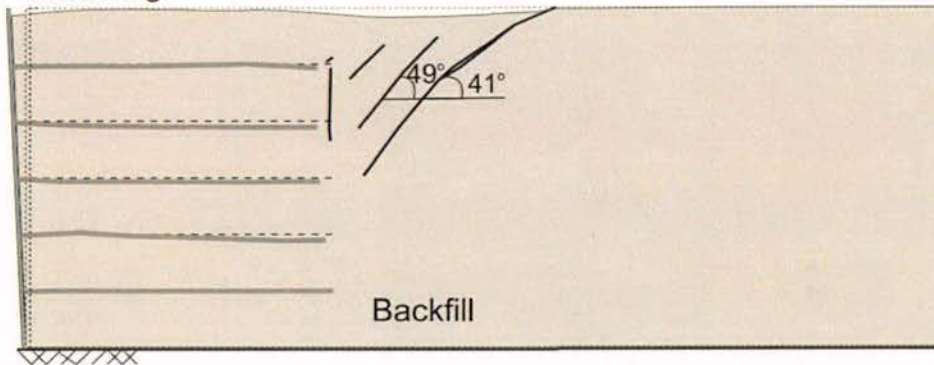
Scale 1:20



Post 0.5g



Post 0.6g



Post 0.7g

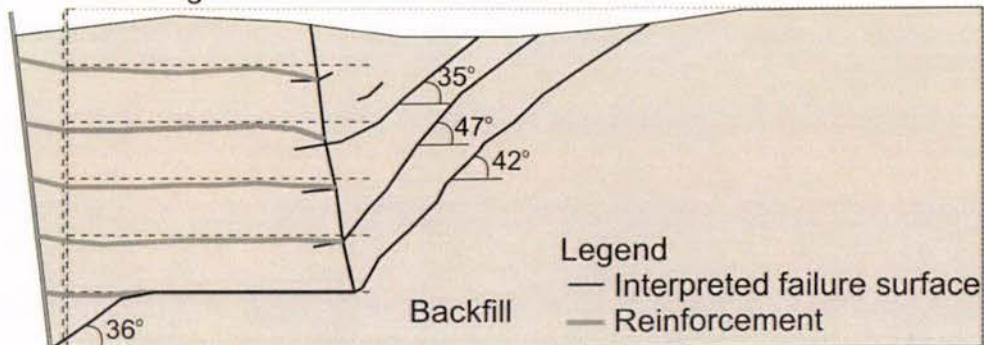
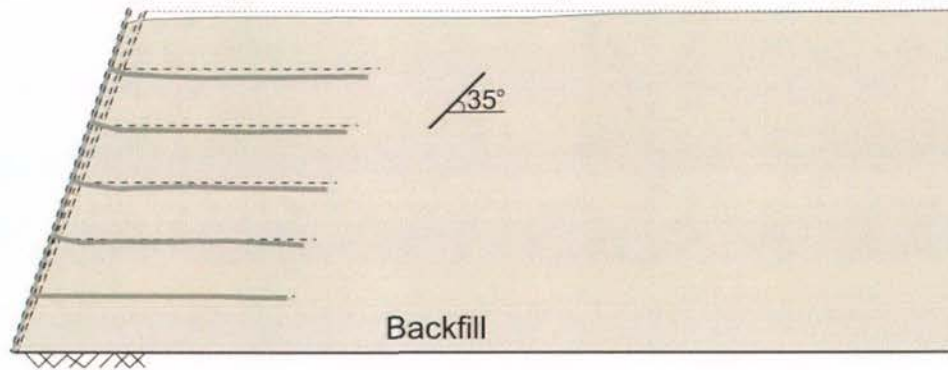
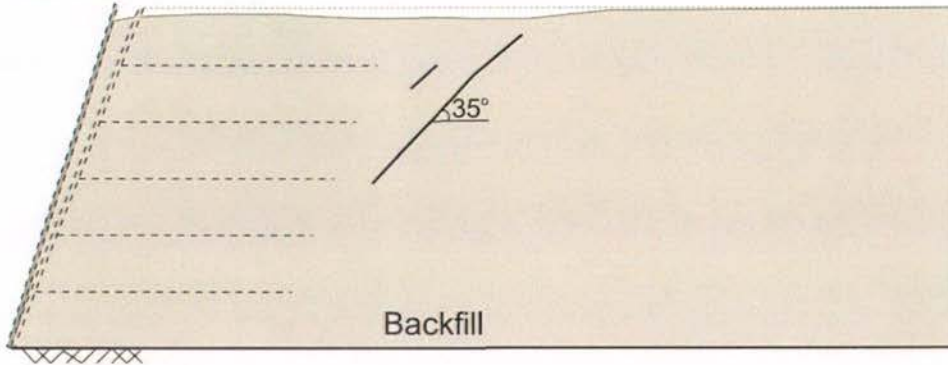


Figure 5-3. Progression of deformation within the backfill in Test-5 reinforced L/H = 0.9 at the completion of: a) 0.3g, b) 0.5g, c) 0.6g, and d) 0.7g (failure).

L/H = 0.75, facing inclined at 70° (Test-7) Post 0.4g Scale 1:20



Post 0.6g



Post 0.7g

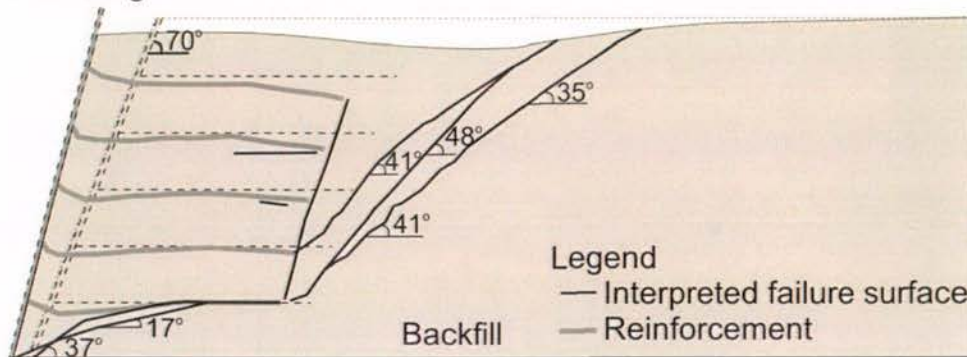


Figure 5-4. Progression of deformation within the backfill in Test-7 reinforced L/H = 0.75 with a facing inclination of 70° at the completion of: a) 0.4g, b) 0.6g and c) 0.7g (failure).

Figure 5-2, 5-3 and 5-4 show the progression of deformation for walls reinforced by L/H = 0.6, 0.9 and 0.75, with the latter wall also inclined at 70° to the horizontal (Tests-6, 5 and 7 respectively). For all tests, multiple failure surfaces at varying inclinations and elevations formed at different acceleration levels. The failure surfaces were accompanied by overturning of the wall face which allowed sliding of an active wedge along the failure surface into the back of the reinforced soil zone to occur. A number of general comments are made with reference to the above plots:

- For Tests-6 and 5, the first and highest shearing surface became visible during 0.3g shaking step. For Test-7, the first and highest shearing surface became visible during the 0.4g shaking step.
- Shaking at higher base acceleration levels either propagated the existing shearing surface (by sliding of the active wedge along the shearing surface), and/or generated a deeper shearing surface. For the vertical walls, this was accompanied by a vertical shearing surface that appeared to propagate downwards from the wall crest and to trace the back of the reinforced soil block.
- Except for Test-7, the angles of subsequent lower shearing surfaces were similar (within 5°) to that of the previously formed failure surface's initial angle.
- Failure surfaces were reasonably planar, especially at lower elevations. The surface became curved near the top of the wall. Slight irregularities in the inclination of the failure surface were possibly due to local strength differences, progressive deformation, the mode of deformation (rotation), and/or measurement error.
- Apart from near the back of the reinforced soil zone, the horizontal reinforcement prevented an inclined failure surface from compromising the reinforced soil block.
- As the failure wedge displaced and deformed, failure surfaces higher up within the wedge became visible and were recorded.
- As the wedge displaced downwards, high settlements occurred behind the reinforced soil block, and the ends of reinforcement were “dragged” downwards. Sabermahani et al. (2009) noted similar down-drag forces acting on reinforcement tails near the back of the reinforced block.
- Except for Test-7, the angles of previously formed failure surfaces were all reduced (became shallower) as the active wedge slid down the failure surface into the reinforced soil block. This possibly indicates that the active wedge rotated clockwise during subsequent shaking steps, as the wall face rotated towards the vertical.

Specific impacts on deformation due to the L/H ratio and wall inclination are discussed subsequently.

### 5.3.2 Effect of L/H ratio on deformation

In general, the deformation patterns for both vertical wall tests was similar even though there was a 50% increase in reinforcement length from Test-6 to Test-5. As noted previously, this increase in reinforcement generated greater stability (a larger critical acceleration). The following comments are made with regard to the influence of L/H ratio on failure surface formation.

- The angles of the failure surfaces formed in Test-6 ( $L/H = 0.6$ ) were steeper than the angle of the failure surfaces formed in Test-5 ( $L/H = 0.9$ ): Approximately  $55^\circ$  compared to  $42^\circ$ .
- Test-6 ( $L/H = 0.6$ ) reinforced soil block exhibited less downward deformation of the reinforcement ends. This perhaps indicates that the  $L/H = 0.6$  reinforced soil block acted in a more rigid manner than the  $L/H = 0.9$  reinforced soil block.

### 5.3.3 Effect of wall face inclination on deformation

Figure 5-4 plots the progression of deformation for Test-7 with a  $70^\circ$  inclined wall face reinforced at  $L/H = 0.75$ . Up until 0.4g shaking, deformation was primarily restricted to rotation of the wall face and no noticeable failure surfaces were formed within the backfill. By the completion of 0.4g shaking step, one failure surface was recorded, at an inclination of  $35^\circ$ . This angle is shallower again than the vertical wall, reinforced at a longer  $L/H = 0.9$ . During the 0.7g shaking step, the deepest failure surface formed and was inclined at  $41^\circ$ , similar in value to that which formed at 0.7g for the vertical wall  $L/H = 0.9$ . Further failure surfaces became visible above this as the active wedge deformed whilst it slipped down and into the back of the reinforced block.

Upon comparison with Figure 5-3 and Figure 5-4, Test-7 exhibited fewer failure surfaces prior to failure at 0.7g, illustrating an increased stability, due to the reduced inclination of the wall.

### 5.3.4 Progressive failure

In limit equilibrium methods, the active wedge is assumed to mobilise peak soil strength at the same time at all points along a potential failure surface. In reality however, progressive failure phenomena means that along a potential failure surface, different strengths according

to location on the stress-strain curve will be mobilised. Thus failure is initiated along the surface when the peak strength is reached at some point and resistance drops (with continued strain) to some residual strength value on the stress-strain curve. This in turn causes a redistribution of stresses along the potential failure surface, and possibly failure at other points along the potential failure surface. Hence peak strength is not mobilised at the same time during shaking and the failure surface is propagated accordingly.

Figure 5-2 and Figure 5-3 provide evidence of progressive failure along each failure surface. During increased base input acceleration, failure surfaces were initiated within the backfill. The failure surface only became visible once sufficient sliding displacement (shear strain) of the active wedge occurred for post-peak reduction of the shear resistance to residual strength values. This redistributed the shear stresses along the potential failure surface. At continued shaking, or higher acceleration shaking, the failure surface was propagated down towards the back of the reinforced soil block.

Watanabe et al. (2003) reported progressive failure within the backfill of conventional gravity-type retaining wall models. In these tests, a failure surface formed which extended from the wall crest to the heel of the wall. Upon application of larger acceleration amplitude shaking a second potential failure surface exploited the localised weakness at the wall heel and initiated a second failure surface up into the backfill inclined at a shallower angle.

In the absence of a reinforcement layer along the solid foundation, the heel of the wall in the current experiments is, in effect, similar to a conventional retaining wall. Figure 5-5 shows the two failure surfaces formed at the wall heel during the final shaking step of 0.5g for Test-6.

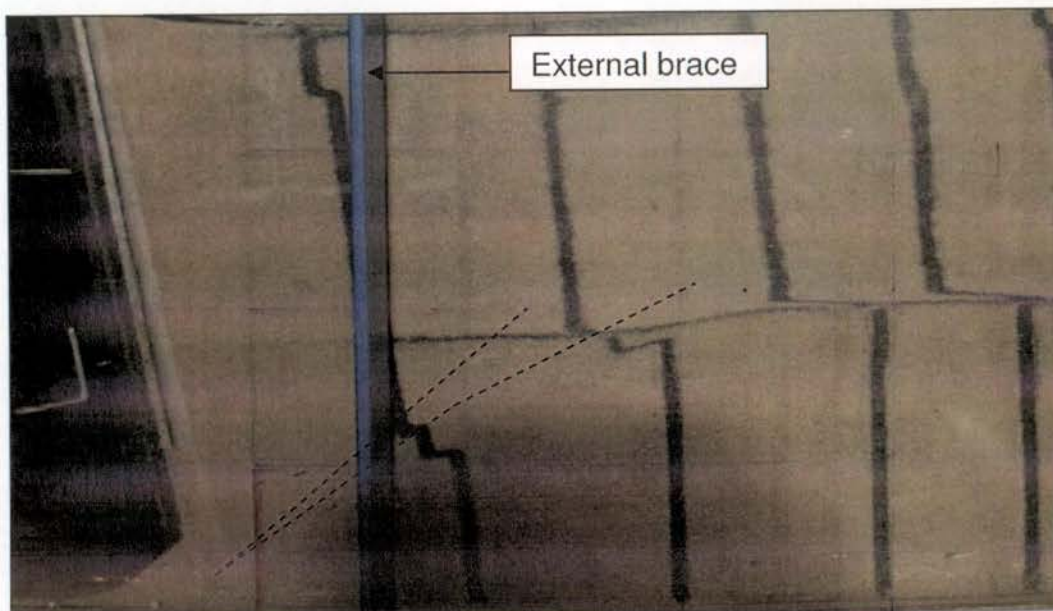


Figure 5-5. Progressive failure at wall heel during the final 0.5g shaking step (Test-6)

Figure 5-5 shows the two failure surfaces intersect the bottom layer of reinforcement, R1 (see Section 3.4.8 for reinforcement numbering). In accordance with similar observations made by Watanabe et al. (2003) noted above, it is likely that during the final shaking step of 0.5g, the steeper failure surface formed first, then, as the wall slid along the bottom layer of reinforcement, the second failure surface formed possibly exploiting the weak region at the toe of the wall (due to strain softening along the previously formed failure surface).

### 5.3.5 Comparison of angle of failure surfaces observed with those predicted by Mononobe-Okabe theory

Mononobe-Okabe (MO) theory is commonly used to calculate pseudo-static earth pressures developed within geotechnical structures under seismic loading, as described in Section 2.2.3. Further, the theory also allows the prediction of the angle of the failure plane which forms the active wedge. As the design acceleration coefficient increases, the seismic component of total earth pressure,  $K_{AE}$ , also increases, and this indicates that the active wedge has increased in volume, and the failure surface becomes shallower.

It has been noted that at large design acceleration coefficients, MO theory is conservative (Murashev 2003), therefore it is important to compare the MO theory predictions of the failure surface angle with that observed in the current tests. The parameters used to calculate the angle of the failure surface for each shaking step were assumed as: Internal angle of

friction of Albany sand,  $33^\circ$ ; Backfill slope,  $0^\circ$ ; Wall inclination to the horizontal,  $90^\circ$ . The angle of friction between the face and soil was assumed equal to  $3/4$  of the internal angle of friction of Albany sand (Koseki et al. 1998) and hence was assumed equal to  $25^\circ$ . Table 5-1 shows the predicted angles of the potential failure surface, and compares these with those observed. Figure 5.6 shows the definition of the angle of the failure surface predicted and observed.

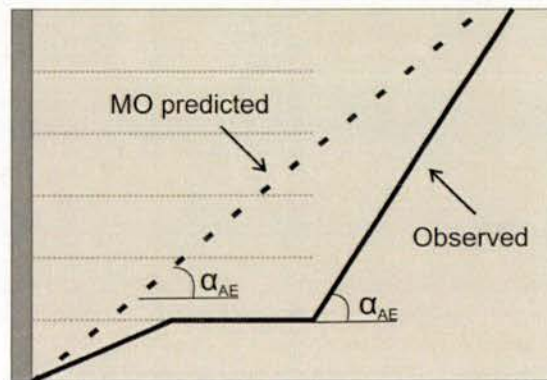


Figure 5-6. Schematic diagram showing the definition of the failure surface angle,  $\alpha_{AE}$ , for the MO prediction and that observed.

Table 5-1. Comparison of angles of failure surfaces at various shaking levels predicted by Mononobe-Okabe theory and observed for Tests-6, 5, and 7 (reinforced by  $L/H = 0.6, 0.9$  and  $0.75$ , the latter wall inclined at  $70^\circ$  to the horizontal, respectively).

Shaking step	MO predicted $\alpha_{AE}$ (vertical walls)	Observed $\alpha_{AE}$		
		Test-6	Test-5	Test-7
0 (static)	$57^\circ$	-	-	-
0.3g	$39^\circ$	$63^\circ$	$47^\circ$	-
0.4g	$31^\circ$	$63^\circ$	$42^\circ$	$35^\circ$
0.5g	$22^\circ$	$53^\circ$	$42^\circ$	$35^\circ$
0.6g	$11^\circ$	-	$41^\circ$	$35^\circ$
0.7g	indeterminate	-	$42^\circ$	$41^\circ$

There are three important points to be made with the derivation of Table 5-1. Firstly, whilst wall inclination can be expected to alter the earth pressure within the wall, MO theory is indeterminate for a slope of  $70^\circ$  to the horizontal given the other parameter values just noted.

Hence, the observed angles for Test-7 are compared with that predicted for a vertical wall. Secondly, because the failure surfaces were observed to be somewhat curved, (becoming shallower at higher elevations within the wall) the angles listed in Table 5-1 were taken from the lower sections of the wall where visible. Finally, the angles recorded were made by the lowest failure surface visible within the wall.

Table 5-1 shows that MO theory predicts shallow failure surfaces at high design accelerations, with an angle of  $11^\circ$  predicted for the 0.6g shaking step. At 0.7g, MO theory is indeterminate, and this corresponds to the condition where the entire wall is assumed unstable and limit equilibrium does not exist. Upon comparison with the angles observed, MO theory can be considered highly conservative, predicting potential failure surfaces far shallower than those observed.

A number of reasons for the disparity between that predicted and that observed are listed below.

- The mechanism of failure between that predicted with the MO theory and observed are different. The MO assumes a single failure wedge, whereas the GRS models instead displayed the two-wedge failure mechanism, as proposed by Horii et al. (1994).
- Progressive failure is shown to occur, contrary to the limit equilibrium assumptions of MO theory (as discussed in Section 5.3.4).
- The MO prediction is sensitive to the soil-wall face interface friction value chosen.
- Multiple failure surfaces develop within the backfill of all models.

Similar differences between that predicted using MO theory, and that observed have also been made by Koseki et al. (1998) and El-Emam and Bathurst (2004) on shaking-table tests of GRS models. The MO predictions of the former were conservative (i.e. shallower), and the latter were un-conservative (i.e. steeper). This indicates the ineffectiveness of MO theory for application to GRS walls.

### **5.3.6 Comment on sidewall friction**

Exact values for the inclination of failure surfaces should be interpreted with caution as the boundary conditions of the acrylic sidewall are not perfectly non-frictional. Watanabe et al.

(2003) investigated the effect of sidewall friction on the formation of failure surfaces during a series of shake-table experiments on conventional and reinforced soil retaining wall models in a strong-box 600 mm wide. In this test, 3 accelerometers were located across the width of the wall at the same elevation. Additionally, a thin brittle wire was run along the box centerline from the wall face to the back wall. The wire was electrified for the purposes of determining the timing of formation of failure surfaces along the centerline: a failure surface would cause the wire to break with a measurable drop in voltage across the circuit.

It was found that there was negligible difference between the accelerations recorded at the sides and centerline of the wall. Further, formation time of the failure surface viewed from the side wall via high-speed camera was the same as that which occurred along the box centre line determined from the brittle electrified wire. However, upon excavation along the box centerline, the angle of the failure surface was found to be 6° shallower from that viewed through the Perspex sidewall.

Considering that no special measures were taken to reduce sidewall friction in the current experimental setup, it is reasonable to presume that the failure surface angles observed through the transparent sidewall would indeed have been shifted by some angle from that at the box centerline.

## **5.4 Geotechnical Particle Imaging Velocimetry**

During testing, high-speed images of two regions: the reinforcement soil block, and the interface region between the reinforced soil block and the retained backfill, were captured for each shaking step. Post-processing of the image data was then undertaken using GeoPIV, to calculate the displacement and strain fields within these regions.

In Section 5.4.1 the background to this technique is first provided followed by possible errors inherent in the process (Section 5.4.2). Section 5.4.3 discusses the regions selected for in-depth GeoPIV analysis. The initial tests undertaken to validate the use of GeoPIV for the current experimental programme are described in Sections 5.4.4 and 5.4.5.

### **5.4.1 Background of GeoPIV technique**

The Particle Image Velocimetry (PIV) technique was originally adapted for experimental fluid dynamics by Adrian (1991) and more recently has been used in varying fields such as

the accurate quantification of particle velocity Fritz et al. (2004); and to measure wall shear rate in blood pumps (Kim et al. 2004). For the purposes of non-intrusive measurement in geotechnical engineering applications, PIV techniques have been developed to measure foundation displacements under load (White et al. 2003); and to identify displacements and shear strains within retaining wall models tested in a centrifuge or on a shake-table (Zornberg et al. 2003; Watanabe et al. 2005).

PIV is a generic term which covers many different image processing techniques (it is also referred to as a “Digital Image Correlation” or DIC). In general the PIV process utilizes high speed cameras, lenses and accurate timing devices to capture image information at a predetermined rate for analysis with PIV software. The GeoPIV software for geotechnical engineering applications developed and described by White et al. (2003) is the particular technique used in the current experiments.

PIV enables image texture, via the different colouration of soil particles, to be identified and displacement measured from successive high speed images (frames) over an accurately known time difference. The image is first divided into a mesh of ‘patches’, sized a certain number of pixels, and the texture of each patch (pattern of light and dark) is recorded. The texture of each patch can then be traced within successive images, to determine patch movement. In contrast to the image measurement procedures used by Zornberg et al. (2003) and Watanabe et al. (2005), GeoPIV does not require sand markers to be placed into the soil; rather GeoPIV utilizes a soil’s texture within an image and thus avoids the need for intrusive calibration devices within the experimental specimen (White et al. 2003).

The texture must be sufficient for the algorithm to recognize discrete patches accurately, otherwise particles need to be “seeded” into the specimen (Bolinder, 1999). “Seeding” involves the use of more visible particles that alter the contrast of the material and allow the texture to be more easily recognised by the GeoPIV software during post processing.

In the current experiments, “Seeding” of small pebbles into the sand layered closest to the side wall window was trialed in Test-2, but the large quantity necessary made this difficult to achieve. Further, “seeding” was not deemed necessary as the Albany Sand and lighting conditions enabled sufficient texture to be visible for analysis with the GeoPIV software. However, it was found that texture was increased with the addition of horizontal and vertical layers of dyed sand, which were used to better visualise failure planes by eye as shown in

Section 5.1 above.

GeoPIV was used to track the texture within ‘patches’ of successive images by matching textures with the highest correlation within the second image taken at a known time interval; this indicates the vector direction of each patch between images. GeoPIV then determines the exact location of the correlation peak through a bi-cubic interpolation of surrounding correlation values which can generate sub-pixel accuracy (Bolinder 1999). The general principles of GeoPIV are summarised in Figure 5-7.

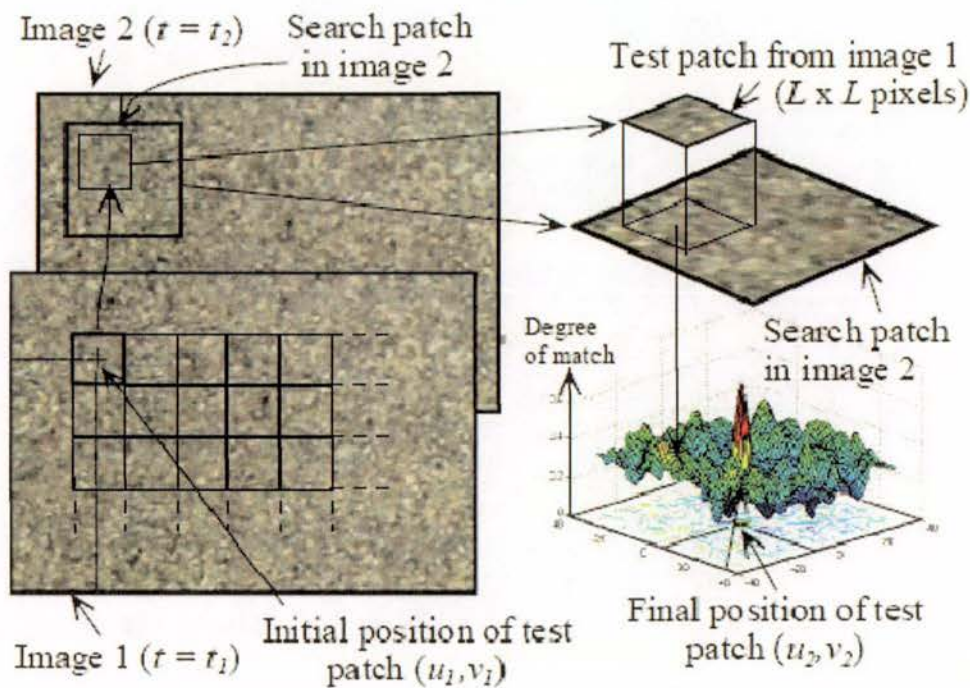


Figure 5-7. Principles of GeoPIV (from White and Take (2002)).

The directions and magnitudes of patch movement as seen in the image captured by the high-speed camera are modified from “image-space” (in pixels) to object-space (measured for instance in mm) by correlation with a grid of fixed points on the surface of the transparent acrylic window built into the box. This process is termed calibration and is discussed in Section 5.4.2 and 5.5.1.

From the PIV data collection process, essential information such as location of failure planes, the timing of formation, and the magnitude of local strains can be obtained.

## 5.4.2 Discussion of error in GeoPIV analysis

The GeoPIV measurement system involves two types of error generation: the precision, and the accuracy of the system. GeoPIV constructs the vector displacement field in image space; the difference between the true movement of patches and that recorded is the precision of the GeoPIV system and data collection methods (camera). Accuracy is dependant on data acquisition methods to transform the displacement field generated in image space to that within real-space. This process is known as image calibration and is discussed in Section 5.5.1.

Both sources of error must be measured and quantified to determine the validity of the system. White et al. (2003) evaluated the precision of the GeoPIV programme in a series of computer simulations and physical experiments on a translating bed of non-deforming Dog's Bay Sand. For the computer simulations an artificial "random" image was translated artificially. For the physical tests, micro-metered incremental translations were applied to a body of sand and images recorded via a rigid-fixed camera. GeoPIV displacement analysis was conducted with varied patch size and compared with the displacements known by the micro-meter instrumentation.

The experiments showed that precision is a strong function of patch size (i.e. the larger the patch the greater the precision), and a weak function of image content (i.e. patches of low texture are more difficult to locate precisely than high texture patches).

For instance, the patch sizes ranged from 5 by 5 to 50 by 50 pixels. For the sand, such an increase in patch size resulted in an increase in the precision of GeoPIV tracking by a factor of 18. For the sand with patches sized 50 by 50, the standard error per pixel was approximately 0.01 (as a fraction of pixels).

The image content is described in terms of its spatial brightness frequency. The spatial brightness of a soil is lower than an artificially created image. This is because for a soil, the brightness of multiple pixels is not necessarily independent, i.e. the pixels could be on the same grain of sand and hence be the same brightness. For instance, a given patch size of 32 by 32 pixels on a random image (where 2 by 2 pixel blocks have a random brightness independent of their neighbours) was tracked using GeoPIV approximately 7 times more precisely than the sand.

Figure 5-8 shows a conservative upper bound on the precision error for a mesh of patches (each sized  $L$  by  $L$  pixels) and the number of patches (measurement point array) within the mesh. Precision is expressed as a fraction of the width of the Field of View (FOV) which is the width of the image under inspection.

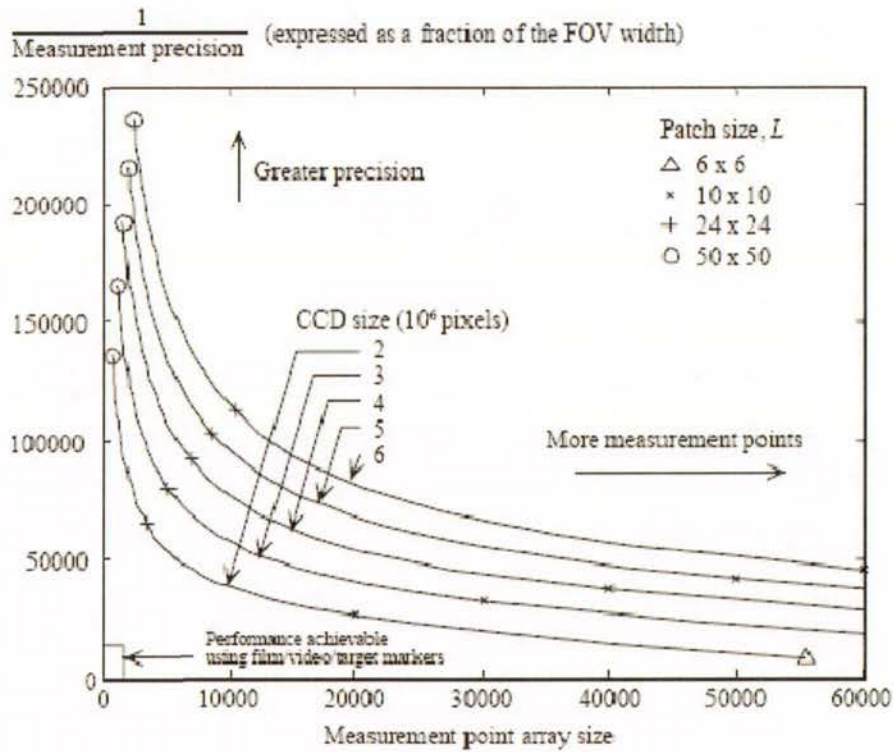


Figure 5-8. GeoPIV precision and measurement array size vs camera CCD resolution (from White and Take (2002)).

Thus a compromise is needed in deciding the optimum patch size: Larger patches can provide improved precision, though in regions of high strain gradients, smaller patches (and hence more measurement points) can reveal greater detail.

The second type of error is generated during calibration of displacements measured in uv-space (pixel) to displacements measured in xy-space (mm) of the physical model. Either a single scale factor is used to convert between pixel and object coordinates or photogrammetry is used. The former is rarely accurate in short focal length digital photography due to spatial variation in image scale caused by: ensuring the camera and object planes are coplanar, radial and tangential lens distortion, refraction through the viewing window and pixel non-squareness (minor) (White and Take 2002).

Because of the above mentioned difficulties, an accurate photogrammetric transformation from uv-space to xy-space is needed. The transformation first determines the spatial variation in scale caused by the abovementioned variables by tracking the location of a set of dots of which the xy-space coordinates are accurately known. A Mylar sheet is typically used for this (White et al. 2003). These accurately known dots are then compared with the reference points located on the inside of the box window (shown below in Figure 5-11) which are later used to calibrate the soil patch displacements from uv-space, to object displacements in xy-space.

Hence the accuracy of the transformed displacements is the geometric summation of the precision of first tracking the reference points, and secondly, the precision of tracking the soil patches with GeoPIV. Again, both these precision errors can be conservatively estimated from Figure 5-8. The precision and accuracy related errors are summed over the course of a GeoPIV analysis of several images and correspond to a random walk of error generation. This random walk determines the error of a GeoPIV analysis.

For the current application, in general each patch was traced between two successive images with a standard error per pixel of 0.1. The FOV (field of view) for the reinforced soil block window shown in Figure 5-11 was 640 pixels. Hence each patch could be traced with a precision error of 0.015%.

The GeoPIV program has an in-built “Leap frog” function, which is used to reduce the accumulation of random walk error. The assigned Leap frog value, indicates how many images will be compared before the initial image is updated. For instance, if Leapfrog is set to 1, then images 1 and 2, 2 and 3, 3 and 4 will be compared. However the errors will be summed in a random walk fashion. If Leap frog is set higher to 3, for example, then images 1 and 2, 1 and 3, 1 and 4 are compared, before updating the initial image and comparing 4 and 5, 4 and 6 etc. This reduces the random walk error, however because images are being compared over larger time frames, patches may deform, and this makes tracking each patch difficult and can result in a larger number of wild vectors.

In the current experiments, Leap frog was used depending on the analysis being run. Where residual strains were investigated, the images compared were pre-selected to occur at cycle peaks or the end of shaking steps and this created a similar leap frog effect. In analyses’ where the cyclic nature of strain was investigated, and hence many images in succession were analysed, leap frog was used to reduce the random walk error during the analysis.

### 5.4.3 Selected regions within the wall for GeoPIV analysis

Camera resolution and memory limited the window size for investigation. A large window may result in insufficient texture, as at larger distances, the sand begins to look homogenous. Additionally, a larger window requires a larger memory built into the camera. In high-speed photography, camera memory is often a limiting factor, and this acts to limit the size of the ‘windows’ under investigation. The camera properties are presented in Section 3.6.3.

Two areas were selected initially as “windows” to focus on during testing and are shown in Figure 5-9. Window C1 captured data of the front region of the reinforced zone along reinforcement layer R4 at 600 mm elevation. This region encompassed the soil layer 75 mm vertically above and below the reinforcement, and its horizontal location was varied between tests. Reinforcement layer R4 was selected because design codes typically cite the location of peak lateral dynamic earth pressure at 60% of the wall height ( $0.6 \times 900 = 540$  vertical height).

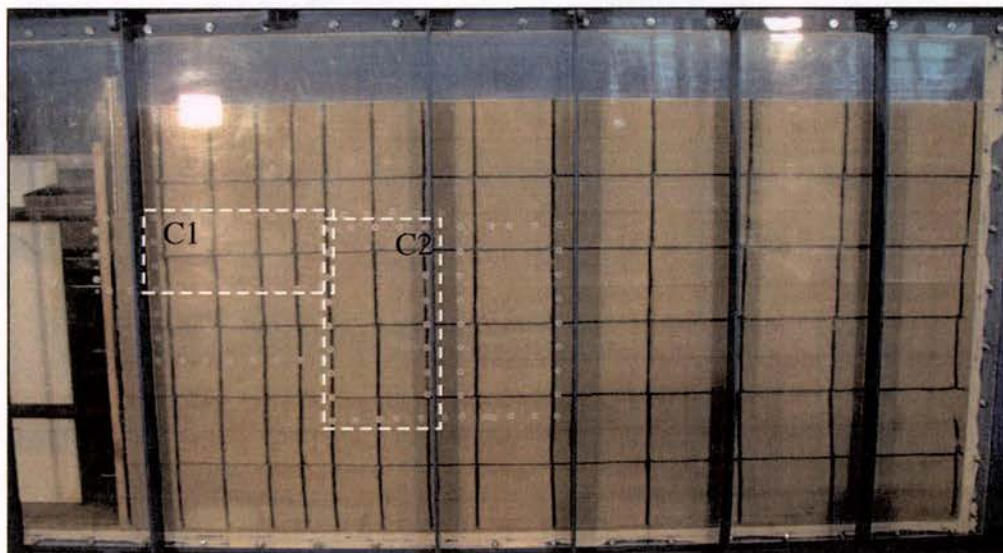


Figure 5-9. Location of “windows” in Test-6 (identified by dashed white lines), used for image capture by cameras C1 and C2. The images captured of these windows were then analysed using GeoPIV.

Window C2 was centred on the interface region between the reinforced block and the retained backfill. The area encompassed 100 mm horizontally either side of the interface and from 75 mm below reinforcement layer, R2, to 75 mm above reinforcement layer, R4.

#### 5.4.4 Validation of GeoPIV for the current application

Validation of the GeoPIV programme was performed during its development by White and Take (2003). The systems accuracy and precision was discussed in Section 5.4.2. Nevertheless, it is important to ensure that the results generated by the programme are reliable for its current use.

To check the image acquisition system and to validate the calibration process for the current experiments, a simple sinusoidal excitation was applied to one wall prior to un-bracing of the wall, and recorded with the three cameras as described above. The displacement time history of the shake-table motion is shown in Figure 5-10.

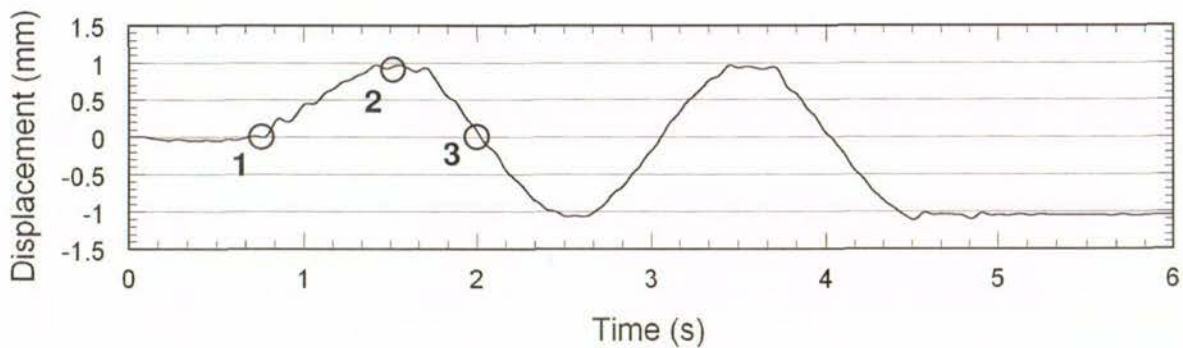
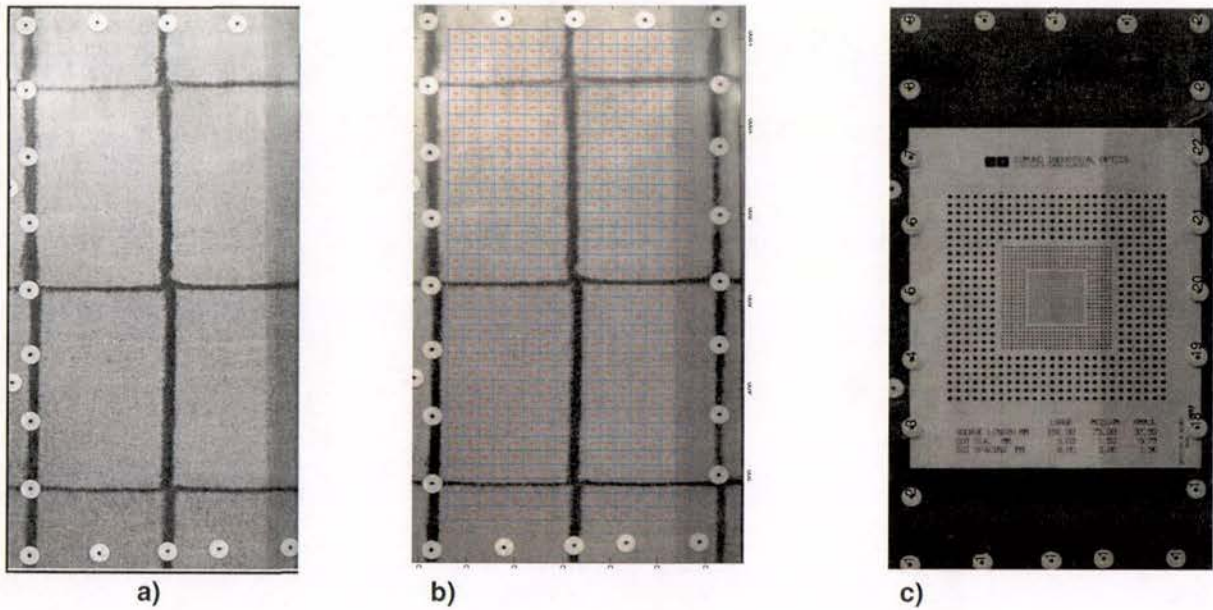


Figure 5-10. Displacement-time history of the shake-table used for PIV validation test. NB: The circled points are images taken for validation of GeoPIV.

As in the testing protocol, camera recording was “triggered” by a 3 volt switch synchronised with the shake-table control system. This ensured that an accurate time zero was established such that the correct image, corresponding to a displacement peak for instance, could be determined.



**Figure 5-11. Calibration of GeoPIV for this application: (a) Window for analysis, (b) mesh of patches to track soil texture, and (c) mesh of patches tracking reference points on the box window.**

In order to determine the performance of GeoPIV for the current investigation, its ability to record displacement over the first half cycle of a 0.1g shaking motion was investigated. A photo of the reinforced soil block and retained backfill interface region taken at point 1 of the shake-table displacement-time history (Figure 5-10) is shown in Figure 5-11 (a). A mesh of patches of 32 by 32 pixels was created for the region shown in Figure 5-11 (b). The GeoPIV programme was then used to track the displacement of each patch between the 3 images corresponding to points 1, 2, and 3 of Figure 5-10.

The displacement vector fields between points 1 and 2, and 2 and 3 are shown in Figure 5-12 (a) and (b). Each vector is plotted in dimensions of pixels in u-v space and has been scaled up 25 times to better view the patch displacement. The vector field traces soil patch displacement field of the wall corresponding to a 1 mm shake-table displacement. As can be seen, there are no “wild” vectors, and this indicates that the soil’s texture is sufficient for tracking.

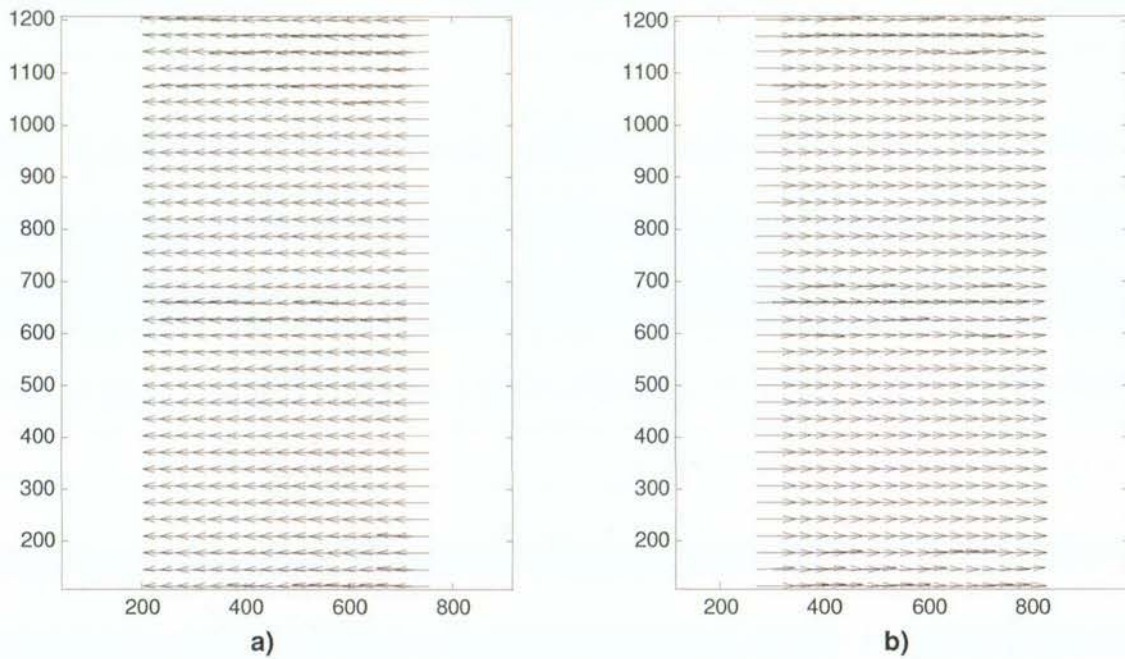


**Figure 5-12. Displacement vector field of interface region in u-v space (pixels). Vectors plotted between: (a) Time history points 1 and 2, and (b) points 2 and 3.**

The above displacement plots tracked patches of soil as it moved with the displacement of the shake-table. Thus the displacement plotted in Figure 5-12 includes the displacement of the shake-table as well. The displacement of the soil relative to the shake-table is determined through the calibration process. In this, the displacement of the reference dots (Figure 5-11(c)) is traced through the image sequence and removed from the displacement of the soil patches shown in Figure 5-11 (b). Thus the relative soil patch displacement can then be plotted in real xy-space (mm) and is shown in Figure 5-13 (a) and (b). Because the wall was braced, and the shake-table motion was gentle, the relative displacement of the soil, as expected, approximates zero.

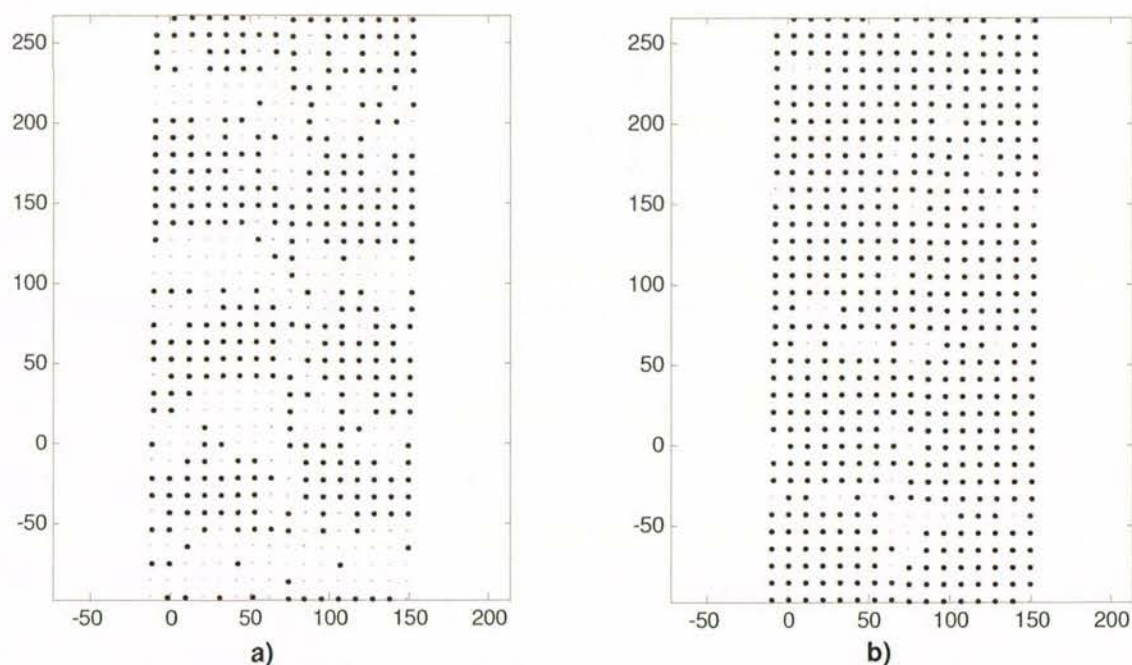


**Figure 5-13. Calibrated displacement vector field of interface region in x-y space (mm). Vectors plotted between: (a) Time history points 1 and 2, and (b) points 2 and 3.**

The above validation process confirms that:

- Patches of Albany sand had sufficient texture and were able to be tracked through a simple sequence of images;
- The tracking process identified simple cyclic displacement;
- The calibration process was able to determine relative soil displacement through the removal of shake-table displacement.

#### **5.4.5 Determination of appropriate patch size**

As noted above, the precision is dependent on the patch size of the mesh. An image sequence for one test was analysed using three patch sizes to determine the most appropriate patch size for subsequent analysis. The patches are square and measured in pixels sized 16 by 16 pixels, 32 by 32 pixels, and 64 by 64 pixels. The calibrated vector plots (i.e. in xy-space) for each analysis is shown in Figure 5-14.

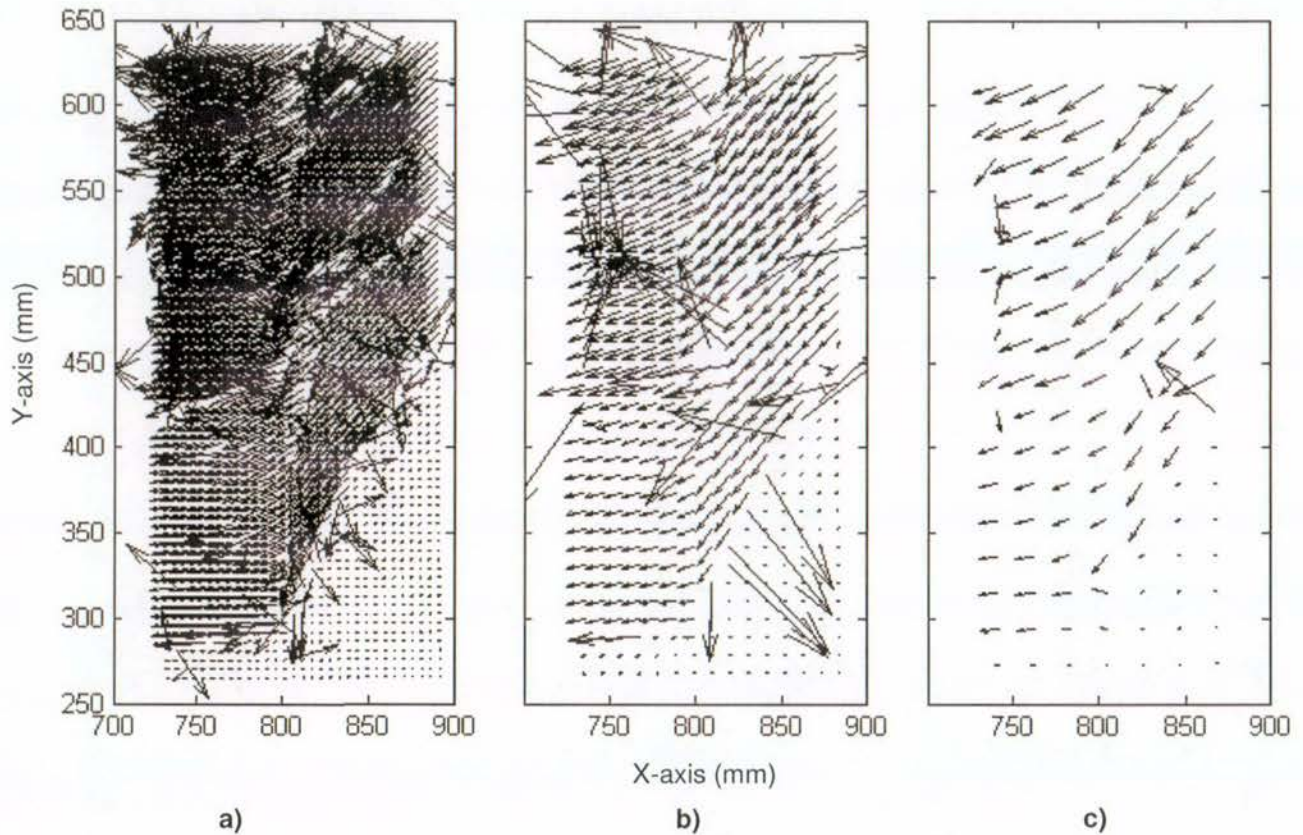


Figure 5-14. Displacement vector plot for comparison of patch size for GeoPIV analysis: a) 16 by 16 pixels, b) 32 by 32 pixels, c) 64 by 64 pixels. Each vector has been scaled up by a factor of 3.

As the patch size increases the accuracy is improved; there is more information in each patch to track through the images. At small patch sizes, an un-manageable number of “wild” vectors are generated in the GeoPIV analysis. In general, wild vectors are removed by manual inspection, however Figure 5-14 (a) shows that too many wild vectors are generated to consider this feasible. However, while large patch sizes generate a smaller number of wild vectors as in Figure 5-14 (c), the displacement field is unnecessarily crude and displacement information is lost. A compromise is needed and it was deemed appropriate to size patches 32 by 32 pixels for subsequent analysis. As shown in Figure 5-14 (b), some post-processing to remove the wild vectors is necessary, however the burden is not large.

## **5.5 Deformation of the reinforced soil block – retained backfill interface prior to failure**

### **5.5.1 Deformation of the Test-6 model using GeoPIV**

GeoPIV was used to analyse the residual deformation of the interface region of Test-6. The region (“window”) under analysis was shown in Section 5.4.3. Residual deformation is analysed as deformation that occurred between the start of the test and the end of each shaking step. The analysis does not consider changes in deformation which occur *within* a shaking step. Rather, images are selected from the start of the test, and at the end of each shaking step, and the deformation is analysed using GeoPIV. This calculates the shear strain accumulated within the reinforced soil block-retained soil interface, from the initial position until wall collapse.

As they were typical of the test results, GeoPIV results from Test-6 are used in this section to demonstrate the GeoPIV analysis procedure. First, the displacement of each patch was determined and shown as a vector field plot in Figure 5-15. This shows the displacement accumulated from the start of the test to the end of the shaking steps 0.1g – 0.4g, as indicated. The final shaking step of 0.5g was not plotted due to the unreliable results that are generated. This was because the mechanism of failure during the final shaking step (in this case 0.5g) involved a failure surface developing below the window used for GeoPIV. The resultant wedge encompasses the entire window under consideration and the soil within translated quickly and outside of the window and image. Thus GeoPIV was unable to track patches reliably during the last shaking step, however, this stage of deformation is clearly visible with the naked eye.

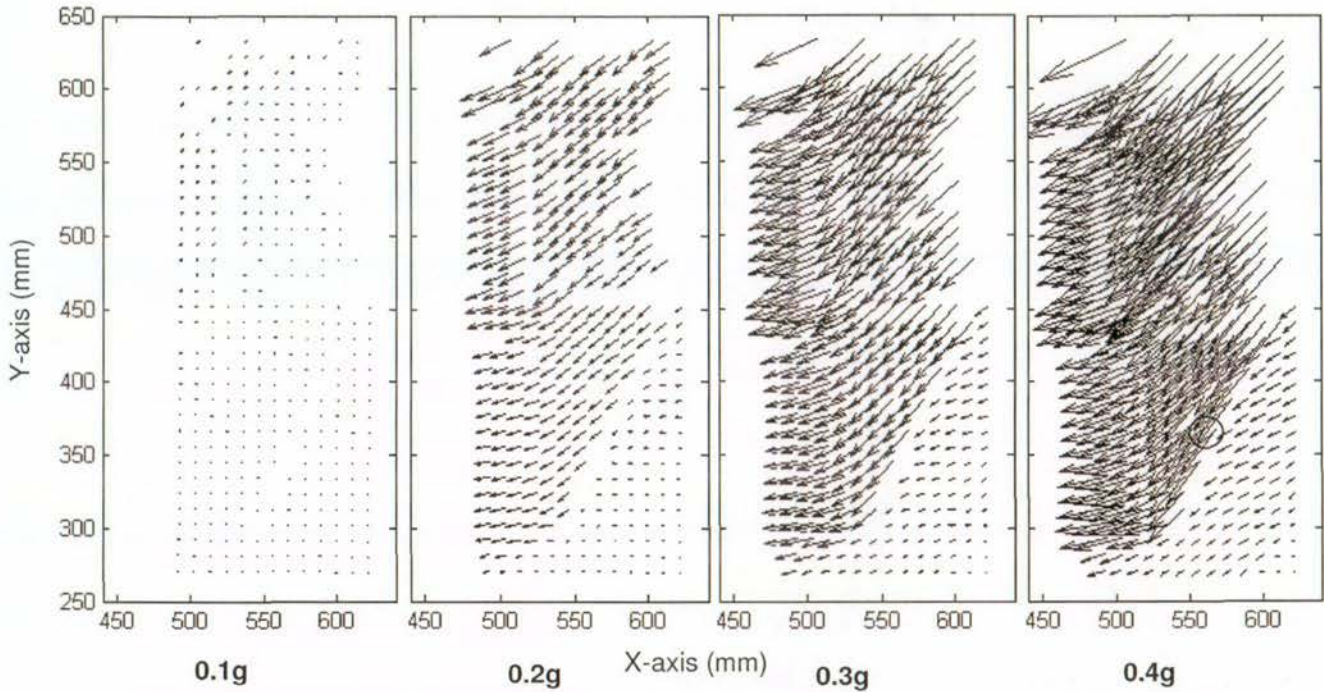


Figure 5-15. Displacement plot of interface region for shaking steps 0.1g, 0.2g, 0.3g and 0.4g. (Note vectors have been scaled by 3). The plotting region is the extent of the viewing window. Vector circled for inspection below.

Figure 5-15 shows the progression of accumulated displacements during testing of Test-6 within the test window, located from 450 to 650 mm in the horizontal x-direction, and 250 to 650 mm in the vertical y-direction. Minimal displacement occurred during the 0.1g shaking step; a steady increase in soil displacement is, however, visible with increasing base input acceleration. The location of a shearing surface is visible after the 0.2g shaking step that extends from the lower left hand corner to mid-height along the right side of the window (x, y coordinates: (500, 275) to (600, 425)).

Significant movement is visible above the shearing surface and can be associated with overturning of the wall face allowing the active wedge to slide downwards and into the back of the reinforced soil block.

The length of a displacement vector, circled in Figure 5-15 (d), and located midway along the shear surface after 0.4g shaking step is 12.9 mm (note that each vector in the above plot has been scaled by 3). The length of an inclined vector on the lower side of the shear surface is 3.7 mm. Hence the differential displacement along the shear surface is 9.2 mm.

Inspection of the vector plot (Figure 5-15) shows that up to 16 mm lateral displacement

occurred at the top of the interface region, corresponding to 25 mm lateral displacement recorded with the displacement transducers at the same elevation at the wall face. Similarly, lateral displacement below the shear surface of approximately 2.0 mm by completion of the 0.4g shaking step compares reasonably well with the sliding displacement of 3.6 mm recorded at the base of the wall face. These results demonstrate a similar order-of-magnitude, however it should be noted that values recorded at the wall face, and at the reinforced soil block – retained backfill interface will never be the same. This is due to the reinforced soil block acting non-rigidly, and hence displacement recorded at the wall face includes deformation of the reinforced soil block.

Also of interest in Figure 5-15, is a near-vertical line defined by a sudden change in the vector direction from inclined to near horizontal. It appears that the line occurs roughly at the interface between the reinforced soil block and retained backfill and is located at roughly  $x = 520$  mm. Note that due to some movement of the wall face, the location of the reinforcement ends has changed from its initial location at  $x = 540$  mm.

In order to better understand the relative deformation of the soil, strains can be calculated using GeoPIV. To do this, GeoPIV creates a triangular mesh of elements which link the centre of patches with its neighbouring patches. Relative patch displacement causes extension or compression of these elements; this is used to calculate various components of strain that include the maximum shear strain, shear strain, linear strain, or volumetric strain. Figure 5-16 shows the triangular element mesh (in uv-space) after “wild” vectors and associated patches within the window were removed during the cleaning process.

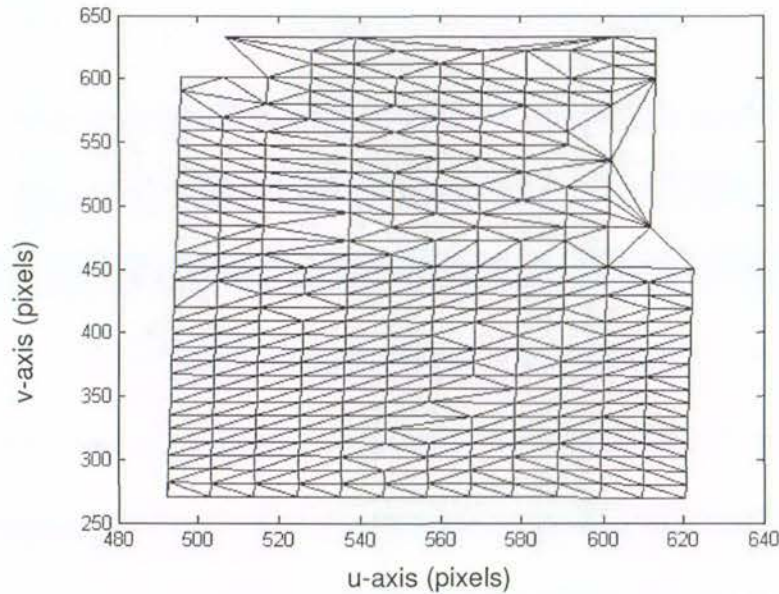


**Figure 5-16. Triangular element mesh for strain calculation plotted in xy coordinates. Note that because some "wild" vectors were evident in the displacement plots, the associated patches have been removed from the element mesh.**

Equation 5-1 presents the maximum shear strain calculated from the relative extension and compression of elements linking adjacent patches.

$$\gamma = \sqrt{(\epsilon_y - \epsilon_x)^2 + \gamma_{xy}^2} \quad (5-1)$$

Where  $\gamma$  is maximum shear strain,  $\epsilon_x$  and  $\epsilon_y$  are linear strains in the x and y directions respectively, and  $\gamma_{xy}$  is the shear strain in the x-y plane. The maximum shear strain,  $\gamma$ , is plotted primarily for the current purposes, however its various components are used to further scrutinise the modes of deformation where necessary.

Figure 5-17 plots the progression of residual maximum shear strain within the soil window accumulated by the completion of 0.1g, 0.2g, 0.3g, and 0.4g shaking steps for Test-6 reinforced at  $L/H = 0.6$ . Colour contours are used to denote percentage values of localised strain.

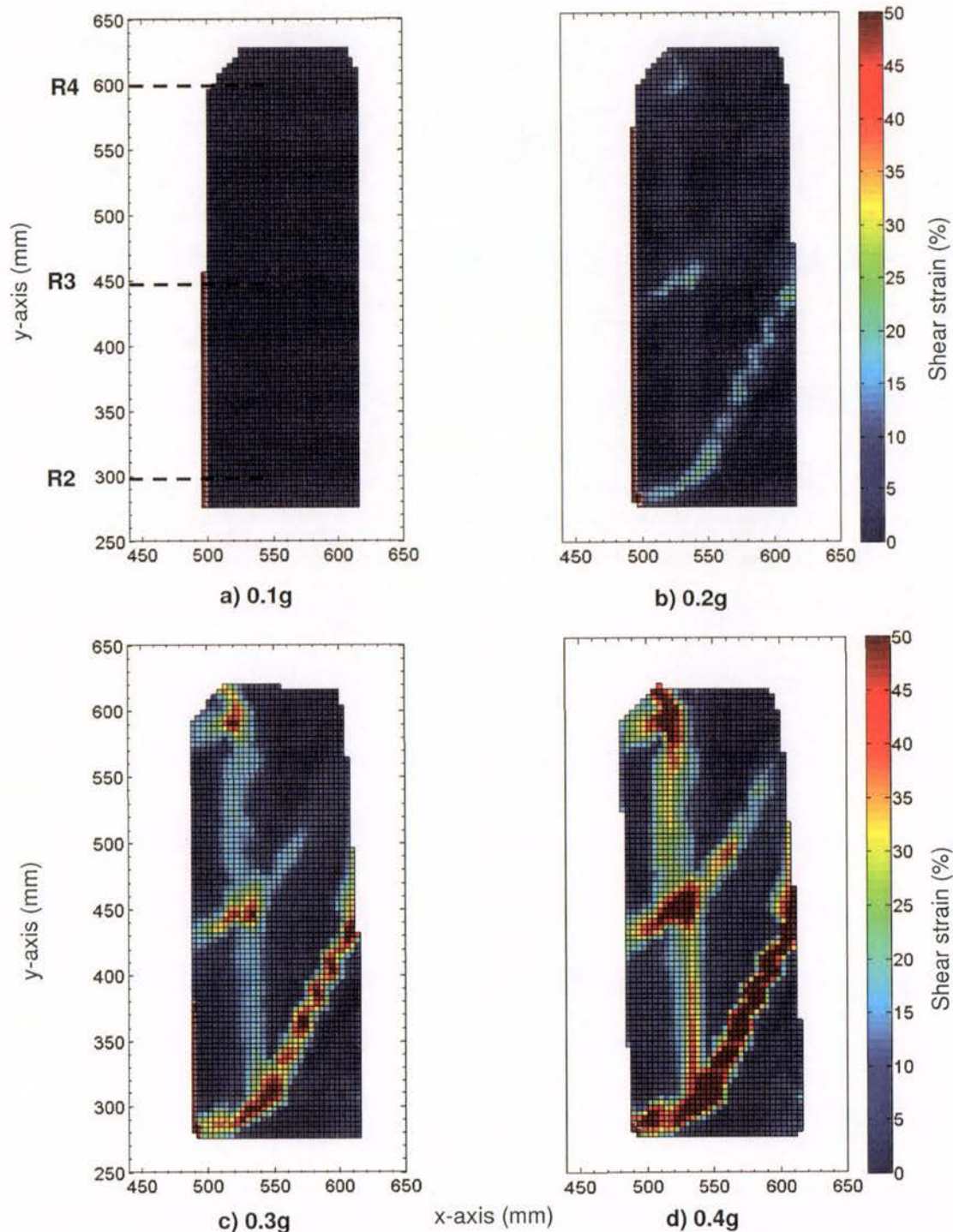
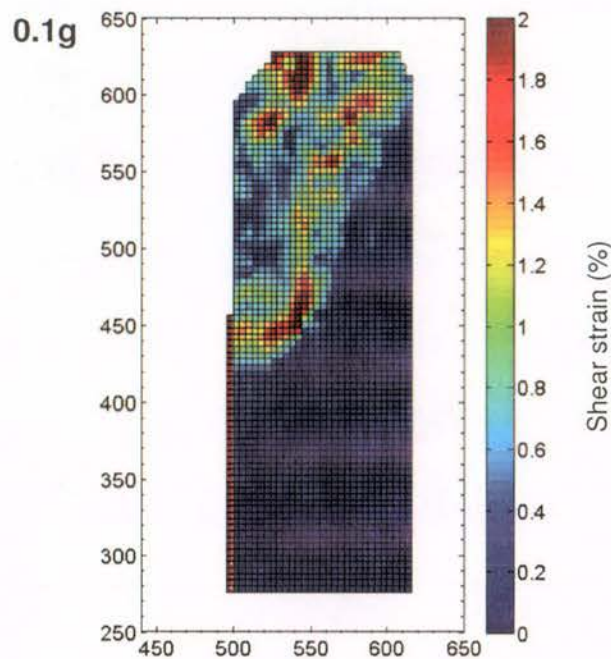


Figure 5-17. Residual shear strain of the reinforced/retained backfill interface of Test-6 reinforced with  $L/H = 0.6$  and accumulated by the completion of: (a) 0.1g, (b) 0.2g, (c) 0.3g and (d) 0.4g shaking steps.

Figure 5-17 shows localised maximum shear strains are evident by the completion of the 0.2g shaking step, with a shear surface formed between the second reinforcement layer from the bottom (R2), and strains beginning to accumulate at the ends of the third and fourth layers of reinforcement (R3 and R4), originally located at 540 mm horizontally and at 300, 450 and 600 mm elevations. The location of each layer of reinforcement is shown with a dashed line

in Figure 5-17 (a). Further shaking at 0.3g and 0.4g contributes to increasing shear strains along well-defined shear surfaces.

Figure 5-17 (b) shows the dominance of an inclined failure surface that intersects with reinforcement R2. Other higher shear surfaces which appear to intersect with reinforcement layers R3 and R4 are visible, but these have not been as well developed. This would appear to be inconsistent with the progressive failure model which prescribes the successive formation of deeper failure planes. The shear strain accumulated by the completion of 0.1g shaking step is replotted with a finer scale to better visualise this initial development of deformation.



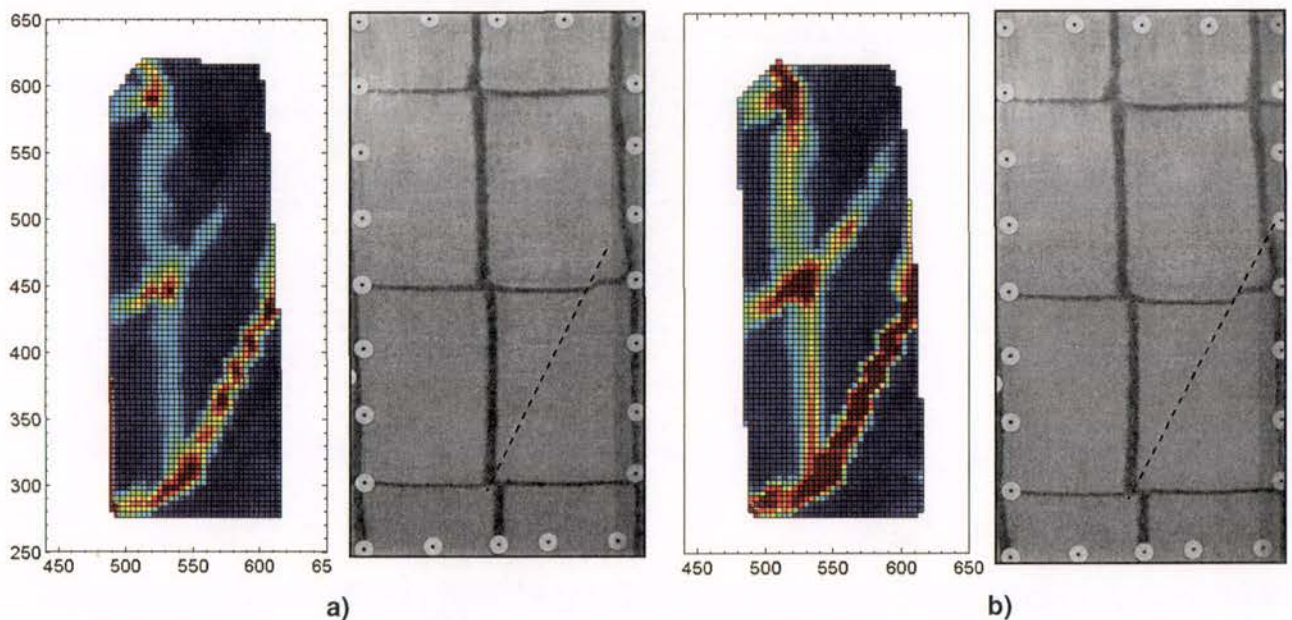
**Figure 5-18. Residual shear strain accumulated by the completion of 0.1g (replotted at a finer scale for better visualisation) of the reinforced/retained backfill interface of Test-6 reinforced with  $L/H = 0.6$ .**

Figure 5-18 shows that, by the completion of 0.1g shaking step, deformation did indeed occur, and that this was confined to near the ends of reinforcement layers R3 and R4. Further, no failure surface which intersects with reinforcement layer R2 was evident. Hence at some point during 0.2g shaking step, the development of higher failure surfaces (reinforcement layers R4 and R3) was exchanged for the development of the lower failure surface (reinforcement layer R2). To inspect this, Section 5.5.3 plots the development of deformation *within* the 0.2g shaking step.

Figure 5-18 shows a vertical shearing surface, not readily visible in the vector plot of Figure

5-15. However, it is important to note that shear strain is calculated based on the differential displacement of patches. Hence the vertical shear surface is the result of differential displacement in the vertical components of the vector plot.

Figure 5-19 compares the failure surfaces determined using GeoPIV at 0.3g and 0.4g, with those visible in the images captured and used for GeoPIV. Obviously they compare well with that visible to the eye. The angle of the lowest failure surface is calculated from Figure 5-19 as  $66^\circ$  to the horizontal, steeper than that shown in Figure 5-2 of  $55^\circ$ . However, it was noted with regard to Figure 5-2 that the failure surface is not exactly planar, and was steeper at lower elevations.



**Figure 5-19.** Comparison of location of failure surfaces plotted and seen within the image after 0.3g (a) and 0.4g (b).

Some general comments are made with regard to the shear surfaces shown within the GeoPIV window, not visible by eye using the sand markers.

- GeoPIV analysis showed deformation to have occurred at the reinforced and retained backfill interface by 0.1g shaking, and prior to these becoming obvious using the sand markers at 0.3g.
- The existence of a near-vertical shear surface that appears to form at the back of the reinforced soil block.
- GeoPIV analysis identified high shearing at the tips of the reinforcement.

- GeoPIV analysis identifies the existence of shear surfaces which appear to enter the back of the reinforced soil block horizontally, and at an angle shallower than that within the retained backfill

A summary of the development of deformation as understood for all walls is made in Section 5.5.5.

### 5.5.2 Interpretation of localised shear strains

In order to interpret the localised shear strains, it is easier, at least initially, to determine what sort of block displacement results from the plotted shear strain. Shear strain is defined in Equation 5-2.

$$\gamma = \frac{\Delta\delta}{t} \quad (5-2)$$

Where  $\gamma$  is the shear strain,  $\Delta\delta$ , the differential displacement, and  $t$  is the thickness over which the displacement occurs, i.e. the thickness of the shear band.

The shear strains identified using GeoPIV in Figure 5-17 (d) were saturated at 50% strain because of the scale used. However, the shear band thickness is increased because a larger thickness of soil has shear strains equal to or greater than 50%; thus the calculation of differential displacement by rearrangement of Equation 5-2 remains the same. Figure 5-19 (d) is replotted at a different scale in Figure 5-20 to show the effect of strain saturation on shear band thickness.

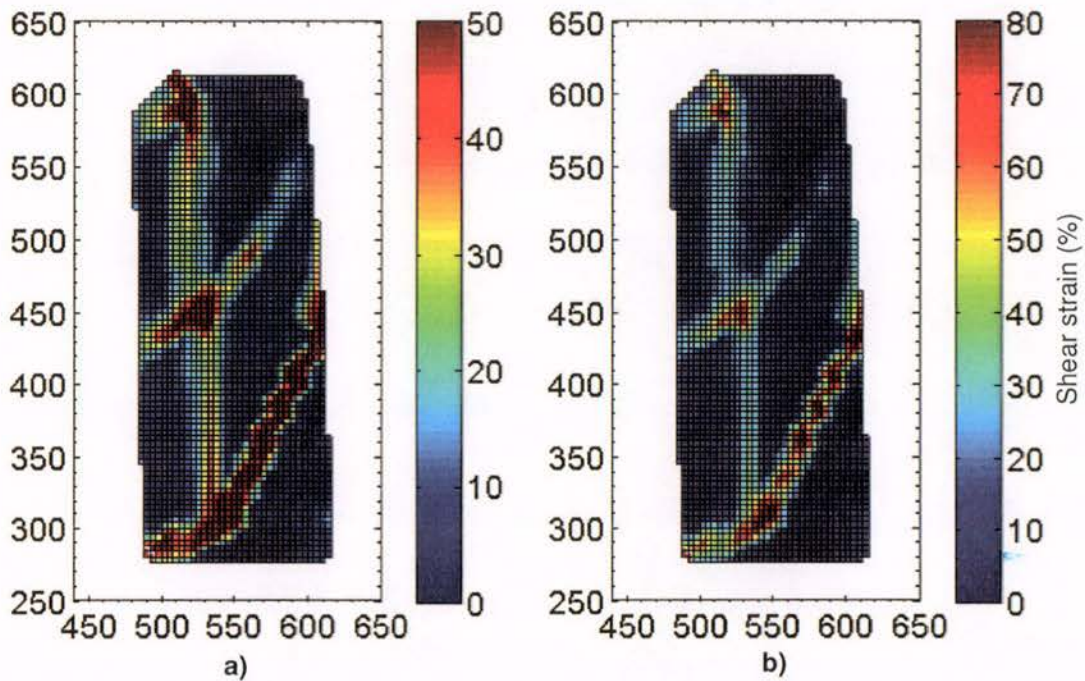


Figure 5-20. Residual shear strain accumulated by the completion of 0.4g shaking step for Test-6 plotted with the maximum strain scale set to: (a) 50% and (b) 80%.

As seen in Figure 5-20 (a), by the completion of 0.4g, the shear strain accumulated in the lowest failure surface was at least 50% along a shear band approximately 15 mm thick. This equates to a block differential displacement of approximately 7.5 mm. In Figure 5-20 (b) the shear band where 80% shear strain is recorded is seen to be a thinner 10 mm thick. Hence the block differential displacement is approximately 8 mm. Note that the difference in block differential displacement is due to inaccuracy in determining a representative shear band thickness across the surface visible.

It is important to compare the displacement predicted by the GeoPIV strain plots with that observed visually, to determine the accuracy of the GeoPIV strain analysis. Hence the displacement along the lowest shear surface was measured from a photo taken similar to Figure 5-19 (b). In the image, the shear band creates a “kink” in the coloured horizontal sand line. Whilst it is difficult to measure the “kink” accurately due to the variable thickness of the horizontal sand layer, it still provides a good indication of the relative soil displacement. The slip movement was measured as 11 mm and agrees roughly with the more accurately determined 9.2 mm shown in the quiver plots presented in Section 5.5.1.

If the reinforced soil block behaved completely rigidly, then the horizontal component of the active wedge movement would be entirely transmitted to the wall face, and would be

recorded with the displacement transducers. The horizontal component of the slip movement is determined by trigonometry; the failure surface is inclined at  $66^\circ$  to the horizontal and at this angle, the lateral displacement of the active wedge is approximately 3 mm. This is significantly less than the 14.5 mm recorded at the wall face at 300 mm elevation as shown in Section 4.4.1. The discrepancy in lateral displacement recorded at the interface between the reinforced and retained backfill and at the wall face is due a number of reasons:

- Multiple sliding surfaces developed within the interface region, and the above calculations considered displacement along only one of these. In reality, displacement along all sliding surfaces contributes to displacement at the wall face.
- The reinforced soil block is not perfectly rigid, hence displacement of the active wedge is not propagated perfectly to the wall face
- Displacement recorded at the wall face includes displacement of the active wedge *and* deformation incurred within the reinforced soil block
- The local shear strains plotted in Figure 5-20 are shown only along a small region of the failure surface. The above calculations are based on average approximations of shear band thickness, inclination angle and shear strain.

### **5.5.3 Development of deformation within the 0.2g shaking step**

GeoPIV analysis enabled shear strain to be recorded during the 0.1g and 0.2g shaking step of Test-6. During 0.1g, an inclined failure surface was seen to intersect with the end of reinforcement R3. However at some time during 0.2g, the development of this higher surface was surpassed by another inclined failure surface seen to extend down to the second layer of reinforcement, R2. Figure 5-21 shows the development of shear strain during the 0.2g shaking step of Test-6.

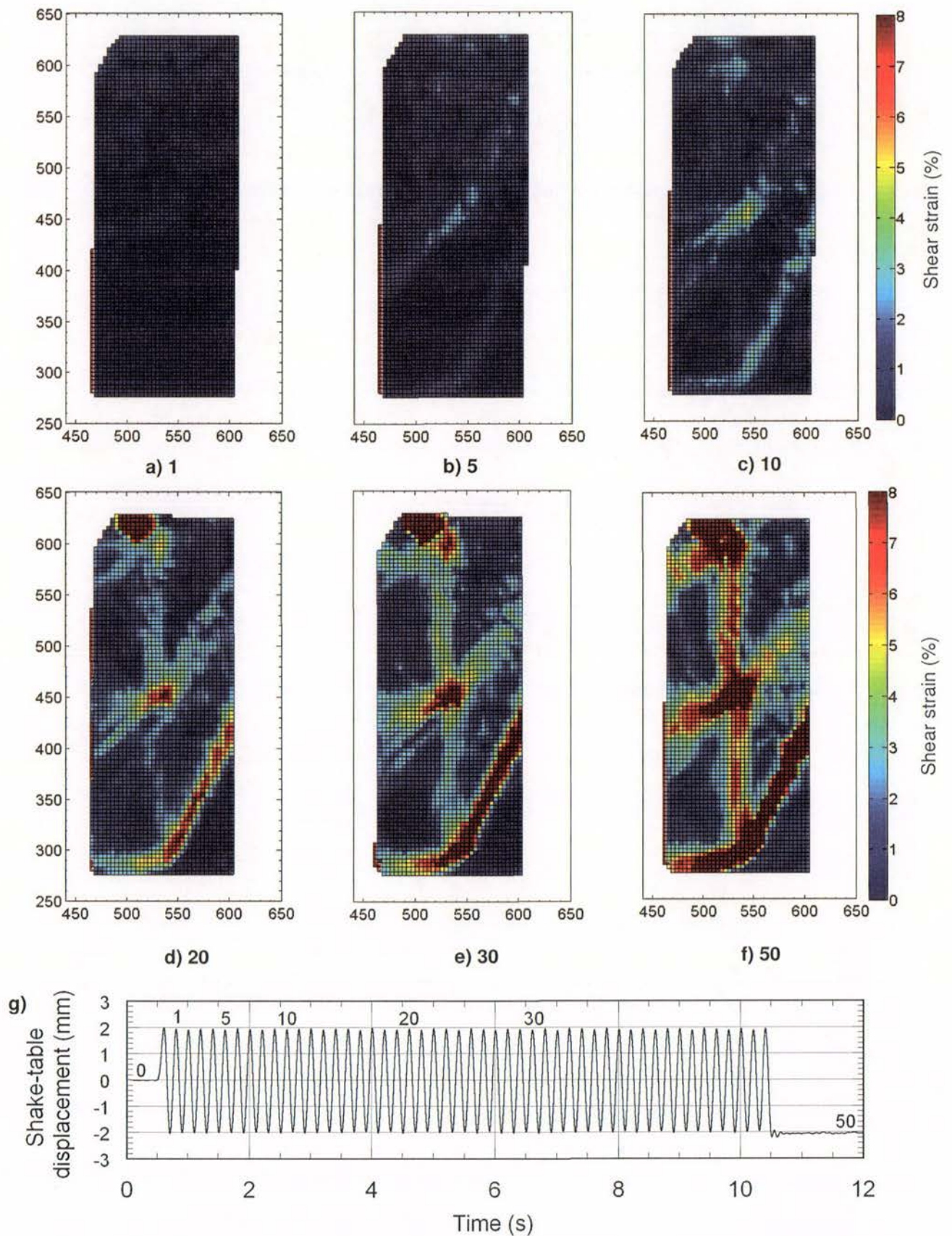


Figure 5-21. Shear strain accumulated during 0.2g shaking step and cycle peak: a) 1, b) 5, c) 10, d) 20, e) 30, f) 50. The cycle peaks are shown in the shake-table time-history (g).

Figure 5-21 shows the development of deformation *during* the 0.2g shaking step. There are several initial points to note with the derivation of the plots. Firstly, the shear strain is accumulated only during 0.2g shaking step, i.e. does not include any shear strain developed during the 0.1g shaking step. Secondly, the shear strain scale has been selected to coincide roughly with the likely shear strain developed at peak strength of Albany sand determined from previous triaxial tests conducted on the same Albany sand by Roper (2006). Hence, recorded shear strain larger than 8% indicate that the peak strength of the sand has likely been reached, and a degraded strength is likely to be mobilised along the shear surface. The shear surface could now be termed a 'failure surface'.

The GeoPIV analysis based on residual strains accumulated by the end of each shaking step shown in Figure 5-17 (b) noted two inclined shear surfaces which extended from the wall crest down to the back of the reinforced soil block and reinforcement layers, R3 and R2 at the end of 0.2g shaking. The figure appeared to show that the lower shear surface developed first as it had the larger shear strain value.

However the development of deformation during 0.2g step is clearly illustrated in Figure 5-21 (a) – (d) which shows, contrary to the residual analysis, that the shear surface which intersects with reinforcement layer R3 is developed first, not the lower surface intersecting with reinforcement R2. The development of the higher shear surface is surpassed by the lower surface by the 20<sup>th</sup> cycle of shaking at 0.2g. Only the lower failure surface was observed by the sand markers on completion of the 0.3g shaking step.

The following points are made with respect to the development of the lowest failure surface during 0.2g shaking step as shown in Figure 5-21 above.

- By the end of the 5<sup>th</sup> cycle (b), a very thin band with 2 – 3% shear strain accumulated was visible at the end of reinforcement, R2.
- By the end of the 10<sup>th</sup> cycle (c), this shear band grew in width and length and propagated both upwards into the retained fill and horizontally along the reinforcement layer, R2.
- By the end of the 20<sup>th</sup> cycle (d), around 8% shear strain was recorded along the failure surface and propagation of shear strain continued as described above for the rest of the shaking step, and, increased shaking steps.

Additionally, Figure 5-21 shows a near-vertical shear surface tracing the back of the reinforced soil block by the 10<sup>th</sup> cycle with roughly 2% shear strain accumulated. It can be seen that the rate of shear strain development along the vertical surface increased once the lowest inclined shear surface likely surpassed peak strength.

#### **5.5.4 Cyclic development of deformation**

GeoPIV is used in this section to show the development of shear strain during the first complete cycle of 0.2g shaking step of Test-6. This is shown in Figure 5-22 below. Five images were selected according to the shake-table displacement time history shown in the figure, such that the shake-table displacement started at its initial positive (left) position. Note that the colour scale has been reduced to 2% of shear strain to better aid in its visualisation.

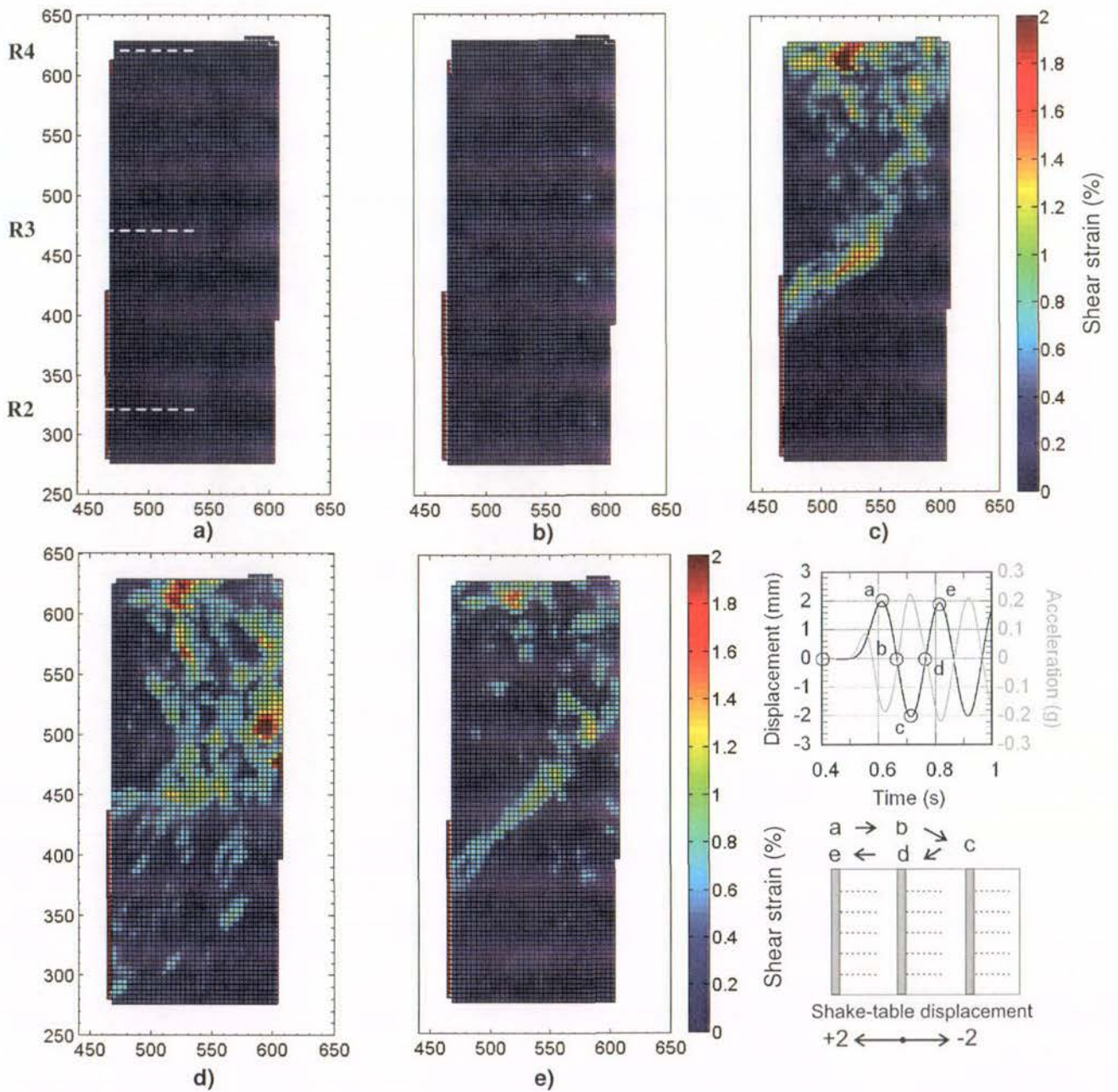
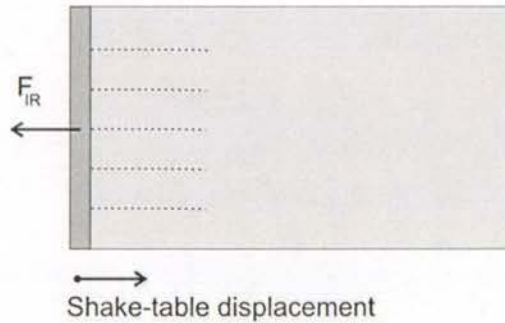


Figure 5-22. Shear strain developed within the first complete shake-table displacement cycle of the 0.2g shaking step for Test-6. The initial position of reinforcement layers R2, R3 and R4 are indicated with a dashed white line in (a).

It can be seen in Figure 5-22 (a) – (c) that, as expected, shear strain is developed within the interface region when the shake-table moves from left-to-right (positive to negative on the shake-table displacement time history). This corresponds to an acceleration time-history exactly opposite (from negative to positive). Hence outwards (positive) inertial forces are induced on the wall face as shown schematically in Figure 5-23.



**Figure 5-23.** Schematic showing the direction of shake-table displacement and the corresponding inertial force,  $F_{IR}$ , acting on the wall face.

Figure 5-22 (c) shows a peak strain of around 2% along the inclined shear surface. The wall is then displaced from the negative to positive (right-to-left) position, and this induces inertial forces acting in the opposite direction towards the backfill. These inertia forces act to stabilise the wall. Figure 5-22 (e) shows that some shear strain is recovered, in that the peak strain recorded along the shear surface is less than the previously recorded 2%.

In order to check whether the above trend of strain continues with further cycles, the strains accumulated within the first four cycles were plotted with GeoPIV and shown in Figure 5-25. Figure 5-24 shows the Displacement transducer (Disp 1) time history recorded at the wall face, and the timing of the images selected for the analysis. Peaks and troughs for cycles 1, 2, and 4 were selected because the facing displacement increased incrementally, whereas cycle 3 showed a reduced response which could have confused the analysis.

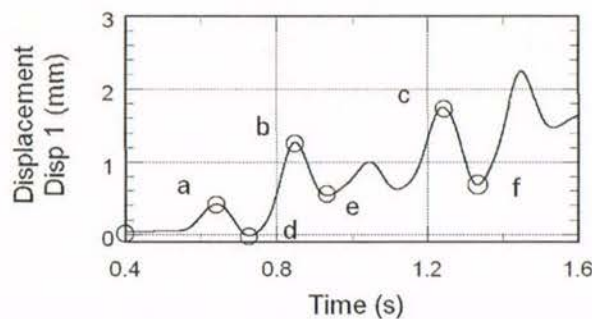


**Figure 5-24.** Selected peaks and troughs of facing displacement transducer Disp 1, for use in the GeoPIV analysis.

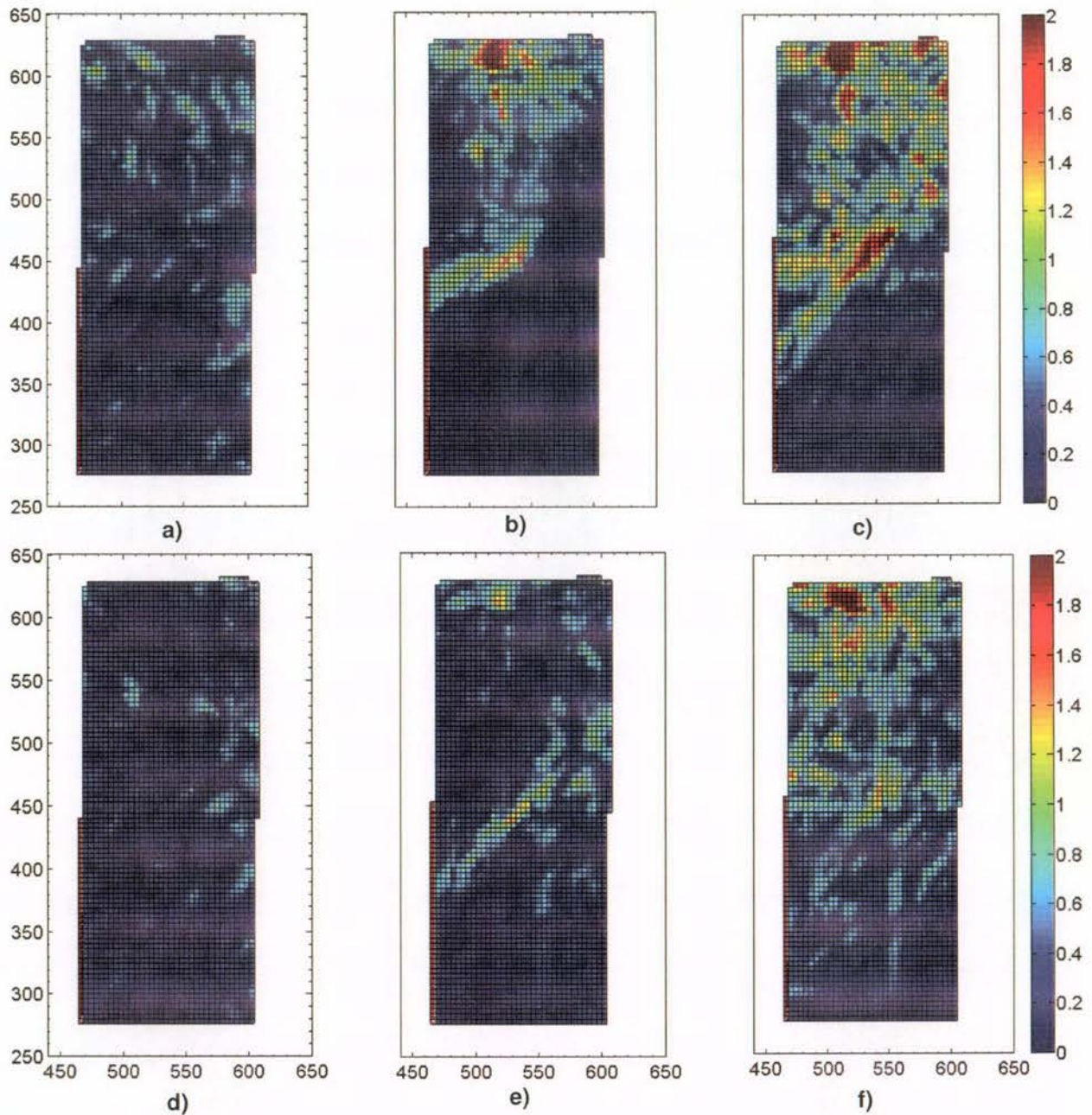


Figure 5-25. Shear strain developed within the complete first four cycles of the 0.2g shaking step for Test-6. The timing of the images was made to coincide with the peaks (a – c) and troughs (d – f) for cycles 1, 2, and 4, respectively, as shown in the attached facing displacement time history.

Figure 5-25 (a – c) show the strain accumulated by the facing displacement peaks, and (d – f) shows the strain accumulated by the facing displacement troughs. As seen, there was a steady accumulation of strain with each peak of cycles 1, 2, and 4 (a – c), and that some strain was recovered with each trough of the same cycle (a – d, b – e, c – f). Again, around 2% strain was localised at the reinforcement layer tips R3 and R4, and that the beginnings of horizontal and inclined failure surfaces became clear (c).

However, it should be noted that the plots show some scatter and the accumulation of strain at other locations is not totally clear. This is a function of the analysis accuracy (and low 2% scale selected), and possibly that the soil response itself was not initially well defined during the first few cycles of shaking.

### 5.5.5 Residual analysis on Tests-5 and 7 interface region

The residual shear strain accumulated at the completion of each shaking step for Test-5 and Test-7 are shown in Figure 5-27 and Figure 5-28 respectively. The "window" locations used by Cameras C1 and C2 for imaging are shown in Figure 5-26.

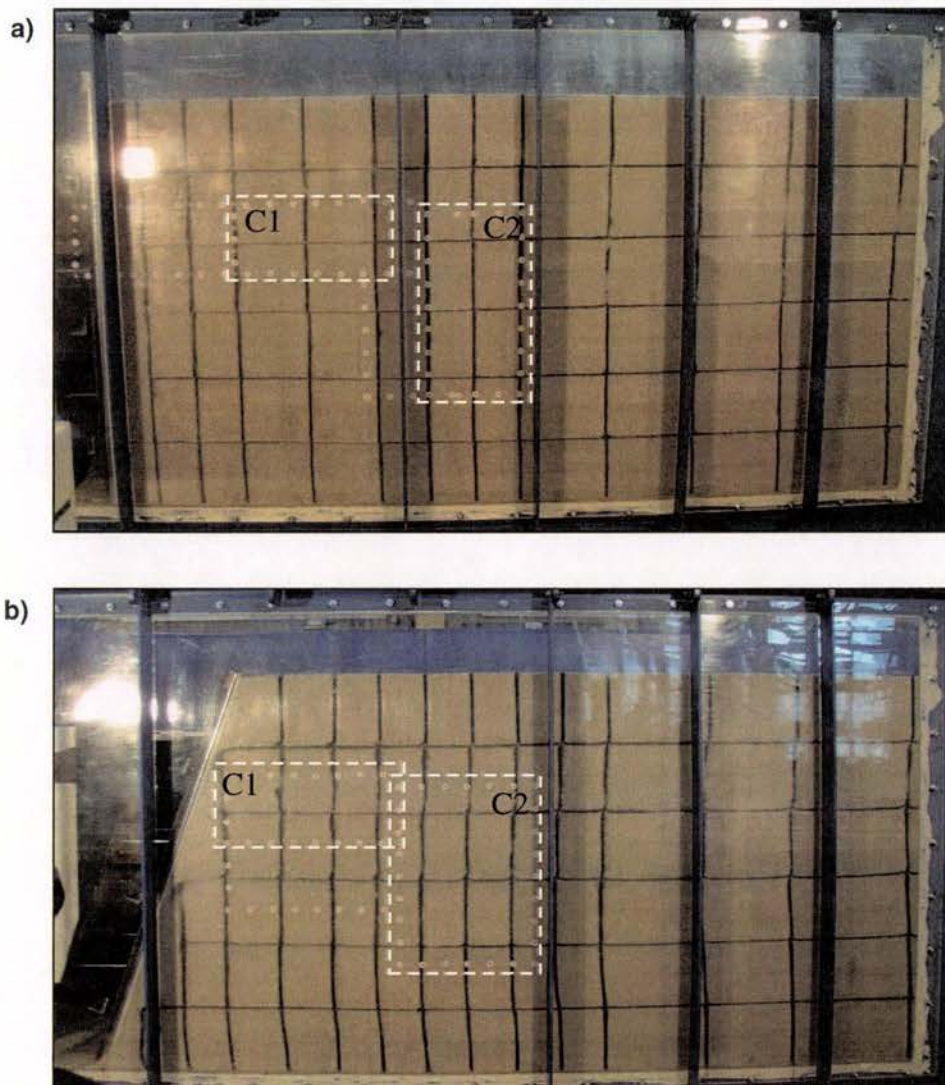


Figure 5-26. The "windows" (identified by dashed white lines) used for image capture by cameras C1 and C2 in Test-5 (a) and Test-7 (b), used for subsequent analysis using GeoPIV.

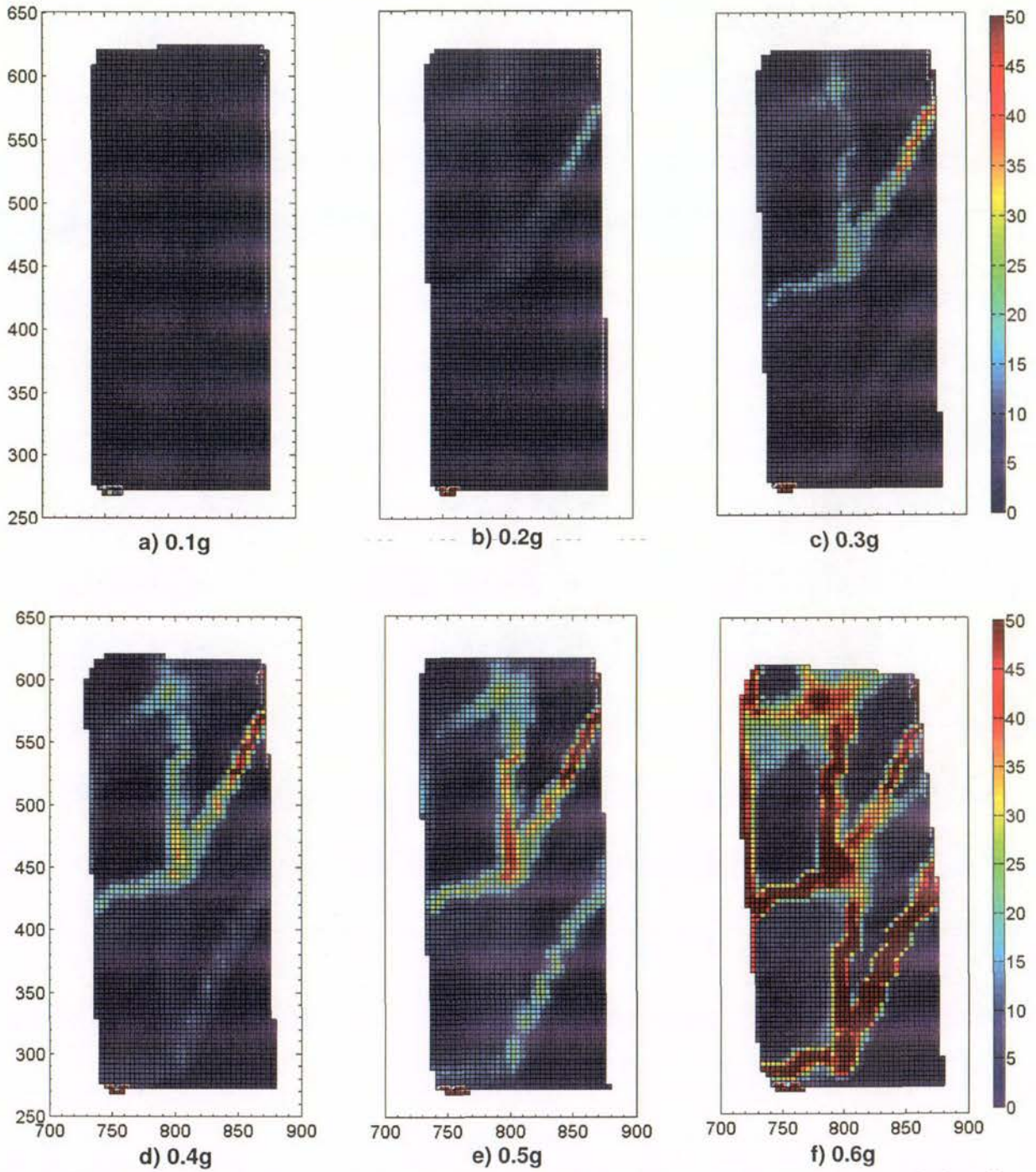


Figure 5-27. Maximum shear strain in Test-5 reinforced at  $L/H = 0.9$  accumulated by the completion of: a) 0.1g, b) 0.2g, c) 0.3g, d) 0.4g, e) 0.5g and f) 0.6g shaking steps.

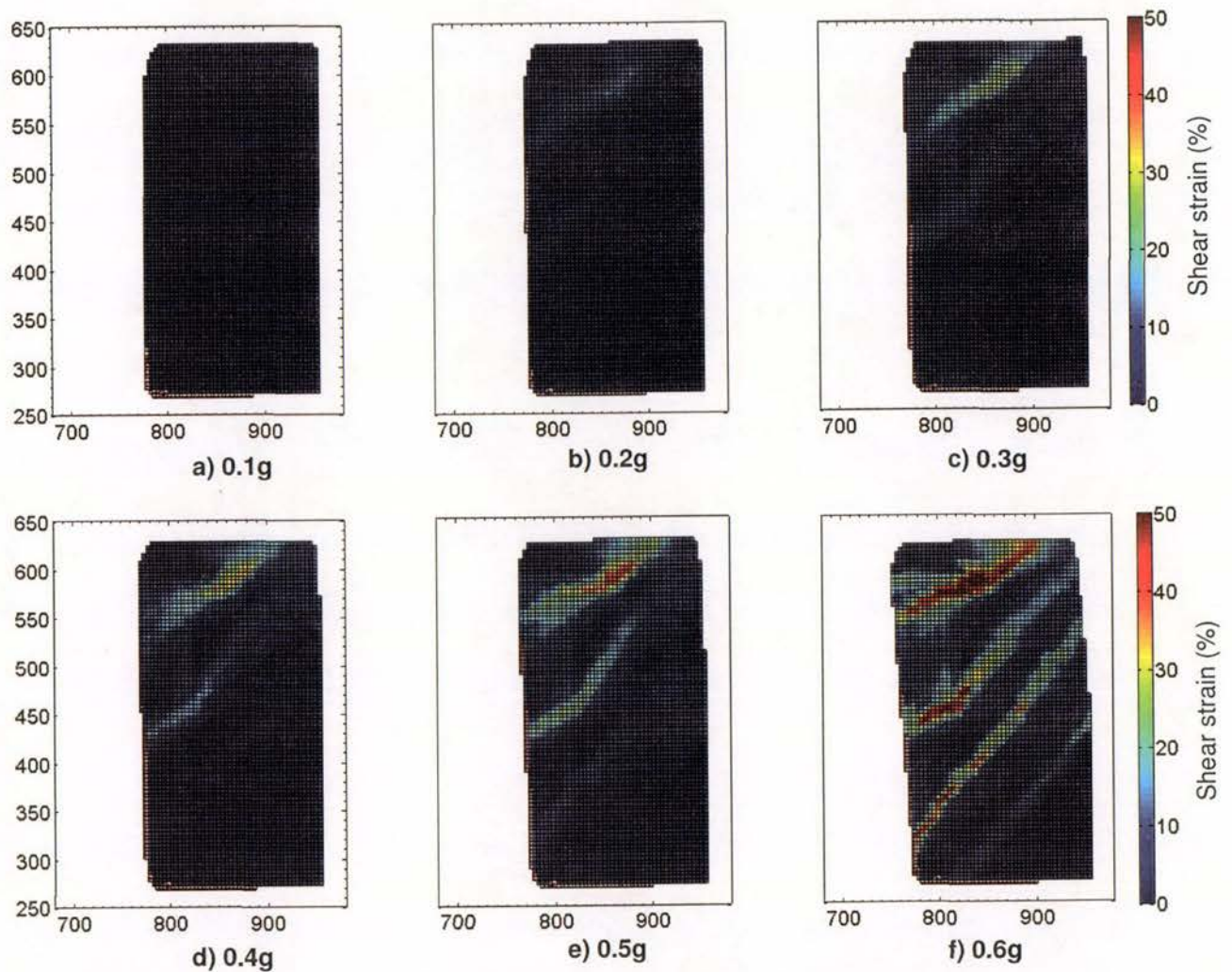


Figure 5-28. Maximum shear strain in Test-7 reinforced at  $L/H = 0.75$  and inclined at  $70^\circ$  accumulated by the completion of: a) 0.1g, b) 0.2g, c) 0.3g, d) 0.4g, e) 0.5g and f) 0.6g shaking steps.

Because GeoPIV can enable shear strains to be identified within the soil at far smaller levels than that rendered visible by the black sand markers, the spatial and temporal development of deformation as well as the complete deformation picture could be visualised.

The general progression of deformation for the vertically faced models is summarised below:

- Shear surfaces first occur at the soil surface and propagate deeper into the deposit, while new shear surfaces continue to develop.
- An inclined shear surface propagates downwards from the wall crest towards the back of the reinforced soil block (Figure 5-27 (b)).
- The failure surface propagates vertically upwards along the back of the reinforced soil block (Figure 5-27 (c)).

- In addition to propagating upwards, the failure surface also propagates: a) along the reinforcement layer and/or, b) at a shallow angle into the reinforced soil block (Figure 5-27 (c)).
- At continued shaking, the failure surface undergoes increasing shear strain (Figure 5-27 (c) – (f)); or,
- At larger acceleration shaking, the process is repeated and deeper failure surfaces propagate downwards towards the back of the reinforced soil block. (The angle of inclination remains approximately the same.) (Figure 5-27 (c) – (f)).

Similarly the development of deformation for the inclined wall in Test-7 is depicted in Figure 5-28 and demonstrates that the behaviour follows a similar pattern. However, there seems to be a decreased vertical interaction between the reinforcement layers, possibly because the reinforcement ends are staggered due to a constant reinforcement length attached to the inclined wall face (Figure 5-28 (f)). It is possible that this leads to the increase in stability noted in Section 4. This is likely due to increased difficulty in forming an active wedge behind the reinforced soil block.

### **5.5.6 Comparison of shear strain development within the interface region**

Figure 5-29 compares the development of strain accumulated by 0.3g shaking test for all Tests-6, 5 and 7. By the completion of the 0.3g shaking step, Test-6 (vertical wall reinforced  $L/H = 0.6$ ) had one well defined failure surface with a maximum shear strain around 50% which intersects with reinforcement layer R2. In comparison, Test-5 (vertical wall, reinforced  $L/H = 0.9$ ) had one defined failure surface at strain levels of around 20%, with the upper portion at 50% shear strain, and that this intersected with reinforcement layer R3. On the other hand, the inclined wall had one defined failure surface, at around 25% maximum shear strain, and this intersected with reinforcement layer R4.

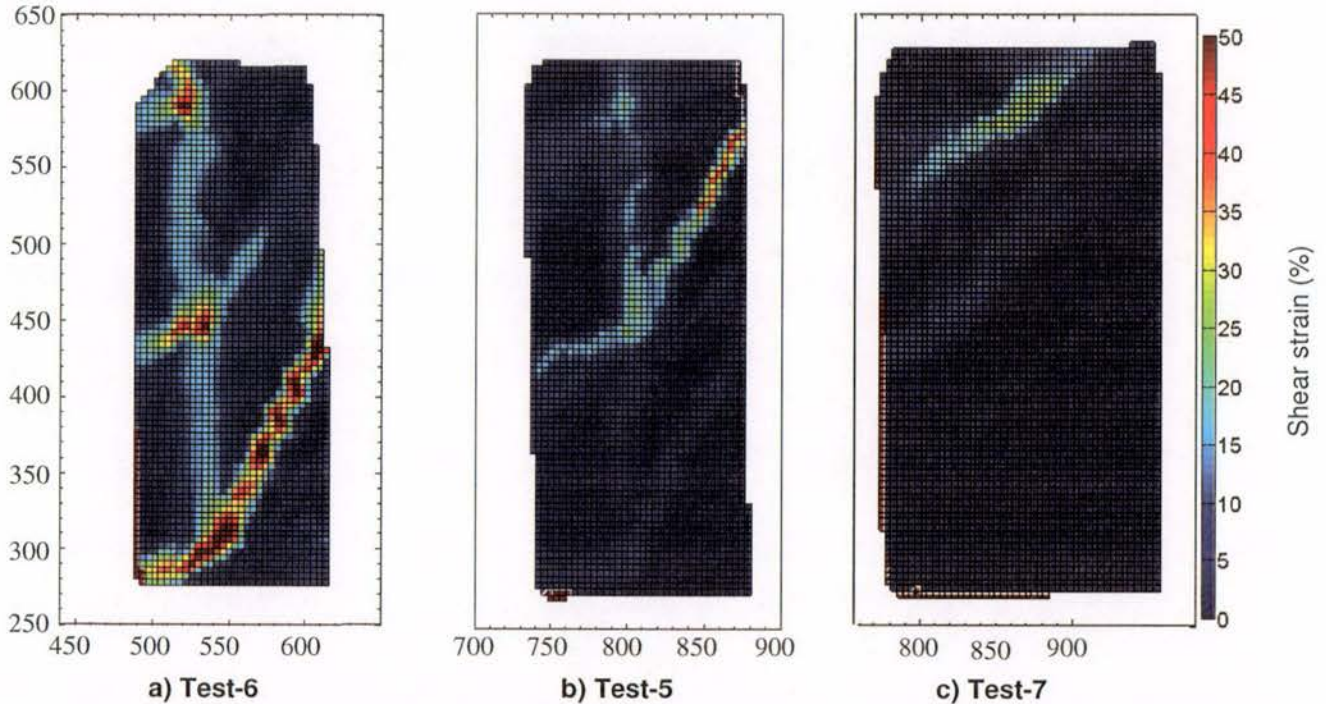


Figure 5-29. Comparison of residual maximum shear strain after 0.3g shaking step for Test-6 (a), Test-5 (b), and Test-7 (c).

The inclined wall accumulated the lowest maximum shear strain by 0.3g when compared to the other vertical walls, and this trend continued throughout further shaking. For instance, at 0.6g prior to failure, only the top most failure surface within the inclined wall had maximum shear strain along its length of around 50%, as compared to the vertical wall Test-5, which shows all visible failure surfaces to exhibit maximum shear strains larger than 50%.

The comparison shows that the development of deformation was more limited in the case of the inclined wall, at both low and high levels of shaking. Further, it is important to note that the inclined wall was only reinforced at  $L/H = 0.75$  (Test-7), shorter than that used for the vertical wall (Test-5 reinforced at  $L/H = 0.9$ ). This demonstrates the significant improvement in performance able to be gained from wall inclination.

## 5.6 Deformation of the reinforced soil block

### 5.6.1 Shear surfaces within the reinforced soil block

Figure 5-30 shows the reinforced soil block regions for Tests-5, 6, and 7. The originally vertical coloured sand marker columns, all show some rotation, and this corresponds to simple shear deformation of the reinforced soil block.

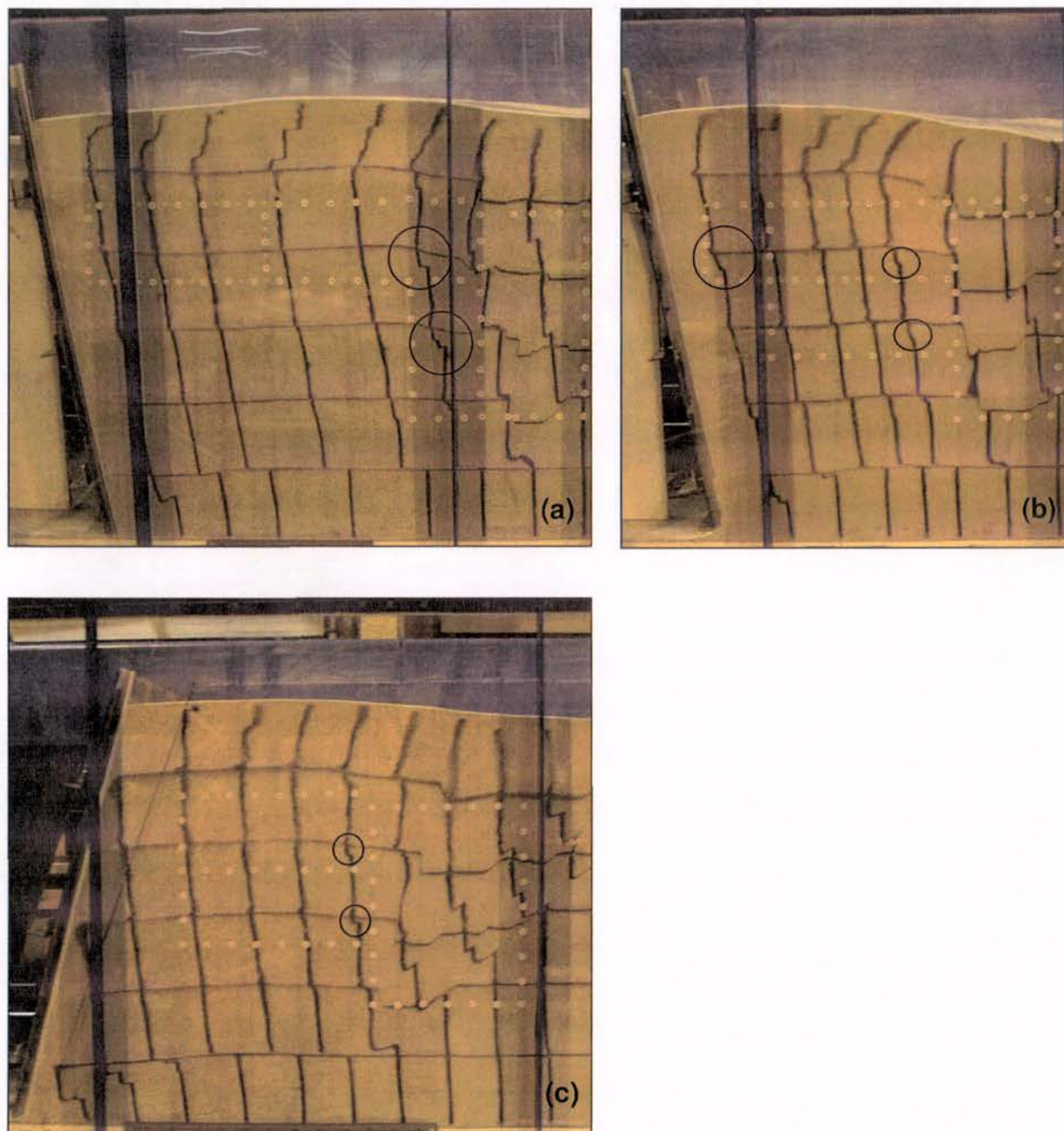


Figure 5-30. Comparison of reinforced block regions post-failure illustrating strain localisations within the reinforced soil block: (a) Test-5,  $L/H = 0.9$ ; (b) Test-6,  $L/H = 0.6$ ; (c) Test-7,  $L/H = 0.75$  and inclined  $70^\circ$  to the horizontal.

As observed by Watanabe et al. (2003) and Sabermahani et al. (2009) while the mode of failure is termed overturning, it actually comprises simple shear within each layer of the reinforced soil block, as the facing rotates about the toe. The mechanism of internal deformation of the reinforced soil block is shown in Figure 5-31.

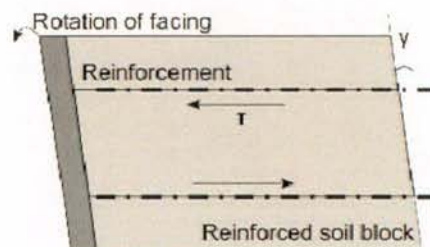


Figure 5-31. Simple shear deformation of the reinforced soil block.

Additionally, Figure 5-30 also shows irregular discontinuities evident in the vertical sand columns for all tests. The FHR facing and overturning mode causes localised shear deformation across the thickness of each reinforcement layer. It is possible that this shear strain will accumulate at localised weaknesses (shear bands), and not necessarily the soil-reinforcement boundary. For instance, localised failure surfaces are evident both at the front (e.g. (b) within the circles) and back (e.g. (a – c) within the circles) of the reinforced soil block. Additionally, dislocations along the reinforcement are readily visible for the shorter,  $L/H = 0.6$  reinforced soil block (b), but are not so apparent for the tests reinforced at a longer  $L/H = 0.9$  and  $0.75$ , (a) and (c) respectively.

Further, it can be seen for all tests that the ends of the reinforced block are dragged downwards as the wedge formed within the backfill slid down and along the failure surface. This was particularly visible for the longer reinforced Test-5 (Figure 5-30 (a)).

It should be noted that for the purposes of external stability and wave propagation, all design codes currently assume rigid block behaviour. This assumption is entirely contrary the behaviour observed above.

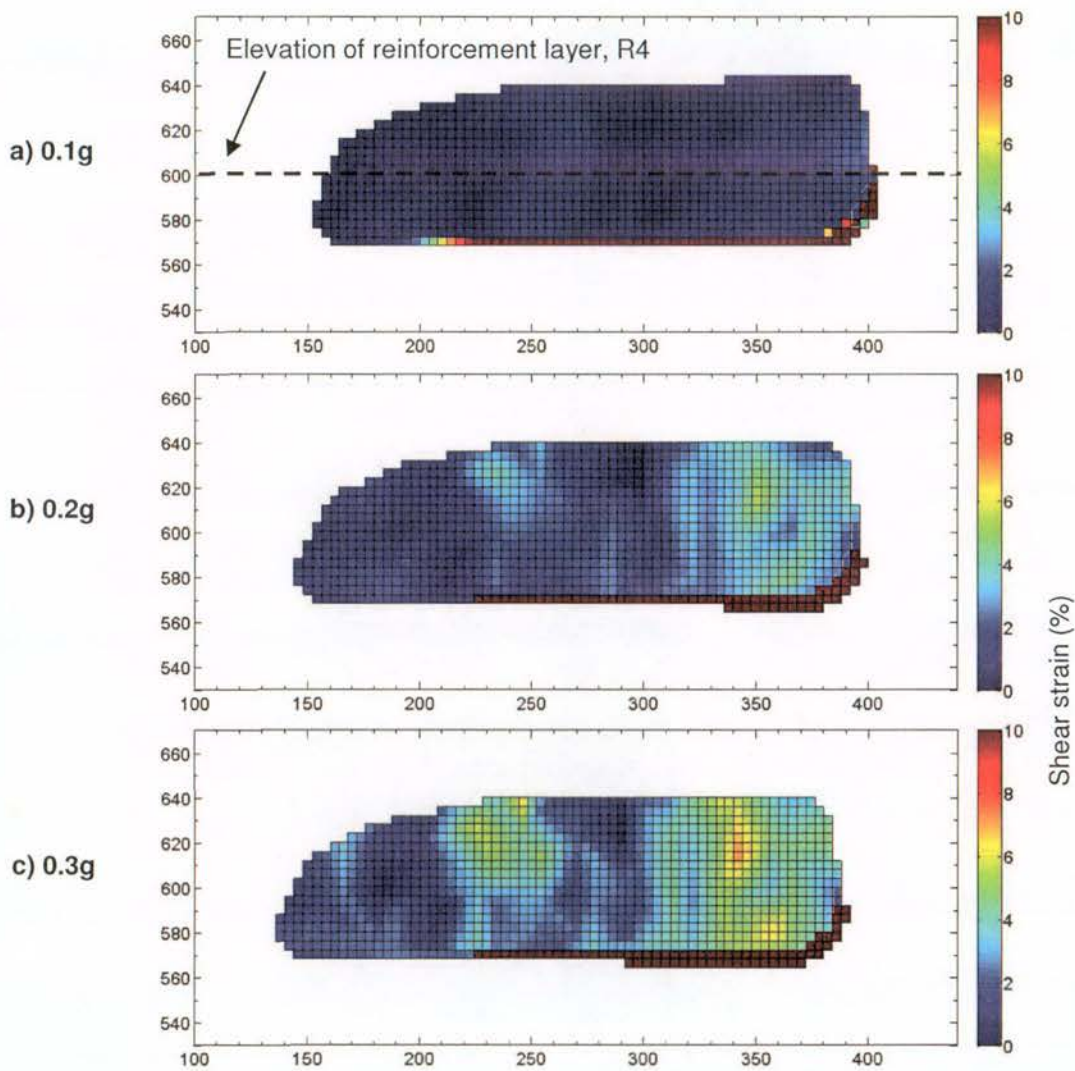
### 5.6.2 GeoPIV analysis of reinforced soil block

Figure 5-30 (a – c) shows that both simple shear, and localised strain deformation occurs along horizontal planes of the reinforced block for Tests-5, 6 and 7. To further investigate these observations, a second “window” wholly within the reinforced zone that straddled reinforcement layer R4, was investigated, as shown in Figure 5-9 and Figure 5-26. The 4<sup>th</sup>

layer of reinforcement was selected because design codes specify 60% of the wall height as the location of the largest dynamic earth pressure component.

For the GeoPIV analysis, patches sized 64 by 64 were used, larger than the 32 by 32 sized patches used for the analysis of the interface region above. While both cameras had similar resolution per square mm, the analysis with patches sized 32 by 32 for the reinforced soil region showed considerably more wild vectors than for the interface region. It is likely that the patches deformed during shaking, leading to erroneous displacement data. Additionally, some scratches were visible on the inside of the acrylic window, and this caused some patches to become 'stuck', rather than trace the actual soil displacement. Hence in order to overcome these limitations, patches sized 64 by 64 pixels were used for the analysis.

Figure 5-32 (a – d) shows the development of maximum shear strain at the completion of shaking steps 0.1g – 0.4g for Test-6. Appendix D displays this information at a lower scale.



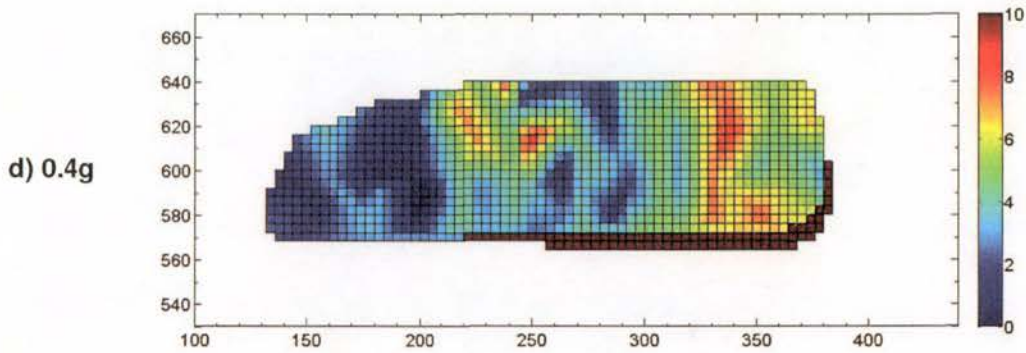
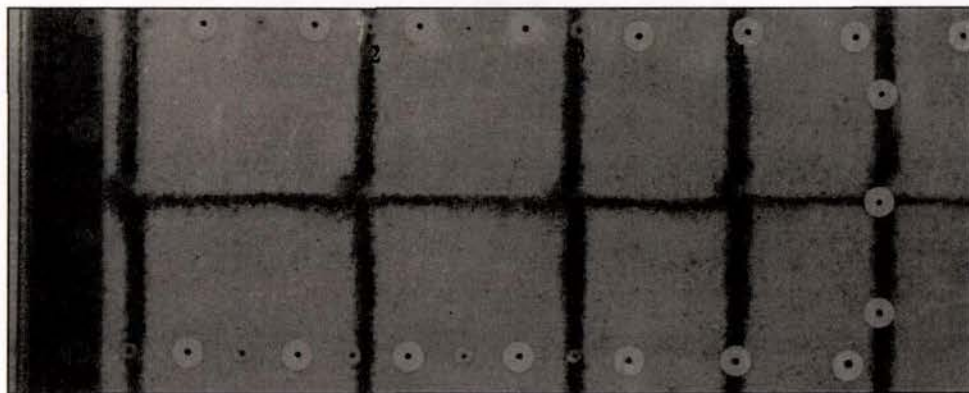


Figure 5-32. Maximum shear strain within the reinforced soil block at reinforcement layer, R4, for Test-6 reinforced at  $L/H = 0.6$  at the completion of: a) 0.1g, b) 0.2g, c) 0.3g, d) 0.4g.

Figure 5-32 (a) shows that some small maximum shear strain of up to 2% developed in two regions located both near the front and back of the reinforced soil block (225 mm and 325 mm from the initial braced position of the wall face) within the first 0.1g shaking step. After 0.2g shaking (Figure 5-32 (b)), the maximum shear strain within these regions was increased to 4 - 6%, whilst much of the upper window was subjected to shearing of approximately 2%. Areas of previous shearing were further developed during 0.3g and 0.4g shaking up to around 10% shear strain, with a background (global) average maximum shear strain of 3 - 4%.

Figure 5-33 shows the high-speed camera images used for the GeoPIV analysis taken at the beginning of testing (a), and end of 0.4g (b) and 0.5g (c) shaking steps. Figure 5-33 (c) shows how the block translates almost more than 100 mm during the 0.5g shaking step, and hence why shear strain was plotted only up to 0.4g (for reasons as discussed in Section 5.5).



1 2 3

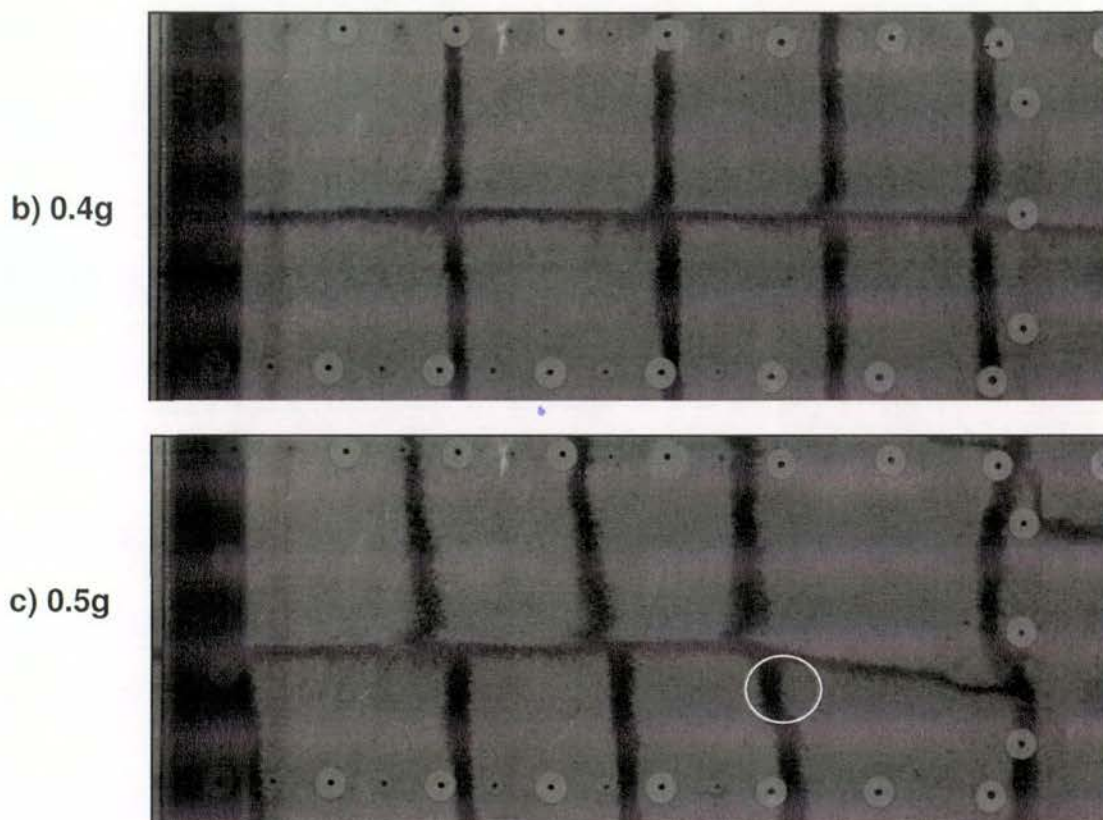


Figure 5-33. High-speed camera images used in the GeoPIV analysis of the reinforced soil block of Test-6: (a) before testing, (b) after 0.4g shaking step, and (c) after failure at 0.5g shaking. The vertical sand marker lines have been numbered to indicate the movement of these lines between shaking steps. Note that a strain localisation is visible in the 5<sup>th</sup> vertical marker line and has been circled.

Also shown in Figure 5-33 (c) is an apparent strain localisation (circled) visible in the coloured vertical marker line after the 0.5g shaking step. The GeoPIV analysis shown in Figure 5-32 shows a region of high shear strain after the 0.3g shaking step (c), near the back of the reinforced soil block from about 375 mm to 400 mm at an elevation of 550 mm to 590 mm. However, because the reinforced soil block translates and overturns significantly during the 0.5g shaking step this deformation has not been able to be shown clearly in the GeoPIV plots up to 0.4g.

Interestingly, a shear surface of similar elevation was also visible in the GeoPIV analysis of the interface region, post 0.3g, shown in Figure 5-17 (c). In this figure, an inclined surface appeared to enter the reinforced soil block at an elevation of approximately 580 mm. It is possible that this shear surface entered into the reinforced soil block and is shown in Figure 5-33 (c) though this is not clear.

In general, the maximum shear strain accumulated by 0.4g and plotted in Figure 5-32 (d) could be associated with the reinforced soil block undergoing simple shearing along horizontal planes (Watanabe et al. 2003). However, Figure 5-32 (a – d) indicates that the shear strain associated with this mechanism accumulated non-uniformly within the layer.

The simple shear within the reinforced soil block can be quantified using the rotational component of displacement recorded at the wall face. For instance, the rotational component of Test-6 calculated up to the 0.4g shaking step was 35 mm. Hence the average shear strain accumulated within the entire reinforced soil block of height 900 mm is calculated in Equation 5-3:

$$\gamma = \frac{\Delta\delta}{t} = \frac{35}{900} = 3.8\% \quad (5-3)$$

The 3.8% shear strain is a theoretical value of shear strain accumulated within the reinforced soil block over the entire wall height. Similar maximum shear strains are shown in the GeoPIV analysis shown in Figure 5-32 (d), with some regions of maximum shear strain higher than 3.8% apparent, as well as regions where no shearing has occurred.

To better understand the behaviour of the reinforced soil block prior to failure, the maximum shear strain,  $\gamma$  can be divided into its components: shear strain,  $\gamma_{xy}$ , and linear strains in the x and y directions,  $\epsilon_x$  and  $\epsilon_y$ , respectively. Figure 5-34 plots the maximum shear strain, (replotted for comparison, a) and those strain components just noted (b – d).

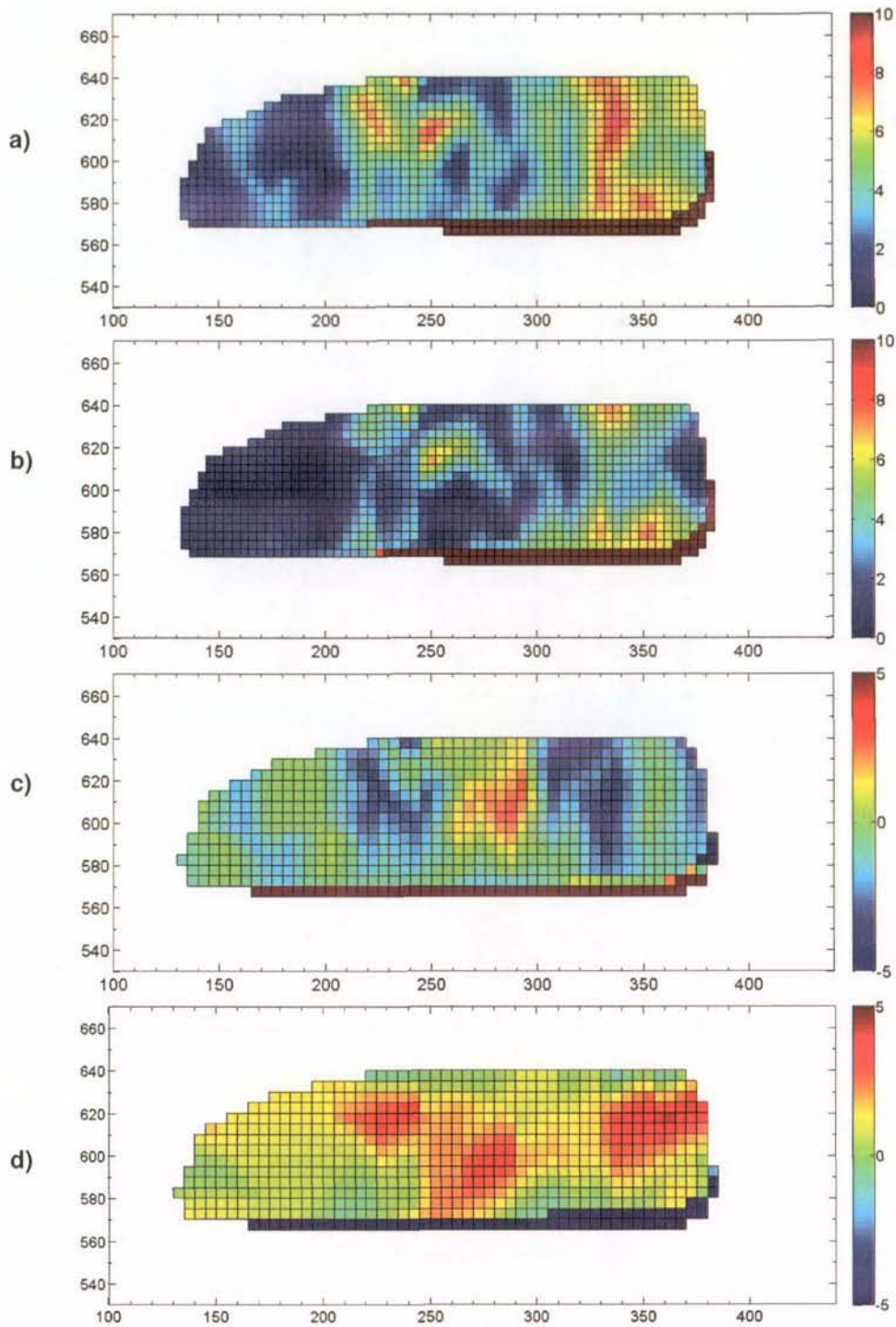
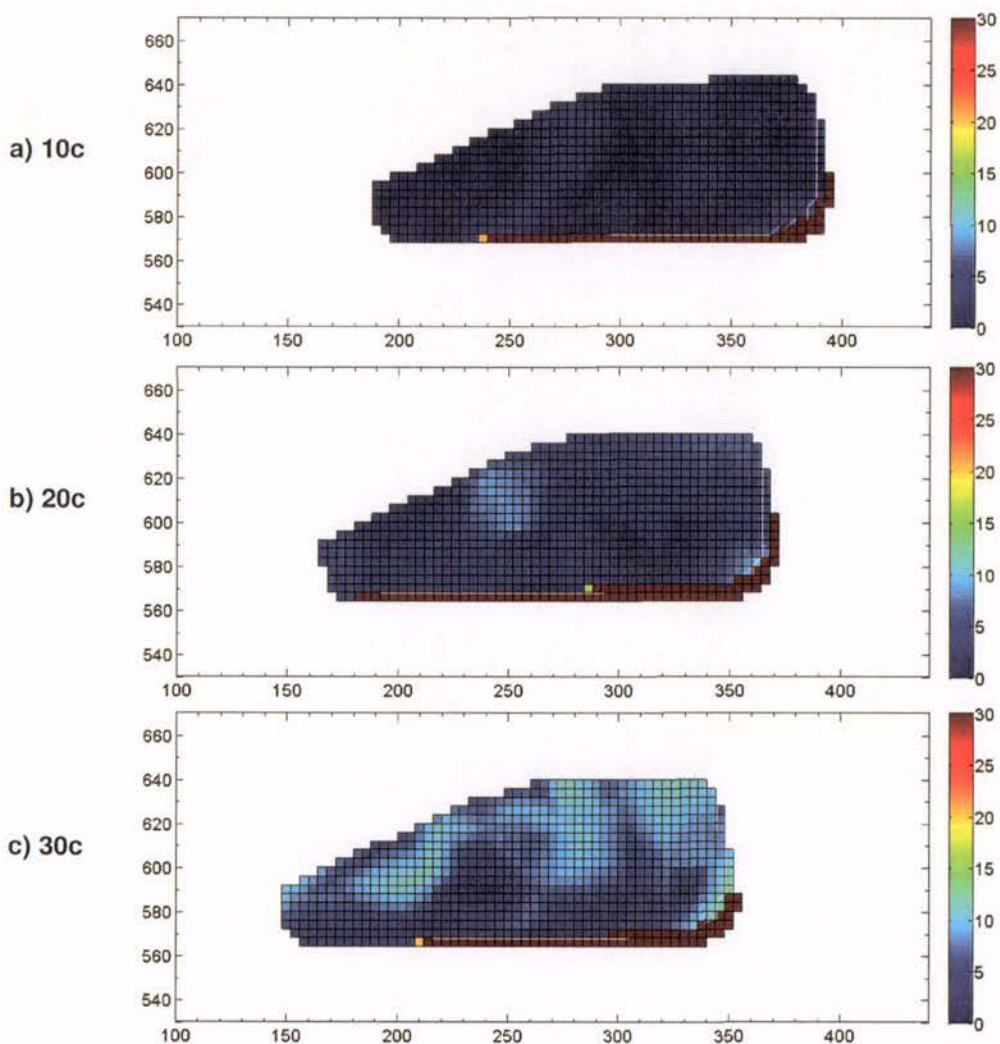


Figure 5-34. Components of strain accumulated up to 0.4g shaking step for Test-6: a) Maximum shear strain,  $\gamma$  (replotted for comparison), b) shear strain,  $\gamma_{xy}$ , c) linear strains in the horizontal direction,  $\epsilon_x$ , and d) linear strain in the vertical direction,  $\epsilon_y$ .

It can be seen in Figure 5-34 that the maximum shear strain (a) is comprised of shear and linear strains (b – d) combined by Equation 5-1. Figure 5-34 (b) shows a background shear

strain of 3 – 4%, which is consistent with that predicted assuming an average strain across the height of the wall. The linear strains in the horizontal direction are largely negative, which indicates extension of the soil along the layer of reinforcement as the block rotates out. The vertical linear strains are all positive, indicating compression in the vertical direction, and hence settlement of the soil within the reinforced soil block.

In order to understand the deformation during failure at 0.5g, GeoPIV was used to analyse the maximum shear strain accumulated *within* 0.5g shaking step. Figure 5-35 (a – e) plots the development of shear strain accumulated from the beginning of 0.5g, every 10<sup>th</sup> cycle through to the 50<sup>th</sup> cycle at the end of the test.



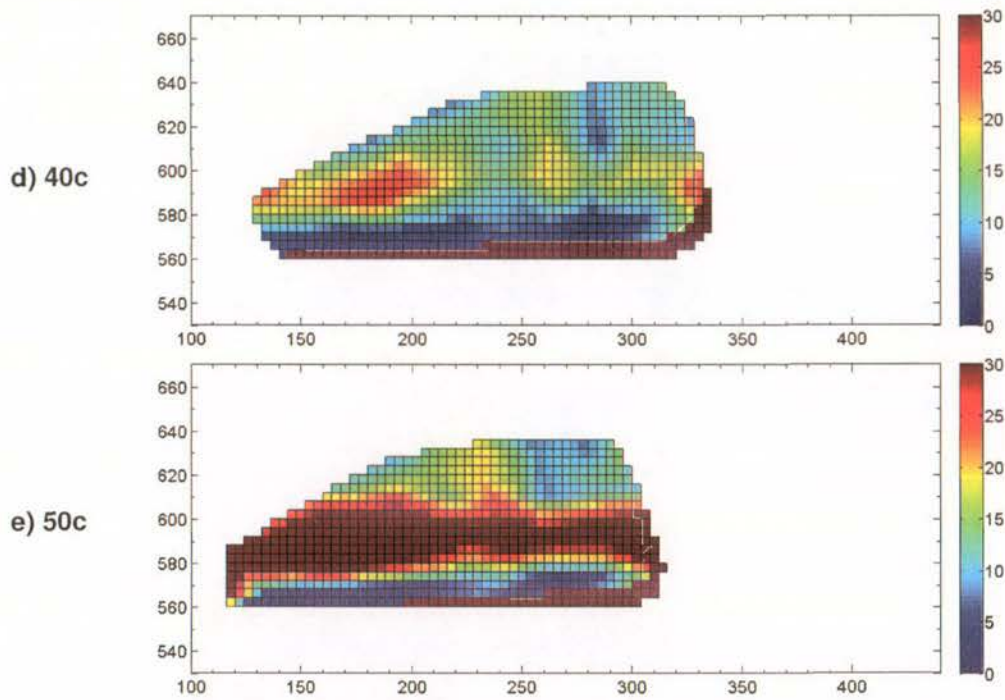


Figure 5-35. Development of shear strain during the 0.5g shaking step for Test-6.

Figure 5-35 demonstrates that, during the final shaking step at 0.5g, there are three mechanisms of failure within the reinforced soil block. The first is that of whole scale sliding, and (a – e) shows the strain plot to translate from the back of the “window” at around 400 mm, to 315 mm away from the original wall face. The second mechanism is the accumulation of simple shear with the general rotation of the wall about the facing toe. For instance, within the first 30 cycles, up 10% maximum shear strain has accumulated in the top half of the window. The third mechanism, which appears dominant between the 30<sup>th</sup> and 50<sup>th</sup> cycles shows a horizontal high strain localisation along the reinforcement layer of up to 30%, while the rest of the window exhibits lower maximum shear strains of between 5% and 20%. This mechanism is consistent with “pullout failure” of the reinforcement from the surrounding soil.

The local response around reinforcement layer R4 exhibited in the GeoPIV plots above can be compared with the global response of the entire wall. Figure 5-36 shows the geometry of failure of the Test-6 wall face during the final shaking step.

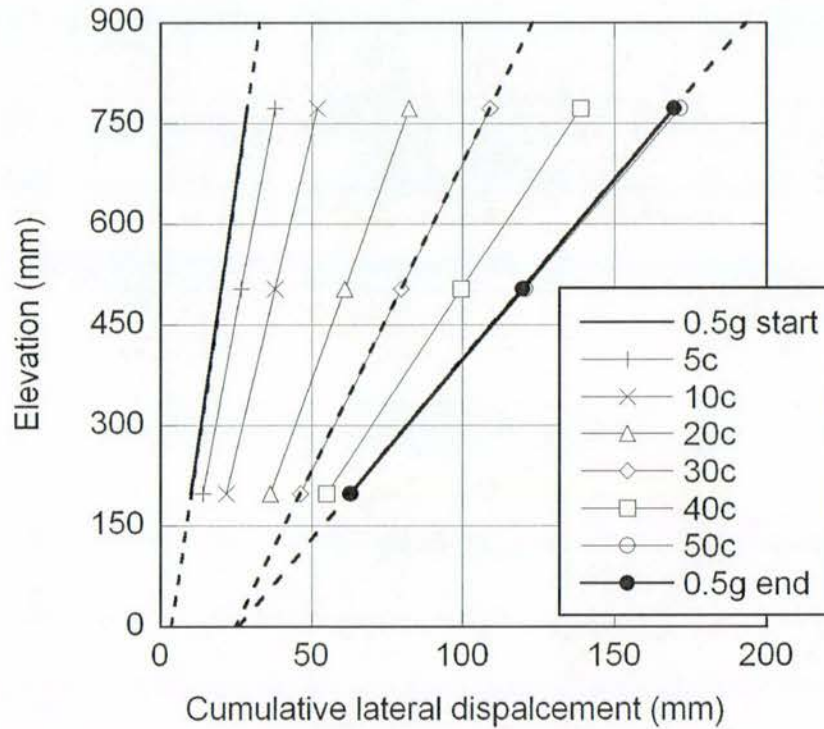


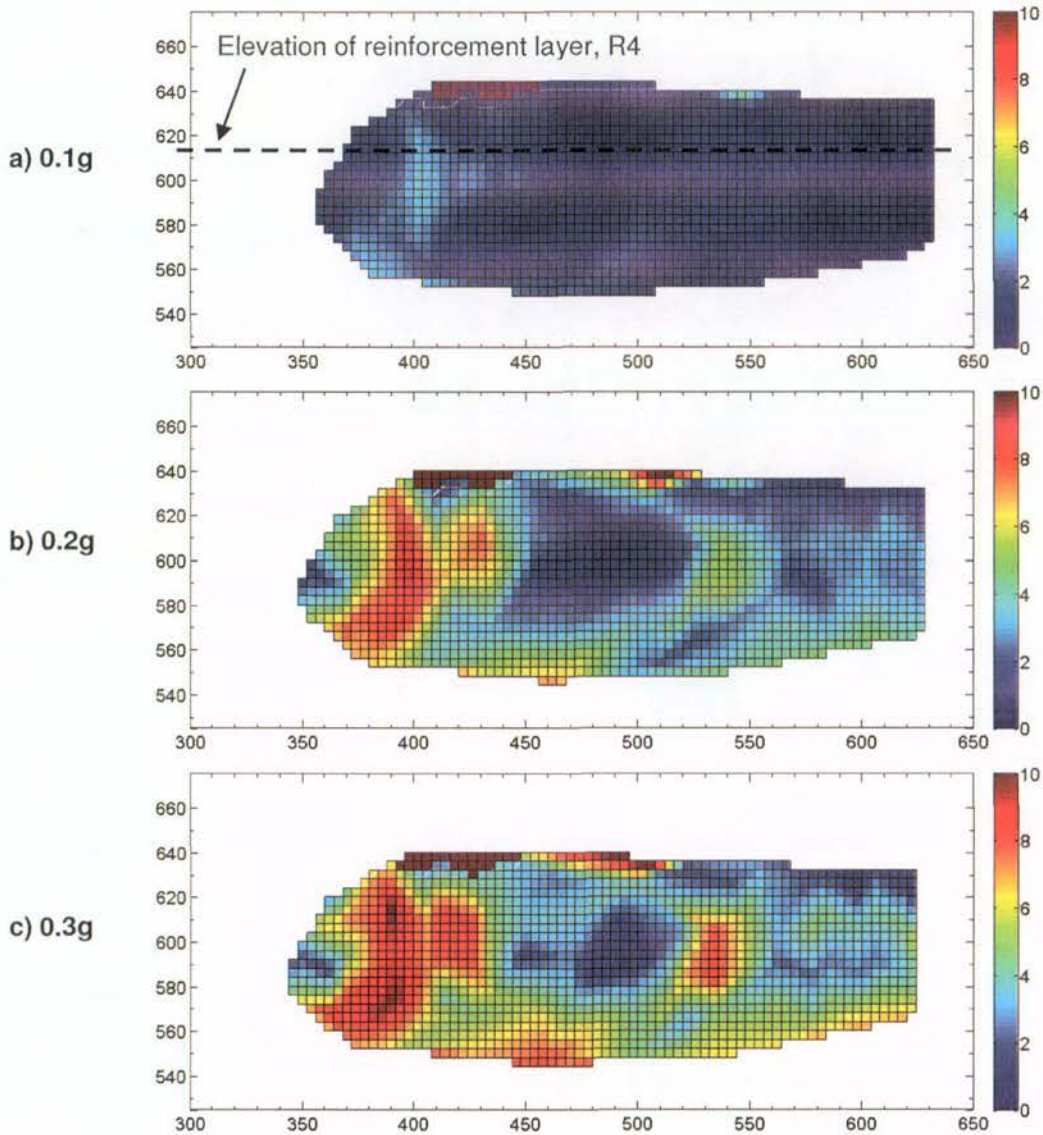
Figure 5-36. Geometry and mode of failure of Test-6 during 0.5g (final) shaking step.

As can be seen in Figure 5-36, both sliding and rotation occur within the first 30 cycles of shaking. However, during the final 20 cycles, only rotation of the wall face is present. This is reflected in the displacement time history (Section 4.3.5) which shows the rate of facing displacement increase within the last 20 cycles, most likely caused by the facing weight, and the added soil resting on the wall, contributing to an increased overturning movement and hence rate of rotation. This could have also led to a decrease in sliding, as evident. The influence of the facing weight could have contributed to the pullout failure made visible using GeoPIV.

Test-5 reinforced the longest at  $L/H = 0.9$ , displayed similar behaviour as to Test-6, in that the deformation accumulated somewhat non-uniformly within the reinforced soil block due to block rotation. However, during the final shaking step at 0.7g, there was no evidence for pullout failure as shown in Figure 5-35. The GeoPIV analysis of the reinforced soil block for the Test-5 is presented in Appendix D.

### 5.6.3 GeoPIV analysis of inclined reinforced soil block

The Test-7 reinforced soil block, which was inclined at  $70^\circ$  to the horizontal demonstrated a higher component of sliding compared to the vertical wall tests. This could be expected to change deformation patterns within the reinforced soil block itself. Figure 5-37 plots the maximum shear strain calculated using GeoPIV centred on reinforcement layer R4 horizontally from 300 mm to 650 mm from the original position of the facing heel.



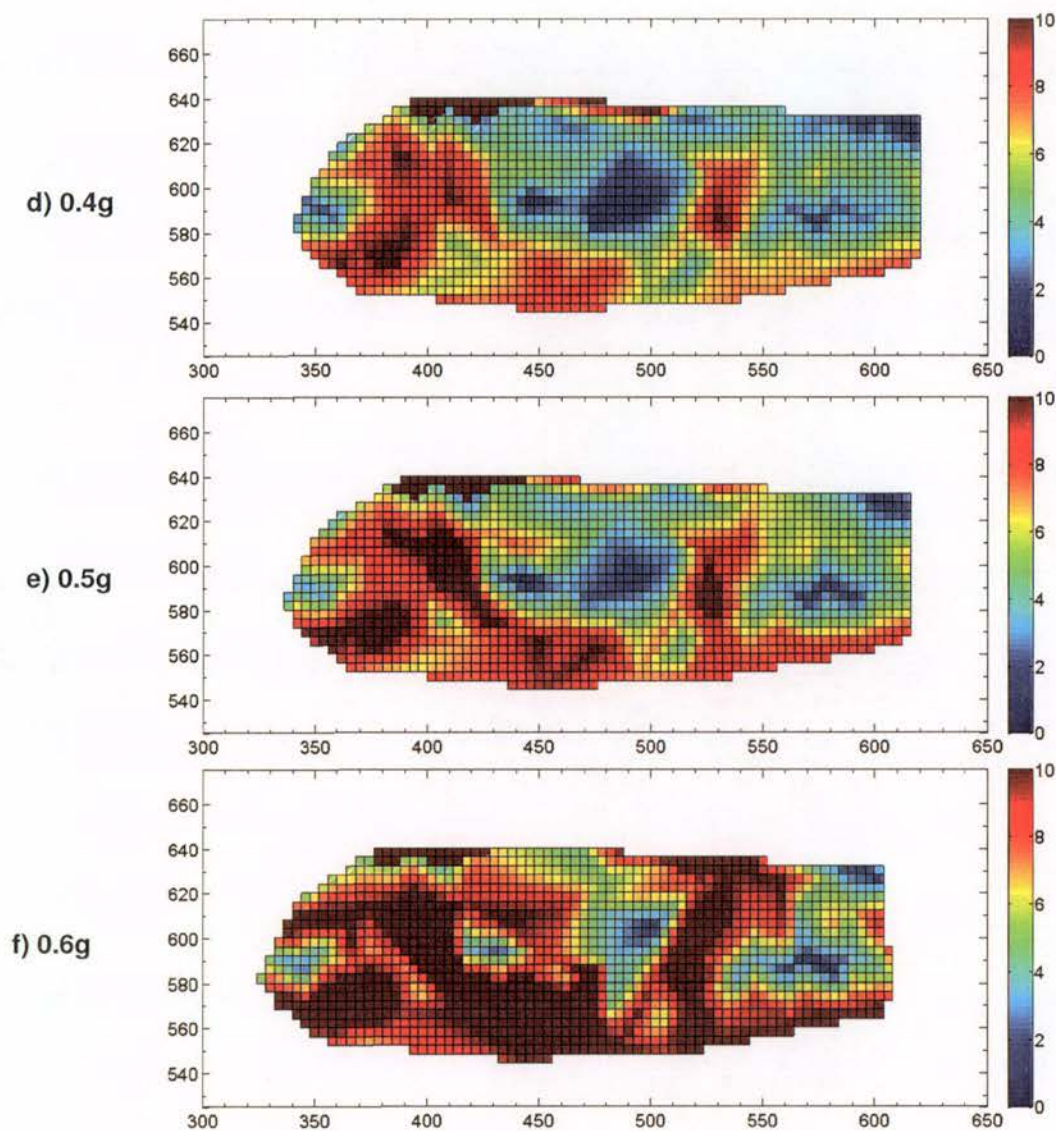


Figure 5-37. Maximum shear strain accumulated within the reinforced soil block by: a) 0.1g, b) 0.2g, c) 0.3g, d) 0.4g, and e) 0.5g shaking steps, centred on reinforcement layer, R4, for Test-7 reinforced at  $L/H = 0.75$  and inclined at  $70^\circ$  top the horizontal. Note that the 0.7g shaking steps are not plotted due to the large sliding component during these steps, impacting on the results as discussed.

Figure 5-37 shows that from 0.1g to 0.6g shaking step (a – c) regions of maximum shear strain around 10% are concentrated at the front of the “window”. Because the wall is inclined, at 600 mm elevation, the front of the “window” is only 80 mm from the back of the wall face, and this could led to the strain localisations here. Contrary to Test-6, no strain localisation along the reinforcement layer R4 (indicated by the dashed line in (a)) is apparent. The development of maximum shear strain during the final 0.7g shaking did not display any pull-out failure, and is presented in Appendix D.

Instead, Figure 5-37 (a – f) shows by the completion of 0.6g, a background (global) shear

strain of at least 3 - 4%, with pockets of high localised shear strain likely due to settlement proximate to the wall face. The background simple shear is generated by the rotation of the wall and was determined in Section 4.5.2 as 23.9 mm, which, over the 900 mm height of the wall corresponds to 2.6% shear strain. This strain is far lower than that observed using GeoPIV.

## 5.7 Idealised model for progression of deformation

### 5.7.1 General model of deformation for vertical walls

Two methods have been presented to show deformation pre- and post-failure. GeoPIV has been used to quantify small strains in selected regions prior at low shaking, and the horizontal and vertical sand markers have been used to show global mechanisms of deformation during and after ultimate failure. The complementary methods have been used to build a complete picture of the mechanisms of deformation for the GRS models under investigation. Figure 5-38 presents a general schematic of the development of deformation within a GRS wall undergoing increasing base input acceleration

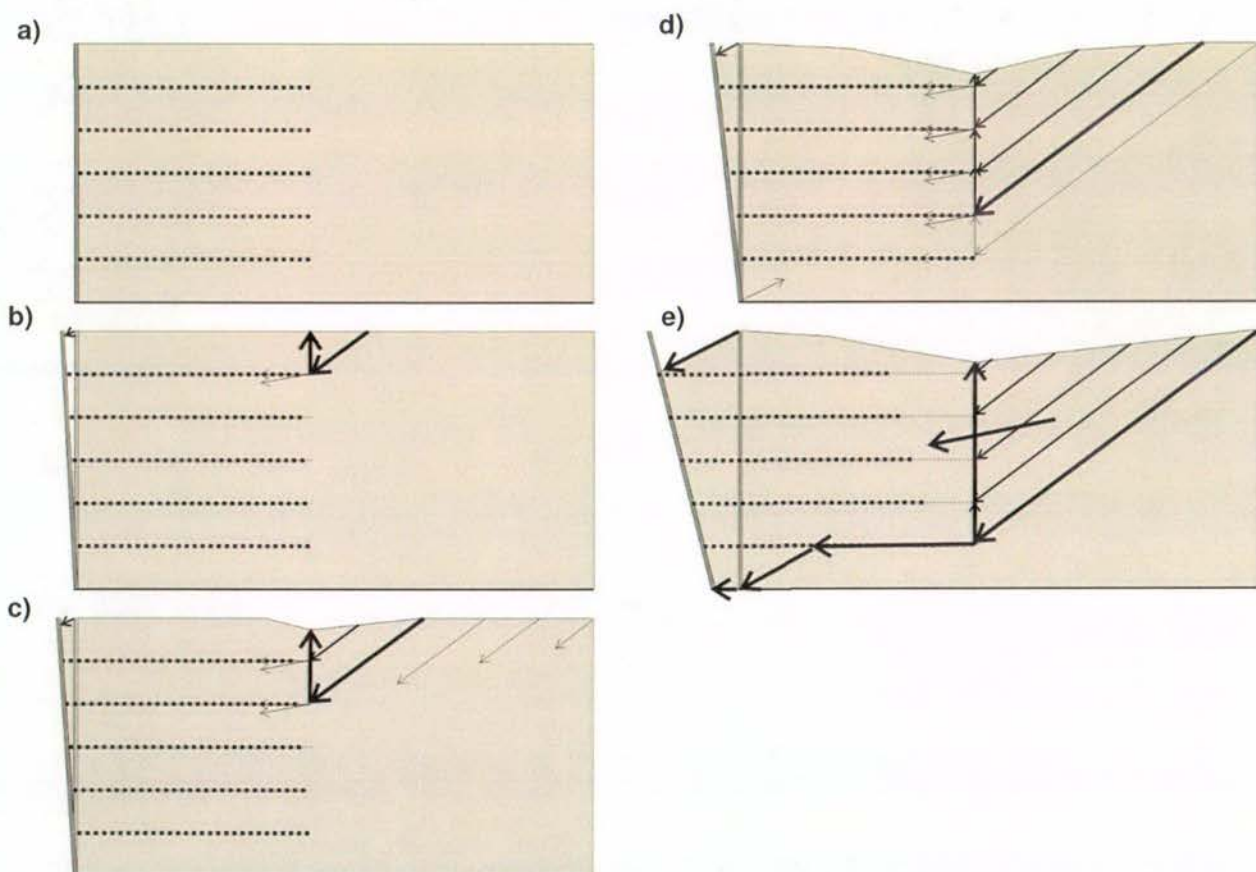


Figure 5-38. Idealised model of progression of deformation mechanism for GRS model walls undergoing increasing stages of seismic excitation from (a) to (e).

An explanation of the progression of deformation with increasing base excitation shown in Figure 5-38 is made with the following:

- a) The GRS wall prior to seismic excitation.
- b) Under the application of a small base acceleration, the wall rotates slightly, and concurrently a shear band begins to develop which extends from the wall crest down towards the tail of the top most layer of reinforcement, R5. A vertical shear band also starts to develop. Once the reinforcement tail has been reached, the shear surface is propagated horizontally along the weakest surface which could be either the reinforcement, or at some angle into the back of the reinforced soil zone, or both.
- c) Application of a higher acceleration causes another shear surface (at the same angle as before) to extend from the wall crest further within the backfill, down towards the back of the reinforced soil block to intersect with the tail of reinforcement layer, R4. Lateral movement of the face allows the active wedge to slide downwards, and this generates settlement behind the reinforced soil block.

Other shear bands beginning at the wall crest and inclined downwards to the tail of the reinforcement layer R4 are developed as the wall overturns.

- d) With application of continued and increasing base acceleration the wall overturns (with further settlement behind the reinforced soil block) and further shear surfaces are developed within the backfill. These are propagated downwards to intersect with the tails of reinforcement layers R3, R2 and R1.

Again, once the shear surface has reached the localised weakness of the reinforcement tail, the surface is propagated either horizontally along the reinforcement, at some angle into the back of the reinforced soil block, or both.

- e) Upon application of the critical acceleration, the final and lowest shear surface is developed until a failure surface is formed. In this case, the rigid foundation confines the soil at this elevation, and the weakest location for the failure surface to propagate is along the reinforcement layer R1.

Continued, or shaking larger than the critical acceleration, causes the active wedge to slide along the lowest formed failure surface. The wall face can then overturn. The active

wedge then slides into the back of the reinforced soil block; generating the largest settlement just behind the reinforced soil block. This movement may also drag the reinforcement tails downwards.

Note that depending on the exact size of each base acceleration step, various shearing surfaces may or may not develop. For instance under a larger acceleration than that applied in (b), the upper shearing surfaces may be skipped, to develop ones at a lower elevation.

Two points concerning the failure surface angles, and the absence of sliding prior to failure requires some explanation:

Firstly, MO theory predicts that the angle of the failure surface is reduced (becomes shallower) with increasing seismic coefficient of acceleration. Such is the case for a conventional gravity retaining wall, where the failure surface originates from the toe of the wall. However, in the current model tests on GRS walls with FHR panel facing, excepting the inclined test (Test-7), the angle of all failure surfaces were reasonably parallel, depending on the L/H ratio. It may be possible that the failure surface angle is related to the critical acceleration of each model, which depends upon stability due to the L/H ratio. For instance, because Tests-6 and 5 were reinforced differently, they failed at different acceleration levels, and hence developed shearing surfaces at different angles.

In contrast, despite different reinforcement L/H and geometry, Tests-5 and 7 both failed at 0.7g, having the same critical acceleration value. The failure surface angles formed in the final shaking step during failure at 0.7g were similar ( $\sim 40^\circ$ ). However, as shown in Figure 5-4, prior to 0.7g, Test-7 failure surfaces were shallower still at around  $30^\circ$ . The difference between the initial angles recorded for Test-7, and those formed subsequently, may be explained by considering that a structure's critical acceleration changes during an earthquake, with the associated change in soil properties and geometry. As the wall became more vertical after increasing shaking, its critical acceleration changed to that of Test-5, hence similar failure surface angles were formed.

Secondly, in the above idealised model, no sliding of the base occurs until a failure surface had formed which intersected with the lowest layer of reinforcement, effectively allowing the reinforced soil block to slide. This was largely verified by the experiments which show only minimal sliding at the wall face until failure occurred. This has also been noted in shake-table experiments reported by Koseki et al. (2006).

Additionally, because the foundation was rigid, there was no subsoil deformation which could contribute to base sliding. Hence, any sliding at the wall face, prior to the formation of the failure surface intersecting with the lowest reinforcement layer could be ascribed to soil-reinforcement interaction. That is, some “pullout” of the reinforcement has to occur before there can be sliding at the toe, and this was not readily seen.

### **5.7.2 Comparison of idealised deformation model with other research**

The general progression of deformation at low base accelerations (and therefore low strain levels) has been identified using GeoPIV. At these low strain levels, the shearing surface is often not visible with the use of coloured sand marker lines, and these are only capable of showing the development of deformation at larger strains, when “kinks” in the sand markers can be seen. Consequently, sand markers can readily identify progression of deformation near failure, and have been used in both the current and other experimental studies (Sabermahani et al. 2009; Watanabe et al. 2003) to identify failure mechanisms.

The general progression of deeper shear surfaces with increasing base acceleration has been observed in experimental studies by Watanabe et al. (2003) and Sabermahani et al. (2009). For instance, two out of the three tests conducted by Watanabe et al. (2003), display two failure surfaces, and in one test, the failure surfaces are not parallel. However, in numerous model tests (11 where the wall failed by overturning and not bulging, out of a total of 20 model tests) the multiple failure surfaces were reported to be parallel, largely confirming the above model.

Additionally, all of the failure surfaces observed by Watanabe et al. (2003) intersected with the lowest layer of reinforcement. In contrast, the failure surfaces observed by Sabermahani et al. (2009) did not extend to the bottom most layer of reinforcement. The difference in behaviour was most likely due to the difference in facing type. The former walls were faced by FHR panel, whilst the latter walls were faced by wrap-around facing. As stated in Section 1.4.2, Tatsuoka (2008) listed one of the main advantages of the FHR panel facing being that all reinforcement layers act in unison to resist deformation. Hence, it is likely that the wrap-around facing models (Sabermahani et al. 2009) failed before the bottom most layer of reinforcement was engaged, and thus no failure surface propagated down towards the bottom most layer of reinforcement.

### **5.7.3 General model of deformation for inclined walls**

The inclined wall follows largely the model as proposed for the vertical wall, except that, as noted in Section 5.6.3, there is reduced interaction between the horizontal layers of reinforcement, and no active failure wedge could form readily. It is for this reason, that the inclined wall demonstrated an increased stability, and a reduced displacement response of the wall top when compared to the other, vertical walls (where a near-vertical shear surface, and hence active wedge, could form easily).

In practice, the top few layers of reinforcement for GRS walls (vertical or otherwise) are often extended, to provide increased wall stiffness and prevent overturning failure (Tatsuoka 2008). In one of the model tests conducted by Watanabe et al. (2003), two of the reinforcement layers were extended; the top most and one just above mid-height of the model. This increased the acceleration required to generate failure by almost 0.1g more than the model with without any extended layers, but same other parameters. Watanabe et al. (2003) noted that the extended reinforcement resisted the formation of the failure plane, and governed strongly its location. It is likely that a similar mechanism contributed to the improved stability of the inclined model in the current tests, when compared to the vertical walls.

## **5.8 Summary**

Deformation within the GRS wall models was observed using a combination of coloured sand markers and GeoPIV. The former was found to be effective at recording mechanisms of ultimate failure, which by definition, occur at medium to large strains. The latter was found able to illustrate deformation at much smaller strains than that visible by eye. The GeoPIV analysis was able to readily show considerable deformation which had occurred during small amplitude shaking, previously not visible using only coloured sand marker lines.

GeoPIV was used to plot the strain field of two regions: the interface between the reinforced soil zone and retained backfill zone. For the interface region between zones, GeoPIV was used to show the development of deformation for the entire test of increasing acceleration shaking steps. This identified the existence of shearing surfaces at higher elevations within the retained backfill and at low acceleration levels.

For all models, failure was predominantly by overturning, with some sliding component.

This was accompanied by the development of inclined shear surfaces which started at the wall crest and extended down to the back of the reinforced soil block. With increasing acceleration amplitude, further surfaces were developed progressively deeper within the retained backfill. Vertical surfaces were also propagated near-vertically up the back of the reinforced soil block to allow the creation of an active failure wedge, and either along the reinforcement layer, or at some angle into the reinforced soil block.

Sliding was very small for accelerations less than the critical acceleration level, whereas at accelerations larger than this, sliding became significant. Failure of the model was observed when a failure surface developed (i.e. with associated post-peak reduction in shear resistance) from the wall crest and was inclined downwards towards the back of the reinforced soil block and intersected with the lowest layer of reinforcement. This mechanism then allowed the model to slide forward, with further overturning.

Failure was accompanied by the active wedge sliding downwards and into the back of the reinforced soil block along the failure surface, and as a result, the highest settlement occurred just behind the reinforced soil block. The block also exerted down-drag forces on the tails of the reinforcement layers, and these were observed to have dipped downwards after testing.

Interestingly, a near-vertical shearing surface, visible in all of the vertical walls tested, was not visible in the GeoPIV analysis of the inclined wall (Test-7) for low accelerations. Because the inclined wall had the same length of reinforcement, the ends of reinforcement did not line up. It is likely that this made it difficult for a vertical shearing surface, and thus the active wedge to develop, and this would have contributed to the increased stability of the inclined wall compared to the vertical walls. It should be noted that a near-vertical surface behind the reinforced soil block became visible at failure, as the wall had rotated enough for such a surface to form more easily.

GeoPIV was also used to show the development of deformation *during* a shaking step, and within a single cycle. The latter showed that deformation of the interface region was related to the inertia force acting on the FHR aluminium panel facing.

The second region considered by GeoPIV was the reinforced soil block, and this was found to be non-rigid for all tests. Whilst the mode of failure is classified as overturning, simple shearing of the reinforced soil block was visible along horizontal planes, not necessarily along the reinforcement layers. For instance, small dislocations in the vertical colour sand

marker lines in between reinforcement layers were visible. GeoPIV showed that the shear strain occurred non-uniformly across reinforcement layer R4, and that pockets of shear strain larger than that predicted using plane strain theory was recorded. This has ramifications for design, where the reinforced soil block is considered a rigid composite mass.

Additionally, pullout failure was shown to occur for one wall reinforced the shortest, during ultimate failure. This was likely due to the geometry of failure and an increase in the overturning moment acting on the wall face due to the facing weight, and soil resting on the back of the facing. This demonstrated the importance of facing weight contribution at during overturning failure.

The failure mechanisms observed agree largely with the two-wedge model proposed by Horii et al. (1994), and the results observed by coloured sand marker lines and GeoPIV were combined to create an ideal model for the progression of deformation for GRS walls with a FHR facing.

## References

- Adrian, R. J. (1991). "Particle imaging techniques for experimental fluid mechanics." *Ann. Rev. Fluid Mech.*, 23, 261 - 304.
- El-Emam, M. M., and Bathurst, R. J. (2004). "Experimental Design, Instrumentation and Interpretation of Reinforced Soil Wall Response Using A Shaking Table." *International Journal of Physical Modelling in Geotechnics*, 4 (2004), 13-32.
- El-Emam, M. M., Bathurst, R. J., and Hatami, K. (2004). "Numerical Modeling of reinforced soil retaining walls subjected to base acceleration." 13th World Conference on Earthquake Engineering, Vancouver, B.C. Canada.
- Fairless, G. J. (1989). "Seismic Performance of Reinforced Earth Walls," University of Canterbury, Christchurch.
- Fritz, H. M., Hager, W. H., and Minor, H. E. (2004). "Near Field Characteristics of Landslide Generated Impulse Waves." *Journal of Waterway, Port, Coastal, and Ocean Engineering*, 130(6), 287-302.
- Horii, K., Kishida, H., Tateyama, M., and Tatsuoka, F. "Computerized Design Method for Geosynthetic-Reinforced Soil Retaining Walls for Railway Embankments." *Recent Case Histories of Permanent Geosynthetic-Reinforced Soil Retaining Walls* Tokyo, Japan, 205 - 218.
- Howard, R., Kutter, B., and Siddharthan, R. "Seismic deformation of reinforced soil centrifuge models." *Geotechnical Earthquake Engineering and Soil Dynamics III*, University of Washington, Seattle, Washington, USA.

- Kim, H.-B., Hertzberg, J., Lanning, C., and Shandas, R. (2004). "Noninvasive Measurement of Steady and Pulsating Velocity Profiles and Shear Rates in Arteries Using Echo PIV: In Vitro Validation Studies." *Annals of Biomedical Engineering*, 32(8), 1067-1076.
- Koseki, J., Bathurst, R. J., Guler, E., Kuwano, J., and Maugeri, M. "Seismic stability of reinforced soil walls." *8th International Conference of Geosynthetics (8ICG)*, Yokohoma, Japan, 51 - 77.
- Koseki, J., Munaf, Y., Tatsuoka, F., Tateyama, M., Kojima, K., and Sato, T. (1998). "Shaking and tilt table tests of geosynthetic-reinforced soil and conventional-type retaining walls." *Geosynthetics International*, 5(1-2), 73-95.
- Ling, H. I., Leshchinsky, D., and Chou, N. N. S. (2001). "Post-earthquake investigation on several geosynthetic-reinforced soil retaining walls and slopes during the ji-ji earthquake of Taiwan." *Soil Dynamics and Earthquake Engineering*, 21(4), 297-313.
- Lo Grasso, A. S., Maugeri, M., and Recalcati, P. (2005). "Seismic Behaviour of Geosynthetic-Reinforced Slopes with Overload by Shaking Table Tests." *Slopes and Retaining Structures Under Seismic and Static Conditions (GSP 140)*, M. A. Gabr, J. J. Bowders, D. Elton, and J. G. Zornberg, eds., Austin, Texas.
- Matsuo, O., Yokoyama, K., and Saito, Y. (1998). "Shaking table tests and analyses of geosynthetic-reinforced soil retaining walls." *Geosynthetics International*, 5(1-2), 97-126.
- Murashev, A. K. (2003). "Guidelines for Design and Construction of Geosynthetic-Reinforced Soil Structures." Transfund New Zealand.
- Roper, M. (2006). "Applications and Procedures of Triaxial Tests." University of Canterbury.
- Sabermahani, M., Ghalandarzadeh, A., and Fagher, A. (2009). "Experimental study on seismic deformation modes of reinforced soil-walls." *Geotextiles and Geomembranes*, 27, 121-136.
- Sakaguchi, M. (1996). "Study of the seismic behavior of geosynthetic reinforced walls in Japan." *Geosynthetics International*, 3(1), 13-30.
- Tatsuoka, F. "Geosynthetic-reinforced soil structures: A cost-effective solution combining two engineering disciplines." *19th Carillo Lecture - Mexican Society for Soil Mechanics*, Aguascalientes.
- Tatsuoka, F., Tateyama, M., and Koseki, J. (1996). "Performance of soil retaining walls for railway embankments." *Soils and Foundations*(Special), 311-324.
- Watanabe, K., Munaf, Y., Koseki, J., Tateyama, M., and Kojima, K. (2003). "Behaviors of several types of model retaining walls subjected to irregular excitation." *Soils and Foundations*, 43(5), 13-27.
- White, D. J., and Take, W. A. (2002). "GeoPIV: Particle Image Velocimetry for use in geotechnical engineering." Cambridge University Engineering Department.

White, D. J., Take, W. A., and Bolton, M. D. (2003). "Soil Deformation measurement using particle image velocimetry (PIV) and photogrammetry." *Geotechnique*, 53(7), 619 - 631.

## **CHAPTER 6**

### **CONCLUSIONS AND RECOMMENDATIONS**

#### **6.1 Geosynthetic Reinforced Soil Walls**

Geosynthetic Reinforced Soil (GRS) systems enable shortened construction time, lower cost, increased seismic performance and potentially improve aesthetic benefits over their conventional retaining wall counterparts such as gravity and cantilever type retaining walls (see Fairless 1989; FHWA 2001; Murahsev 2003; El-Emam and Bathurst 2004 as examples). Further, soil reinforcement meets many of the goals associated with sustainable development such as reduced carbon emissions and embodied energy (Jones 1996; Tatsuoka 2008).

Experience in previous earthquakes such as Northridge (1994), Kobe (1995), and Ji-Ji (1999) indicate good performance of reinforced soil retaining walls under high seismic loads. During these earthquakes, significant damage of conventional retaining wall structures was reported, whilst reinforced soil structures demonstrated limited to no damage (Ling et al. 2001; Sandri 1997; Tatsuoka et al. 1996). However, this good performance is not necessarily due to advanced understanding of their behaviour, rather this highlights the inherent stability of reinforced soil against high seismic loads and conservatism in static design practices (White and Holtz 1997).

Hence the seismic performance of GRS walls has been the object of investigation in this study, and in particular the observation of the mechanisms and development of deformation

prior to failure. The influence of the L/H ratio and the inclination of the wall on seismic performance was also examined as these are two important design parameters.

A series of seven reduced-scale model tests was conducted using the University of Canterbury shake-table. The L/H ratio and wall inclination was varied from test to test and wall facing displacement, acceleration within the backfill, and deformations of the wall were measured during testing at varying levels of shaking intensity.

## **6.2 Conclusions from the experimental study**

The specific objectives of the project were to:

- Develop testing procedures for shake-table tests on GRS walls.
- Quantify the influence of the L/H ratio and wall inclination on seismic behaviour.
- Identify deformation patterns and failure mechanisms of GRS walls under seismic loading.
- Identify critical issues for further research studies.

### **6.2.1 Shake-table tests**

Based on previous model studies on reinforced soil, a strong box 3.0 m long, 0.8 m wide and 1.1 m high was constructed. The box included a 20 mm thick transparent acrylic window, which enabled visual observation of failure patterns within the physical model. A procedure for the construction and testing of reduced-scale GRS wall models on the University of Canterbury shake-table was also developed.

The five most important considerations for the experimental design were as follows:

- The model was constructed in 12 layers, each 75 mm thick, up to the required 900 mm soil deposit height. The soil deposit (Albany sand) was compacted by vibration of each layer by the shake-table and a weighted steel plate placed on top of the layer. The wall face was braced during model construction, which was then removed prior to testing. A reasonably consistent model relative density was achieved across all tests, and the average relative density of the models was 92%.

- The model was faced by an FHR panel, and the model was reinforced with a stiff Microgrid reinforcement. A rigid connection between the facing and reinforcement was ensured. These details were representative of GRS walls with FHR facing for the observation of deformation patterns and ultimate failure.
- In addition to accelerometers within the backfill and displacement transducers at the wall face, the experiment also utilised high-speed cameras to record deformation within the backfill during testing. The captured images were analysed using GeoPIV for interpretation of deformation prior to, and during failure.
- Care was taken to develop procedures for experimental details such as model preparation, the seal between the wall face and box sidewalls, and construction of vertical and horizontal coloured sand marker lines.
- A series of seven model tests were conducted and the reinforcement ratio  $L/H$  and the wall inclination were varied. Facing displacements, accelerations within the backfill, settlements, as well as deformation observations within the backfill were made. Importantly, the experimental design allowed the effect of model parameters such as  $L/H$  and wall inclination on model behaviour to be observed.

### **6.2.2 Influence of $L/H$ ratio and wall inclination on seismic performance**

The experimental series involved a parametric study which varied the  $L/H$  ratio between  $L/H = 0.6, 0.75$  and  $0.9$ , and wall inclination from the vertical, to  $70^\circ$  with the horizontal over four tests, namely Tests-1, 5, 6, and 7. The testing regime involved subjecting the models to successively increasing base excitation in 10 second duration steps, with a sinusoidal acceleration wave of frequency 5 Hz. At each stage, the amplitude of shaking was increased by 0.1g, with the initial shaking at 0.1g. The following conclusions are made with respect to an increase in the  $L/H$  ratio from  $L/H = 0.6$  to  $0.9$ , across Tests-6, 1, and 7, respectively.

- An increase in the  $L/H$  ratio increased both the critical acceleration (and by definition, the acceleration at which ultimate failure occurred) from 0.4 to 0.6g. Thus a 50% increase in  $L/H$  ratio resulted in an increase of the acceleration level at which failure occurred by 40%.

- An increase in the L/H ratio caused the displacement-acceleration curve to be shallower, and hence the wall deformed less at low levels of acceleration.
- An increase in L/H ratio resulted in a reduction in the amplification of accelerations within the backfill prior to, and during failure. This can be attributed to the longer reinforcement generating an increase in stability.

The following conclusions are made with respect to a decrease in wall inclination from the vertical (Tests-1 and 7).

- A decrease in wall inclination from  $90^\circ$  to  $70^\circ$  to the horizontal, increased the critical acceleration (and by definition, the acceleration at which ultimate failure occurred), from 0.5g to 0.6g.
- A decrease in wall inclination caused the displacement-acceleration curve to be shallower, and hence to deform less at low accelerations levels, than the vertical walls.

### **6.2.3 Development of deformation**

All models were observed through the transparent acrylic window on one side of the strong box during testing. For all models, failure was predominantly by overturning, with some sliding component. For all tests, sliding was very small for accelerations less than the critical acceleration level. For accelerations larger than the critical acceleration level, sliding was significant.

Two methods for the observation of deformation were employed. The first of these methods utilised horizontal and vertical coloured marker lines of sand placed within the backfill during construction. Dislocations in the coloured marker lines were able to show failure mechanisms which formed at medium to large strains.

The second of these methods utilised high-speed camera imaging during testing of two regions within the soil deposit: 1) centred on the second reinforcement layer from the top, and 2) the interface between the reinforced soil block and the retained backfill. These images were then analysed with Geotechnical Particle Imaging Velocimetry (GeoPIV) software. GeoPIV was able to show deformation which developed at low acceleration levels (small

strains), not visible by the naked eye. GeoPIV therefore provided a more complete picture as to the development of deformation.

With both of these methods, an idealised model for the progression of deformation with increasing base acceleration was presented. The model basically confirms the use of the two-wedge mechanism for ultimate failure.

Overturning of the wall was observed to be accompanied by inclined shear surfaces which started at the wall crest and extended down to the back of the reinforced soil block. With increasing acceleration amplitude, further surfaces were developed progressively deeper within the retained backfill. Upon reaching the back of the reinforced soil block, these surfaces were propagated upwards to allow the creation of an active failure wedge, and either along the reinforcement layer, or at some angle into the reinforced soil block.

Failure of the model was only initiated when a failure surface developed (i.e. with associated post-peak reduction in shear resistance) from the wall crest and was inclined downwards towards the back of the reinforced soil block and intersected with the lowest layer of reinforcement. This mechanism then allowed the model to slide forward, with further overturning, until failure occurred. This was accompanied by the active wedge sliding downwards and into the back of the reinforced soil block along the failure surface, and as a result, the highest settlement occurred just behind the reinforced soil block.

The inclined model demonstrated similar behaviour, with only slightly more sliding components before and after failure. For instance, sliding contributed to 40% of the total displacement of the wall top, compared to only 30% for the vertical walls. Again, the active wedge slid down the failure surface and into the back of the reinforced soil block, however this movement was observed to be slightly rotational.

With the inclined test, the length of reinforcement was kept constant, and this resulted in a back-tilted reinforced soil block, with the ends of reinforcement also inclined. It should be noted that vertical failure surfaces appeared to form with difficulty because of this. Hence an active failure wedge was not formed easily until the wall had overturned some, and this may have contributed to it having the shallowest and lowest acceleration-displacement curve, and resultant increased stability.

The reinforced soil block was found to be non-rigid for all tests. Whilst the mode of failure is classified as overturning, a combination of simple shearing of the entire reinforced soil block, and localised shearing along horizontal planes was visible. This shearing deformation was found to occur, at least at high elevations (the reinforcement layer second from the top) non-uniformly within each layer. For instance pockets of shear strain larger than that predicted using an average shear strain up the wall were developed, and horizontal dislocations were visible along the reinforcement layer or between reinforcement layers near the back of the reinforced soil block. This was combined with the tail of the reinforcement being dragged downwards as the active wedge slid down into the back of the reinforced soil block.

#### **6.2.4 Implications to design**

##### *Deformation prior to ultimate failure*

A major assumption for design purposes is that the reinforced soil zone behaves as a rigid composite block. However, experimental observations show that overturning failure is accompanied by inclined shearing surfaces within the retained backfill, and along horizontal planes within the reinforced soil block. Further, this deformation occurs even at low acceleration levels. Deformation of the reinforced soil block was shown to be non-uniform between each layer of reinforcement, and not necessarily along the reinforcement layers.

##### *Wall inclination*

A reduced wall inclination was found to contribute to the stability of the wall significantly. Additionally, even after multiple shaking steps, deformation was small and the wall was likely to be serviceable. This is because pre-failure, the wall deformed by overturning, and this only increased the inclination of the wall towards the vertical. Therefore the wall did not actually overturn past the vertical before (and during) failure.

##### *Acceleration Amplification*

Amplification of acceleration was found for all tests to be non-linear up the wall face, and to generally increase with increasing base input acceleration. An increase in the L/H ratio was effective at reducing this amplification.

The New Zealand Guidelines (Murahsev, 2003) specify a maximum amplification factor of 1.3, and a downwards trend of amplification with increasing base acceleration. An opposite trend of increasing amplification with increasing base acceleration was observed in the current experiments with an FHR panel facing.

### **6.3 Model limitations**

As with all model tests, there are limitations as to the applicability of results generated at model scale to full-scale. An attempt at model similitude was made to generate behaviour representative of prototype scale. Of particular concern was the scaling of soil properties associated with model studies at 1-g, and this could impact the failure mechanisms observed. However as the model was only able to fail by overturning and sliding (and pullout failure could not be quantified) it is unlikely that this had a major effect on the mechanisms observed.

Further, possible modes of failure were constricted to those three stated, and where other modes are allowed (by careful scaling of the soil-reinforcement interaction, inclusion of foundation sub-soil, etc) this could impact on the failure patterns observed.

It should be noted that the progression of deformation observed is only valid for GRS models with an FHR facing panel, as the facing rigidity ensured that all reinforcement layers were engaged in actively resisting deformation of the wall. Other facing types would result in different failure patterns to be observed.

Additionally, the model was subject to boundary effects, though where possible, these were minimised. For instance, acceleration data was recorded at the box centreline. However, it should be noted that deformation observations made at the sidewall of the box could have incurred the maximum possible boundary effects. It should be repeated that Watanabe et al. (2003) showed that there was a difference in angle of the failure planes measured at the transparent sidewall and along the centreline of the box, but not in the timing of formation. However it is unlikely that such a shift in angles would impact on the actual mechanisms observed.

## 6.4 Recommendations for future research

This was the first study of a longer research programme which investigates the seismic performance of GRS walls. Hence, much work was devoted to the experimental detail and methods of model preparation to enable future studies to possibly investigate, among other things:

- The use of local soils as backfill, and its impact on seismic performance.
- The addition of a surcharge load and its effect on deformation during seismic excitation.

The high-speed camera imaging employed in this study generated considerable data for subsequent analysis using GeoPIV. Additionally, the data can be presented in a variety of ways depending on the information required. For instance, total maximum shear strain, volumetric strain, linear strains and shear strain can be isolated and scrutinised. However, due to time constraints, not all of the data has been analysed in such a comprehensive manner, and only the most interesting results have been presented in this study. Hence, with regards to the GeoPIV analysis, the following points are noted:

- The strain data obtained by GeoPIV for both “windows” and all tests could be further scrutinised using the abovementioned components of strain to better isolate the mechanisms of deformation.
- The deformation of the reinforced soil block was not able to be quantified exactly using GeoPIV for all tests due to camera resolution and the location chosen for investigation (at 66% of model height). However, the use of GeoPIV was able to identify deformation within the reinforced soil block-retained fill interface well, and it is likely that a redesign of the camera location and/or resolution used for investigation of the reinforced soil block could be met with better results.
- Failure was governed by the development of a failure surface which intersected with the lowest layer of reinforcement. However, the reinforced soil block – retained backfill “window” was located too high to visualise the development of this deformation. The “window” could be lowered in future tests to rectify this.

- Camera resolution is governed by the camera's RAM memory, and hence the selected frame rate. The analyses in this study showed that much information can be obtained from residual analysis of images taken just before and after shaking, i.e. without the need for high-speed imaging. Thus it would be possible to capture larger images at a higher resolution separately before and after testing, for analysis of residual deformation using GeoPIV. Subsequent imaging at 200 fps (and reduced resolution and window size) could then continue as per normal, to analyse response *during* shaking.

Recommended research to further investigate the influence of L/H ratio and wall inclination on seismic performance includes:

- The existence of an 'optimum' L/H ratio, whereby an increase in reinforcement length, is not met by a proportional increase in seismic performance.
- The effect of wall inclination on behaviour could be better investigated with further tests conducted on inclined walls with a more gradual transition of  $10^\circ$  increments from the vertical case.
- The Microgrid reinforcement used in the current tests was 'inextensible' at model scale. No comparison was made with other reinforcement types, and hence it is difficult to ascertain the influence of this parameter on seismic performance. This could be investigated with further testing using a larger range of reinforcement types and stiffness's.

Finally, it is envisaged that the depiction of mechanisms of deformation can lead to more accurate performance based methods of design. For instance, while Newmark-type rigid-block methods have been shown to be reasonably accurate at predicting deformation during failure (Matsuo et al. 1998), the present study demonstrated that deformation occurred even at low levels of shaking intensity, predominantly by rotation of the wall about the toe. Given that these mechanisms of deformation at low levels of shaking have largely been identified in this work, future research can focus on the development of performance-based methods to quantify small-strain deformation, to aid in better prediction of seismic performance that meets SLS criteria.

## References

- Fairless, G. J. (1989). "Seismic Performance of Reinforced Earth Walls," University of Canterbury, Christchurch.
- Jones, C. J. F. P. (1996). *Earth reinforcement and soil structures*, Thomas Telford London.
- Ling, H. I., Leshchinsky, D., and Chou, N. N. S. (2001). "Post-earthquake investigation on several geosynthetic-reinforced soil retaining walls and slopes during the ji-ji earthquake of Taiwan." *Soil Dynamics and Earthquake Engineering*, 21(4), 297-313.
- Matsuo, O., Yokoyama, K., and Saito, Y. (1998). "Shaking table tests and analyses of geosynthetic-reinforced soil retaining walls." *Geosynthetics International*, 5(1-2), 97-126.
- Sakaguchi, M. (1996). "Study of the seismic behavior of geosynthetic reinforced walls in Japan." *Geosynthetics International*, 3(1), 13-30.
- Sandri, D. (1997). "Performance summary of reinforced soil structures in the Greater Los Angeles area after the Northridge earthquake." *Geotextiles and Geomembranes*, 15(4-6), 235-253.
- Tatsuoka, F. "Geosynthetic-reinforced soil structures: A cost-effective solution combining two engineering disciplines." *19th Carillo Lecture - Mexican Society for Soil Mechanics*, Aguascalientes.
- Tatsuoka, F., Tateyama, M., and Koseki, J. (1996). "Performance of soil retaining walls for railway embankments." *Soils and Foundations*(Special), 311-324.
- Watanabe, K., Munaf, Y., Koseki, J., Tateyama, M., and Kojima, K. (2003). "Behaviors of several types of model retaining walls subjected to irregular excitation." *Soils and Foundations*, 43(5), 13-27.
- White, D. M., and Holtz, R. D. (1997). "Performance of geosynthetic-reinforced slopes and walls during the Northridge, California Earthquake of January 17, 1994." *Earth Reinforcement*, 2, 965-972.



**APPENDIX A**

**WALL DESIGN AND SOIL PROPERTIES**

## A.1 Model Wall Design

The model wall was designed at prototype scale, initially setting  $L/H = 0.75$ .

### Wall geometry at prototype scale

Wall height	H	4.50m
L/H ratio		0.75
Reinforcement length	L	3.375m
Inclination	$\theta$	$90^\circ$

### Microgrid properties

Factored allowable tension	$T_{al}$	14kN/m
----------------------------	----------	--------

### Soil Properties

Unit weight of fill	$\gamma_f$	16.7 kN/m <sup>3</sup>
Internal friction angle	$\Phi$	$33^\circ$
Active Earth Pressure Coefficient	$K_{af}$	0.295
Angle of failure plane angle	$\psi$	$61.5^\circ$

Static horizontal wall thrust,  $F_A$

$$F_A = 0.5 K_{af} \gamma_f H^2$$

$$F_A = (0.5 \times 0.295 \times 16.7 \times 4.5^2) = 74.7 \text{ kN/m}$$

External stability: Check sliding failure

$$F_h^* \leq \Phi F_v^* \tan \Phi$$

$$F_h^* \leq (1.0 \times 253 \times \tan(33)) = 165 \text{ kN/m}$$

SLIDING OK

External stability: Check overturning failure

$$M_d^* \leq \Phi M_r^*$$

$$M_d^* = (74.7 \times 0.5 \times 4.5) \leq \Phi M_r^* = (0.75 \times 253 \times 0.5 \times 3.375)$$

$$M_d^* = 168 \text{ kN/m} \leq \Phi M_r^* = 321 \text{ kN/m}$$

OVERTURNING OK

Check number of reinforcement layers,  $N$ , required

$$N = F_A / T_{al} = 5.3$$

Hence 5 Layers of reinforcement, spaced vertically by 0.75 m has been selected.

*Internal stability: Check pullout failure*

Maximum tensile force in reinforcement,  $F^*_j$ :

$$F^*_j = \sigma^*_{hj} S_{vj}$$

Factored design soil interaction strength against pullout,  $T^*_{di,l}$ :

$$T^*_{di,l} = \Phi \Phi_n F^* \alpha \sigma^*_{vi} L_e C$$

Where,  $\Phi$  is the uncertainty factor for soil-reinforcement interaction (assumed 0.8),  $\Phi_n$  reduction factor associated with consequence of failure (1.0),  $F^*$  is pullout resistance (manufacturer tested as 0.8),  $\alpha$  is the scale correction factor (1.0),  $L_e$  is the reinforcement length in the resistant zone, and  $C$  is the reinforcement effective unit perimeter (2.0 for geogrid and geotextiles).

Hence, the reinforcement strength must satisfy:

$$F^*_j \leq T^*_{di,l}$$

Reinforcement Layer	$L_e^1$ (m)	Vertical stress at layer, $\sigma^*_{vj}$ (Kn/m <sup>2</sup> )	Factored soil interaction strength, $T_{il,1}$ (Kn/m)	Max Tensile force in reinforcement, $F^*_j$ (Kn/m)
1	2.97	62.6	268	13.9
2	2.56	50.1	185	11.1
3	2.15	37.6	117	8.31
4	1.75	25.0	63	5.54
5	1.34	12.5	24	2.77

<sup>1</sup> Calculated from assumed failure surface angle,  $\psi = 61.5^\circ$

PULLOUT OK

## A.2 Seal Friction Measurements

Reduction of the seals influence on model behaviour involves minimising the friction force between model wall facing and box sidewall. The friction force is calculated as below:

$$F_f = \mu_s F_N$$

Where  $F_f$  is the friction force,  $\mu_s$  is the static coefficient of friction, and  $F_N$  is the force normal to the box sidewall. The normal force against the box sidewall comprises the earth pressure force along the vertical length of the seal, in addition to the outwards force provided by the seal against the box sidewall. Thus reduction of the friction force can occur by reducing the coefficient of static friction and / or reduction of the normal force provided by the seal. While we cannot change the earth pressure on the seal, appropriate material selection, and a reduction of the seal's contact area will reduce the friction against the side wall.

### *Static coefficient of friction*

The friction between various materials, Ployester plastic (PE), Teflon tape (TE), grease and steel was trialed via simple tilt table tests, and the static coefficient of friction,  $\mu_s$ , calculated by:

$$\mu_s = \tan \theta$$

The test results are shown in Table A-1.

**Table A-1. Tilt-table tests on different seal materials to determine coefficient's of friction**

Material	Trial 1	Trial 2	Trail 3	Trail 4
<u>PE - PE</u>				
$\theta$	22	23	23.5	21
$\mu_s$	0.404	0.42	0.44	0.38
<u>Teflon – PE (semi-rough) contact</u>				
$\theta$	20	18	18	18
$\mu_s$	0.36	0.32	0.32	0.32
<u>Teflon – PE (smooth) contact</u>				
$\theta$	16	16	16	16
$\mu_s$	0.28	0.28	0.28	0.28
<u>Teflon – greased PE (semi-rough) contact</u>				
$\theta$	23	23	22	21
$\mu_s$	0.42	0.42	0.404	0.38
<u>Teflon – steel contact</u>				
$\theta$	18	18	18	18
$\mu_s$	0.32	0.32	0.32	0.32

Hence the Teflon PE (smooth contact was selected) as explained in Section 3.3.3.

A spring force was attached to the top of the facing panel whilst inside the box. Multiple spring force trials were made on the seal comprising a Teflon and PE contact, and only 1 N of force was required to generate wall rotation about the toe.

### A.3 Particle Size Distribution

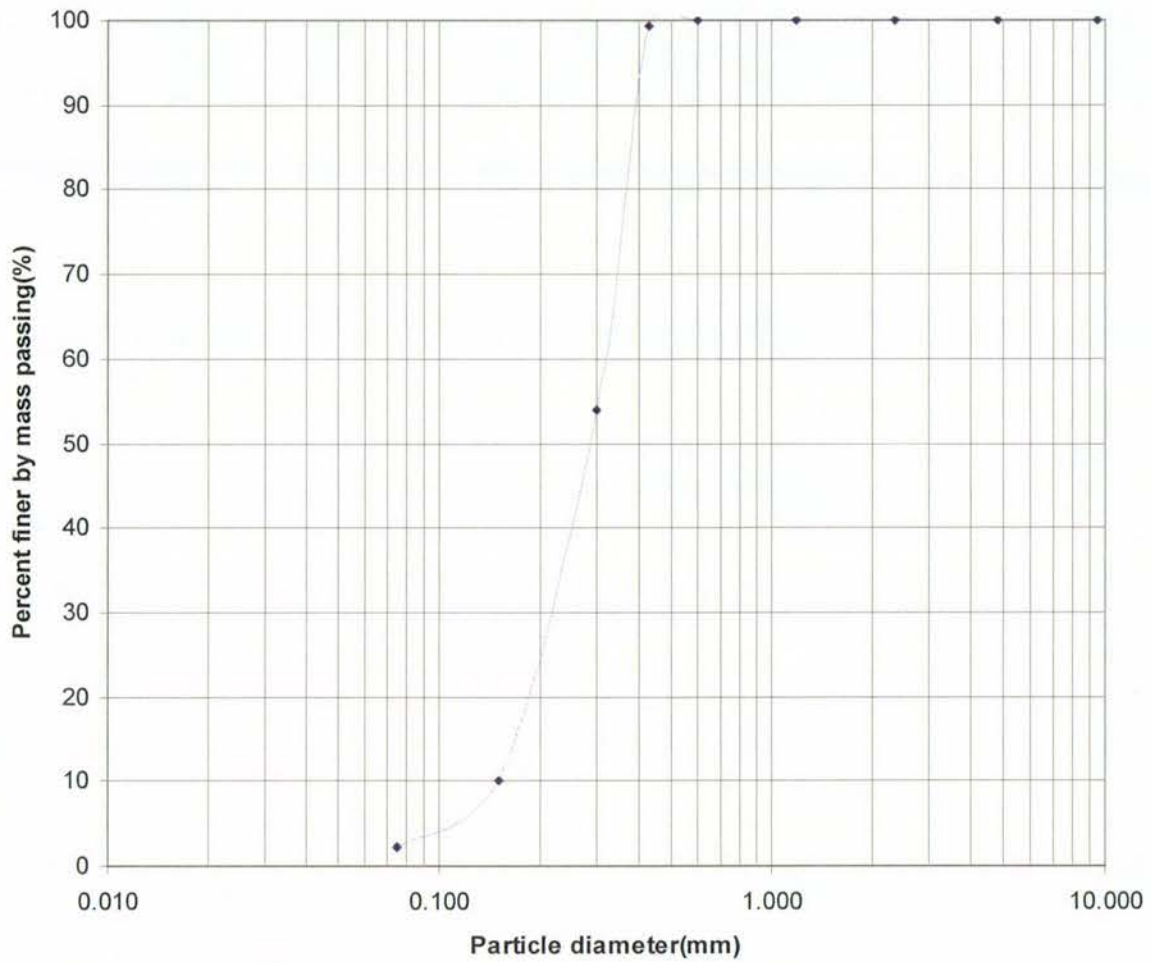


Figure A-1. Particle Size Distribution of Albany Sand

Coefficient of Uniformity  $C_U$  is calculated as:

$$C_U = \frac{d_{60}}{d_{10}} = \frac{0.121}{0.103} = 1.17$$

**APPENDIX B**  
**TIME HISTORIES**



## B.1 Test-1 Time Histories

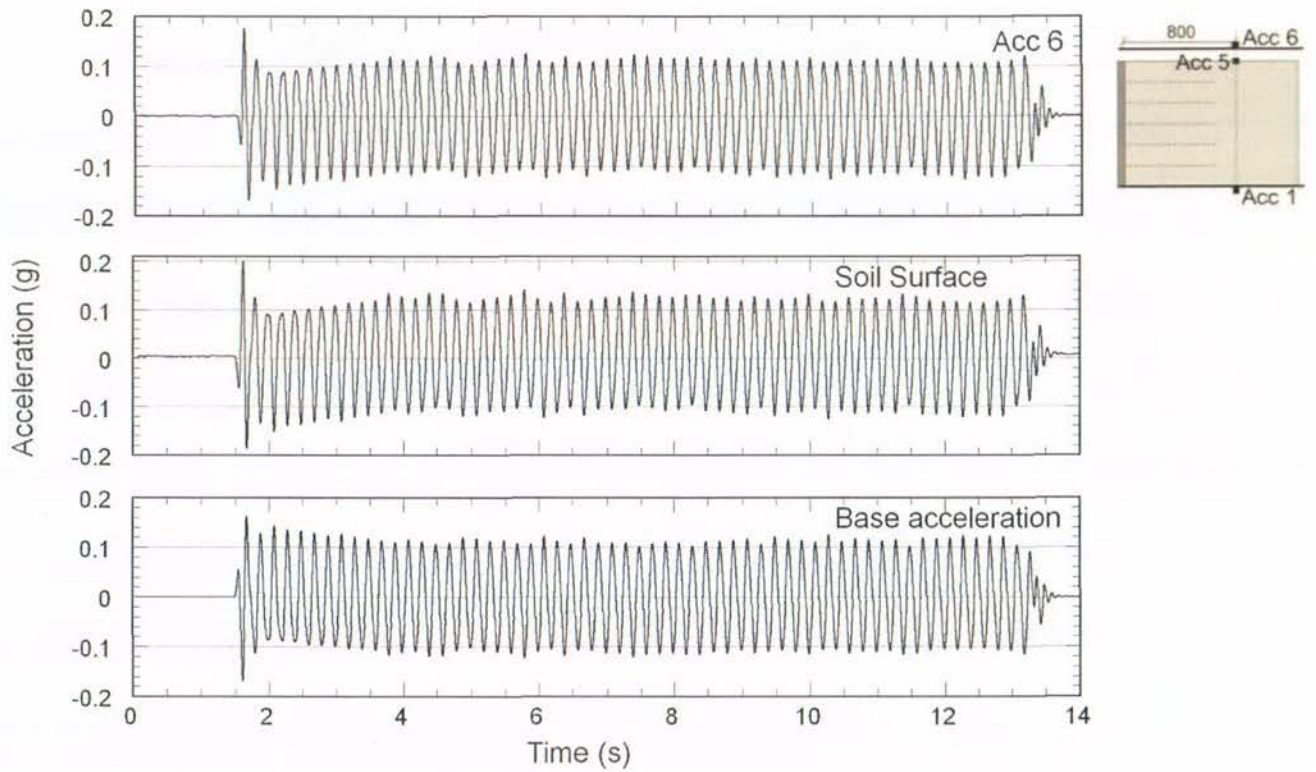


Figure B-1. Test-1 acceleration time histories at 0.1g shaking step

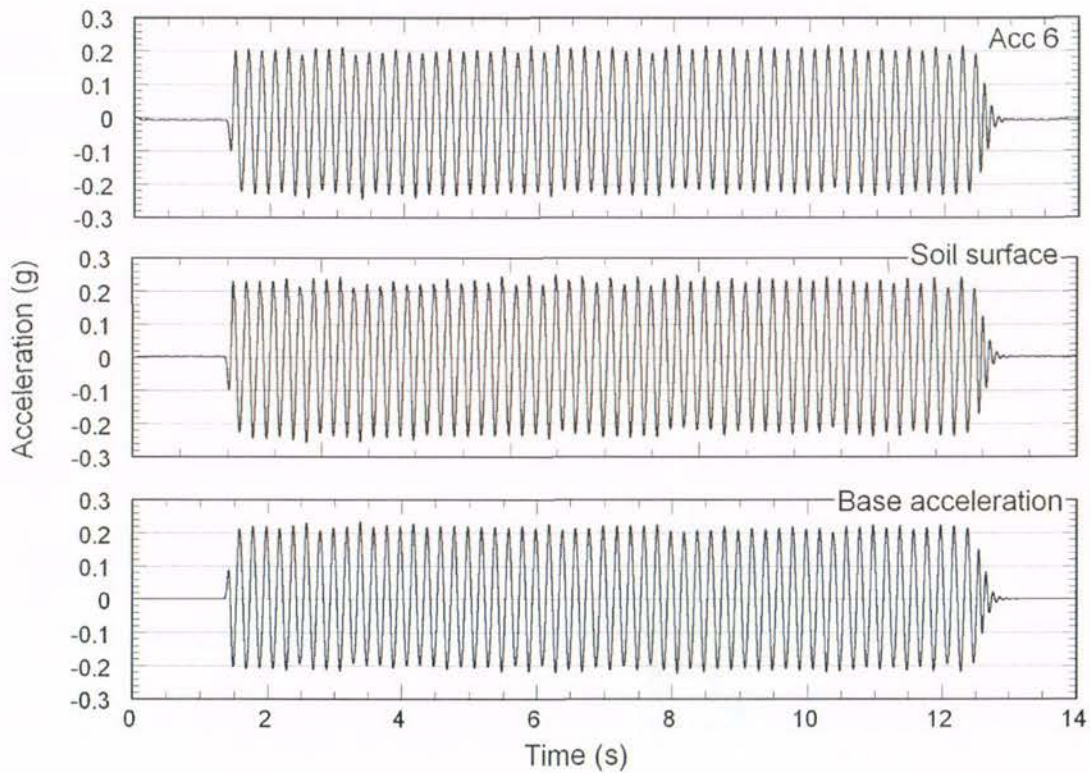


Figure B-2. Test-1 acceleration time histories at 0.2g shaking step

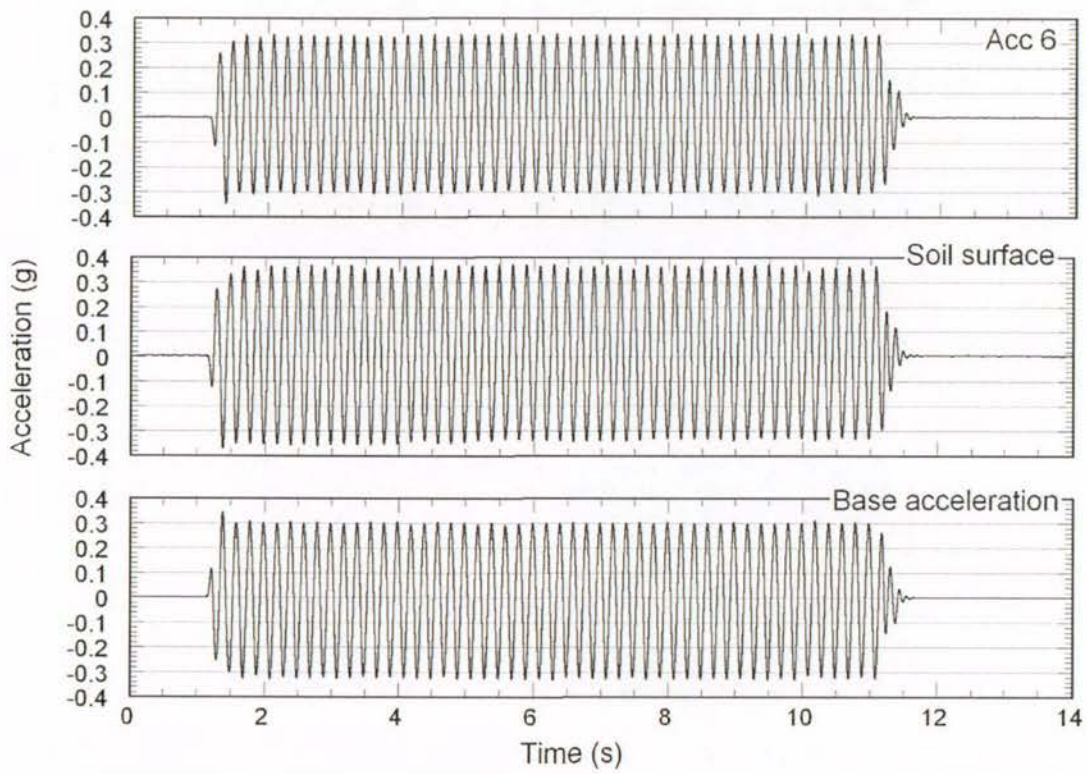


Figure B-3. Test-1 acceleration time histories at 0.3g shaking step

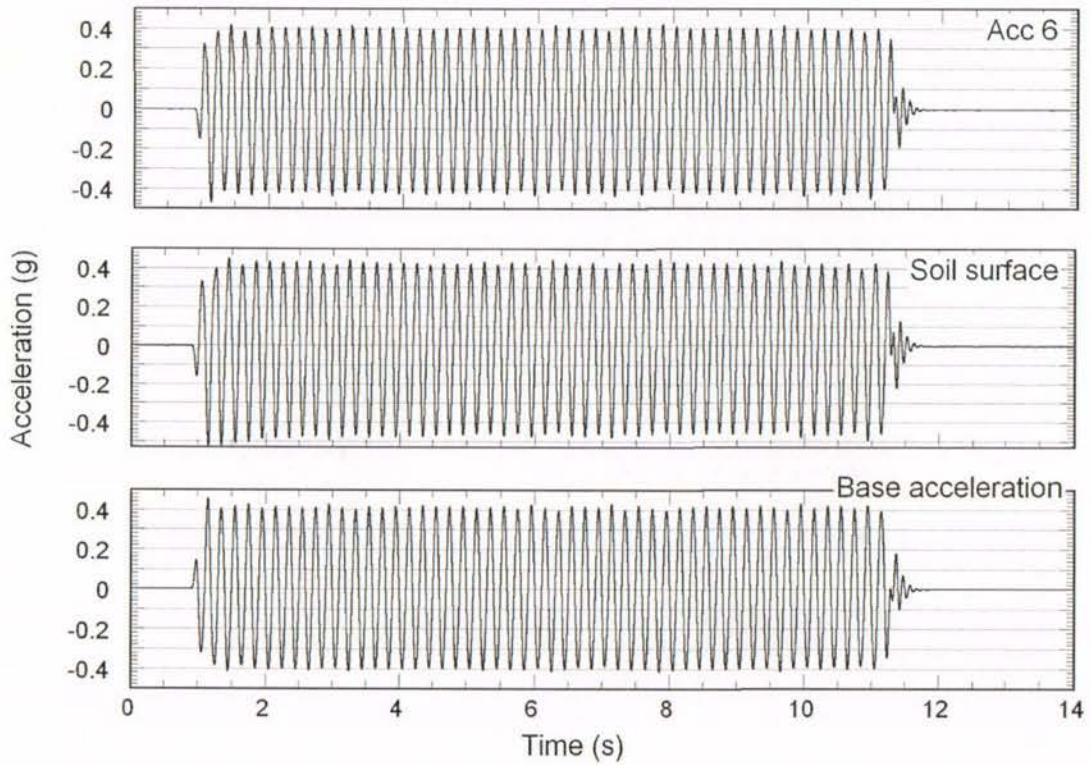


Figure B-4. Test-1 acceleration time histories at 0.4g shaking step

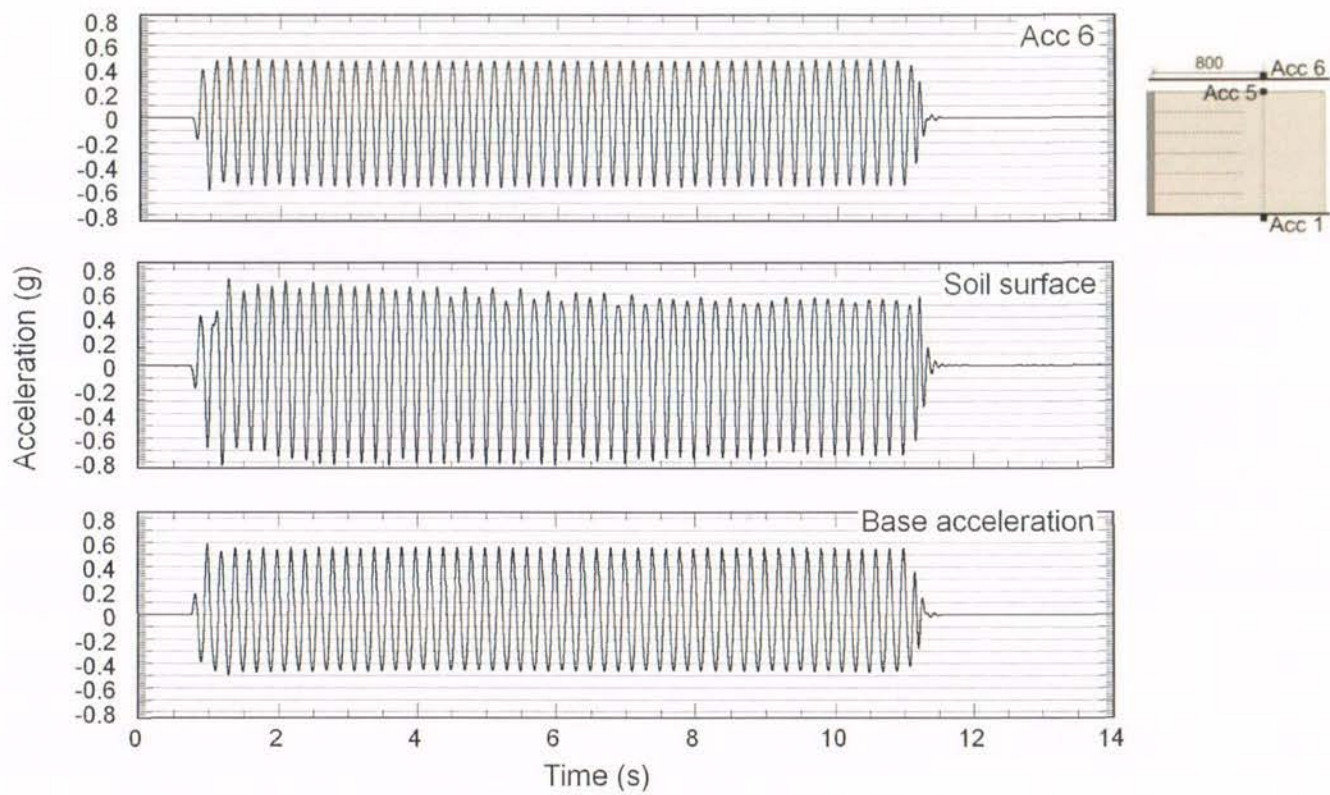


Figure B-5. Test-1 acceleration time histories at 0.5g shaking step

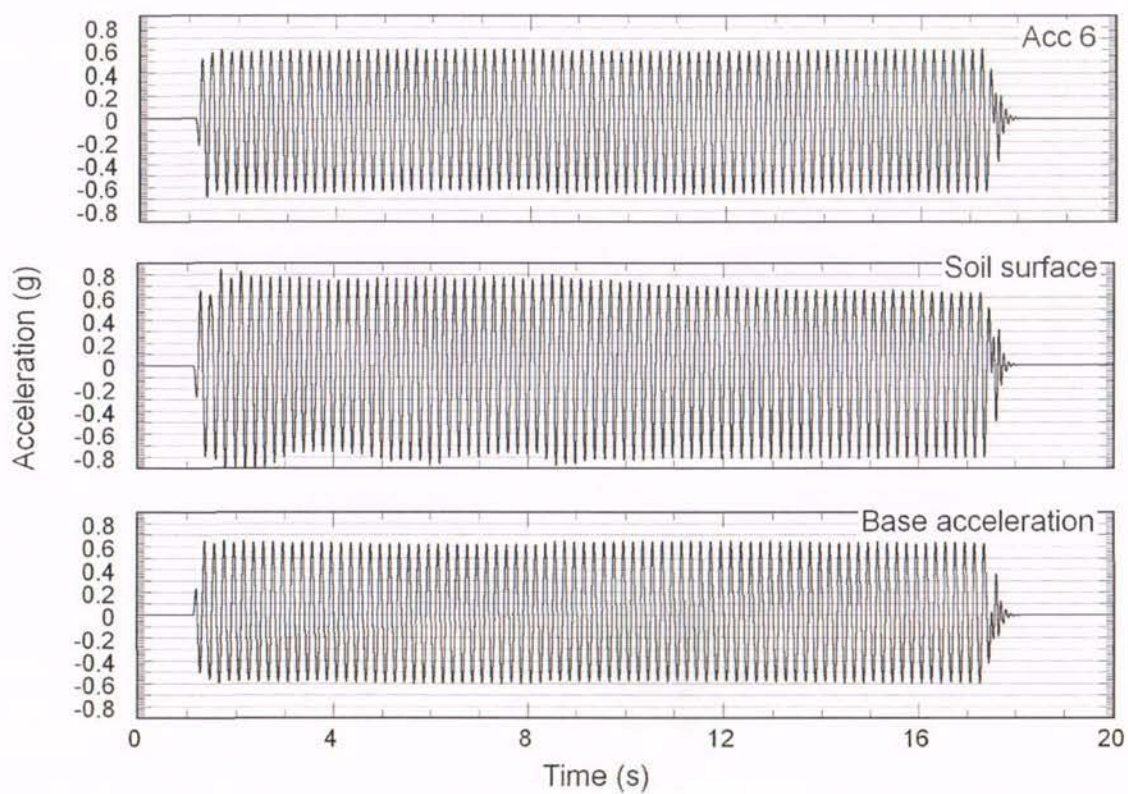


Figure B-6. Test-1 acceleration time histories at 0.6g shaking step

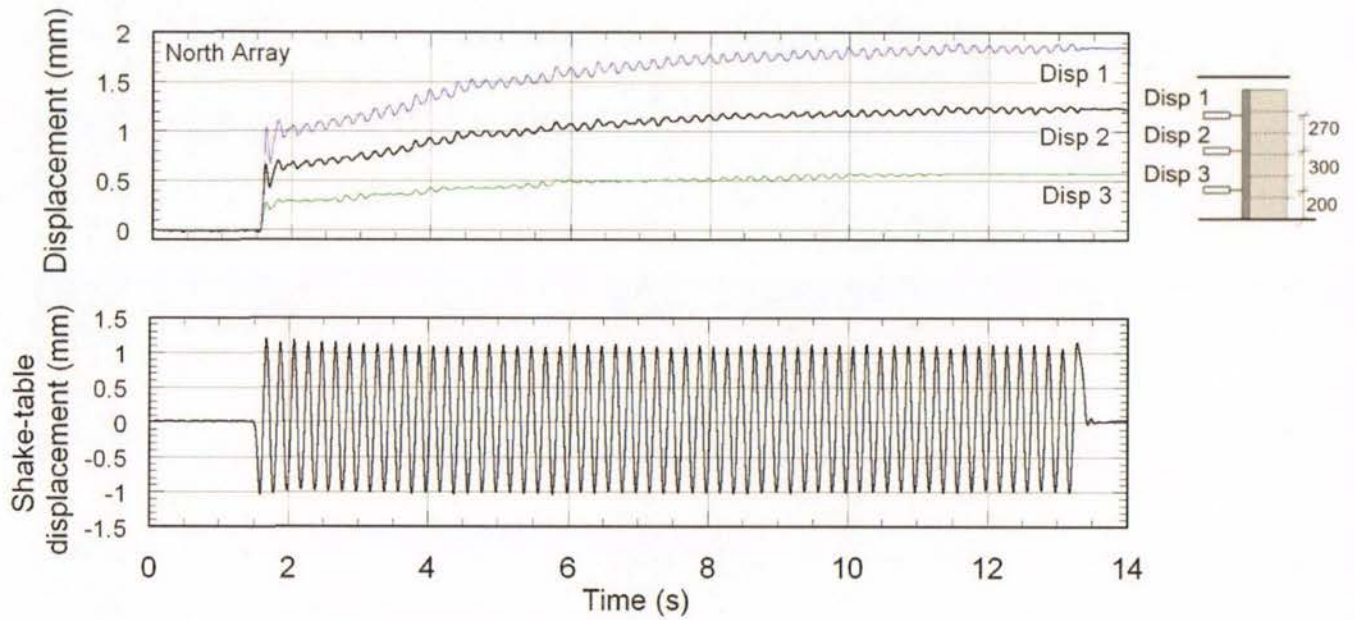


Figure B-7. Test-1 displacement time histories at 0.1g shaking step

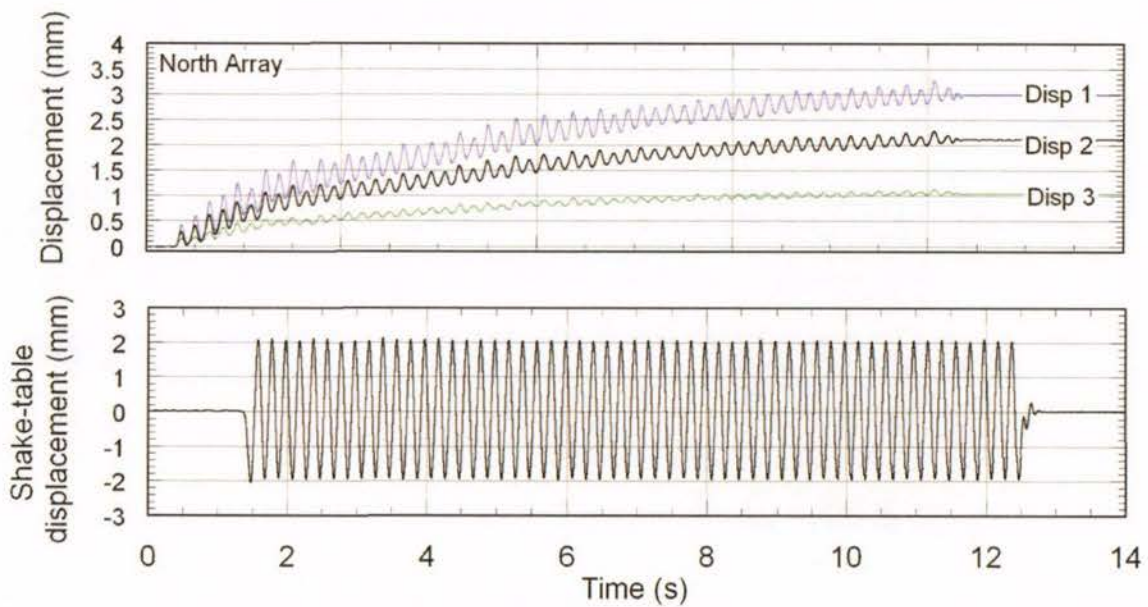


Figure B-8. Test-1 displacement time histories at 0.2g shaking step

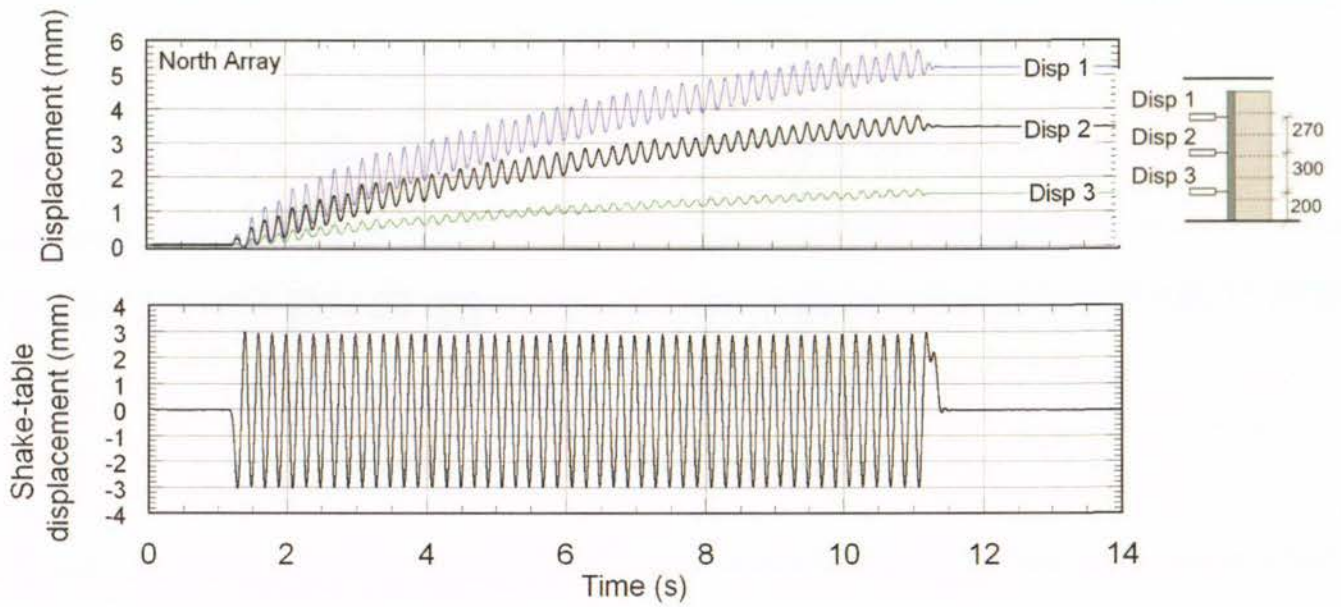


Figure B-9. Test-1 displacement time histories at 0.3g shaking step

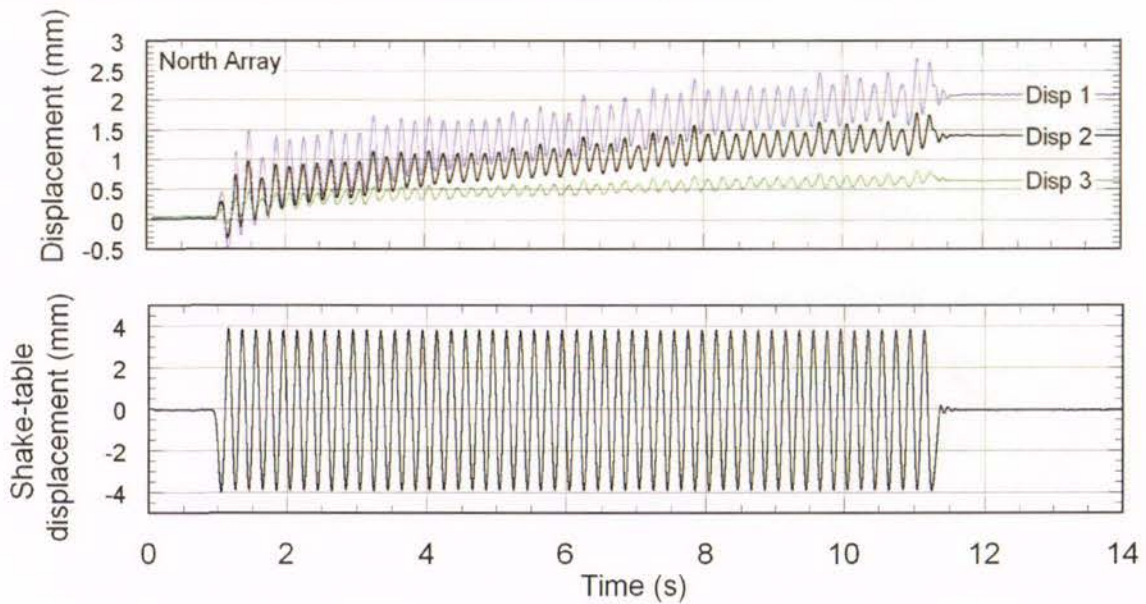


Figure B-10. Test-1 displacement time histories at 0.4g shaking step

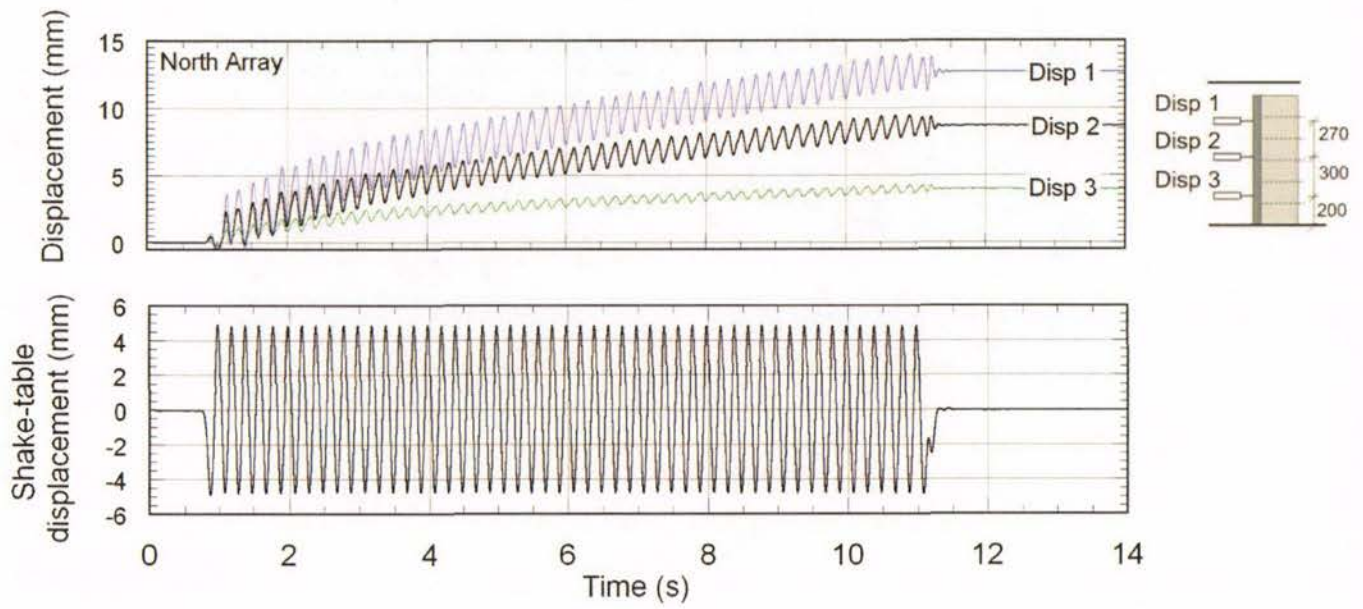


Figure B-11. Test-1 displacement time histories at 0.5g shaking step

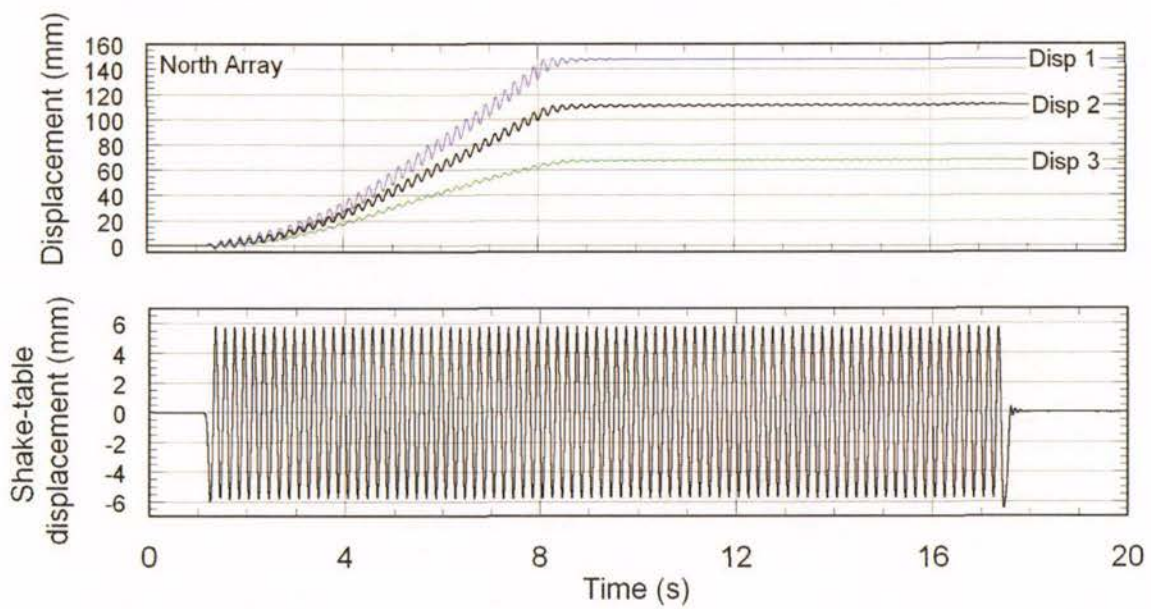


Figure B-12. Test-1 displacement time histories at 0.6g shaking step

## B.2 Test-2 Time Histories

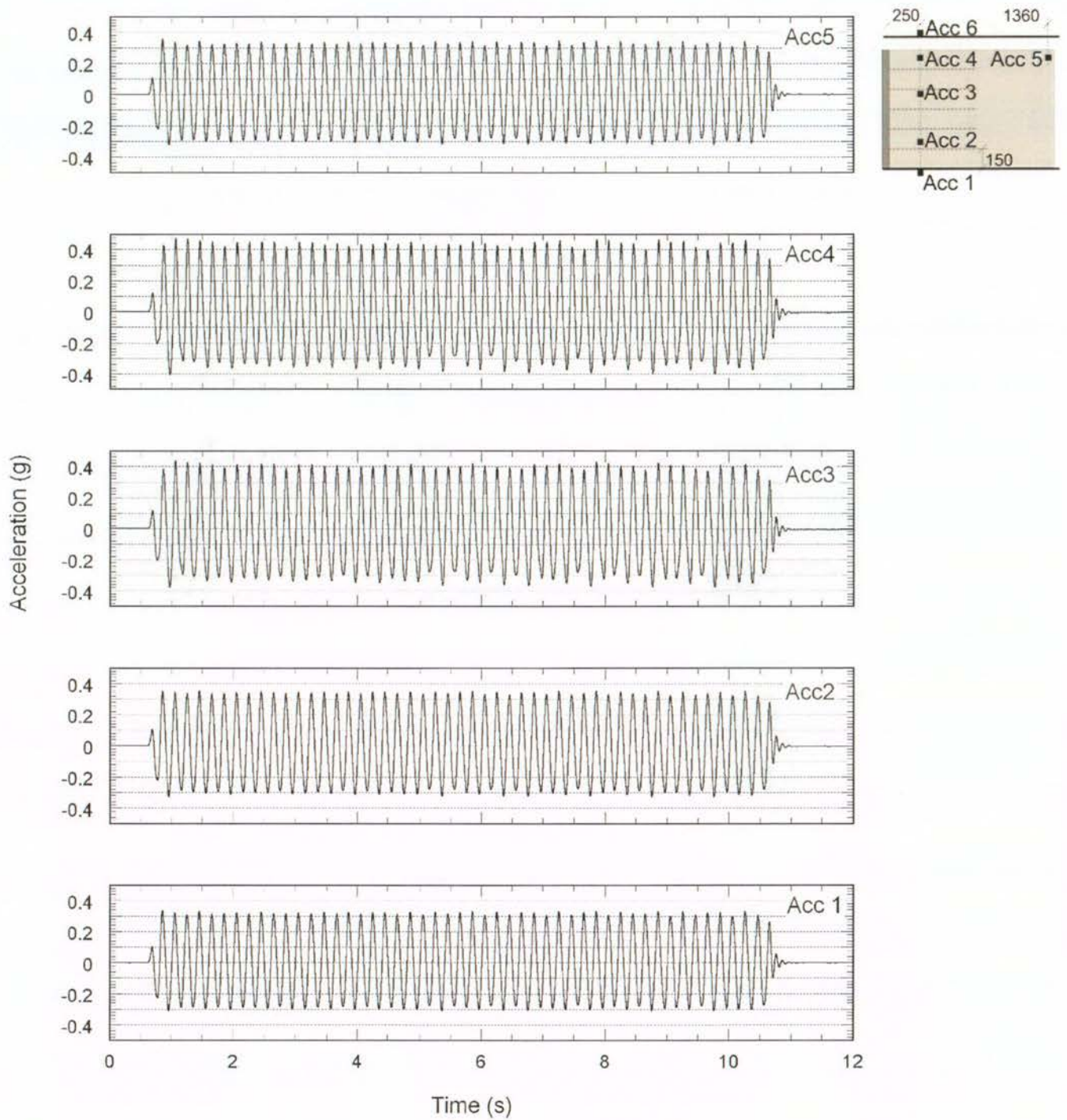


Figure B-13. Test-2 acceleration time histories at 0.3g shaking step

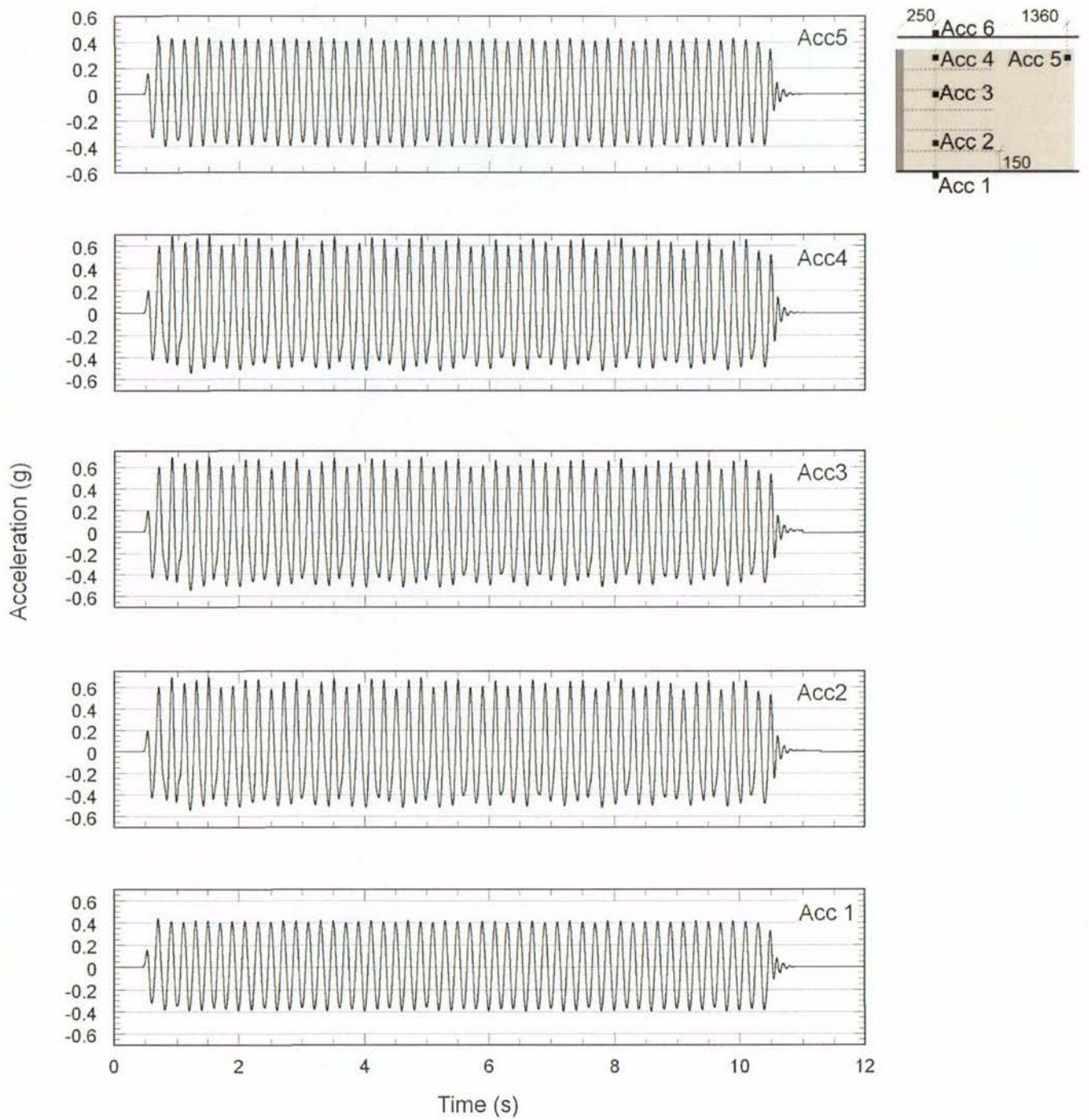


Figure B-14. Test-2 acceleration time histories at 0.4g shaking step

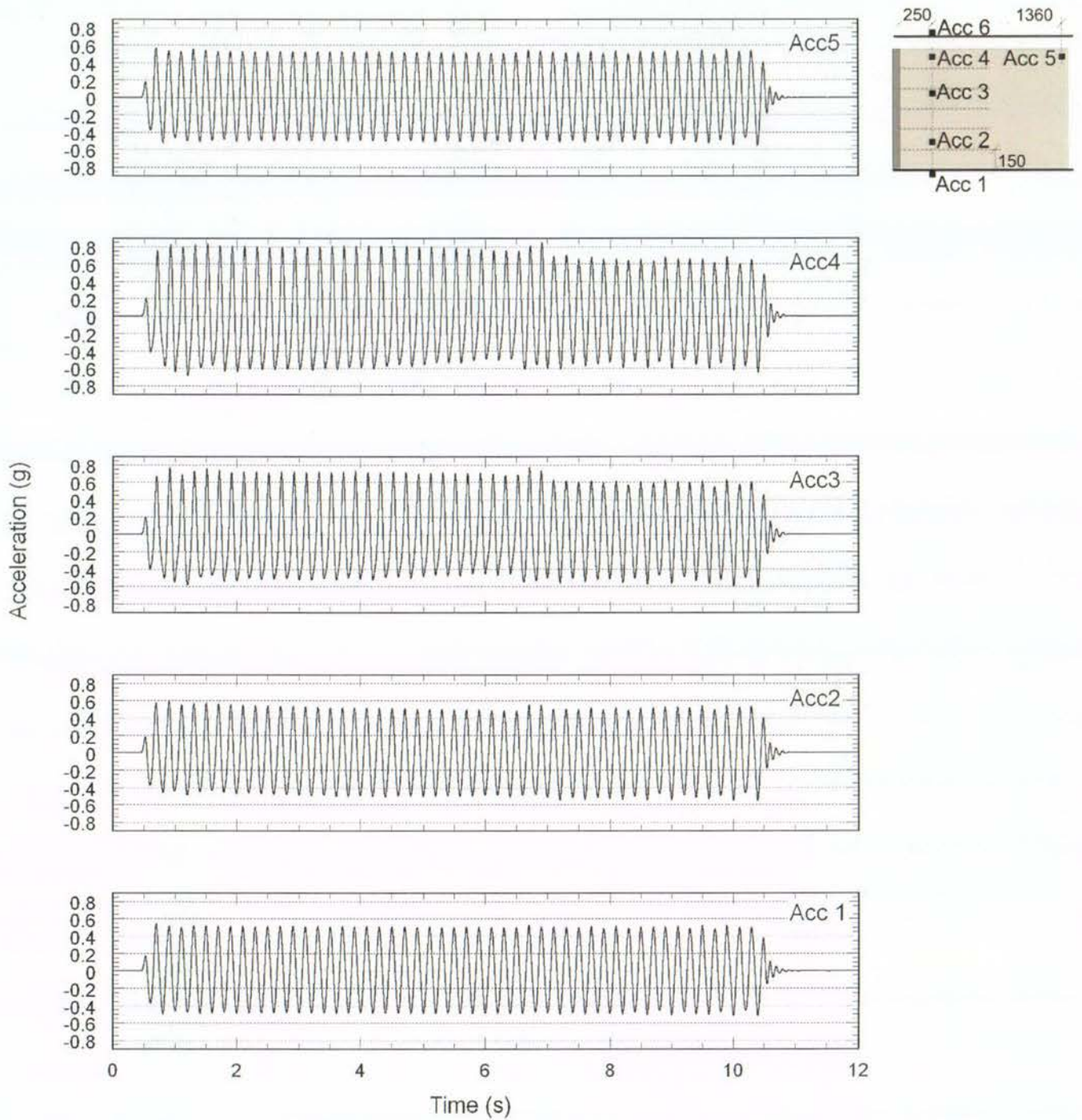


Figure B-15. Test-2 acceleration time histories at 0.5g shaking step

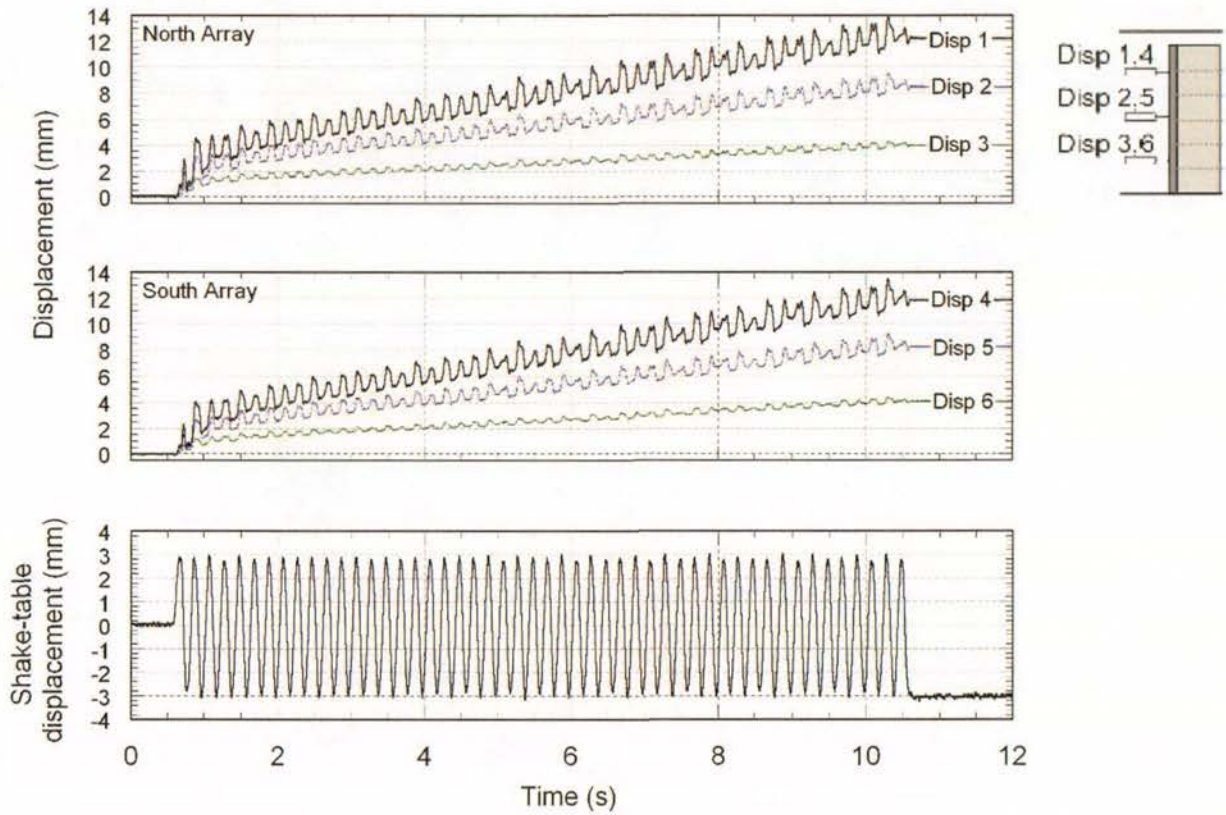


Figure B-16. Test-2 displacement time histories at 0.3g shaking step

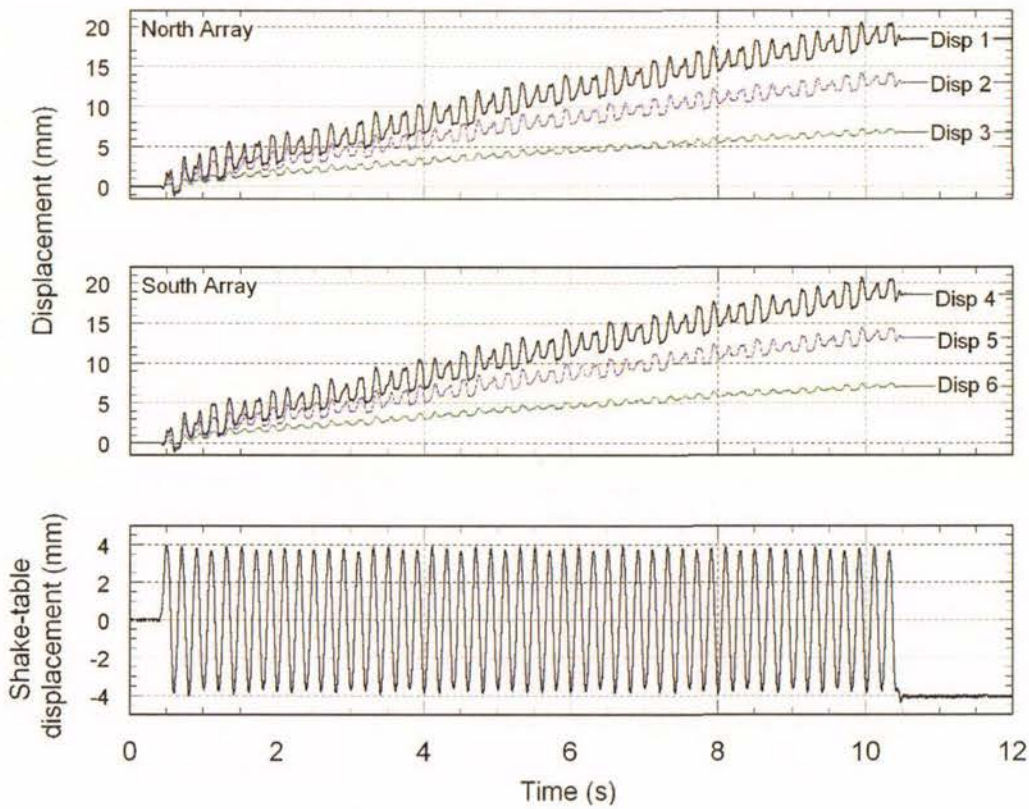


Figure B-17. Test-2 displacement time histories at 0.4g shaking step

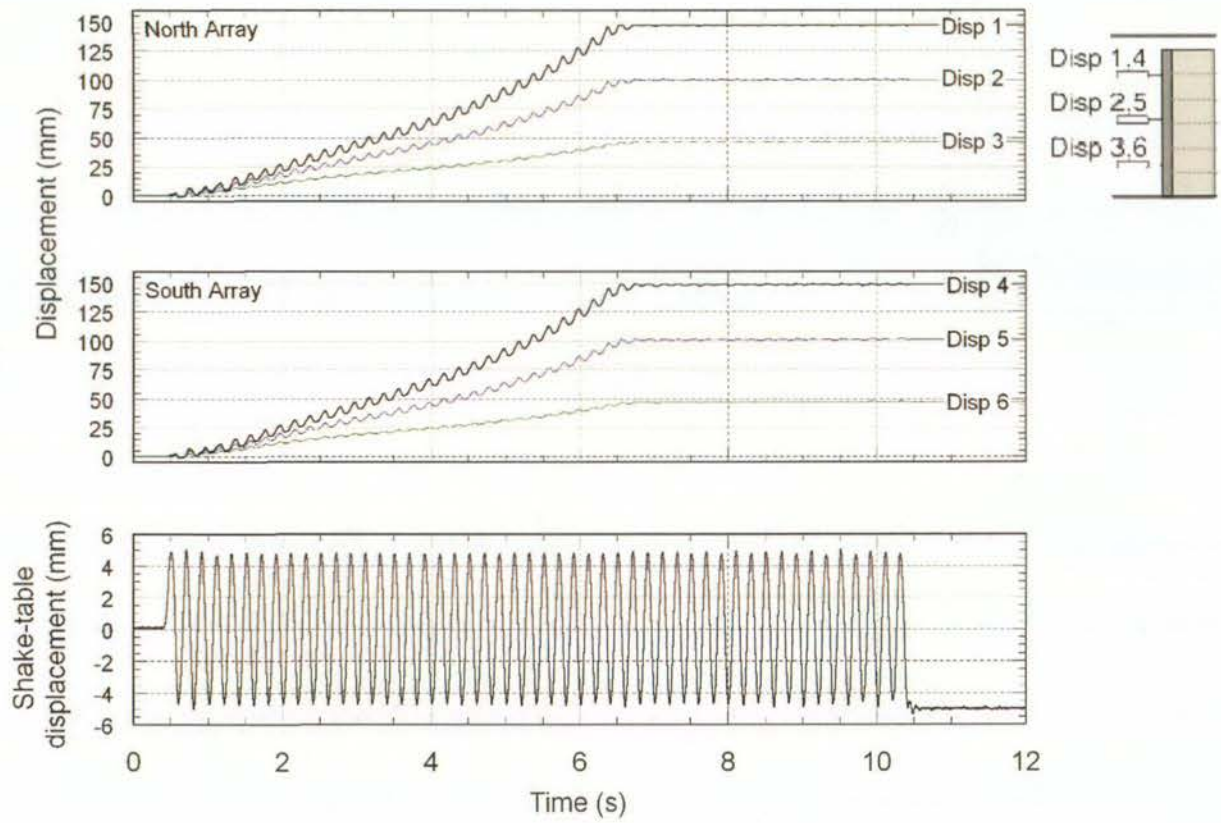


Figure B-18. Test-2 displacement time histories at 0.5g shaking step

### B.3 Test-3 Time Histories

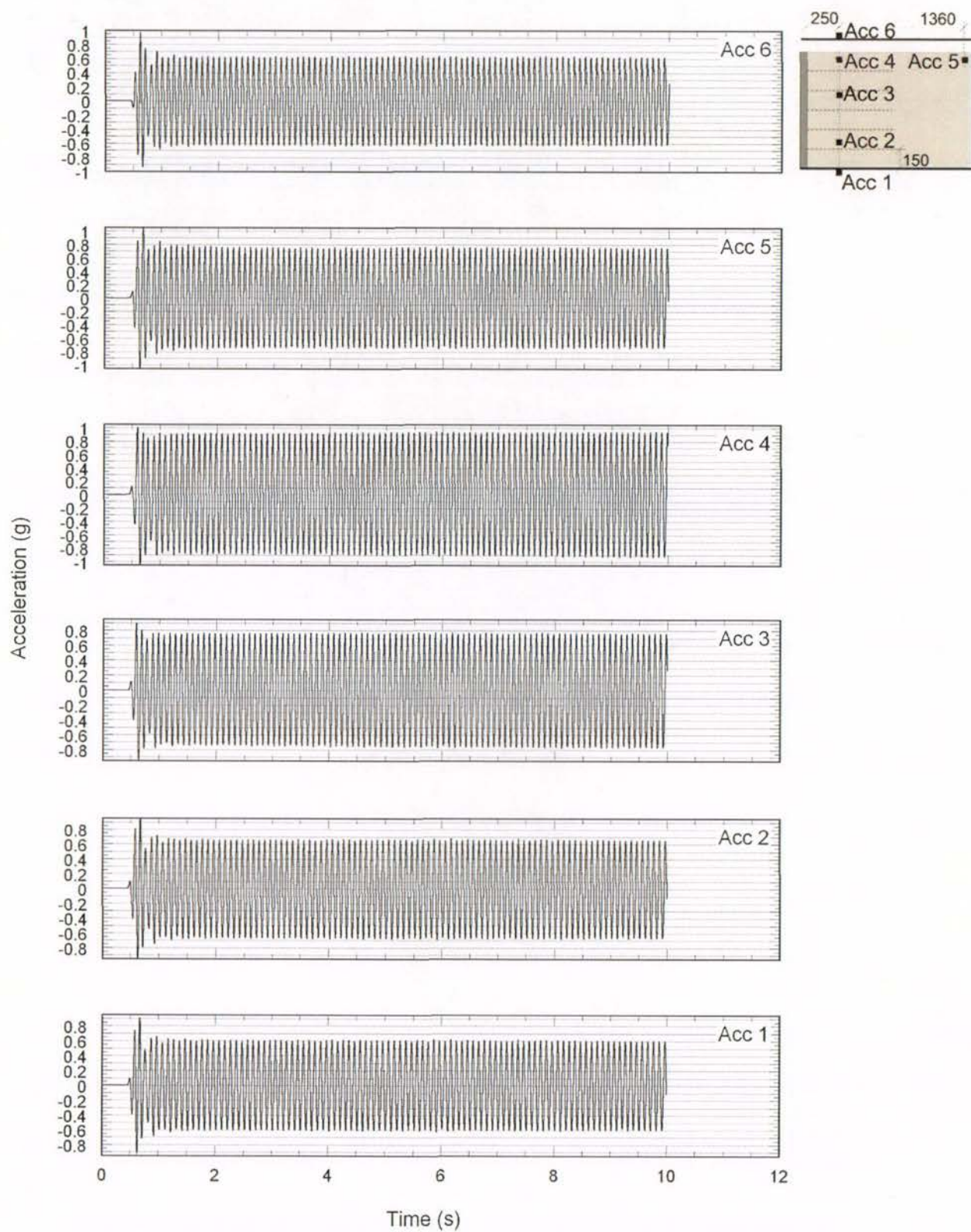


Figure B-19. Test-3 acceleration time histories at 0.6g, 10 Hz frequency shaking step

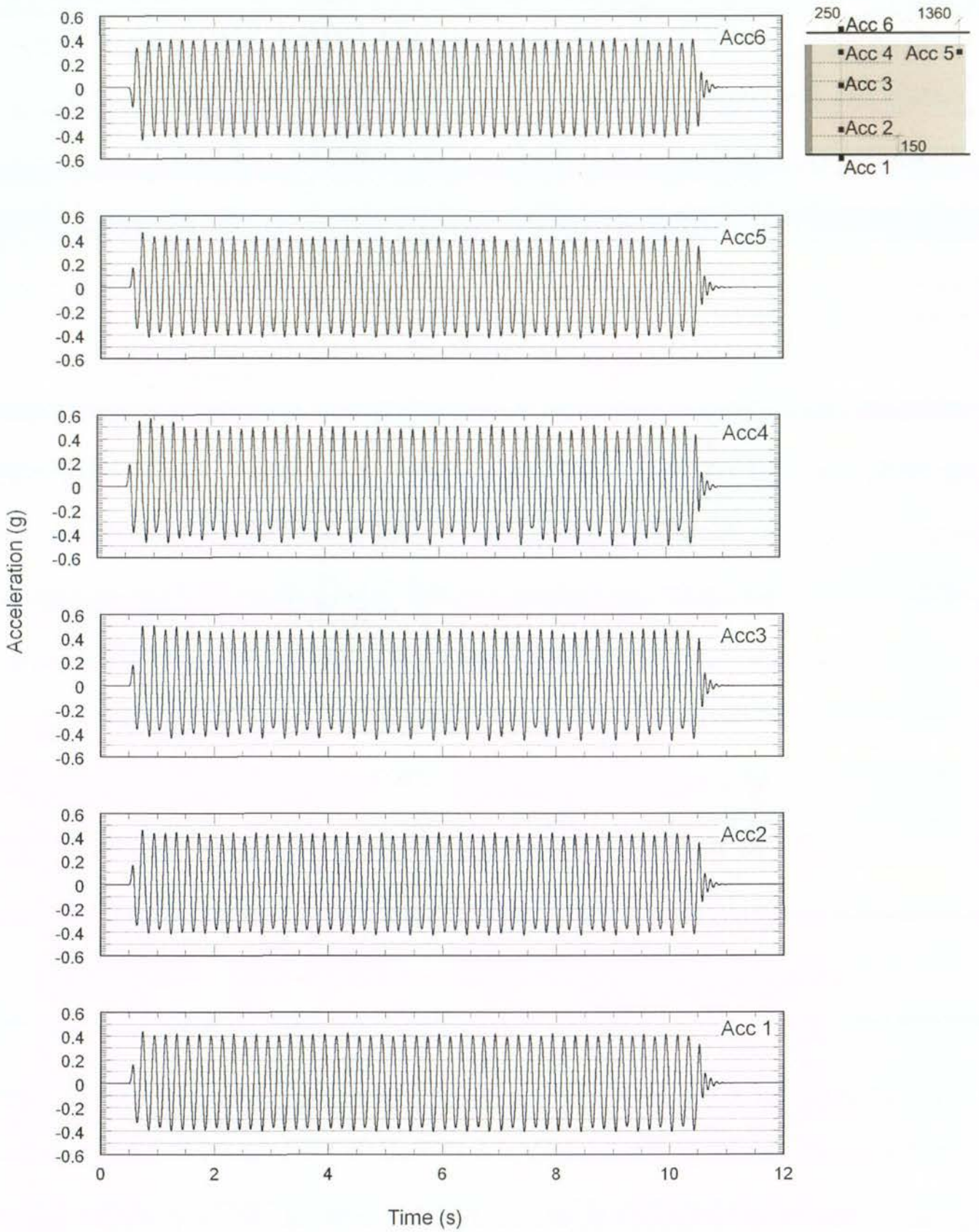


Figure B-20. Test-3 acceleration time histories at 0.4g, 5Hz shaking step, as per standard protocol

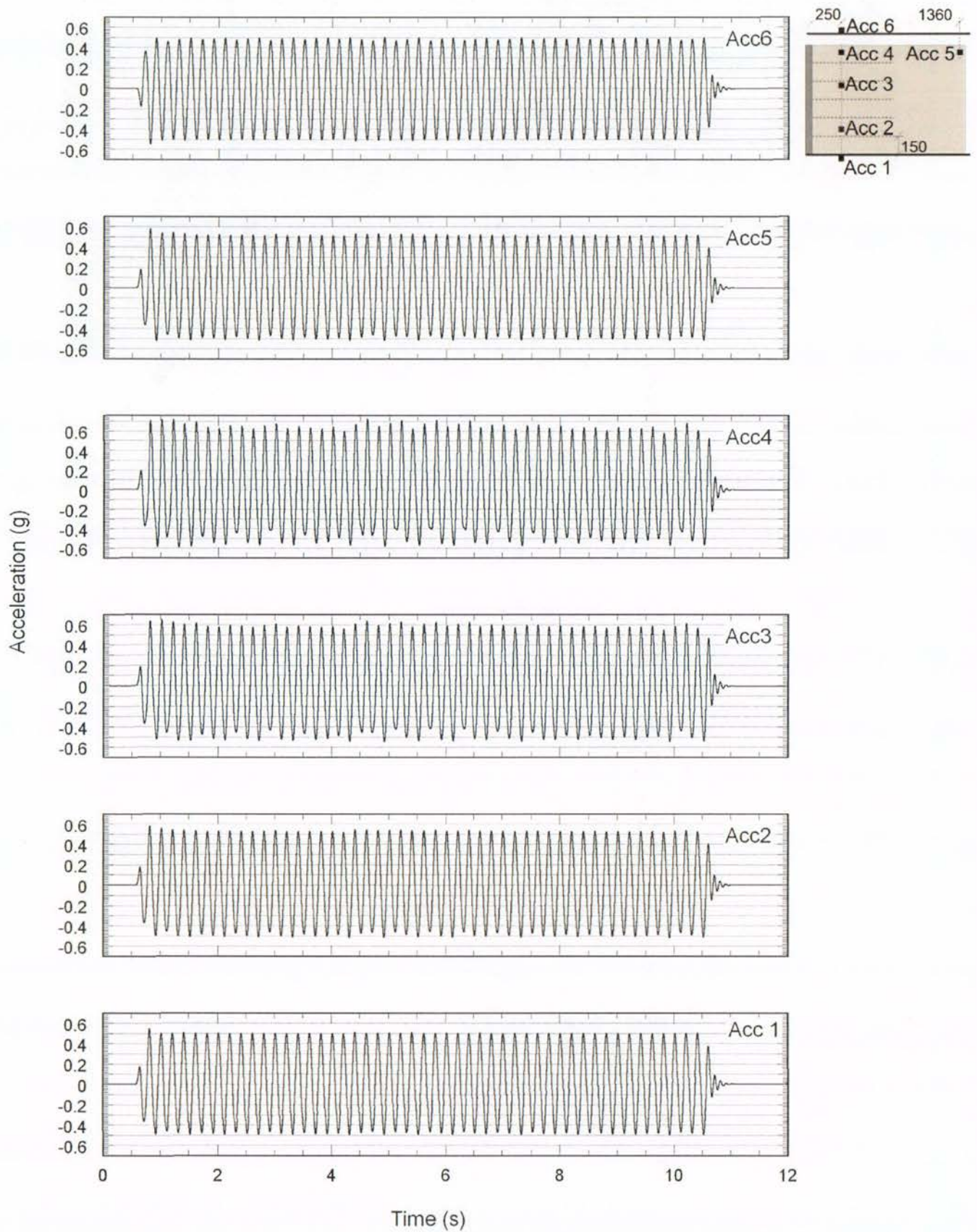


Figure B-21. Test-3 acceleration time histories at 0.5g shaking step

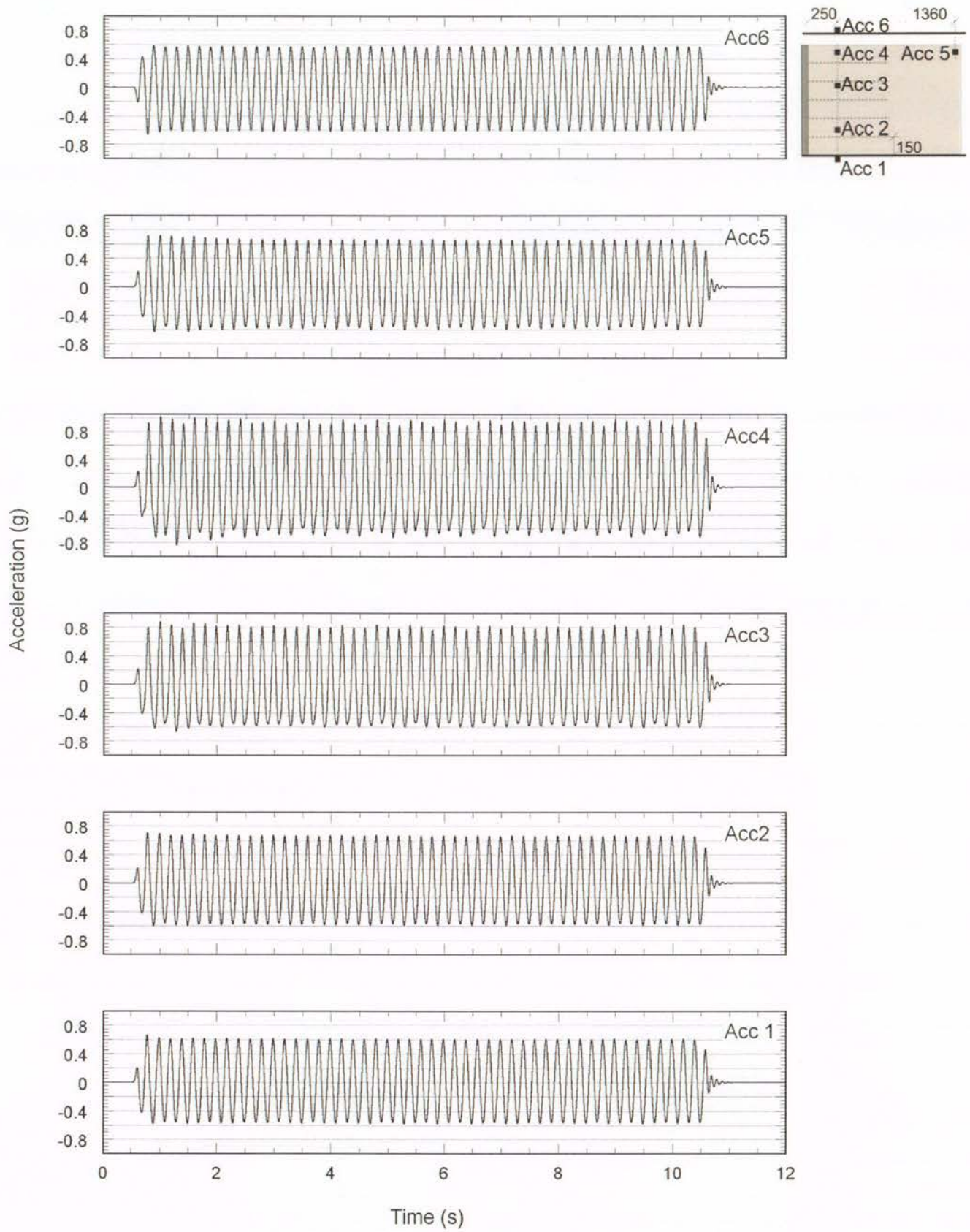


Figure B-22. Test-3 acceleration time histories at 0.6g shaking step

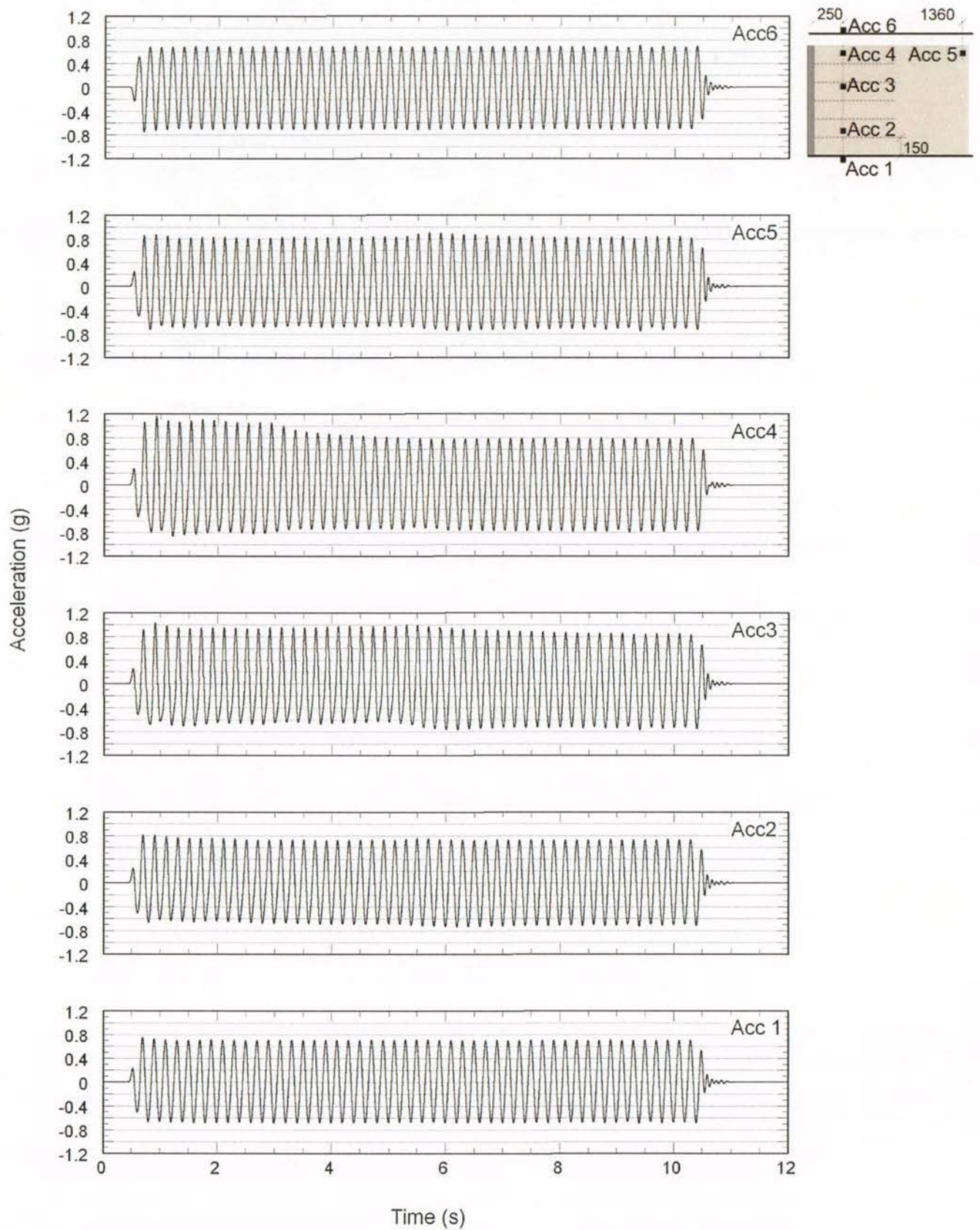


Figure B-23. Test-3 acceleration time histories at 0.7g shaking step

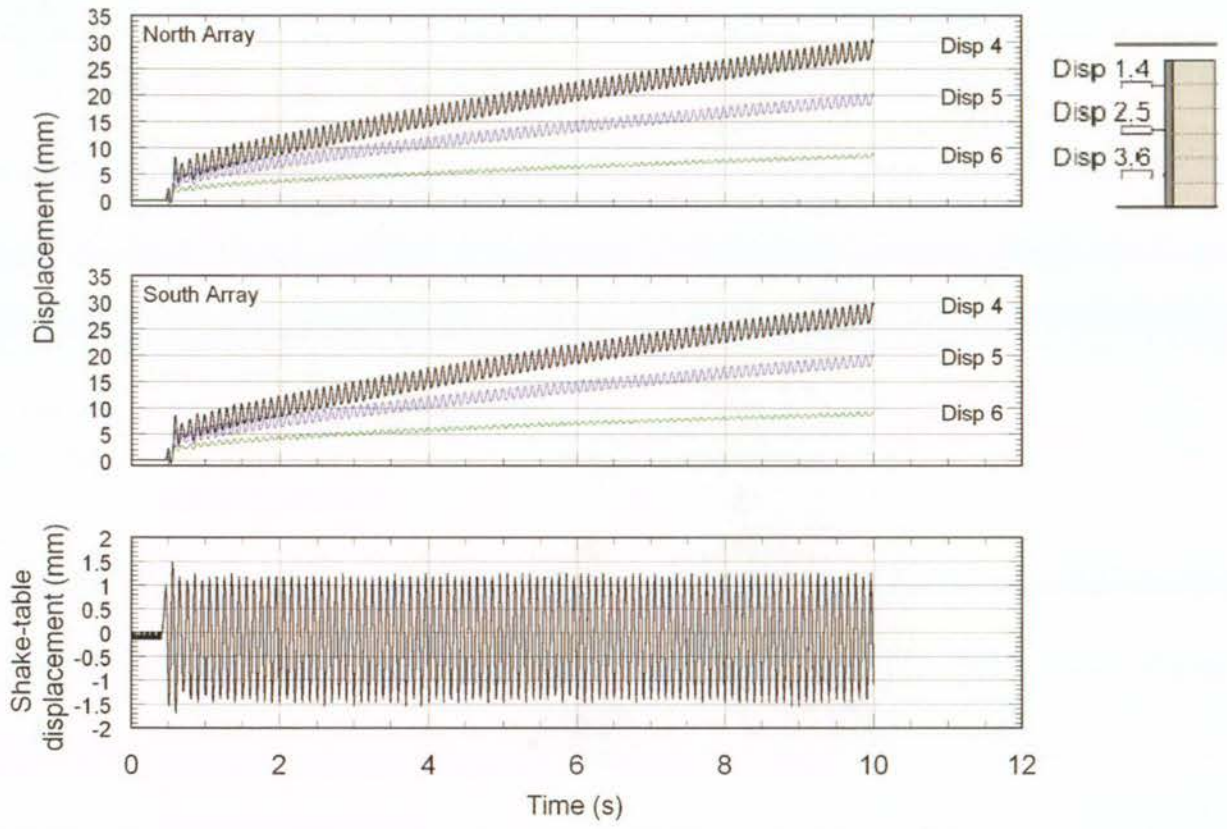


Figure B-24. Test-3 displacement time histories at 0.6g, 10 Hz frequency shaking step

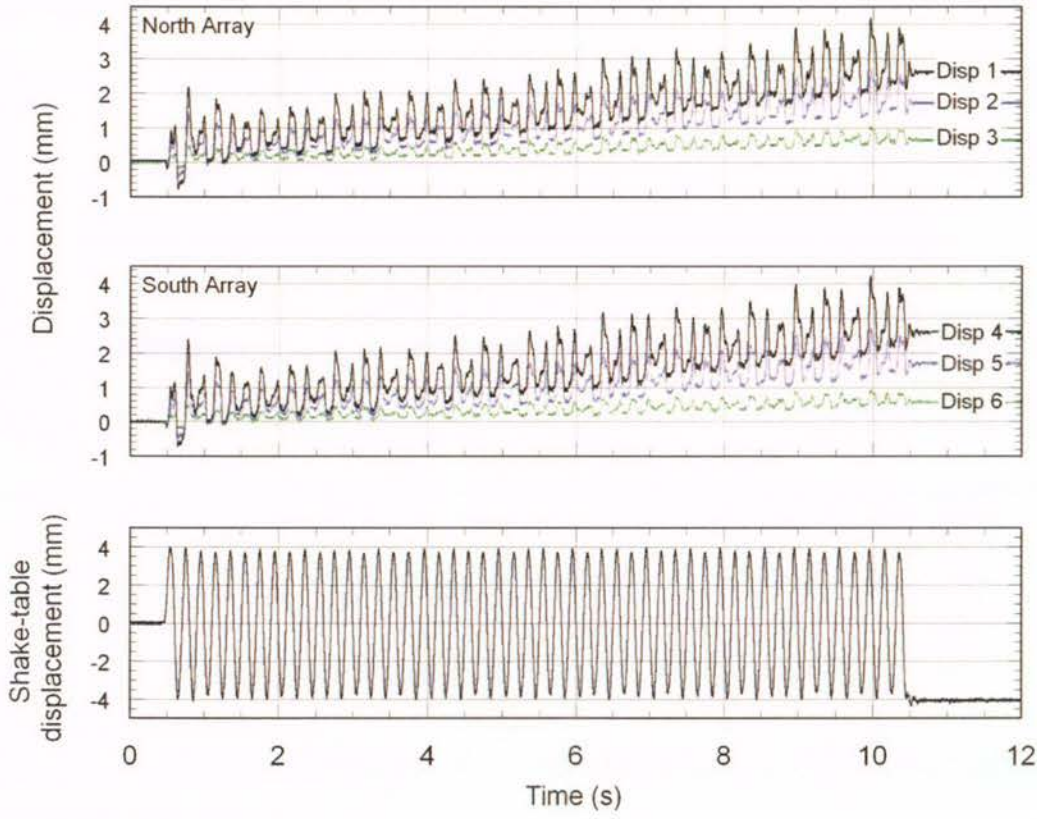


Figure B-25. Test-3 displacement time histories at 0.4g shaking step

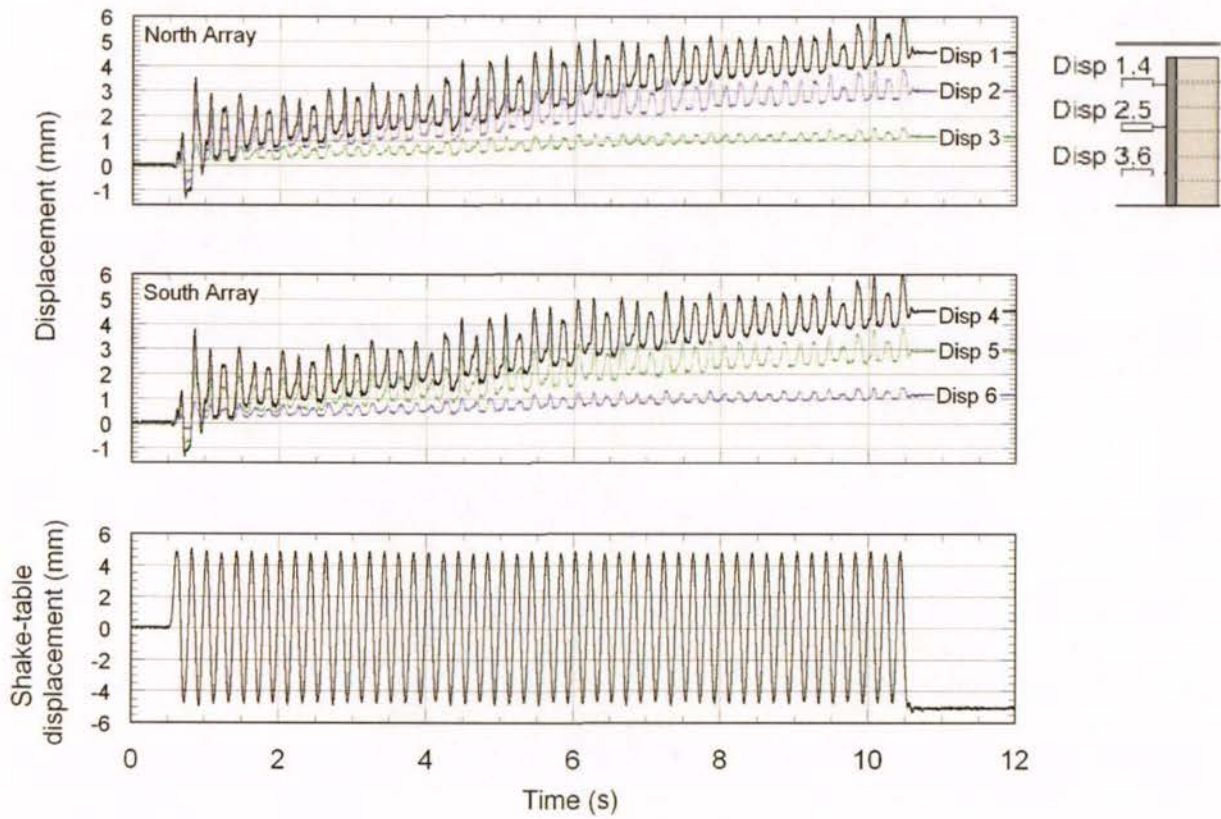


Figure B-26. Test-3 displacement time histories at 0.5g shaking step

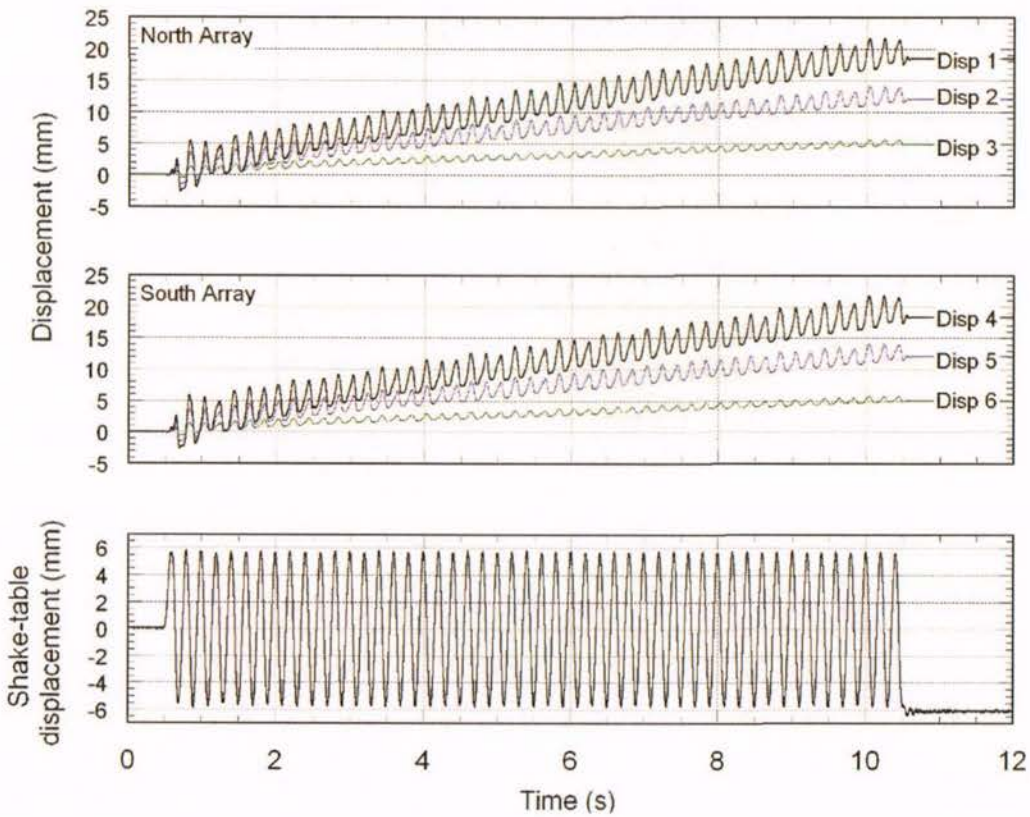


Figure B-27. Test-3 displacement time histories at 0.6g shaking step

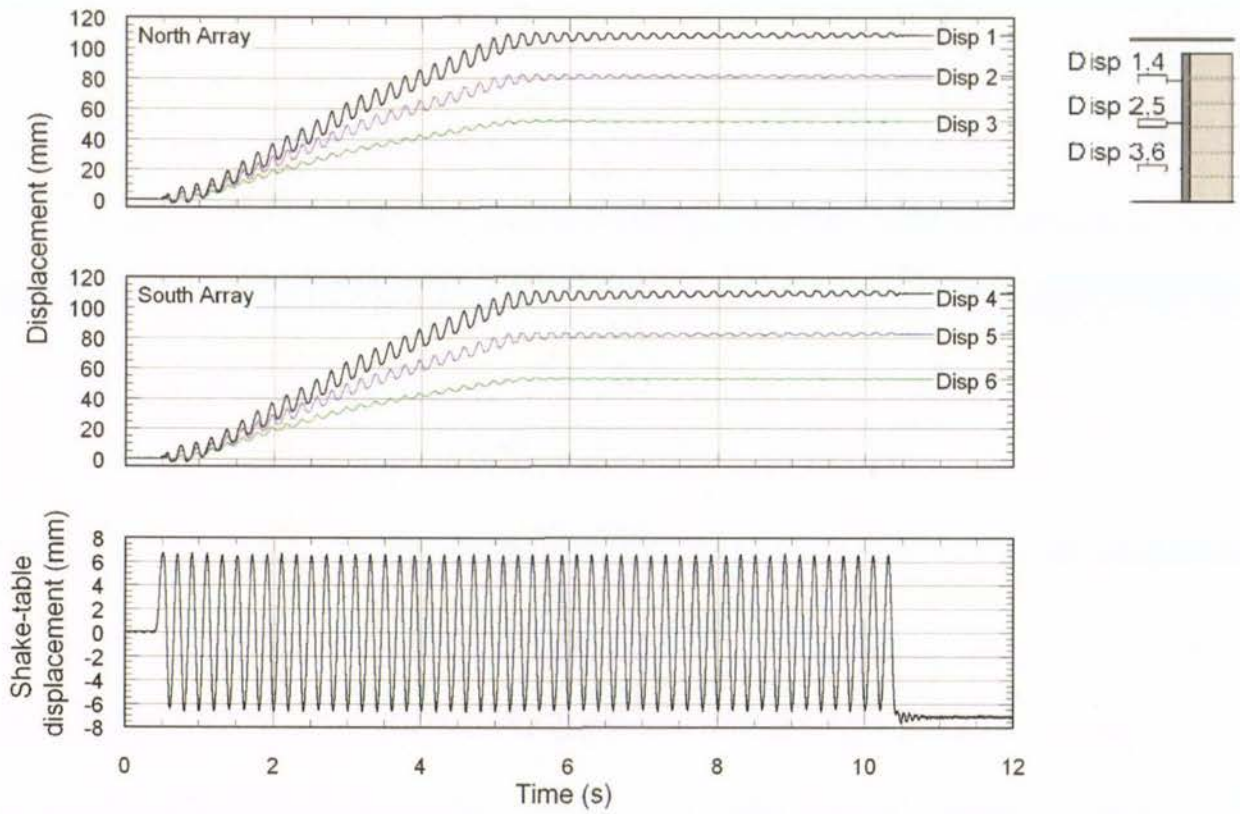


Figure B-28. Test-3 displacement time histories at 0.7g shaking step

## B.4 Test-4 Time Histories

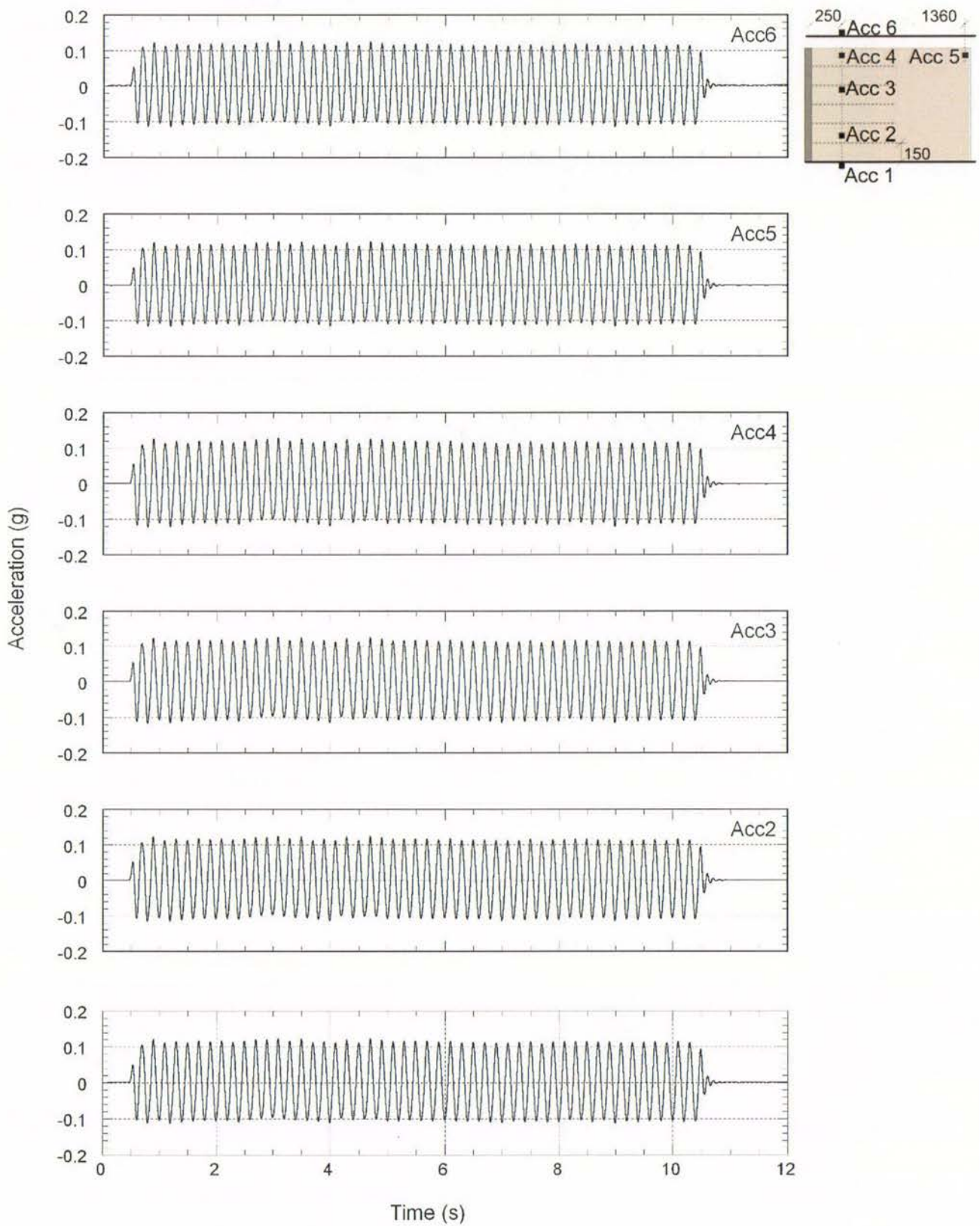


Figure B-29. Test-4 acceleration time histories at 0.1g shaking step

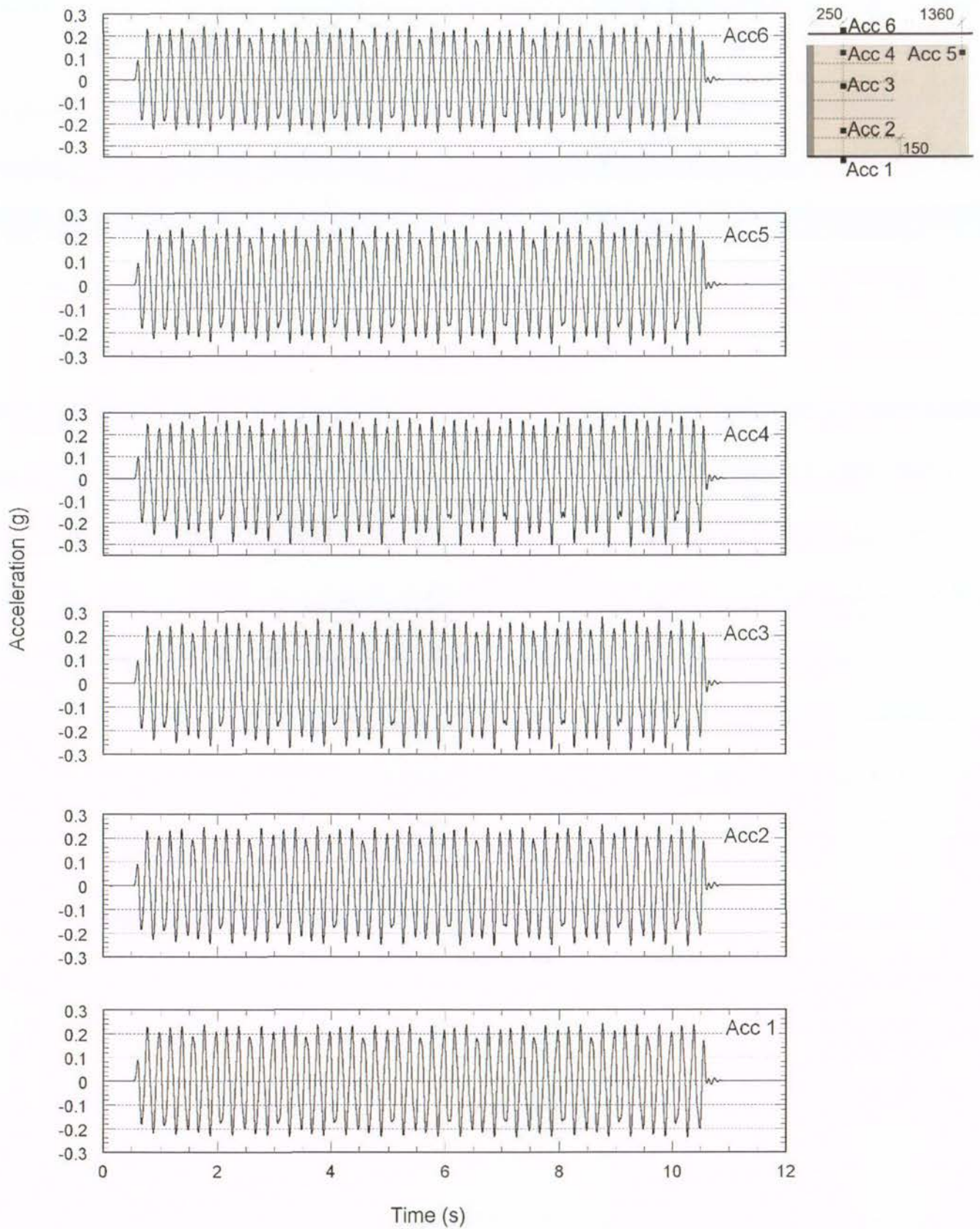


Figure B-30. Test-4 acceleration time histories at 0.2g shaking step

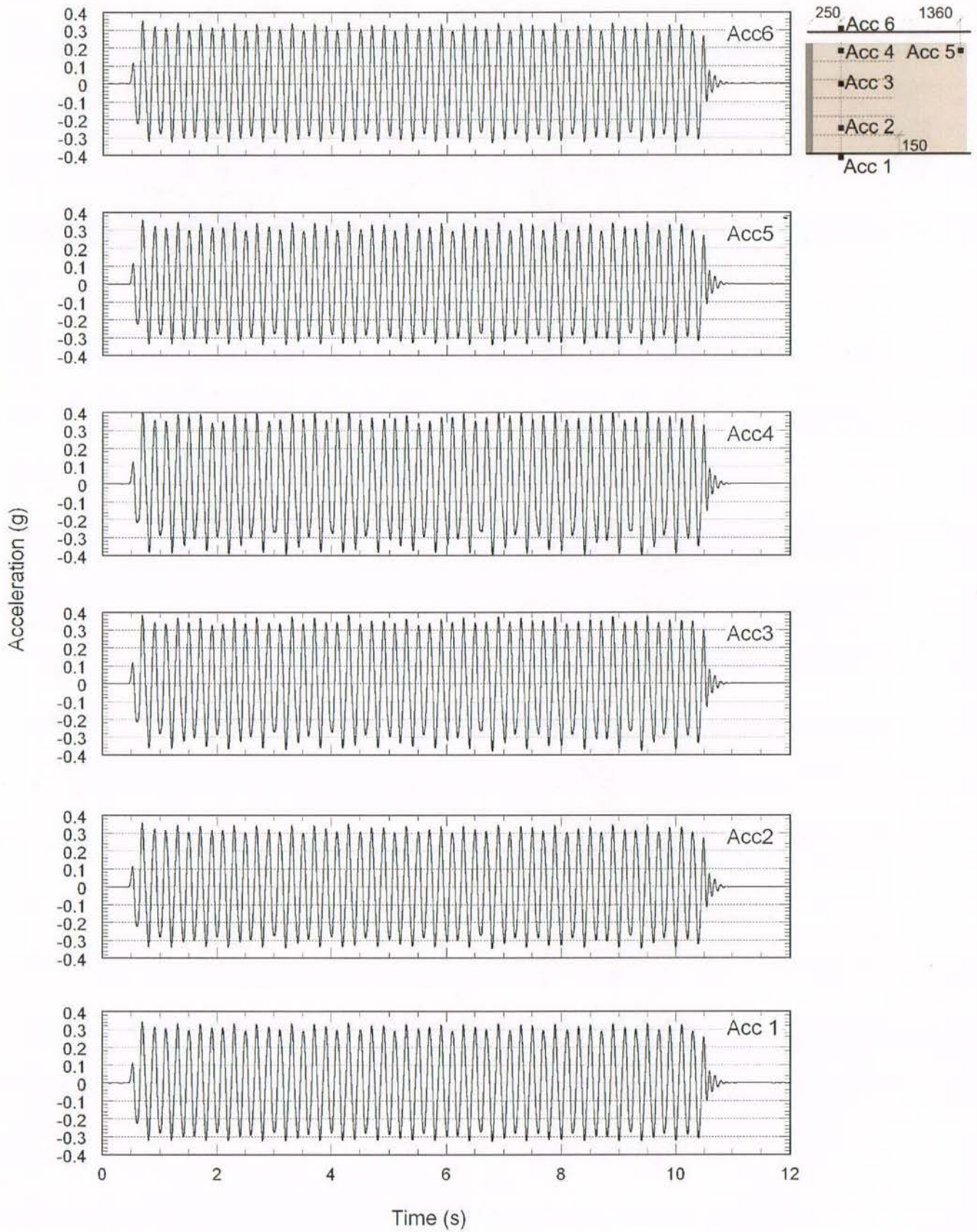


Figure B-31. Test-4 acceleration time histories at 0.3g shaking step

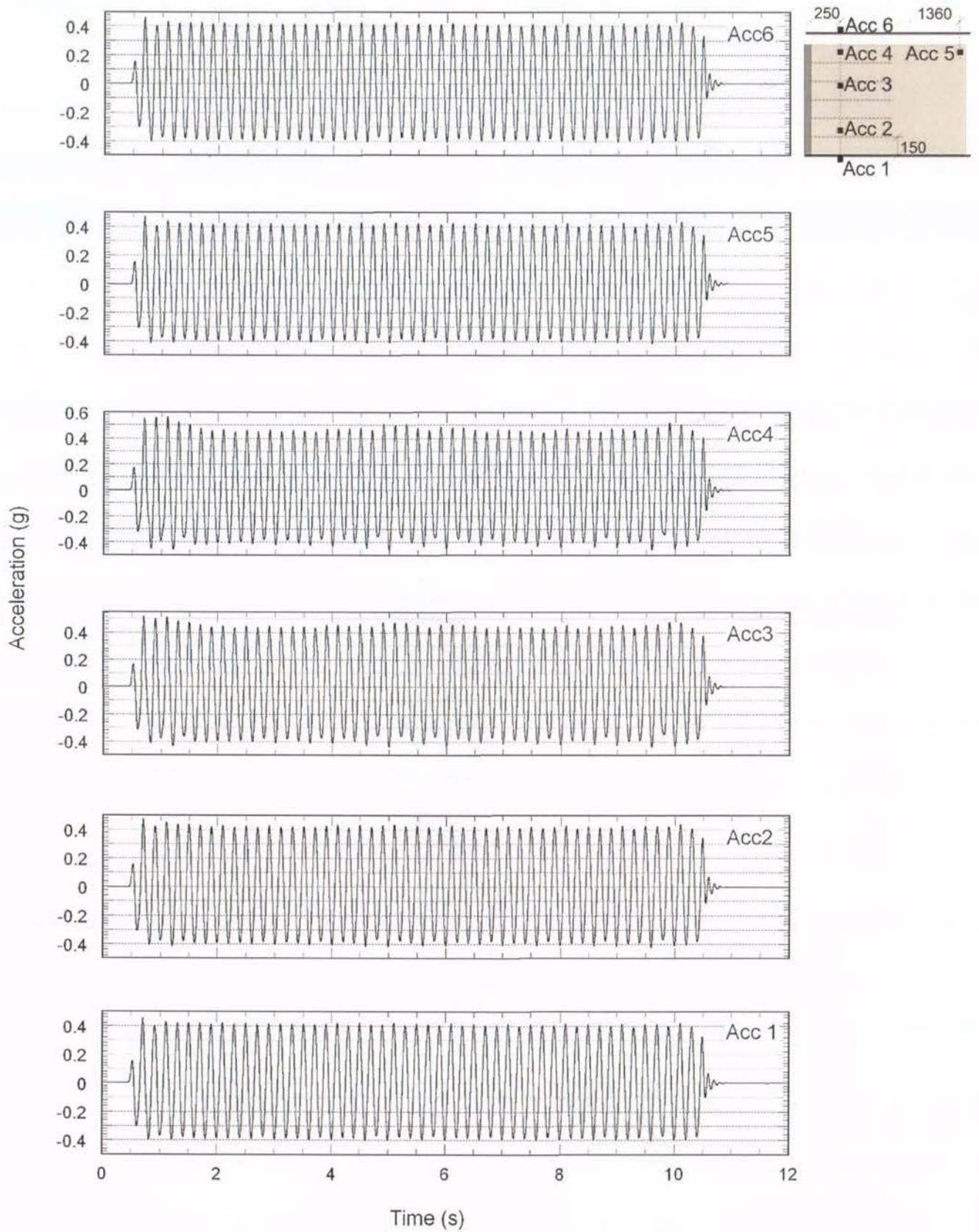


Figure B-32. Test-4 acceleration time histories at 0.4g shaking step

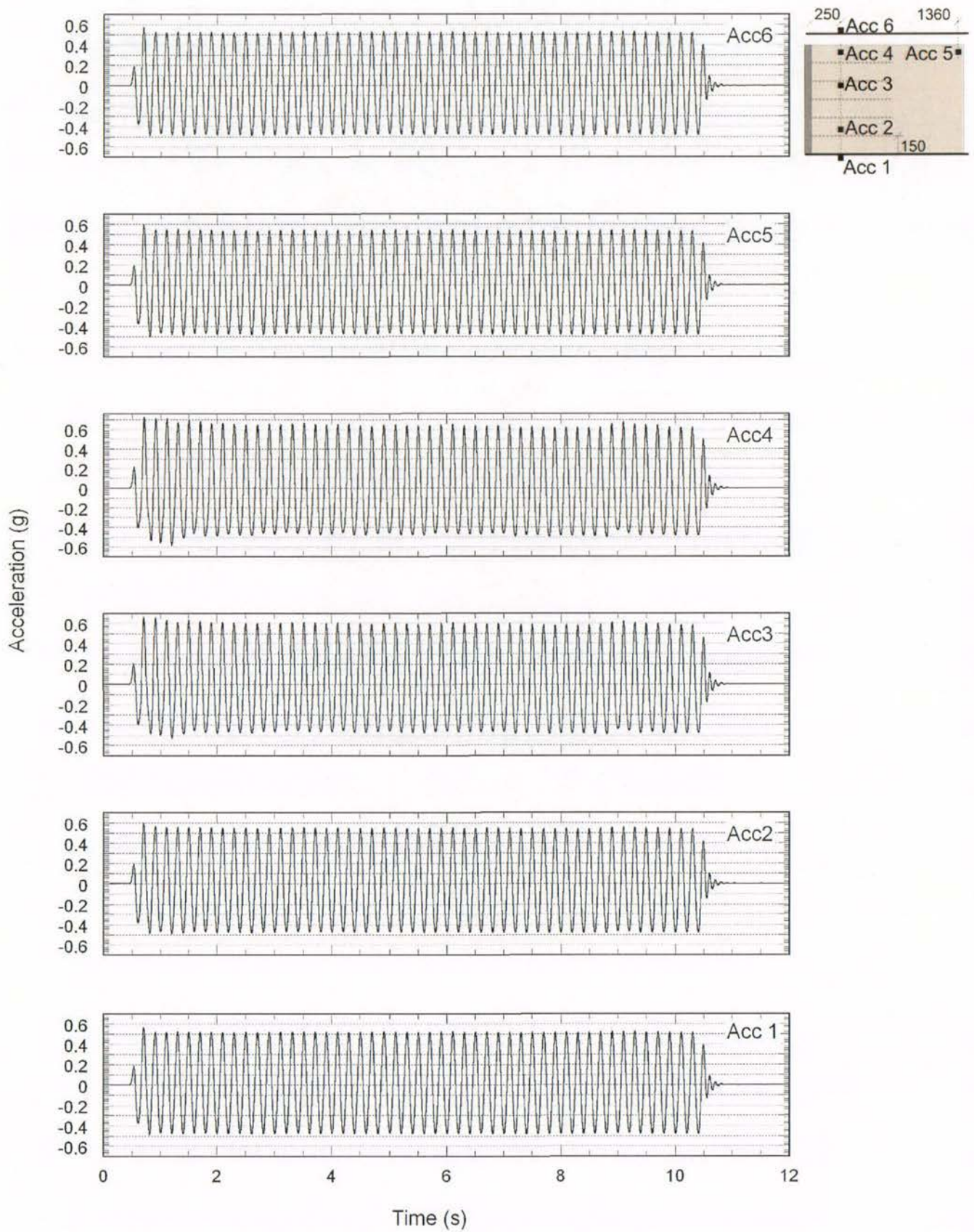


Figure B-33. Test-4 acceleration time histories at 0.5g shaking step

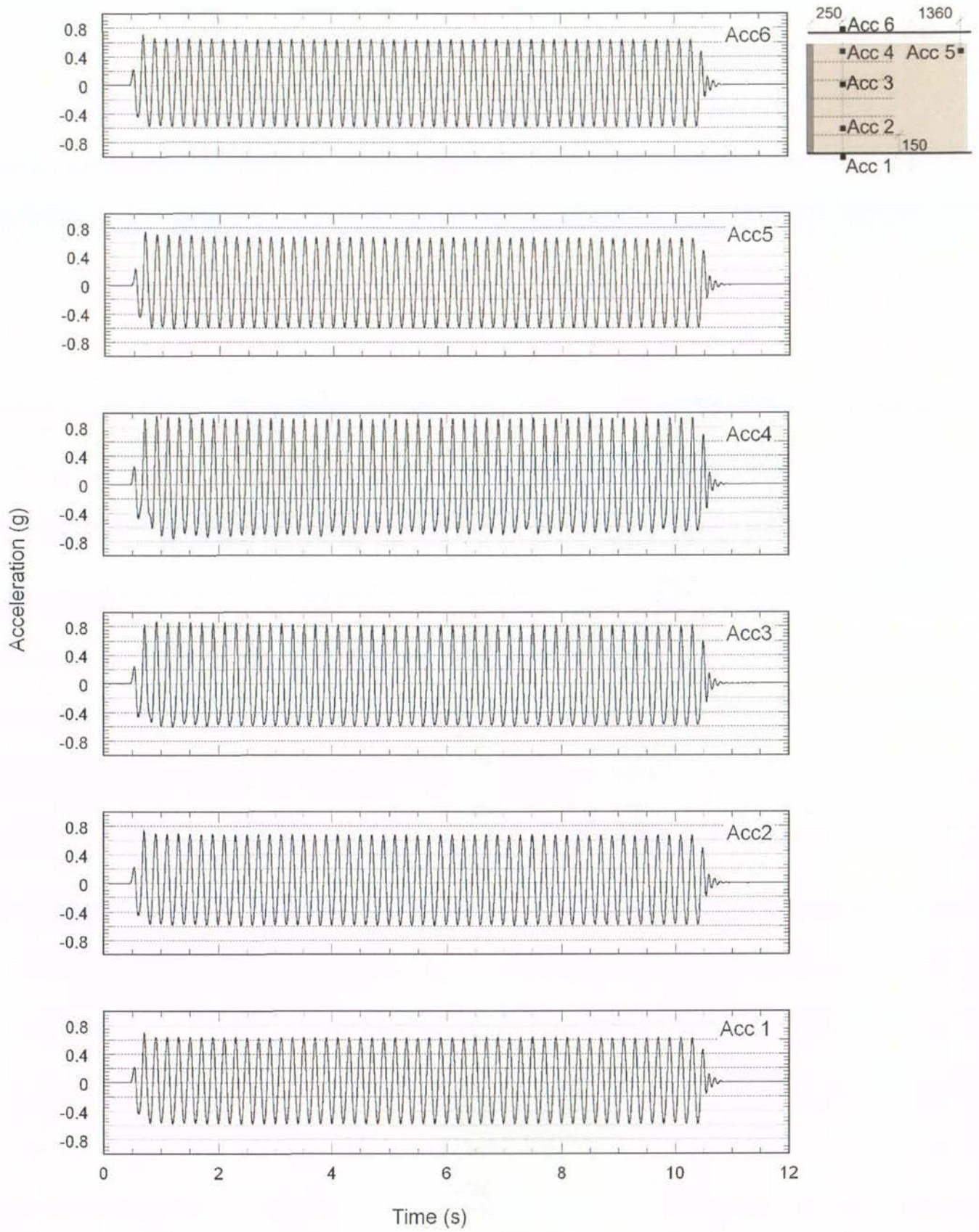


Figure B-34. Test-4 acceleration time histories at 0.6g shaking step

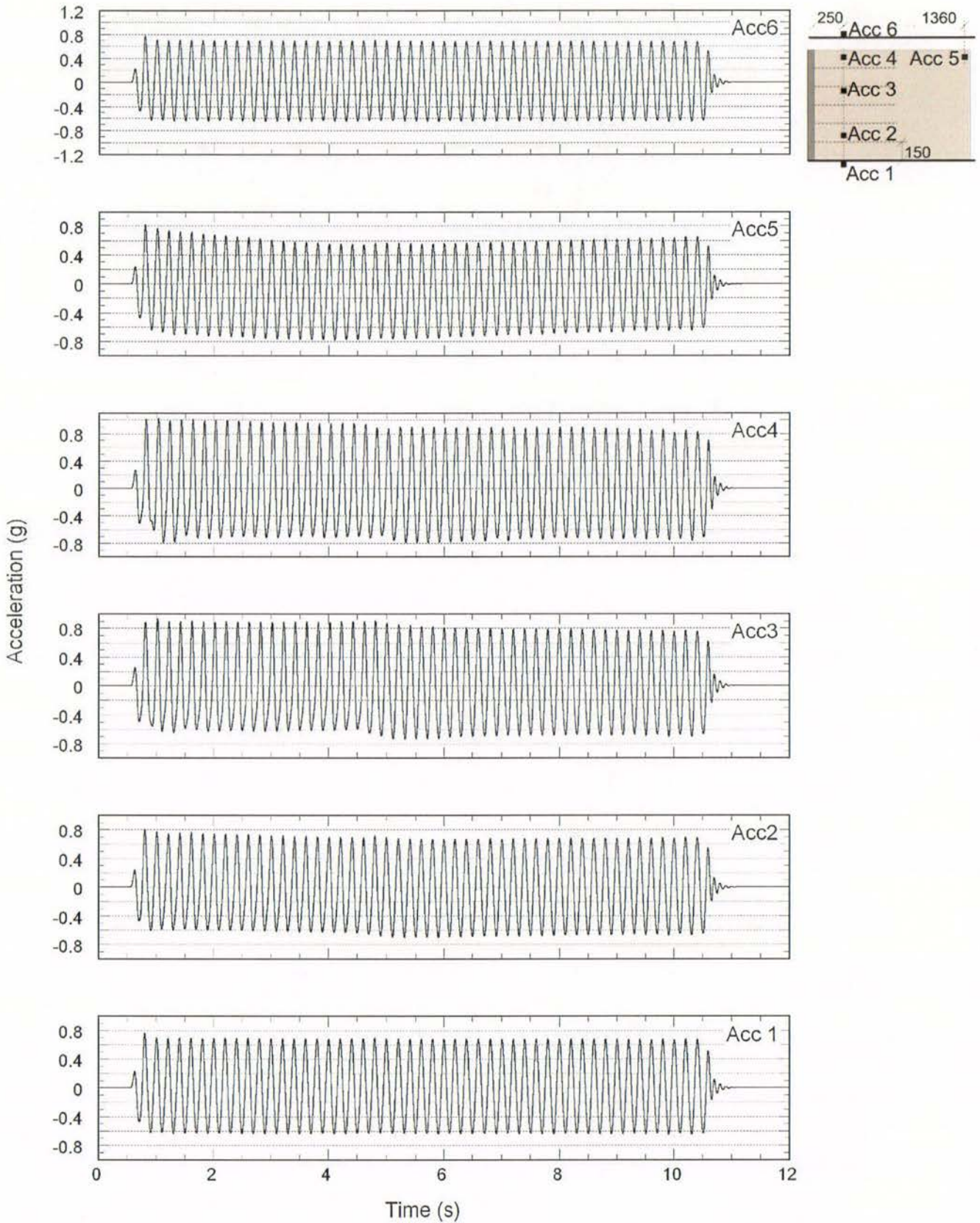


Figure B-35. Test-4 acceleration time histories at 0.65g shaking step

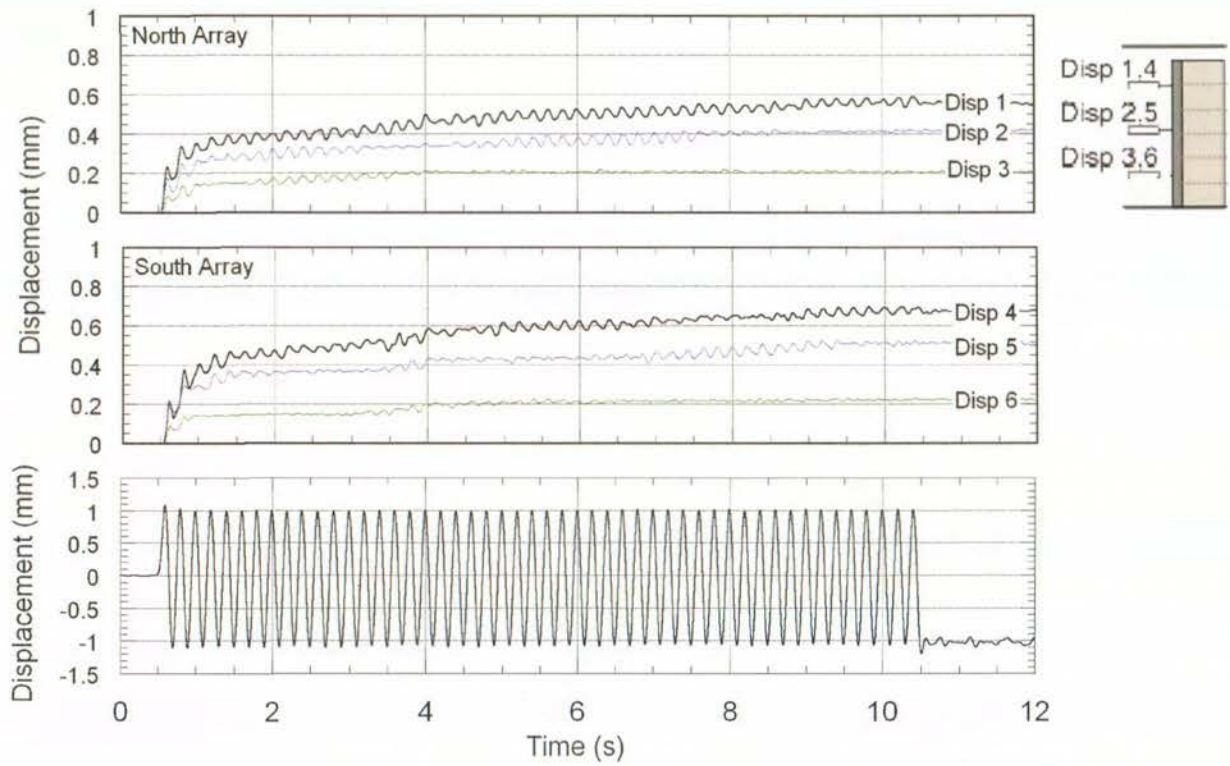


Figure B-36. Test-4 displacement time histories at 0.1g shaking step

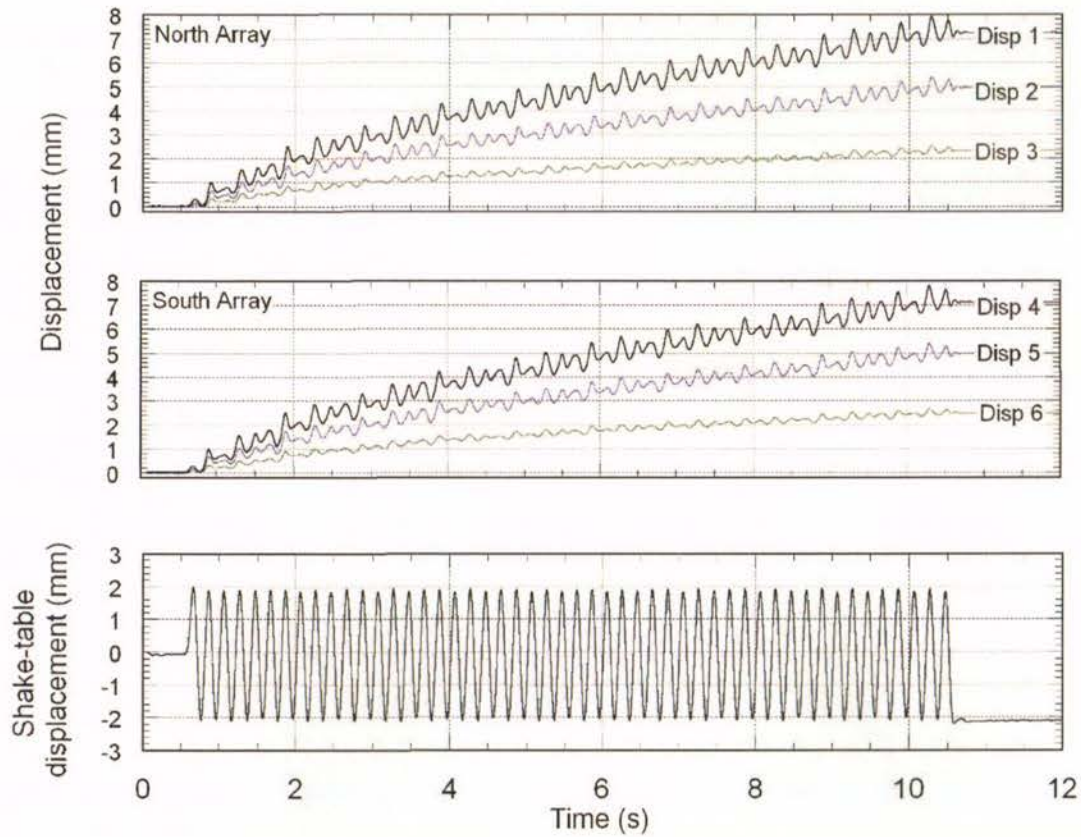


Figure B-37. Test-4 displacement time histories at 0.2g shaking step

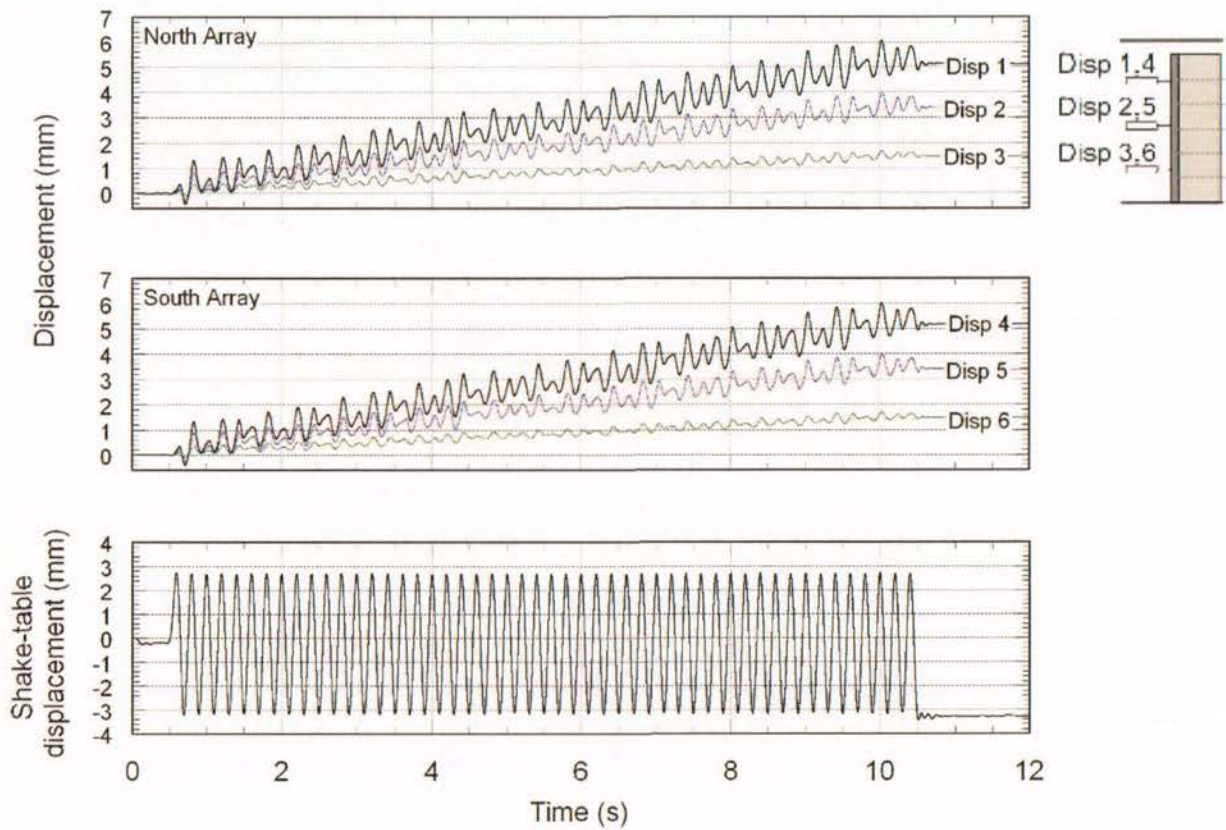


Figure B-38. Test-4 displacement time histories at 0.3g shaking step

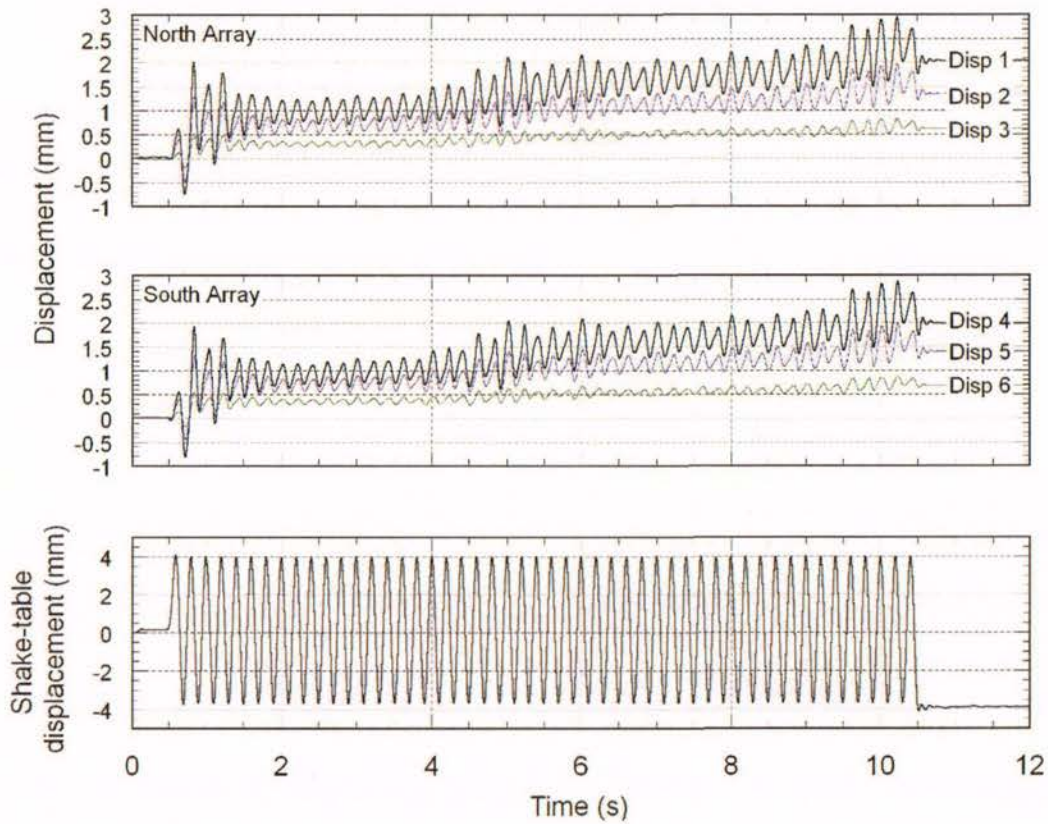


Figure B-39. Test-4 displacement time histories at 0.4g shaking step

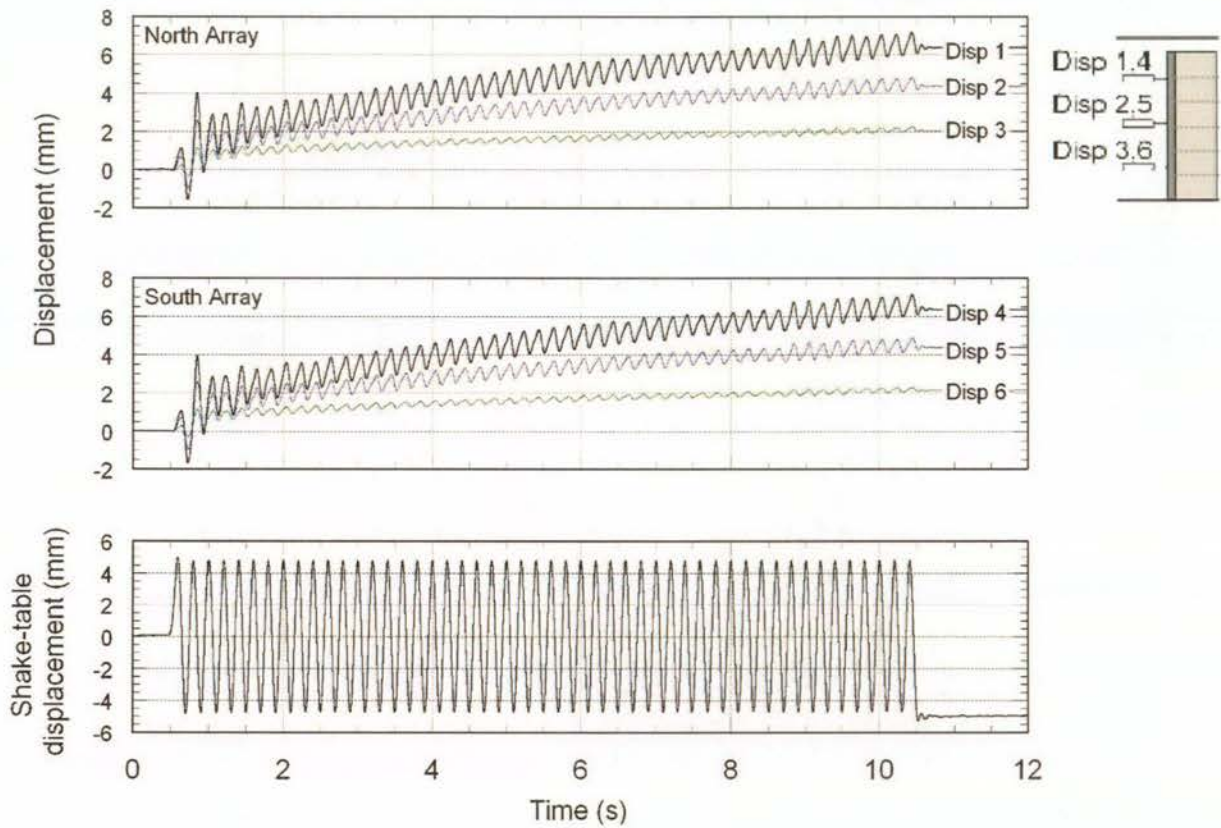


Figure B-40. Test-4 displacement time histories at 0.5g shaking step

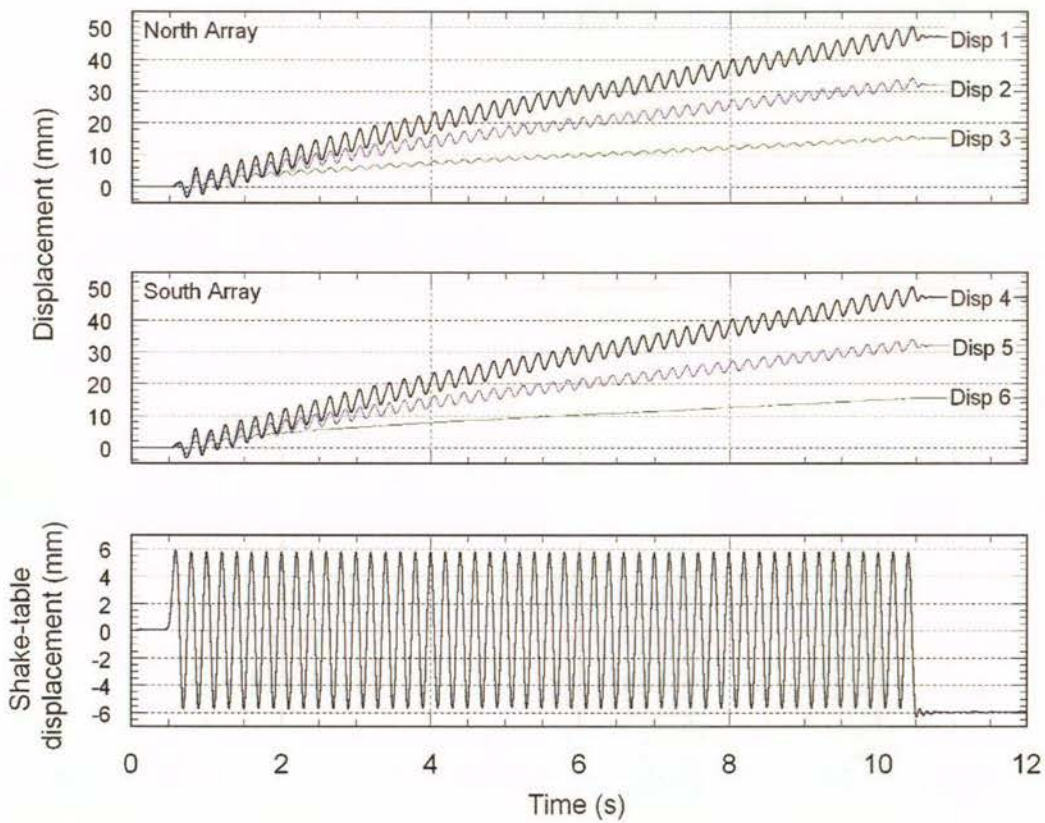


Figure B-41. Test-4 displacement time histories at 0.6g shaking step

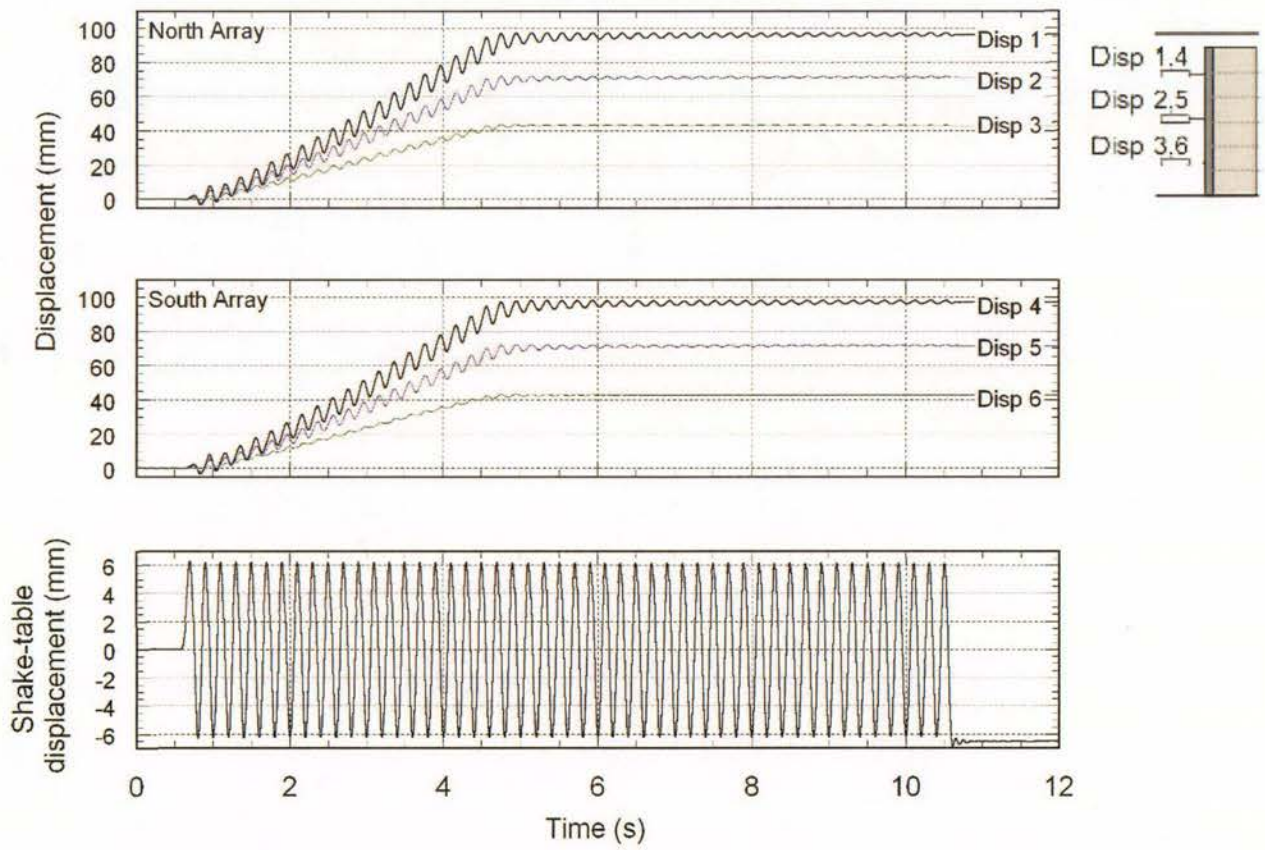


Figure B-42. Test-4 displacement time histories at 0.65g shaking step

## B.5 Test-5 Time Histories

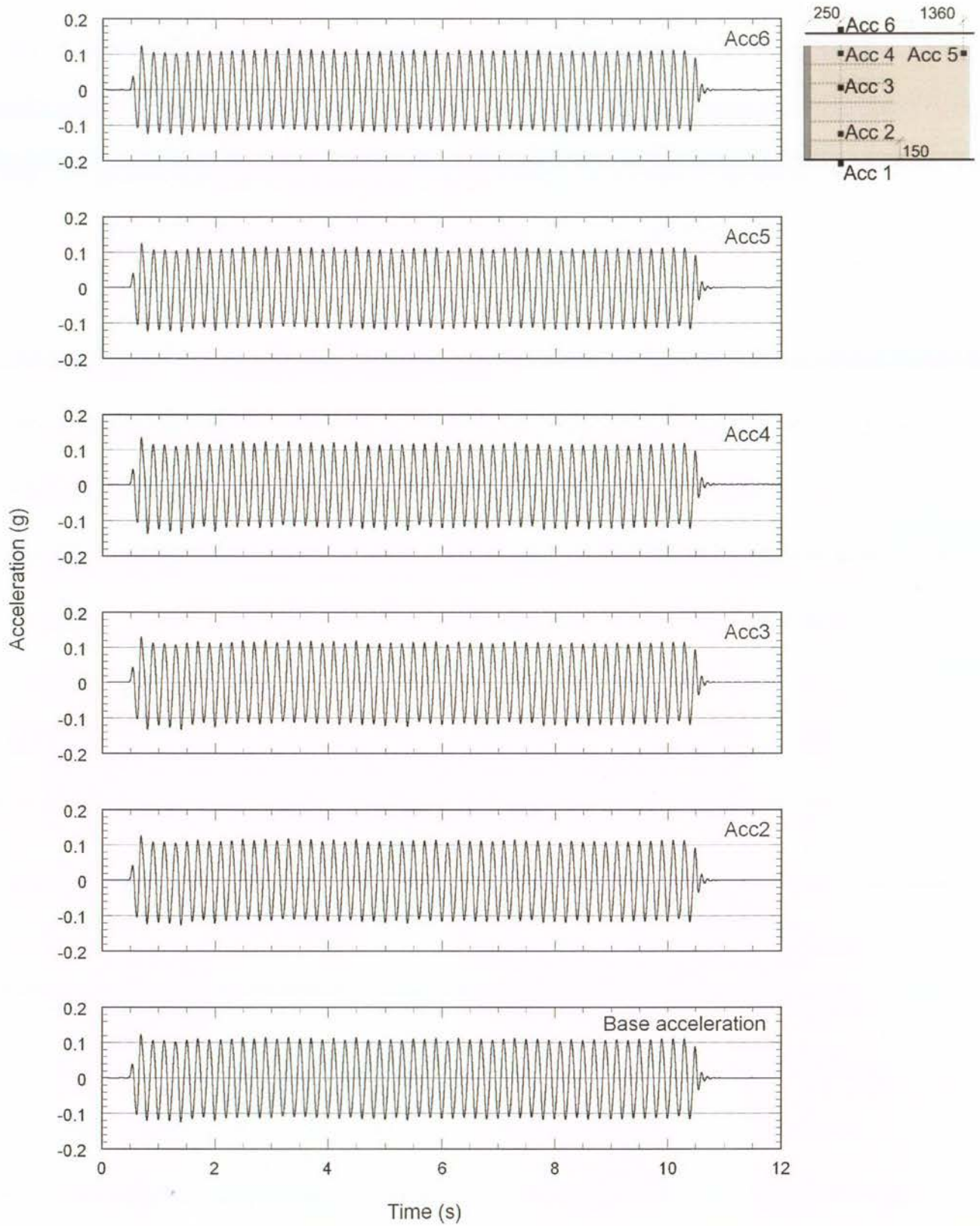


Figure B-43 Test-5 acceleration time histories at 0.1g shaking step.

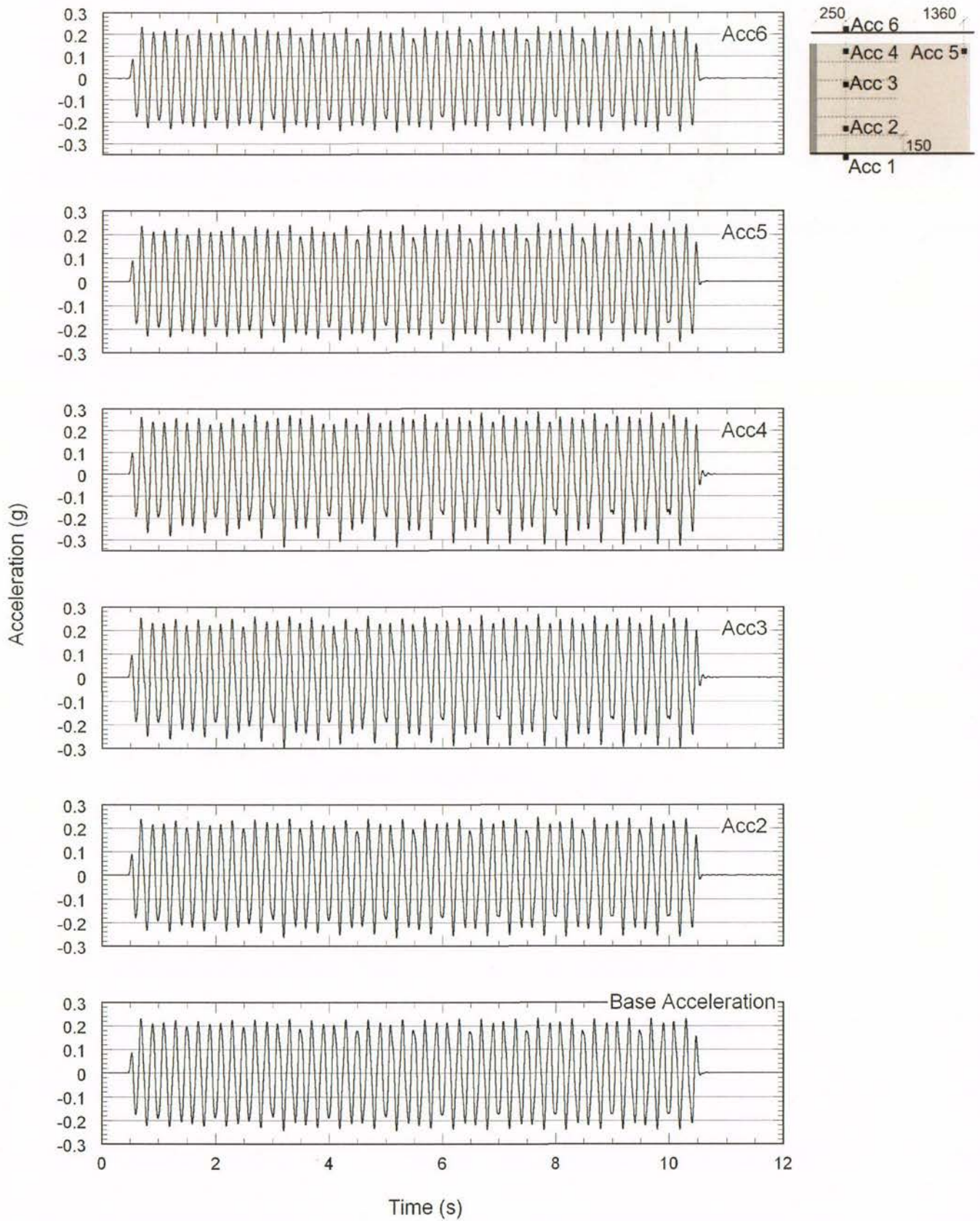


Figure B-44. Test-5 acceleration time histories at 0.2g shaking step.

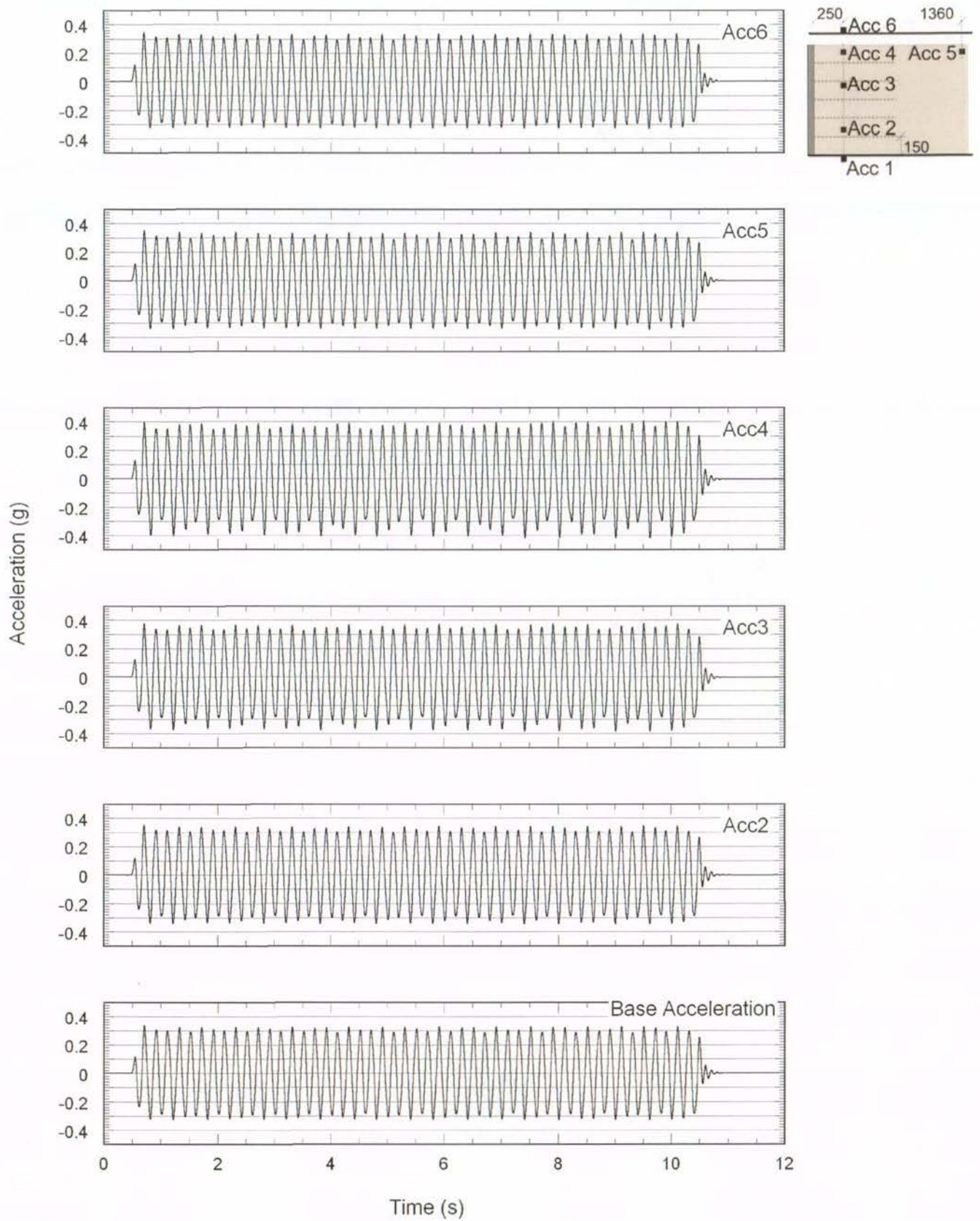


Figure B-45. Test-5 acceleration time histories at 0.3g shaking step.



Figure B-46. Test-5 acceleration time histories at 0.4g shaking step.

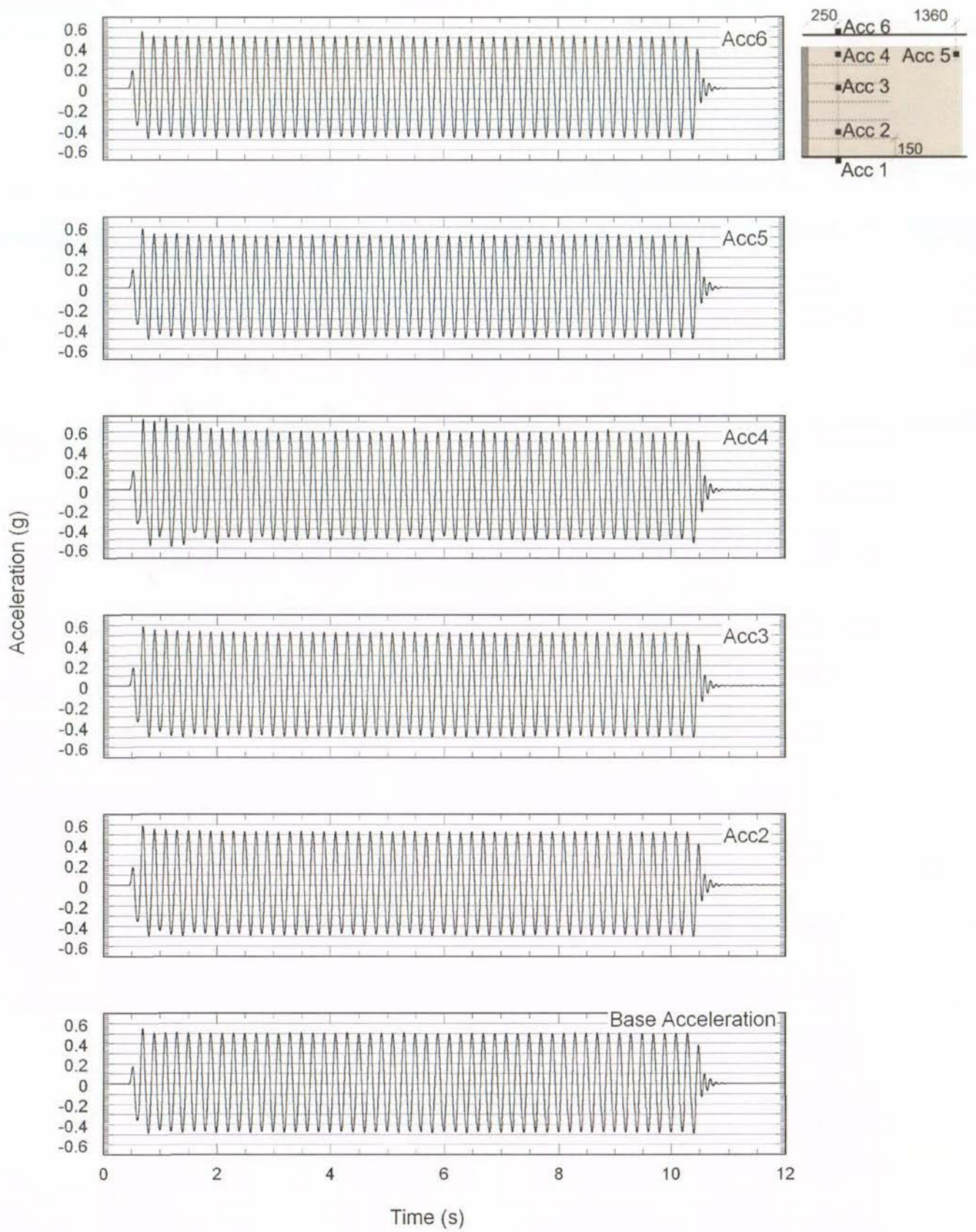


Figure B-47. Test-5 acceleration time histories at 0.5g shaking step.

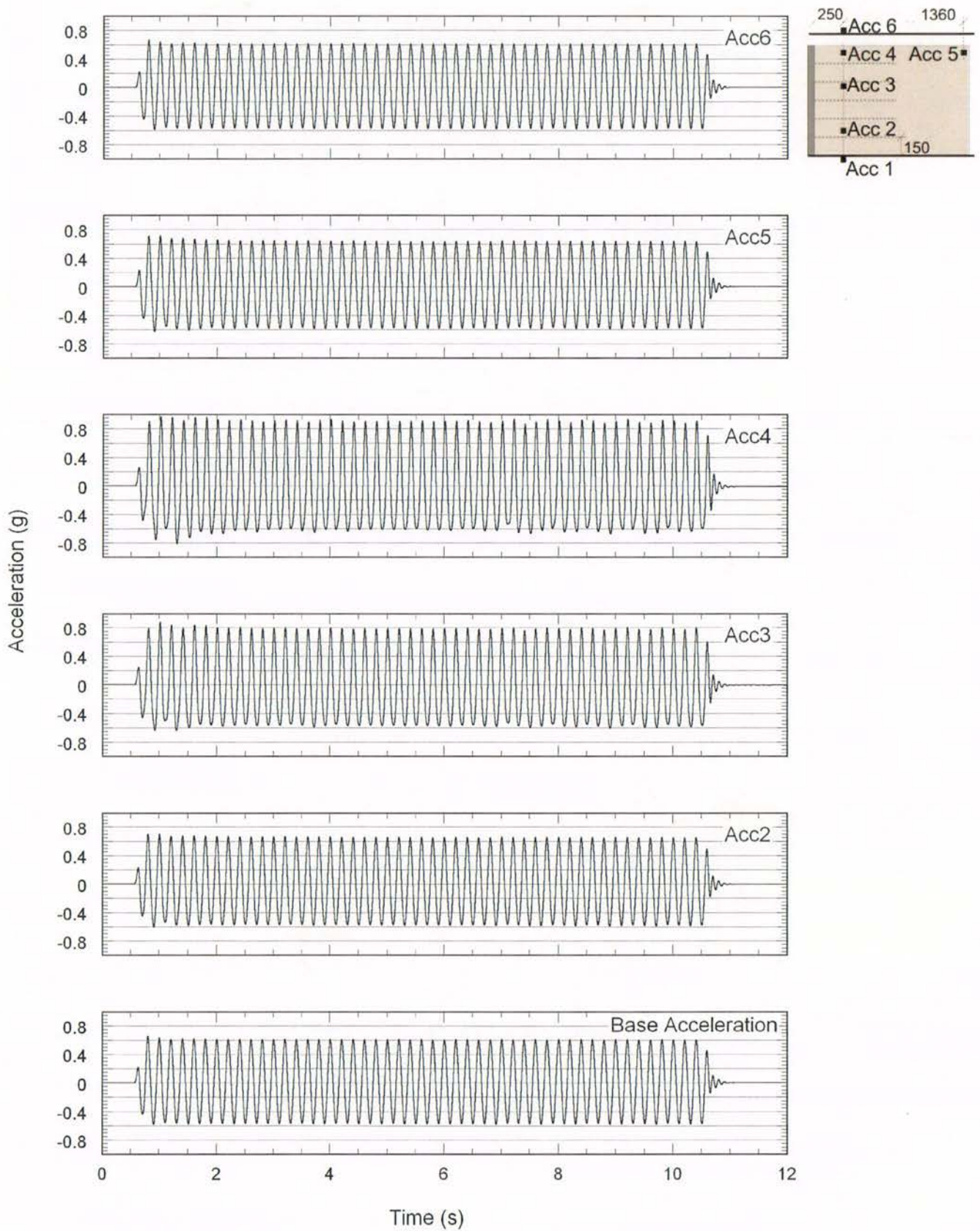


Figure B-48. Test-5 acceleration time histories at 0.6g shaking step.



Figure B-49. Test-5 acceleration time histories at 0.7g shaking step.

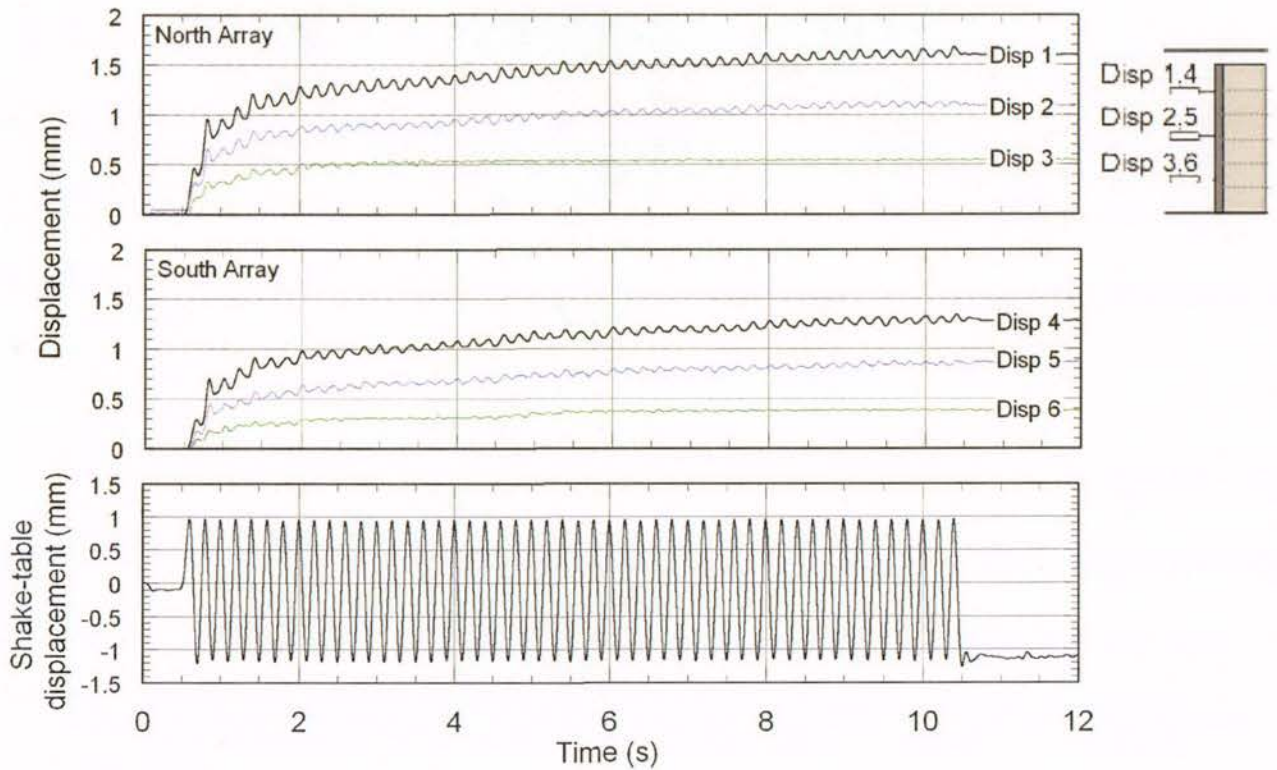


Figure B-50. Test-5 displacement time histories at 0.1g shaking step

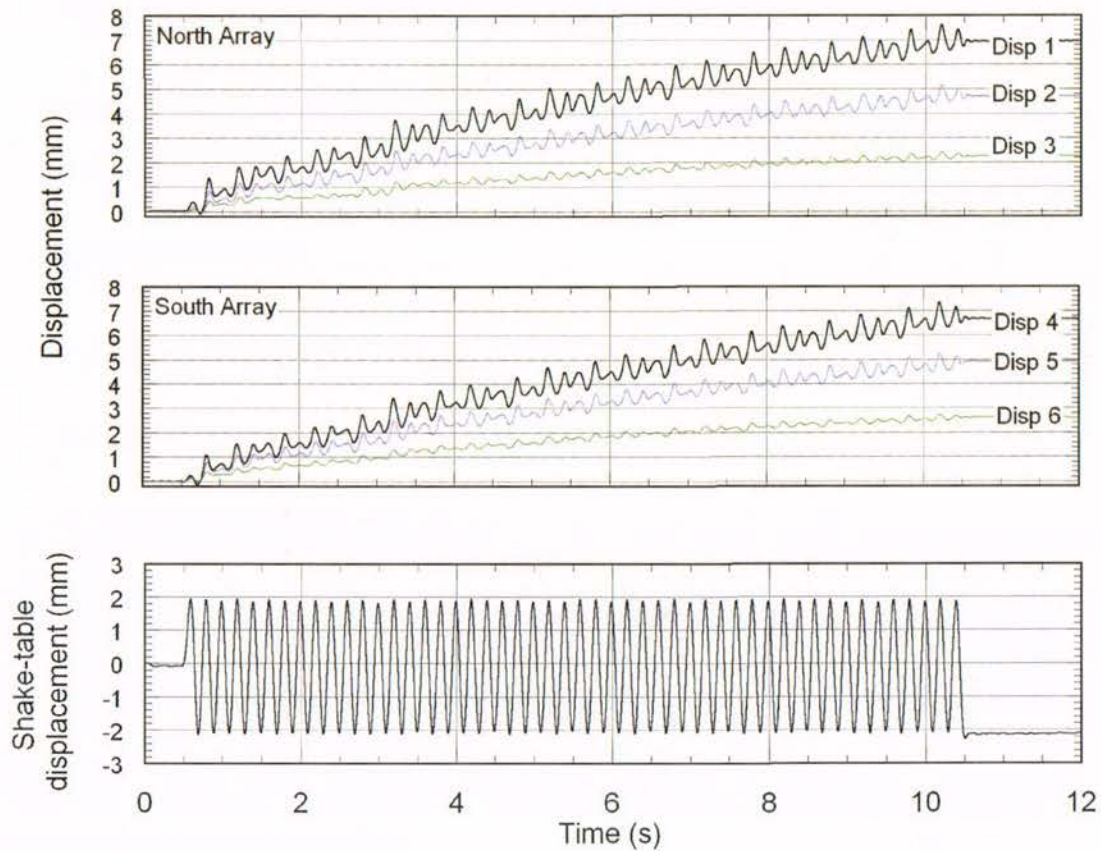


Figure B-51. Test-5 displacement time histories at 0.2g shaking step

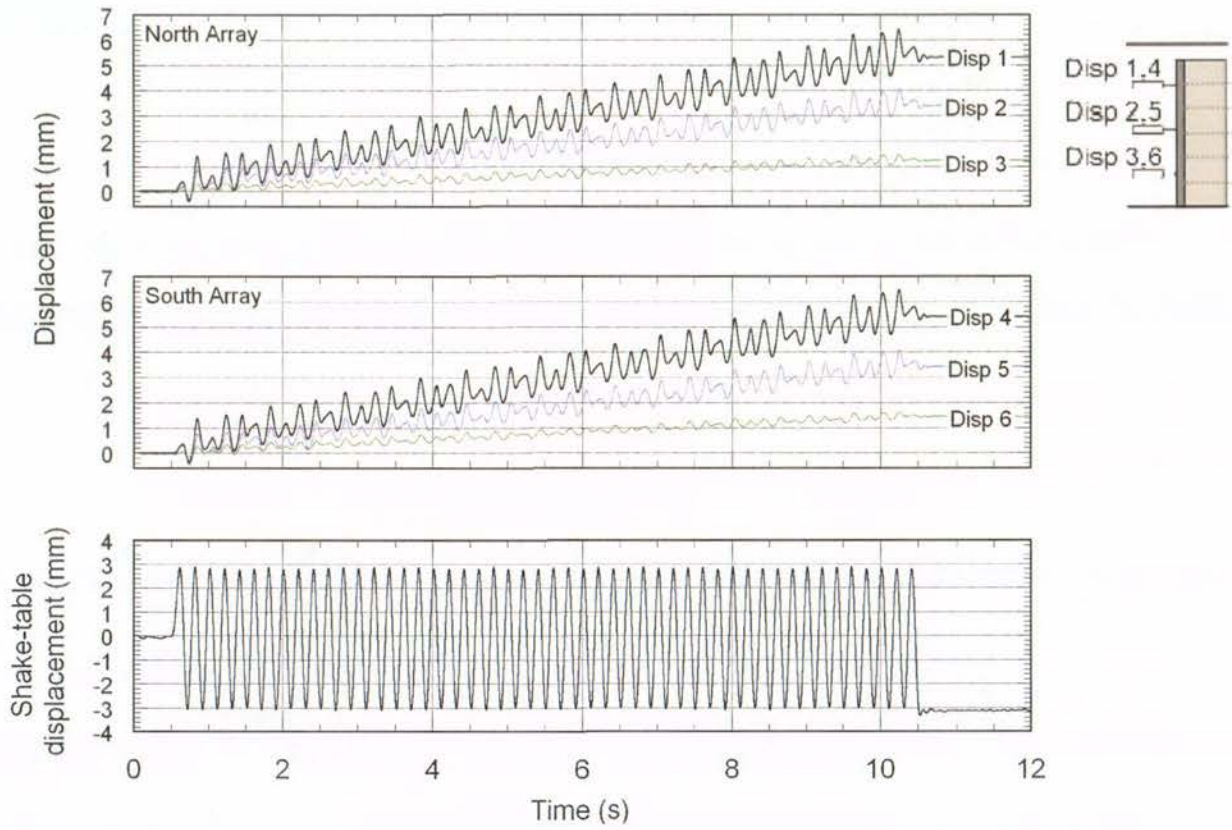


Figure B-52. Test-5 displacement time histories at 0.3g shaking step

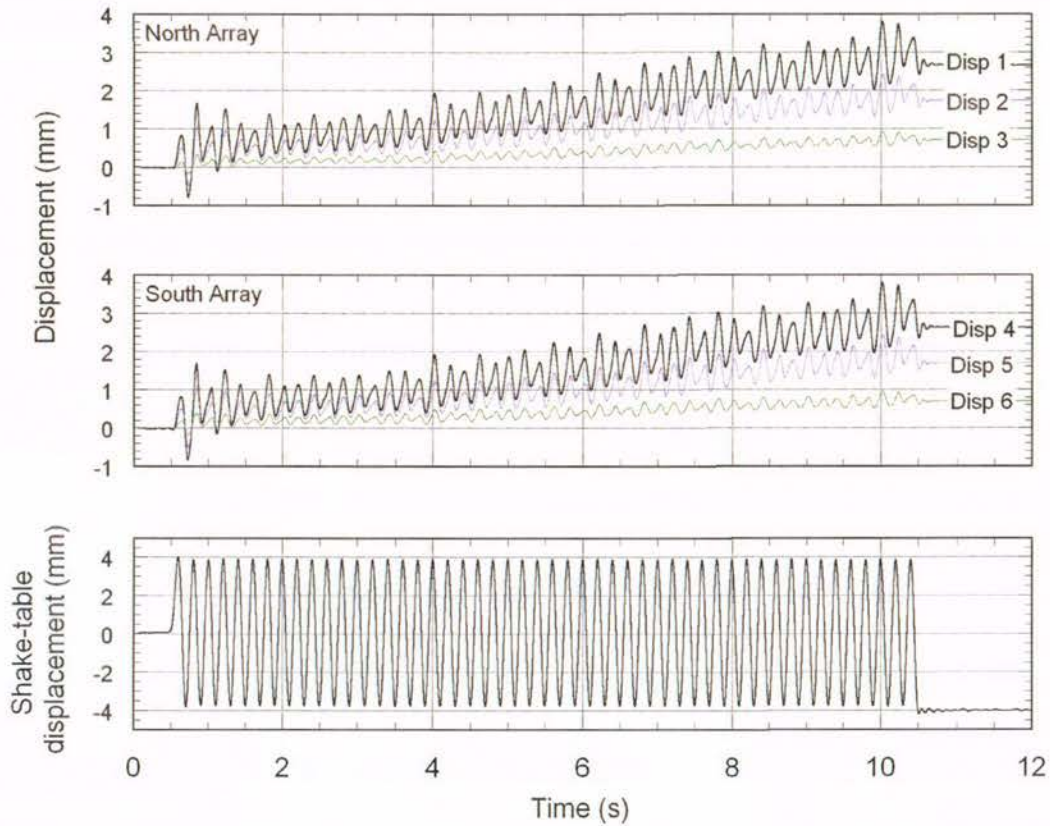


Figure B-53. Test-5 displacement time histories at 0.4g shaking step

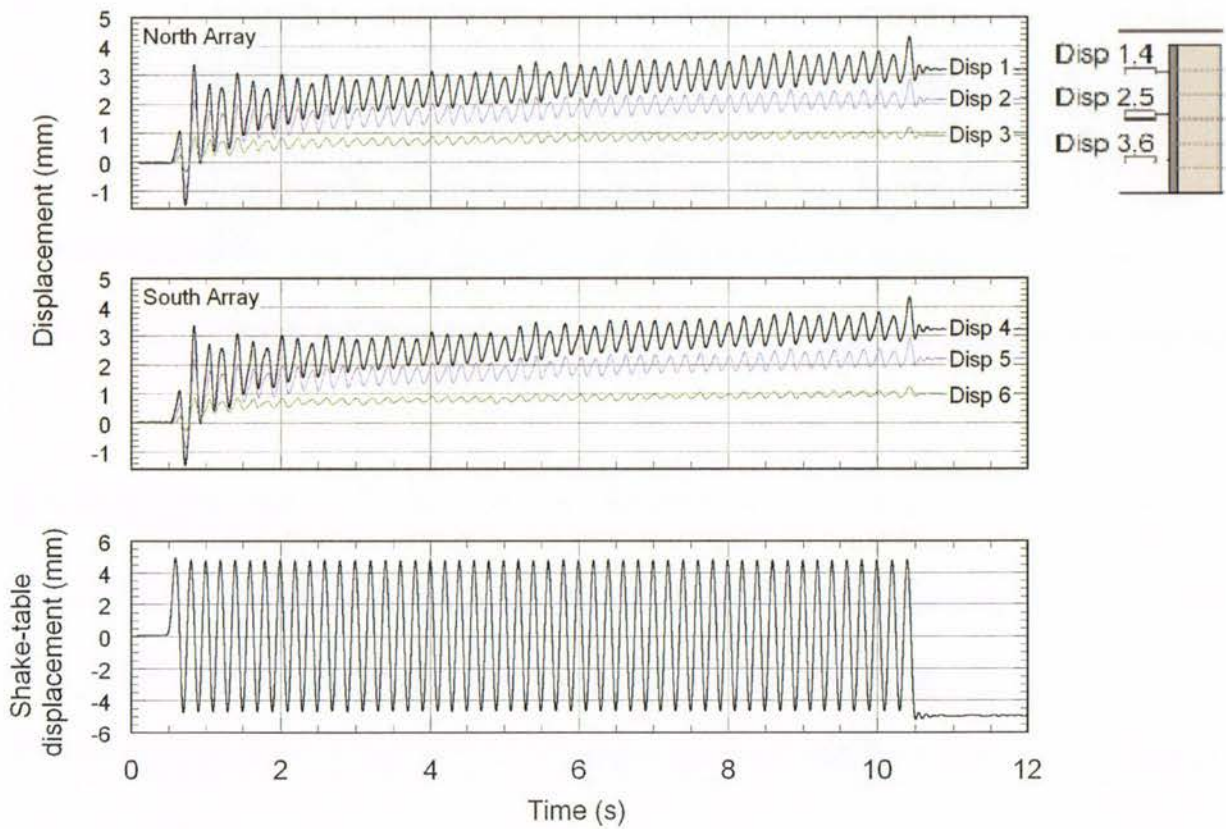


Figure B-54. Test-5 displacement time histories at 0.5g shaking step

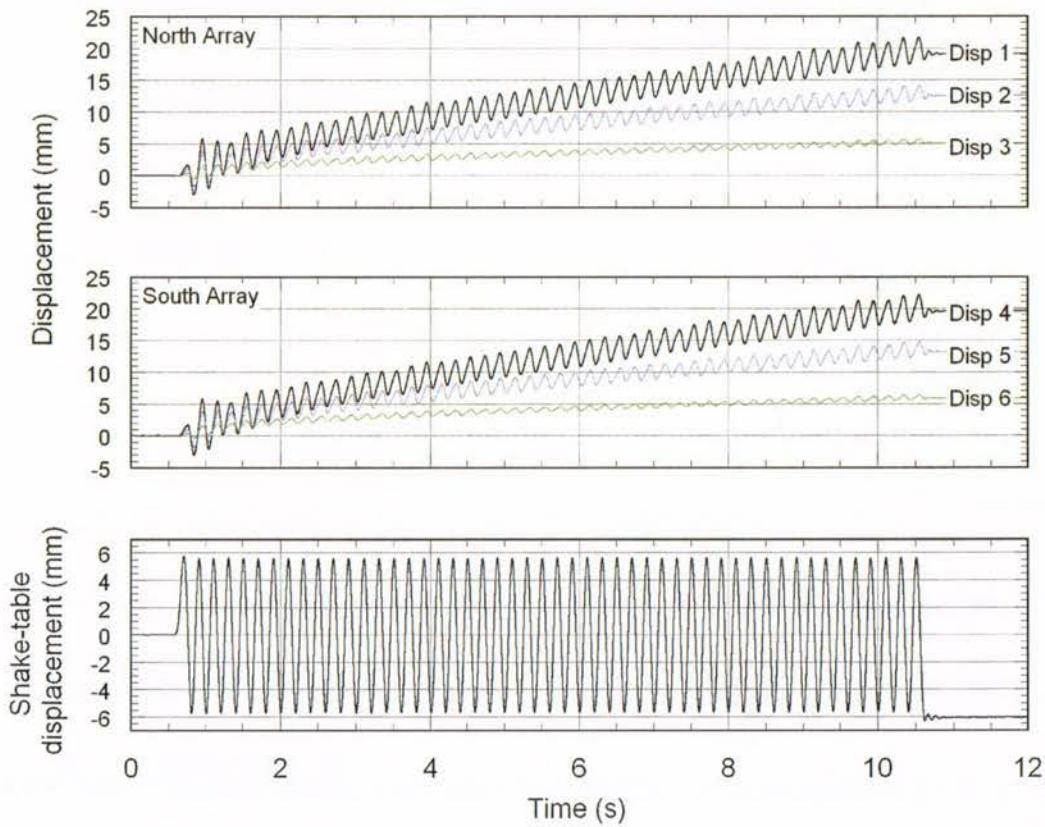


Figure B-55. Test-5 displacement time histories at 0.6g shaking step

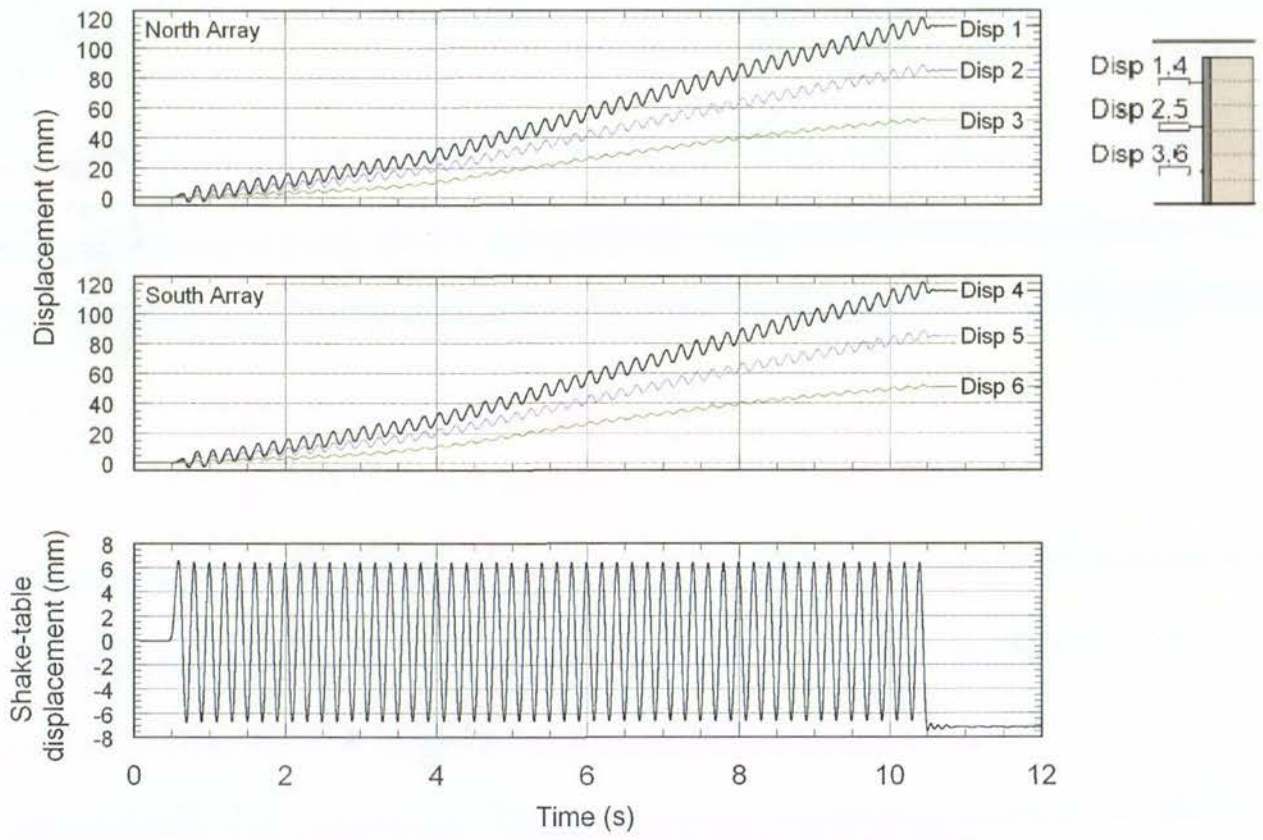


Figure B-56. Test-5 displacement time histories at 0.7g shaking step

## B.6 Test-6 Time Histories



Figure B-57. Test-6 acceleration time histories at 0.1g shaking step.

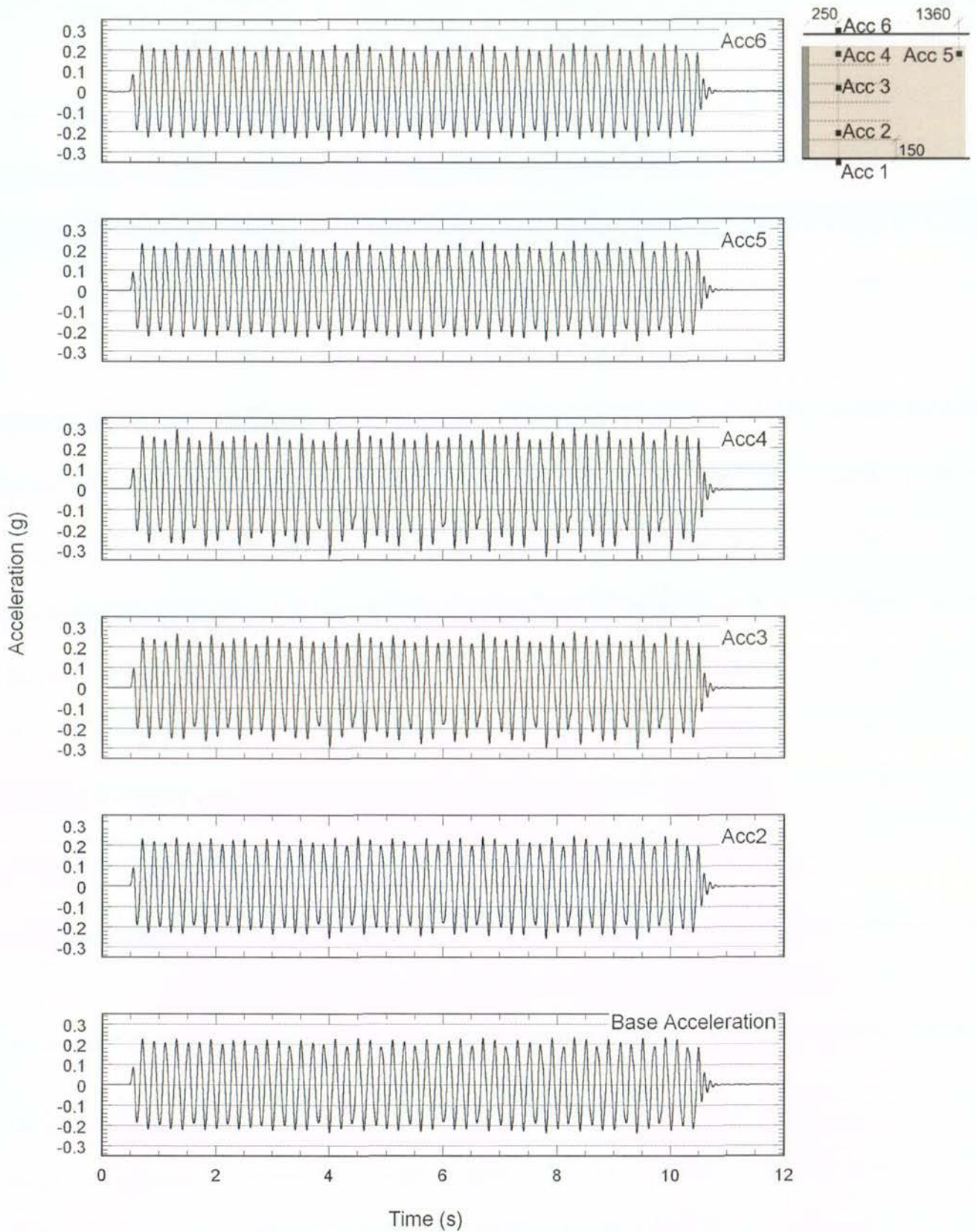


Figure B-58. Test-6 acceleration time histories at 0.2g shaking step.

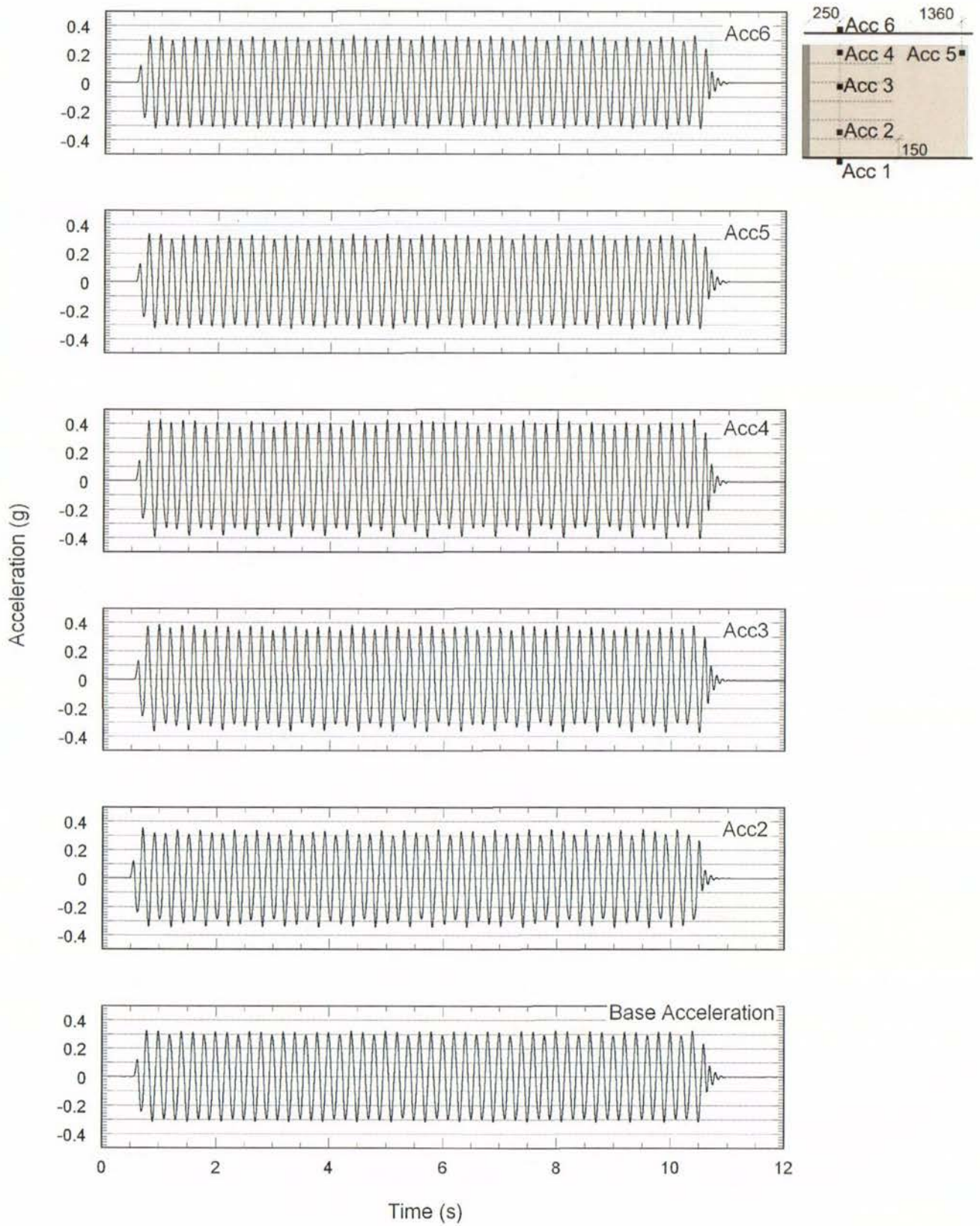


Figure B-59. Test-6 acceleration time histories at 0.3g shaking step.

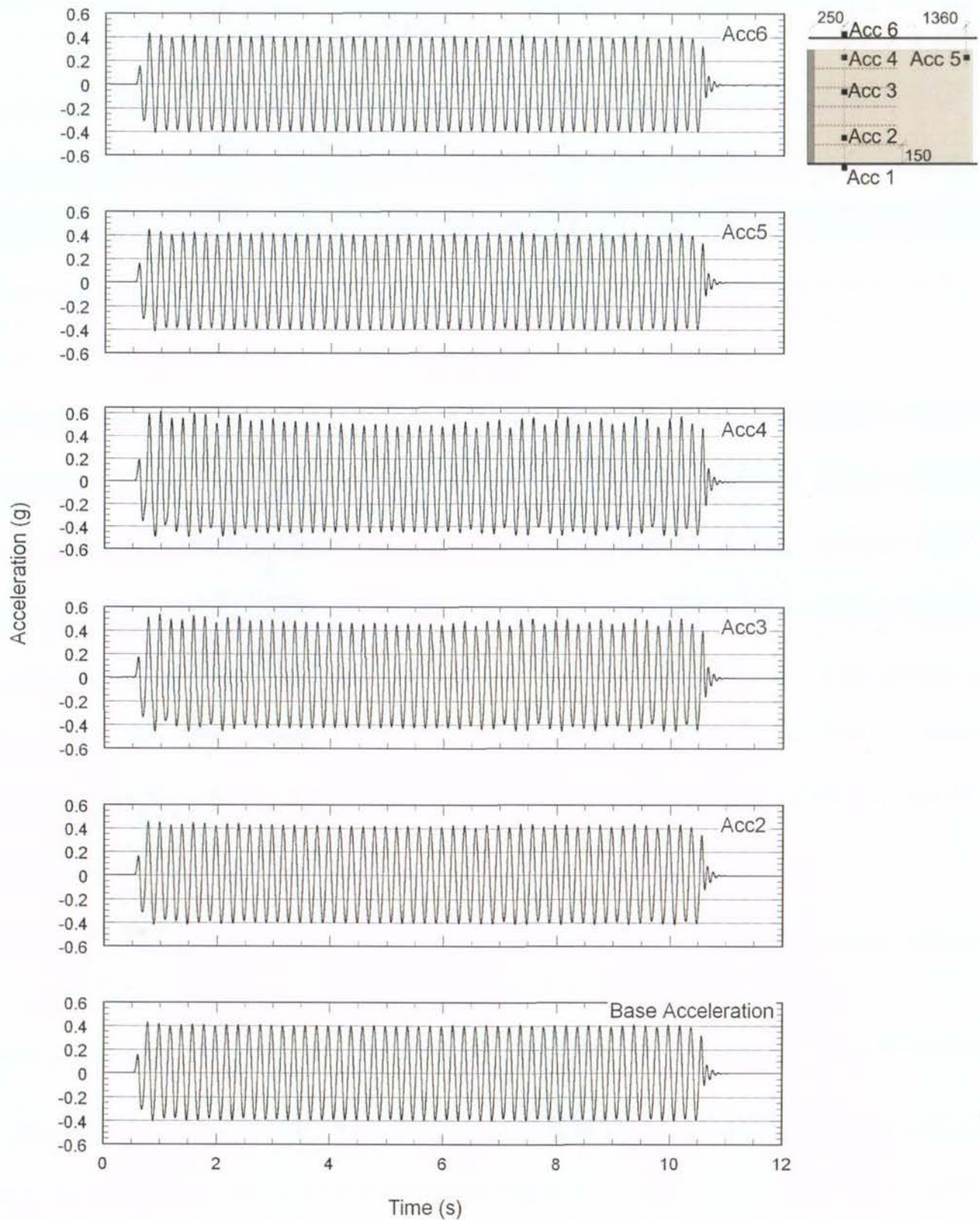


Figure B-60. Test-6 acceleration time histories at 0.4g shaking step.

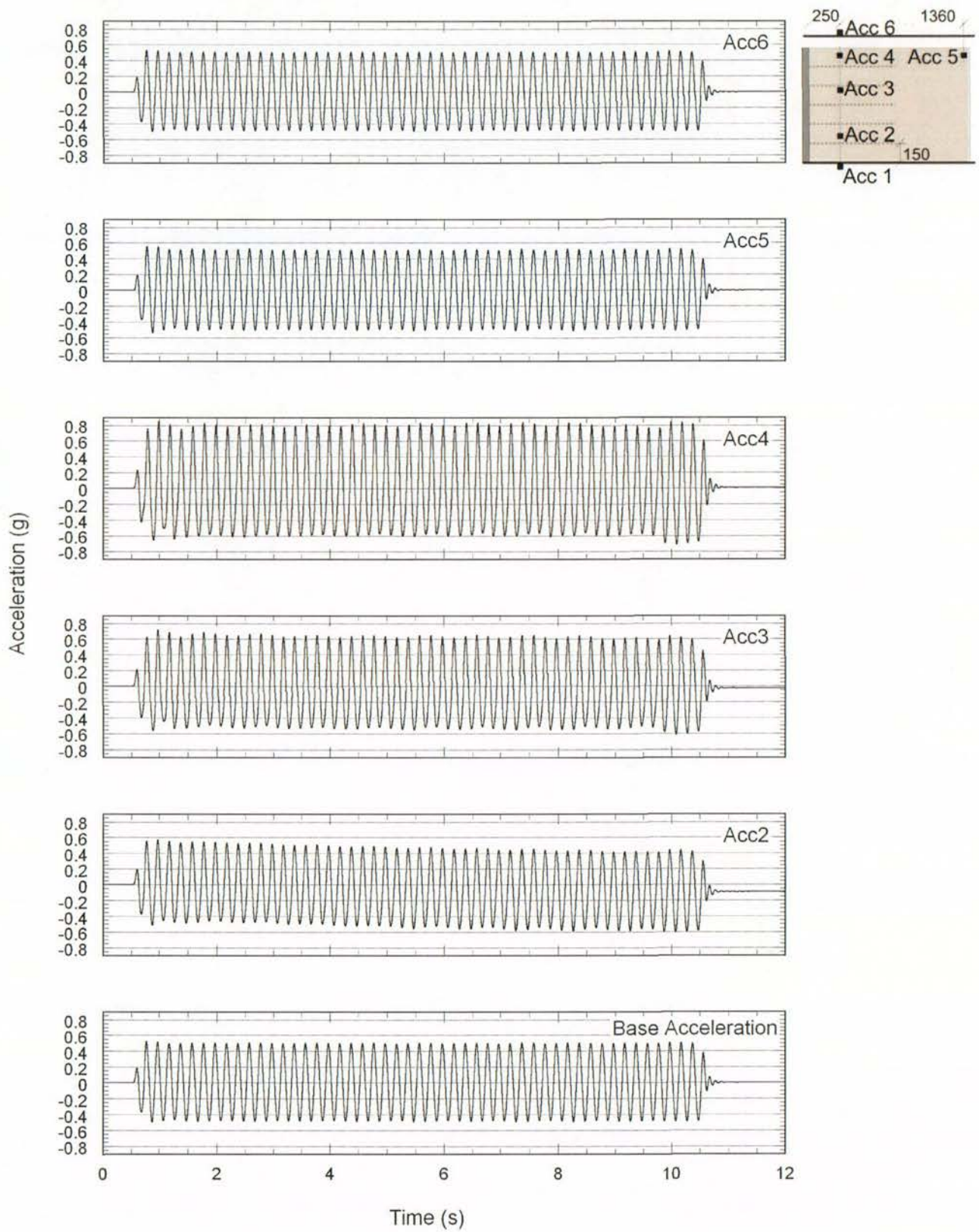


Figure B-61. Test-6 acceleration time histories at 0.5g shaking step.

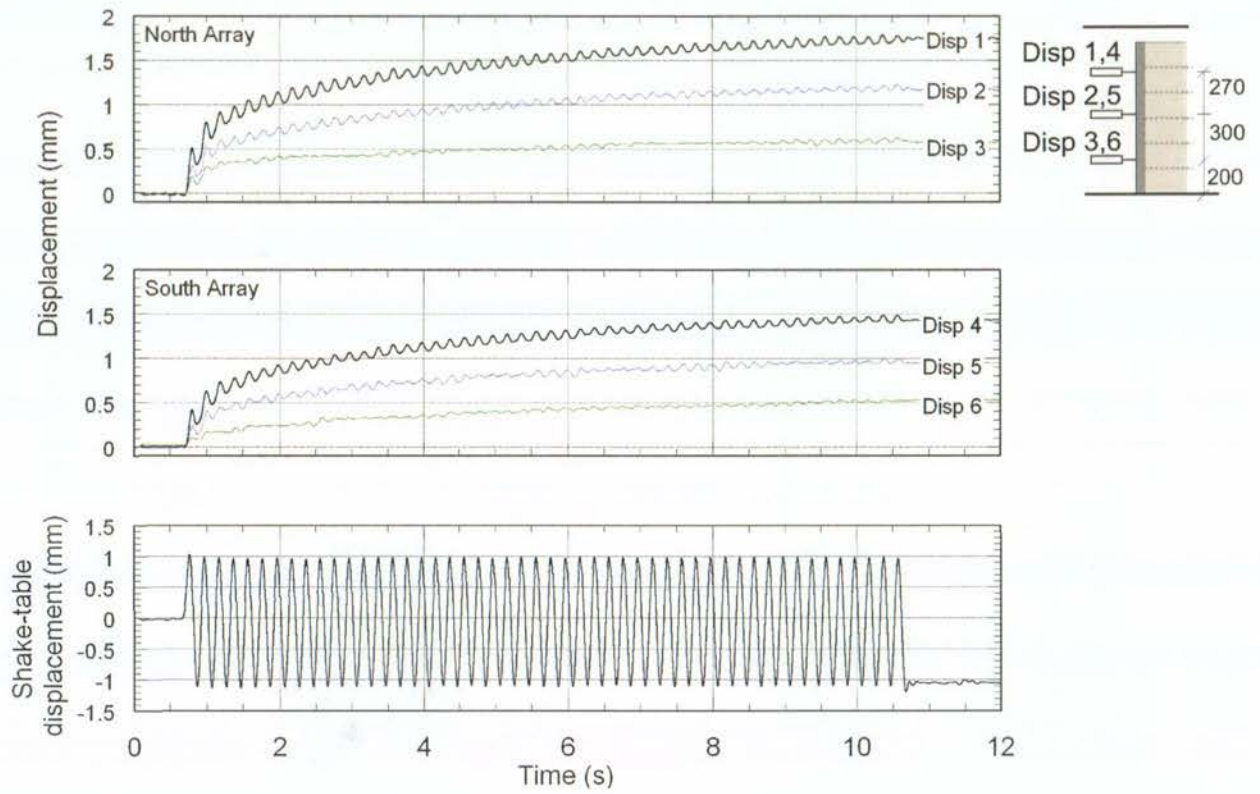


Figure B-62. Test-6 displacement transducer time histories at 0.5g shaking step.

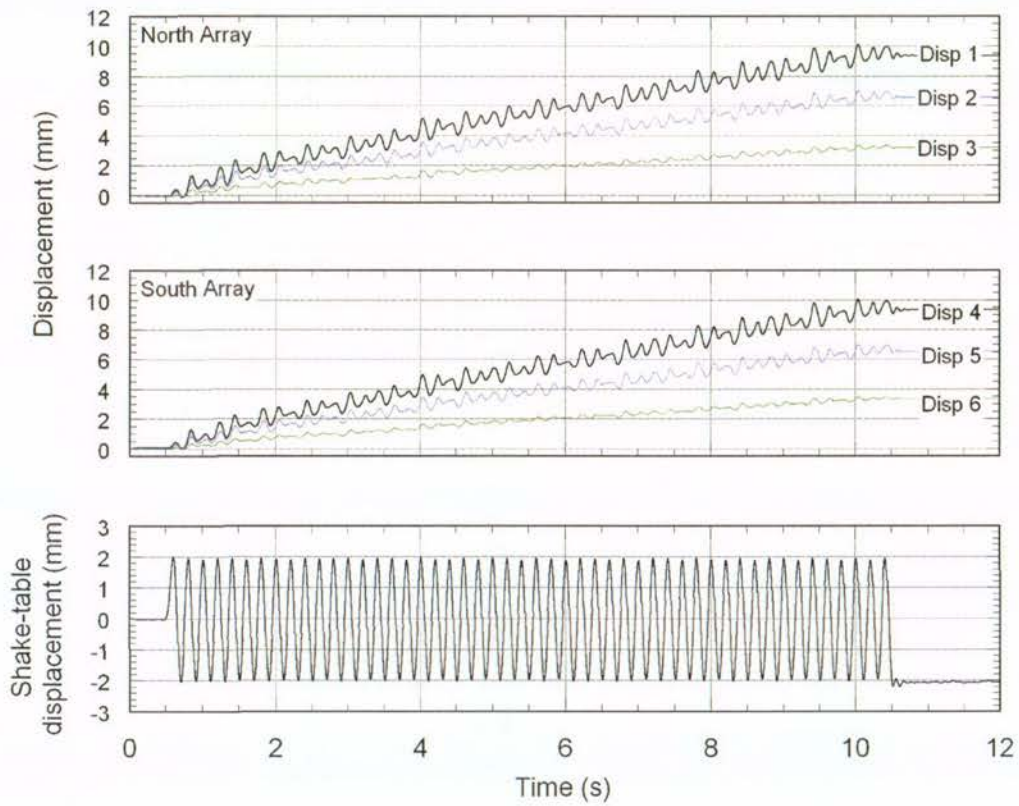


Figure B-63. Test-6 displacement time histories at 0.2g shaking step.

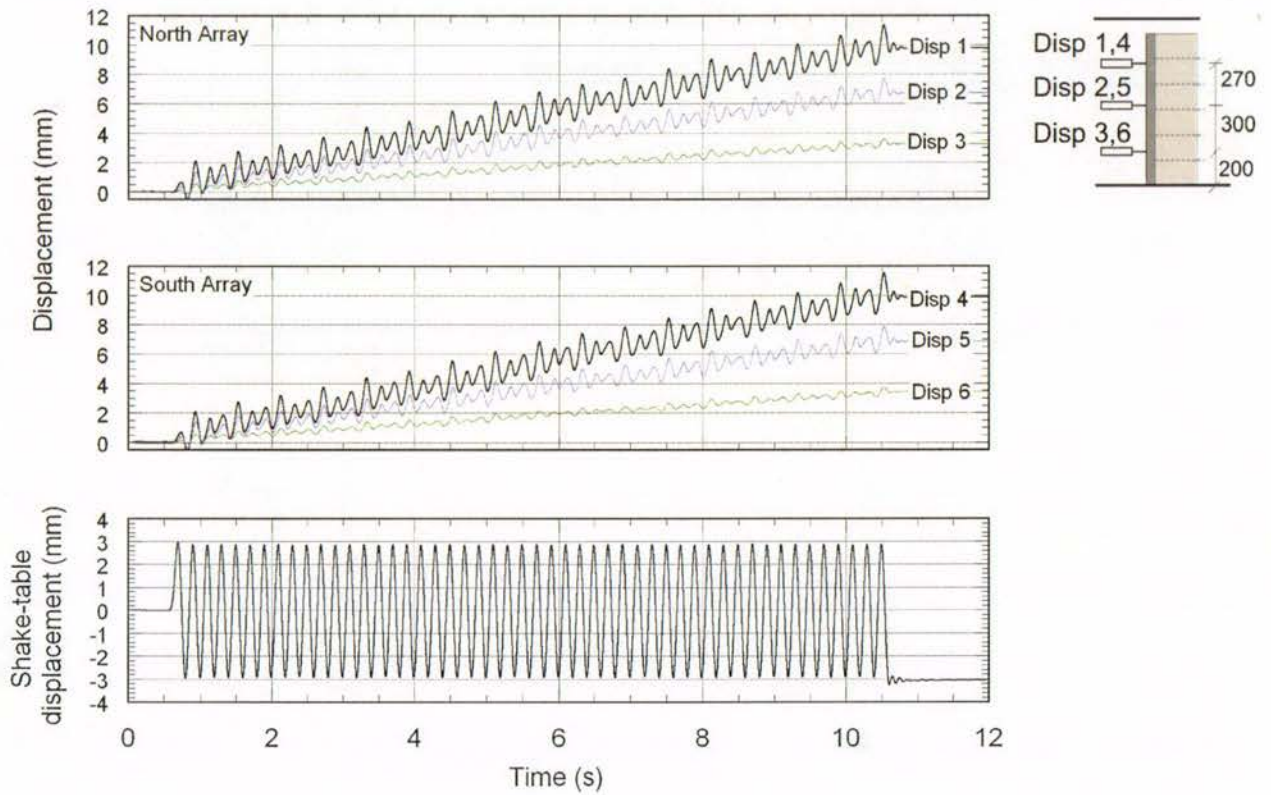


Figure B-64. Test-6 displacement time histories at 0.3g shaking step.

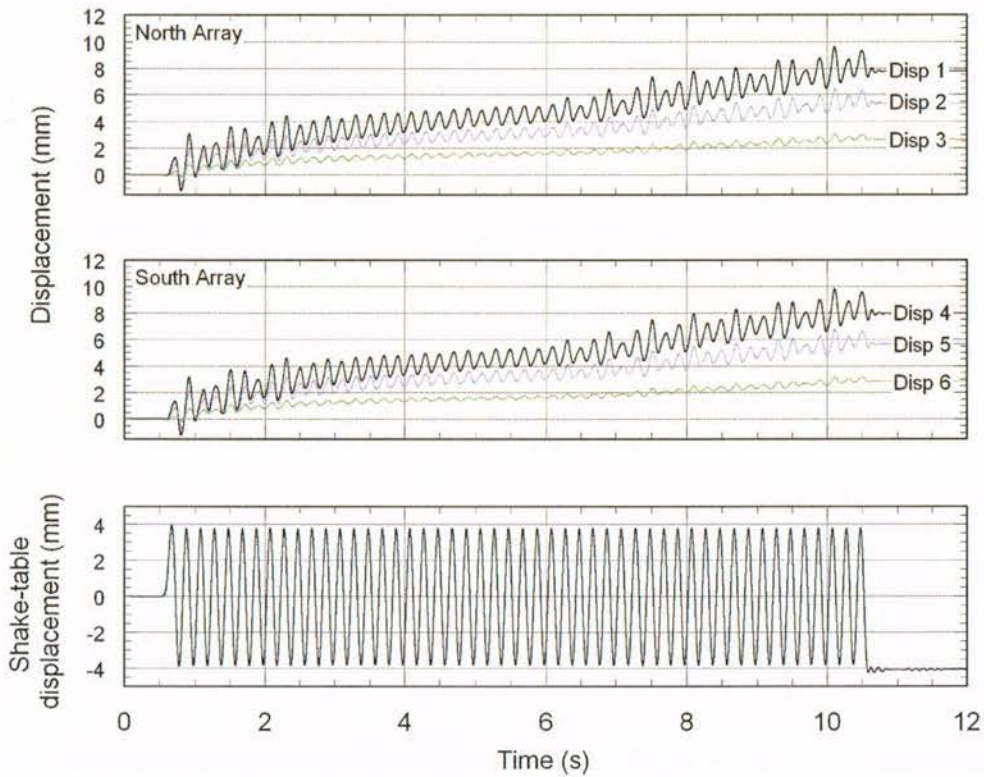


Figure B-65. Test-6 displacement time histories at 0.4g shaking step.

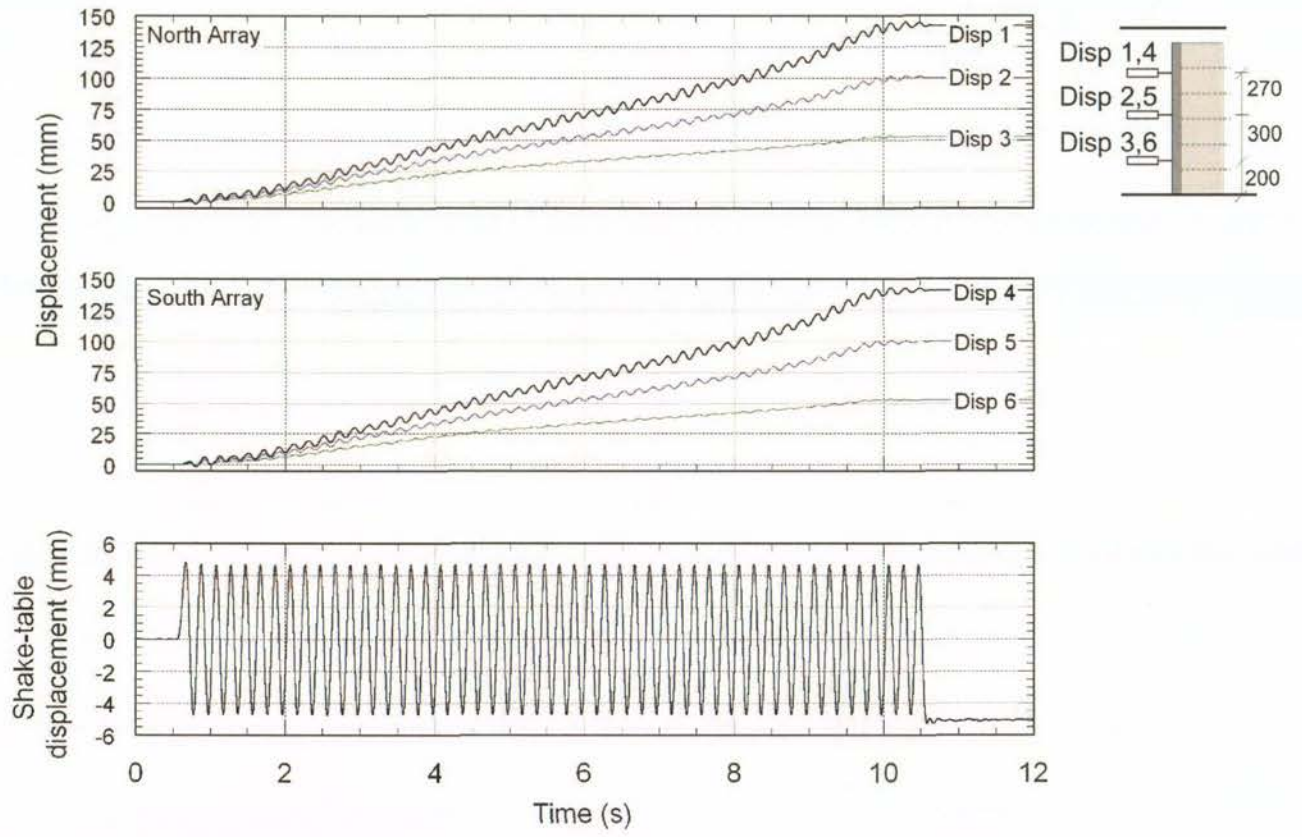


Figure B-66. Test-6 displacement time histories at 0.5g shaking step.

## B.7 Test-7 Time Histories

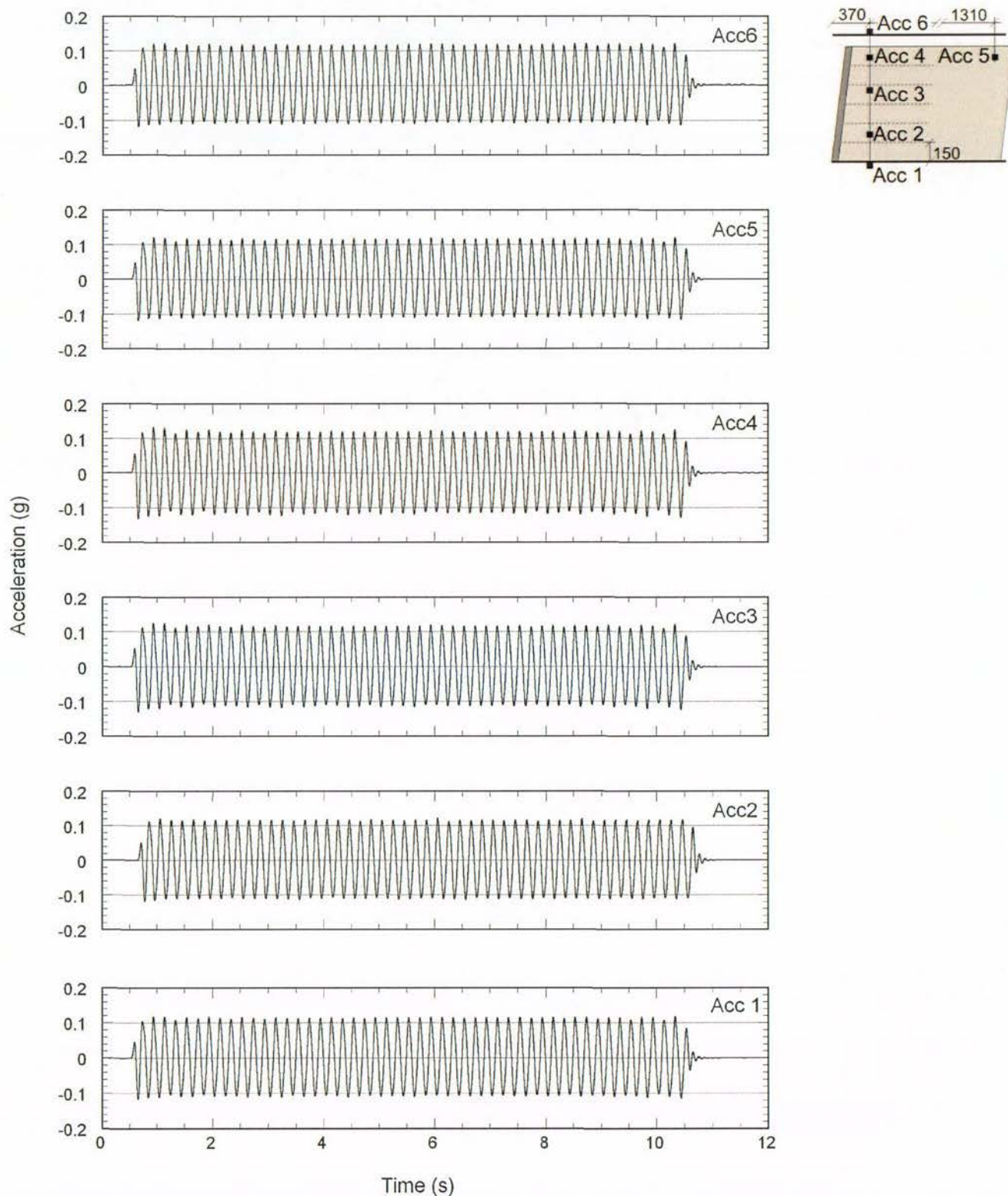


Figure B-67. Test-7 acceleration time histories at 0.1g shaking step.

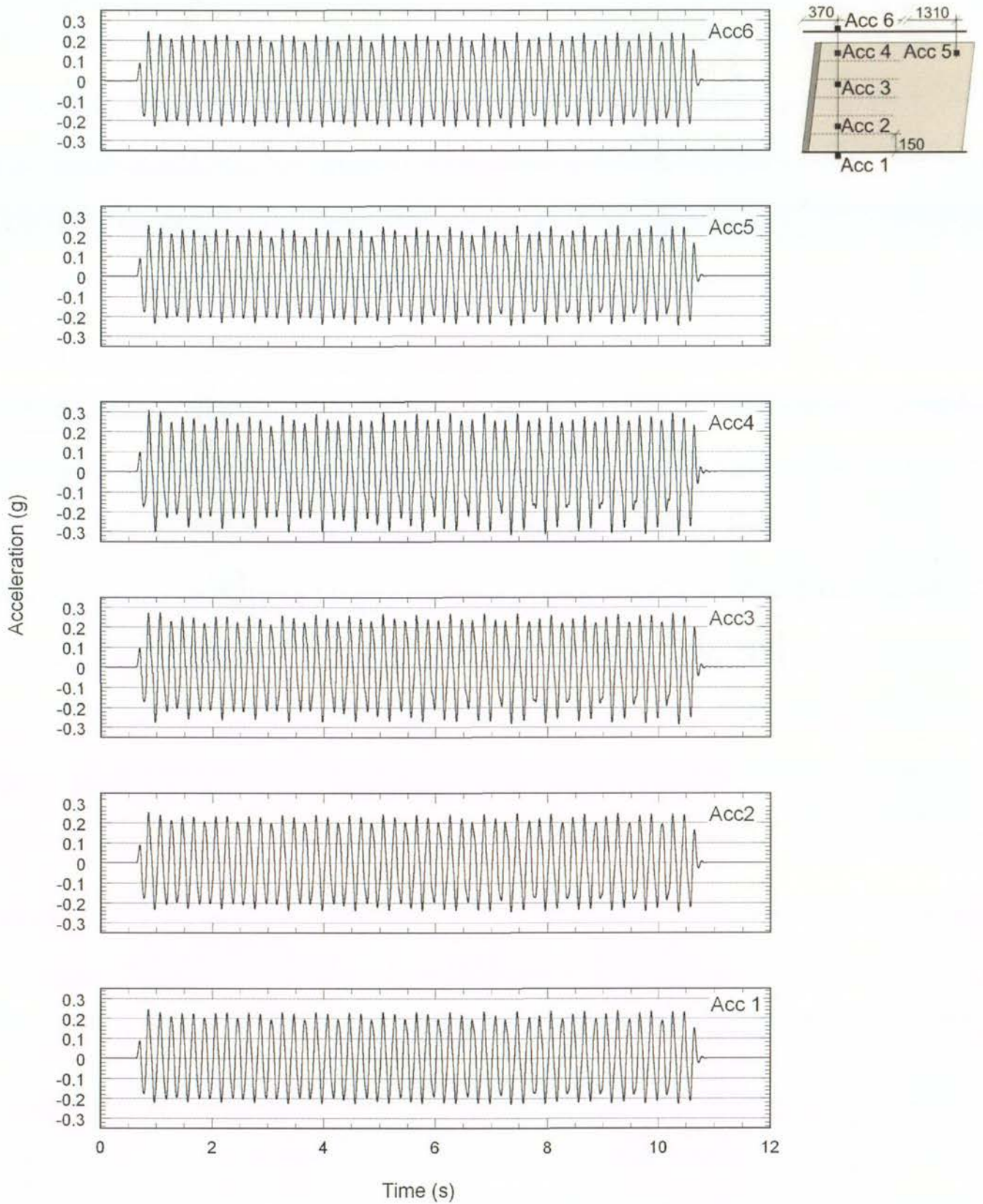


Figure B-68. Test-7 acceleration time histories at 0.2g shaking step.

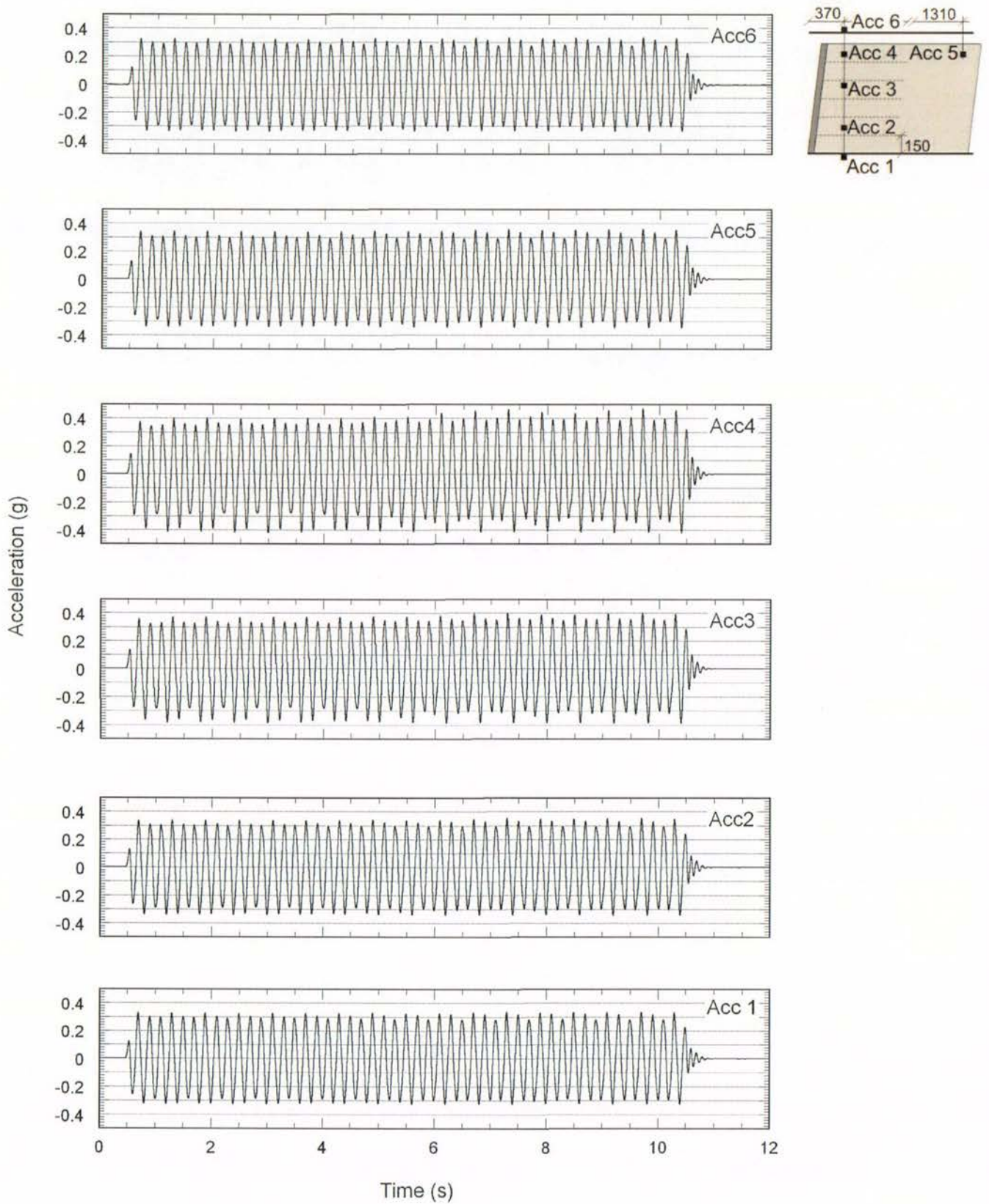


Figure B-69. Test-7 acceleration time histories at 0.3g shaking step.

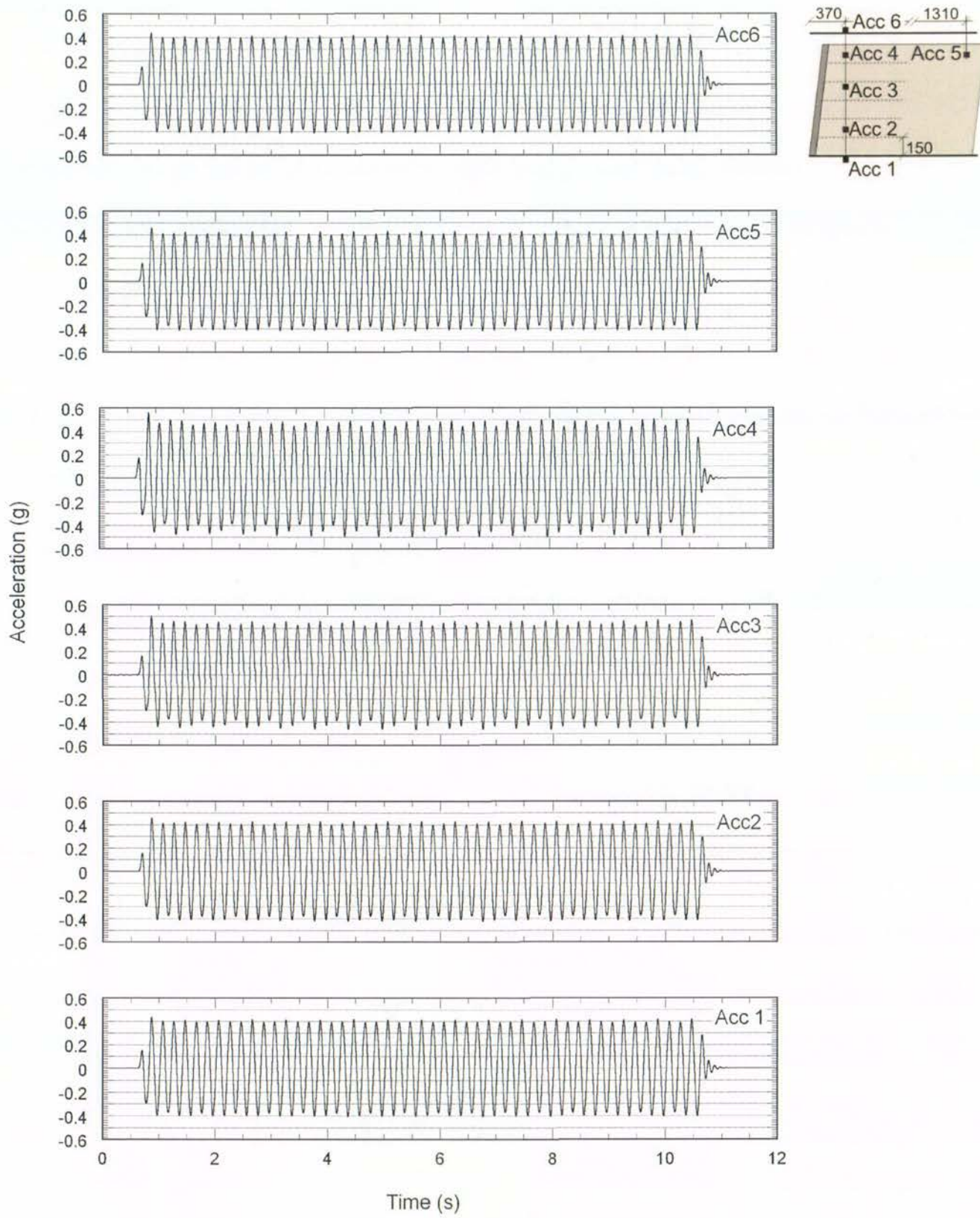


Figure B-70. Test-7 acceleration time histories at 0.4g shaking step.

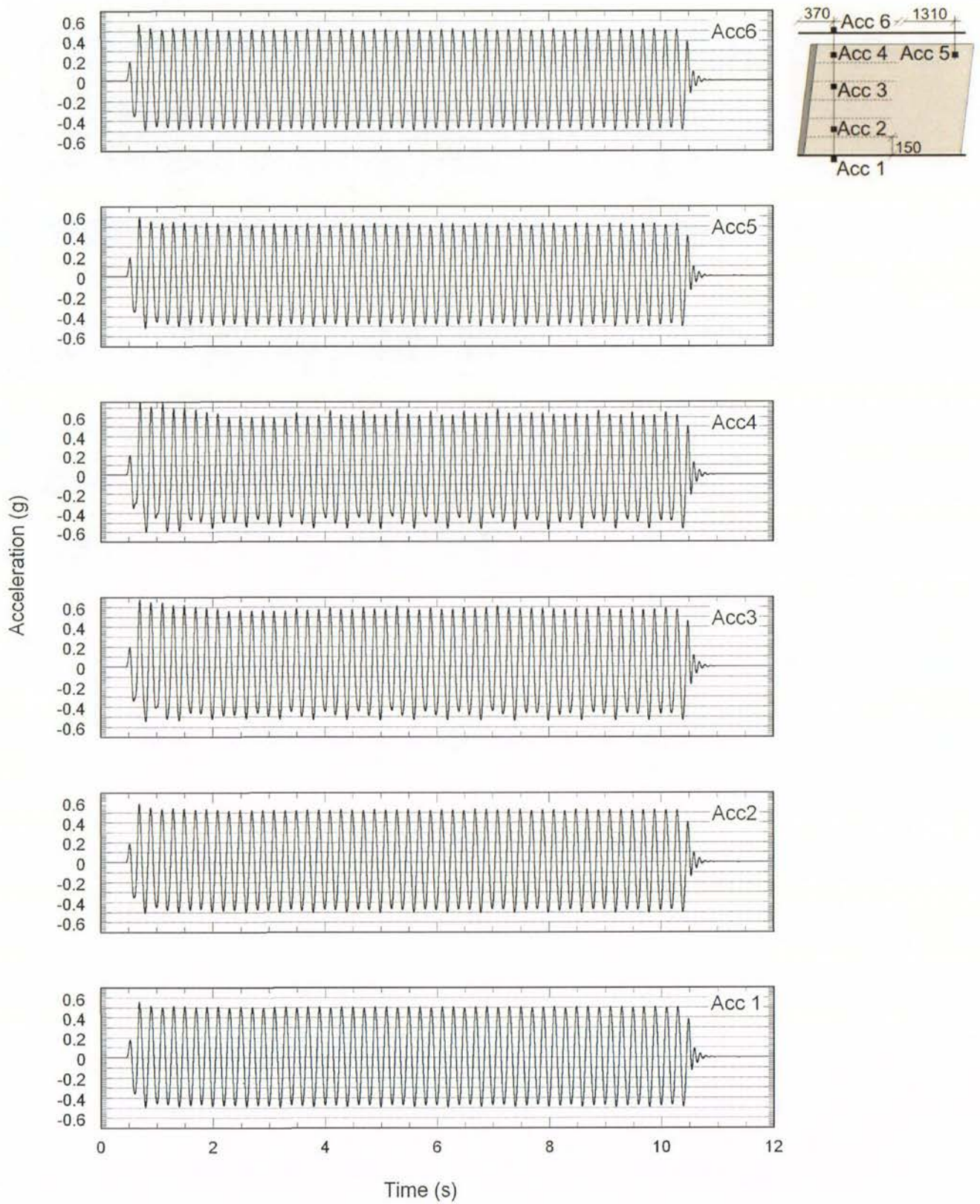


Figure B-71. Test-7 acceleration time histories at 0.5g shaking step.

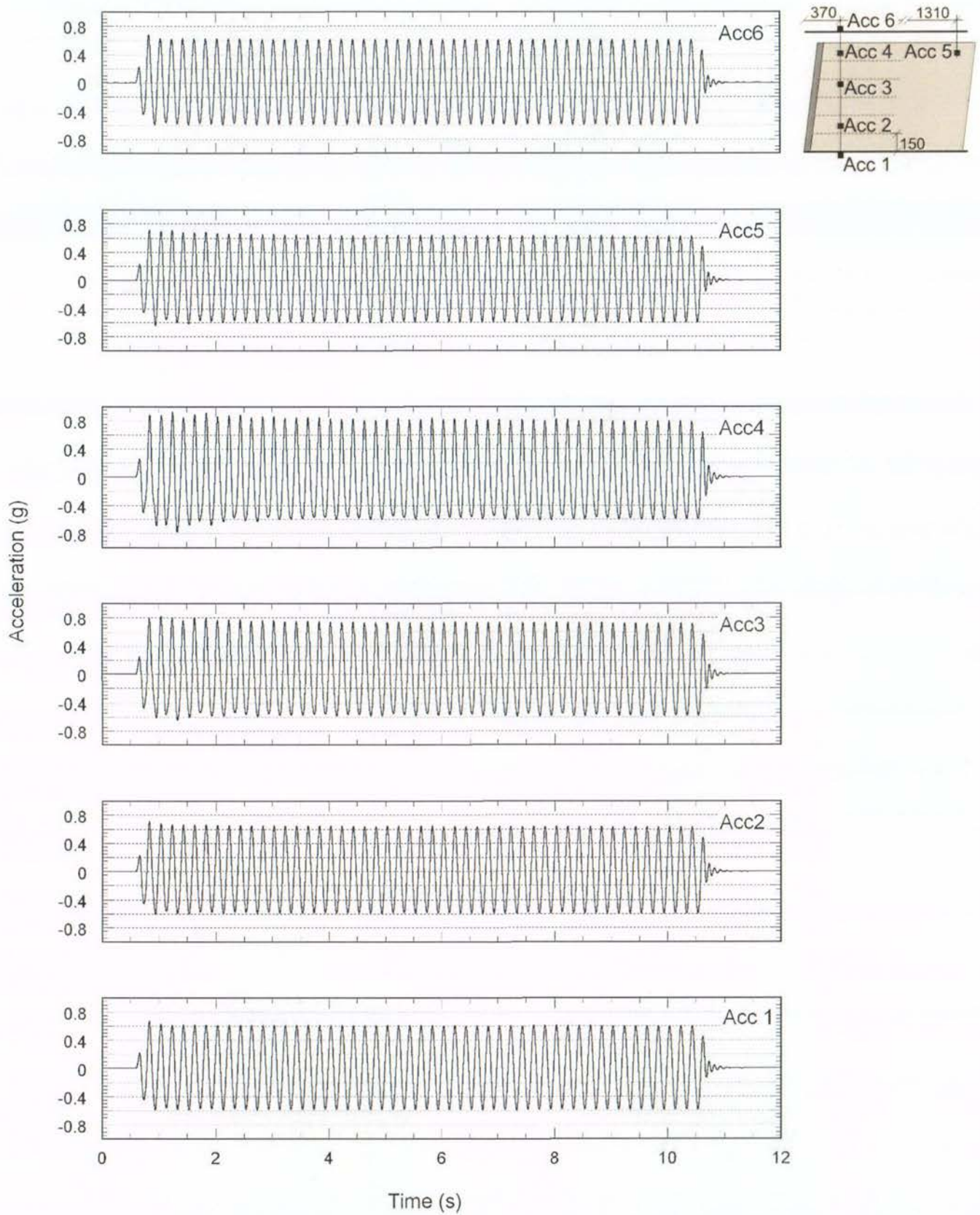


Figure B-72. Test-7 acceleration time histories at 0.6g shaking step.



Figure B-73. Test-7 acceleration time histories at 0.7g shaking step.

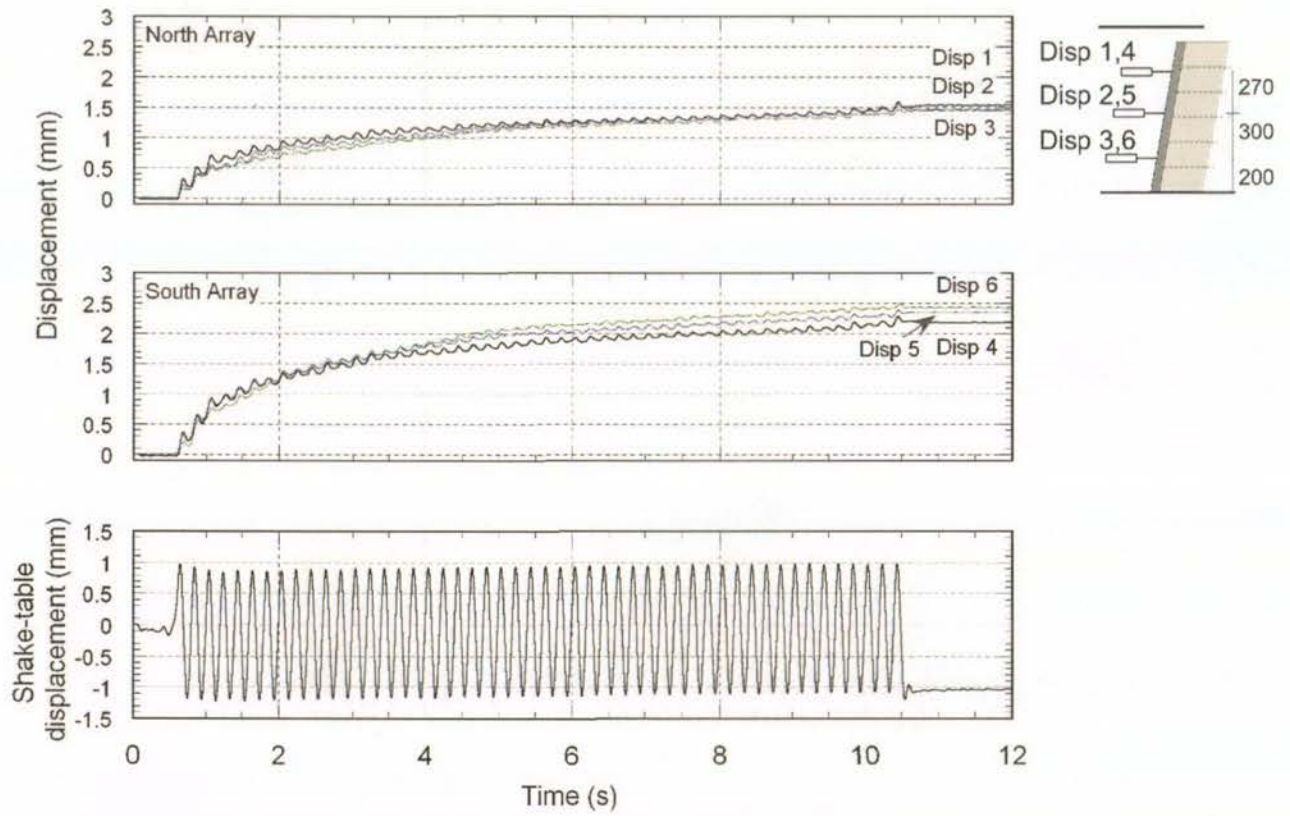


Figure B-74. Test-7 displacement transducer time histories at 0.1g shaking step.

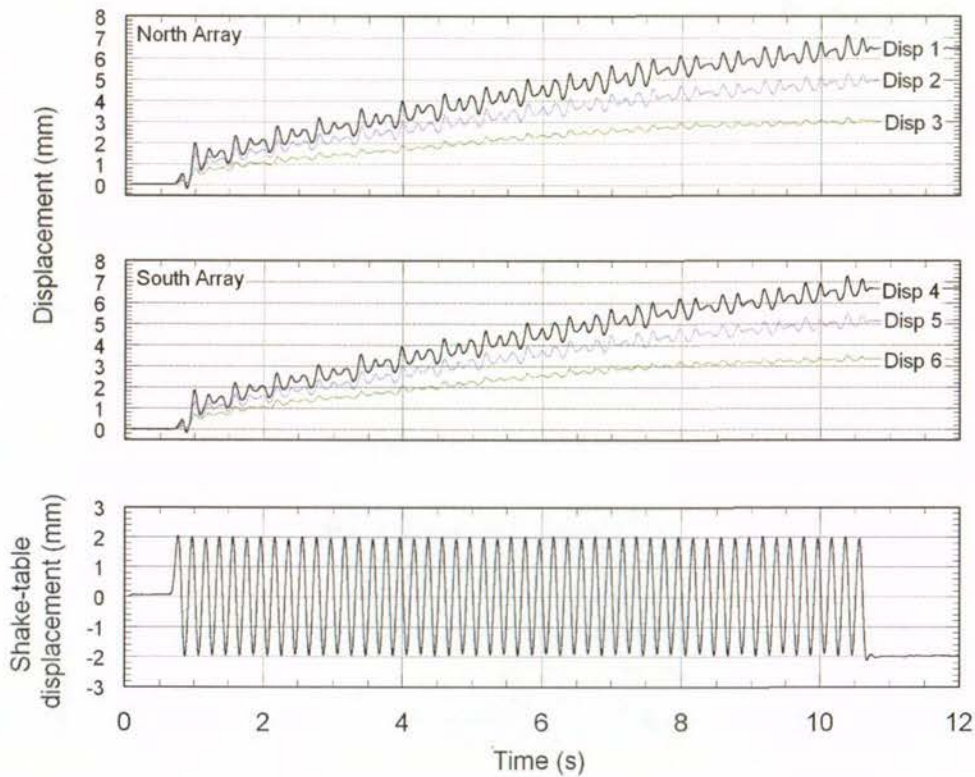


Figure B-75. Test-7 displacement transducer time histories at 0.2g shaking step.

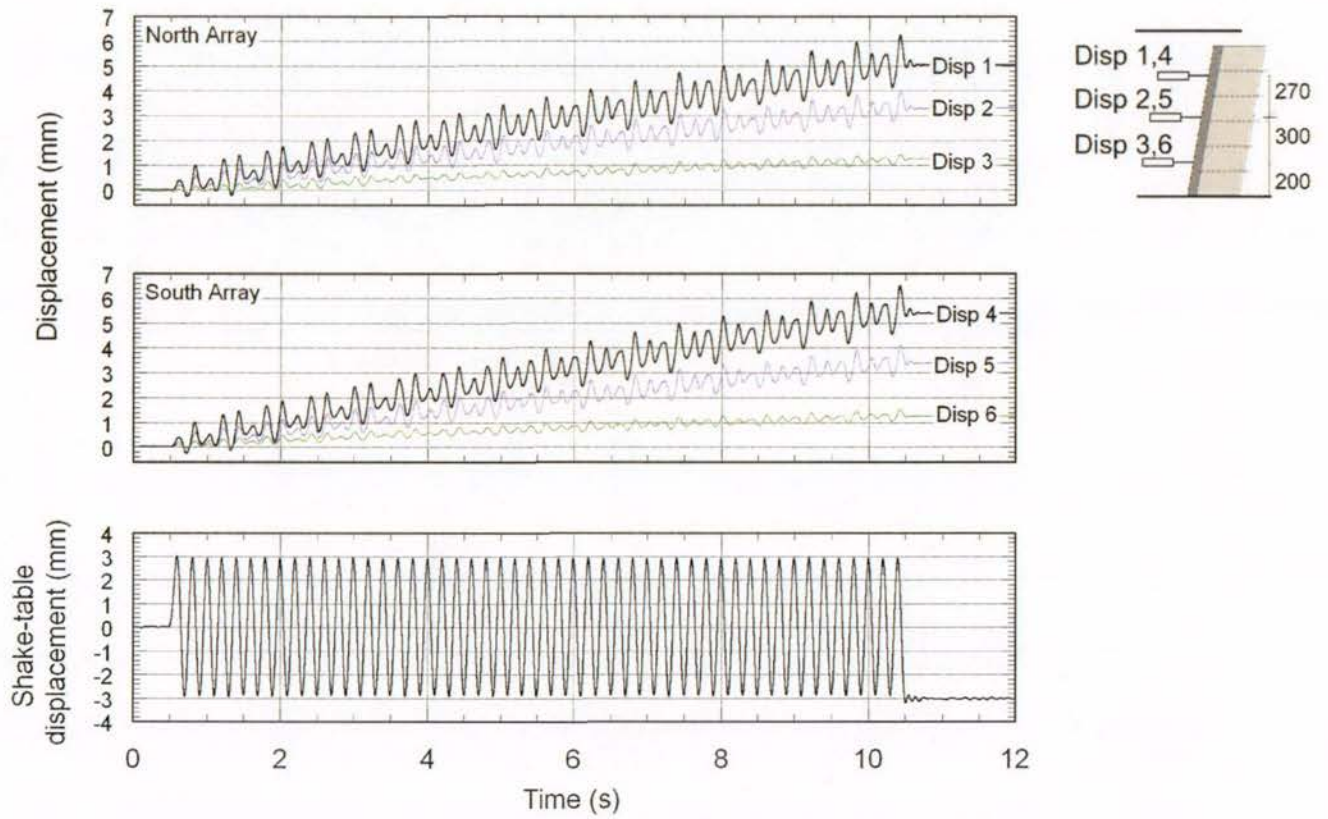


Figure B-76. Test-7 displacement time histories at 0.3g shaking step.

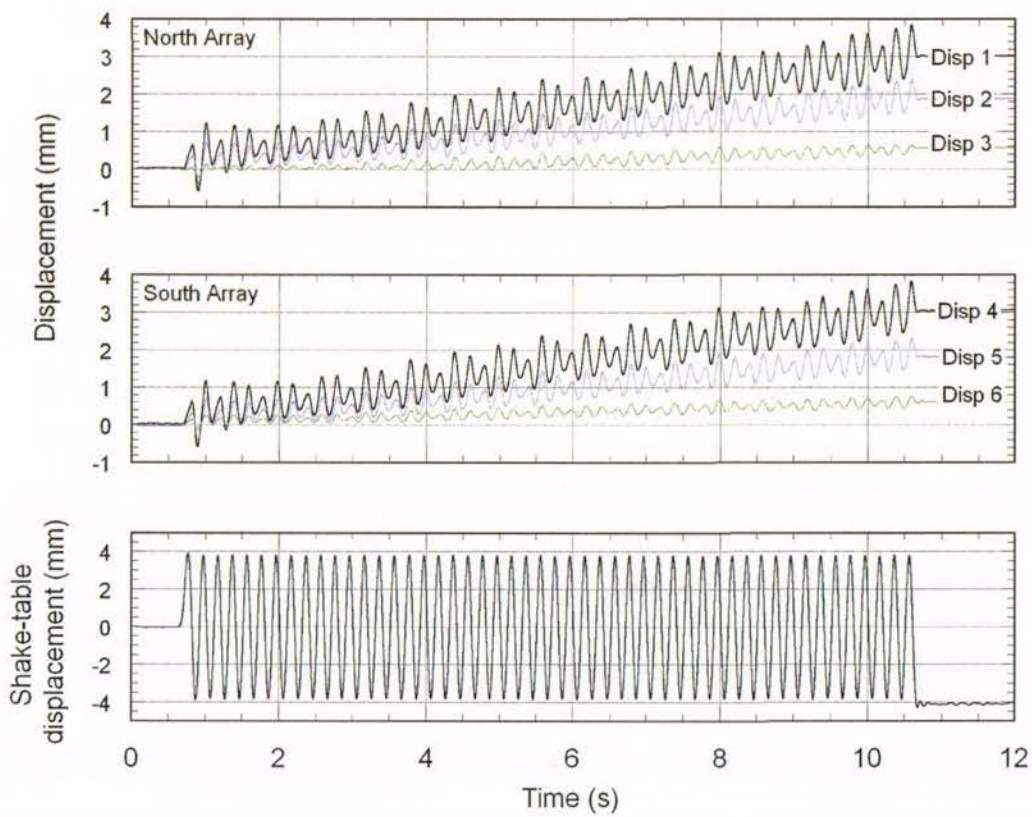


Figure B-77. Test-7 displacement time histories at 0.4g shaking step.

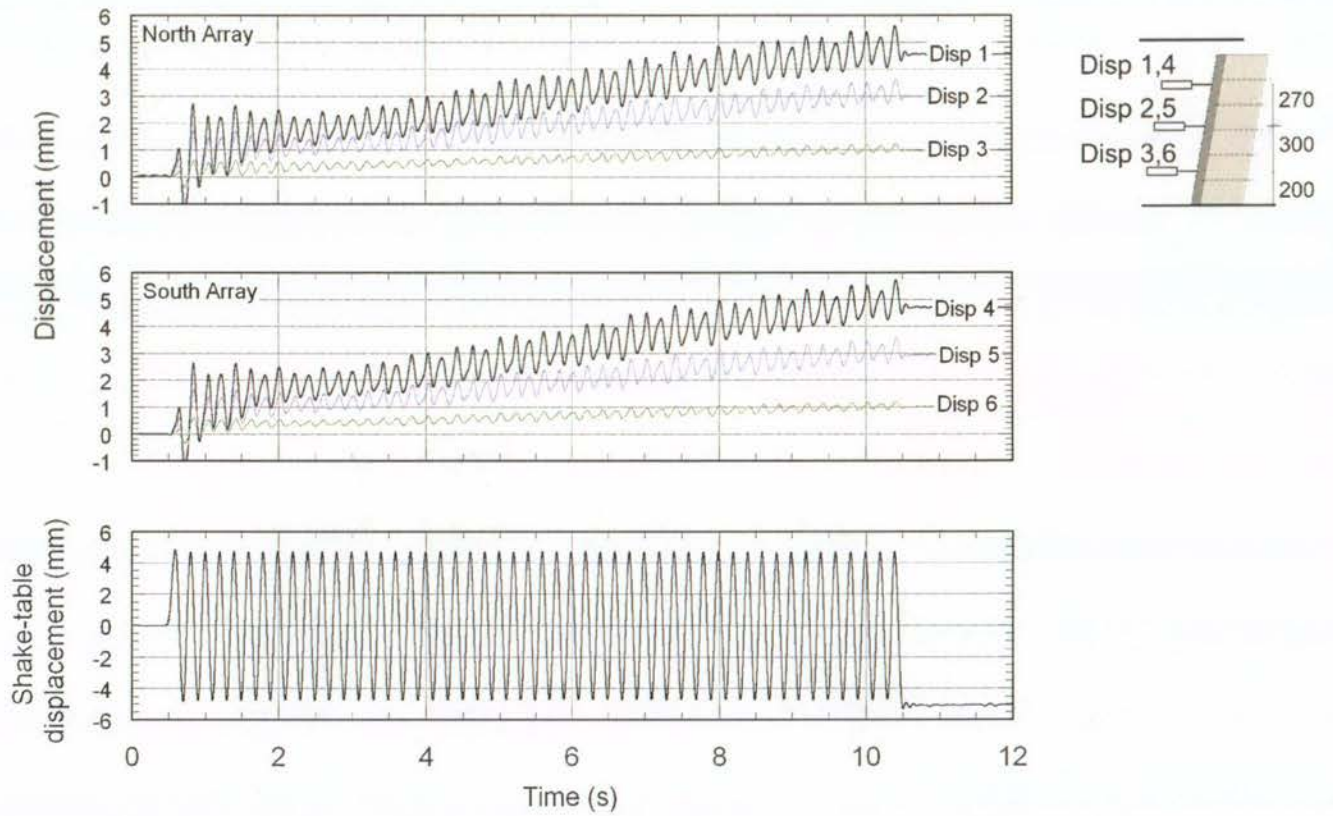


Figure B-78. Test-7 displacement time histories at 0.5g shaking step.

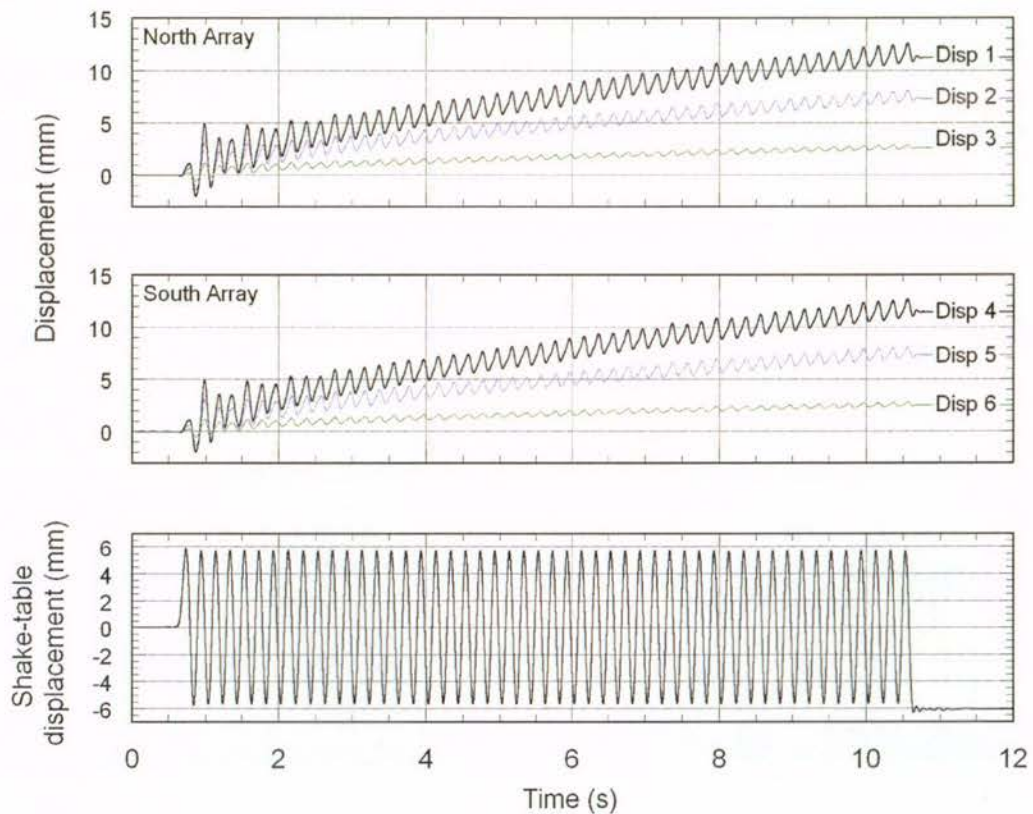


Figure B-79. Test-7 displacement time histories at 0.6g shaking step.

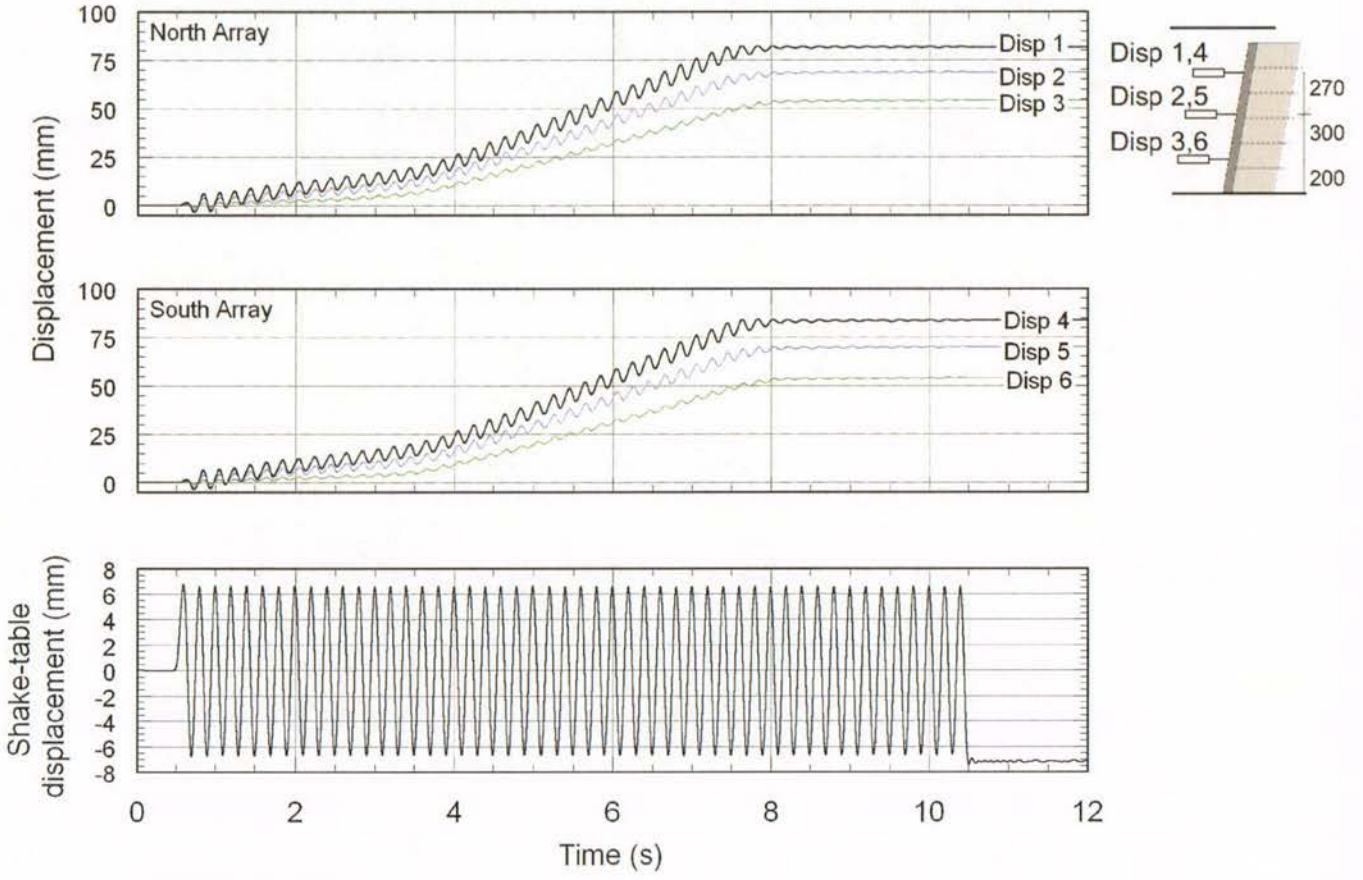


Figure B-80. Test-7 displacement time histories at 0.7g shaking step.

APPENDIX B TIME HISTORIES

VII

B.1	Test-1 Time Histories .....	IX
B.2	Test-2 Time Histories .....	XV
B.3	Test-3 Time Histories .....	XX
B.4	Test-4 Time Histories .....	XXVIII
B.5	Test-5 Time Histories .....	XXXIX
B.6	Test-6 Time Histories .....	L
B.7	Test-7 Time Histories .....	LVIII

Figure B-1.	Test-1 acceleration time histories at 0.1g shaking step	IX
Figure B-2.	Test-1 acceleration time histories at 0.2g shaking step	IX
Figure B-3.	Test-1 acceleration time histories at 0.3g shaking step	X
Figure B-4.	Test-1 acceleration time histories at 0.4g shaking step	X
Figure B-5.	Test-1 acceleration time histories at 0.5g shaking step	XI
Figure B-6.	Test-1 acceleration time histories at 0.6g shaking step	XI
Figure B-7.	Test-1 displacement time histories at 0.1g shaking step	XII
Figure B-8.	Test-1 displacement time histories at 0.2g shaking step	XII
Figure B-9.	Test-1 displacement time histories at 0.3g shaking step	XIII
Figure B-10.	Test-1 displacement time histories at 0.4g shaking step	XIII
Figure B-11.	Test-1 displacement time histories at 0.5g shaking step	XIV
Figure B-12.	Test-1 displacement time histories at 0.6g shaking step	XIV

Figure B-13. Test-2 acceleration time histories at 0.3g shaking step	XV
Figure B-14. Test-2 acceleration time histories at 0.4g shaking step	XVI
Figure B-15. Test-2 acceleration time histories at 0.5g shaking step	XVII
Figure B-16. Test-2 displacement time histories at 0.3g shaking step	XVIII
Figure B-17. Test-2 displacement time histories at 0.4g shaking step	XVIII
Figure B-18. Test-2 displacement time histories at 0.5g shaking step	XIX
Figure B-19. Test-3 acceleration time histories at 0.6g, 10 Hz frequency shaking step	XX
Figure B-20. Test-3 acceleration time histories at 0.4g, 5Hz shaking step, as per standard protocol	XXI
Figure B-21. Test-3 acceleration time histories at 0.5g shaking step	XXII
Figure B-22. Test-3 acceleration time histories at 0.6g shaking step	XXIII
Figure B-23. Test-3 acceleration time histories at 0.7g shaking step	XXIV
Figure B-24. Test-3 displacement time histories at 0.6g, 10 Hz frequency shaking step	XXV
Figure B-25. Test-3 displacement time histories at 0.4g shaking step	XXV
Figure B-26. Test-3 displacement time histories at 0.5g shaking step	XXVI
Figure B-27. Test-3 displacement time histories at 0.6g shaking step	XXVI
Figure B-28. Test-3 displacement time histories at 0.7g shaking step	XXVII
Figure B-29. Test-4 acceleration time histories at 0.1g shaking step	XXVIII
Figure B-30. Test-4 acceleration time histories at 0.2g shaking step	XXIX
Figure B-31. Test-4 acceleration time histories at 0.3g shaking step	XXX
Figure B-32. Test-4 acceleration time histories at 0.4g shaking step	XXXI

Figure B-33. Test-4 acceleration time histories at 0.5g shaking step	XXXII
Figure B-34. Test-4 acceleration time histories at 0.6g shaking step	XXXIII
Figure B-35. Test-4 acceleration time histories at 0.65g shaking step	XXXIV
Figure B-36. Test-4 displacement time histories at 0.1g shaking step	XXXV
Figure B-37. Test-4 displacement time histories at 0.2g shaking step	XXXV
Figure B-38. Test-4 displacement time histories at 0.3g shaking step	XXXVI
Figure B-39. Test-4 displacement time histories at 0.4g shaking step	XXXVI
Figure B-40. Test-4 displacement time histories at 0.5g shaking step	XXXVII
Figure B-41. Test-4 displacement time histories at 0.6g shaking step	XXXVII
Figure B-42. Test-4 displacement time histories at 0.65g shaking step	XXXVIII
Figure B-43 Test-5 acceleration time histories at 0.1g shaking step.	XXXIX
Figure B-44. Test-5 acceleration time histories at 0.2g shaking step.	XL
Figure B-45. Test-5 acceleration time histories at 0.3g shaking step.	XLI
Figure B-46. Test-5 acceleration time histories at 0.4g shaking step.	XLII
Figure B-47. Test-5 acceleration time histories at 0.5g shaking step.	XLIII
Figure B-48. Test-5 acceleration time histories at 0.6g shaking step.	XLIV
Figure B-49. Test-5 acceleration time histories at 0.7g shaking step.	XLV
Figure B-50. Test-5 displacement time histories at 0.1g shaking step	XLVI
Figure B-51. Test-5 displacement time histories at 0.2g shaking step	XLVI
Figure B-52. Test-5 displacement time histories at 0.3g shaking step	XLVII
Figure B-53. Test-5 displacement time histories at 0.4g shaking step	XLVII

Figure B-54. Test-5 displacement time histories at 0.5g shaking step	XLVIII
Figure B-55. Test-5 displacement time histories at 0.6g shaking step	XLVIII
Figure B-56. Test-5 displacement time histories at 0.7g shaking step	XLIX
Figure B-57. Test-6 acceleration time histories at 0.1g shaking step.	L
Figure B-58. Test-6 acceleration time histories at 0.2g shaking step.	LI
Figure B-59. Test-6 acceleration time histories at 0.3g shaking step.	LII
Figure B-60. Test-6 acceleration time histories at 0.4g shaking step.	LIII
Figure B-61. Test-6 acceleration time histories at 0.5g shaking step.	LIV
Figure B-62. Test-6 displacement transducer time histories at 0.5g shaking step.	LV
Figure B-63. Test-6 displacement time histories at 0.2g shaking step.	LV
Figure B-64. Test-6 displacement time histories at 0.3g shaking step.	LVI
Figure B-65. Test-6 displacement time histories at 0.4g shaking step.	LVI
Figure B-66. Test-6 displacement time histories at 0.5g shaking step.	LVII
Figure B-67. Test-7 acceleration time histories at 0.1g shaking step.	LVIII
Figure B-68. Test-7 acceleration time histories at 0.2g shaking step.	LIX
Figure B-69. Test-7 acceleration time histories at 0.3g shaking step.	LX
Figure B-70. Test-7 acceleration time histories at 0.4g shaking step.	LXI
Figure B-71. Test-7 acceleration time histories at 0.5g shaking step.	LXII
Figure B-72. Test-7 acceleration time histories at 0.6g shaking step.	LXIII
Figure B-73. Test-7 acceleration time histories at 0.7g shaking step.	LXIV
Figure B-74. Test-7 displacement transducer time histories at 0.1g shaking step.	LXV

Figure B-75. Test-7 displacement transducer time histories at 0.2g shaking step.	LXV
Figure B-76. Test-7 displacement time histories at 0.3g shaking step.	LXVI
Figure B-77. Test-7 displacement time histories at 0.4g shaking step.	LXVI
Figure B-78. Test-7 displacement time histories at 0.5g shaking step.	LXVII
Figure B-79. Test-7 displacement time histories at 0.6g shaking step.	LXVII
Figure B-80. Test-7 displacement time histories at 0.7g shaking step.	LXVIII

**APPENDIX C**  
**TESTING IMAGES**



### C.1 Test-2 Testing Images

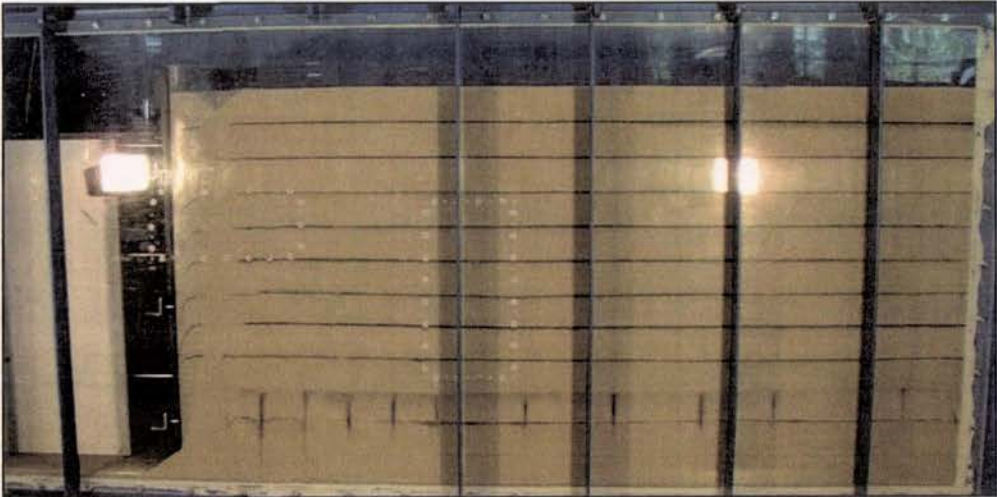


Figure C-1. Test-2 prior to testing

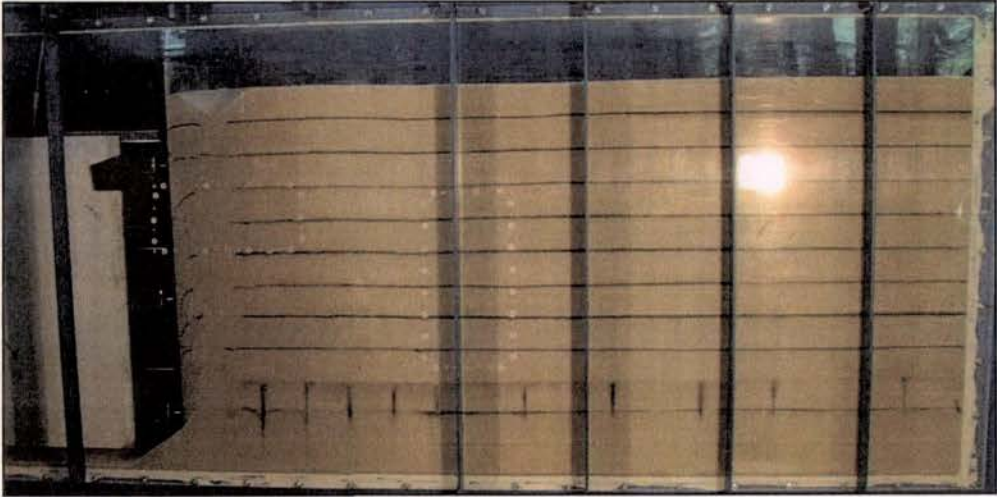


Figure C-2. Test-2 after 0.3g shaking (first step to reduce sand leakage).

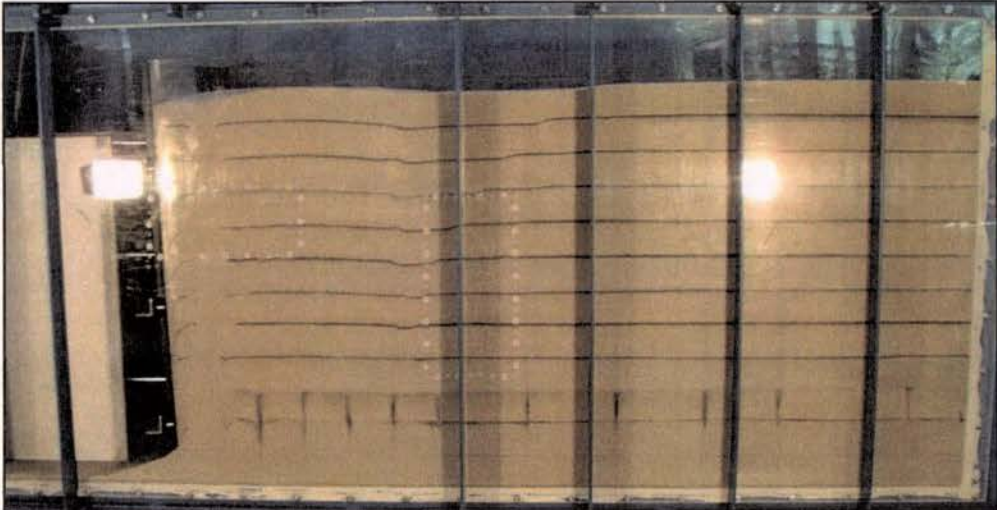


Figure C-3. Test-2 after 0.4g shaking.

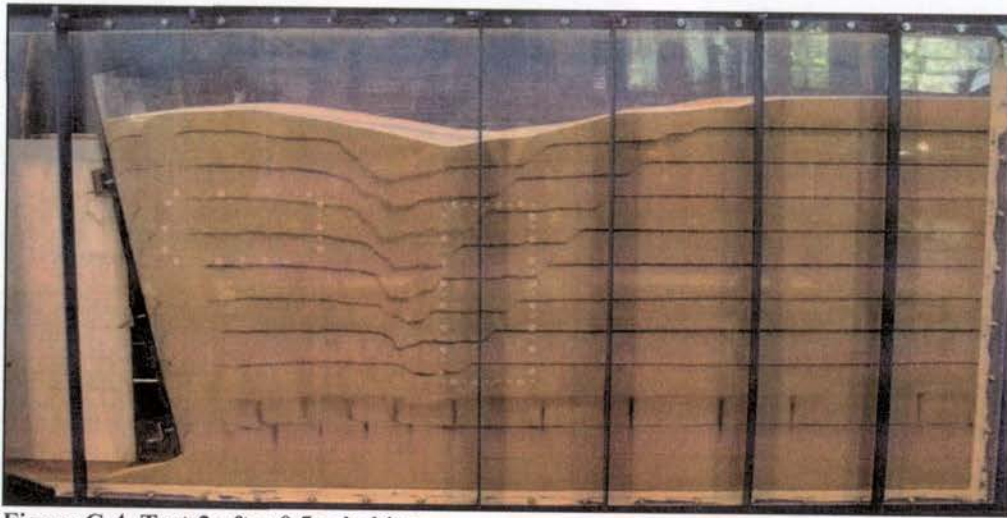


Figure C-4. Test-2 after 0.5g shaking.

## C.2 Test-3 Testing Images

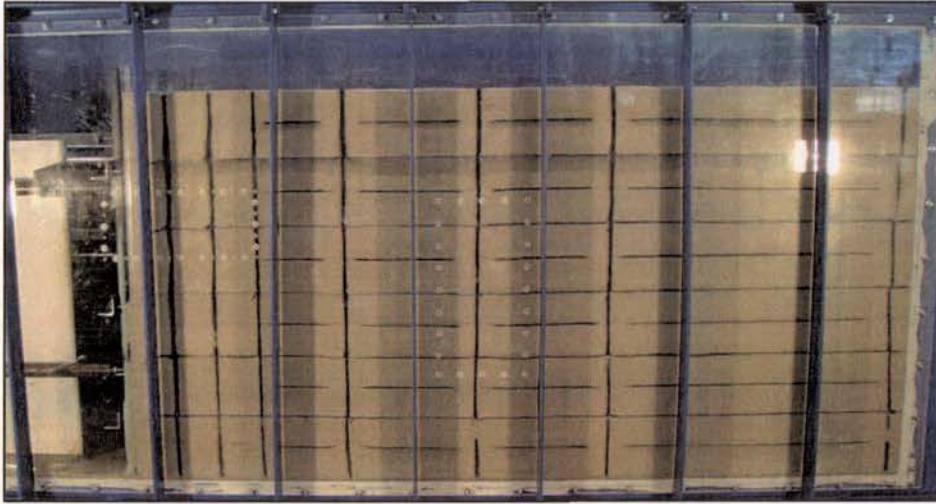


Figure C-5. Test-2 prior to testing

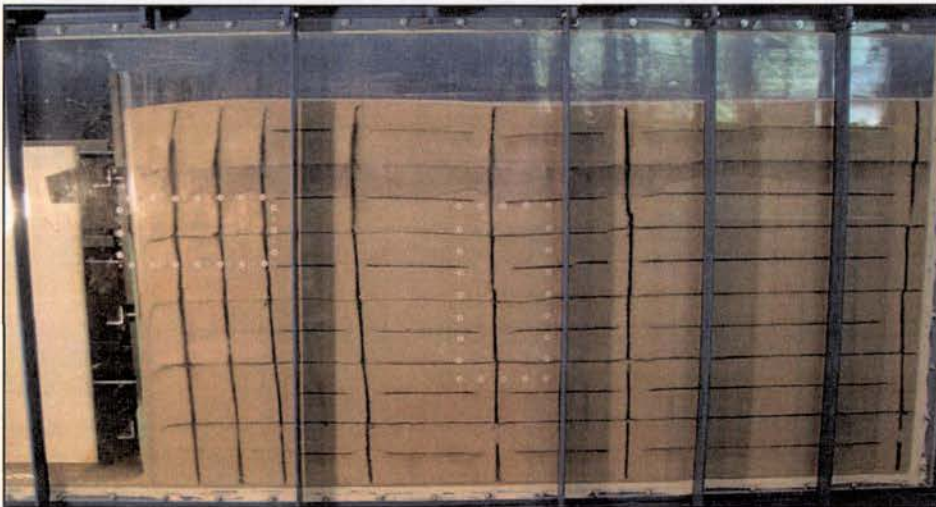


Figure C-6. Test-3 after first shaking step of 0.6g, at 10Hz (due to experimental error).

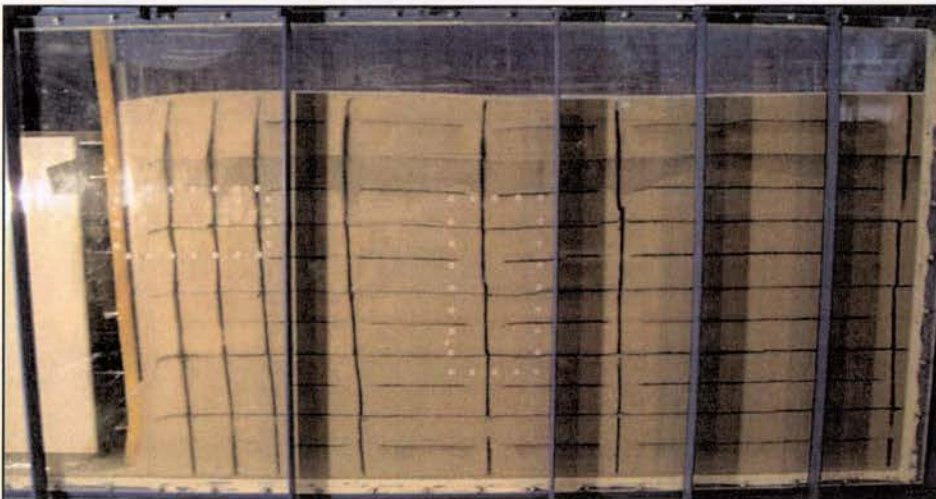


Figure C-7. Test-3 after 0.4g, 5 Hz shaking step (standard testing protocol resumed).

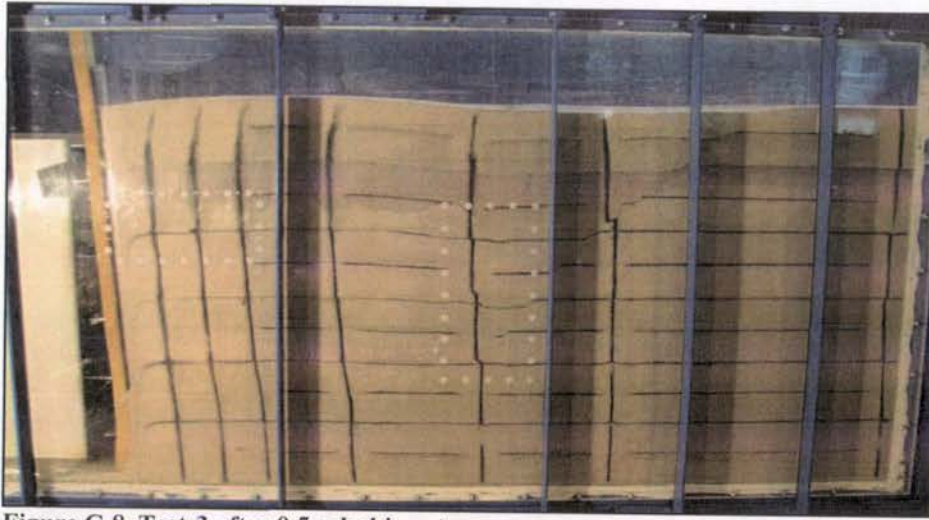


Figure C-8. Test-3 after 0.5g shaking step.

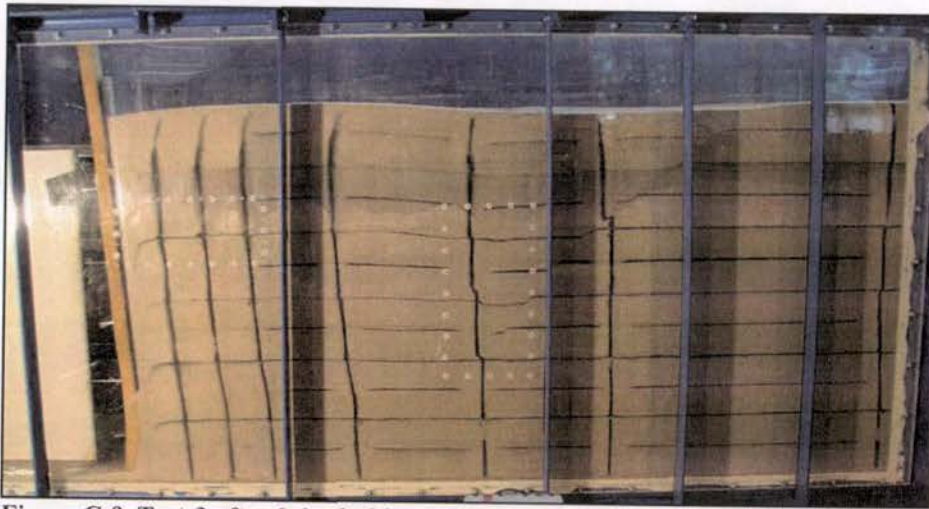


Figure C-9. Test-3 after 0.6g shaking step.

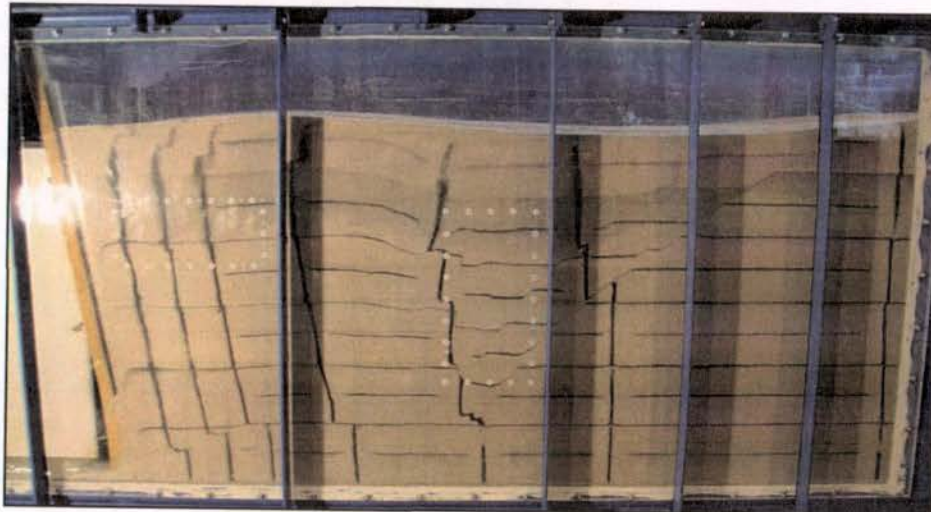


Figure C-10. Test-3 after 0.7g shaking step.

### C.3 Test-4 Testing Images



Figure C-11. Test-4 prior to testing

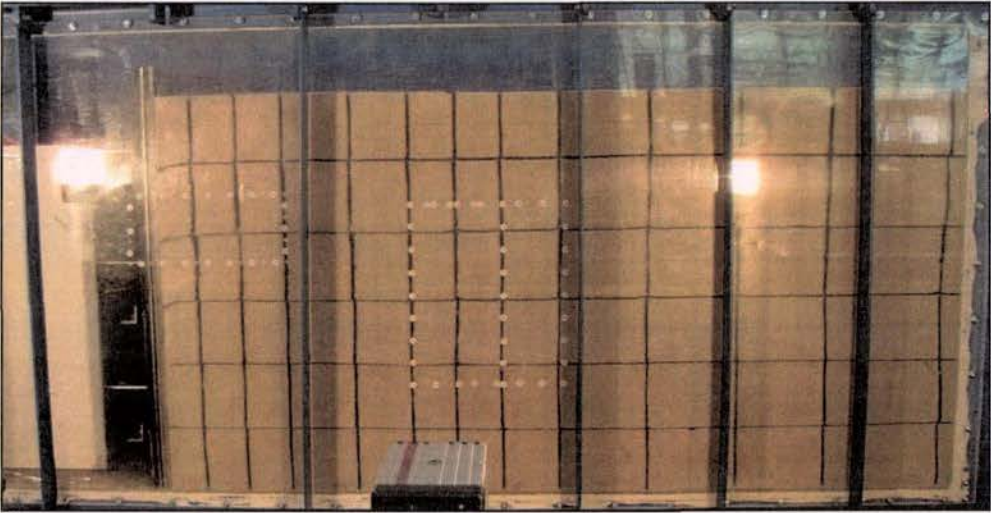


Figure C-12. Test-4 after 0.1g shaking step.

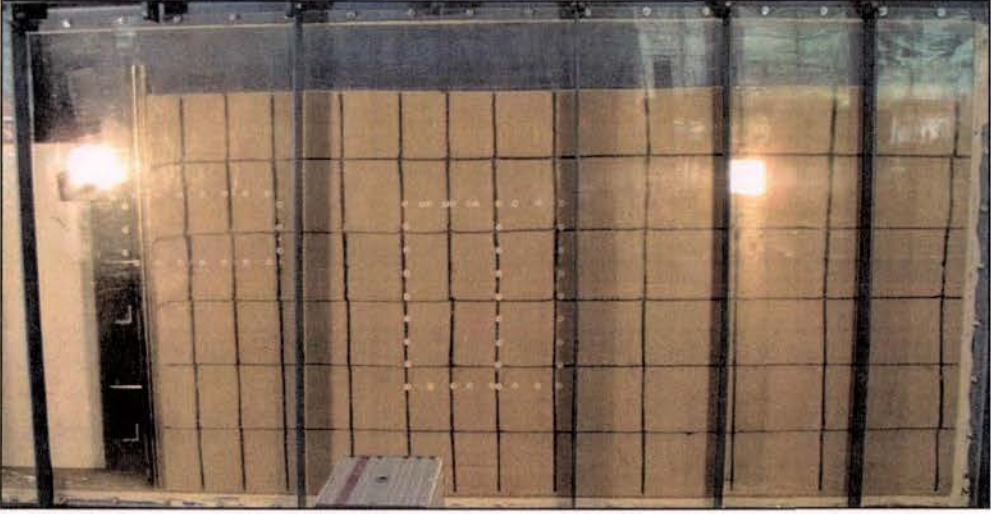


Figure C-13. Test-4 after 0.2g shaking step.



Figure C-14. Test-4 after 0.3g shaking step.

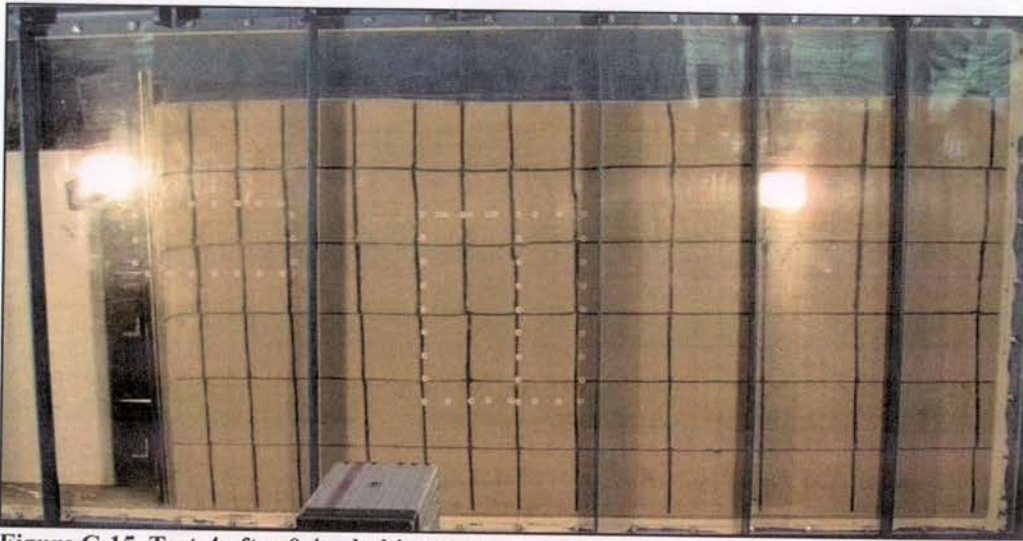


Figure C-15. Test-4 after 0.4g shaking step.

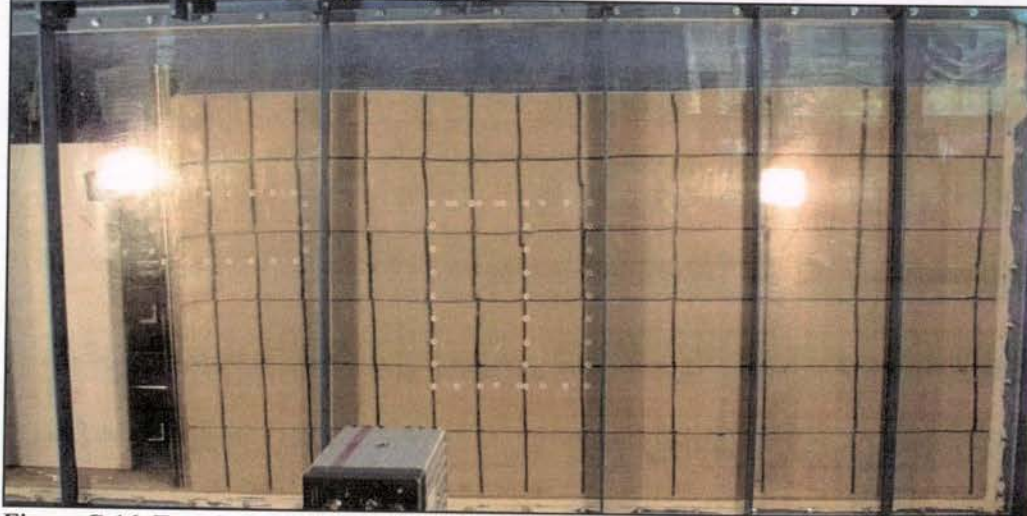


Figure C-16. Test-4 after 0.5g shaking step.



Figure C-17. Test-4 after 0.6g shaking step.



Figure C-18. Test-4 after 0.65g shaking step.

#### C.4 Test-5 Testing Images

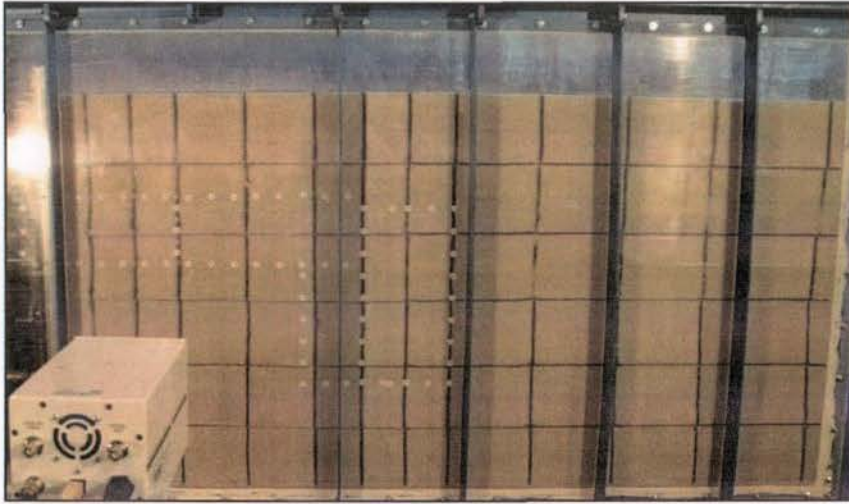


Figure C-19. Test-5 prior to testing.

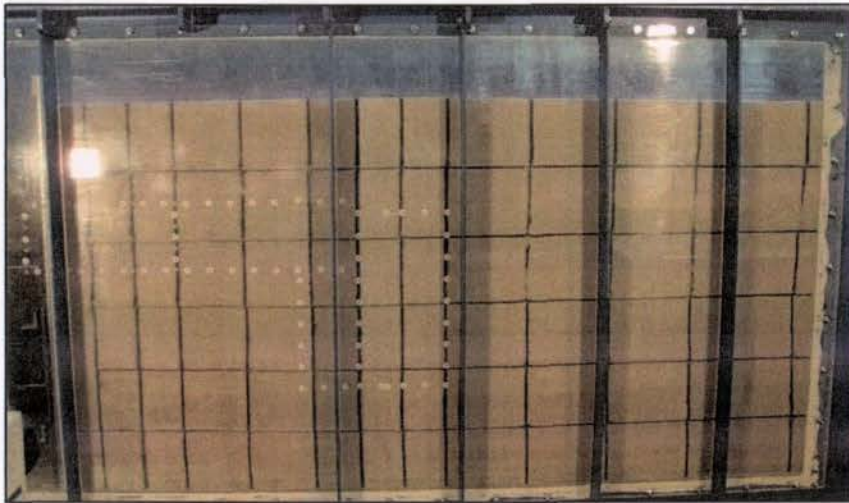


Figure C-20. Test-5 after 0.1g shaking step.

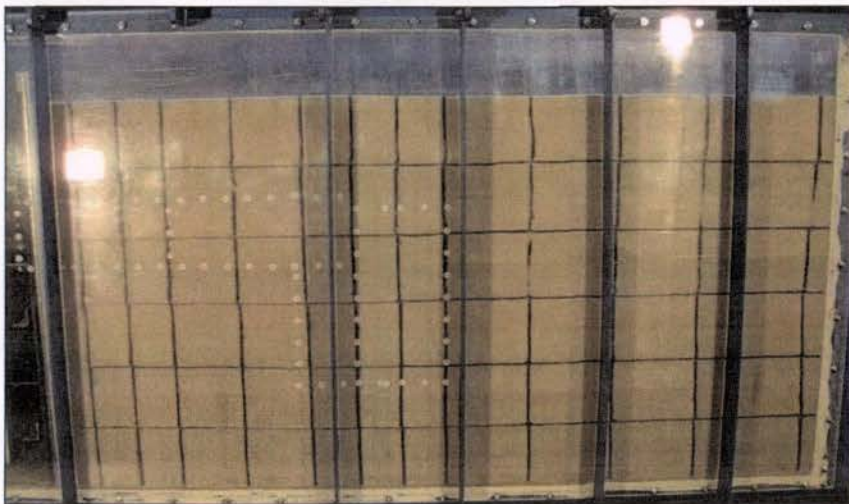


Figure C-21. . Test-5 after 0.2g shaking step

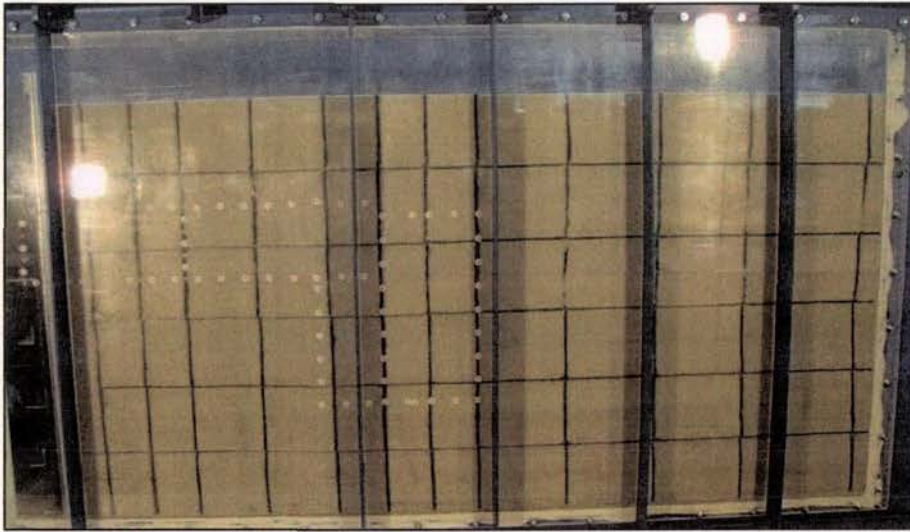


Figure C-22. Test-5 after 0.3g shaking step

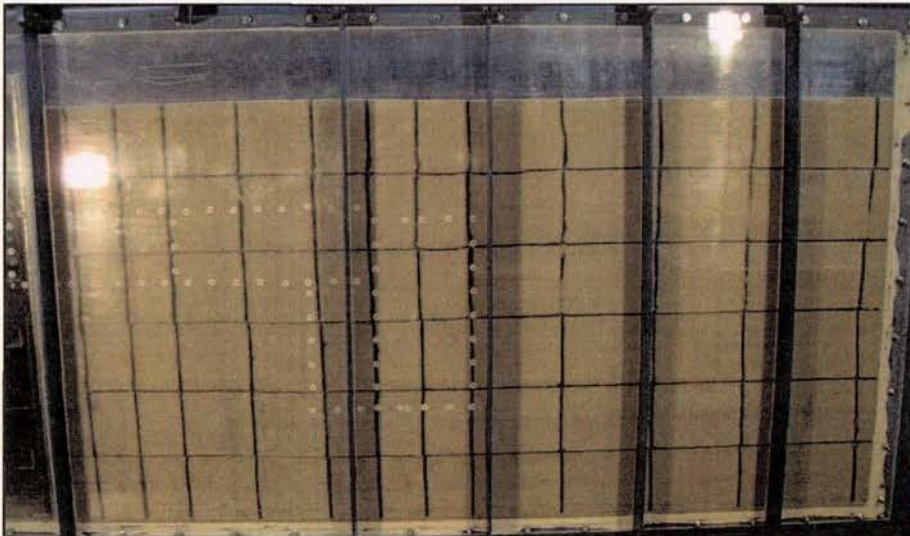


Figure C-23. Test-5 after 0.4g shaking step

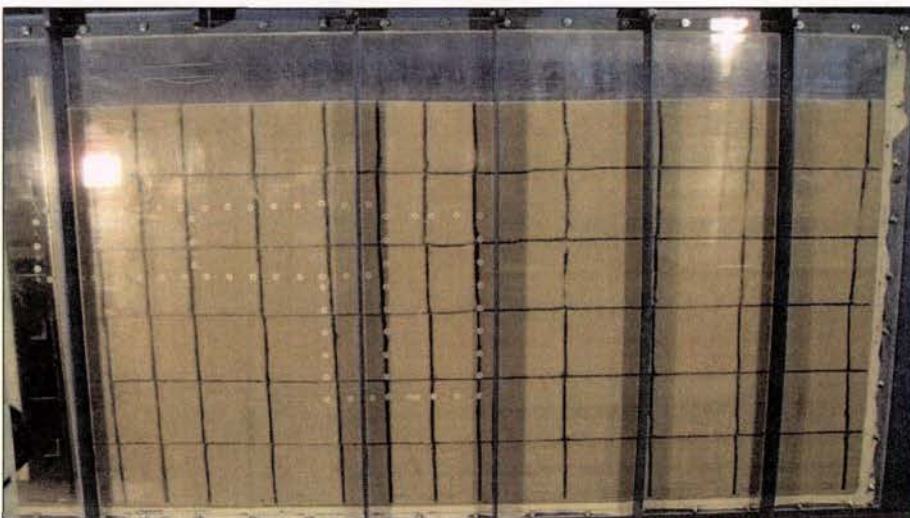


Figure C-24. Test-5 after 0.5g shaking step

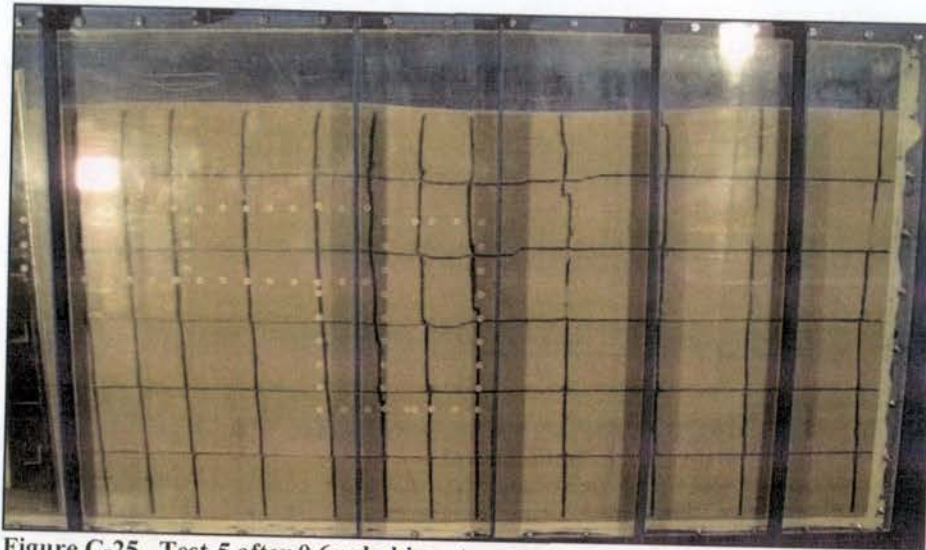


Figure C-25. Test-5 after 0.6g shaking step

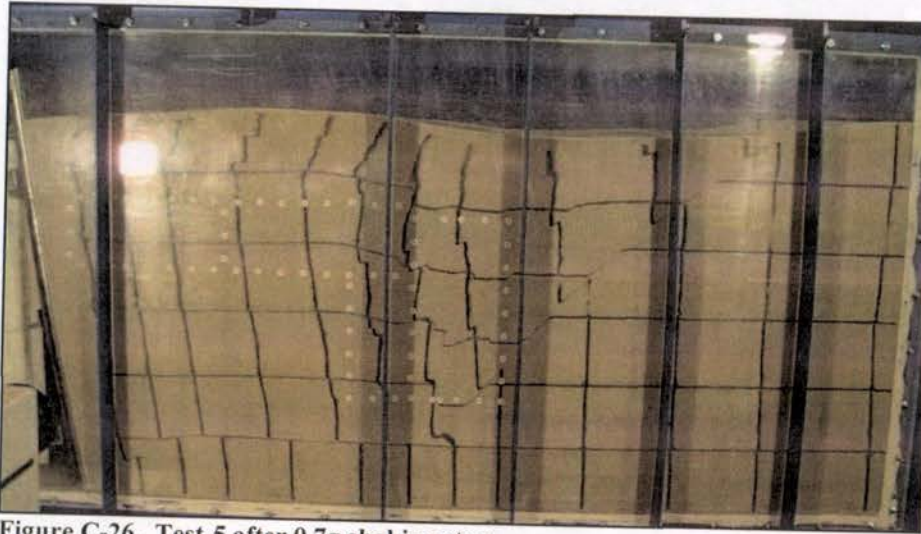


Figure C-26. Test-5 after 0.7g shaking step

## C.5 Test-6 Testing Images

Are presented in Section 4.3.3.

**C.6 Test-7 Testing Images**

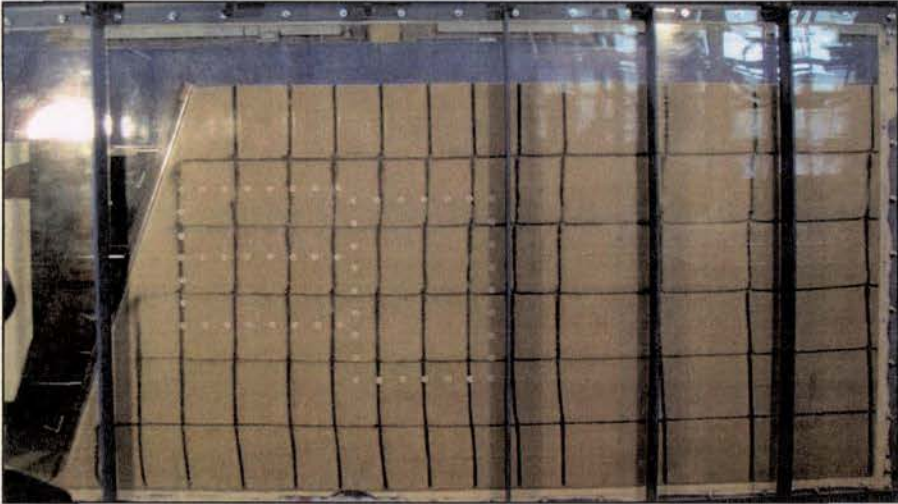


Figure C-27. Test-7 prior to testing.

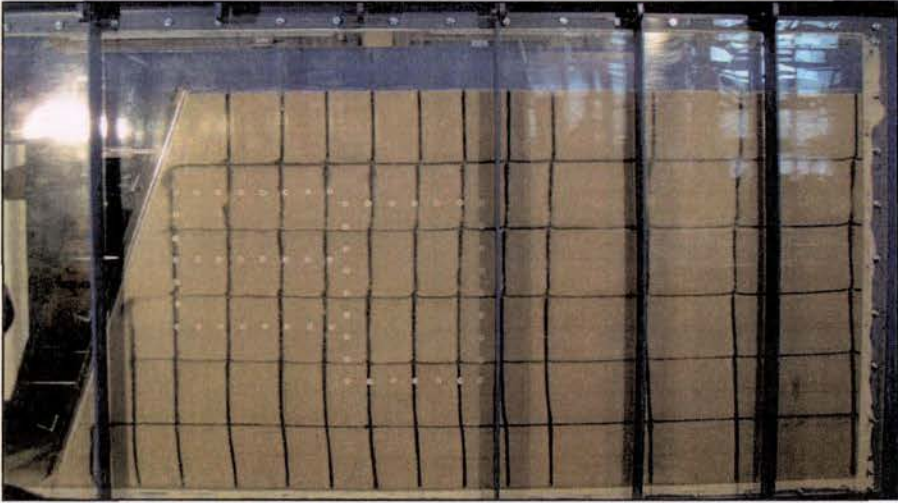


Figure C-28. Test-7 after 0.1g shaking step.

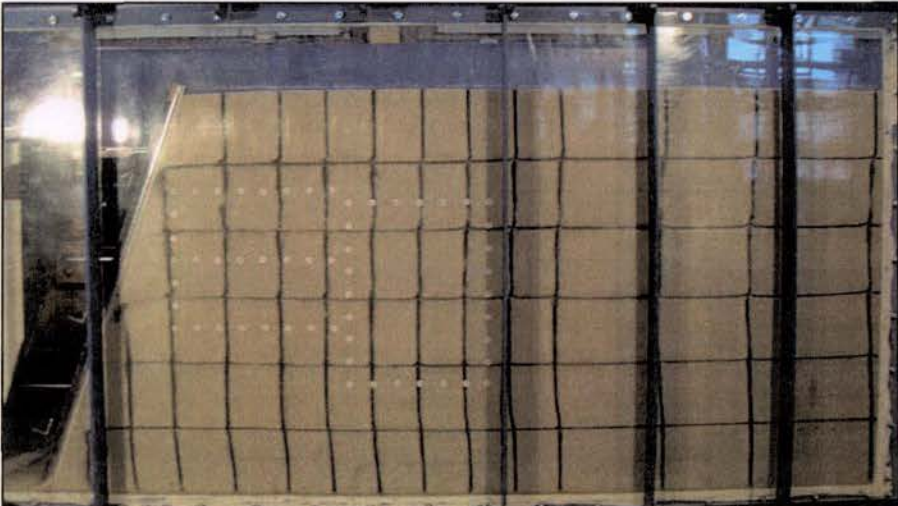


Figure C-29. Test-7 after 0.2g shaking step.

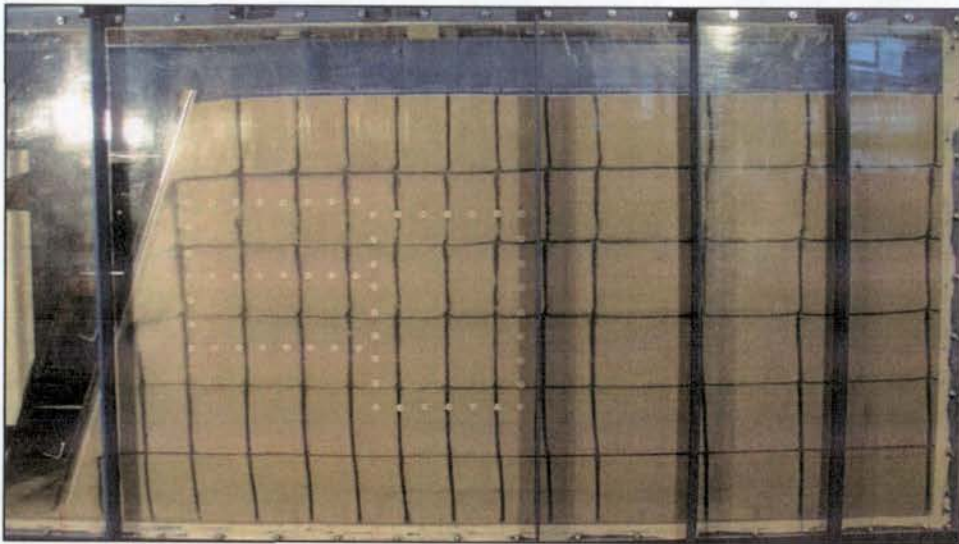


Figure C-30. Test-7 after 0.3g shaking step.

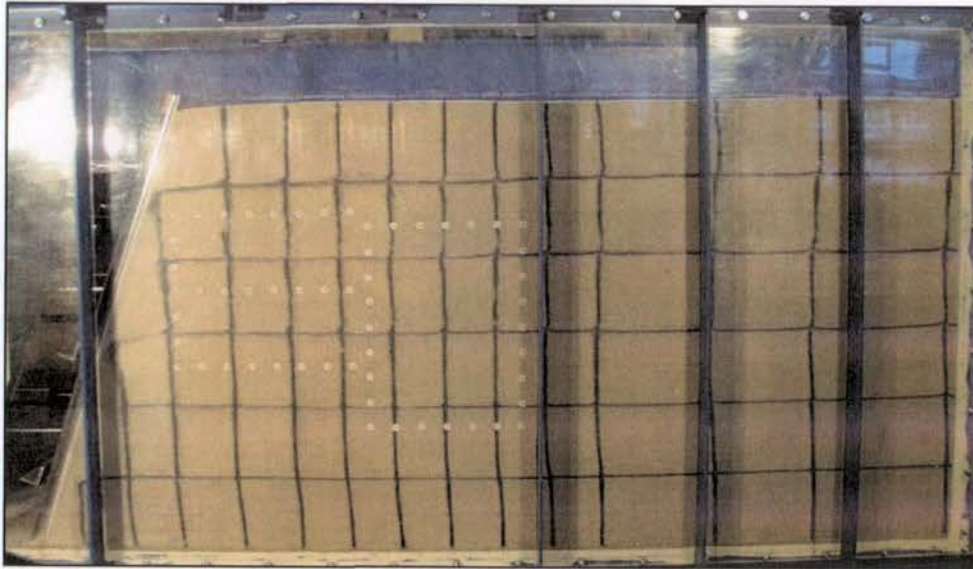


Figure C-31. Test-7 after 0.4g shaking step.

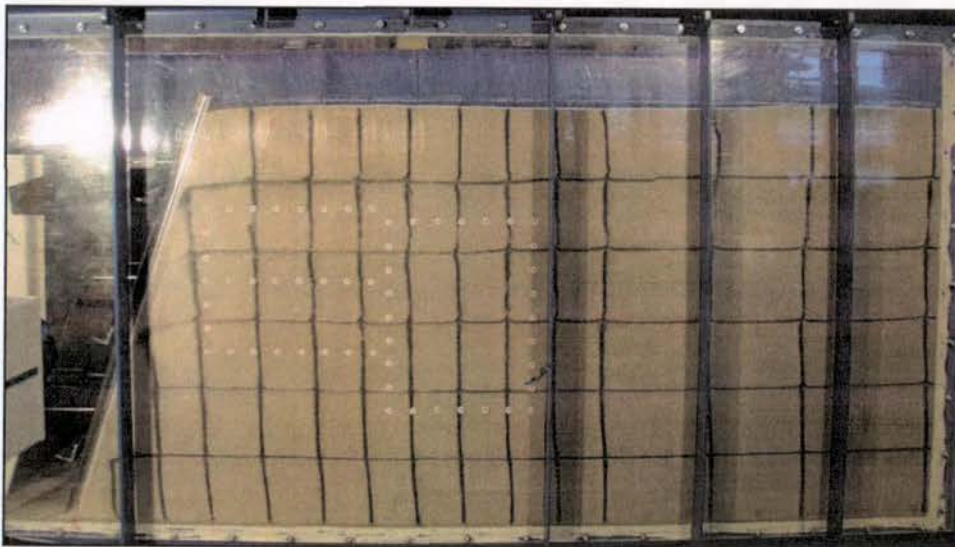


Figure C-32. Test-7 after 0.5g shaking step.

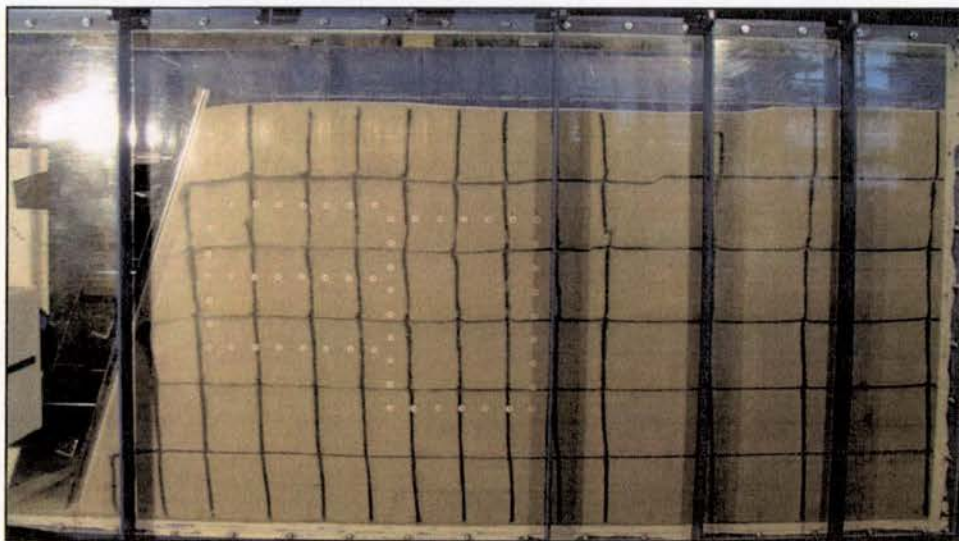


Figure C-33. Test-7 after 0.6g shaking step

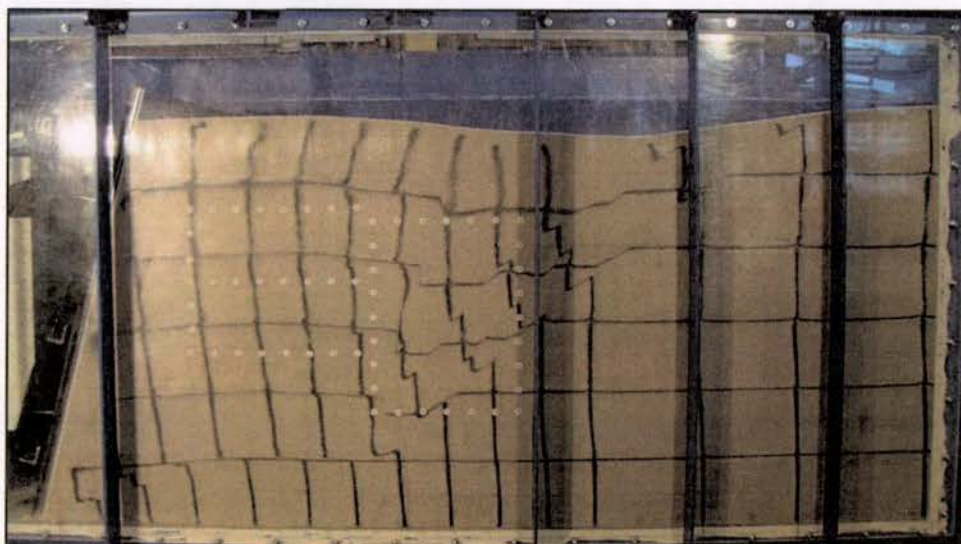


Figure C-34. Test-7 after 0.7g shaking step



## Contents

APPENDIX C	TESTING IMAGES	LXIX
C.1	Test-2 Testing Images.....	LXXI
C.2	Test-3 Testing Images.....	LXXIII
C.3	Test-4 Testing Images.....	LXXV
C.4	Test-5 Testing Images.....	LXXVIII
C.5	Test-6 Testing Images.....	LXXX
C.6	Test-7 Testing Images.....	LXXXI
Figure C-1.	Test-2 prior to testing	LXXI
Figure C-2.	Test-2 after 0.3g shaking (first step to reduce sand leakage).	LXXI
Figure C-3.	Test-2 after 0.4g shaking.	LXXI
Figure C-4.	Test-2 after 0.5g shaking.	LXXII
Figure C-5.	Test-2 prior to testing	LXXIII
Figure C-6.	Test-3 after first shaking step of 0.6g, at 10Hz (due to experimental error).	LXXIII
Figure C-7.	Test-3 after 0.4g, 5 Hz shaking step (standard testing protocol resumed).	LXXIII
Figure C-8.	Test-3 after 0.5g shaking step.	LXXIV

Figure C-9. Test-3 after 0.6g shaking step.	LXXIV
Figure C-10. Test-3 after 0.7g shaking step.	LXXIV
Figure C-11. Test-4 prior to testing	LXXV
Figure C-12. Test-4 after 0.1g shaking step.	LXXV
Figure C-13. Test-4 after 0.2g shaking step.	LXXV
Figure C-14. Test-4 after 0.3g shaking step.	LXXVI
Figure C-15. Test-4 after 0.4g shaking step.	LXXVI
Figure C-16. Test-4 after 0.5g shaking step.	LXXVI
Figure C-17. Test-4 after 0.6g shaking step.	LXXVII
Figure C-18. Test-4 after 0.65g shaking step.	LXXVII
Figure C-19. Test-5 prior to testing.	LXXVIII
Figure C-20. Test-5 after 0.1g shaking step.	LXXVIII
Figure C-21. . Test-5 after 0.2g shaking step	LXXVIII
Figure C-22. Test-5 after 0.3g shaking step	LXXIX
Figure C-23. Test-5 after 0.4g shaking step	LXXIX
Figure C-24. Test-5 after 0.5g shaking step	LXXIX
Figure C-25. Test-5 after 0.6g shaking step	LXXX
Figure C-26. Test-5 after 0.7g shaking step	LXXX
Figure C-27. Test-7 prior to testing.	LXXXI
Figure C-28. Test-7 after 0.1g shaking step.	LXXXI
Figure C-29. Test-7 after 0.2g shaking step.	LXXXI

Figure C-30. Test-7 after 0.3g shaking step.	LXXXII
Figure C-31. Test-7 after 0.4g shaking step.	LXXXII
Figure C-32. Test-7 after 0.5g shaking step.	LXXXII
Figure C-33. Test-7 after 0.6g shaking step	LXXXIII
Figure C-34. Test-7 after 0.7g shaking step	LXXXIII

**APPENDIX D**

**GEOPIV PLOTS OF MAXIMUM SHEAR STRAIN**



## D.1 Test-6 Residual Maximum Shear Strain

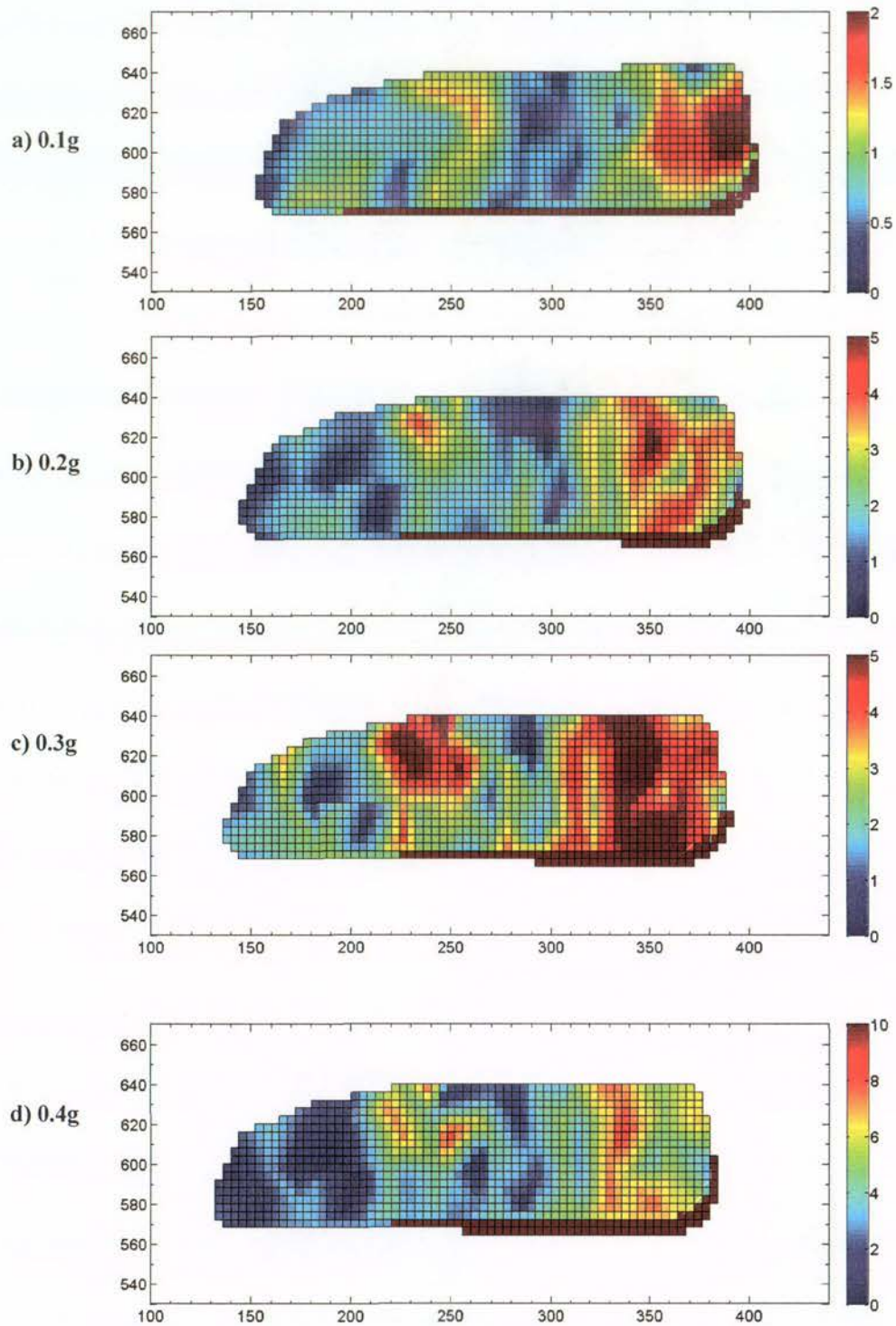
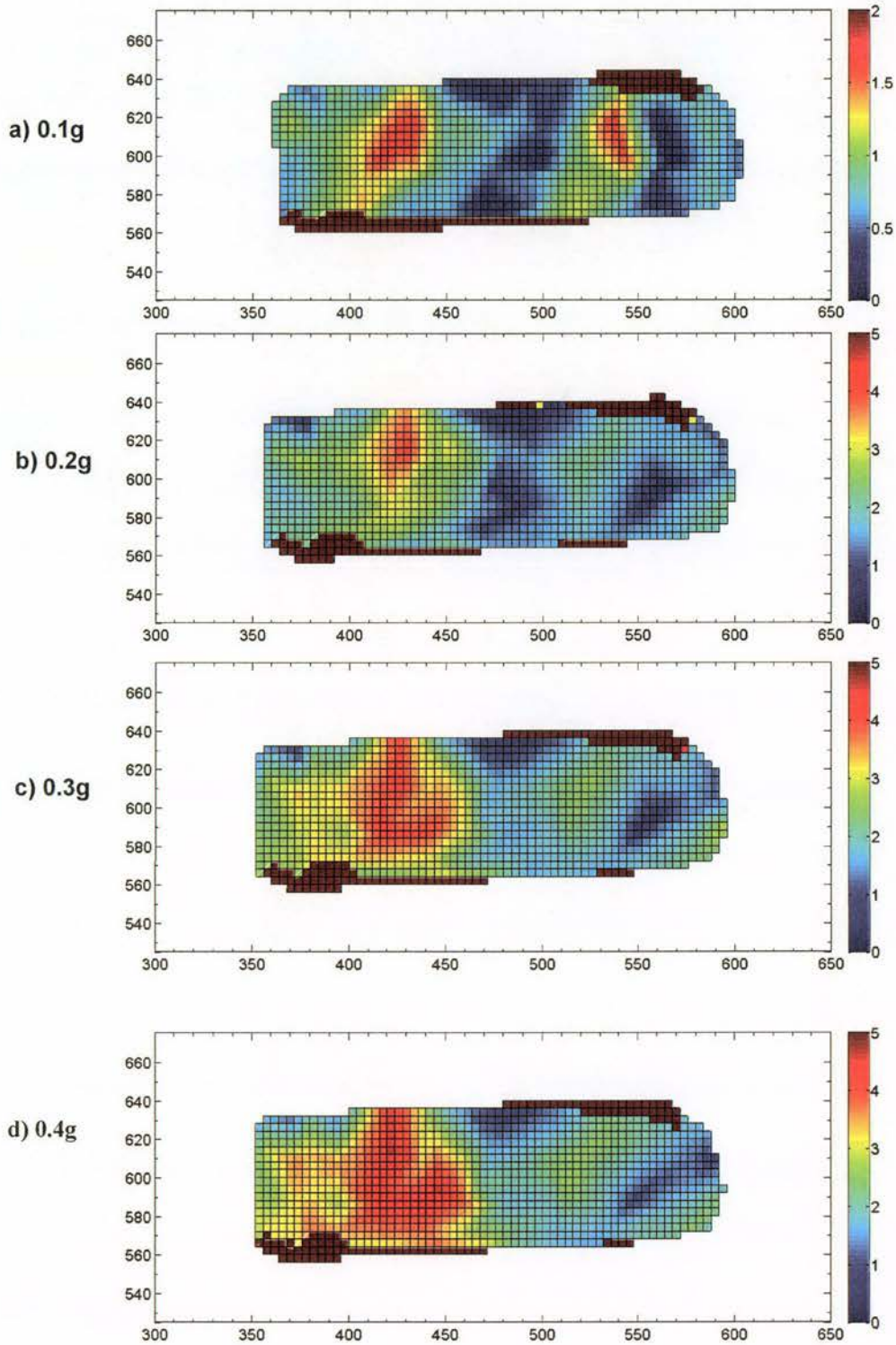


Figure D-1. Maximum shear strain within the reinforced soil region for Test-6, vertical wall reinforced at  $L/H = 0.6$ , by shaking steps: a) 0.1g, b) 0.2g, c) 0.3g, d) 0.4g.

## D.2 Test-5 Residual Maximum Shear Strain



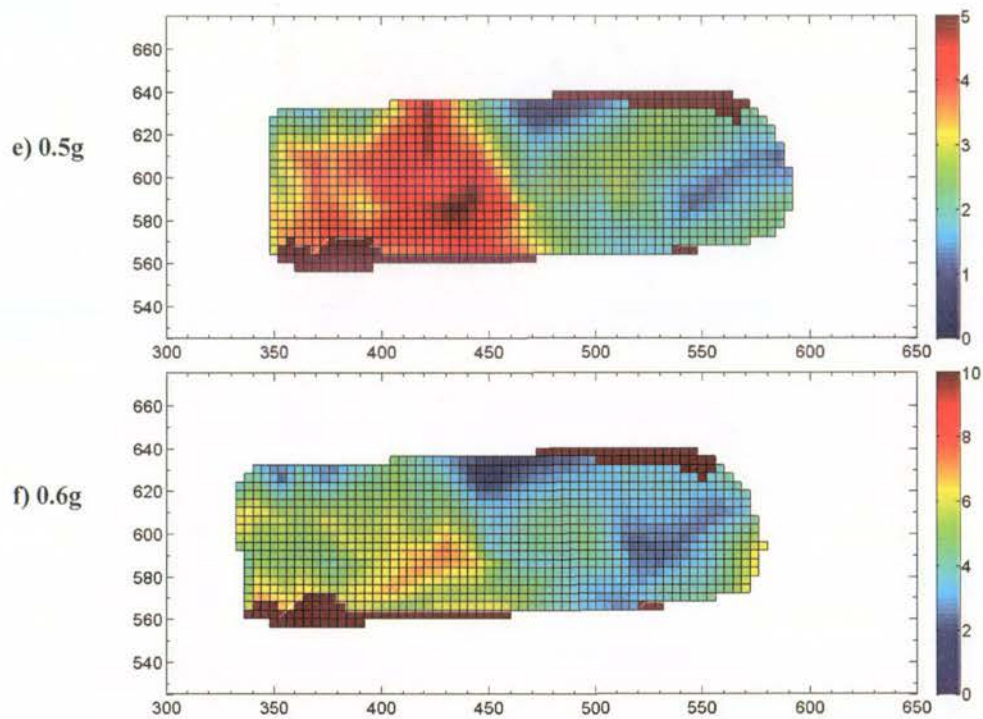
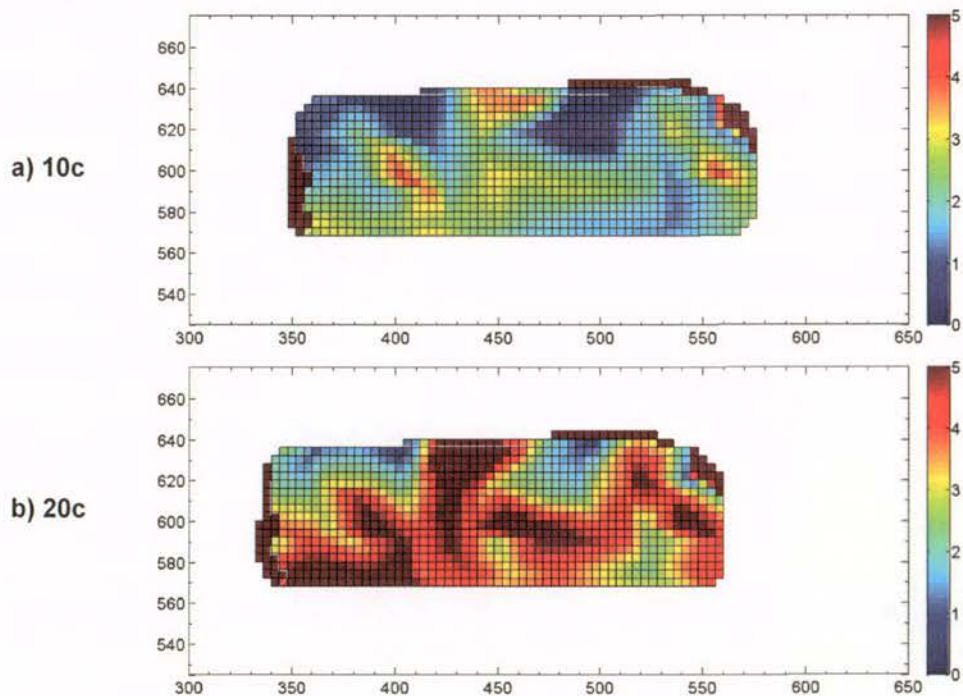


Figure D-2. Maximum shear strain within the reinforced soil region for Test-5, vertical wall reinforced at  $L/H = 0.9$ , by shaking steps: a) 0.1g, b) 0.2g, c) 0.3g, d) 0.4g, e) 0.5g, and f) 0.6g.

### D.3 Test-5 Maximum Shear Strain developed during 0.7g shaking step



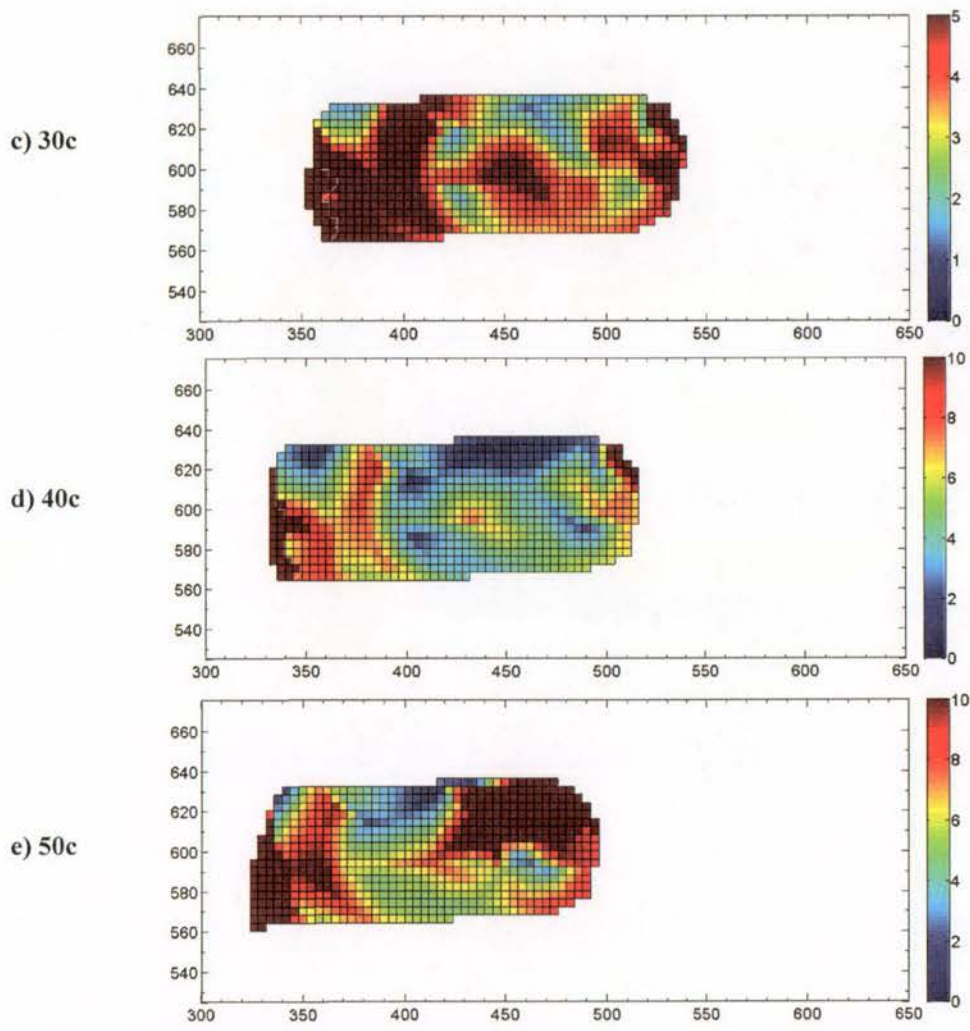
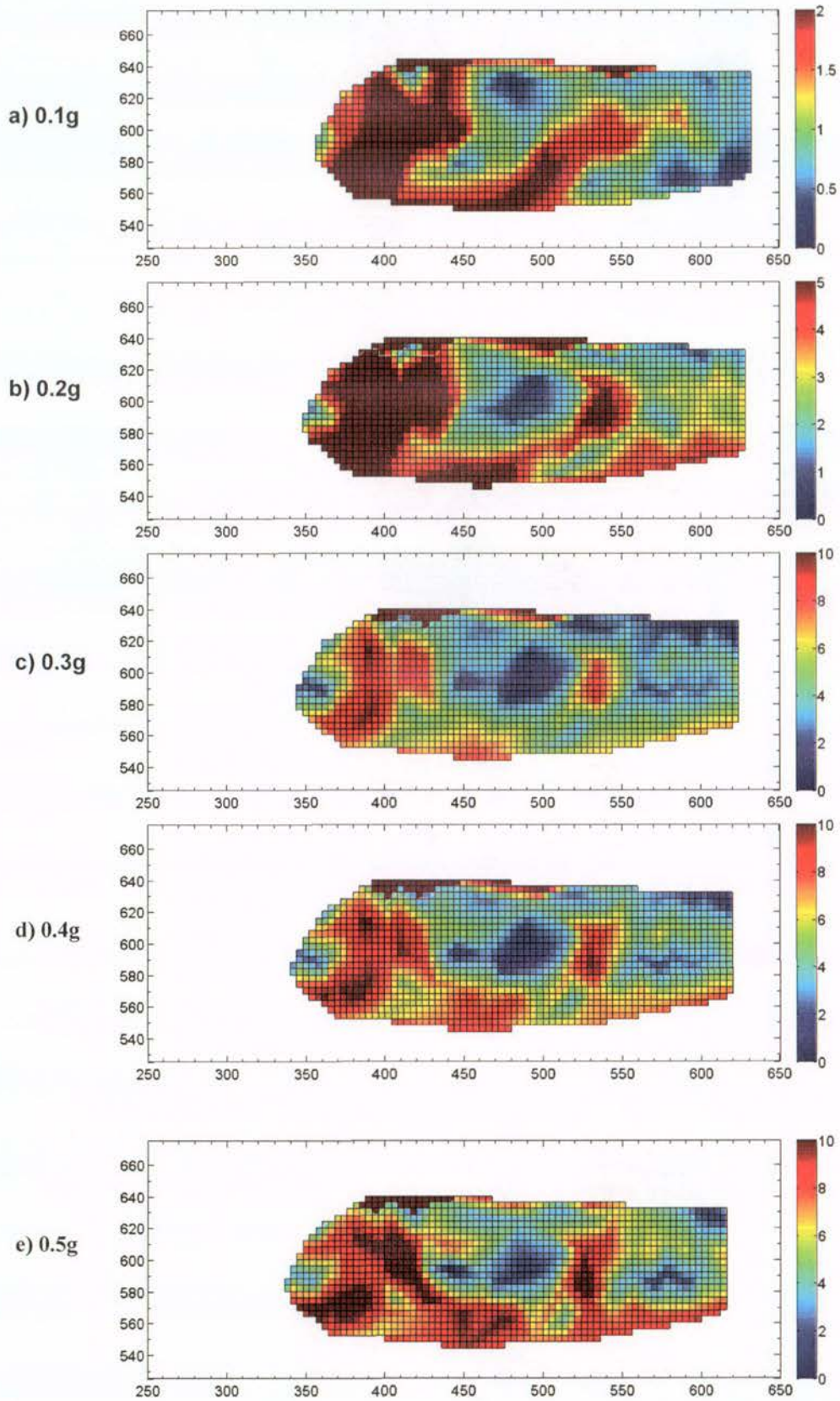


Figure D-3. Development of maximum shear strain within the reinforced soil region during 0.7g shaking step for Test-5, vertical wall reinforced at  $L/H = 0.9$ . Strains accumulated from the end of 0.6g shaking step to: a) 10 cycles (c), b) 20 cycles, c) 30 cycles, d) 40 cycles, and e) 50 cycles.

## D.4 Test-7 Residual Maximum Shear Strain



XCI

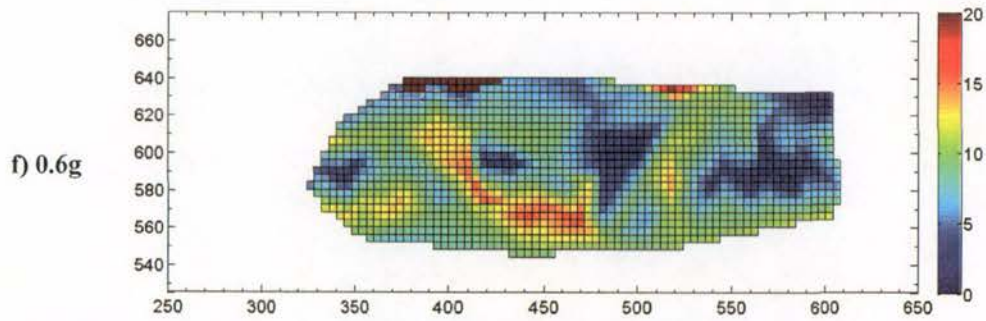
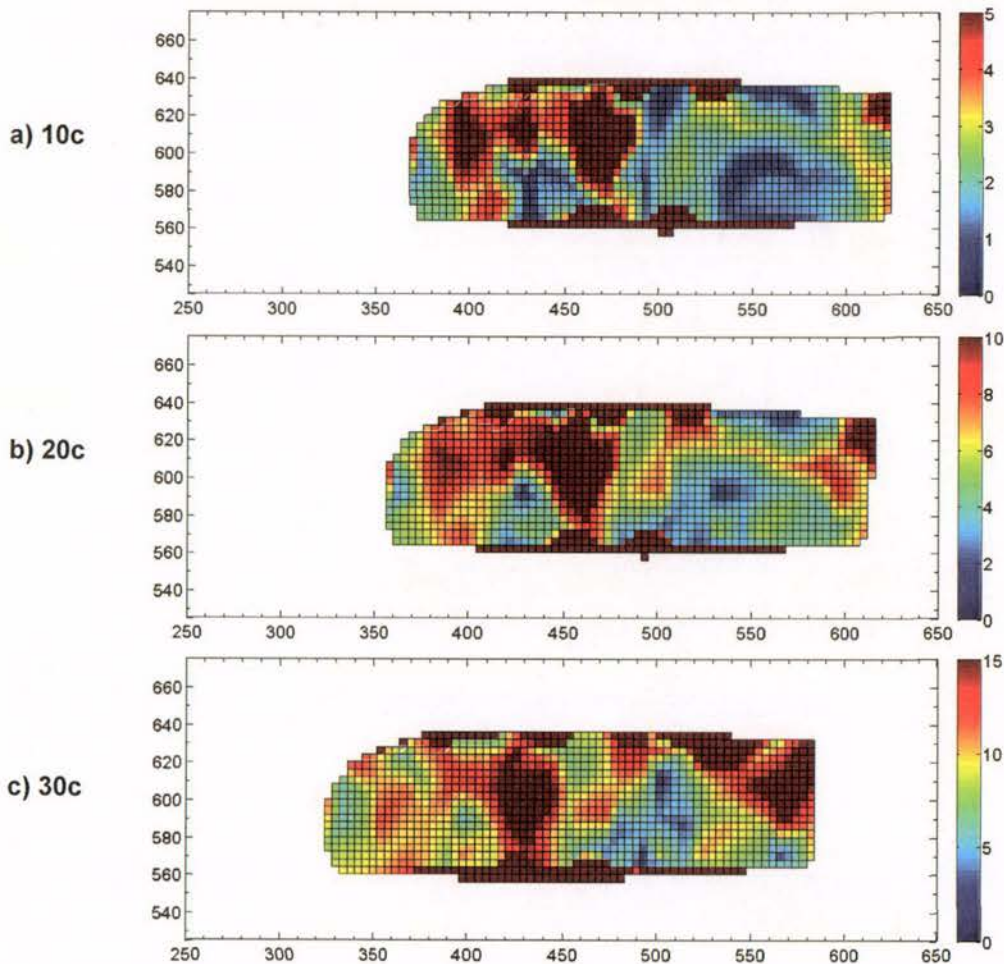


Figure D-4. Maximum shear strain within the reinforced soil region for Test-7, wall reinforced at  $L/H = 0.9$  and inclined at  $70^\circ$  to the horizontal, by shaking steps: a) 0.1g, b) 0.2g, c) 0.3g, d) 0.4g, e) 0.5g, and f) 0.6g.

### D.5 Test-7 Maximum Shear Strain developed during 0.7g shaking step



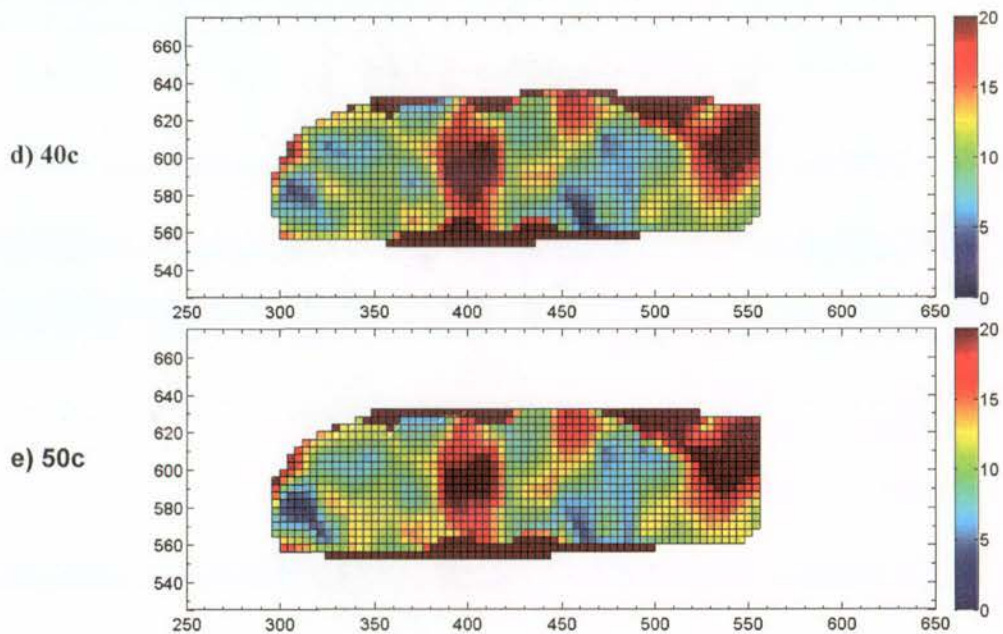


Figure D-5. Development of maximum shear strain within the reinforced soil region during 0.7g shaking step for Test-7, wall inclined at  $70^\circ$  to the horizontal and reinforced  $L/H = 0.75$ . Strains accumulated from the end of 0.6g shaking step to: a) 10 cycles (c), b) 20 cycles, c) 30 cycles, d) 40 cycles, and e) 50 cycles.